Broadband Submillimeter Instrumentation for the Detection of Distant Galaxies

Thesis by

Dominic James Benford

In Partial Fulfillment of the Requirements

for the Degree of

Doctor of Philosophy

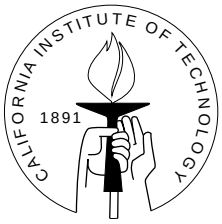

California Institute of Technology

Pasadena, California

1999

(Submitted February 5, 1999)

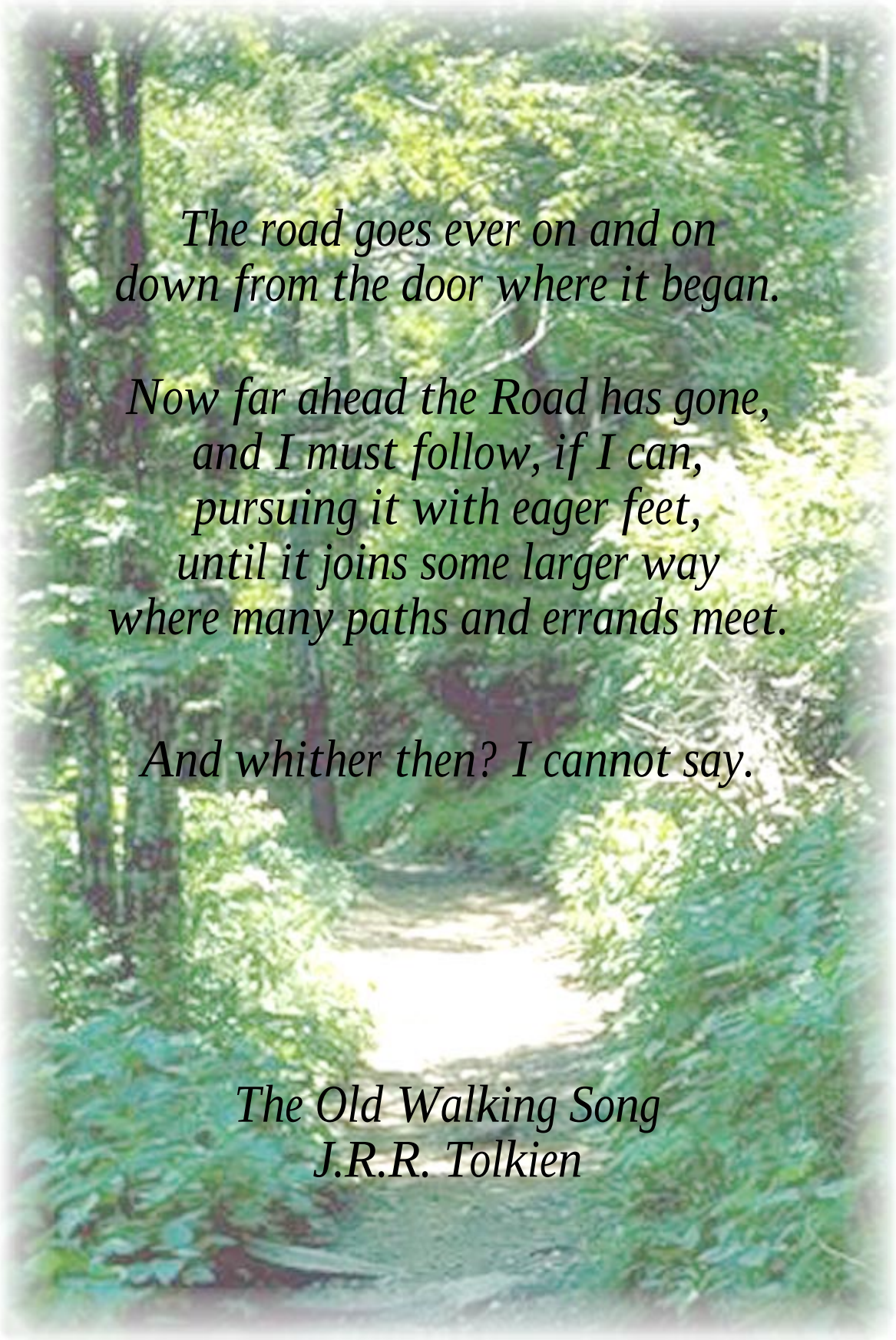

The road goes ever on and on
down from the door where it began.

Now far ahead the Road has gone,
and I must follow, if I can,
pursuing it with eager feet,
until it joins some larger way
where many paths and errands meet.

And whither then? I cannot say.

The Old Walking Song
J.R.R. Tolkien

Acknowledgements

This thesis is dedicated to Trudi.

Without her, I might never have done any of this, and I certainly would have had trouble getting through it. She was my inspiration in the morning, the resuscitation in the afternoon, and the drive in the evening. The work embodied herein is as much hers as it is mine. ♡ ♩

Special thanks go to Todd R. Hunter† ("Gravity is down to point eight!"), who taught me immeasurable amounts of astronomy, and with whom I spent some of the best times at Caltech. Further thanks are due to Robert A. Knop† ("Steege! Put gravity on automatic!"), who imparted knowledge of computers and without whom I would have had much less pizza, Star Trek, frisbee golf, and humor in my time here. Still more thanks are due to Tom Phillips (my advisor, in case anybody reading this isn't in the know): he provided me with plenty of opportunities, just the right amount of nudging in directions to keep me going, wry British humor which I haven't had since I left Lafayette, and the good sense and kindness to wind me up and let me go.

Other people who were important to me in a great variety of ways: Alycia Weinberger (thank goodness you & Todd Rosentover† finally moved to within a parsec of each other!), Gene "Navel Lint" Serabyn, Pat Schaffer† ("built like a brick shithouse - that's as good as it gets!"), Gerry & Marcia Neugebauer, Taco (Raoul Taco-Slime Naamgozaar Abu Zalaam Machilvich Harbor Young), Anthony "Tuer Porcus" Schinckel, Tom "Red Baron" Murphy, Ning Wang, André Clapp, James "Licence to Reduce" Larkin, Jason "Trapped in IRAF Hell" Surace & Atiya Hakeem the simianologist, Jacob "van Gogh" Kooi, Keith "the Wizard" Matthews, Lee "Sphincter Boy" Armus the Skin of Evil, Tom Soifer (*at the bat*) and his athletic family, Doug Warden† of the VRWC, Jonas Zmuidzinas, Jocelyn Keene, Mike Gaidis, Mei Bin, Todd "Minesweeper God" Groesbeck, Rob Schoelkopf, Darek "stuntdriver" Lis, John

†Member, Vast Right-Wing Conspiracy

Ward† (the führer of Unix), Darren Dowell, Jeff Groseth†, Jon Kawamura, Matt the mëtalhead, Shimpei the Linux guru, Attila the Hungarian. Without Susan, Rena, Diana, Margie, Lydia, and Dheera, I would have been terribly disorganized and would have probably died from lack of *sympathique* contact at work. François Pajot, Cyrille Rioux and Bruno Maffei are to be thanked for their hard work in a faraway land to bring an instrument to Caltech a few months before my defense. A multitude of nights with my co-observers made all the oxygen-starved hours worthwhile, especially with Pierre Cox, Min-Su Yun, Sangeeta Malhotra, Casey Lisse, Jean Turner, & David Meier. Without the Hawai′i crew, I would never have gotten any data whatsoever: Martin Houde, Richard Chamberlin, Allen, Mac, Pat, and of course the three Roys (Steve, Toby "State Penn?", and Po the Hash-man).

At GSFC, S. Harvey Moseley provided the support, opportunities, and moments of wisdom that helped inspire me to better things. Christine A. Allen deserves more thanks than she'll ever receive for her tireless efforts to fabricate state-of-the-art micromachined devices. Tim Powers and Ernie Buchanan gave me help in the lab, interesting stories about horrible winters ("It was... minus 95 degrees, with 60 mph winds... the copper cables were shattering from the cold...") and the true pessimist's view of life.

I'd never have gotten through my homework without Stephen Ouelette, Mike Pahre, Luisa DeAntonio, Adam Leibovich, David Hogg & others. Instrumental theses have physical foundations; mine were laid by the machinists Marty "Zen" Gould, Ricardo Paniagua, Richard Borup, and Terry/Armando/Phil/Dave/Fernando/etc. Electronics would have taken forever for SHARC and the spectrometer were it not for the dedication of Ben "Blacker Armored Division" Smith.

Thanks to: Led Zeppelin, Metallica, Alice in Chains, Marilyn Manson ($\begin{smallmatrix}we\ hate\ love\\we\ love\ hate\end{smallmatrix}$), Adam & Dr. Drew, Mark & Brian, Kevin & Bean ($\begin{smallmatrix}\text{No! Lots of serial killers had cows!}\\\text{Manson had a Holstein!}\end{smallmatrix}$), Bill Handel, Mr. KFI, Bill & Ted ($\begin{smallmatrix}\text{Be ... excellent to each other.}\\\text{Party on, dudes!}\end{smallmatrix}$), KNAC (`www.knaclive.com`), Dr. Pepper, Earl Grey, Hawaiian Sun, Astérix, Tintin, Phil Foglio, Scott Douglas, Elizabeth Peters, Tom Clancy†, Ayn Rand, the DNRC, Jĭhâd Ågā͡ĩñst Stàrbüçks, and Steeges Worldwide.

For friends and family: Judy's wry humor; John's consistency; Yetta's sense of perspective; Steve & Vicki's optimism; Sue & Walt's realism; Johnathan's perseverance; Julie & Dave's solidness; Julie & David's Bohemian-ness; Charlotte and Emily's affection.

Last, but certainly not least, of my helpers are those who provided support during my whole life. To Gran and Granddad for their support over the years. To Vanessa, for being perhaps the most mainstream person on this list and providing a reference for life in the real world. To Greg[†], because of his enthusiasm for the novel. To Joan, because she exhibited more strength than I could imagine. To Mom and Dad, whose support, teaching and nurturing made me the kind of person who could achieve this... I love you both.

Finally, the serious stuff... Much of this work has been funded by NSF contract #AST 9615025 which provides support for the Caltech Submillimeter Observatory. The studies of the immersion grating spectrometer were funded by NASA contract #NAG5-4196. The development of the CO Fabry-Perot filter relied upon Gene Serabyn's NASA grant #NAG5-4200 for the study of planetary atmospheres. Developing the Fabry-Perot spectrometer drew from many funding sources, including the IAS collaborators' funding and a Caltech President's Grant. During the majority of my thesis work, I was partially supported by a NASA Graduate Student Fellowship through NASA's Goddard Space Flight Center and Harvey Moseley.

Abstract

This research details my efforts to search the universe for the faint far-infrared emission of galaxies as far away as possible. I first describe the design, construction, use, and performance evaluation of the Submillimeter High Angular Resolution Camera (SHARC), a 24-element bolometer camera for imaging at 350μm and 450μm from the Caltech Submillimeter Observatory (CSO). This instrument achieves background-limited performance and has been available for use by the international community since 1996.

In the following two chapters, I detail the astronomical results attained with this instrument when used to observe the thermal dust emission from a sample of nearby galaxies (chapter 3) and a sample of sources as distant as 90% of the way across the spacetime universe (chapter 4). The nearby sample is well-characterized by a single-component greybody dust emission model with a temperature of 37 ± 4K and a spectral emissivity index of $\beta = 1.7 \pm 0.4$. Our cosmologically distant sample provides the first systematic study of these objects at wavelengths probing near the emission peak at a rest-frame wavelength of $\sim 80\mu$m. We find an average temperature of 53 ± 8K and determine a median luminosity of $(2 \pm 1) \times 10^{13}\, L_\odot$ and a median dust mass of $(3 \pm 2) \times 10^8\, M_\odot$. This makes these objects some of the most massive and luminous ever observed, with an inferred star formation rate of 2000 $M_\odot$ per year.

To balance the continuum emission results described above, I have observed both local and high-redshift galaxies with the CSO facility heterodyne receivers in an effort to detect the emission lines of CO, CII, and NII. We have observed a sample of 22 nearby ($0.02 \leq z \leq 0.13$) ultraluminous infrared galaxies in the $J = 2 \rightarrow 1$ and $J = 3 \rightarrow 2$ transitions of CO. Using published $1 \rightarrow 0$ intensities, we find that the $3 \rightarrow 2$ emission most likely arises from an optically thick region, implying that future observations in the higher-J lines can be used to constrain the temperature of the molecular gas in these galaxies. We find a most likely temperature in the range

$20 \leq T \leq 60$K and a molecular gas density of $n_(H_2) \approx 1500$ cm^{-3}. At high redshifts ($z > 2$), however, most of our observations have resulted in nondetections, but not without merit. The emission in the NII 205μm line from the Cloverleaf quasar is found to be below the amount predicted for a galaxy similar to M82. For two $z > 4$ quasars, our upper limits to the CII 158μm line emission show that the ratio of the line luminosity to the total luminosity is less than 0.01%, ten times smaller than has been observed locally.

Finally, I shall detail our effort to design a novel submillimeter spectrometer using a linear bolometer array as a detector element and relying on Fabry-Perot or immersed grating optics to provide the spectral dispersion. This approach promises to provide bandwidths several times larger than are available with existing heterodyne spectrometers, making the detection of cosmologically distant galaxies in their submillimeter line emission a reality.

Contents

List of Figures

List of Tables

Chapter 1 Introduction:

The Far-Infrared Emission from Primæval Galaxies

1.1

In the beginning, there was light (James 1611; Weinberg 1977). The universe was photon-dominated for the first 700,000 years, until the era of recombination, when ions combined to form neutral atoms and the last light left over from the Big Bang was released to travel through the rapidly expanding universe. The light was red-colored visible radiation with a wavelength of about 1μm, corresponding to a temperature of 3,000 K[1]. Since this time, as the universe has expanded and cooled, so has the radiation, until today this "Cosmic Microwave Background Radiation" (CMBR) is found to have a wavelength of about 1mm (3K, Penzias & Wilson 1965). This was an early indicator that observations at millimeter and submillimeter wavelengths are key in our efforts to understand the high-redshift universe.

Much of our knowledge about this early time comes from the results of the Cosmic Background Explorer (COBE) satellite, launched by NASA in 1989. In particular, the Far Infrared Absolute Spectrophotometer (FIRAS) experiment proved that the CMBR has a thermal spectrum[2] with a temperature of 2.735K (Mather et al. (1990); Figure 1.1). Also, the Differential Microwave Radiometer (DMR) demonstrated that there were fundamental fluctuations (anisotropies) in the CMBR, outlining the exis-

[1] Our Sun has a surface temperature of about 5500 Kelvin, which yields a peak wavelength of roughly 0.5μm, which is green light. 1μm peaks slightly to the long wavelength side of red light.

[2] A *thermal spectrum* is the spectrum radiated by a perfectly emissive (black) object; we are all familiar with this kind of radiation from hot objects such as the sun or the element of an electric range stove.

tence of structures in the universe when it was less than a million years old (Smoot et al. (1992); Figure 1.2).

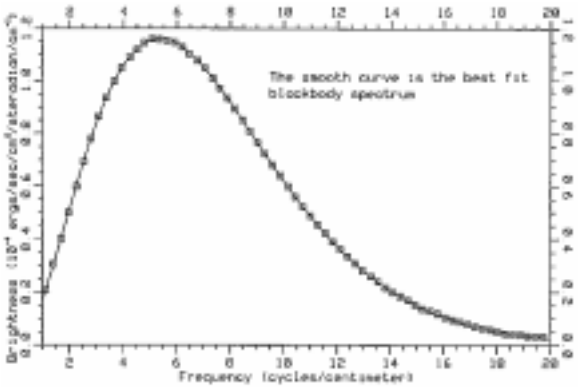

Figure 1.1 Best-fit blackbody spectrum to the CMBR, as measured by the FIRAS instrument on COBE.

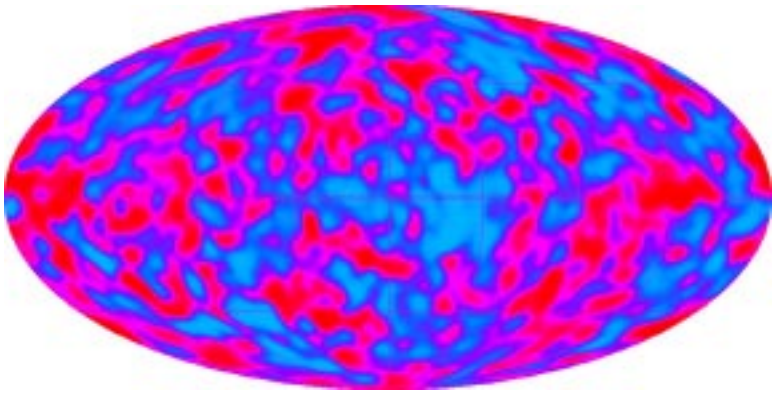

Figure 1.2 Fluctuations in the CMBR at roughly one part per 100,000 as measured by the DMR instrument on COBE. The objects in this map are galaxy superclusters.

Our next information about the universe's evolution is probably best illustrated by the Hubble Deep Field (HDF–Williams et al. (1996); Figure 1.3), which contains images of galaxies from when the universe was already a billion years old. What happened during that first billion years? At what epoch did the relatively smooth, gargantuan structures seen by COBE develop into the finely structured universe evident in the HDF? Also, when did the first stars - those whose light is seen in the HDF - form?

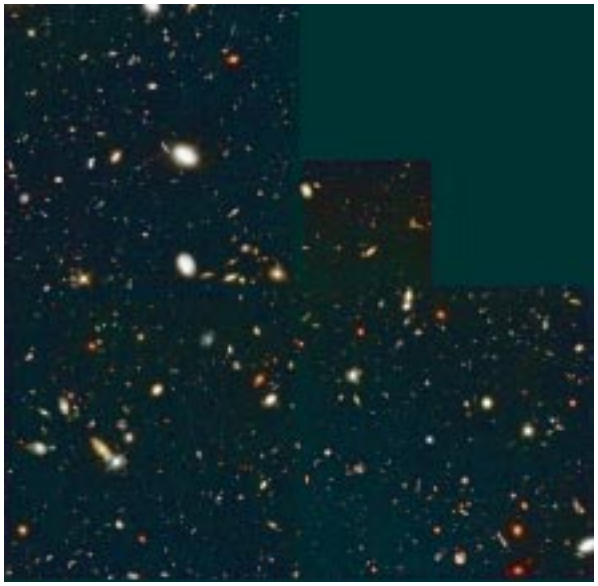

Figure 1.3 Deep image of the distant universe, made by the WFPC/2 instrument on the Hubble Space Telescope. These objects are individual galaxies.

1.1.1 The Formation of Galaxies at High Redshift

Spectacular advances in our knowledge of galaxy formation have been realized through observations with the Hubble Space Telescope and the new large, ground-based Keck observatories. However, all these observations were made at optical and near-infrared wavelengths. This provides us with an only partial view of galaxy evolution: some fraction of star formation is hidden by dust obscuration, which absorbs the rest-frame UV and visible radiation and reradiates it in the mid- to far-infrared. It is known in the local universe that about one-third of the total bolometric luminosity of galaxies is emitted in the far-infrared (Soifer & Neugebauer 1991). This "optically dark" side of galaxy evolution was studied primarily by the IRAS[3] satellite, which probed galaxy evolution as far as a redshift[4] of $z \sim 0.2$ (Ashby et al. 1996). When compared to the HDF, which detected objects to $z \sim 5$, it is apparent that much remains to be done to improve our understanding of the evolution of galaxies as traced by far-infrared emission.

[3]IRAS (Neugebauer et al. 1984) was a 57cm telescope with detectors at 12, 25, 60 and 100μm, which conducted an all-sky survey in 1983.

[4]A *redshift*, z, is the amount by which the wavelength λ of light is shifted redward due to the expansion of the Universe: $z = \frac{\lambda_{\rm observed} - \lambda_{\rm emitted}}{\lambda_{\rm emitted}}$. (See, e.g., Weinberg (1972).)

Theoretical arguments based on galaxy formation and evolution models have predicted a substantial amount of far-infrared radiation[5] from cosmologically distant source since at least the work of Partridge & Peebles (1967). Perhaps the first truly comprehensive work on this subject appeared in Bond, Carr & Hogan (1986). It is increasingly the case that models of the integrated[6] emission from very distant protogalaxies (those forming their first generation of stars) yield very strong emission at wavelengths between 1μm and 1 mm[7] For technical reasons, workers in this broad region of wavelengths have been relatively late to develop the kind of instrumentation necessary to detect this integrated light. The most definitive results to date are the measurements made by COBE of the integrated light of distant galaxies. For a proper historical perspective (where history is defined as the last decade), one should first discuss the negative results of protogalaxy searches in the optical.

1.1.2 Searches for Primæval Galaxies

I shall take as an Ansatz that a *protogalaxy* is a galaxy seen during its phase of maximum star-formation-derived luminosity. While this may at first blush seem like a purely pragmatic definition, it has a physical basis: the act of forming the first generation of stars during an initial gravitational collapse (possibly due to merging and coalescing) must release a large amount of energy. Most of this energy is likely to be from the burning of hydrogen to helium in the first massive stars, which dominate the luminosity (Djorgovski & Weir 1990). We can then stipulate properties of such an object (e.g., Pritchet 1994): a spectrum consistent with star formation, large luminosity, a redshift of formation of roughly $2 \lesssim z \lesssim 5$, and a compact (but possibly clumpy) nucleus of star formation activity. A quick survey of the literature will show that several objects can be found which satisfy one or more of these criteria, perhaps

[5]The *far-infrared* region of the electromagnetic spectrum is roughly light with a wavelength of 20μm to 200μm, while the mid-infrared is roughly 2μm to 20μm and the submillimeter from 100μm to 1 mm.

[6]Here, integrated refers to summing the light over the whole sky, so that individual sources are not resolved but the average properties are derived.

[7]In a kind of inverse Olber's Paradox, the darkness of the night sky at optical and radio wavelengths (with the exception of the CMBR) has forced theories to predict brightness of the night sky at wavelengths between them.

(in the case of quasars) even all of them. The problem with our current expectations is in one more property: the number of protogalaxies we anticipate. With billions of galaxies in the universe, there must be a surface density[8] of protogalaxies of order a few per square arcminute (Baron & White 1987). Of course, this depends on the merger history of the universe and the mean redshift and lifetime of the protogalactic phase, but more sophisticated calculations also yield a surface density of ~ 10 per arcmin^2 (Djorgovski 1992). At this surface density and the expected brightness (roughly 3×10^{-15}erg cm^{-2} s^{-1}, for a luminosity of 3×10^{43}erg s^{-1} $\sim 10^{10}\, L_\odot$[9], there are fewer than ~ 0.1 sources per arcmin^2 (Pahre & Djorgovski 1995) - one hundredth of what is expected! The question is thus: where are the protogalaxies?

In an attempt to answer this question, several surveys have been conducted in the past decade (see, e.g., the review article of Pritchet (1994) and references therein). The first surveys were broadband surveys aimed at detecting the continuum emission from starlight from the early stars. Efforts along these lines have typically yielded detections of fainter, more local objects than the desired protogalaxies. The most common method of recent surveys has been a narrowband search for emission lines. Of such searches, narrow-band imaging (using some filter such as a Fabry-Perot to restrict the search to a small redshift range) of Ly α[10] or another bright line has proved the most used method, reaching very faint levels over large areas. An increase in the redshift coverage can be achieved by slitless or long-slit spectroscopy, but only at the price of sensitivity or areal coverage. So far, the result of each of these surveys is the same: no protogalaxies have been seen. When compared to the models, the observations are more sensitive than should be necessary by more than two orders of magnitude in surface density and one order of magnitude in luminosity.

What, then, could be done to resolve this quandary? There is the possibility that quasars are associated with protogalaxies. One can explain this association by hypothesizing that quasars harbor an AGN, driven by a merger, which initiates

[8] *Surface density* is the number of objects per unit area on the sky.

[9] The solar luminosity is $L_\odot = 3.83 \times 10^{26}$ W.

[10] The recombination line of ionized hydrogen at 1216Å is called the Lyman-α line and is often the brightest line in galaxies.

star formation. However, this explanation does not provide enough protogalaxies. Perhaps dust absorption is significant even in very early galaxies, and the optical light is strongly absorbed. However, recent observations of Lyα at high redshifts (De Propris et al. (1993) and references therein) imply that some not insubstantial fraction of the starburst phase will be unobscured. One further possibility is that the protogalaxies coalesced in a clumpy manner on angular scales of a few arcseconds, which would be difficult to detect with standard techniques.

Recently, progress has been made by Steidel et al. (1996) and Madau et al. (1996) using the Lyman dropout technique. In this method, three-color images are used to try to estimate the redshift of galaxies by the location of the Lyman break (912Å rest frame wavelength). With a substantial number of detections of galaxies at $z \sim 3$, they are able to determine that there is a substantial population of galaxies with a star forming rate of perhaps as much as $10\,M_\odot\,\mathrm{yr}^{-1}$ [(11)]. While this level is still a factor of several (5-10) below that which would imply a rapid, single star formation epoch, it is a good start. However, the surface density is still too low. It would appear that finding the truly massive, luminous protogalaxies is not yet possible using optical and near-infrared surveys.

1.1.3 The Cosmological Far-Infrared Background

There have been substantial efforts made in the past decade towards detecting the background from cosmologically distant galaxies emitting in the near- to far-infrared. The IRAS satellite provided the survey of the local universe, yielding lower limits to the number of distant, dusty galaxies based on source counts in the 25-100μm bands. Theorists spent trillions of clock cycles on their workstations generating many models which fit the IRAS data and predicted varying amounts of emission in the far-infrared from the integrated light from high redshift galaxies (see, e.g., the review of Lonsdale (1996) and references therein).

Such arguments were justified by the detection of a far-infrared cosmic background

[11] The solar mass is $1\ M_\odot = 1.99 \times 10^{30}\,\mathrm{kg}$.

radiation (CIRB) made by Puget et al. (1996) using the data from the FIRAS instrument aboard COBE, making careful subtraction of the local backgrounds. The detected spectrum is shown in Figure 1.4 and shows the Rayleigh-Jeans part of a thermal spectrum. Verification of this detection by Fixsen et al. (1998), together with a detection of the CIRB at 3.5μm (Dwek & Arendt 1998) and limits in the mid-infrared (Hauser et al. 1998) have constrained the integrated spectrum of galaxies at cosmological distances. A recent survey of all the efforts has been encapsulated in Figure 1.5 from Hauser et al. (1998). It shows that the CIRB intensity peaks somewhere in the 10-100μm range, indicative of dust emission at temperatures of $\sim$ 100K. There has been a substantial effort to determine the characteristics of the galaxies giving rise to this background. Some recent results include the first detections of galaxies discovered by their far-infrared emission (e.g., Clements et al. 1998; Kawara et al. 1998; Smail, Ivison & Blain 1997). These galaxies, if comprised of the first generation of stars formed in a massive early starburst, could be the progenitors of the rogues gallery of galaxies around us. If we can learn about them, perhaps we can understand the process of galaxy formation and evolution from the era of first star formation to the present epoch.

1.2 Fingerprints of the Past

These detections of the CIRB, integrated over both space and frequency, are like a set of fingerprints left at the scene of a crime: an indication that there is something there, but not useful without careful interpretation and analysis. Providing some idea of the nature of the individual galaxies making up the CIRB is the realm of astronomer sleuths modeling the properties and number density of galaxies in a variety of ways. In this section, I present some of these methods and results from the literature. I further present my own, empirically-based model of the far-infrared emission from a prototype star-forming galaxy at high-redshift. Finally I shall discuss the considerations of observing this emission with current instrumentation.

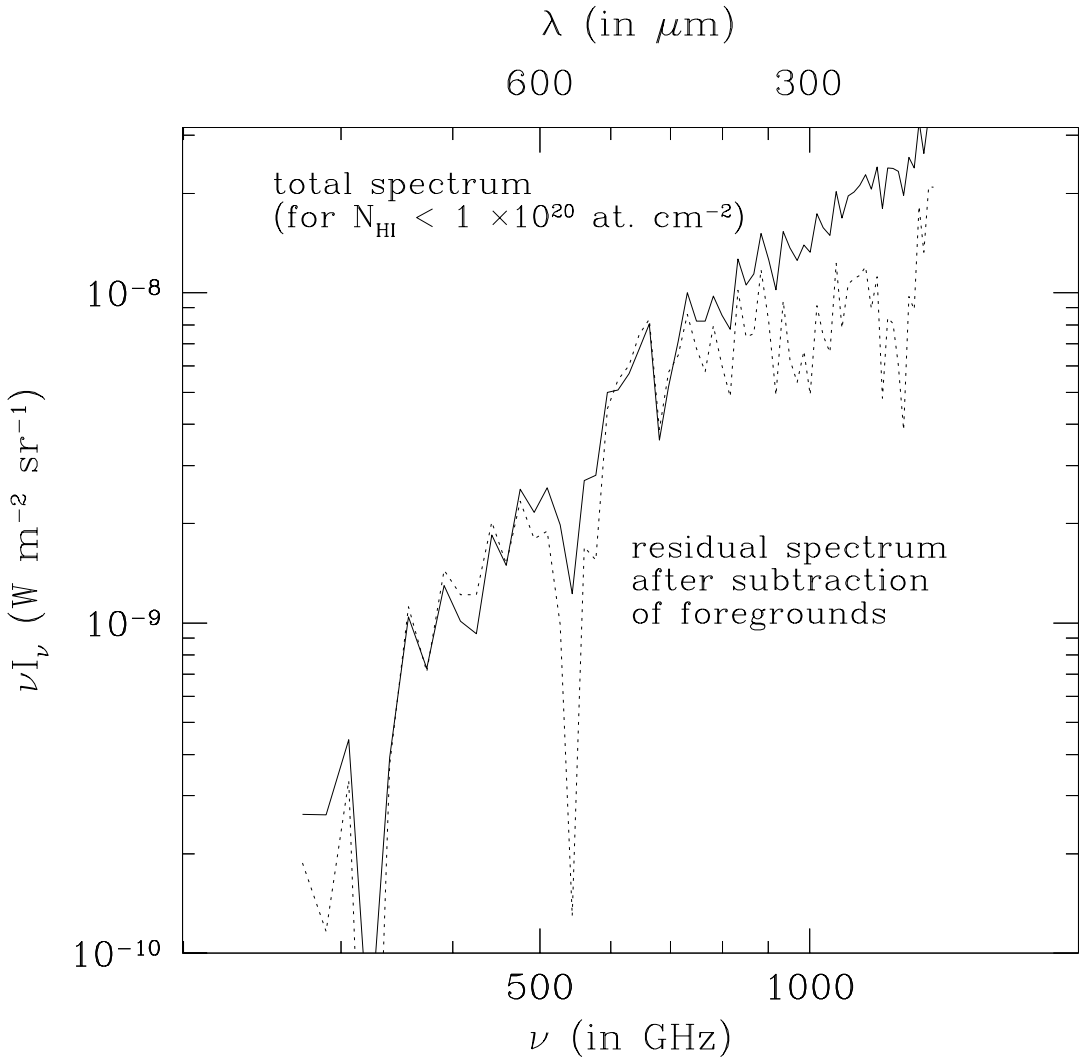

Figure 1.4 Detection of the Cosmological Far Infrared Background, as seen by Puget et al. (1996) and Fixsen et al. (1998).

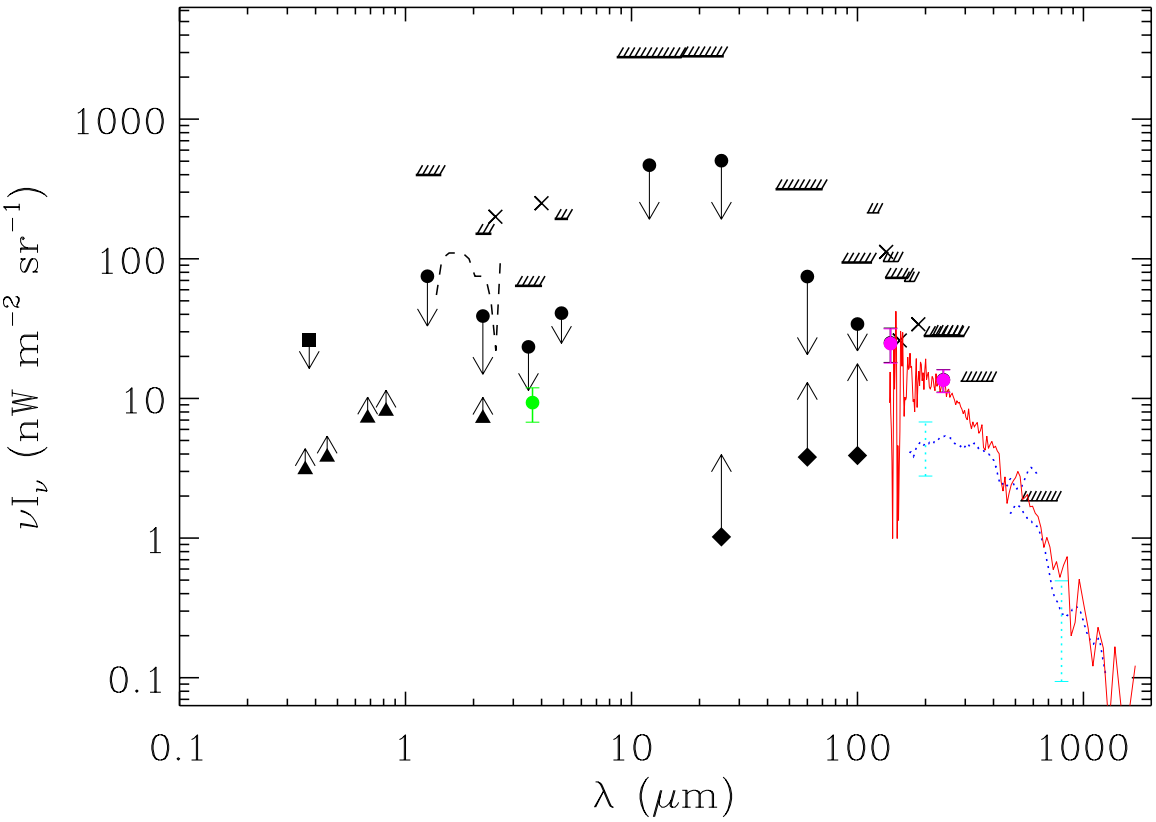

Figure 1.5 Cosmic background intensity I_ν times the observed frequency ν as a function of the observed wavelength λ, from Hauser et al. (1998). The circles with error bars are the detections based on DIRBE data after removal of foreground emission at 140 and 240 μm, while those with arrows are 2σ upper limits with the arrows extending to the measured residuals at $1.25 - 100$ μm. The hatched thick lines are dark sky limits (95% CL) from the DIRBE data at $1.25 - 240$ μm, while the hatched thin lines are dark sky "broadband" limits (95% CL) from FIRAS data at $120 - 650$ μm (Shafer et al. 1998). The crosses are upper limits derived from rocket experiments at $134 - 186$ μm (Kawada et al. 1994) and $2.5 - 4.0$ μm (Matsuura et al. 1994). The dashed line from $1.4 - 2.6$ μm is residual radiation after foreground removal from the rocket data of Noda et al. (1992). The diamonds with arrows are lower limits derived from *IRAS* counts at $25 - 100$ μm (Hacking & Soifer 1991); 60 μm limit from Gregorich et al. (1995). The dotted curve from $170 - 1260$ μm shows the tentative infrared background determined from FIRAS data by Puget et al. (1996), while the solid curve is the average of the two DIRBE-independent methods of FIRAS analysis used by Fixsen et al. (1998). The triangles are lower limits derived from the Hubble Deep Field at $3600 - 8100$ Å (Pozzetti et al. 1998) and K-band galaxy counts at 2.2 μm (Cowie et al. 1994). The square is an upper limit derived from sky photometry at 4400 Å (Mattila 1990).

1.2.1 Far-Infrared Emission Models

Modeling the emission from galaxies is a field with ample possibilities for the direction of approach. Most of the information available is that gleaned from the local universe, including stellar abundances and evolution, the properties of dust, and (to redshifts of $z \sim 0.1$) the evolution of galaxies. It is fairly common, though, to assume that the bulk of star formation occurred in a relatively short time span at fairly high redshift; models often assume redshifts in the range $z_{\rm formation} \sim 2-3$. An evolution in the star formation rate (SFR) is usually invoked to apply to the evolution of galaxies. This is usually a power law, so that the luminosity of galaxies goes as $L \propto (1+z)^n$, where $0 \leq n \leq 3$ (following the study of quasars by, e.g., Marshall et al. 1983). Furthermore, it can be assumed that galaxies have been merging constantly since their formation, so the number density of galaxies has been decreasing with time. Looking back in time, therefore, we see an increase in the number density if galaxies with a power law of $(1+z)^m$ where $0 \leq m \leq 4$ (from the IRAS-based models of Hacking, Condon & Houck (1987), for example). These corrections are called *evolutionary terms*, from which we derive the phrase "strong evolution" in the case of a term which varies rapidly with redshift.

1.2.1.1 Theoretical Modeling

Perhaps the most fundamental, physical approach is the bottom-up theoretical model: begin with a model of cosmology and galaxy evolution, then propagate it forward in time to solve for the emission as a function of wavelength and redshift. The general approach is shown in Figure 1.6. The specifics of each model vary by which physical processes are included and how these are treated.

One method of determining the emission from dust is to model the chemical evolution of the universe, which then determines the amount and temperature distribution of the dust. This has been done by Wang (1991a), who determined that (assuming an IRAS-derived average temperature) the mass of dust in high-redshift galaxies can be up to 4 times that found in local galaxies, while (for models with strong evolution)

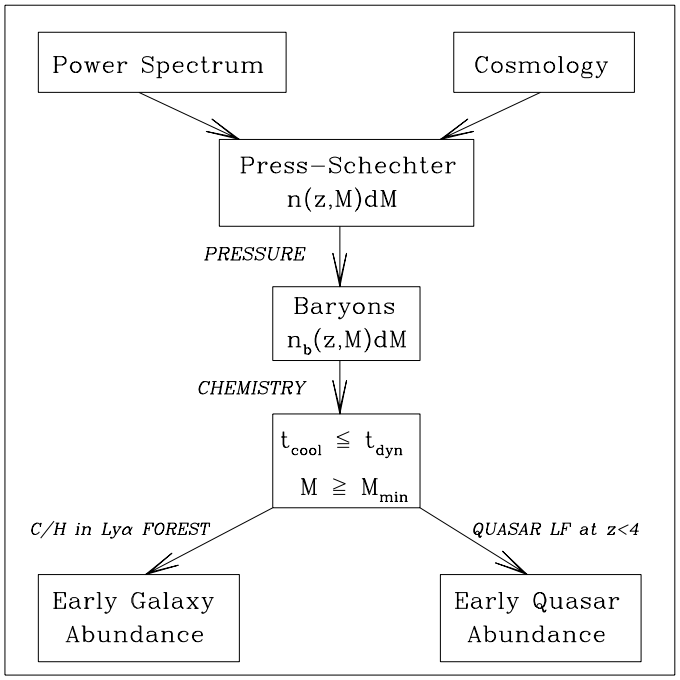

Figure 1.6 Flowchart for the construction of models of galaxy evolution, from Haiman (1998). While the specific stages vary greatly, the general path of all bottom-up models is the same.

the luminosity can be up to 100 times larger. Furthermore, this galaxy distribution predicts that the CIRB should peak at $\sim 115\mu$m and dominate over the CMBR for wavelengths shorter than 400μm (Wang 1991b).

In contrast to this result, a series of papers by Eales and Edmunds (Eales & Edmunds 1996; Eales & Edmunds 1997; Eales & Edmunds 1998) uses chemical modeling in comparison to observations to show that the higher dust masses are difficult to reproduce without substantial amplification by gravitational lensing[12]. Furthermore, they find that the maximum mass of dust possible in a galaxy is only $M_{\rm dust} \leq 0.002 M_{\rm total}$. This implies that a galaxy with $10^9 M_\odot$ of dust – as is found in some studies, (e.g., Hughes, Dunlop & Rawlings 1997; Lewis et al. 1998) – is a very massive galaxy indeed.

In addition to chemical modeling, it is also possible to include the photometric evolution of the stellar populations providing the radiant heat source for the dust. A good example of this kind of model can be found in Franceschini et al. (1994).

[12]Gravitational lensing is the apparent amplification of light from cosmologically distant sources due to the light being focused in our direction by an intervening galaxy or galaxy cluster. While this may sound incredibly unlikely, the high density of galaxies and substantial bending of light due to their gravitational pull makes this a reasonably common event.

Another variation on the photometric evolutionary model is that of Dwek & Smith (1996), in which the formation and destruction of dust grains is also included.

1.2.1.2 Semi-Analytic Modeling

Rather than beginning with fundamental physics and deriving a result, it is possible to assume that certain observed processes are present in the population of high-redshift galaxies, but modified in some way to accommodate the effects of the earlier epoch. This is the field of "semi-analytic" modeling, which was first introduced by Désert, Boulanger & Puget (1990), and applied to the infrared to submillimeter spectrum of galaxies by Guiderdoni et al. (1998). Following the prescription of Maffei (1994), they modeled certain physical processes, including dissipative and non-dissipative collapse of galaxies, star formation, the metal enrichment of the ISM through stellar feedback, and stellar evolution. Summing all these processes results in a spectrum like that in Figure 1.7.

In this model, the absorption of starlight and subsequent reemission is apparent. Furthermore, emission features from Polycyclic Aromatic Hydrocarbons (PAHs) are apparent in the mid-infrared, superposed on the emission from very small, transiently-heated grains. The thermal emission from large (thermalized) grains is the dominant source of luminosity, peaking at around 100μm. Recent results surveying the whole spectrum from nearby galaxies using the ISO satellite has shown the validity of these models (Fischer et al. 1999).

1.2.2 Purely Empirical Model

I have attempted to model the far-infrared to millimeter spectrum of a prototypical starburst galaxy using a purely empirical model. Unlike the semi-analytic model, the physical processes are determined by a statistical approach: observe enough low-redshift galaxies to extrapolate these properties to higher redshift. This process begins by selecting the continuum emission spectral energy distribution (SED[13]) of 26 star-

[13]The SED is the distribution of emission energy as a function of wavelength or frequency.

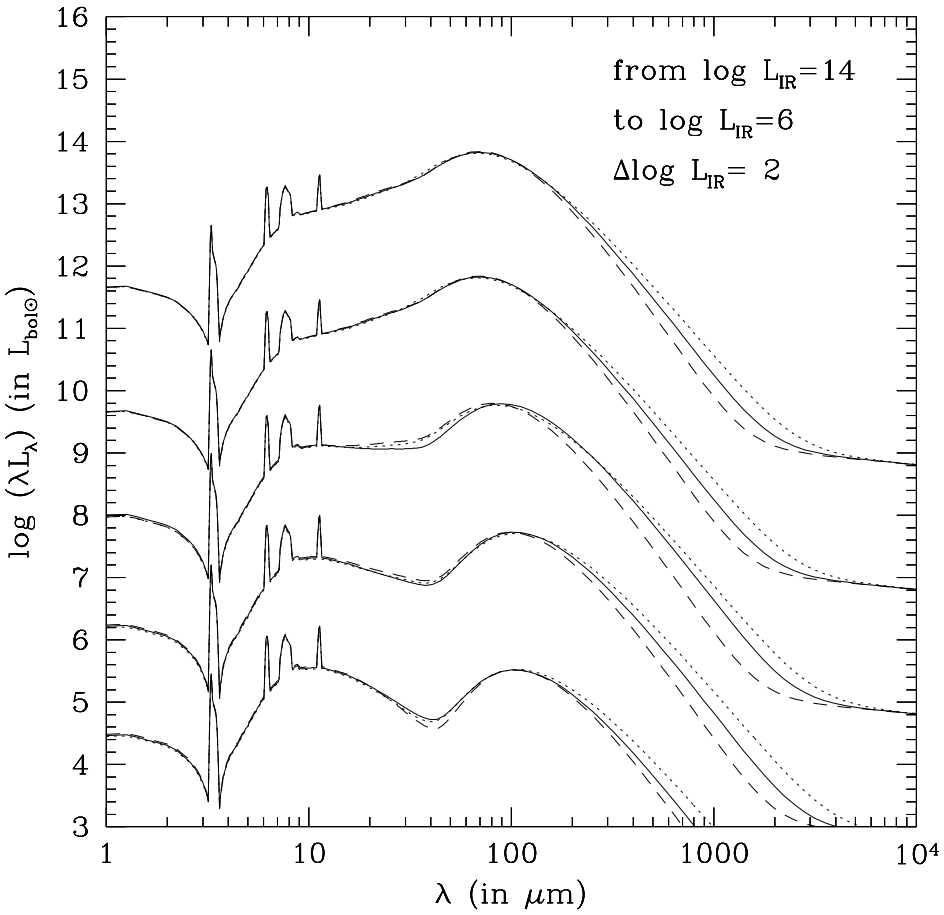

Figure 1.7 Model spectra for IR luminosities 10^6, 10^8, 10^{10}, 10^{12}, and $10^{14} L_\odot$. This range covers galaxies from the smallest dwarf to the most luminous known. The primary difference in the shape of the spectra is in the amount of cold dust emission (that part which peaks near 100μm) in each galaxy. The different submillimeter curves correspond to an emissivity index of $\beta = 2$ (dashes), $\beta = 1.5$ (solid lines), and $\beta = 1$ (dotted lines). From Guiderdoni et al. (1998).

burst galaxies[14] found in the literature (Schmitt et al. (1997) and references therein). Selecting the emission of 15 highly reddened starbursts with the fluxes normalized at 7μm, a composite SED can be determined. This includes several data points in the optical to mid-infrared, the IRAS points in the far-infrared, and fluxes from synchrotron radio emission. A modified blackbody can be fit to the submillimeter range, of the form

$$F_\nu(\nu, T) = B_\nu(T)\Omega_{\rm source}\left[1 - \exp(-\nu/\nu_0)^\beta\right]. \tag{1.1}$$

The SED of these galaxies is well fit by a temperature 50K and index $\beta = 1.5$ with $\nu_0 = 1.5$ THz (200μm), following the prescription of Hildebrand (1983). Combining the dust emission with the optical and radio SED produces an empirical model of the continuum emission from a local dusty starburst galaxy (Figure 1.8). The heavy curve shows the average emission, while the lighter curves illustrate the variance of the data. Note that emission around the PAH features near 10μm is seen as an increase in the variance.

In order to estimate properly the contribution of discrete line emission to the submillimeter portion of the spectrum[15], we need an idea of the flux emitted in various lines in a galaxy. Little data of this sort exist, because of the difficulty in measuring faint lines over a broad band, particularly with the atmospheric opacities hindering ground-based observatories. An estimate models of the far-infrared to millimeter line emission from a star-forming molecular cloud is shown in Figure 1.9.

The best observational data on the bright (and therefore, more likely to be detected) lines comes from the COBE – FIRAS survey of our own galaxy. The spectrum, shown in three stages of reduction in Figure 1.10, was initially presented in Wright et al. (1991) and Bennett et al. (1994) and has recently been updated by Fixsen, Ben-

[14] A starburst galaxy is one undergoing a phase of forming stars at a great rate, usually several solar masses per year.

[15] I shall neglect the important contribution made by emission lines at other wavelengths because they are beyond the scope of this work. It should be noted that searches for high-redshift emission based on observations of such lines turn up no sources, possibly implying that dust obscuration hides emitting regions in protogalaxies.

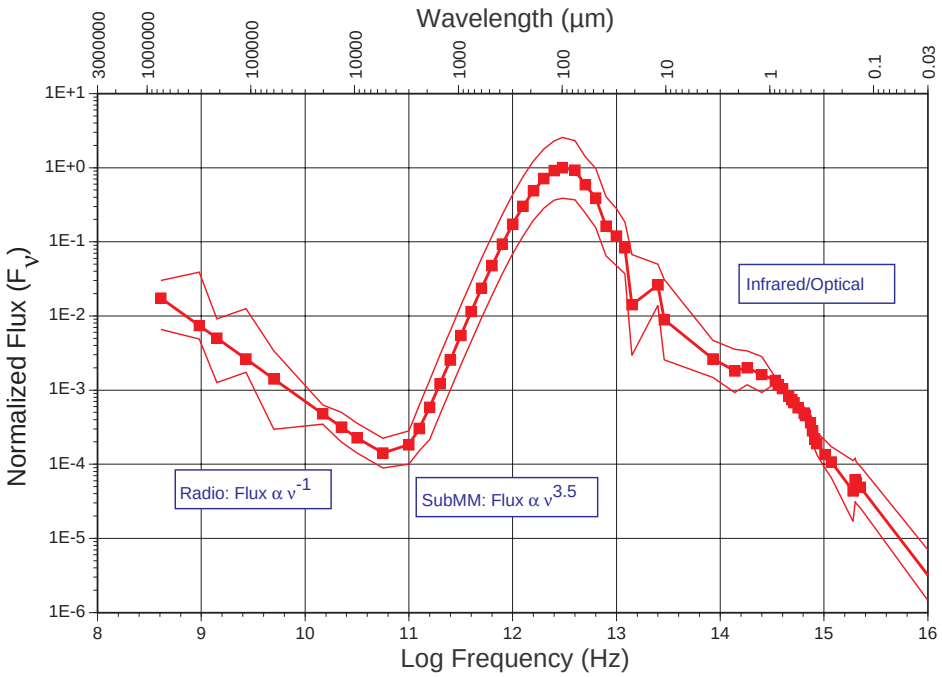

Figure 1.8 Continuum model of the SED of a starburst galaxy. The light bars around the data points indicate the variance of the normalized spectra from the 15 galaxies included in the average.

nett & Mather (1998). It demonstrates clearly that the lines most likely to be seen in galaxies like the Milky Way are those of carbon monoxide (CO), atomic carbon (CI), ionized carbon (CII), ionized nitrogen (NII) and atomic oxygen (OI). These lines, and the problems associated with detecting them at cosmological distances, will be discussed in section 1.3.

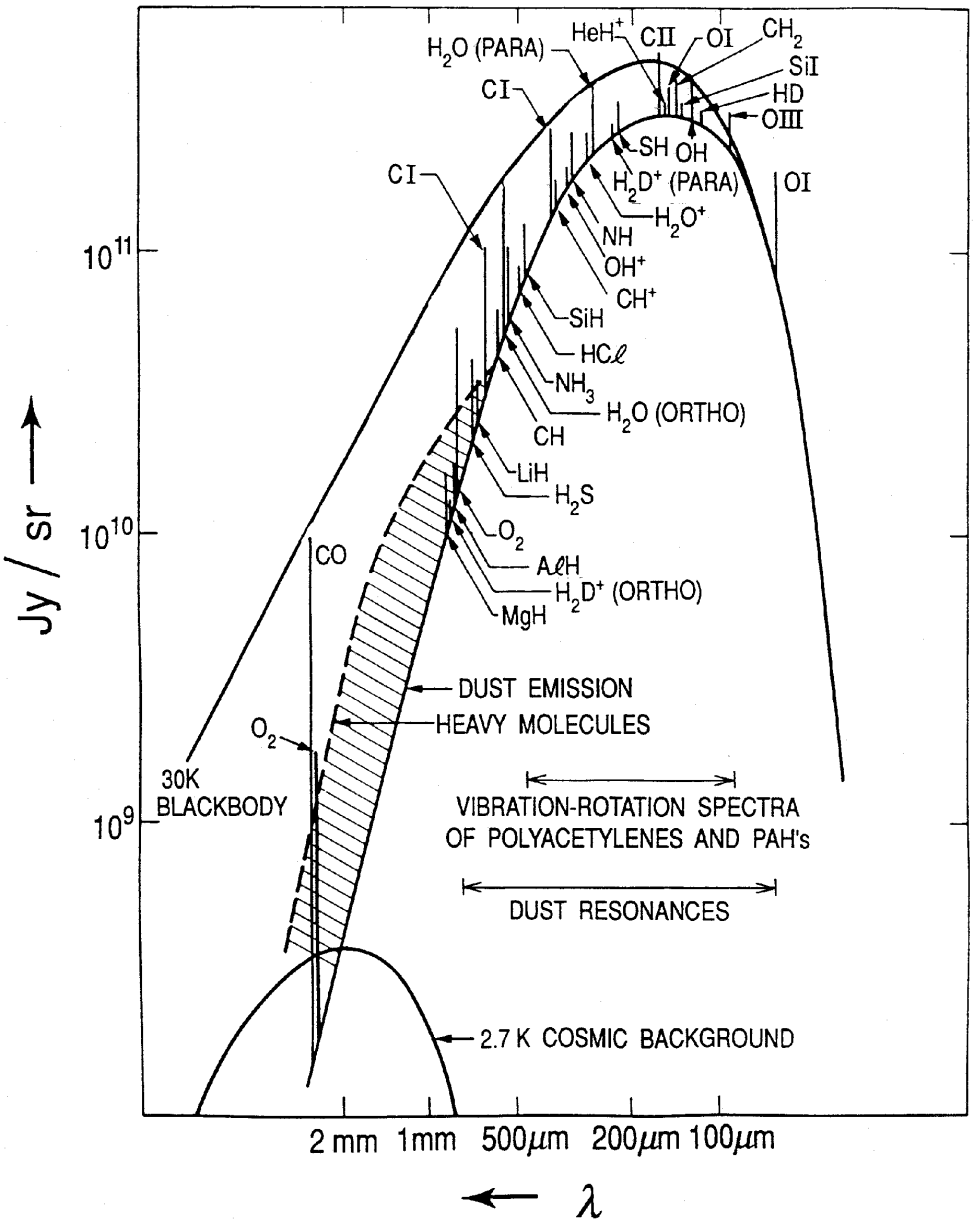

Figure 1.9 Model emission spectrum of a molecular cloud, from Phillips & Keene (1992).

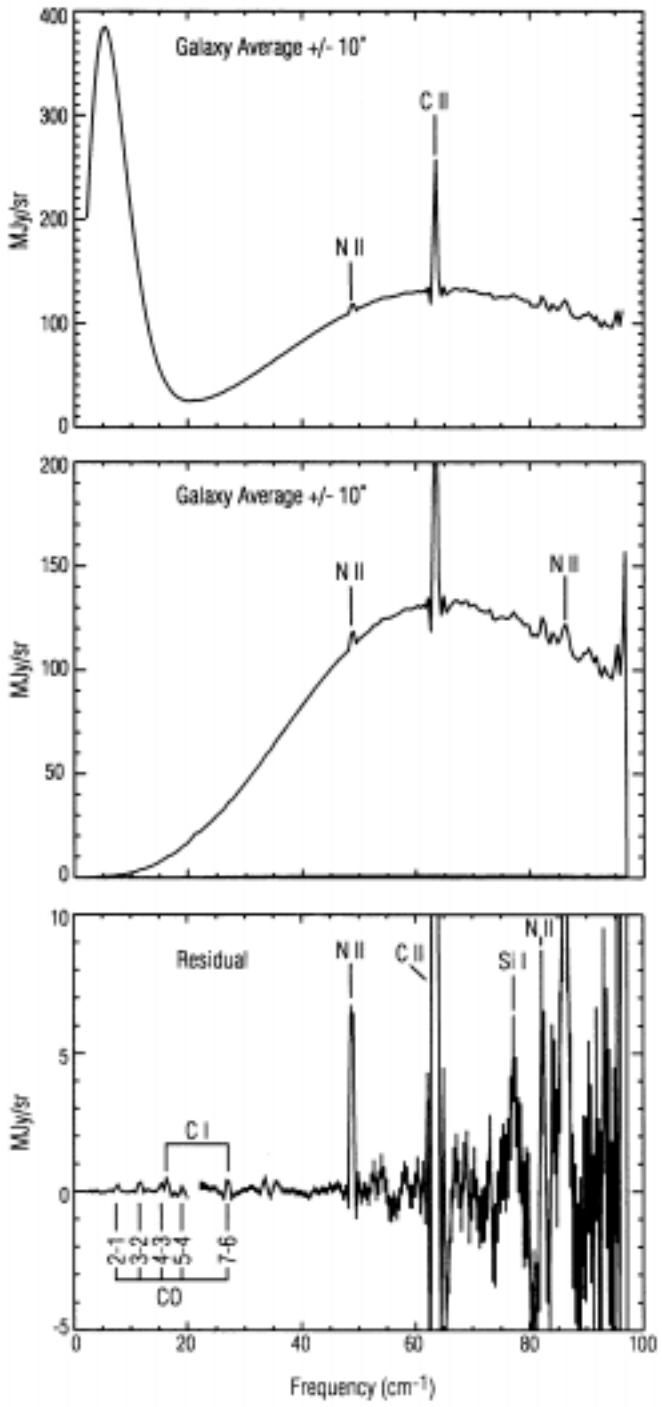

Figure 1.10 FIRAS spectrum of: (Top) the whole sky; (Middle) the Milky Way with CMBR subtracted; (Bottom) the line emission from the Milky Way with Galactic continuum also subtracted. While the continuum emission dominates, over narrow bands certain lines are quite strong and, in the case of CII, even dominate over the continuum.

In Figure 1.11, the FIRAS lines detected in the Milky Way have been scaled to the Galactic continuum flux at 100μm, then added into the starburst SED. I have made an assumption about the width of the lines which yields somewhat greater fluxes for the lower-frequency transitions; this derivation appears to be reasonably appropriate to the CO transitions I have measured in a sample of galaxies (section 5). This yields an empirically derived continuum SED of a starburst galaxy with the submillimeter lines.

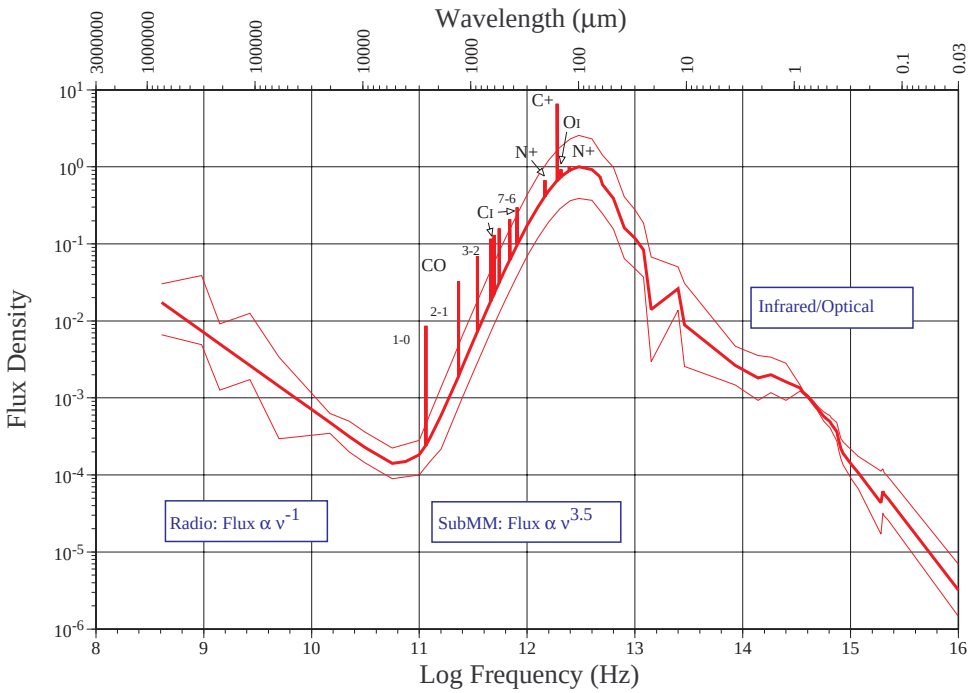

Figure 1.11 The empirically-modeled SED of a starburst galaxy.

For comparison, we include a very complete model fit to Arp 220 of Silva & Danese (1998) in Figure 1.12. The agreement in the general shape of the optical to submillimeter spectrum is quite good, providing verification that the empirical model is well justified. Note the change in both ordinate and abscissa.

This SED can now be redshifted, under the assumption that no change in the luminosity is present. The redshifting of a spectrum is dependent on cosmology, with the observed flux F_ν of a source of luminosity L_ν being given by

$$F_{\nu_{\rm observed}} = \frac{L_{\nu_{\rm emitted}}}{4\pi D_L^2 (1+z)}, \tag{1.2}$$

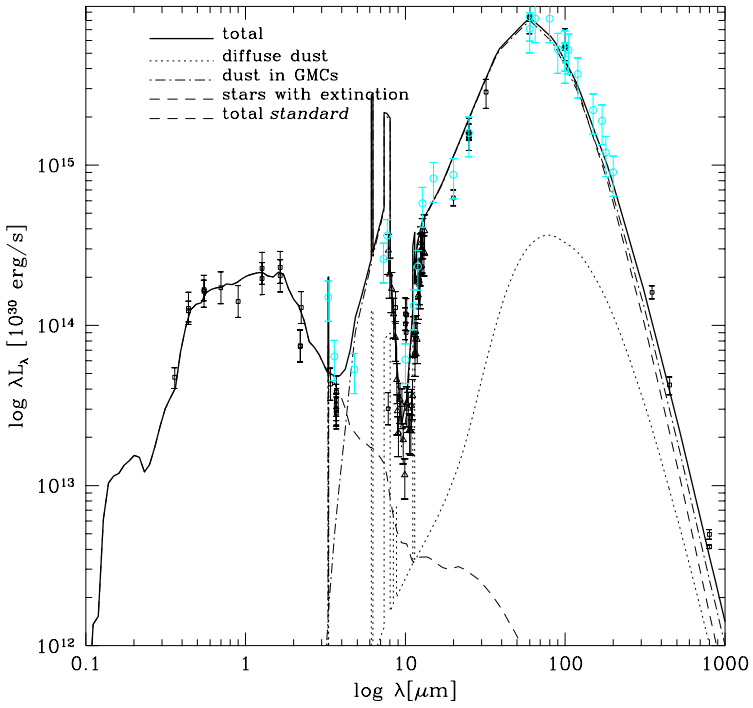

Figure 1.12 Model and data for the optical to submillimeter continuum emission of Arp 220. Note the similarity in general shape to the model of Figure 1.11, although the axes are different. From Silva & Danese (1998).

where the luminosity distance D_L is given by (Weinberg 1972)

$$D_L(z) \equiv \frac{c}{\mathrm{H}_0}\Big(\Omega_0 z + (\Omega_0 - 2)\big[\sqrt{\Omega_0 z + 1} - 1\big]\Big). \tag{1.3}$$

Naturally, the luminosity of a source is independent of distance, whereas the flux density (as shown in Figures 1.8 & 1.11) is not. Therefore, the model has been scaled to match the 100μm flux of Arp 220, a starburst galaxy with luminosity of $L_{\mathrm{IR}} \sim 10^{12} L_\odot$, 110Jy at a redshift of $z = 0.018$ (Soifer et al. 1984). The resultant spectrum is shown in Figure 1.13, for a variety of redshifts. The assumed cosmology is $\mathrm{H}_0 = 100$ km s^{-1} Mpc^{-1} and $\Omega_0 = 1$. At millimeter and submillimeter wavelengths, the "negative K-correction" is easily seen as an overlap of all the models: i.e., the flux density is not strongly dependent on redshift. All other things being equal, it is then best to search for distant objects at wavelengths of $\sim 400\mu$m to yield the largest flux density with the least sensitivity to redshift. However, all is not equal, with atmospheric absorption and background being less in the millimeter than the submillimeter. It is therefore fairly comparable given current instruments to observe

at longer wavelengths, but then the submillimeter flux density remains a necessary measurement if one wishes to constrain the temperature (and hence the luminosity and mass) of an object. Later, I shall show that an accurate measurement of the dust temperature can be used to determine a photometric redshift in the case of a galaxy with no spectroscopic data (section 4.3). This approach is qualitatively similar to the successful UV-dropout technique of Steidel et al. (1996).

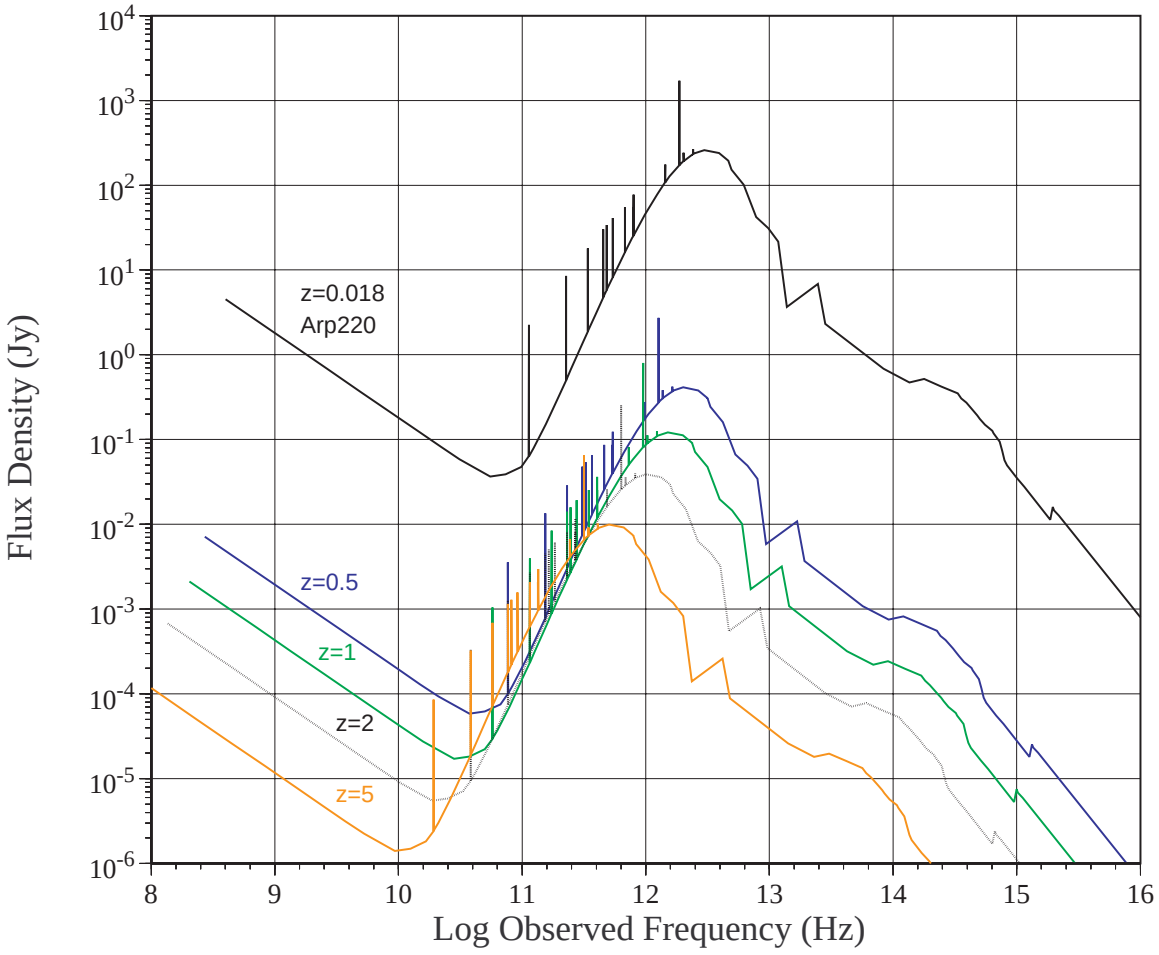

Figure 1.13 Redshifted spectrum (i.e., in the observer's frame) of a model starburst galaxy at several cosmological distances. The cosmology $H_0 = 100$ and $\Omega = 1$ has been used (see text).

1.3 Observing the Far-Infrared Emission from Primævals

There are two primary ways to look at the far-infrared emission from galaxies, dictated by the available instrumentation (Phillips 1998). The most straightforward is to observe the continuum emission from dust, integrating all the light over a fairly broad bandwidth of $\lambda/\delta\lambda \sim 10$. Currently, this is the realm of bolometer-based instruments, and is perhaps the best way to survey large areas of sky to look for distant, dusty objects. The second method for studying galaxies is through looking at the line emission, usually at high enough resolution to measure the linewidth and shape, which is useful for understanding the kinematics of the galaxy. The instruments used are typically heterodyne radio receivers using superconducting-insulating-superconducting (SIS) junctions, (see, e.g., Carlstrom & Zmuidzinas (1996) and references therein).

In this section I shall discuss the considerations necessary for observing the emission from local to cosmologically distant galaxies in the rest-frame submillimeter. It is a field in its relative infancy compared to the optical, infrared, and radio region. Therefore much of our estimates of the emission from distant objects is highly speculative, but it will serve to illustrate the relative difficulty of certain observations.

1.3.1 Continuum Emission

At wavelengths between 50μm and 2mm, the continuum emission from galaxies is dominated by the thermal radiation from cold dust. Given the generally sparsely-sampled spectra of galaxies, this dust emission from galaxies can be empirically fit by a modified blackbody with a single temperature component. This function, a *greybody*, is easily described as the Planck blackbody multiplied by a function which yields a power law index β at long wavelengths. For my modeling, I used an exponential function to roll off smoothly (equation 1.1):

$$F_\nu(\nu, T) = B_\nu(T)\Omega_{\rm source}\left[1 - \exp(-\nu/\nu_0)^\beta\right] \tag{1.4}$$

where $\nu_0 = 1.5$ THz (200μm). The frequency ν_0 corresponds approximately to the frequency at which the dust emission becomes optically thick, and is unfortunately rather imprecisely known. This parameter only changes the shape of the spectrum near the peak, and therefore an accurate knowledge is not critical; Hildebrand (1983) suggests that $\nu_0 \sim 2$ THz is a reasonable guess.

The spectral emissivity index β is a parameter used to model the variation of the effective emissivity of dust grains in the regime where the wavelength is very long compared to the dust size. In this limit, the effective emitting area is very much less than the geometric area, so that the optical depth tends to be substantially smaller than at short ($< 50\mu$m) wavelengths. The parameter β is poorly known, however, so that at wavelengths of ~ 1 mm, the flux varies widely depending on the value assumed. A survey of several regions in the Galaxy yields $\beta = 2$ (Gordon 1988). Observations of the Orion starforming region (Lis et al. 1998) have found β to vary depending on the physical conditions (most notably the ionizing flux) and can take values of $1.5 \leq \beta \leq 2.5$. The best estimates from theory (Draine & Lee 1984) yield $\beta \simeq 1.8$ for cold (19K) dust grains composed of graphites and silicates. Aannestad (1975) finds values for quartz of $\beta = 1.6$, for olivine of $\beta = 2.2$, and for ice-coated grains $\beta \sim 3$. A summary of the properties of galactic and extragalactic dust by Helou (1989) demonstrate that the index is truly not known, though most observational results constrain it to $1 \lesssim \beta \lesssim 2$. Except where noted in this thesis, I shall take $\beta = 1.5$, as this is a reasonable mean value for a range of theoretical and experimental results.

If we assume a dust temperature and dust mass of a galaxy, the observed flux density of that galaxy at arbitrary redshift can be calculated using equation 1.2 and the knowledge that the luminosity is given by:

$$L_\nu \;=\; 24\left(\frac{\nu}{2.4\,\mathrm{THz}}\right)^{\beta} B_\nu(T_d)\, M_d \tag{1.5}$$

where the assumptions of Hildebrand (1983) and Hunter (1997) have been made regarding the mass emissivity of the dust. Our own galaxy contains only $\sim 10^8\, M_\odot$

of dust, and the ultraluminous infrared galaxy Arp 220 contains about $4 \times 10^8\,M_\odot$ of dust. An upper limit of around $10^9\,M_\odot$ is appropriate on both theoretical (e.g., Eales & Edmunds 1998) and observational (e.g., Hughes, Dunlop & Rawlings 1997; Lewis et al. 1998) grounds. Figure 1.14 illustrates the result of this calculation for $10^8\,M_\odot$ of dust with a temperature of 50K, the median temperature of high redshift quasars from the sample of Benford et al. (1999). Gravitational lensing will increase the apparent mass by the amplification factor, which can be around 10 (Alloin et al. 1997; Downes, Solomon & Radford 1995). For comparison purposes, the detection limits (3σ) in one hour for available instruments and telescopes have been plotted.

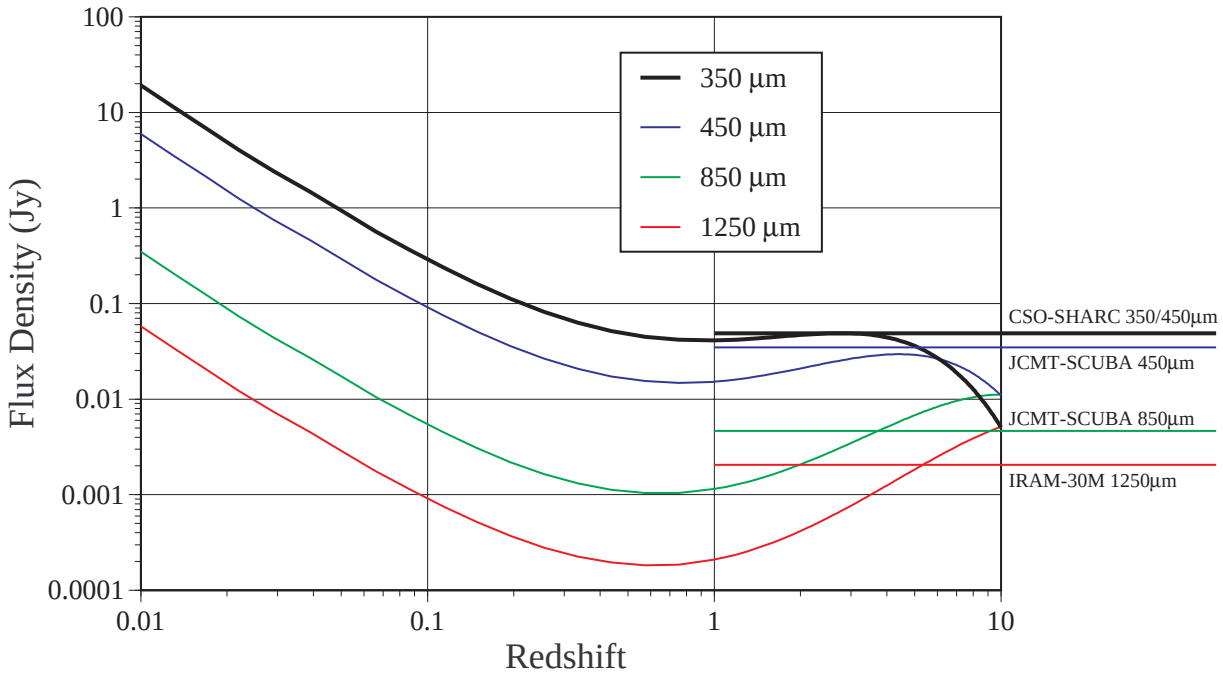

Figure 1.14 Predicted flux density from $10^8\ M_\odot$ of dust as a function of redshift for four wavelengths. Sensitivity for state-of-the-art instrumentation in each band is shown, assuming one hour of on-source integration in good weather conditions.

1.3.2 Line Emission

When attempting to predict the observed flux of a given line as a function of redshift, the cosmology is perhaps the best constrained part of the model. The observed flux density of a line of luminosity $L_{\rm line}$ and width $\Delta v \equiv c(\Delta\nu/\nu)$ and frequency $\nu_{\rm emitted}$

is:

$$F_{\nu_{\rm observed}} = \frac{L_{\rm line}}{4\pi D_L^2 [\frac{\Delta v\, \nu_{\rm emitted}}{c(1+z)}]} \tag{1.6}$$

where the luminosity distance D_L is given by equation 1.3. In the case of $\Omega_0 = 1$, the flux density is given by:

$$F_{\nu_{\rm observed}} = 90 \left(\frac{L_{\rm line}}{10^9\, L_\odot}\right) \frac{1}{(z+2) - 2\sqrt{z+1}} \left(\frac{\Delta v}{300{\rm km/s}}\right)^{-1} \left(\frac{\nu_{\rm emitted}}{\rm GHz}\right)^{-1} \quad {\rm Jy.} \tag{1.7}$$

Whereas the temperature and total dust mass of many nearby galaxies (and a number of high redshift ones) is known, the luminosity $L_{\rm line}$ carried by a line is highly uncertain. For instance, the brightest far-infrared line in our galaxy, the CII 158μm fine structure line of singly ionized atomic carbon, carries nearly 1% of the total bolometric luminosity of the entire Milky Way. However, measurements of CII in the starburst galaxy Arp 220 (Luhman et al. 1998) find that the line-to-dust luminosity ratio is two orders of magnitude less! This was shown by Gerin & Phillips (1998) to be due to the high gas density and high internal UV intensity in Arp 220. It is therefore a very uncertain exercise to attempt to model the flux received by line emission from highly redshifted objects.

If we assume a reasonably conservative model of a galaxy with a total far infrared luminosity of $10^{12} L_\odot$ and a CII/$L_{\rm FIR}$ ratio of 10^{-3} or 10^{-2}, we calculate the curves shown in Figure 1.15. Cosmological models of $\Omega_0 = 1.0$, $h = 1$ and $\Omega_0 = 0.2$, $h = 0.5$ are used, where $h = {\rm H}_0/100$ km/s/Mpc. A rough estimate of the sensitivity (1σ detection limit in an hour of on-source integration time) of available ground-based instrumentation is shown as a heavy curve. The detections of ultraluminous infrared galaxies from Luhman et al. (1998) are also shown for comparison; extrapolation of these data would lead one to deduce that current instruments would not detect these objects at high redshift.

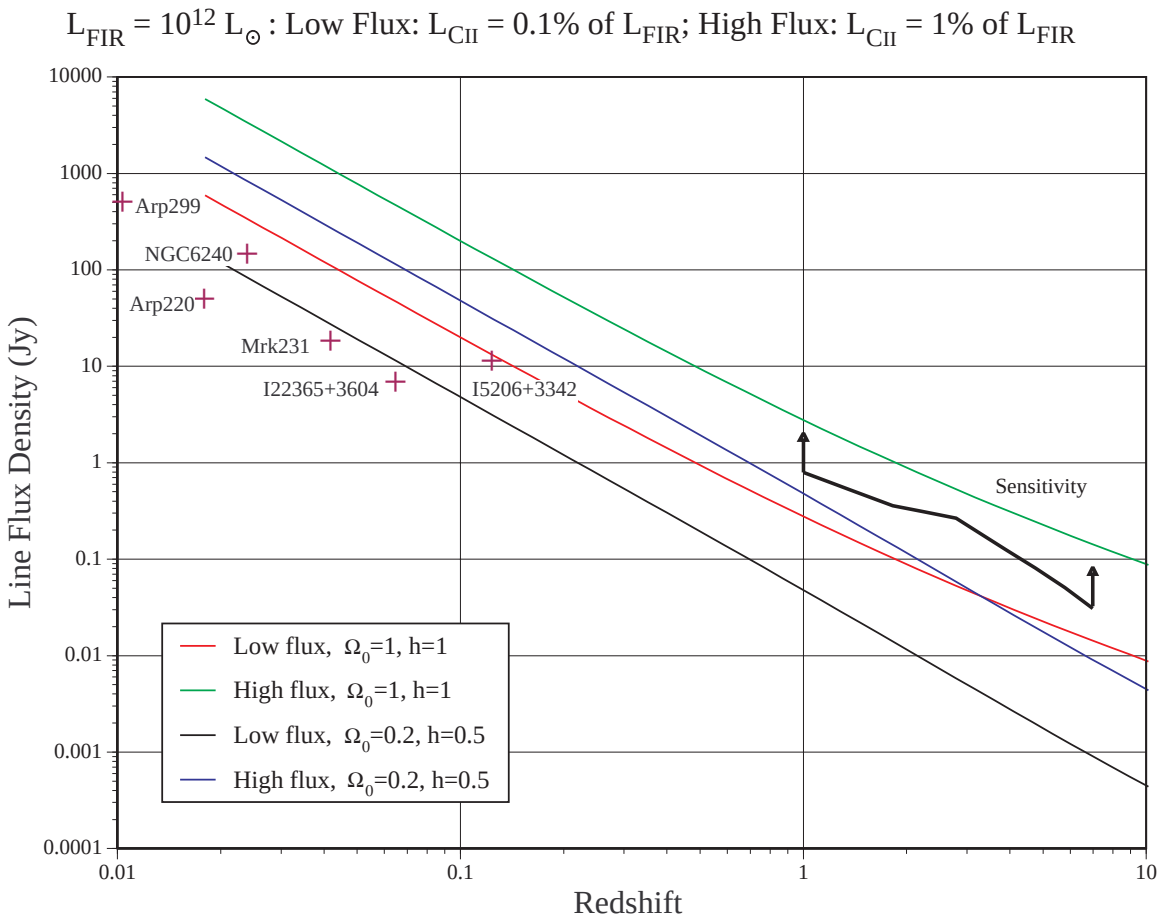

Figure 1.15 Predicted flux density in the CII line as a function of redshift. Two different cosmological models are plotted for each of two estimators: $L_{\rm CII} = 0.01 L_{\rm FIR}$ and $L_{\rm CII} = 0.001 L_{\rm FIR}$. The approximate sensitivity of ground-based instruments ($1\,\sigma$ in one hour) is shown as a heavy curve.

1.3.3 The Need for New Instruments

As shown in the past two figures, available instruments on currently operating telescopes are only barely able to detect emission, either continuum or line, from highly redshifted sources. It is therefore of critical importance to push forward the existing technology or open up new technologies in order to realize the potential for scientific advancement available from the study of cosmologically distant objects at submillimeter wavelengths.

In the following chapter, I shall discuss my contributions to the development of one advanced instrument for continuum studies, SHARC (listed in Figure 1.14). Com-

missioned in 1995, this instrument and its direct competitor SCUBA (also listed in the figure and commissioned in 1996), have helped open up the universe for study at submillimeter wavelengths. In chapters 3 and 4 I describe the results of my observations using SHARC to detect local and cosmologically distant galaxies, respectively. chapters 5 and 6 highlight the use of existing spectrometers to detect the emission lines of local and cosmologically distant galaxies, respectively. The searches for line emission from distant galaxies have not been fruitful, so new instrumentation is being developed at Caltech to enable this kind of search to be conducted more easily. This effort is a multi-part project, and is described in chapters 7, 8 and 9.

Chapter 2

The Submillimeter High Angular Resolution Camera (SHARC)

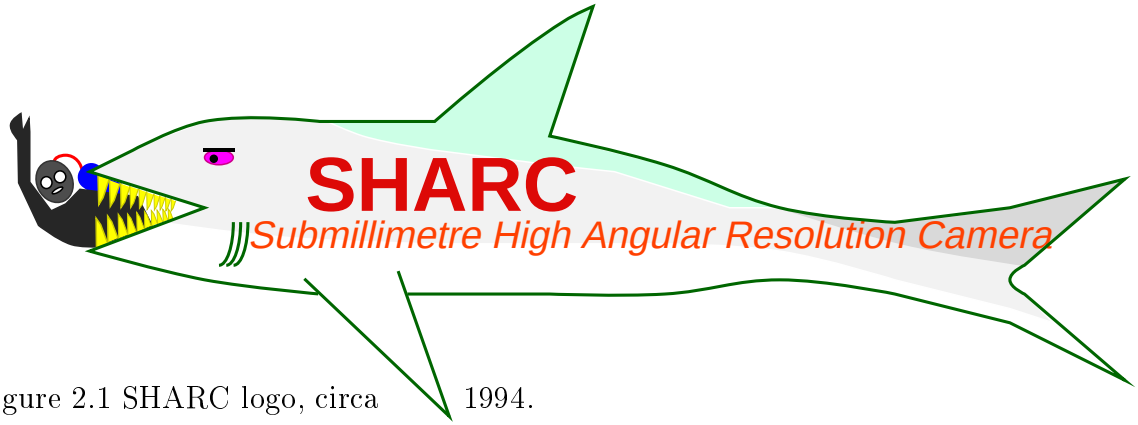

Figure 2.1 SHARC logo, circa 1994.

2.1 An Array of Continuum Detectors: the Submillimeter Bolometer Camera

The successful deployment of large format – hundreds or thousands of pixels – array detectors on near-infrared telescopes has revolutionized astronomy over the past two decades (Elston 1991; McLean 1994) and driven the development of longer wavelength arrays. Longward of the mid-infrared atmospheric windows at 10μm and 20μm, the next infrared wavelengths observable from the ground are in the submillimeter band from 300-1000μm. For studies of nearby star formation to galaxies near the edge of the universe, a current goal in astronomy is to gather high spatial resolution images using the large aperture ($\geq$ 10m) ground-based submillimeter telescopes. This includes the Caltech Submillimeter Observatory (CSO)[1], located near the summit of Mauna Kea, Hawaii. The CSO consists of a 10.4-meter parabolic primary dish with excellent

[1]The CSO is run by Caltech under contract to the National Science Foundation, grant #AST9615025.

surface accuracy and a hyperbolic secondary mirror which together form a classical Cassegrain telescope. Operating at frequencies from 200 to 1000 GHz, the telescope employs numerous cryogenic heterodyne and bolometric instruments. In the first half of this decade, however, the only instrument available for continuum observations was a single-element bolometer with far-from-ideal performance.

Since 1990, the Caltech submillimeter group has been involved with the development of bolometer array instruments in collaboration with Dr. S. Harvey Moseley and his colleagues in the infrared, X-ray, and microelectronics fabrication groups at the National Aeronautics and Space Administration's Goddard Space Flight Center (NASA/GSFC) in Greenbelt, Maryland. The first result of this collaboration is the Submillimeter High Angular Resolution Camera (SHARC), a state-of-the-art instrument for the detection of continuum emission at 350μm and 450μm (Wang et al. 1996). Installed at the CSO in Fall 1995, the camera has been in active use monthly since this date and was opened for external proposals beginning in September 1996. The numerous advantages of the 24-pixel linear bolometer camera over the single channel bolometer system has revolutionized the field of ground-based submillimeter continuum observations. Its main advantages include: 1) A nearly twenty-fold increase in mapping speed of extended sources such as nearby external galaxies and Galactic molecular clouds; 2) Improved sky subtraction by removing correlated noise and noise spikes from all pixels; 3) Doubling of the on/off integration time on point sources when performing pointed observations; and 4) Confirmation of the detection of point sources by direct measurement of the diffraction-limited source size using the Nyquist-sample array. In this chapter, I give an overview of the theory of thermal bolometer detectors, which will be of importance later in this thesis. This is followed by the theory of noise from atmospheric emission in the context of designing an instrument which will have intrinsic noise less than the atmospheric (Benford, Hunter & Phillips 1998). I then discuss briefly the optical design and optical performance of SHARC (Hunter, Benford & Serabyn 1996). Finally, I briefly describe the data reduction software for both mapping and pointed observations, and conclude with measurements of the sensitivity of the instrument in astronomical applications.

2.2 Instrument Overview

At wavelengths longer than 200μm (1500GHz), photoconductors cease to work due to insufficient photon energy compared to the energy gap in the semiconducting detectors (stressed Germanium) (Richards & Greenberg 1982). Heterodyne instruments suffer from a limited bandwidth, making them insensitive for broadband (continuum) studies at frequencies above 100GHz (3mm). In the region between these two limits, thermal detectors are the only available choice. Historically, many researchers have used Golay cells and thermopiles for laboratory work, as these room-temperature detectors are convenient and easy to use. However, in the realm of photon-starved astronomical applications, the only suitable instrument is the cryogenic bolometer. The following section describes the performance of this class of devices.

2.2.1 Bolometer Theory

The idea of the thermal detector has been around since ancient times, in scientific terms. Herschel (1800) used a thermal detector – in his case a mercury thermometer – to discover the existence of infrared radiation from thermal sources at the end of the 18th century. Less than a century later, Langley (1881) invented a much more sensitive device which he called the *bolometer*. His thermal detector used a pair of matched platinum strips forming arms in a Wheatstone bridge, as shown in Figure 2.2. When one strip was exposed to the light and the other kept in the dark, the tiny change in temperature changed the resistance of the illuminated strip and unbalanced the bridge. In this way, a temperature change as minute as 10μK was detectable. The modern definition of a bolometer is somewhat more general; it is a device which changes its temperature in response to light of any wavelength from radio waves to X-rays falling upon it.

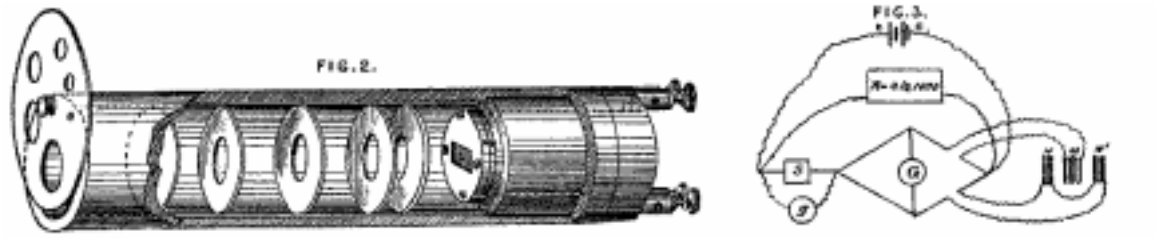

Figure 2.2 Langley's original bolometer instrument.

2.2.2 Bolometer Performance

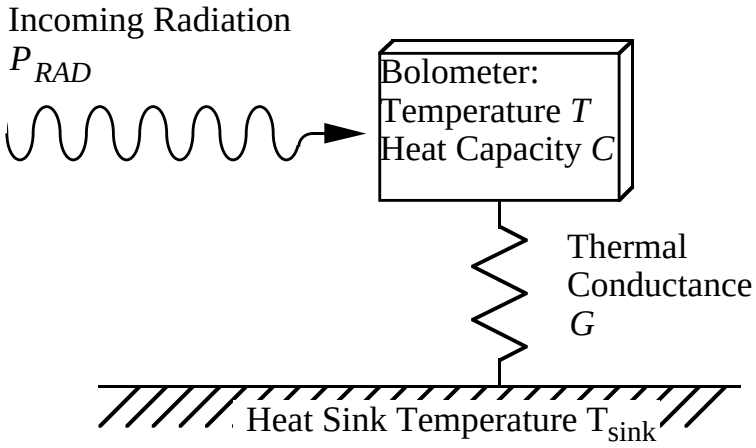

Figure 2.3 A simplified diagram of a bolometer from a thermal point of view.

The bolometers we shall consider are similar to Langley's, using a chip of doped silicon which has an electrical resistance dependent upon temperature. On the absorption of incident radiation, the temperature of a bolometer rises, causing a change in electrical resistance of the active element. A bolometer has a heat capacity

$$C \equiv \frac{dQ}{dT} \qquad [C] = \text{Watts/Kelvin} \tag{2.1}$$

where dQ is the additional thermal energy stored in the device after a temperature change of dT. I shall use the notation $[X]$ to indicate the units of X. Because it is connected to a heat sink of fixed temperature T_{sink}, as is shown in Figure 2.3, the

heat will be conducted away from the bolometer at temperature $T_{\rm bolo}$ at the rate P:

$$P = \int_{T_{\rm sink}}^{T_{\rm bolo}} G(T)dT \quad \text{which can be inverted as} \quad \overline{G} = \frac{dP}{dT}. \qquad [P] = \mathrm{W} \tag{2.2}$$

where $G(T)$ is the thermal conductance as a function of temperature and $\overline{G}$ is the averaged thermal conductance between $T_{\rm sink}$ and $T_{\rm bolo}$. The magnitude of the bolometer's temperature response can be increased by making $\overline{G}$ as small as possible with the constraint that C is also reduced in order that the response time, defined as

$$\tau \equiv \frac{C}{\overline{G}}, \qquad [\tau] = \text{seconds} \tag{2.3}$$

remains below the value required in the experiment.

The change in resistance of the active element is governed by the temperature coefficient of resistance defined by

$$\alpha \equiv \frac{1}{R}\frac{dR}{dT}. \qquad [\alpha] = \mathrm{Kelvin}^{-1} \tag{2.4}$$

Unlike normal metals, the resistance of ion-implanted thermometers in silicon bolometers at $T < 10$K has empirically been found to increase as T decreases (e.g., Downey et al. 1984):

$$R = R_0 \exp\left[\left(\frac{T_0}{T}\right)^{\frac{1}{2}}\right], \qquad [R] = \Omega \tag{2.5}$$

$$\alpha = -\frac{1}{2}\left(\frac{T_0}{T^3}\right)^{\frac{1}{2}}, \tag{2.6}$$

where R_0 and T_0 are constants depending on the level of implantation. This behavior is consistent with the prediction of the model for variable-range hopping[2] with a Coulomb gap (Pignatel et al. 1994; Zhang et al. 1993). Hence, incident radiation on

[2]Variable-range hopping is conduction where an electron can make a jump from one spot in a lattice to another, possibly distant spot.

the bolometer causes a change in resistance

$$dR = \alpha R dT = -\frac{1}{2} R_0 \exp\left[\left(\frac{T_0}{T}\right)^{\frac{1}{2}}\right]\left(\frac{T_0}{T^3}\right)^{\frac{1}{2}} dT. \tag{2.7}$$

For completeness, it must be pointed out that the hopping-conduction model of the resistance of thermistors breaks down at lower temperatures due to electrical nonlinearities. A hot-electron model can be used to explain the difference qualitatively: at low temperatures, the electron-phonon coupling becomes weak so that the electrons reach an equilibrium before the lattice can conduct away the heat. Quantitatively, the resistance should be written as

$$R = R_0 \exp\left[\left(\frac{T_0}{T_\mathrm{e}}\right)^{\frac{1}{2}}\right]; \qquad T_\mathrm{e}^{\beta+1} = \frac{\beta+1}{g_0}\frac{P}{V} + T_l^{\beta+1}, \tag{2.8}$$

where T_e and T_l are the electron and lattice temperatures, P/V the power per unit volume transferred between the two, g_0 the thermal conductance, and β is typically about 5 (Zhang et al. 1998). Having said all this, a simple calculation reveals that at typical bias powers the difference between electron and lattice temperatures amounts to a few percent at the lowest temperatures, a negligible amount for operation.

A bolometer is typically used in a circuit similar to that indicated in Figure 2.4. A change in resistance as given by equation 2.7 can be measured as a change in voltage at constant bias current I

$$dV = IdR = -\frac{1}{2} I R_0 \exp\left[\left(\frac{T_0}{T}\right)^{\frac{1}{2}}\right]\left(\frac{T_0}{T^3}\right)^{\frac{1}{2}} dT = -\frac{IR\sqrt{T_0}}{2T^{3/2}} dT. \qquad [dV] = \mathrm{V} \tag{2.9}$$

The bolometer responsivity S characterizes the response to an incident power P:

$$S \equiv \left|\frac{dV}{dP}\right| \simeq \frac{IdR}{\overline{G}dT} = \frac{I(dR/dT)}{\overline{G}} = \frac{IR\sqrt{T_0}}{2\overline{G}T^{3/2}}, \qquad [S] = \mathrm{V/W} \tag{2.10}$$

where we have made the approximation that the self-heating effect of the bias current remains small. This equation simply illustrates the advantage of low temperature

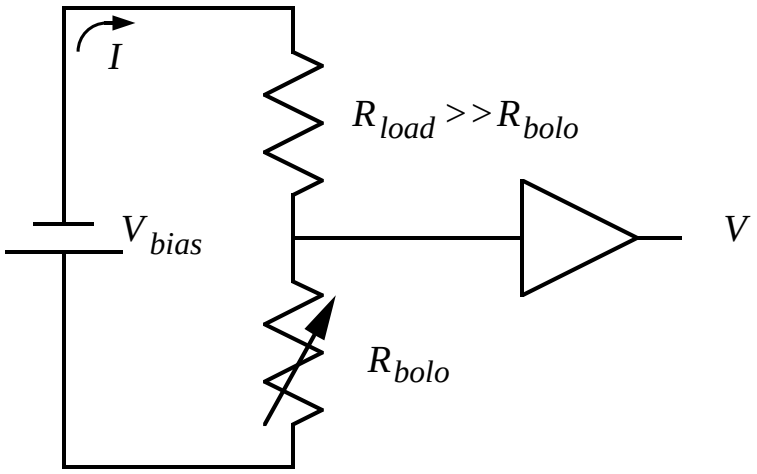

Figure 2.4 A simplified schematic for a bolometer using the classic unlooped voltage amplifier.

operation of ion-implanted silicon bolometers: a smaller T yields a larger responsivity. The responsivity S is, in the full description, a complex value due to the effective thermal phase error or electrical nonlinearities introduced when one considers the responsivity for a time-varying incident power (Mather 1984b).

2.2.3 Noise in Bolometers

As in all detectors, there is a fundamental noise floor for a given device which can be determined by a number of sources. I shall compare the known sources of noise in bolometers using the conventional figure of merit, the *Noise Equivalent Power (NEP)*. NEP is the signal power which would yield a unity signal to noise ratio. There is some area for confusion with this parameter, however, in that the signal power is imprecisely defined. In various places in the literature, it can be the power *absorbed* by the bolometer, the power *incident* upon the bolometer, the power incident upon the entrance of the *cryostat*, or even the power *emitted* by the source. In the following discussion, I shall refer to the power absorbed by the bolometer.

The fundamental sensitivity limit[3] of a bolometer or any other thermal detector is

[3]For those familiar with heterodyne instruments, I point out that a bolometer is fundamentally different from a mixer in that the single-photon detection process of a thermal detector has no quantum limit, while the two-photon process in heterodyne mixing does.

determined by temperature fluctuations in the active element (Jones 1953; Low 1961; Mather 1982; Mather 1984a). Physically, the number of phonons in the device will vary due to communication with the phonons in the heat sink, as shown in Figure 2.3. This is called *phonon noise* and is given by:

$$NEP^2_{\text{phonon}} = 4kT^2G \qquad [NEP] = \text{W}/\sqrt{\text{Hz}} \tag{2.11}$$

for a bolometer at temperature T and conductance G.

Perhaps the next most fundamental limit is Johnson noise, the random fluctuations in the apparent resistance R of the bolometer element. This noise can be thought of as the noise in a circuit containing a noise-free resistor and an impedance-matched noise source, in which blackbody radiation of power spectral density kT is communicated between the two when in thermal equilibrium. The current through the resistor and impedance-matched load is $I_N = V_N/2R$, so the power $I_N^2R = V_N^2/4R = kT$. Dividing by the responsivity yields the well-known value of the Johnson noise:

$$NEP^2_{\text{Johnson}} = \frac{4kTR}{|S|^2} \tag{2.12}$$

where the real portion of the responsivity S has been used. The load resistor as shown in Figure 2.4 will also inject some Johnson noise, given by:

$$NEP^2_{\text{R}_{\text{Load}}} = \frac{4kT_LR_L}{|S|^2}\left(\frac{R}{R_L+R}\right) \tag{2.13}$$

where R_L is the resistance of the load at temperature T_L. Since a bolometer instrument typically uses $T_L = T$ and $R_L > R$, it can be seen that the value of this noise term actually *decreases* with increasing load resistance (Figure 2.5), since the load resistor acts as a voltage divider with the bolometer with the majority of the load resistor noise being seen across the load resistor's terminals themselves.

Every bolometer circuit needs an amplifier, and all amplifiers introduce noise. A conventional bolometer amplifier is a Junction Field-Effect Transistor (JFET) source follower with unity gain, used for impedance transformation. Bolometers typically

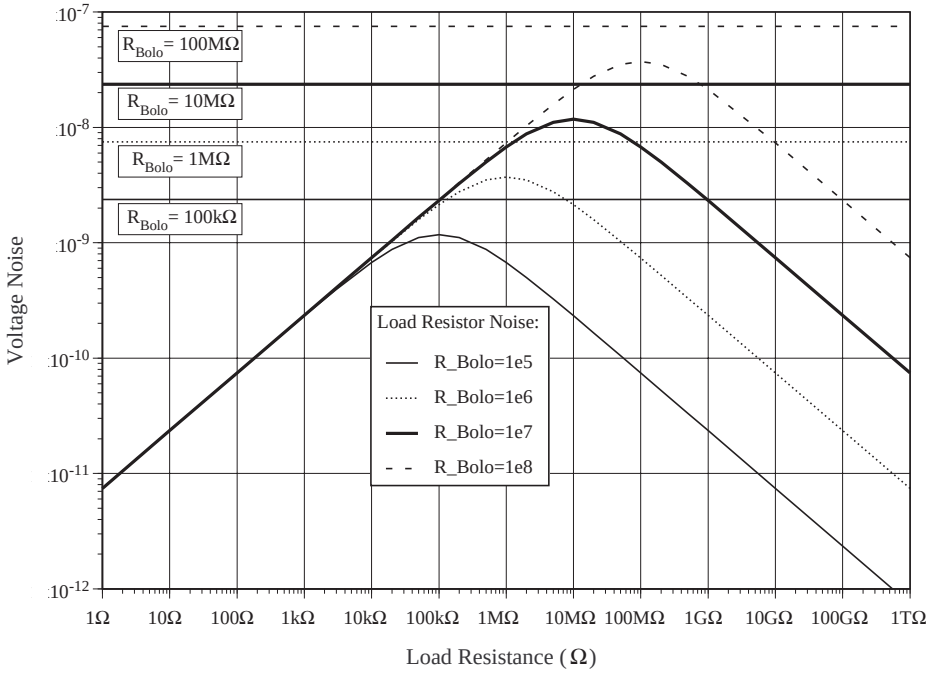

Figure 2.5 Voltage noise (in $\mathrm{nV}/\sqrt{\mathrm{Hz}}$) for a load resistor at 1K, as a function of its resistance and the bolometer resistance. For reference purposes, the bolometer's Johnson noise is also plotted.

have resistances of order 10MΩ, which may make the system sensitive to microphonic noise pickup, whereas JFET output impedances are merely kΩ. The noise from a JFET can often be characterized well by using two parameters, the most important of which is the voltage noise V_N which can be considered as the Johnson noise for an effective FET resistance. One must also consider the current noise I_N, which can be considered as shot noise in the gate current (electrons moving through a potential barrier), with value $I_N \sim \sqrt{2qI_{\rm gate}}$). Then the NEP contribution from these sources is

$$NEP^2_{\rm amplifier} = \frac{V_N^2 + R^2 I_N^2}{|S|^2}. \tag{2.14}$$

Typical values of V_N and I_N for a very good, cooled JFET are about $1{\rm nV}/\sqrt{\rm Hz}$ and $10^{-17}{\rm A}\sqrt{\rm Hz}$, respectively. Voltage noise is a parameter which can be found in the manufacturer's specifications for a given FET (e.g., InterFET Inc.). There is usually a $1/f$ component to this noise such that $V_N = V_{N_0}(1 + f_{\rm knee}/f)$ (e.g., Netzer 1981), with a knee at a frequency of about 10 Hz (though there is a great deal of variability in this parameter). Current noise specifications are harder to find, but can be deduced from a gate leakage current estimation. At room temperature (300K), leakage currents tend to be less than 10^{-10} A, corresponding to a current noise of $I_N \sim 5 \times 10^{-15}$ A$/\sqrt{\rm Hz}$. However, the gate current for silicon JFETs decreases a factor of 2 for every 10K the die is cooled (Horowitz & Hill 1989). Cooling to 130K therefore ought to reduce the current by a factor of 10^5, decreasing the current noise to roughly $10^{-17}{\rm A}\sqrt{\rm Hz}$. This level of performance has been verified experimentally (Moseley, Mather & McCammon 1984). Because bolometer resistances are typically less than $10^8\Omega$, the current noise power is usually negligible compared to the voltage noise power.

Finally, noise can be introduced by fluctuations in the sink temperature. This noise is harder to estimate, but has the value

$$NEP^2_{\rm sink} = G^2 T_N^2 \tag{2.15}$$

where T_N is the spectrum of fluctuations in the bath temperature. The "bath" here is the heat sink actually seen by the bolometers, usually a slab of metal with some finite heat capacity and conductance to the ultimate bath, such as a boiling cryogen. The noise spectrum of fluctuations in the temperature of the heat sink drops above frequencies corresponding to its own time constant. A typical heat sink is $\sim$ 50g of Invar, which probably has a heat capacity of 5mJ/K at 300mK (White 1979), connected to a ^{3}He bath with conductance 5mW/K. This yields a time constant of about 1 second, and is relatively insensitive to temperature due to the fact that both heat capacity and thermal conductance scale linearly with temperature.

At typical infrared modulation frequencies of a few Hz, a ^{3}He sorption-pumped refrigerator has a temperature fluctuation density of $T_N \sim 50\mathrm{nK}/\sqrt{\mathrm{Hz}}$ (Holzapfel et al. 1997). With a conductance of $G \sim 10^{-9}\mathrm{W/K}$, this yields an NEP of $5{\times}10^{-17}\mathrm{W}/\sqrt{\mathrm{Hz}}$, roughly half the phonon noise. An ADR with active temperature control achieves a fluctuation spectrum of perhaps $100\mathrm{nK}/\sqrt{\mathrm{Hz}}$ with $G \sim 10^{-11}\mathrm{W/K}$, for an NEP of $10^{-18}\mathrm{W}/\sqrt{\mathrm{Hz}}$, slightly below the phonon noise. It is therefore prudent to design the time constant of the sink relative to the bath to be longer than the IR modulation period by a factor of at least 4, which would fairly well prevent temperature fluctuation noise from contributing.

There are other sources of noise which have been observed (Richards 1994), including the "popcorn" noise in FET amplifiers and anomalous noise with a $1/f$ spectrum attributed to shot noise at poor electrical contacts. Another insidious form of noise is in microphonics, caused by small motions of the electrical components. For instance, a wire with a capacitance $\mathfrak{c}$ to ground held at voltage $\mathfrak{V}$ is mechanically susceptible to generating an AC current $\mathfrak{V}d\mathfrak{c}/dt$. Microphonic noise is reduced in two ways: (1) tensioning or anchoring of all leads such that the resonant frequencies are very high, so that mechanical vibrations cause electrical signals out of the frequency band of interest and (2) JFET preamplifiers used as impedance transformers, placed near the bolometers to reduce the impedance (and therefore the microphonic voltage noise) by roughly three orders of magnitude. There is also the possibility of current noise from radio frequency pickup on signal leads; this is minimized by using RF isolators at the

cryostat entrance to form a Faraday cage for the bolometers. Hence, through careful design and fabrication, it is possible to reduce all these sources of noise to the point of insignificance. I shall assume that is the case here.

We can now sum the noise terms in quadrature, yielding the bolometer noise equivalent power:

$$NEP^2_{\rm bolometer} = 4kT^2G + G^2T_N^2 + \frac{4kTR + 4kT_LR_L(R/(R+R_L))^2 + V_N^2 + R^2I_N^2}{|S|^2}. \tag{2.16}$$

It should be pointed out that in the full nonequilibrium treatment of the bolometer, the Johnson noise is approximately half of the equilibrium value, due to the effect of electrothermal feedback (Mather 1982). Furthermore, the phonon noise is similarly reduced by $\sim 25\%$.

2.3 Noise from Atmospheric Emission

With the advent of large submillimeter telescopes at high, dry sites, the atmospheric background noise in a moderate bandwidth can be low enough to challenge the ability of instrument designers to produce sufficiently low noise bolometers to be background limited. In this section, I compare the predictions for the noise power of a bolometer observing through an emissive atmosphere, considering the effect of atmospheric absorption, telescope optical efficiency, and detector optical efficiency, with measurements through the atmosphere over Mauna Kea.

A *background limited* detector is defined as one in which the NEP of the detector is less than the NEP from the photons it detects. Recently, the development of bolometers for submillimeter telescopes in the 1.3 mm to 350 μm range has focused on the production of background limited bolometer arrays. Two recent examples are SHARC on the Caltech Submillimeter Observatory (CSO) (Wang et al. 1996), the subject of this chapter, and SCUBA on the James Clerk Maxwell Telescope (JCMT) (Holland et al. 1996). Having background limited bolometers is especially important for ar-

ray detectors, as this implies that any spatially correlated component of atmospheric noise (sky noise) will be easily detected in all elements and can therefore be removed. Furthermore, as bolometers are employed in moderate bandwidth spectroscopy (Maffei et al. 1994; Benford et al. 1998a), which will be discussed in chapter 7, background power is further reduced, allowing the use of even more sensitive bolometers. These advances require a careful evaluation of the photon background noise limit to determine the constraints on future bolometer design.

2.3.1 Noise Power of Blackbody Radiation

In the case of a practical ground-based submillimeter telescope observation, the detected radiation is typically dominated by the atmosphere emitting as a blackbody in a diffraction-limited beam (Phillips 1998). Following a thermodynamic approach, we can take the emitted photon rate spectral density per spatial mode as $n = (e^{\frac{h\nu}{kT}} - 1)^{-1}$. It can be shown (Kittel 1980) that the mean square fluctuations in the equilibrium number of photons per mode is $< (\Delta n)^2 >= n(1+n)$. Following Fellgett, Jones & Twiss (1959), for a telescope of main beam efficiency $\eta_{\rm MB}(\nu)$, a blackbody emissivity $\epsilon(\nu)$, and an optical efficiency (the product of optics transmission and detector absorptivity) $\eta(\nu)$, the mean square fluctuation in the number of photons *detected* per mode is given by:

$$< (\Delta n)^2 >= n(1 + \epsilon(\nu)\eta_{\rm MB}(\nu)\eta(\nu)n) \tag{2.17}$$

where the first term can be regarded as shot noise in the incident photon stream (the "particle" term) and the second term is commonly referred to as photon bunching (the "wave" term) (Lewis 1947). The efficiencies appear in the second term because wave fluctuations are a quadratic effect in the mean photon rate.

Multiplying the above expression by the energy per photon and the number of modes, N, then yields the spectral density of the mean square fluctuations in the

radiation power detected:

$$< (\Delta P_\nu)^2 >= 2N \frac{h^2\nu^2}{e^{\frac{h\nu}{kT}} - 1} \left[1 + \frac{\epsilon(\nu)\eta_{\rm MB}(\nu)\eta(\nu)}{e^{\frac{h\nu}{kT}} - 1} \right]. \tag{2.18}$$

The factor of 2 derives from the fact that a thermal detector is a square law detector and consequently doubles the mean square fluctuations (Robinson 1979). To determine the total mean square fluctuations in the detected radiation, one must integrate over the frequency band of detection. We must now refer the noise power to that of a blackbody with perfect optical efficiency in order to take into account this variation:

$$< (\Delta P)^2 >= \int 2N \frac{\epsilon(\nu)\eta\eta}{e^{\frac{h\nu}{kT}} - 1} h^2\nu^2 d\nu \left[1 + \frac{\epsilon(\nu)\eta\eta}{e^{\frac{h\nu}{kT}} - 1} \right]. \tag{2.19}$$

Given that the physical temperature of the atmosphere from ground-based telescopes is ~ 260 K, the Rayleigh-Jeans approximation introduces a $< 10\%$ error for frequencies < 1000 GHz, small enough to be neglected in the interest of simplicity. The throughput of the telescope is $A\Omega$, where A is the area of the telescope and Ω the solid angle on the sky seen by the detector. In the diffraction limited case, the number of modes is $N = \frac{2A\Omega}{\lambda^2} \approx 2$, where a factor of 2 has been included to allow for both polarizations of light. Assuming a narrow bandwidth instrument used to observe a source comparable to or smaller than the beam size (and where the beam-defining optics emit considerably less power than the atmosphere), the number of modes is independent of frequency so the above expression becomes

$$< (\Delta P)^2 >= \int 4\epsilon(\nu)\eta_{\rm MB}(\nu)\eta(\nu)\ kTh\nu d\nu \left[1 + \epsilon(\nu)\eta_{\rm MB}(\nu)\eta(\nu)\frac{kT}{h\nu} \right]. \tag{2.20}$$

2.3.2 Noise Equivalent Power

The Noise Equivalent Power (NEP) is defined as the *signal* power required to obtain a unity signal to noise ratio in the presence of some known (detector or background) noise. If we assume that the detector noise is less than the background noise, as is desirable, then the background noise power given by equation 2.20 can be used. It is

important to note that if one's efficiency for collecting signal photons increases, the signal power needed to equal the noise (the NEP) decreases. Similarly, if the amount of noise increases, the NEP must increase. The relative scaling of these quantities is shown schematically in Figure 2.6. When the detector is used at a telescope to observe an astronomical source, the signal strength must be included and therefore the optical efficiencies affect the NEP in the following manner:

$$NEP \propto Noise/Signal \tag{2.21}$$

$$Signal \propto \eta_{\rm MB}(\nu)\eta(\nu)(1-\epsilon(\nu)) \tag{2.22}$$

$$Noise \propto \sqrt{\epsilon(\nu)\eta(\nu)} \tag{2.23}$$

$$\therefore NEP \propto \sqrt{\frac{\epsilon}{\eta_{\rm MB}(\nu)^2\eta(\nu)(1-\epsilon)^2}} \tag{2.24}$$

which is valid under the assumption of a source comparable to or smaller than the beam size, and the atmospheric background contributes in both the main and error beams. Hence the NEP calculated from the atmospheric noise will underestimate the actual background limited NEP. In the submillimeter, where typically $0.2 < \epsilon < 0.8$ and $\eta_{\rm MB} < 0.8$, this introduces a substantial difference. To take note of this difference explicitly, henceforth all values shall be referred to above the atmosphere unless otherwise stated.

At this point we shall make some simplifying approximations. Typically, the bandwidth of bolometric instruments is relatively narrow ($\Delta\nu/\nu < 1/10$), so the telescope and optical efficiencies can be taken as constant. We do this with the understanding that the bandwidth of integration is limited by the optical efficiency (e.g., $\eta(\nu) = 0$ outside some region $\nu \pm \Delta\nu/2$), so that there is an implicit frequency dependence. However, the atmosphere is known to contain large variations in emissivity in the submillimeter, down to $\Delta\nu/\nu \approx 1/1000$; therefore, one must integrate over frequency in most cases. We choose to neglect, but wish to point out, that hot spillover adds excess noise as given by equation 2.20, with appropriate $\eta_{\rm hot}$ and $T \sim 280$K, $\epsilon = 1$.

We can then write the *Background Radiation Equivalent* (BRE) NEP, which we

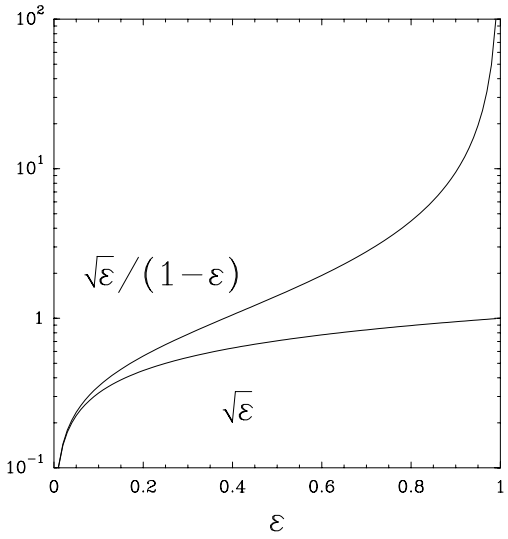

Figure 2.6 Comparison of the scaling of noise and NEP.

shall define as the source noise power yielding a signal to noise of 1 when observing a source through the atmosphere. We term this noise power Background Radiation Equivalent to imply that the noise power is not *from* the background (atmosphere), but is equivalent to it.

$$(NEP)^2 = \int \frac{4\epsilon(\nu)}{\eta_{\rm MB}^2 \eta (1-\epsilon(\nu))^2} kTh\nu d\nu \left[1 + \epsilon(\nu)\eta \frac{kT}{h\nu}\right]. \tag{2.25}$$

In the limit where the integration range $\Delta\nu$ is small and $\epsilon(\nu)$ is nearly constant, this becomes

$$(NEP)^2 = \frac{4\epsilon}{\eta_{\rm MB}^2 \eta (1-\epsilon)^2} kTh\nu\Delta\nu \left[1 + \epsilon\eta \frac{kT}{h\nu}\right]. \tag{2.26}$$

This is the source power incident upon the atmosphere which will yield a signal to noise of 1. As the emissivity of the atmosphere increases, the required source power must also increase. Equation 2.26 differs from equation (8) of Phillips (1998) in that the BRE NEP is larger by a factor of $\sqrt{1/\eta_{\rm MB}}$.

Because the submillimeter atmospheric windows are not equally transmissive over such broad bands, and bandpass filters do not have top hat transmission functions,

the integral formulation is necessary for a more exact calculation. Performing this analysis yields values of $\lesssim 2$ times higher for a bandpass filter well matched to the 650/850 GHz atmospheric windows; for instance, a full analysis of SHARC predicts a BRE NEP of $\sim 2 \times 10^{-14}$ W/$\sqrt{\text{Hz}}$ at 850 GHz.

When measuring the noise of a bolometric detector in the laboratory, a conventional method is to use a reimaging system which observes a chopped hot and cold load. The electronic noise is then measured and translated into an NEP. However, because of the absorptive effects of the atmosphere and telescope, the noise measured in this fashion is an underestimate of the true BRE NEP by the factor:

$$\frac{BRE\ NEP}{Lab\ Noise} = \frac{\epsilon\sqrt{(1+\epsilon\eta\frac{kT}{h\nu})/(1+\eta\frac{kT}{h\nu})}}{\eta_{\text{MB}}\eta(1-\epsilon)} \tag{2.27}$$

At 350 GHz this factor is around 1, while at 650 and 850 GHz, it will typically be over 10.

In an optimal bolometer, the dominant source of temperature fluctuations will be in the rate of absorption and emission of photons, called the background limit. In the case of a practical submillimeter telescope observation, the detected radiation is typically dominated by the atmosphere emitting as a greybody (a blackbody of finite optical depth) into the telescope beam (Phillips 1998).

For the case of SHARC, we can estimate the values of the parameters in equation 2.26, using the atmospheric emissivity shown in Figure 2.7. We can separate the optical efficiency η into a foreoptics efficiency η_{optics} and a bolometer absorption efficiency η_{bolo}. With the appropriate values for SHARC at the CSO:

$$\eta_{\text{optics}} = 0.85, \qquad \eta_{\text{bolo}} = 0.35, \tag{2.28}$$

$$\Delta\nu_{850\text{GHz}} = 103\ \text{GHz}, \qquad \Delta\nu_{650\text{GHz}} = 68\ \text{GHz}, \tag{2.29}$$

$$\eta_{\text{MB:850 GHz}} \approx 0.30, \qquad \eta_{\text{MB:650 GHz}} \approx 0.40, \tag{2.30}$$

$$\epsilon \approx 0.6, \qquad T \approx 260\ \text{K}, \tag{2.31}$$

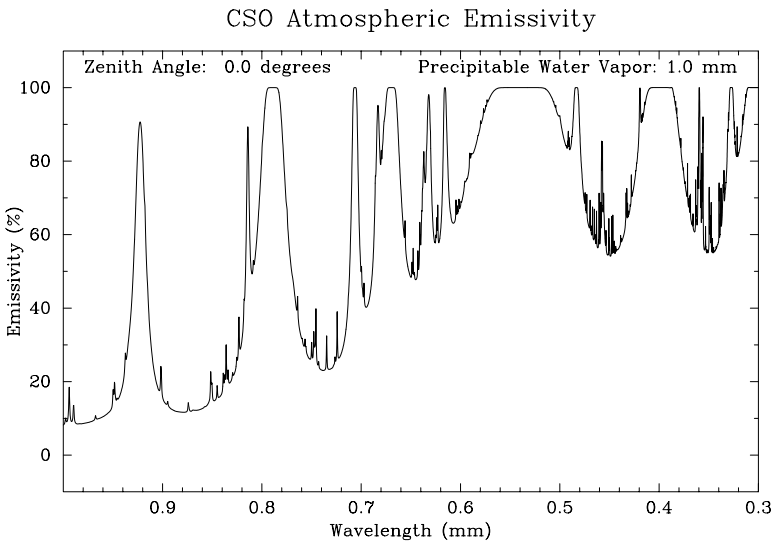

Figure 2.7 The submillimeter zenith atmospheric emissivity from Mauna Kea on a good night.

the calculated background NEPs in the two highest frequency submillimeter windows (referenced to a position above the atmosphere) become:

$$NEP_{650\text{GHz}} = 9.1 \times 10^{-15} \text{ Watt}/\sqrt{\text{Hz}} \tag{2.32}$$

$$NEP_{850\text{GHz}} = 1.6 \times 10^{-14} \text{ Watt}/\sqrt{\text{Hz}} \tag{2.33}$$

In computing these values, it is interesting to note that the contributions to the background NEP from the "particle" and "wave" terms (the additive terms in brackets in equation 2.26) are comparable at a frequency of 850 GHz: 1 and 1.1, respectively. With appropriate consideration, the NEP can be related to a useful observational parameter to the practicing astronomer, the Noise Equivalent Flux Density ($NEFD$). The $NEFD$ provides a measure of the expected integration time required to attain signal to noise ratio of 1 on a source with a given flux density in Janskys (Jy). The $NEFD$ can be estimated given the bandwidth of detection $\Delta\nu$ and the telescope geometric collecting area A:

$$NEFD = \frac{2\ NEP}{A\Delta\nu\eta_{\text{demod}}\eta_{\text{chop}}} \tag{2.34}$$

where η_{demod} is the electronic demodulation efficiency of the lock-in detection process

and $\eta_{\rm chop}$ is the mechanical efficiency of the chopping secondary mirror beyond the factor of 2 explicitly introduced for standard optical chopping ($\sqrt{2}$ because the on-source time is half the total time, and $\sqrt{2}$ because the result is a differenced measurement).

In periods of good submillimeter transparency on Mauna Kea (about 20% of the time), ϵ can be as low as 0.6 across most of the 350 and 450μm filter bands. Under these conditions, with $A = 85$ m^2, $\eta_{\rm demod}\eta_{\rm chop} = 0.58$, the background-limited $NEFD$ becomes:

$$NEFD_{650\rm GHz} = 0.53 \text{ Jy}/\sqrt{\rm Hz}, \tag{2.35}$$

$$NEFD_{850\rm GHz} = 0.62 \text{ Jy}/\sqrt{\rm Hz}. \tag{2.36}$$

However, because ϵ varies with frequency within the filter bandpass (increasing near the edges and at several significant absorption lines as can be seen in Figure 2.21), equation 2.26 must be integrated properly over frequency. The resulting background-limited $NEFD$s can easily become a factor of 2 higher than those listed in equations 2.35 and 2.36. In addition, correlated sky noise not removed by the optical chopping technique will raise the $NEFD$ further.

The background-limited $NEFD$ available to broadband bolometric detectors can be compared to that of the current generation of high frequency heterodyne receivers (e.g., Kooi et al. 1994). Using the Dicke radiometer equation (Kraus 1986), a system noise temperature of 1000 K, a bandwidth of 1 GHz, and the same telescope efficiencies listed above, the background-limited $NEFD$s are 9 and 12 Jy/$\sqrt{\rm Hz}$ at 650 and 850 GHz, respectively. The advantage of a broad bandwidth is clearly evident in this comparison.

2.3.3 Coupling Light into Bolometers

Because photoconductive detectors are not available beyond a wavelength of $\sim 200\mu$m, continuum detectors used in the submillimeter range have traditionally been composite bolometers. A composite bolometer consists of a separate thermistor physically attached to a radiation-absorbing substrate which is suspended from the cold bath

by leads of low thermal conductance (e.g., Nishioka, Richards & Woody 1978). Due to the crowding of suspension leads, it is difficult to construct a closely-packed array of composite bolometers, even for a one-dimensional array. In addition, the low absorptivities of the bolometers have typically required the use of compound parabolic concentrating horns and integrating cavities in order to collect light over a sufficient diameter in the focal plane and deliver it to the bolometer (Winston 1970; Hildebrand 1982). At the same time, these horns, commonly referred to as Winston cones, limit the solid angle of ambient radiation viewed by the detectors. In a similar vein, straight-sided conical horns can be used to produce nearly Gaussian beam profiles with the appropriate horn aperture chosen to deliver high efficiency (Cunningham & Gear 1990; Kreysa et al. 1993). In both cases, however, the large horn input diameter ($d \sim 2F\lambda$) conflicts by a factor of 4 with the goal of Nyquist sampling of the highest spatial frequencies available in the focal plane pattern of a large aperture submillimeter telescope ($d \sim F\lambda/2.5$). The image plane filling factor is then about 1/25.

On the other hand, during the last decade it has become possible to construct monolithic bolometer arrays using microelectronic fabrication techniques (Moseley, Mather & McCammon 1984). In a monolithic bolometer array, the substrate and thermal/mechanical leads are etched from a silicon wafer. The thermistor and electrical leads are ion-implanted directly into the silicon substrate. This technology allows large bolometers (~ 1 mm) to be manufactured in very densely packed linear arrays or fairly densely packed two-dimensional arrays from a single silicon wafer. The closely-packed pixels allow an optical configuration which Nyquist samples the spatial frequencies available in the focal plane along the linear dimension of the array.

The problem then becomes absorbing the incident light. The broadband absorption of far-infrared radiation by Silicon is poor since it is very transparent and has a high refractive index (Loewenstein, Smith & Smith 1973). For instance, a 10μm thick silicon wafer absorbs only 0.1% of the light passing through it at 100μm wavelength, in addition to an averaged 20% loss from reflection at normal incidence. However, with a proper impedance-matching coating, 50% absorption can be achieved (Clarke

et al. 1977). A typical procedure is to coat the back side of the silicon with a thin layer (~ 1100Å) of bismuth, which yields a reasonable resistance per square[4]. If one can tailor the bismuth impedance to be $Z_0/R_\square = n - 1$, where $Z_0 = 377\Omega/\square$ and $n = 3.4$ is the refractive index of silicon, then the absorption will be frequency independent. A simple calculation then yields the absorption:

$$A_{\rm bolo} = \frac{4(n-1)}{(n+1)^2} = 50\% \tag{2.37}$$

which applies for $R_\square = 157\Omega/\square$. A complete calculation of the absorption for a typical span of frequencies and surface resistivities is shown in Figure 2.8. It is evident that at frequencies below 1 THz, anything thinner than a relatively thick 10μm silicon bolometer will be optimized with the $157\Omega/\square$ bismuth coating. At shorter wavelengths, however, Fabry-Perot resonance can enhance the absorption substantially. Unfortunately, tuning the thickness of the coating is difficult: the bismuth resistance will depend on the surface quality of the silicon and the temperature and vacuum during evaporation. Furthermore, the final coating cannot be measured electrically, since the DC resistivity deviates from the IR resistivity. The coating impedance will also change when cooled.

Assuming one can produce a reasonably good bismuth absorber, the large size of the pixels enables them to efficiently absorb radiation with $\lambda \leq d_{\rm pixel}$. As at optical and infrared wavelengths, there is no inherent throughput limitation to this type of coupling (Richards & Greenberg 1982). This characteristic eliminates the earlier requirement for a concentrating cone, and indicates that the pixels can be optically coupled in the focal plane with geometric optics techniques.

2.3.4 Optimizing Your Bolometer

We can now choose optimum parameters for a bolometer with intrinsic noise given by equation 2.16 for observations with a background noise given by equation 2.26.

[4]The conventional term "resistance per square" is the resistance of a planar material with an aspect ratio of 1:1. As you change the aspect ratio, the effective resistance seen by a photon incident on the center of the material must change.

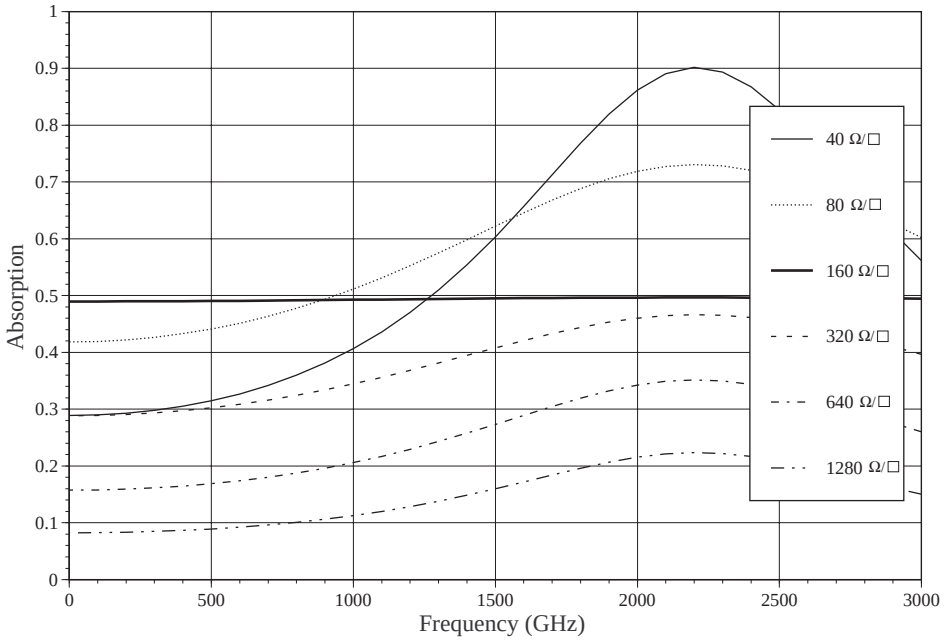

Figure 2.8 Absorption of a second-surface-coated Bismuth-on-Silicon bolometer as a function of frequency. The curves are for a 10μm thick Silicon sheet; scaling to 1μm would require the frequency scale to be multiplied by 10.

In order to attempt an optimization, we must confine ourselves to considering a semiconducting bolometer with dielectric mechanical supports. At low temperatures, the thermal conductance $G(T)$ is well represented by

$$G(T) = G_0 T^3 \ [G] = \mathrm{W/K} \tag{2.38}$$

where G_0 depends on the geometry of the mechanical supports connecting the bolometer to the heat sink. I shall further select a good bolometer resistance to match the available FET amplifiers. Since the voltage noise of a good FET[5] is $V_N \sim 1\mathrm{nV}/\sqrt{\mathrm{Hz}}$ and the approximate current noise is $I_n \lesssim 10^{-16}\mathrm{A}/\sqrt{\mathrm{Hz}}$, the optimum bolometer resistance is $R \gtrsim 10^7\Omega$.

Picking up from equation 2.10 for the responsivity S of the bolometer with small bias current I:

$$S \simeq \frac{IR\sqrt{T_0}}{2GT^{3/2}} \quad \therefore \quad S^2 \simeq \frac{I^2R^2T_0}{4G^2T^3} \tag{2.39}$$

The optimum amount of bias power I^2R has been solved (Grannan, Richards & Hase 1997) and found to be $\sim GT/10$, although it can be varied by at least a factor of two with negligible effects on the sensitivity. Substituting this value and equation 2.38, we can write

$$S^2 \simeq \frac{RT_0}{40G_0T^5}. \tag{2.40}$$

Here we recall equation 2.16 for the total intrinsic noise. Substituting for the responsivity, we obtain:

$$\begin{aligned} NEP^2_{\mathrm{bolometer}} \ = \ & 4kT^5G_0 + G_0^2T_N^2 \\ & + \frac{40G_0T^5(4kTR + 4kT_LR_L(R/(R+R_L)^2) + V_N^2 + R^2I_N^2)}{RT_0} \end{aligned} \tag{2.41}$$

To get a feeling for the magnitude of the NEP, we note that an optimized bolome-

[5]The NJ132L from InterFET Inc. is such a device.

ter operated at pumped liquid ^{3}He temperatures and below, as is now the case for millimeter and submillimeter telescopes, has $T_0/T \sim 100$ (Griffin & Holland 1988). This is easily seen if we consider the dimensionless sensitivity A:

$$A \equiv \left| \frac{T}{R} \frac{dR}{dT} \right| = \frac{1}{2} \sqrt{\frac{T_0}{T}} \sim 5 \tag{2.42}$$

The dimensionless sensitivity has an optimal range of $3 \lesssim A \lesssim 10$ (Mather 1984a), where the lower bound is to achieve a low NEP and the upper bound is the maximum readily realized in semiconducting bolometers. The thermal conductance G_0 can be estimated by requiring that the optical power on the bolometer should not drive it substantially warmer than the temperature of the heat sink; therefore, $G_0 \sim \frac{2P}{T^4}$ where P is the optical power received by the detector. The Rayleigh-Jeans limit of Planck's law can be used to determine P in the case of a high-background environment (external to the cryostat) of emissivity ϵ at temperature $T_{\rm bkgnd}$:

$$P = 2\epsilon\eta_{\rm optics} k T_{\rm bkgnd} \Delta\nu, \tag{2.43}$$

where the detector receives a single mode with $\Delta\nu$ bandwidth with an optical efficiency of $\eta_{\rm optics}$. Then the optimum value of G_0 becomes

$$G_0 = 4\epsilon\eta_{\rm optics} k T_{\rm bkgnd} \Delta\nu / T^4. \tag{2.44}$$

Cooled JFETs have low enough current noise such that when multiplied by the bolometer resistance, the voltage noise typically dominates. Furthermore, the voltage noise of a transistor is typically chosen to be less than the Johnson noise, as shown in Figure 2.9. We shall hereafter assume that the bolometer temperature and resistance are designed or chosen such that the amplifier noise is smaller than the Johnson noise. We shall also assume that the load resistor is at temperature $T_L = T_{\rm sink}$, and that $R_L \simeq 10R$ so that the Johnson noise of the load resistor is negligible. Finally, we assume that the refrigeration system is implemented such that the temperature fluctuations in the signal band – as defined by the optical chopping frequency and

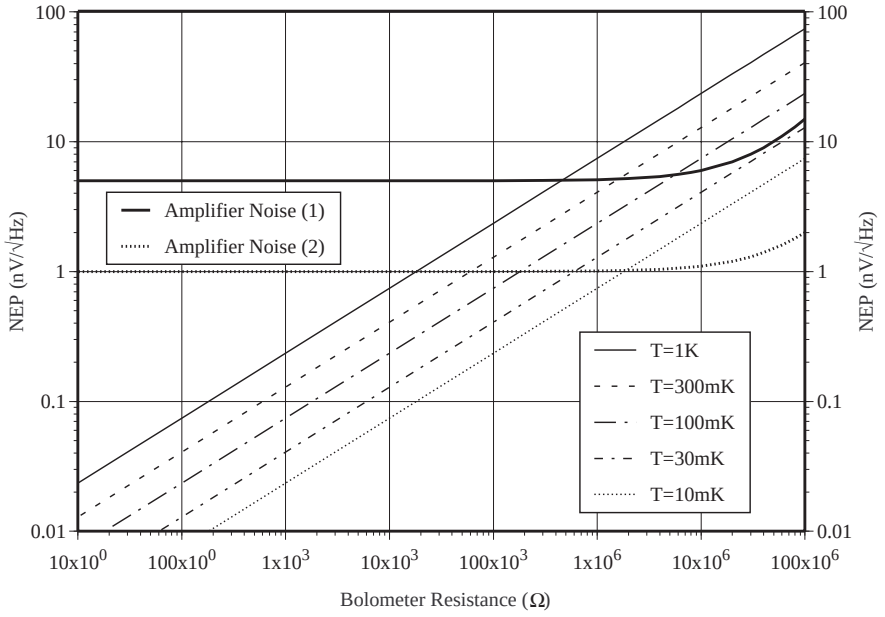

Figure 2.9 Comparison of the Johnson noise at several temperatures and JFET amplifier noise in a bolometer circuit. Amplifier (1) corresponds to a voltage noise of $5\text{nV}/\sqrt{\text{Hz}}$ and a current noise of $10^{-16}\text{A}/\sqrt{\text{Hz}}$; amplifier (2) has a voltage noise of $1\text{nV}/\sqrt{\text{Hz}}$ and a current noise of $10^{-17}\text{A}/\sqrt{\text{Hz}}$.

the integration time constant – are small. Now the NEP can be rewritten as:

$$NEP^2_{\text{bolometer}} \sim 4kT^5G_0(\text{phonon}) + 2kG_0T^5(\text{Johnson}). \tag{2.45}$$

$$\simeq 6kT^5G_0 \tag{2.46}$$

By inserting the various efficiency factors, we can refer this value of the NEP to the power of a source above the atmosphere. That is, the *astronomical* source power which would be required to yield a unity signal-to-noise ratio, rather than the power absorbed by the bolometer:

$$NEP^2_{\text{bolometer}} \sim \frac{6kT^5G_0}{\eta^2_{\text{MB}}\eta^2_{\text{optics}}(1-\epsilon)^2} \tag{2.47}$$

We now substitute in for the conductance in the above equation to obtain:

$$NEP^2_{\rm bolometer} \sim \frac{24k^2T_{\rm bolo}T_{\rm bkgnd}\Delta\nu\epsilon}{\eta^2_{\rm MB}\eta_{\rm optics}(1-\epsilon)^2} \tag{2.48}$$

To compare the bolometer NEP to the background limited NEP, we recall equation 2.26:

$$(NEP_{\rm atmos})^2 = \frac{4\epsilon}{\eta^2_{\rm MB}\eta_{\rm optics}(1-\epsilon)^2}kT_{\rm bkgnd}h\nu\Delta\nu\left[1+\epsilon\eta_{\rm optics}\frac{kT_{\rm bkgnd}}{h\nu}\right]. \tag{2.49}$$

We recall equation 2.48, and find that the optical efficiencies cancel out to reveal:

$$\frac{NEP^2_{\rm bolometer}}{NEP^2_{\rm atmos}} \sim \frac{6kT_{\rm bolo}}{h\nu}\left[1+\epsilon\eta_{\rm optics}\frac{kT_{\rm bkgnd}}{h\nu}\right]. \tag{2.50}$$

For most applications, the second term in the brackets is small, so in order to achieve a value of $NEP_{\rm bolometer} \ll NEP_{\rm atmos}$, we must lower the temperature sufficiently such that

$$\lambda_{\mu\rm m}T_{\rm bolo} \lesssim 240. \tag{2.51}$$

Thus, for an instrument required to operate in a background-limited mode with a wavelength as long as 500μm, we must achieve a bolometer temperature of lower than 500mK, which is most easily reached using a ^{3}He refrigerator operating at a temperature near 300mK.

2.3.5 Monolithic Bolometer Array

The bolometer array detector used in SHARC is a monolithic silicon package of linear geometry developed and fabricated by Harvey Moseley, Christine Allen, Brent Mott and their colleagues at NASA/GSFC. Similar arrays have been constructed there for instruments flown on the Kuiper Airborne Observatory (KAO[6]) (Moseley 1995) and

[6]The KAO was a $\sim$ 1m telescope in an airplane, allowing atmospheric transparencies close to those achieved in space, but with a somewhat higher thermal background. It was grounded in 1994,

the Advanced X-ray Astronomical Facility (AXAF) (Moseley, Mather & McCammon 1984; McCammon et al. 1987; McCammon et al. 1989). Each array originates on a silicon wafer large enough to supply several arrays. The arrays are fabricated using conventional wet etching photolithographic techniques, as illustrated in Figure 2.10. Because the final dopant concentration is difficult to predict, a series of wafers are doped by increasing amounts in order to obtain wafers with a range of values of R_0 and T_0. Specifically, the SHARC array came from the MIRA-2 series (Mid-InfraRed Array) of 1 by 24 pixel arrays. Each pixel is 1mm by 2mm, a geometry shown schematically in Figure 2.11. After cutting and mounting the arrays, a measurement of R_0 and T_0 determines their optimum operating temperature for photon sensitivity. In order that the background photon noise dominate over thermal noise in the detector during broadband submillimeter continuum observations, the SHARC array was selected to operate at 0.3 K.

A thin bismuth film (110 nm) is applied as an absorber to match the impedance of free space. Each of the 24 pixels is rectangular (1 mm by 2 mm by 12μm[7]) with four thermally-conducting support legs of size 2 mm by 12μm by 14μm wide (see Figure 2.12).

The total thermal conductance of the four legs at 0.3 K was measured to be 10^{-9} W K^{-1} (Wang et al. 1996). The heat capacity of the silicon plus the bismuth coating plus the arsenic contact leads is estimated to be approximately 2×10^{-12} J K^{-1}. These two values yield a time constant of $\sim$ 2 millisecond which is much shorter than the typical telescope beam switching rate of several Hz. Four of the pixels were damaged during fabrication, so there are 20 working pixels in the current version of the camera.

2.3.6 Cryogenics and Electronics

The bolometer array has been installed in a ^{3}He cryostat backed by liquid ^{4}He and liquid N_2 cooled shields. The brief cryostat operating manual, the "Pundit's Guide" to

to be replaced by SOFIA, a 2.5m telescope in a 747, which will be operational in the early 2000s.

[7] To get a feel for these dimensions, consider that a nickel is about 2mm thick, and that a human hair is about 75μ in diameter.

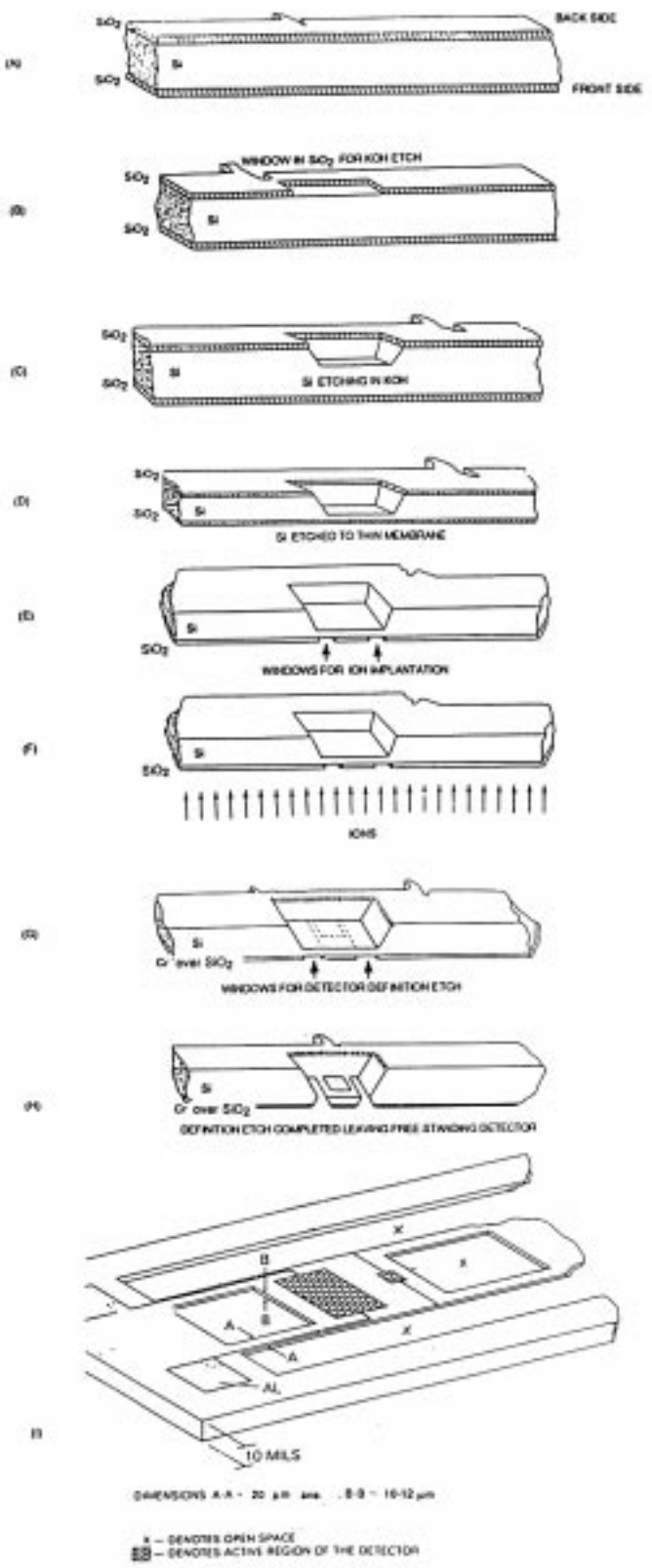

Figure 2.10 Diagram of the steps in processing of a silicon wafer into a monolithic silicon bolometer.

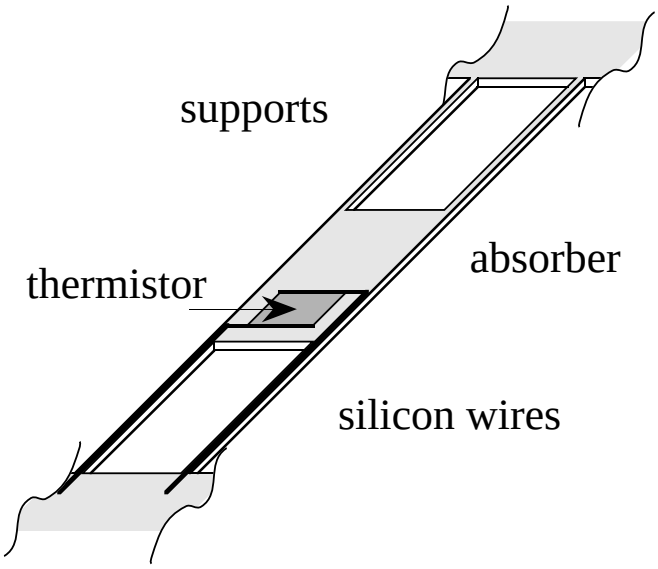

Figure 2.11 Schematic diagram of a single monolithic silicon bolometer element.

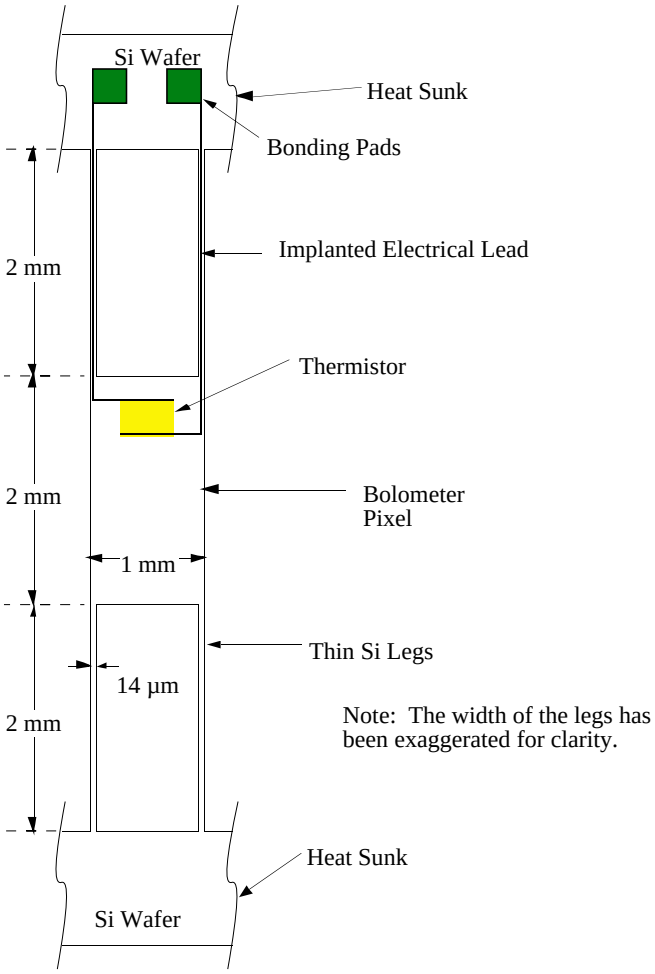

Figure 2.12 Dimensions of a single monolithic silicon bolometer element. The thickness (in the direction perpendicular to the page) is roughly 12μ, but depends on the etching.

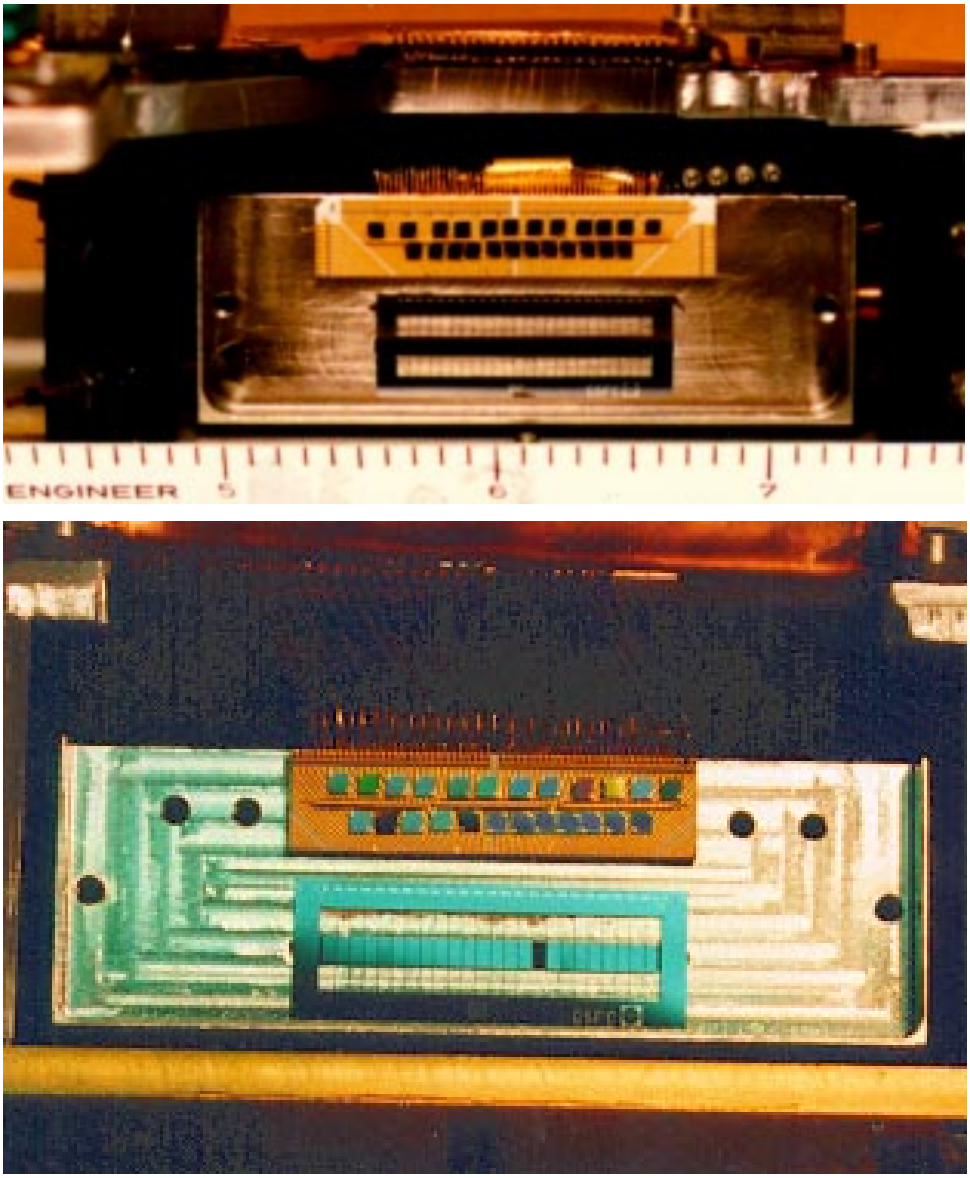

Figure 2.13 (TOP) A close-up photograph showing the configuration of the bolometer array detector in SHARC. The minor divisions on the ruler at the bottom are tenths of inches. Just above the ruler is the rectangular Invar block cooled to 0.3 K and suspended from the rest of the housing via Kevlar cords for thermal isolation. Mounted in two rows near the top of the Invar block are the square 30 MΩ load resistors. Below these resistors lies a rectangular annulus of silicon with all of the interior etched away except for the bisecting line of pixels and their narrow support legs. Manganin leads (0.001 inch diameter) under tension bridge the thermal stages near the top and carry the signals to the JFET stage mounted nearby. (BOTTOM) The current array in SHARC. This photograph has been expanded to show the pixels' support legs more clearly. Near the middle is the dead pixel (note #16 is missing). When in operation, the array is aligned vertically, with the left-hand edge nearer the Zenith.

SHARC, is provided in Appendix A. The first stage electronics are three eight-channel FET packages which operate at 130 K inside the dewar and serve as impedance transformers of the signal. Located just outside the dewar are three four-layer, eight-channel, battery-powered, low-noise preamplifier boards. These boards yield a nominal gain of 500 from 3 to 300 Hz, with a high gain setting of 8000 used for most astronomical sources. The amplified signals are subsequently sent to 16-bit A/D boards with a ± 3 volt range and a sampling rate of 1 kHz. The digitized signals are transferred via fiber optic cables to a digital signal processor (DSP) board inside a Macintosh Quadra 950 computer which performs digital lock-in detection at the chopping frequency. More detail on the readout electronics can be found in section 7.7 and in Wang et al. (1996).

2.4 Optical Design

While most of the optical design was carried out by Todd Hunter, I helped in several ways, including the design of the optical filtering, the optical alignment, the development of a spray-to-apply submillimeter black coating, and the calculation of the geometric optics pixel efficiency. In designing the optics for the CSO's camera, we considered all of the optical elements beginning with the telescope itself, including the CSO tertiary relay optics, which I shall describe briefly and are discussed in detail by Serabyn (1997). Much of the description of the optical design is described in detail by Hunter, Benford & Serabyn (1996).

2.4.1 Tertiary Relay Optics System

Most of the recent and future CSO instruments are mounted at the Cassegrain area of the CSO where a large unvignetted field of view ($\sim 3'$ square) is available (Serabyn 1994; Padman 1994). However, because of the large focal ratio (f/12.36) at the Cassegrain focus, the focal plane plate scale of $1.65''$/mm implies that our millimeter-sized detectors would oversample the $\sim 10''$ diffraction pattern of the telescope by a large factor. A system of relay optics was designed to reduce the focal ratio to a

value (f/4.48) more suitable for illuminating such detectors with an appropriate-sized diffraction spot. The relay optics provide dual mounting ports, each of which can support an instrument cryostat simultaneously. A flat steering mirror selects one of the two ports and an off-axis ellipsoidal mirror creates a 32 mm diameter tertiary image of the primary mirror that lies 50.8 mm above the instrument mounting surface. The tertiary image of the sky then lies 142.2 mm beyond the image of the primary mirror. This design allows the window of downward-looking cryostats to be placed before the image of the primary, which can then be used as a cold aperture (Lyot) stop.

2.4.2 Design Requirements for the Camera

In order to make an optically efficient, high performance imaging instrument, we considered several optical design constraints. These include the detector and cryostat geometry and cryogenic needs.

2.4.2.1 Optical Geometry Constraints

Due to the process used to manufacture our bolometer arrays, the detector elements are closely spaced. Twenty-four array elements of size 1 mm by 2 mm are aligned with their long axes adjacent as shown schematically below in Figure 2.14, after Wang et al. (1994). There is only a small ($\sim$ 15 μm) gap between the pixels so that the filling factor of the array is 98.5% over its full extent of 24mm by 2mm. In order to provide approximately Nyquist sampling of the sky brightness distribution along the array axis, the plate scale of the final image must provide $\sim$ 2 pixels per telescope diffraction beamsize in the focal plane. To simplify the optical design, the camera is optimized for operation only in the 350 and 450μm atmospheric windows, although an 870μm filter is available for observing in inclement weather. If we restrict our consideration to 400μm wavelength, a single, fixed plate scale is sufficient for the optical design. In order for the CSO diffraction beamsize at 400μm ($9\farcs7$) to be roughly 2 mm in diameter at the focal plane (1.22Fλ $\sim$ 2 mm), we need to illuminate the detectors

with an f/4.10 beam. Thus, the camera optics must transform the f/4.48 relay optics input beam to f/4.10. With a 10.4 meter telescope of effective tertiary Cassegrain focal length 40.41m at f/4.0, the plate scale is $4''.97$ per mm. Hence, the 24 mm bolometer array subtends $\approx 120'' = 2'$ on the sky.

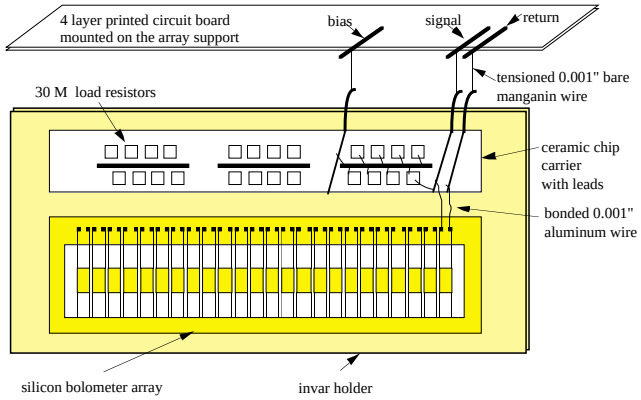

Figure 2.14 Schematic diagram of the configuration of the SHARC detector array.

2.4.2.2 Optical Quality Requirement

In addition to the plate scale requirement, the quality of the final focus must be excellent. This must be true not only for the central detector, but also for off-axis detectors, even when the chopping secondary slews the image another $2'$ off-axis. We use the Strehl ratio as our figure of merit, defined as the fraction of the power falling within the diffraction-limited spot, or in the words of Virginia Trimble (Trimble & McFadden 1998), "the ratio of peak intensity to what you would get if diffraction were the only thing against you." We chose the requirement that the Strehl ratio would be > 0.95 for secondary chop angles $< 2'$ off-axis) over a field of view as large as the foreseeable detector arrays. To allow for expansion of future arrays in the perpendicular direction, the optics should therefore maintain high quality imaging over a square field $2' \times 2'$, or about 25 by 25 mm in the focal plane (a maximum radius of ~ 18 mm). Also, the distortion of the focal plane from barrel, coma, pincushion,

and field curvature must be negligible with respect to the diffraction beamsize; i.e., the separation of two point source images must be linear across the $2'$ field with respect to the angular separation of the sources on the sky.

2.4.2.3 Thermal Requirements

Background radiative loading of the cold bolometer array must be reduced to an absolute minimum ($<$ 10pW, to be less than 10% of the expected optical power) by proper cold stops, baffling against stray light, and bandpass and blocking filters. With the exception of a selected bandpass originating from the small solid angle of the sky targeted by the bolometer array, all ambient temperature radiation entering the dewar window must be rejected by filters at liquid nitrogen and helium temperatures. Because they emit as blackbodies, the stops and camera optics must lie within the helium work space of the cryostat.

2.4.2.4 Spectral Requirements

In order to be scientifically useful, the wavelengths of light received by the camera must be well known. Therefore it is imperative to be able to select a narrow band ($\delta\lambda/\lambda \sim 0.1$) where the response to an optical signal is large, but is small outside this band. For the camera, a reasonable criterion is that the total out-of-band power received by the detectors must be small ($<$10%) of the in-band power received.

2.4.2.5 Geometrical Requirements

The total volume available to the camera optics is limited by the size of the available helium work space of the cryostat. The diameter of the cold plate is 25 cm while the height of the helium stage radiation shield is limited to $\sim$ 50 cm due to mechanical rigidity concerns and cryogen usage. In effect, these sizes limit the focal lengths of the optical imaging components. It is best to minimize the use of folding mirrors so as to reduce the number of optical elements, which simplifies the optical alignment and reduces the effect of stray light in the system.

2.4.3 Early Camera Designs

In order to match the above requirements for the camera, several reimaging designs were explored. All of the optical designs were modeled on a VAXStation with the software package CODE V (Optical Research Associates) in order to determine ray clearance and measure image quality. The models included all of the optical elements beginning with the CSO primary surface so that the distortions introduced by the relay optics could be adequately accounted for. Three general configurations were explored: standard spherical lenses, a pair of off-axis paraboloidal mirrors, and a single off-axis ellipsoid. The first design, using silicon lenses, was rejected due to high reflection and absorption losses and the necessity for fold mirrors. The paraboloid design yielded high Strehl ratios, but a field curvature of $\sim 20''$ across $120''$ and a variable plate scale were deemed too poor optically.

2.4.4 Camera Optical Design

The breakthrough came with the realization by Gene Serabyn and subsequent verification by Todd Hunter that larger mirrors can be used if we include the relay optics ellipsoidal mirror in our concept of the "camera." Since the tertiary relay optics already incorporate one off-axis ellipsoid, potentially superior imaging quality is then obtainable by using a second off-axis ellipsoid in the camera optics. By orienting the ellipsoids properly, the second mirror can be used to compensate for the coma aberration introduced by the first. Furthermore, because a far-field focus and primary image lie between two ellipsoids, cold aperture and field stops can be provided while requiring only one of the ellipsoidal mirrors to be inside the cryostat (see Figure 2.15).

Ellipsoids are an interesting optical element, resulting from the fact that they have two foci. Rays emergent from one geometrical focus of the ellipse are reflected by the surface to the second focal point. Moving the source closer to the surface will displace the image further along the reflected chief ray. In this way, the input and output focal ratios can be chosen in many possible positions in the ellipse. This

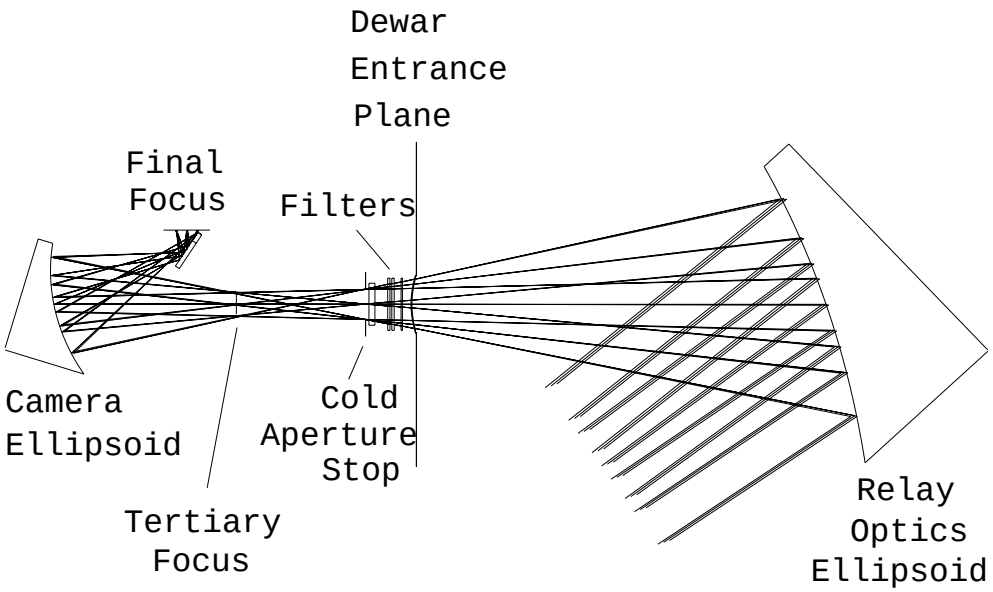

Figure 2.15 Layout of the ellipsoidal mirror re-imager used for SHARC. The large ellipsoidal mirror is part of the CSO relay optics and the rest of the optics are cryogenically cooled. The rays plotted span an angle of 2′ on the sky.

effect provides flexibility in using elliptical mirrors in which degradation of the on-axis image is traded for improvements in the off-axis imaging. There should exist a best compromise between moving closer on-axis and deflecting the image; such a compromise was determined for the CSO relay optics. The existing relay optics ellipsoid has an eccentricity of 0.7606, an input focal length of 3500 mm, and an output focal length of 547.5 mm. The object distance (the Cassegrain focus) is 1803 mm.

Since the camera optics require a small focal ratio change from f/4.48 to f/4.0, focal displacement was again exploited in designing the camera optics ellipsoid. In this case, a shorter focal length was necessary in order to fit the mirror into the available cryostat length. A focal length of the generating ellipse of 300 mm was chosen. Distortion becomes the most significant aberration at focal lengths less than 300 mm, and the Strehl ratios also degrade. A deflection angle of 22.5° was required on the ellipsoidal surface in order to yield sufficient clearance for the detector assembly at the focal plane. Determined from CODE V optimization, the ellipsoid giving best imaging in this configuration has an eccentricity of 0.4129, an input focal length of

200.0 mm and an output focal length of 178.5 mm. For two 24-pixel linear arrays separated by 10 mm (a feasible expansion of the current detector), the required size including an extra 10% for clearance is only 13.5 by 8.4 cm which easily fits on the 25 cm diameter cold plate. This mirror was constructed for SHARC at Caltech by Ricardo Paniagua with an automated milling machine performing successive circular cuts about the axis of the ellipsoid followed by hand polishing to an optically smooth finish.

From analysis in CODE V, the ellipsoidal mirror configuration described above provides excellent diffraction-limited imaging (Strehl > 0.95) in the final focal plane across a $2' \times 2'$ square field even with the secondary mirror chopping up to $4'$ throw on the sky. The Strehl ratios as a function of secondary chop angle at the field center, and ends of the array are plotted in Figure 2.16. Since the depth of focus $\sim F^2\ \lambda$ is ~ 6 mm, a small to moderate amount of field curvature is not a critical problem in this application.

Spot diagram footprints of the $2'$ by $2'$ focal plane are given in Figure 2.17. To envision the diffraction beam, these spot diagrams must be convolved with a spot size of $\sim$ 1.6 mm (at a wavelength of 350μm). There is essentially no distortion in direction along the array. A small distortion ($\sim 2''$ over $120''$) exists across the field in the direction perpendicular to the array, but it is negligible compared to the diffraction beamsize ($8''.5$ at the shortest operating wavelength of 350μm).

2.4.5 Optical Stops

Simply placing a reimaging mirror in a dewar does not a camera make. As shown in Figure 2.15, upon entering along the axis of the cylindrical cryostat, the relay optics deliver an image of the primary mirror 5.6 cm in from the dewar entrance along the converging f/4.48 beam. The tertiary focus lies an additional 14.2 cm beyond the primary image. After this focus, the beam re-expands to fill the cold ellipsoid. Upon reflection, the chief ray moves away from the dewar axis at 22.5° and is redirected by a small folding mirror onto the bolometer array mounted perpendicular to the helium

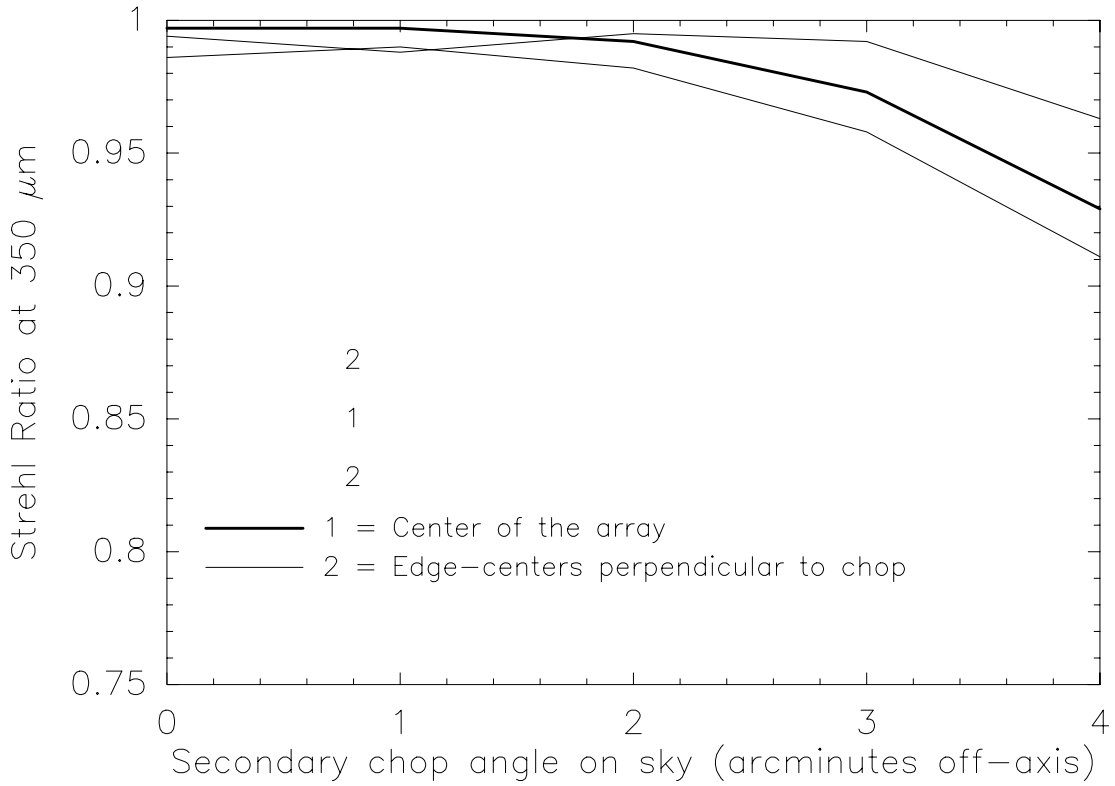

Figure 2.16 Strehl ratios across the 2′ field of view of the camera focal plane as a function of the secondary chopper angle. The solid and dashed lines represent, respectively, the center and edges of the current linear array (which is oriented in zenith angle). The graph shows the performance at the best composite focus of the three positions at each setting of the chopper.

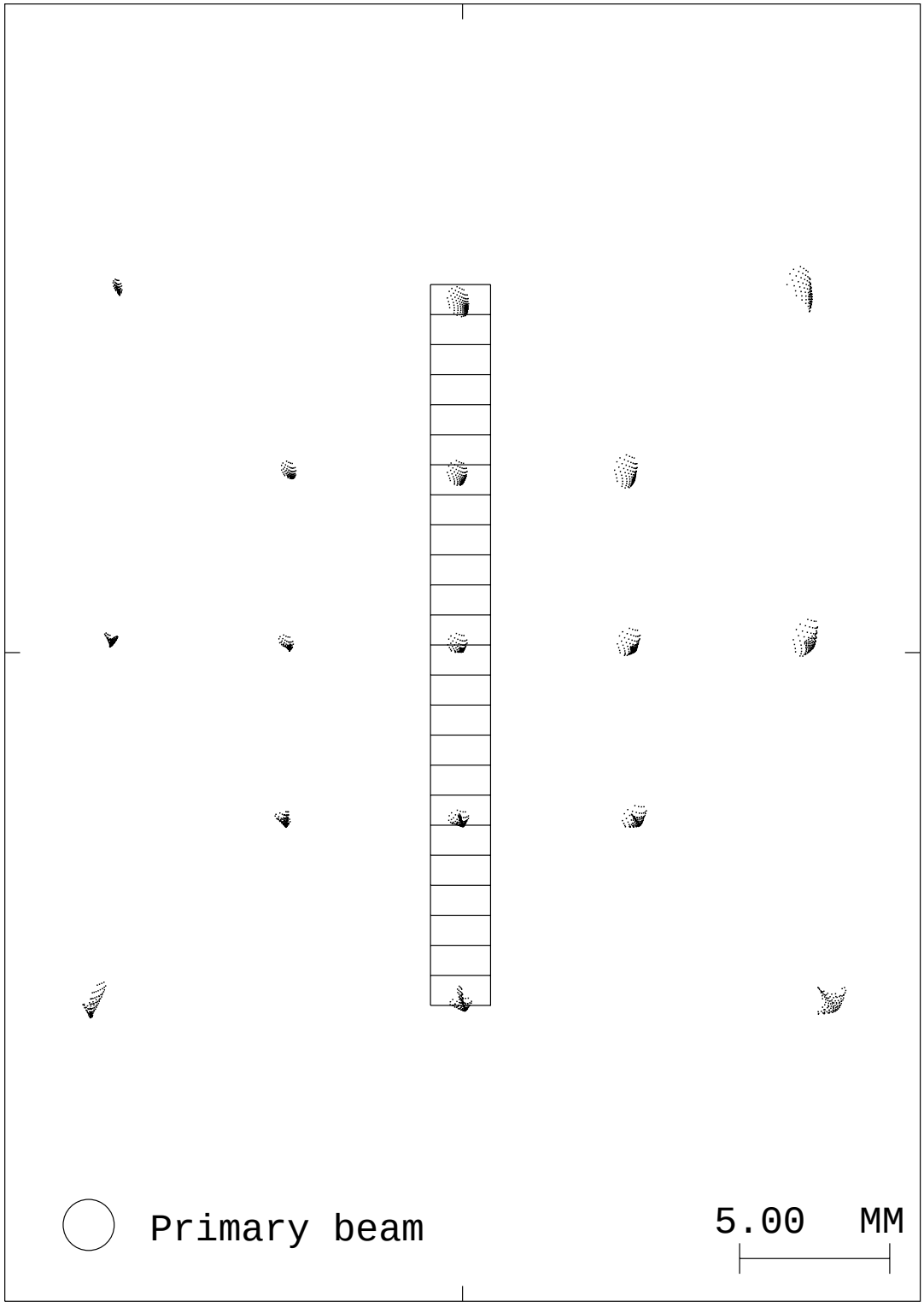

Figure 2.17 Spot diagram of the SHARC focal plane. The spots lie at the center, corners and edges of a $1'$ and a $2'$ square field, corresponding in the focal plane to 12 mm and 24 mm respectively. The diameter of the primary diffraction beamsize of $8''.5$ is shown.

work surface.

With direct illumination, as in any optical or infrared camera, the solid angle for light acceptance must be precisely defined. In our case, we wish to avoid hot spillover past the edge of the primary mirror by using a cold physical stop in the optics (Hildebrand 1986). For this reason, we place a 32 mm diameter cold aperture stop at the primary image to define the illumination pattern of the array pixels. This ensures that each pixel sees radiation originating only from the primary mirror. Scattered ambient radiation, which lowers bolometer sensitivity through loading and degrades the beam, must be prevented as much as possible from entering the optical path after the aperture stop. To achieve this goal, we completely surround the reimaging optics with absorptive baffling. A crucial part of this baffling is the field stop which lies at the tertiary focus. Together, these two stops define the total throughput of light from an astronomical object which is admitted to the detector. The field stop is a thin stainless steel plate with a rectangular slit machine-punched to match the scaled size of the bolometer array at the tertiary focus with 25% clearance. Because these elements limit the throughput of the source, they also limit the background radiation transmitted to the detector. However, since the stops lie beyond the optical filtering, both the aperture and field stop must be cooled to $T < 4$K in order to minimize the blackbody emission reaching the detector.

2.4.6 Mechanical Design

Because the optical design requires that the detector, aperture and field stops be completely enclosed in a light-tight baffle, a significant mechanical support structure is needed to support and fix these elements with respect to the ellipsoidal and flat mirrors and the detector array. The mechanical support was designed to be symmetric about a plane in order to simplify the optical arrangement as much as possible and to allow for accurate positioning of the mirrors and stops. Thus the optical system is reflection-symmetric about the plane of the chief ray.

In order to minimize the required dewar length without adding extra folding mir-

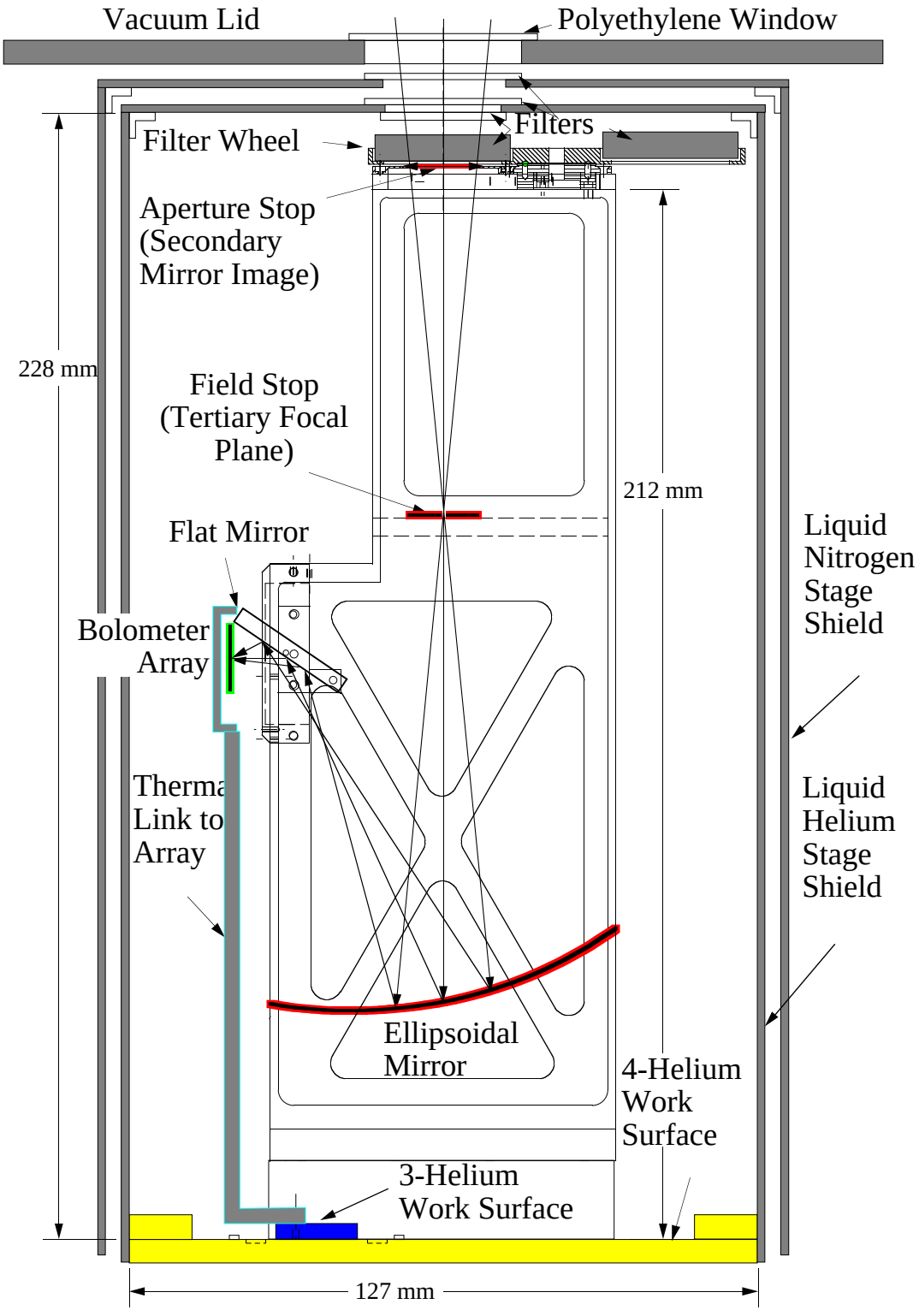

Figure 2.18 A scale drawing of the cryostat optics with dimensions in units of millimeters.

rors, the ellipsoidal mirror was placed as close as possible to the helium work surface with the chief ray aligned with the entrance window along the dewar axis (see Figure 2.18). All of the optical elements from the aperture stop to the array are fixed in place. Thus there is no alignment to perform other than the lateral positioning of the bolometer array housing which is accomplished by means of a sliding surface. As all mirror surfaces are polished to be reflective in visible light, this adjustment is performed with a diffuse white light source.

To insure proper alignment of the aperture stop and field stop with the ellipsoidal mirror, the support structure attaches directly to the mirror with self-consistent stop locations defined by tapped holes machined to specification. This arrangement also allows easy removal of the entire optics assembly including the detector housing, either with or without the ellipsoidal mirror. All sides of the main optics assembly are covered with 0.625 mm OFHC copper baffle sheets to block stray light from reaching the detectors. The inside surfaces are blackened (as described in section 2.4.8) to reduce the propagation of stray light.

2.4.7 Filtering

Optical filtering is crucial in a submillimeter camera for two main reasons, the most fundamental of which is to define the bandpass of the observations. In the case of our high sensitivity, low temperature detectors, it is further necessary to limit the radiative heat load.

Because of the broad wavelength response of the detectors, far-infrared through optical radiation must be rejected by a stack of blocking filters. The filters are mounted at the entrance to the liquid N_2 and He-cooled shields of the cryostat. In order to accurately determine the amount of filtering needed to meet our requirements of high efficiency and low total out-of-band power transmission, I have developed a filter modeling program. Given the transmissivity and absorptivity of a variety of filter materials as a function of both temperature and wavelength, a solution to any geometry of filter transmission can be found through simple numerical methods. A beam

originating in a blackbody at room temperature is assumed, then propagated through a customized filter stack consisting of elements at different temperatures. The resulting power emergent from the end of the filter stack is then determined, which yields the effective transmission of the filter stack. The model of the filter stack chosen for SHARC is shown in Figure 2.19. The constraint for SHARC's filter stack is that only temperatures of 77K and 4K can be used. With this requirement, a filter stack with $\sim 40\%$ transmission is possible, with most of the total transmitted power from in-band wavelengths.

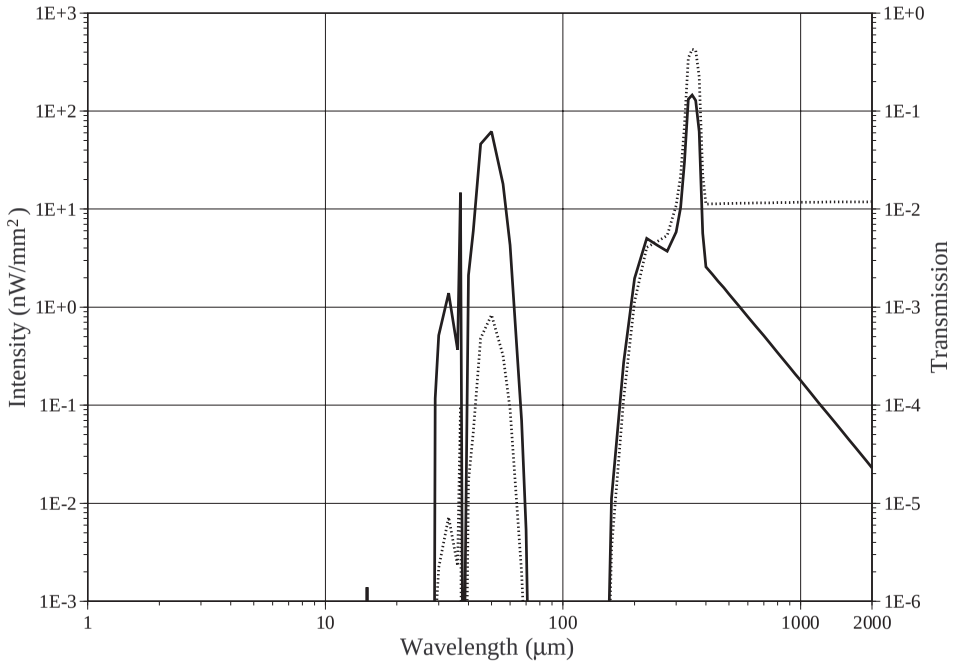

Figure 2.19 Modeled transmission (dotted line) and total intensity (solid line) in unity bandwidth for the SHARC filter stack.

A schematic of the filter arrangement is shown in Figure 2.20. First, the vacuum window of the cryostat is a 1.0 mm thick disk of high density clear white polyethylene which provides long-term durability and water impermeability (Bussone 1989) coupled with low loss at submillimeter wavelengths (Birch, Dromey & Lesurf 1981; Stützel, Tegtmeier & Tacke 1988; Birch 1990; Kawamura, Paine & Papa 1996). The thickness is chosen such that the regions of best transmission coincide well with the 350μm and 450μm atmospheric windows. Next, a 1.5 mm thick quartz filter

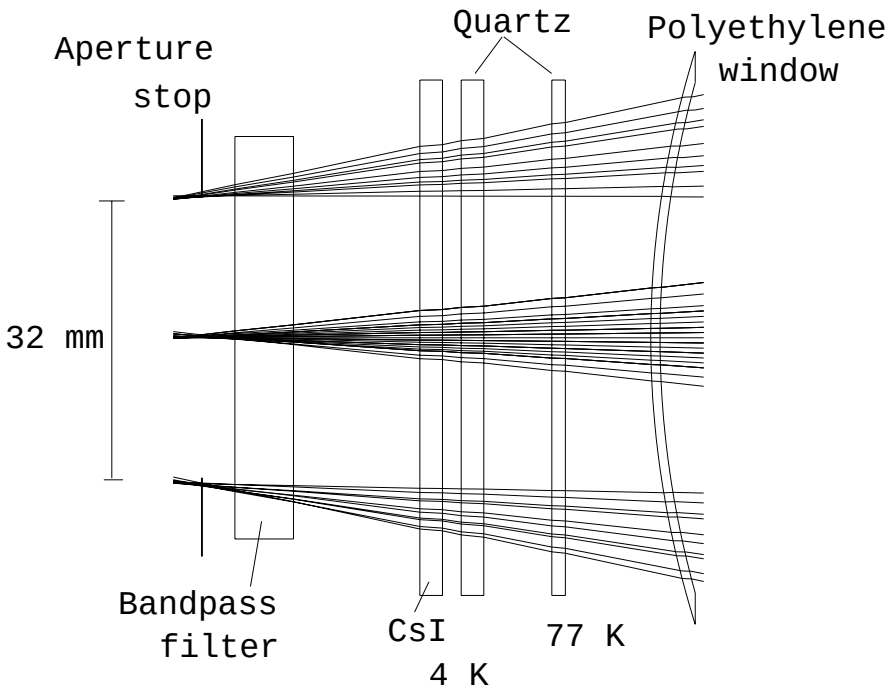

Figure 2.20 The filter arrangement at the entrance of the SHARC cryostat. The filters (and thicknesses) are: high density clear polyethylene vacuum window (1.01 mm); quartz (1.5 mm) with black polyethylene AR coating; quartz (2.5 mm) with a diamond scattering layer on the top and a black polyethylene AR coating on the bottom, Cesium Iodide (2.5 mm) with a clear polyethylene AR coating on both sides; metal-mesh bandpass filter (6.5 mm). The bandpass filters lie in a manually-driven filter wheel with space for four different filters.

with a black polyethylene antireflection coating on both sides is mounted at the window of the nitrogen shield lid. At its operating temperature of about 90K, quartz is essentially opaque to radiation between 5 and 40μm (Eldridge 1991), becoming transmissive at longer wavelengths (Randall & Rawcliffe 1967; Loewenstein, Smith & Smith 1973; Bréhat & Wyncke 1997). The black polyethylene also serves to block optical and near-infrared radiation shortward of 5μm (Blea et al. 1970) A second long-wavelength-pass quartz filter, this one 2.5 mm thick, is mounted as the window of the helium shield. On its top surface is a diamond scattering layer opaque from about 5 to 100μm (Infrared Laboratories; Armstrong & Low 1974). Again, a black polyethylene antireflection coating is applied on the bottom surface of the quartz to block the near-infrared photons originating from the 77 K filter and shield. At this point, power from light shortward of 100μm is completely blocked by a factor of $> 10^3$.

The quartz filter on the helium shield lid is followed by a 2.5 mm thick crystalline cesium iodide (CsI) filter with clear polyethylene anti-reflection coating (Josse, Gerbaux & Hadni 1993) on both sides. The clear polyethylene also serves to protect the CsI from hydration, as it is quite hygroscopic. As an ionic crystal, CsI exhibits a reststrahlen reflective band in the far-infrared ($\sim$100-170 μm) due to lattice vibrations (Mitsuishi, Yamada & Yoshinaga 1962; Yamada, Mitsuishi & Yoshinaga 1962; Eldridge 1991). At 4 K, the CsI filter yields nearly zero transmission of incident radiation between 80 and 150μm while rising to 90% transmission at 350μm (Hadni et al. 1962; Vergnat et al. 1969). There may be a small peak of transmission at about 50μm, where neither the quartz nor the CsI block efficiently. The height of this peak is then sensitive to the scattering and absorption caused by the diamond and black polyethylene, neither of which is a well-specified quantity. The model in Figure 2.19 represents a worst-case assumption.

The bandpass of the camera is defined by one of a trio of narrow-band ($\lambda/\delta\lambda \sim 10$) metal mesh filters mounted on a liquid He-cooled filter wheel which is located just above the aperture stop. According to measurements made by the manufacturer (Cochise Instruments), the bandpass filters effectively block all wavelengths

$\lambda > 150\mu$m except, of course, for their specified bandpass at 350μm, 450μm, or 870μm. However, they do typically have a few percent transmission at the third harmonic, which corresponds to the absorption band of the CsI filter. The bandpass filter wheel is a 152 mm diameter geared circular plate with four round milled slots that can hold metal-mesh bandpass filters of 46 mm clear aperture. The filter wheel is mounted at the top of the optics chamber just below the lid of the He temperature shield. A drive shaft for the filter wheel extends from the bottom of the dewar up along the inside of the helium shield to a 9.5 mm diameter pinion. The pinion drives the filter wheel with a 16:1 turn ratio with manual operation from the outside. A blankoff filter (painted black as described in section 2.4.8) with a thermometer was also installed to enable testing. The thermometer verifies that the bandpass filters, the last filtering element before the bolometers, are kept below 5K.

The SHARC filter transmission curves are plotted in Figure 2.21 along with the atmospheric transmission over Mauna Kea as a function of frequency. The bandwidths and effective frequencies of the filters are also listed for sources with different submillimeter spectral indices $2 + \beta$, where $F_\nu \propto \nu^{2+\beta}$. Blackbodies correspond to $\beta = 0$, whereas dust grains with power-law emissivities generally correspond to $\beta = 1$ or 2.

2.4.8 Submillimeter Black Paint

As in all sensitive cameras, it is necessary to minimize unwanted reflections and scattered light inside the optical path. Since the detectors are similar in size to the telescope diffraction spot, scattered light reaching the pixels will cause apparent spreading of the beam shape. In addition, with cryogenic bolometers sensitive to broadband radiation, all of the low temperature surfaces must be highly absorptive so that only emission from low temperature materials can be seen by the detector. To ensure this property, we coated the inner surfaces of the optics support and baffles with a specially-mixed "submillimeter" black paint. The far-infrared properties of various types of optical black coatings have been measured (Smith 1984; Pompea et

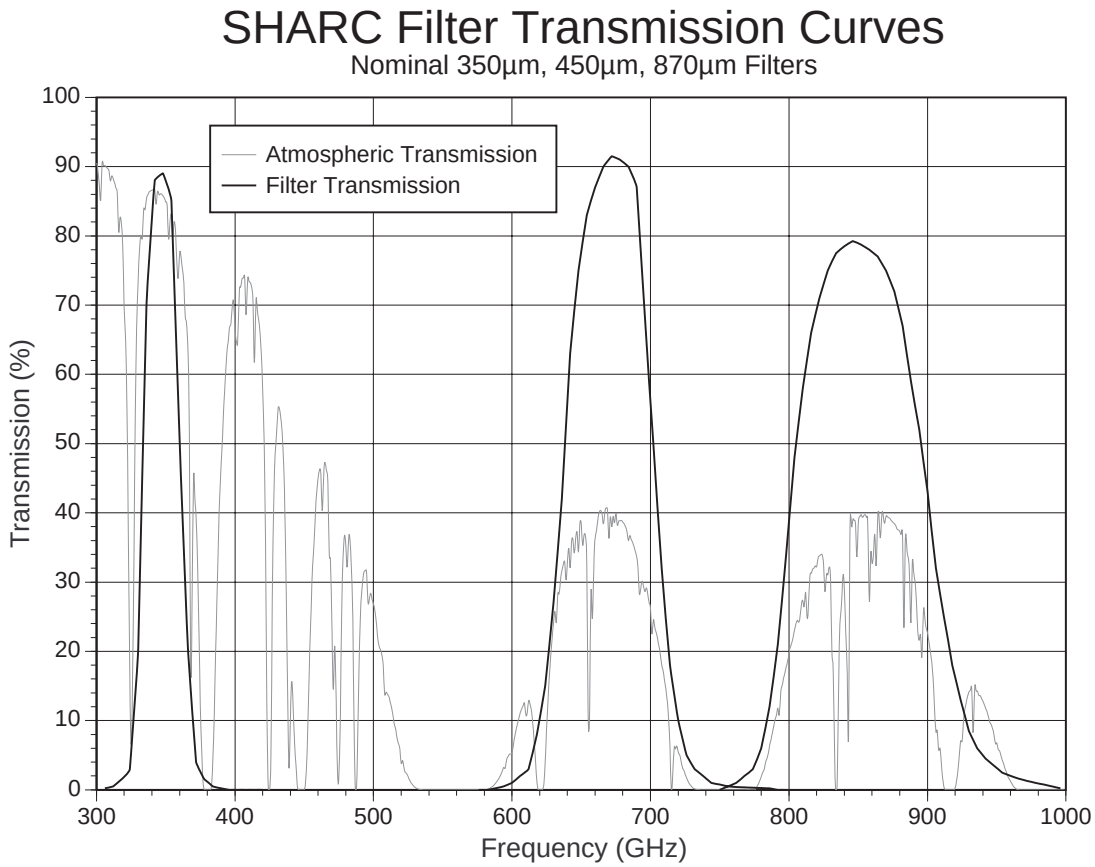

870 μm Filter:	450 μm Filter:	350 μm Filter:
Effective Wavelength (Frequency):	Effective Wavelength (Frequency):	Effective Wavelength (Frequency):
871.4 μm (344.3 GHz) with β = 0	448.9 μm (668.3 GHz) with β = 0	353.2 μm (849.4 GHz) with β = 0
870.6 μm (344.6 GHz) with β = 1	448.3 μm (669.2 GHz) with β = 1	352.4 μm (851.3 GHz) with β = 1
869.7 μm (344.9 GHz) with β = 2	447.6 μm (670.2 GHz) with β = 2	351.7 μm (853.0 GHz) with β = 2
Bandwidth 74.2 μm (29.4 GHz)	Bandwidth 45.5 μm (67.9 GHz)	Bandwidth 42.6 μm (102.9 GHz)

Figure 2.21 The SHARC filter transmission curves superimposed on the atmospheric transmission over Mauna Kea during good weather ($\tau_{225\mathrm{GHz}} = 0.05$). The computed bandwidths and effective frequencies of the filters are also listed for different submillimeter spectral indices $2 + \beta$.

al. 1984). The base of the mixture we chose is a black polyurethane paint, Aeroglaze Z-306 (Lord Corporation Industrial Coatings 1995). A 2-part wash primer was applied to the roughened metal surfaces prior to the black topcoat. Tests of the submillimeter absorptivity of the paint, performed by inserting metal samples coated with a layer of thickness ~ 0.1 millimeter into the beam of the 650 GHz heterodyne receiver at the CSO (Kooi et al. 1994), revealed that the paint absorbs less than 10% of incident submillimeter radiation.

To improve the absorption of the paint, we mixed varying amounts of absorbing or scattering substances into the topcoat base. Varying ratios of carbon black powder (Fisher Scientific 1995) and both hollow and solid glass beads with a variety of diameters (Potters Industries 1995) were mixed into the paint. Carbon black effectively absorbs optical and infrared radiation while dielectric glass beads of radius a extend the attenuation to longer wavelengths $\lambda < 2\pi a$ (Sato et al. 1989). Generally, it was found that the greater the mass of glass, the better the absorption.

The final paint we chose used a mixture of carbon black powder 3% by volume filtered to remove large congealed clumps that could clog the air brush used to apply the paint and solid glass beads 10% by volume with a distribution of diameters from 50-200 microns. A significant amount of Aeroglaze 9958 paint thinner ($\sim$25% by volume) was also added to lower the viscosity of the total mixture sufficiently to be sprayed with the air brush. Multiple coats were required to obtain sufficient thickness of ~ 0.3 mm (0.010 inch). With these additives, the submillimeter absorptivity of the metal samples was raised to $\sim 65\%$. The paint adheres well to aluminum and copper surfaces of thickness over 0.5 mm (0.020 inch). When applied to thinner sheet metal, the paint will buckle and peel under repeated thermal stress.

2.4.9 Field Rotation

The current observing method employed with millimeter and submillimeter bolometers relies on rapid beam switching on and off the source in order to subtract sky emission. At the CSO, this switching is accomplished by chopping the secondary

mirror in azimuth at a rate of $\simeq 4$ Hz. Raster scan "On-The-Fly" maps are acquired by scanning the telescope in azimuth at successive elevation settings and numerically restoring the individual dual beam pixel measurements to a single beam image in celestial coordinates. Because this rapid scanning method works well to suppress correlated sky fluctuations, the preferred observing mode for SHARC is to align the array axis in the elevation direction and have the CSO secondary mirror chop in azimuth. Deep integrations are performed by repeated mapping scans.

A new observing mode has recently been made available which maintains a fixed alignment of the linear detector array along a specified position angle on the sky by rotating the dewar on its mounting plate as the telescope tracks. However, because the optics contain off-axis elements, this rotation varies the imaging performance. Best imaging is obtained when the two ellipsoidal mirrors lie with the concave directions pointing away from each other and in the same plane, as discussed above. However, to align the linear bolometer array with the elevation direction, the dewar must be rotated 14° with respect to this configuration, in order to compensate for an angular offset introduced by the two flat mirrors of the relay optics, which send the beam out of the symmetry plane of the primary mirror. The imaging quality across the bolometer array remains excellent in the elevation-aligned configuration, despite the small misalignment of the mirror axes. A plot of the Strehl ratios as a function of dewar rotation is given in Figure 2.22. The three lines plotted represent Strehl ratios at the center and ends of the array as in Figure 2.16 and with the secondary mirror rotated off-axis by $2'$ on the sky. The allowance for dewar rotation was not a major concern during the original design given our customary fixed orientation observing mode. However, the Strehl ratios across the central line of the focal plane remain above 0.8 over $\pm 60°$ of position angle, and because sources are typically observed only within a few hours of local transit time (with parallactic angles between $\pm 45°$), this range of performance is satisfactory for observations relying on field de-rotation. To determine what range in RA, Dec, and Hour Angle of objects is usefully trackable, the plots in Figure 2.23 illustrate the range of parallactic angles exhibited by a source as a function of its declinations. Only sources passing through the Zenith present

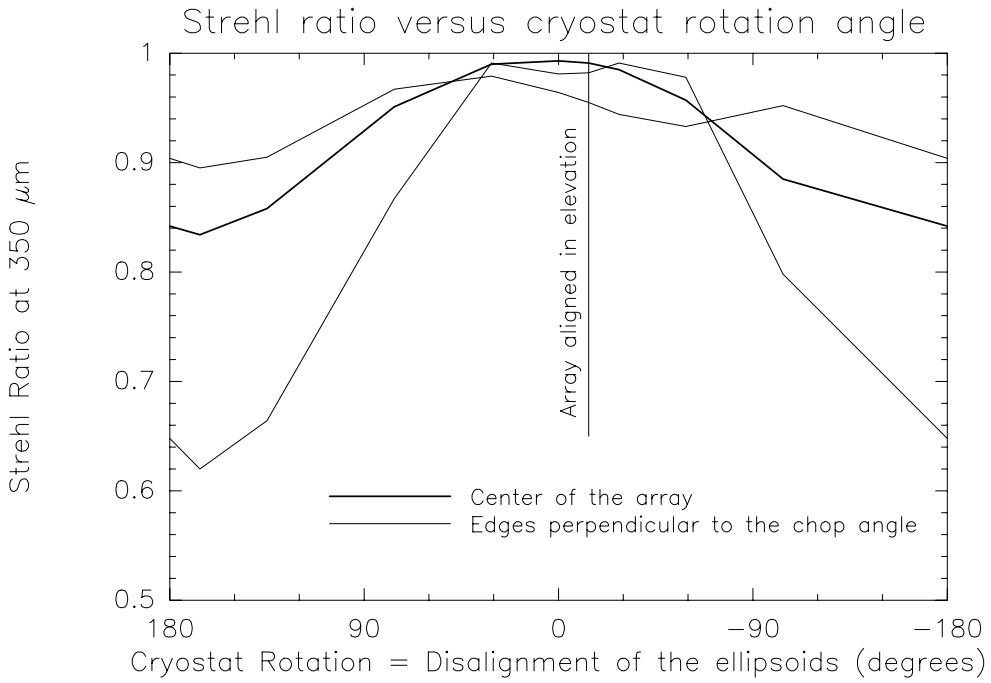

Figure 2.22 The Strehl ratio of the camera optics across the 2′ field of view in the focal plane as a function of the dewar rotation angle. The heavy and solid lines represent, respectively, the center and edges of the linear detector array. The results plotted are with the secondary mirror rotated off-axis by 2′ on the sky.

difficulties.

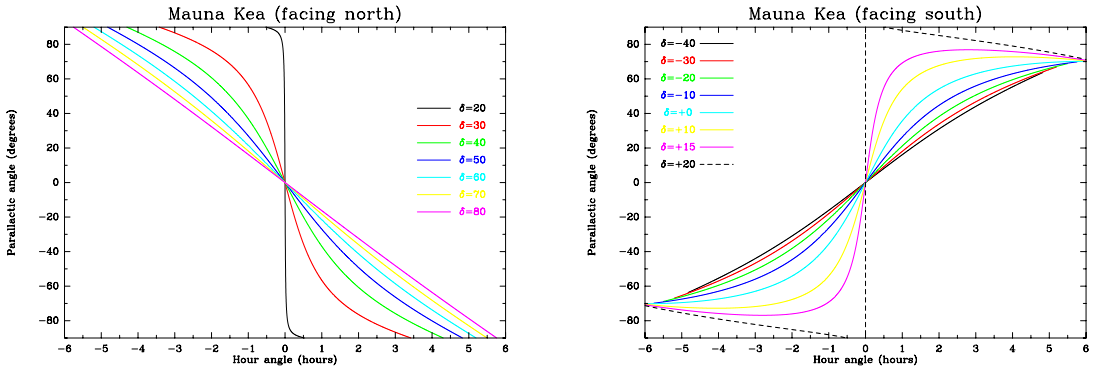

Figure 2.23 The parallactic angle for a source at the specified Dec and Hour Angle for (left) sources transiting in the north (with an assumed 180° flip in the sense of the array) and (right) in the south.

2.5 Optical Performance

Shown in Figure 2.24 is a beam map of SHARC obtained at the CSO at a wavelength of 350μm. The map, obtained in November 1998, is constructed from a sum of 11 SHARC scans (about 10 minutes of telescope time) recorded while the telescope was driven across the planet Mars (diameter $5\farcs07$) at a rate of $2\farcs0$ s^{-1}. The array was stepped in elevation by $3\farcs0$ in order that neighboring pixels sample a slightly different portion of the beam on each pass. The finest possible pixel scale recorded is then $0\farcs5 \times 1\farcs0$, with an on-source integration time of roughly 0.31s per pixel. In order to achieve an excellent signal-to-noise ratio (Mars, even though bright, is seen at a theoretical signal-to-noise ratio of about 280 in this integration time), the final map was binned into $3''$ pixels, which quadruples the signal-to-noise ratio. The secondary mirror was chopping $28''$ in azimuth (the scan direction) at 4.098 Hz during the scans. The solid contour levels are 1,2,5,10-90% by 10% of the peak flux density; the dashed contour is -1%. At this level, the map consists of only real emission and processing artifacts. A 1/10th scale bar indicates the orientation of the array during the map. The circle at lower left is roughly diffraction beamwidth convolved with the planetary

disk, 10″. This should be compared with the observed half power level, indicated by the heavy contour. Some beam smearing in the scan direction is observed, a residual of the imperfect chopping secondary throw. Some residual from poor knowledge of the chopper throw is observed as the sharp dropoff in the contours to the lower right.

Because of the small angular size of Mars ($\theta = 5\farcs07$ on 25 November 1998) and its large flux density, it is a good source with which to measure the beam pattern. The brightness temperature ($T_{\rm B}$) of Mars varies with wavelength and time, and was calculated to be 211 ± 1K at the time the map was made (Stapelfeldt, private communication).

Thus, the expected blackbody flux density from Mars at 350μm (849 GHz) can be computed from the Planck function:

$$F_\nu = B_\nu(T_{\rm B})\Omega = \frac{2h\nu^3}{c^2\left[\exp\left(\frac{h\nu}{kT_{\rm B}}\right) - 1\right]}\frac{\pi\theta^2}{4} = 2.009 \times 10^{-23}\ {\rm J\ m^{-2}\ s^{-1}\ Hz^{-1}} = 2009\ \ {\rm Jy}. \tag{2.52}$$

Because SHARC uniformly illuminates the secondary mirror, the response to a point source should be an Airy pattern. With a 10.4-meter telescope operating at 350μm, the theoretical full-width at half-maximum (FWHM) of the main lobe of the Airy disk is $7\farcs2$. The under-illumination of the primary by the secondary widens the CSO's Airy disk slightly, while its central obstruction of roughly 12% (linear) narrows it slightly (Schroeder 1987). In the case of the CSO, these effects virtually cancel each other, so they are neglected here. If we convolve the $7\farcs2$ FWHM Airy disk over the area of the rectangular detector, the expected half power beamwidths become $9\farcs4$ along the long axis (azimuth) by $8\farcs0$ along the short axis (elevation).

Strip scans were extracted from the map of Mars by cutting in the azimuth and elevation directions (Figure 2.25). Fitting an Airy pattern to the image of Mars yields a size of $9\farcs4$ in azimuth by $9\farcs2$ in elevation, close to the expected size. However, the low level wings of beam pattern evident in the contour plot are not well fitted by the single Airy-like components because at this short wavelength, the surface roughness of the CSO primary and secondary mirrors degrades the imaging performance. Surface

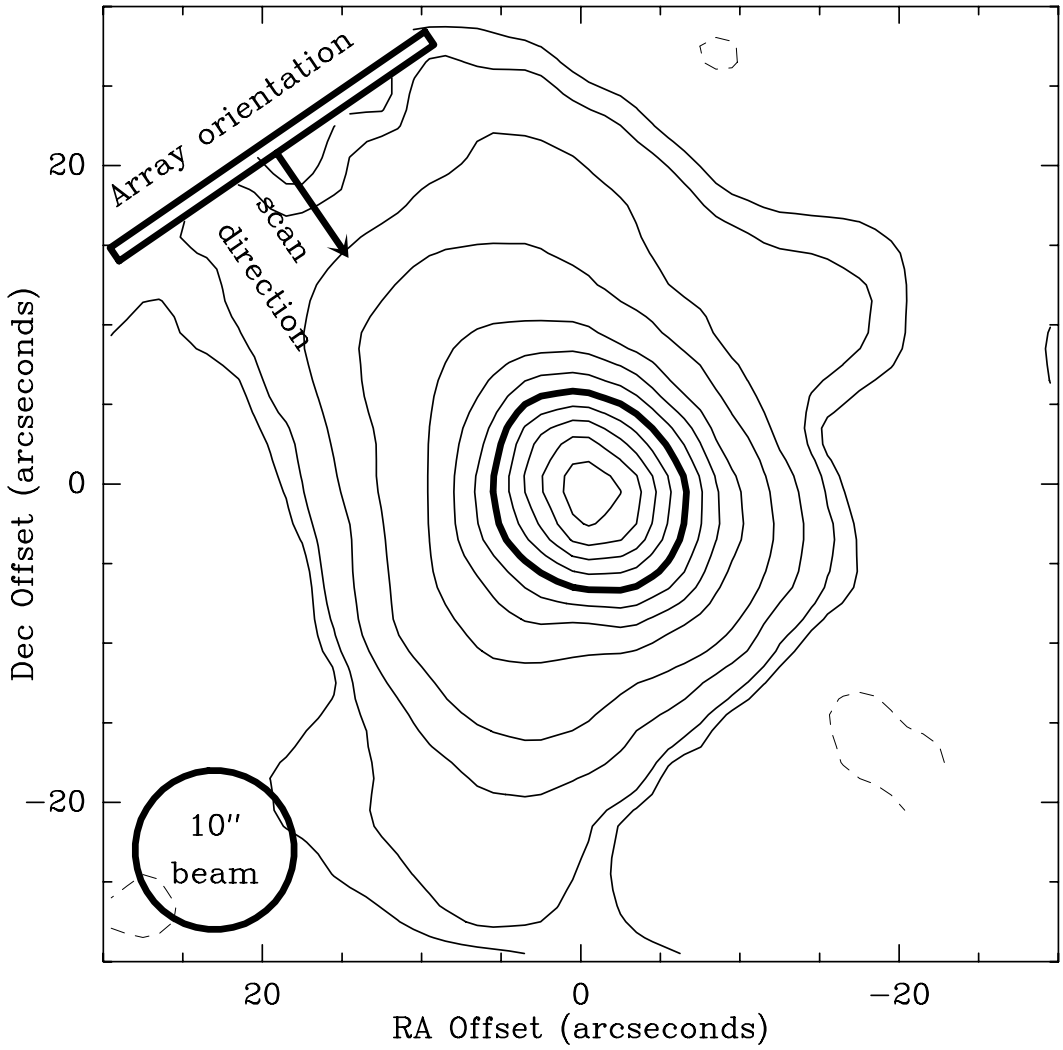

Figure 2.24 A CSO/SHARC beam map at 350μm constructed from a sum of 11 SHARC scans (about 10 minutes of telescope time) recorded while the telescope was driven across the planet Mars (diameter 5.″07). The solid contour levels are 1,2,5,10-90% by 10% of the peak flux density. The dashed contour is −1%, and a 1/10th scale bar indicates the orientation of the array during the map. The heavy contour is the half-power level, which can be compared to the circle at lower left, which is roughly the convolved beamsize, 10″. Some beam smearing in the scan direction is observed, a residual of the imperfect chopping secondary throw. Some residual from poor knowledge of the chopper throw is observed as the sharp dropoff in the contours to the lower right.

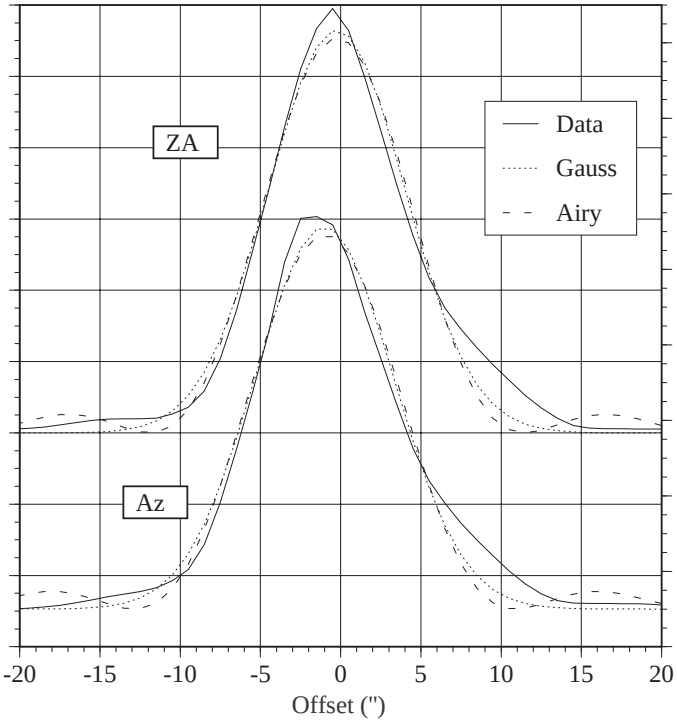

Figure 2.25 Strip-scans across Mars in Azimuth (lower trace) and Zenith Angle (elevation; upper trace). The best fit Airy and Gaussian functions are shown as dashed and dotted lines, respectively.

inaccuracies (on the scale of $\sim \lambda/20$), flexure, obstruction from the feed legs, defocus and decenter of the secondary divert a portion of the flux into sidelobes, called the telescope error pattern, which can have a complex shape. We attempt to account for this error pattern by fitting the azimuth and elevation cuts through the image of Mars with a Gaussian pattern. In this model, the fitted FWHM of the Gaussian function is $10\farcs2$ in azimuth by $10\farcs0$ in elevation.

In addition to maps, several pointed observations were made of Uranus at 350μm. In this mode, the array is held at a fixed position as it tracks the source, resulting in a very high signal-to-noise strip scan in zenith angle across the planet. Fitting a Gaussian beam to this scan results in a very good determination of the beamwidth. The results of these observations are given in Table 2.1. The theoretical Gaussian beamwidth of the CSO at 350μm is $8\farcs5$, which, when convolved with the bolometer size and the $\sim 3\farcs6$ planetary disk diameter, yields an expected Gaussian beamwidth of $9\farcs4$. Our measurement of $9\farcs7$ is 3% larger than the expected, quite a good agreement. This results in a Gaussian-deconvolved beamwidth of $9\farcs0$.

Table 2.1 SHARC beamwidth measurements using the Gaussian-fitted width of Uranus seen in pointed observing mode.

UT Date	Planet Diameter	Measured Size (″)	Deconvolved Beamwidth	Airmass
09 Jul 96	3.7	8.7 ±0.6	7.9	1.3
09 Jul 96	3.7	11.3 ±0.5	10.7	1.3
09 Jul 96	3.7	10.0 ±0.2	9.3	1.3
14 Jul 97	3.7	10.1 ±0.04	9.4	1.5
17 Jul 97	3.7	13.6 ±0.2	13.1	1.9
18 Jul 97	3.7	10.4 ±0.05	9.7	1.4
18 Jul 97	3.7	9.4 ±0.03	8.6	1.7
24 Oct 97	3.5	9.3 ±0.05	8.6	1.3
24 Oct 97	3.5	10.5 ±0.05	9.9	1.6
24 Oct 97	3.5	9.8 ±0.06	9.2	2.0
25 Oct 97	3.5	9.0 ±0.06	8.3	1.3
25 Oct 97	3.5	8.8 ±0.06	8.1	1.5
25 Oct 97	3.5	10.7 ±0.08	10.1	1.8
26 Oct 97	3.5	9.5 ±0.1	8.8	1.3
Mean		9.69 ±0.02	9.0	

2.6 Instrument Control System

Another portion of the work on SHARC which I was involved in is the development and implementation of the control software for the CSO bolometer array camera. Traditionally, the heterodyne spectrometers on millimeter and submillimeter telescopes have been managed by a small "backend computer" responsible for setting system parameters, and processing and delivering data to the main telescope computer. In the case of the continuum bolometer array system at the CSO, the instrument control computer, or "camera computer," is an Apple Macintosh.

2.6.1 System Requirements

The requirements of the software package for the CSO bolometer array camera were well defined at the outset of the project. First, the digital signal processing board (DSP) that performs digital lock-in of the bolometer signals was designed by engineers

at the Goddard Space Flight Center (GSFC) on a Macintosh NuBus board and thus required a Macintosh computer for operation. Second, much of the low level communication to the DSP board was written by Kevin Boyce (GSFC) in the LabVIEW (National Instruments) software package, a graphical programming language originally written for the Macintosh (but now available for Windows and Unix platforms). This body of code is known as the DogKAO (Digital Overseer and Go-between for the Kuiper Airborne Observatory). Rather than recreate this code, the control software was based on the existing LabVIEW architecture. Third, the main CSO control program, the User Interface Program (UIP), runs under the VMS operating system on a VAXStation 3100 or Alpha 300 located in the telescope building. The UIP exerts ultimate control over the 68000-based computer which controls the antenna computer as well as the Power-PC (Cetia) backend computer for the acousto-optic spectrometers used with the heterodyne instruments. For uniformity, it was decided in consultation with the CSO staff that the Macintosh computer that operates the DSP board would also be controlled by the UIP over Ethernet in a manner similar to the backend computer. Finally, since the Macintosh performs the actual data gathering, rapid communication with the antenna computer is required in order to know when the antenna has reached and acquired the selected position.

2.6.2 Hardware

The original control computer for SHARC is a Macintosh Quadra 950 computer outfitted with 24 Megabytes of RAM, a 1 Gigabyte hard drive and a SuperMatch 20 inch color monitor. The CPU in the Quadra 950 is a 33 MHz 68040 which currently runs LabVIEW version 3.0.1 (National Instruments). The extra memory was required to compile and run the complex virtual instruments (VIs) that communicate with the VAX and display the data on the Mac. Also purchased was a multi-purpose analog and digital I/O board, the AT-MIO-32 board from National Instruments, Inc., to allow the source acquisition status bit (the "acquire bit") and the telescope tracking status bit (the "idle bit") generated by the antenna computer to be monitored in real

time by the Macintosh software. The Quadra 950 allows space for 5 NuBus boards of which at least 2 are required: the DSP board and the I/O board. The extra slots available in the Quadra plus its high processor speed (second fastest of the NuBus line) influenced the decision to buy it. One important modification was needed to the mechanical housing of the Quadra itself. A second fan was added inside the case in order to increase the convective cooling rate of the microprocessors on the mother board and the NuBus boards in order to prevent the overheating problems frequently faced by visiting groups using Macintosh computers at the CSO.

In 1997, the Quadra 950 died and was replaced by a Centris 650, running at 25 MHz. It has only 3 slots, but serves well as the SHARC server. The repaired Quadra 950 is now in Pasadena as development for the upcoming Fabry-Perot bolometer spectrometer, which requires 3 additional boards for operation (chapter 8). It is also planned to be used with an upgraded camera with a larger number of pixels, SHARC II.

2.6.3 Communication between the Computers

The communication between the Macintosh and the CSO control computer (the VAXStation 3100) is modeled after the system configured for the heterodyne receivers by Ken "Taco" Young at the CSO. All of the communication occurs asynchronously using the Transmission Control Protocol/Internet Protocol (TCP/IP) implemented over a local Ethernet. Fortunately, the LabVIEW package supplies built-in VIs for TCP/IP communication. On the VAX side, the communication software is written in C in order to use the built-in TCP/IP socket routines for VAX C in the Multinet software package (TGV Inc.). To initialize observing with the bolometer array, the server VI must be started within LabVIEW on the Macintosh, which is configured as a Startup item upon reboot of the system. After initializing the display panel on the Macintosh, the server sits and waits for a connection to be made on the TCP/IP port 5000 of the Macintosh.

Sometime later, the observer issues the SHARC command in the UIP, which

spawns a client program called SHARC_CLIENT, written in VAX C. The client program creates two VMS mailboxes called TO_SHARC and FROM_SHARC which are used to transfer commands to and receive responses from the Macintosh (the server). The client also assigns a communications channel to a socket to be used for TCP/IP communication to the remote Macintosh and initiates a connection to port 5000 on the Macintosh. When the server receives this connection request, it opens the connection and returns a prompt character (>) which the client perceives as the "Connection OK" response. The client then enters a permanent loop waiting for a message to appear in the TO_SHARC mailbox (as will occur when SHARC-related commands are issued in the UIP). When a message appears, it searches for the termination character (~) and relays the message as a string to the Macintosh over TCP/IP, then waits for a return string message(s). When the client receives the prompt symbol (>), it stops waiting for further messages from the Macintosh and instead waits for or acts upon the subsequent mailbox message from other UIP commands.

Once the client has connected to the server, the Mac initiates three more TCP connections to the VAX: one for error messages (through port 5001 on both machines), event flags (port 5002), and data (port 5003). Multinet is configured on the VAX so that when the Mac sends a connection request to these ports, the appropriate server program will be initiated on the VAX. The connection to port 5001 starts the program SHARC_EVENT_FLAG_SERVER, port 5002 starts the SHARC_ERROR_SERVER, and port 5003 starts the SHARC_SCAN_WRITER. All error conditions on the Mac are sent to the error server process on the VAX and appear as messages on the UIP operator's terminal. The event flag channel is used to clear the backend wait (BEWAIT) status on UIP observing commands when the Mac has gathered the appropriate number of data. Finally, data are sent to the scan writer process along with some header variables when appropriate.

2.6.4 Data Display on the Macintosh

The two main data acquisition modes for bolometer observing at CSO are the scanning mode (known as OTF_MAP) and the pointed observation mode (known as CHOP_SLEWY). Both modes involve the use of the CSO's chopping secondary.

2.6.4.1 OTF_MAP

The term OTF_MAP ("on-the-fly" mapping) refers to the observing mode in which the antenna computer directs the telescope to scan across the source at a constant rate, usually in azimuth at a rate of a few arcseconds per second, while data is gathered "on-the-fly." Because rapid sampling of the lock-in signal allows for the best possible sky noise subtraction, we sample after each chop period of the secondary mirror which is the maximum rate possible. This method allows extended maps to be constructed more rapidly than with a series of pointed observations. The raw signal is sampled by the A/D system at 1 kHz and sent to the DSP via a fiber optic link. Performing digital lock-in detection, the DSP demodulates the data with a sine wave template function and reports a signal level at the chopping rate. The demodulated bolometer signals are displayed in real time on the Macintosh in the form of 24 separate strip chart graphs.

The basic display is modeled on the "Display Data" module written by Kevin Boyce of GSFC. As integrations are obtained they are sent back to the VAX over Ethernet in real time. The data are accumulated at the socket on the VAX and written to disk all at once at the end of each row of the map. This strategy has the advantage of requiring only a single open and close of the data file for each OTF_MAP row. The data consist of 4 byte integers in DSP units. The data header of each scan contains the scale factor for the proper conversion from DSP units to millivolts. The conversion from DSP units to actual voltage (post-amplification) is:

$$V(\text{volts}) = \left(\frac{\text{DSP units}}{32 \times 10^6}\right)\left(\frac{f}{c}\right)\left(\frac{750}{T}\right)2^{s-6} \tag{2.53}$$

where f is the chopping frequency in Hz, c is the number of chop cycles per integration

(usually 1), T is the unitless amplitude of the sine wave template (defaults to 750), and s is the right shift (in bits) applied to the data by the DSP (defaults to 6). The chopping frequency is generated on the DSP board in the Macintosh in the form of a 0 to 5 volt square wave and can take on quantized values satisfying the equation:

$$f(\text{Hz}) = \frac{1000}{n} \text{ where } 2 \leq n \leq 512. \tag{2.54}$$

The chopper throw is determined by the amplification and offset applied to the square wave signal by the chopping secondary control circuitry built by Martin Houde at CSO. Currently, the throw must be tuned manually. However, a simple closed-loop circuit has been designed and is being built that will interface with the I/O board in the Macintosh to enable it to automatically set and monitor the chopper throw (via the standard UIP command SECONDARY on the VAX).

2.6.4.2 CHOP_SLEWY

The term CHOP_SLEWY refers to the standard pointed observation combining two motions: constantly chopping the secondary mirror (at a few Hz) while frequently nodding the telescope (every few seconds) to move the target source between the positive and negative beams and provide better subtraction of atmospheric fluctuations and beam asymmetries. As in OTF_MAP mode, the demodulated bolometer signals are displayed on the Macintosh as strip charts. Upon the completion of each nodding segment, data are sent to the VAXStation which immediately appends it to the current file. At the conclusion of the specified number of chopping cycles, the average and RMS value of the data in each channel are written to the file after the scan data. Since the multiplex advantage of a (continuum) linear array is best exploited in mapping mode, the pointed observing mode of SHARC was not fully-commissioned until August 1996. It has since been used for deep integrations on point sources, the most sensitive of which are described in Benford et al. (1999). Measurements of the time efficiency of this observing mode, which yields the greatest on-source efficiency for point sources, are given in Figure 2.26.

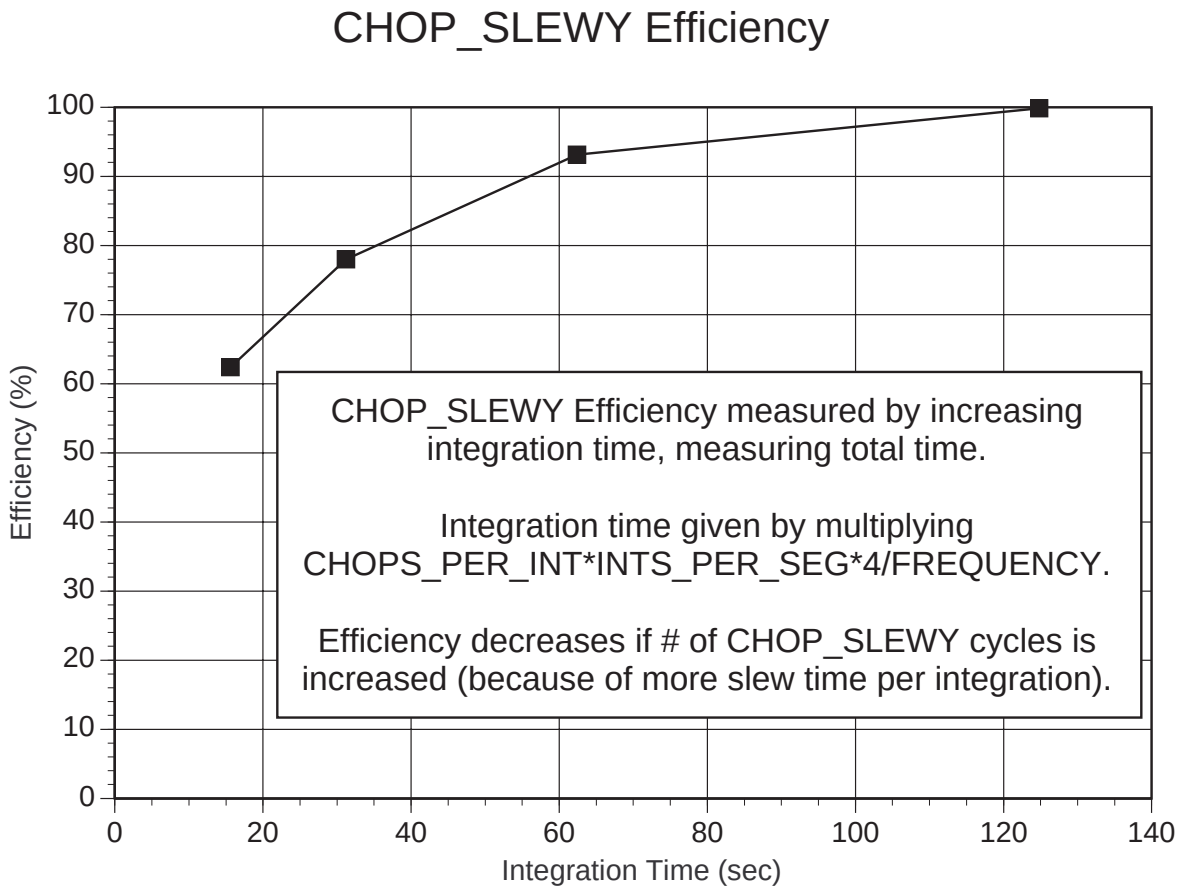

Figure 2.26 Efficiency of CHOP_SLEWY observations as a function of integration time. Telescope overheads are fixed, so that efficiency grows as on-source time grows.

2.6.4.3 THREE_POINT

I developed this routine, written in 1997 well after SHARC's initial commissioning, after a need for improved pointing became apparent. Not only is pointing via mapping a fairly slow process, requiring about 2 minutes for each point, but it is inaccurate in that the observer is required to determine new pointing offsets by eye. Furthermore, since the faintest observable source for pointing is about 20 Jy, there are only about 20 pointing sources in the whole sky accessible from Mauna Kea.

THREE_POINT commands the telescope to take data (similar to CHOP_SLEWY) while pointed at one of three positions, nominally on source and symmetrically off to either side in azimuth, usually by $10''$. A Gaussian is fit to all three scans, yielding the zenith angle offset term. Then a fourth Gaussian is fitted to the peak of the three scans, yielding the azimuth offset term.

In addition to being highly accurate (stability less than $1''$ typical in good weather), approximately 10 seconds of data are taken per point, allowing the use of sources as faint as ~ 5 Jy. This opens up the use of quasars for pointing. In fact, the initial testing of THREE_POINT used the quasar 3C273, at a redshift of $z = 0.16$ (NED Database), with excellent results.

2.7 Data Reduction for Imaging (OTF_MAP)

Since all demodulated SHARC data are stored on a workstation, it is most convenient to run the data reduction software on a UltraSPARC running Solaris, as this is the fastest data-crunching machine currently available. Darek Lis, with some help from Todd Hunter and myself, has written a FORTRAN program named *CAMERA* for the reduction of data taken with the `OTF_MAP` command. It uses the NOD-2 dual beam restoration algorithm (Haslam 1974; Emerson, Klein & Haslam 1979), with an interface specific to observing at the CSO with SHARC. The program queries the user (or can be scripted) for responses at each step through the data reduction: (1) pixel-to-pixel gain calibration, (2) automatic or manual de-spiking, (3) de-striping,

(4) constant offset or linear baseline removal, (5) airmass correction, (6) dual beam restoration, (7) azimuth and elevation pointing correction, and (8) transformation to equatorial coordinates. There are four modes available in *CAMERA*: (A) pointing mode, used at the telescope to correct the telescope pointing and to provide sky transmission measurements, (B) scan mode, wherein a single slew of the array across the sky is used to create a snapshot, (C) gain mode, used for calibration of the pixel-to-pixel gains, and (D) map mode, which treats each bolometer pixel as a single element instrument making a two-dimensional raster map across the source. In a separate FORTRAN program called *REGRID*, the restored images written by CAMERA are summed together into a regular grid in equatorial coordinates with sigma-weighting and flux calibration applied. The output image file from REGRID is in FITS format (Wells, Greisen & Harten 1981) and can be read into a variety of software packages. The plotting package *GRAPHIC* of the Insitut de Radio Astronomie Millimétrique (IRAM) was used for the data plotted in this work.

2.7.1 Pixel Gain Calibration

Because of small differences in the responsivities (based on slightly varying thermal and electrical properties) of each pixel and in the variation of optical efficiency across the focal plane, each pixel of the SHARC bolometer array exhibits a slightly different level of response when centered on a given source. This is the pixel-to-pixel gain variation, and has a standard deviation of 2%. Four gain scans on different runs are shown in Figure 2.27; the largest excursions are typically less than 10%. Even though the magnitude of the effect is generally small enough that mapping with multiple pixels will even out all variations, it is still good practice to correct for the variations before reducing the data. The relative gains of the pixels are measured at the CSO by scanning the array quickly in zenith angle through a bright planet quickly enough that atmospheric changes are minimal during the scan. This is accomplished with elevation scans invoked by the UIP command `OTF/SIDEWAYS`, or through the flat-field macro `FF_SHARC`. The planet is placed in the positive beam for one scan followed

by the negative beam for a second scan. Each scan is analyzed in the gain mode of *CAMERA* which writes out a file with the computed gains normalized to unity. These gains are then averaged to create the gain file named `CAMERA.DAT` to be subsequently used in data reduction.

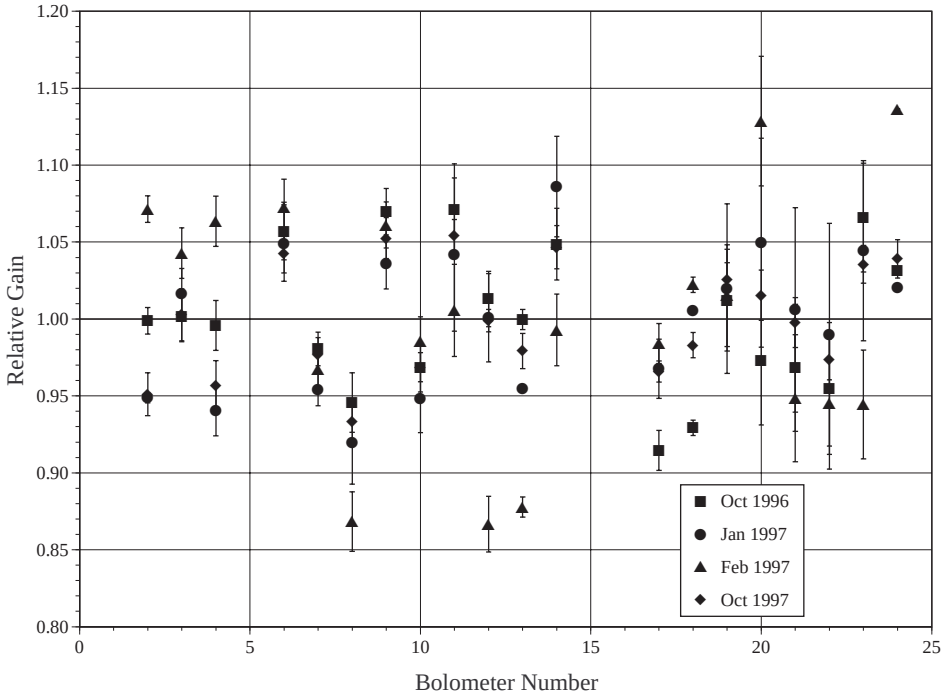

Figure 2.27 Four runs' pixel-to-pixel gain averages. The averaged standard deviation is 2%.

2.7.2 Despiking

Cosmic ray hits to the bolometers and electronic glitches are occasionally seen as spikes in the time series of data. Spikes may appear in a single pixel or in all pixels at once (in the case of noise on the power supply rails). Spikes can be automatically identified and flagged in *CAMERA* by their magnitude with respect to the RMS background level. The value of the spike is replaced by the average of four values: the two adjacent integrations from that pixel and the integration from the two adjacent pixels (if they have not previously been flagged). An avoidance range can be specified within which spikes will not be removed by the automatic procedure. Alternatively,

spikes can be flagged manually in *CAMERA*, although this is impractical for the case of large maps.

2.7.3 Destriping

After despiking, there will be some residual pixel-to-pixel correlated noise remaining on the array which appears as stripes in the scan data along the direction of the array. On nights of unstable or windy conditions, the dominant source of correlated noise originates above the telescope. This is thought to be due to cells of water vapor blowing through the two beams faster than the chopping period ($\sim$ 0.25 seconds). Removal of these stripes is a riskier process than despiking, especially when extended emission is present, but can also be very lucrative, as shown by the Uranus scan in Figure 2.28. For this reason, an avoidance region in the scan can be specified in *CAMERA* within which the data will not contribute to the calculation of the destriping correction. Using an avoidance region enables one to ensure that the structure of specified sources will not be altered by this noise reduction algorithm, but it also can leave a residual rectangular "plateau" of emission in the avoidance region.

2.7.4 Offset or Baseline Removal

During long scans, a drift in the signal zero level can conceivably occur. Although this effect is usually not detectable in SHARC scans, *CAMERA* allows the removal of a constant offset or a baseline computed from a specified number of integrations on each end of the scan. However, if the data has already been destriped, no offset should remain at this point.

2.7.5 Airmass Correction

As a source being observed rises and sets, the varying airmass (optical depth through the atmosphere) will result in a varying atmospheric transmission. In order to compensate for this effect, the signal being recorded by SHARC must be corrected for the

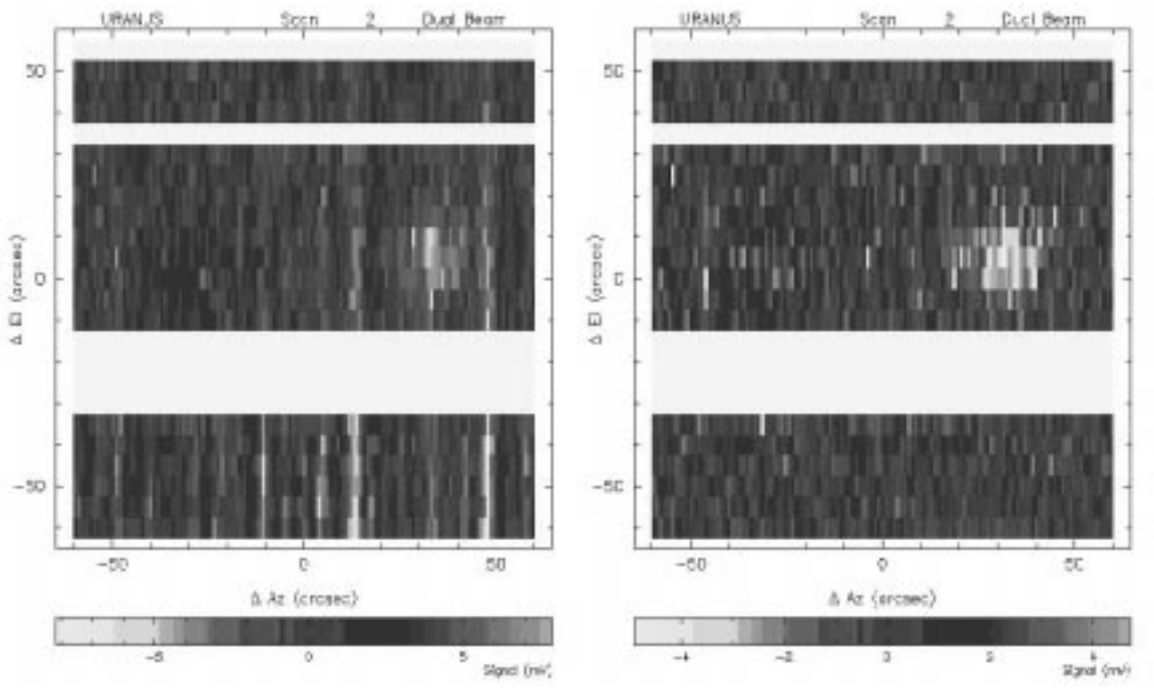

Figure 2.28 (Left) Raw dual-beam scan across Uranus. (Right) The same data, but with destriping applied. Note the change in scale.

attenuation, usually to the attenuation at the zenith. The signal $S(t)$ recorded as a function of time while looking through an airmass of $A(t)$ with zenith optical depth τ is given by:

$$S(t) = S_0 \exp\left[-A(t)\tau\right] \quad \text{where} \quad A(t) = \sec\left[\text{zenith\_angle}(t)\right], \tag{2.55}$$

where S_0 is the signal that would be recorded above the atmosphere.

Even in excellent conditions on Mauna Kea, the zenith optical depth of the atmosphere τ at 350 and 450μm is always greater than 0.5. (This optical depth τ corresponds to an emissivity $\epsilon = 0.39$ via the relation: $\epsilon = 1 - e^{-\tau}$). In order to properly calibrate the continuum flux density of all the sources observed, it is essential to measure the optical depth each night, preferably on several sources observed at many different airmasses. I have written a program called *SHARCTAU* into which the observer can enter these measurements which then calculates the optical depth and gives the uncertainty and the zenith flux (suitable for determining the conversion factor from millivolts to Janskys). Once the optical depth has been computed,

the scans of each source can be calibrated to a fixed airmass with *CAMERA* before summing the scans into a map.

In the near future, we will be testing a hardware skydip solution to solve the problem of measuring the optical depth. A synchronous chopper has been built which enables SHARC to chop between a fixed temperature (designed to be roughly 200K) load and the sky. Measurement of the effective sky temperature as a function of elevation can then be made, which (in the Rayleigh-Jeans limit) is easily converted into an optical depth.

2.7.6 Dual Beam Restoration

After processing the raw data to remove spurious and correlated noise and to calibrate it for atmospheric attenuation, the scans can be restored from a dual beam response pattern into a single beam sky intensity. This is accomplished in *CAMERA* with the NOD2 libraries. The raw dual beam scan can be thought of as a derivative of the sky intensity with a fixed spatial scale. The restoration process uses the edges of the scan as a zero level which is propagated across the scan using a maximum entropy approach (but introducing some additional noise) in order to properly reconstruct the extended emission. Before and after the restoration, the scans are written to GREG format RGDATA files named `CAMERA.DUAL` and `CAMERA.REST`.

2.7.7 Pointing Correction

Occasionally it is necessary and valid to correct the pointing offsets listed in the scan header for telescope tracking drifts or known encoder errors. Also, a thermal pointing shift of the telescope may have occurred since the most recent pointing scan, which shifts the pointing in an unknown direction by an unknown amount. Because the OTF scans are recorded in azimuth-elevation coordinates, these telescope-based pointing shifts can be corrected in data reduction after the observation. The offsets to shift the image are specified in *CAMERA* as the direction the image is to move in azimuth and elevation.

2.7.8 Coordinate Transformation

After restoration, the two-dimensional map seen by each pixel is transformed by *CAMERA* from azimuth-elevation coordinates to celestial equatorial coordinates using the appropriate header information of the local sidereal time and telescope offsets. The data are treated as if the telescope was pointed at the requested location during the scan. A typical single map file will then contain 20 integrations (for the 20 good pixels) which are written out after transformation to the file `CAMERA.RADEC`.

2.7.9 Regridding, Summing and Flux Calibration

Multiple maps of a given source (in the form of multiple `CAMERA.RADEC` files) can be summed by the program *REGRID*. A center position in right ascension and declination and an RA-Dec aligned rectangular grid of pixels about that point must be specified. Each integration of each `.RADEC` map file is placed into the appropriate pixel of the final grid, being added in with sigma weighting (where sigma is the standard deviation of the integration). Each map file can be given an absolute flux calibration conversion from millivolts (mV) to Janskys (Jy) which will be applied individually. The flux calibration changes smoothly with opacity, with larger opacities resulting in fewer mV per Jy. Like the optical depth, it is vital that the flux calibration factor be computed for each night relative to some consistent reference airmass (typically 0.0 or 1.0). When referenced to zero airmasses (above the atmosphere), the conversion factor is typically 0.3 Jy/mV.

In *REGRID*, individual integrations (corresponding to the map from a single pixel) can be flagged in any or all map files if necessary. The pixel-to-pixel gain calibration can also be invoked at this point if it has not already been applied. The output of *REGRID* is a FITS image. At the CSO, smoothing and customized display of these images is achieved in the GRAPHIC package developed at the Insitut de Radio Astronomie Millimétrique (IRAM).

2.8 Data Reduction for Pointed Observations (CHOP_SLEWY)

I have written the *Bolometer Array Data Reduction Software* (BADRS, pronounced Bad-Riss) package, an interactive, scriptable software language for the cleaning, calibration, and display of pointed observations with SHARC. The command line interface uses the SIC package developed at IRAM for heterodyne spectroscopy and featured in *CLASS* and *GRAPHIC*. A full guide to the use of *BADRS* is given in Appendix D.

It is crucial in the processing of CHOP_SLEWY observations that one understand how the data are taken and stored. A single CHOP_SLEWY command directs the telescope to move between the "on" and the "off" beams of the telescope (since the chopping secondary is running), integrating for some time in each beam and writing the data to disk. After some number of these integrations, each of which lasts about 10 seconds of telescope time, the average is written to disk. This is called a *scan* and represents somewhere in the neighborhood of 50 up to 250 seconds of on-source integration time. Because the raw data is written as well as the averages, a standard deviation can be calculated for each data point in the data set of scans. In order to represent the true standard deviation closely, a minimum of ten raw data points must be used in the determination (Bevington 1969). One of the most important functions of *BADRS* is the determination of the standard deviation, which is used for weighting sums or removal of spikes, and ultimately determines the noise remaining in the final summed data.

Upon entering *BADRS*, the *DEVICE* command will open a graphics window and the *FILE IN* command will read in the file. If, for some reason, the source was observed in the off beam instead of the on beam, the *FLIP* command will invert them. *LIST* will detail the individual data scans in the file. *PLOT* is used to display the scans to the screen or the printer.

An avoidance region can be specified in *BADRS* by means of the *SET WINDOW* command.

2.8.1 BADRS Processing for Maximum Signal-to-Noise

One of the first things to do in *BADRS* is to calibrate the data to correct for atmospheric opacity and pixel-to-pixel gain variations. As these calibrations bring the data into real units (Janskys/beam), the concept of a true standard deviation becomes valid. The data set can then be viewed as a two-dimensional array, with the vertical axis being position on the sky along the detectors and with the horizontal axis being time, since each scan is just another sampling of the same astronomical source. After calibrating, removal of a constant offset from each bolometer in each scan is necessary. This is analogous to the destriping algorithm in mapping mode. After removing these offsets, the despiking as outlined above is applied. *BADRS* allows the removal of spikes using a cutoff based either on the data viewed as a time sequence (taking the standard deviation in the signal from one bolometer) or as a spatial sequence (each scan has its own standard deviation in the detectors). Finally, another baseline is subtracted to compensate for the despiked pixels. Once this processing has been applied, the standard deviation for every data point in the two-dimensional array using the raw data from that point and the neighboring two points in time (i.e., the same pixel immediately before and after). The array is then ready for final summation. The effects of this processing are shown in figures 2.29 and 2.30. A final reduced scan is shown compared to its preprocessed version in Figure 2.31.

Adding together the processed scans into a final, single scan can be done in a variety of ways. The simplest is to weight all scans by the time taken to acquire them, so that the final scan is equivalent to what would have been recorded at the telescope if it had simply been integrating for the entire time, and then wrote only the final result. This can be improved upon if one weights scans more heavily if the noise level is less (sigma weighting). This is a valid approach in that the true signal-to-noise changes during the observation due to the rising and setting of the source through a varying amount of atmosphere. The sigma used for this weighting can be either the standard deviation of each pixel or of each scan as a whole. After summing, a baseline (usually linear) can be removed to subtract off any remaining spurious offset.

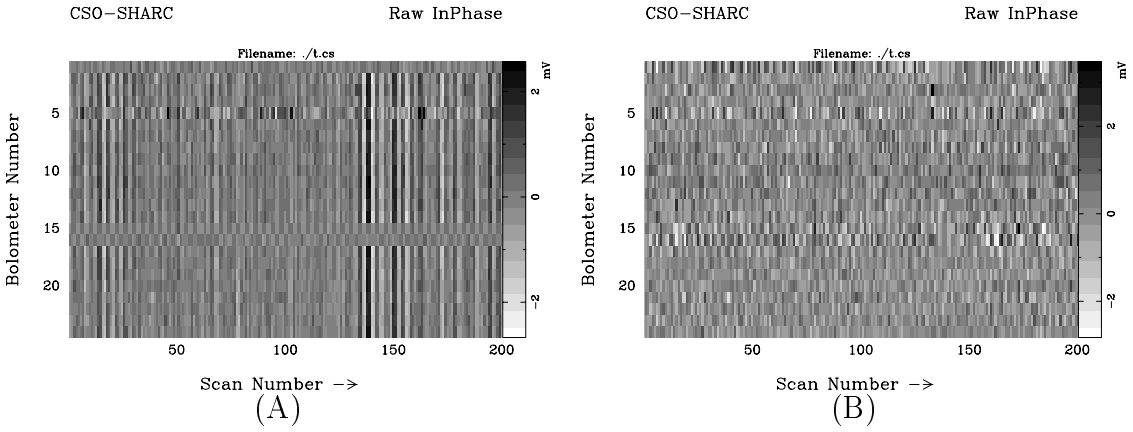

Figure 2.29 Raw in-phase data from CHOP_SLEWY observations of NGC6000 (A) before processing and (B) after data reduction. When correcting for atmospheric opacity, the reduced data was multiplied by a factor of 2.5, so the processed data is actually much less noisy than the raw data than is apparent here.

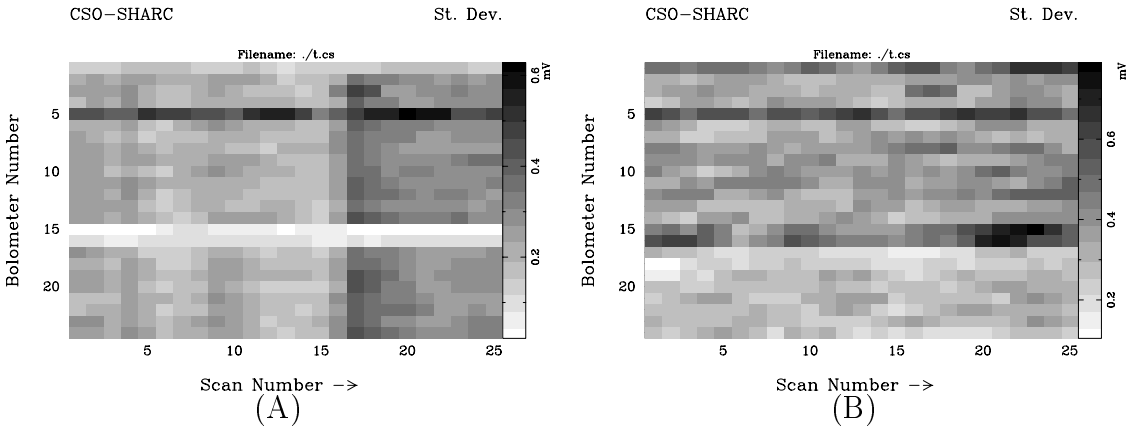

Figure 2.30 Standard deviations of the raw data from the CHOP_SLEWY (A) before processing and (B) after data reduction. Again, the factor of 2.5 has been introduced in the final data. The dead pixels (1,5,15 & 16) are clearly visible.

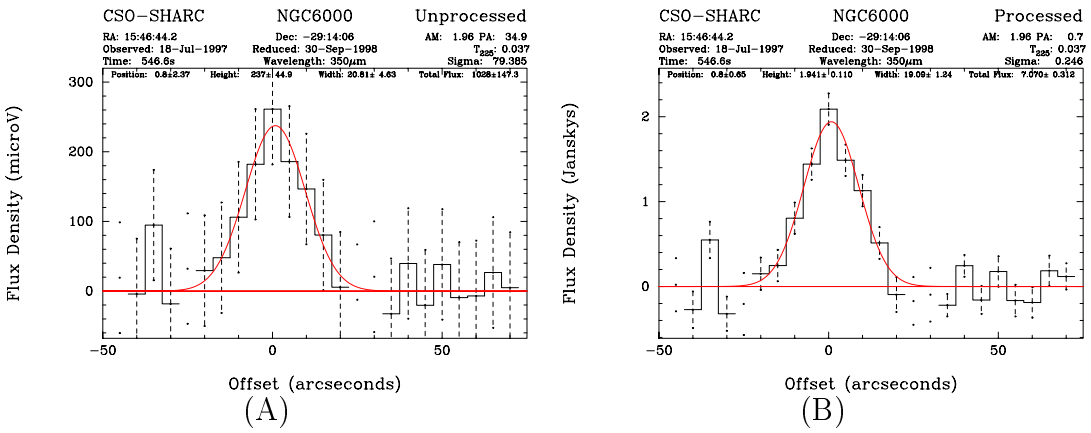

Figure 2.31 Summed data resulting in detections of NGC6000 (A) with no processing and (B) after complete data reduction. Gaussian fits to the data show the effect of the BADRS correcting algorithms: the peak flux density results in a 5σ detection with no processing, but 18σ with processing.

One more subtlety exists: there is a low-level discrepancy in the digitizing electronics for SHARC in that odd and even bolometers use equivalent but separate channels of a dual digital-to-analog converter. There is, therefore, a small amount of residual signal which varies consistently from channel to channel, like a square wave of fixed amplitude. Accordingly, this can be modeled and subtracted, and is typically (for long integrations, appropriate to observations of distant galaxies) a correction on the order of a few mJy. Nevertheless, it contributes to the overall standard deviation of the final scan.

BADRS has a routine for fitting a Gaussian to the final data and can plot the results for inclusion in publications. A fully-reduced observation of the $z = 4.7$ quasar BR $1202 - 0725$ is shown in Figure 4.1 to illustrate the excellent quality of data obtainable.

2.9 Sensitivity

This chapter concludes with a demonstration of the sensitivity achieved with SHARC at the telescope. To begin with, I shall discuss measurements of the short-term (timescales of a minute) sensitivity as compared to the atmospheric limit, to verify the expressions derived in section 2.3. Afterwards, I present the sensitivity achievable during long (more than a minute) integrations.

2.9.1 Atmospheric Noise Equivalent Power Measurements

2.9.1.1 Measurements with SHARC

Noise and BRE NEP measurements were made at the Caltech Submillimeter Observatory in October 1995 and April 1996 using the facility bolometer array camera SHARC (Wang et al. 1996; Hunter, Benford & Serabyn 1996). The noise was measured with the telescope tipped at several different zenith angles, yielding the detector-referenced noise power as a function of atmospheric emissivity. We have also measured the BRE NEP, determined by tracking a source of known brightness through several different airmasses and determining the signal-to-noise ratio in a fixed integration time.

The results are shown in Figure 2.32, where best fits to the expected functions are shown: the noise (solid triangles) and the NEP (solid squares) as measured with SHARC. The noise has been fit as the sum of an atmosphere dependent noise term and a constant instrument noise term added in quadrature. A lab measurement (equivalent to no atmosphere) is plotted as a hollow triangle; it matches the telescope measurement prediction quite closely. The BRE NEP data covers only a small range in emissivity, but clearly would not be well fit by a $\sqrt{\epsilon}$ dependence. A measurement of the NEP using the SuZIE receiver at the CSO (Holzapfel et al. 1997) is plotted as a hollow square, lying exactly on the curve predicted by SHARC measurements. This shows that both the noise power and the BRE NEP follow the expected equations, so that calculating only the background noise does not yield the proper value of the BRE NEP. Quantitatively, the noise calculation of $\sim 2 \times 10^{-14}$ W/$\sqrt{\text{Hz}}$ for SHARC

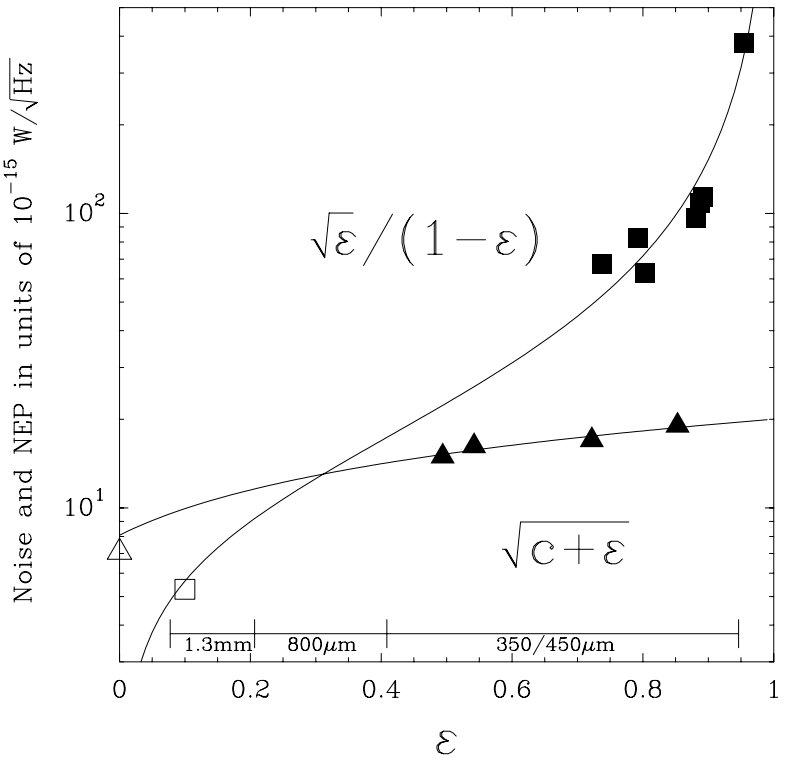

Figure 2.32 Measured atmospheric noise (solid triangles) at 350 μm fit by equation (4) and BRE NEP (solid squares) at 450 μm fit by equation (7) from Mauna Kea. The open triangle is a lab noise measurement, while the open square is a 1.3mm NEP measurement. Scale is in 10^{-15} W/$\sqrt{\text{Hz}}$. Typical ranges of emissivities for several wavelength bands are indicated at the bottom for good to moderate weather.

is quite close to the prediction from the measured values.

It is important to note that the BRE NEP is a complete description of the signal to noise level of an astronomical source passing through an absorptive and emissive atmosphere. Therefore, it can be related to a useful observational parameter to the practicing astronomer, the Noise Equivalent Flux Density (NEFD). NEFD is a measure of the celestial source's strength required to attain unity signal-to-noise ratio in one second of integration. The NEFD can be estimated given the bandwidth of detection $\Delta\nu$ and the telescope effective geometric collecting area A:

$$NEFD = \frac{2\,NEP}{A \times \Delta\nu} \tag{2.56}$$

where a factor of 2 has been introduced assuming optical chopping is used: $\sqrt{2}$

because the on-source time is half the total time, and $\sqrt{2}$ because the missing half of the time is not only a lack of signal, but a source of noise. The NEP is calculated from equation 2.26. Then, for $\Delta\nu \sim 50$ GHz and $A \sim 100$ m^2, this yields:

$$NEFD_{350GHz} = 0.03 \text{ Jy}/\sqrt{\text{Hz}}$$
$$NEFD_{650GHz} = 0.32 \text{ Jy}/\sqrt{\text{Hz}}$$
$$NEFD_{850GHz} = 0.46 \text{ Jy}/\sqrt{\text{Hz}}$$

A calculation of the expected NEFD at 850 GHz with $\epsilon \sim 0.8$ for the CSO bolometer camera yields a value of 1.4 Jy/$\sqrt{\text{Hz}}$ (when corrected for 70% chopping secondary duty cycle at 4 Hz), quite close to the 1.9 ± 0.3 Jy/$\sqrt{\text{Hz}}$ measured on IRC10216, a secondary calibrator (assuming the published flux of 19 Jy at 850 GHz (Sandell 1994).) At $\epsilon \sim 0.74$, we have measured 2.0 ± 0.3 Jy/$\sqrt{\text{Hz}}$, within a factor of 2 of the predicted value of ~ 1.0. Thus the measured value of the NEFD closely matches the prediction based on a calculated BRE NEP. The small deviations from the prediction seen here could be due to instrumental noise, varying sky emissivity during the integrations, and the contribution from hot spillover. If $\eta_{\text{hot}} \sim 0.1$, the BRE NEP will be higher by about 10%.

2.9.1.2 NEP of Other Instruments

Using information from Holland et al. (1998), we estimate the NEFD for SCUBA at 350 GHz, 650 GHz, and 850 GHz to be around 0.045, 0.40, and 0.50 Jy/$\sqrt{\text{Hz}}$, respectively. The quoted values are 0.075, 0.45, and 1.0, which are within a factor of 2 of the predictions. The calculated NEFD at 650 GHz, where SCUBA has been well characterized, is in very good agreement with the data.

The instrumental noise of the SuZIE millimeter-wave bolometric receiver at the CSO was measured at 217 GHz (Holzapfel et al. 1997). The NEP measured on the sky is 5×10^{-16} W/$\sqrt{\text{Hz}}$ which corresponds to 0.030 Jy/$\sqrt{\text{Hz}}$. This is comparable to the CSO BRE NEP & NEFD calculated for this frequency, 4×10^{-16} W/$\sqrt{\text{Hz}}$ and 0.025 Jy/$\sqrt{\text{Hz}}$, respectively. This implies that sky noise is fairly insignificant.

A formalism for calculating sky noise has been developed by Church (Church 1995). Using this method yields a sky noise component of ~ 0.010 Jy/$\sqrt{\text{Hz}}$. If we apply the same theory to SHARC/SCUBA, we find a sky noise of ~ 0.050 Jy/$\sqrt{\text{Hz}}$ at 650/850 GHz in good weather, worsening to $\gtrsim 1$ Jy/$\sqrt{\text{Hz}}$ in bad weather. Sky noise is a highly variable quantity, depending on the temperature and distribution of water along the line of sight as well as wind speed and direction, in addition to telescope parameters.

Hertz, the submillimeter polarimeter at the CSO (Dowell et al. 1998), is an 850 GHz dual bolometer array with a half-wave plate to split polarizations. Its estimated optical NEP (based on electrical NEP and optical efficiency measurements) is $\sim 7 \times 10^{-14}$ W/$\sqrt{\text{Hz}}$ and its measured point-source NEFD is ~ 4 Jy/$\sqrt{\text{Hz}}$. Calculation of the theoretical BRE NEP and NEFD yields 5×10^{-14} W/$\sqrt{\text{Hz}}$ and 1.1 Jy/$\sqrt{\text{Hz}}$, respectively. Again, these results are quite close, even though Hertz differs from the other instruments in that each bolometer receives only one polarization and the total optical efficiency is somewhat lower (0.017 for Hertz vs. 0.10 for SHARC or 0.42 for SuZIE).

At higher frequencies, current heterodyne spectrometers are limited in total instantaneous bandwidth to a coverage of approximately $\Delta\nu \sim 1$ GHz. Since extragalactic line emission typically has spectral features of order ~ 100 MHz, the NEP for a receiver operating with T_{sys} $\sim$2000 K (a low value for observations in the 650-850 GHz region) is 2.8×10^{-16} W/$\sqrt{\text{Hz}}$. At the CSO, this corresponds to about 10 Jy/$\sqrt{\text{Hz}}$. We are currently building a spectrometer (Benford et al. 1998a) using bolometers which will have a resolution of 500 MHz, yielding an NEFD of around 4 Jy/$\sqrt{\text{Hz}}$, but with a total bandwidth of 9 GHz. This corresponds to velocity coverage of 3500 km/s, which will enable extragalactic lines of uncertain redshift to be detected much more easily.

2.9.1.3 Results of Theory and Experiment

The full expression for the background radiation equivalent NEP was derived in section 2.3.2, and is given by equation 2.26. This allows for the calculation of the effective

noise limit imposed upon a thermal detector used for astronomical observations. A background limited detector must have a detector noise referred to above the atmosphere of at least a few times lower than this value. Since a calculation of atmospheric emission noise alone neglects the absorbing effect of the atmosphere, it is therefore strictly a measure of noise, not of true NEP. The NEFD can be calculated from the BRE NEP, allowing the astronomer to calculate the minimum detectable source flux for a given integration time. Experimental measurements in astronomical situations have verified the validity of the expressions for NEP and NEFD.

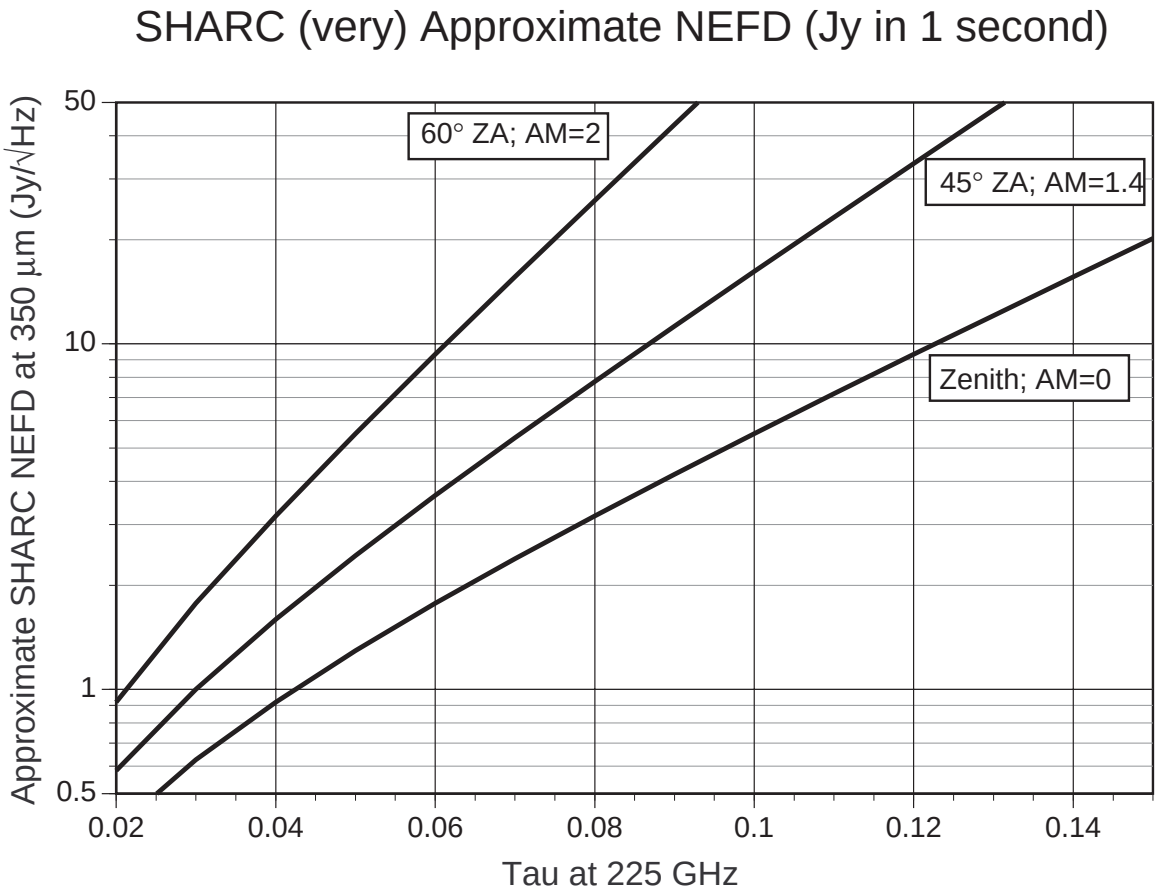

Figure 2.33 Noise Equivalent Flux Density as a function of atmospheric opacity.

2.9.2 Long Integrations

In order to test the camera sensitivity during long integrations, it is necessary to consider a series of data taken during constant sky conditions. The longest map-

ping integration performed to date with SHARC is the CSO deep field survey for protogalaxies which contains the sum of 1,007,270 0.244-second pixel integrations. This corresponds to 4370 seconds of integration in each $10''$ resolution element in the map. Therefore, the RMS noise achieved in the final map (95 mJy at 450μm) implies an average $NEFD = 6.2$ Jy/$\sqrt{\text{Hz}}$. However, these data are spread over a large field ($3'$) and acquired over many nights with varying weather conditions and may not represent the effective $NEFD$ for long integrations on a single position with the CHOP_SLEWY mode.

In the course of observing high-redshift quasars (as described in chapter 4), several extremely long integrations were made. The longest of all was the observation, made over several nights, of BRI $1335-0417$ at $z = 4.4$. A total of $28,421$ seconds of on-source data were acquired, equivalent to 158 hours with a single-element bolometer. The NEFD of the five longest integrations has been calculated and is shown in Table 2.2. The mean NEFD is 1.1 Jy/$\sqrt{\text{Hz}}$, verifying that SHARC continues to integrate down as $^1/_{\sqrt{t}}$ for the longest conceivable integration times.

Table 2.2 SHARC sensitivity during long integrations.

Source Name	Time (s)	Noise (mJy)	NEFD (Jy/$\sqrt{\text{Hz}}$)
BRI $1335-0417$	28421	6.30	1.06
BR $1202-0725$	14451	9.24	1.11
Q $0842+3432$	6952	13.39	1.12
PHOT $1608+5444$	5509	10.17	0.75
BR $0302-0019$	4941	21.60	1.52
Mean			1.11

Chapter 3

Nearby Ultraluminous Infrared Galaxies

3.1 The Characteristics of Dust

The thermal emission from cold ($T \sim 40$K) dust in luminous infrared galaxies (LIRGs[1]) is an important tracer of the physical conditions in this class of objects. Not only does this emission tend to dominate the total luminosity, but the cold component contains most of the dust mass in the galaxy. It is therefore important to have a good understanding of this emission, especially since our understanding of the properties of protogalaxies and other objects at cosmological distances require a thorough understanding of dust emission in nearby galaxies.

With this goal in mind, we have undertaken a survey of nearby luminous infrared galaxies. All are detected by the IRAS satellite, providing useful 60μm and 100μm measurements. Using SHARC, we have constrained the spectral energy distribution of each galaxy. Using the spectrum in concert with other information allows us to infer the properties and structure of the dust itself. This effort is being prepared for publication under the authorship of myself, Gerry Neugebauer, Todd Hunter, and Tom Phillips.

3.2 Observations

Our scientific goal was to obtain measurements of the submillimeter flux densities and sizes of a representative sample of luminous infrared galaxies. This is accomplished most easily by observing at 350μm, the shortest wavelength available from the ground. In this band, SHARC is at its most sensitive in terms of signal-to-noise in a fixed

[1]Herein I take a very broad view of "luminous": $L_{\rm IR} \geq 10^{10}\,L_{\odot}$.

integration time, and the diffraction-limited beamwidth is the smallest. Furthermore, observations at wavelengths of $\sim 1200\mu$m are available from the literature for many such sources, greatly assisting in the fitting of spectra. In order to determine the size of a galaxy, a signal-to-noise ratio of order 10 is needed; this sets a practical lower limit on the brightness of the galaxies we observe given the finite telescope time assigned to the project. In one hour of telescope time in good weather, SHARC at the CSO can detect a galaxy with a flux density of roughly 1 Jy at this signal-to-noise ratio[2]. Since galaxies are typically a factor of 20 fainter in flux density units at 350μm than at 100μm, this sets a reasonable minimum flux density cutoff at 20 Jy at 100μm.

We selected a sample to observe drawing largely from the list of Wynn-Williams & Becklin (1993, hereafter WWB93) of luminous infrared galaxies with sizes measured at 12 and 25μm. Two of the galaxies of WWB93 were removed to yield the flux cutoff at 100μm of 20Jy. In order to better understand the galaxies at the high luminosity end of the sample, we added the ultraluminous galaxies IRAS 09320 + 6134 and Mrk 231, distant enough to be point sources yet above our flux cutoff. We also include the nearby starburst galaxy NGC 1068 as a test case for a galaxy that will be clearly resolved. The final list then contains 20 galaxies with mean infrared luminosity of $5 \times 10^{11}\, L_\odot$, but varying from $1.3 \times 10^{10}\, L_\odot$ (NGC 4818) to $3 \times 10^{12}\, L_\odot$ (Mrk 231). Not surprisingly, Mrk 231 – along with NGC 4102 – defines the limits of the redshift range of the sample, $0.003 \leq z \leq 0.042$ with mean of $z = 0.016$. If we assume that the luminosity of each galaxy is driven primarily by star formation, then we can estimate the star formation rate using the relation of Thronson & Telesco (1986):

$$\mathrm{SFR} \sim \Psi 10^{-10} \frac{L_{\mathrm{FIR}}}{L_\odot}\ M_\odot \mathrm{yr}^{-1} \text{ with } \Psi \sim 0.8 - 2.1. \tag{3.1}$$

In this case, our sample contains galaxies with star formation rates of $2 - 300 M_\odot \mathrm{yr}^{-1}$ and mean value $\mathrm{SFR} = 50 M_\odot \mathrm{yr}^{-1}$. The sample list and IRAS measurements are summarized in Table 3.1.

This observing project was used as filler time between objects being observed

[2]See the SHARC memo *On the Calculation of SHARC Observing Time* by Benford & Lis.

Table 3.1 Positions and IRAS data for the 20 galaxies of the local infrared-luminous galaxies survey.

Source Name	Velocity (km/s)	Distance† (Mpc)	RA (B1950.0)	DEC (B1950.0)	Flux 10^{-12} W/m^2	Flux Density (Jy) 12μm	25μm	60μm	100μm	Log L_{IR} ($L_\odot$)
NGC 520	2281	30.4	01:21:59.7	+03:31:53	2.62	0.77	2.87	30.9	45.8	10.9
NGC 1068	1136	15.1	02:40:07.1	−00:13:31	28.10	39.7	85.0	176.2	224.0	11.3
NGC 1614	4778	63.7	04:31:35.5	−08:40:56	2.98	1.44	7.29	32.3	32.7	11.6
NGC 2339	2206	29.4	07:05:25.1	+18:51:42	1.66	0.598	2.147	17.47	31.43	10.7
NGC 2388	4134	55.1	07:25:38.2	+33:55:17	1.42	0.452	2.078	16.0	23.66	11.1
NGC 2623	5535	73.8	08:35:24.9	+25:55:50	1.73	0.212	1.74	23.13	27.88	11.5
UCG 5101	11812	157.5	09:32:04.8	+61:34:37	1.02	0.250	1.034	11.54	20.23	11.9
NGC 4102	837	11.2	12:03:51.3	+52:59:22	4.26	1.509	6.76	46.93	69.74	10.2
NGC 4194	2506	33.4	12:11:41.2	+54:48:15	1.98	0.834	4.312	21.38	25.88	10.8
NGC 4418	2179	29.1	12:24:20.8	−00:36:04	3.43	0.935	9.32	40.68	32.8	11.0
Mrk 231	12642	168.6	12:54:05.0	+57:08:38	3.14	1.872	8.662	32.0	30.3	12.5
NGC 4818	1155	15.4	12:54:12.7	−08:15:13	1.87	0.839	3.85	20.0	25.2	10.1
NGC 5135	4112	54.8	13:22:56.2	−29:34:23	1.62	0.638	2.40	16.9	28.6	11.2
Mrk 273	11326	151.0	13:42:51.7	+56:08:14	1.60	0.235	2.28	21.7	21.4	12.1
Arp 220	5434	72.5	15:32:46.9	+23:40:08	7.44	0.484	7.91	103.8	112.4	12.1
NGC 6000	2110	28.1	15:46:44.3	−29:14:06	3.24	1.245	5.06	35.5	52.6	10.9
NGC 6240	7339	97.9	16:50:27.6	+02:28:58	1.93	0.558	3.42	22.7	27.8	11.8
IC 5135	4842	64.6	21:45:19.8	−35:11:07	1.51	0.588	2.12	16.5	25.6	11.3
NGC 7469	4892	65.2	23:00:44.4	+08:36:16	2.58	1.348	5.79	25.9	34.9	11.5
Mrk 331	5541	73.9	23:48:54.1	+20:18:29	1.55	0.497	2.50	18.6	21.6	11.4

† Assuming H_0=75 km/s/Mpc.

for the SHARC high redshift quasar survey, detailed in chapter 4. As a result, the observations were spread over 9 observing runs over the course of more than two years as given in Table 3.2. In all cases, however, the following observational details held. Firstly, absolute calibration was provided by observations of Mars, Saturn, or Uranus, all of which are bright, compact, and reasonably well-understood. Using these sources or a secondary calibrator such as IRC 10216, we measured the atmospheric transmission to calibrate our observations. Additionally, these sources were used as pointing references, and in general our pointing was stable to approximately $3''$. In each of these runs, the weather was excellent, with 225 GHz atmospheric opacities of $\tau < 0.05$, corresponding to an in-band atmospheric opacity of roughly unity.

3.3 Analysis

We were able to obtain data for 18 of the 20 sample galaxies, detecting all 18 at a signal-to-noise ratio of at least 3. Since the SHARC array is linear, the data consist of a cut through each galaxy at some mean position angle (determined by the orientation of the sky during the observation). This cut yields a flux density (in Janskys/beam) at each position, sampled every $5''$ along the array. Plots of this data are shown in figures 3.1–3.18, along with the Palomar Observatory Sky Survey (POSS) digitized image for each one. A Gaussian emission profile is assumed for each source, yielding a one-dimensional size and a peak flux density. Under the assumption that the source distribution is circularly symmetric, the total integrated flux density can be estimated approximately for the resolved sources by a simple geometric model. In the case of unresolved sources, we assume that all the flux has been observed by the SHARC array.

Table 3.2 Observation dates using SHARC at the CSO.

Source Name	Observation Dates									Calibrators			Integration Time† (s)
	7/96	10/96	1/97	2/97	4/97	7/97	10/97	1/98	11/98	Mars	Saturn	Uranus	
NGC 520		•				•			•	•	•	•	1366
NGC 1068		•	•	•						•	•		148
NGC 1614			•				•			•	•		678
NGC 2339							•	•			•		219
NGC 2388								•			•		186
NGC 2623									•	•	•		765
UGC 5101							•		•	•	•		929
NGC 4102					•					•		•	426
NGC 4194								•			•		1224
NGC 4418					•					•			623
Mrk 231			•		•					•			1651
NGC 4818					– *no data* –						–		–
NGC 5135					– *no data* –						–		–
Mrk 273			•	•						•		•	1115
Arp 220	•			•	•	•				•		•	197
NGC 6000					•	•				•		•	536
NGC 6240						•				•			1082
IC 5135						•	•			•		•	1509
NGC 7469	•					•				•	•	•	700
Mrk 331						•					•	•	1082

† Total net on-source integration time used in the final data; in some instances, data taken in poor conditions were not used. To convert to wall-clock time, multiply by roughly 3.5. The total on-source time for this project is 14 436s.

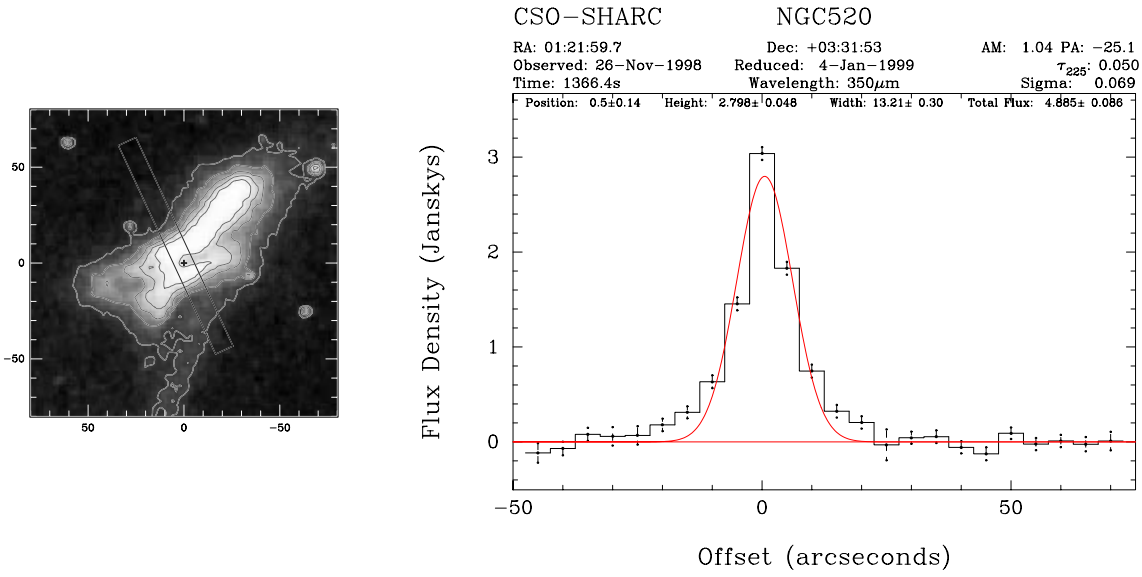

Figure 3.1 POSS image and 350μm observation of NGC 520. The horizontal axis is the displacement in arcseconds, while the vertical is the flux density in units of Jy/beam. The mean orientation of the array is shown as the rectangular box superimposed on the POSS image, while a cross denotes the central position.

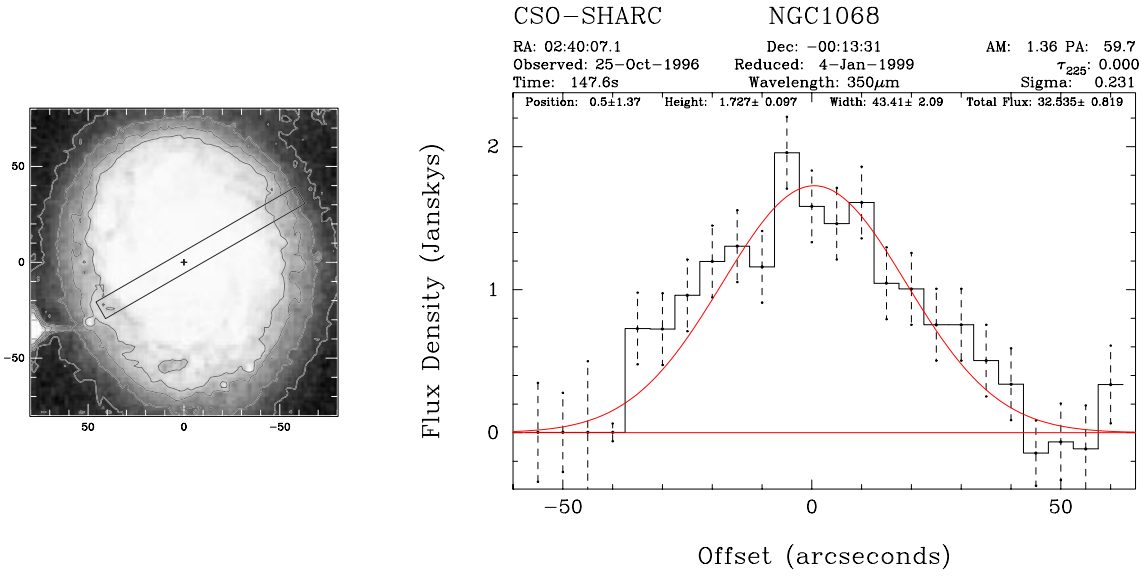

Figure 3.2 POSS image and 350μm observation of NGC 1068.

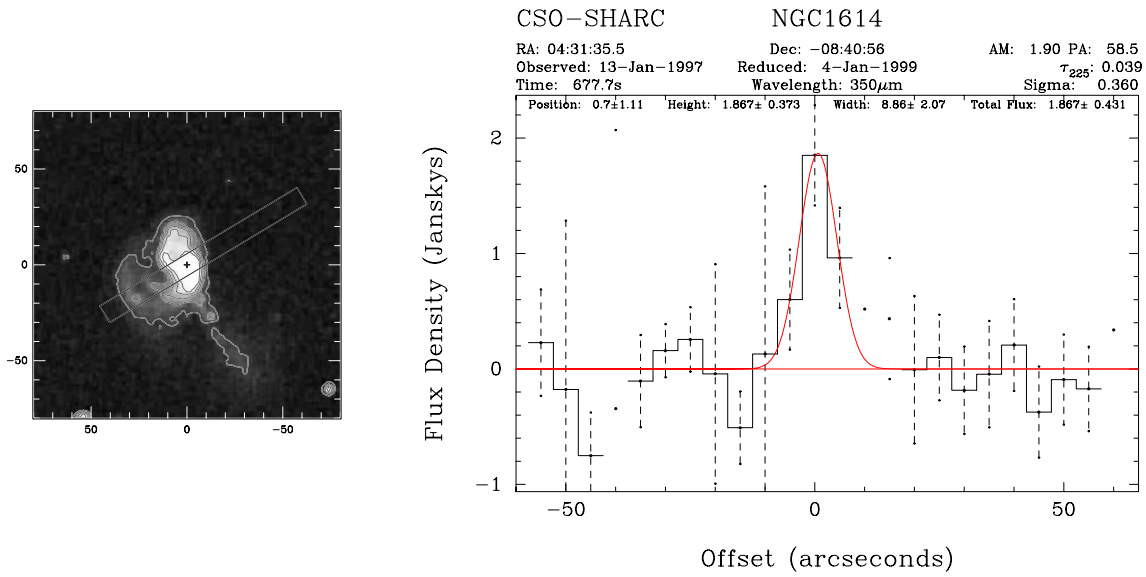

Figure 3.3 POSS image and 350μm observation of NGC 1614.

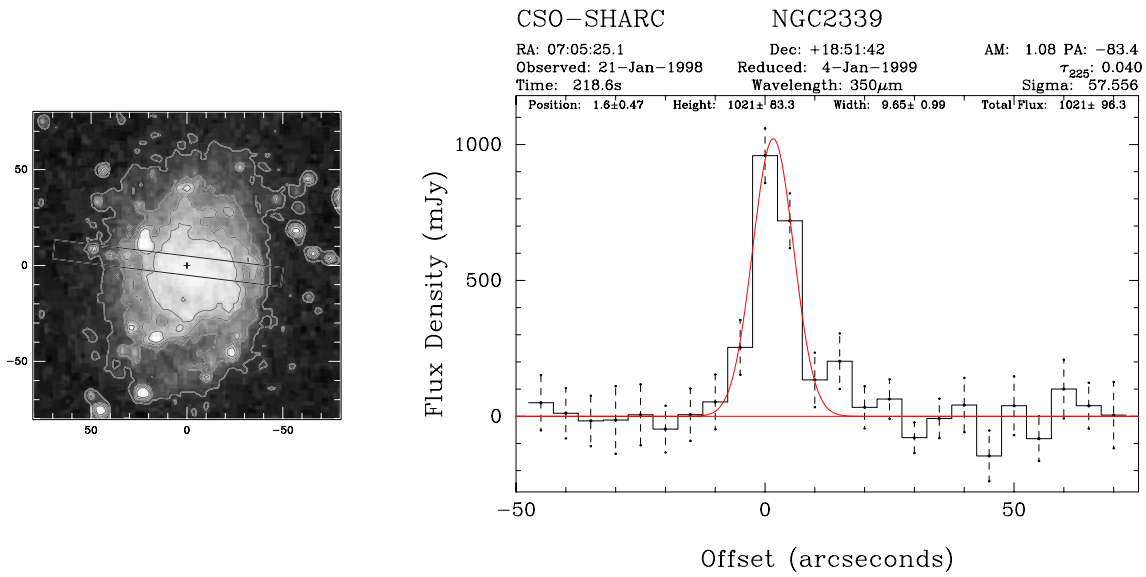

Figure 3.4 POSS image and 350μm observation of NGC 2339.

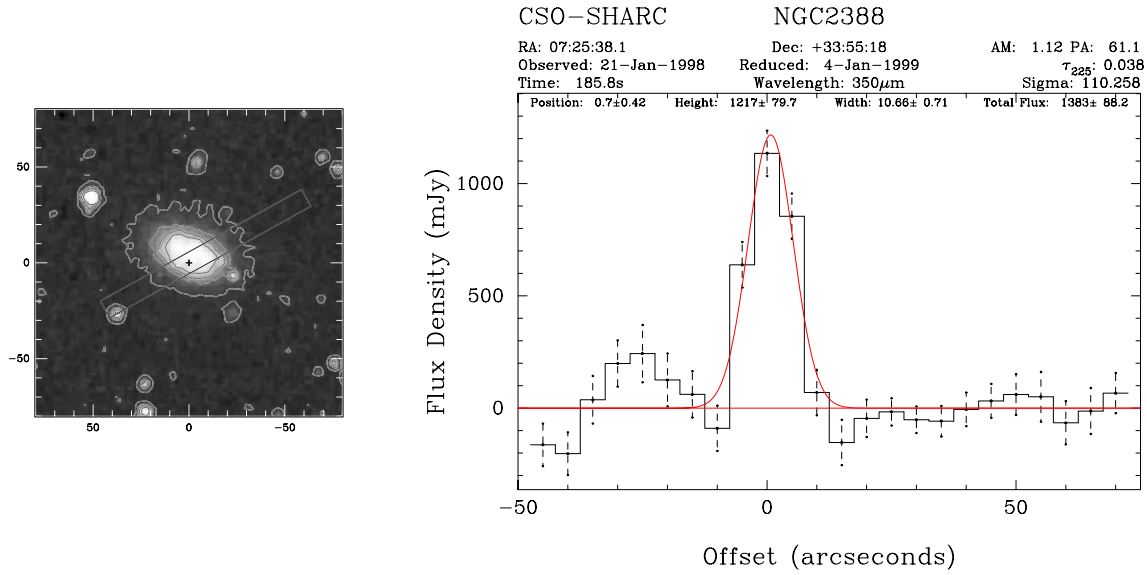

Figure 3.5 POSS image and 350μm observation of NGC 2388.

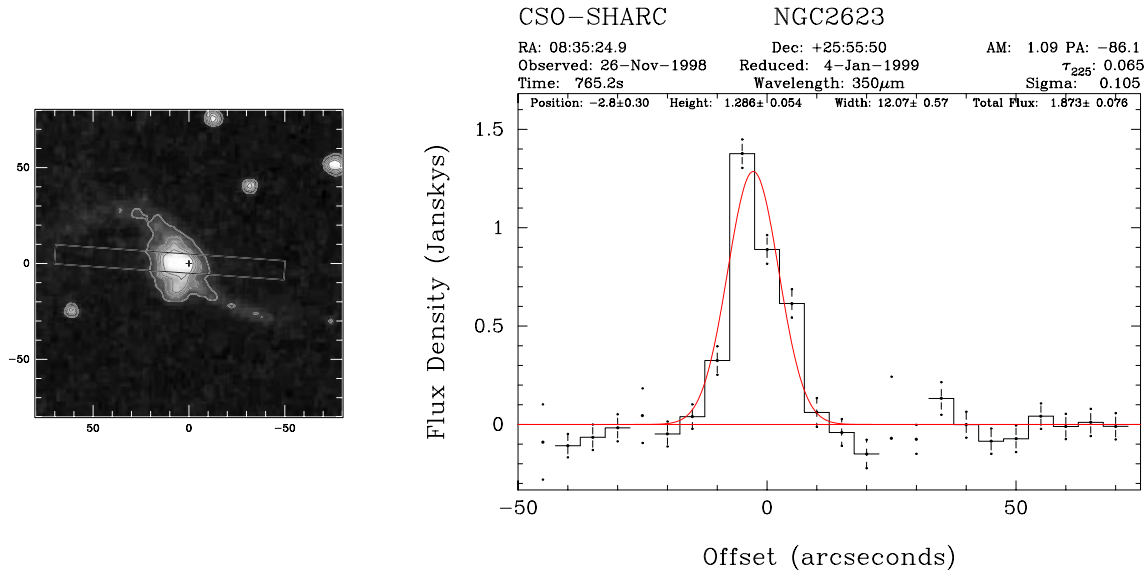

Figure 3.6 POSS image and 350μm observation of NGC 2623.

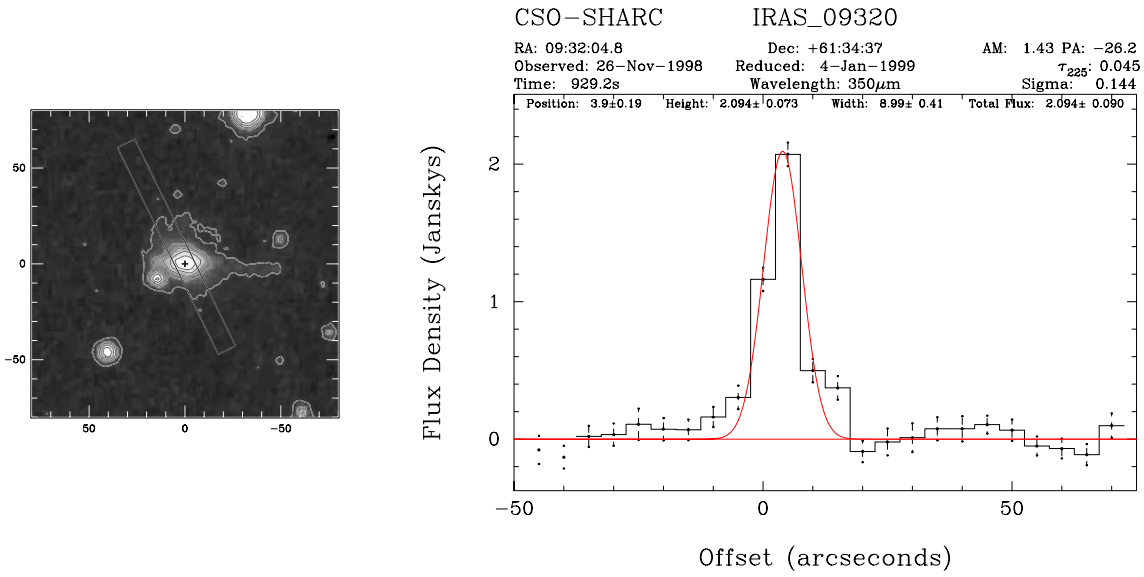

Figure 3.7 POSS image and 350μm observation of UGC 5101 (IRAS 09320+6134).

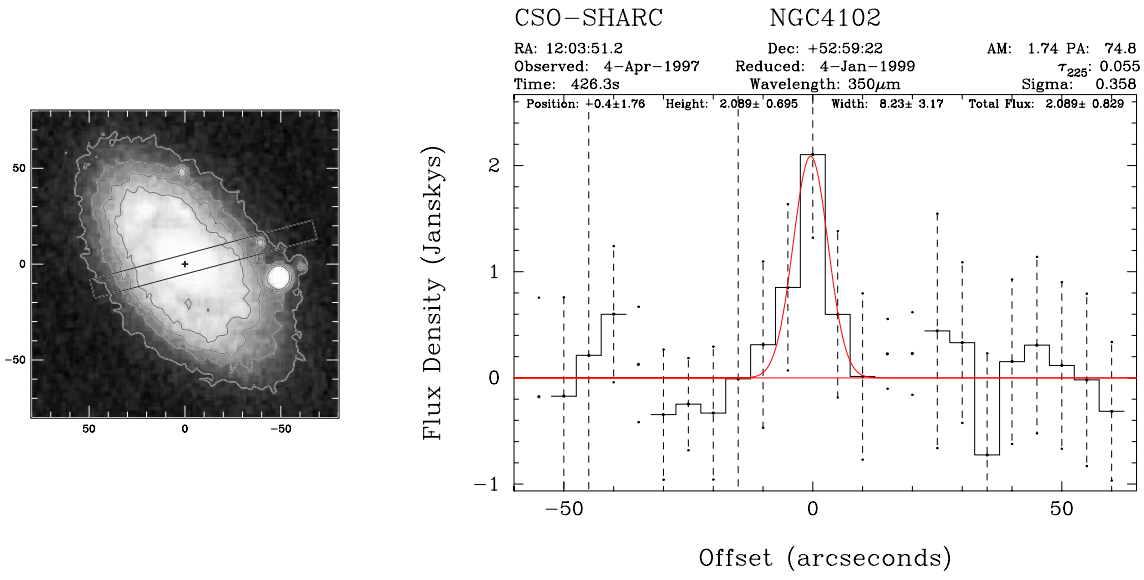

Figure 3.8 POSS image and 350μm observation of NGC 4102.

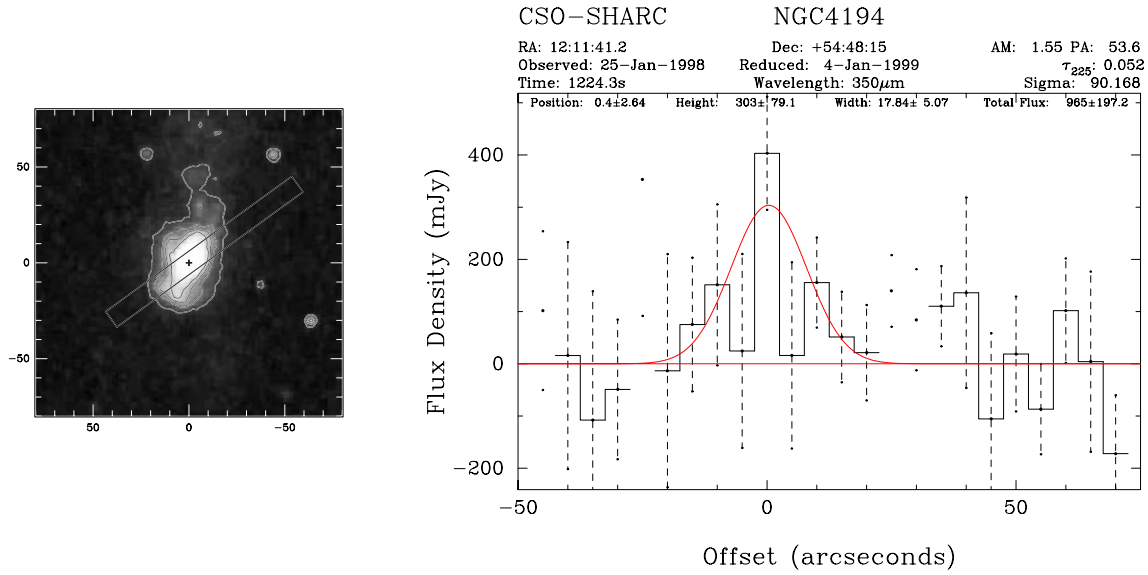

Figure 3.9 POSS image and 350μm observation of NGC 4194.

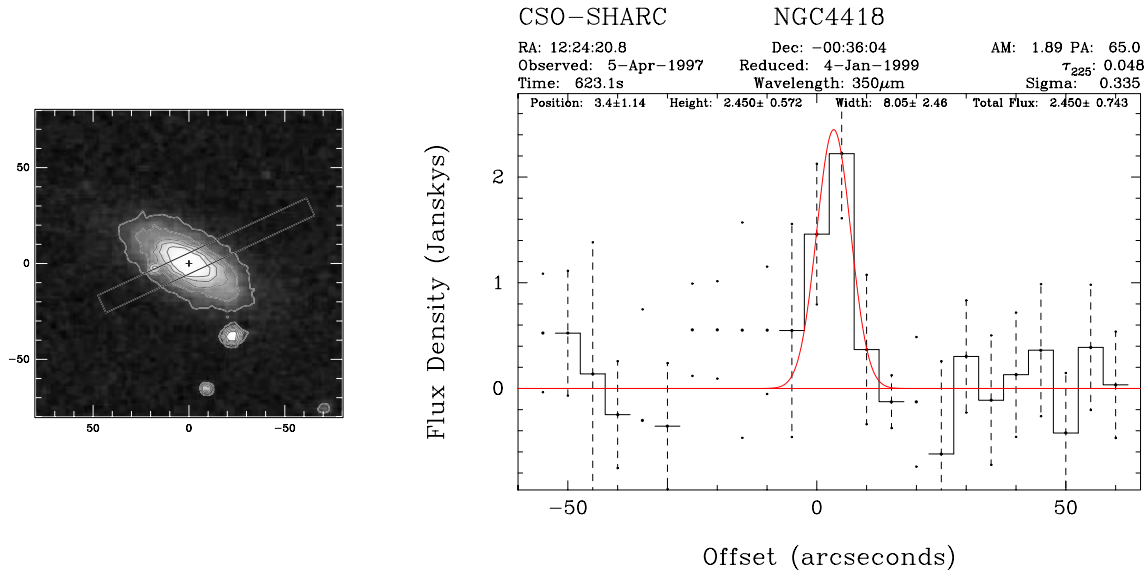

Figure 3.10 POSS image and 350μm observation of NGC 4418.

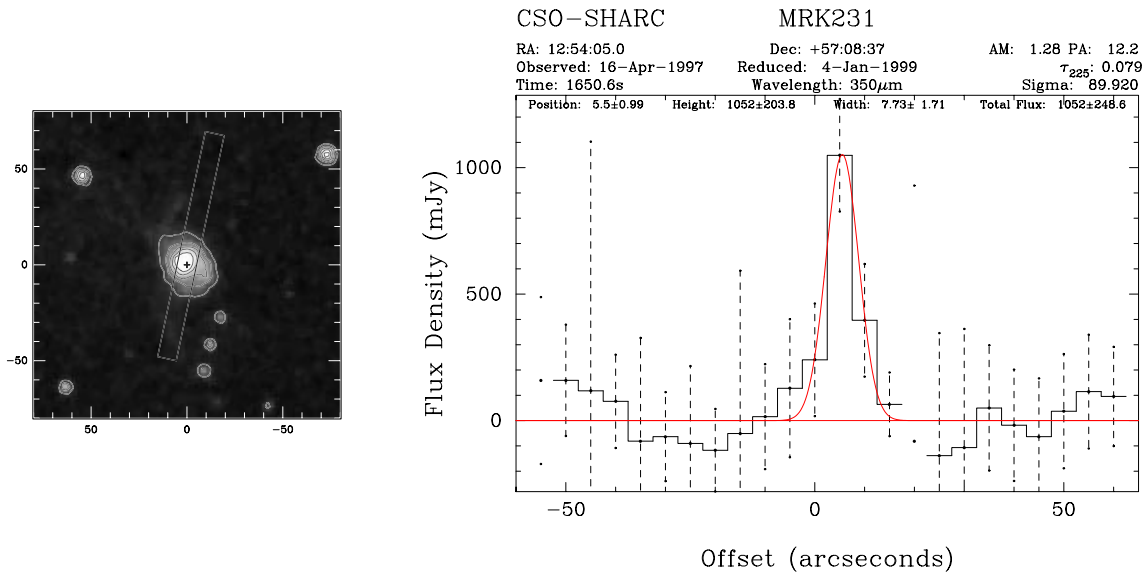

Figure 3.11 POSS image and 350μm observation of Mrk 231.

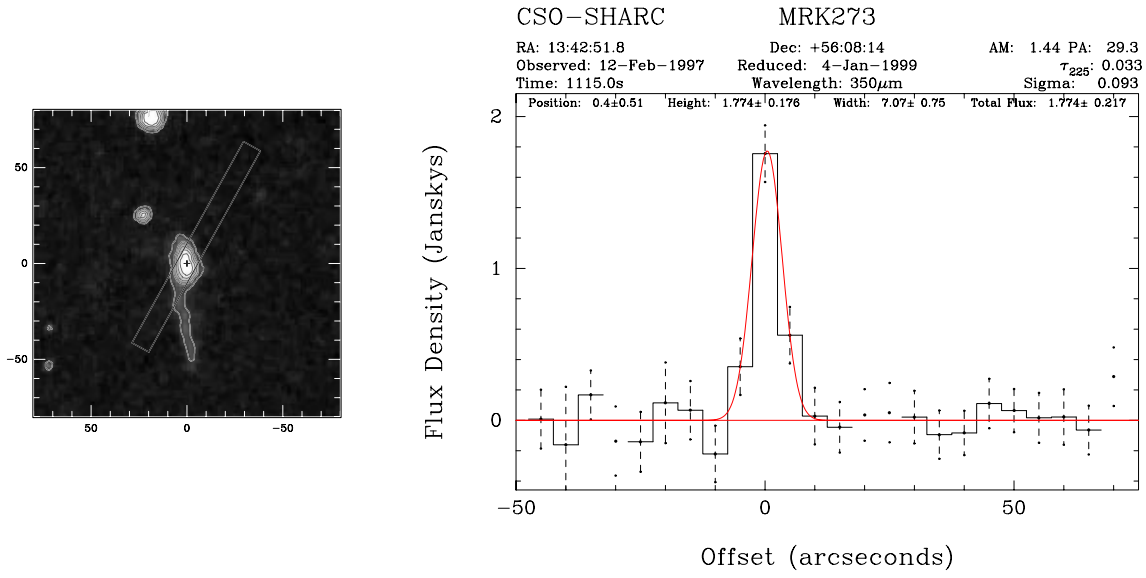

Figure 3.12 POSS image and 350μm observation of Mrk 273.

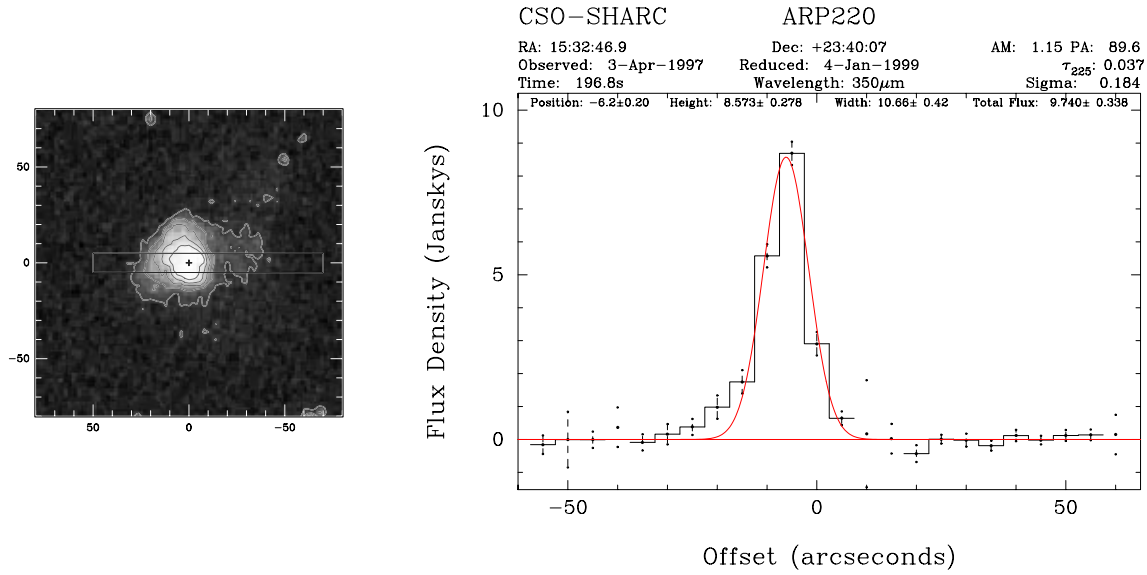

Figure 3.13 POSS image and 350μm observation of Arp 220.

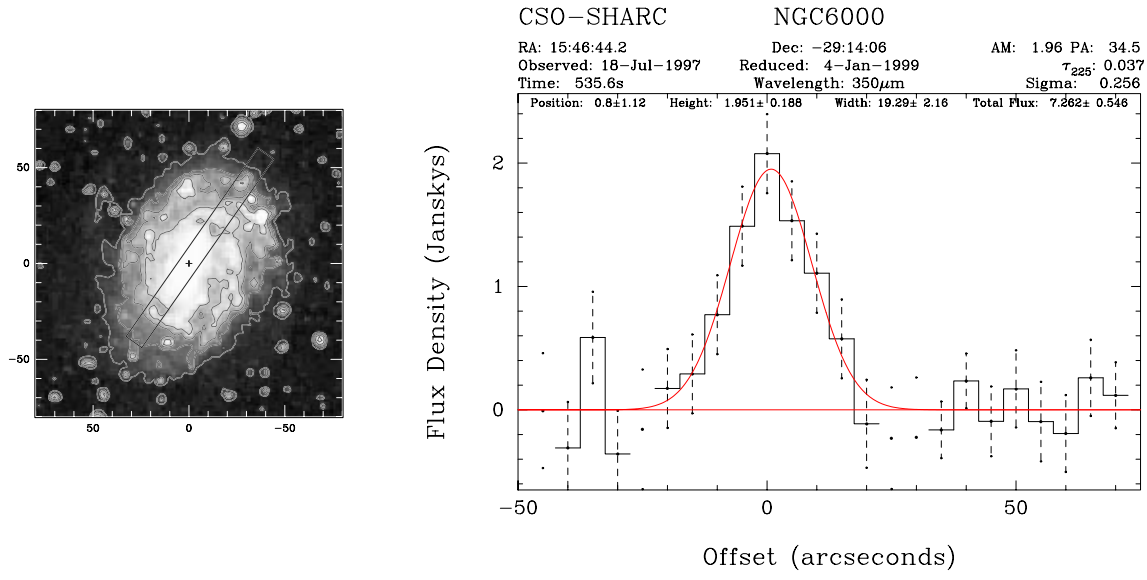

Figure 3.14 POSS image and 350μm observation of NGC 6000.

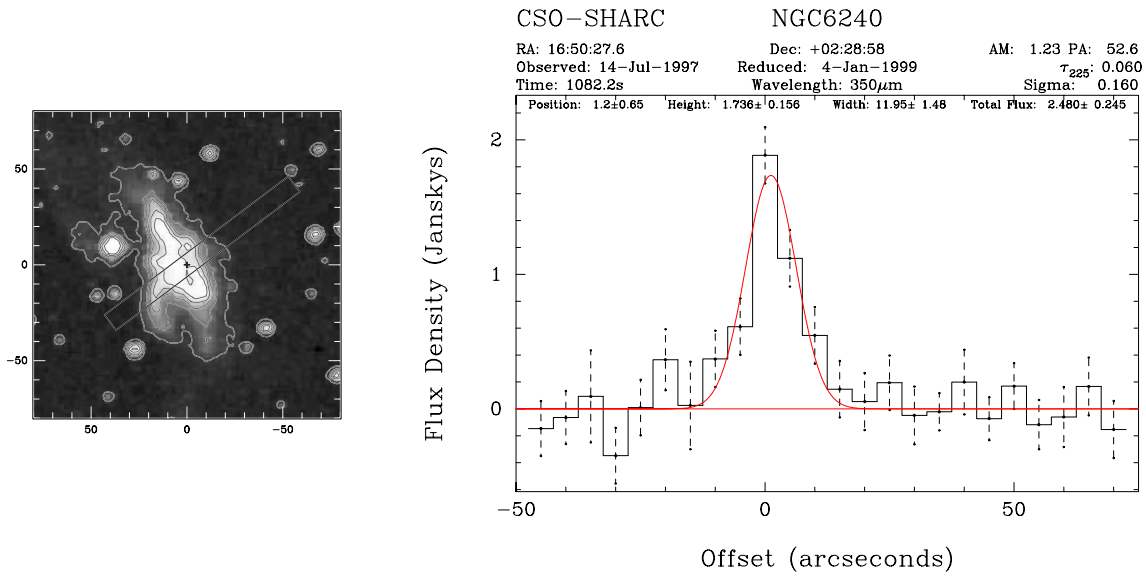

Figure 3.15 POSS image and 350μm observation of NGC 6240.

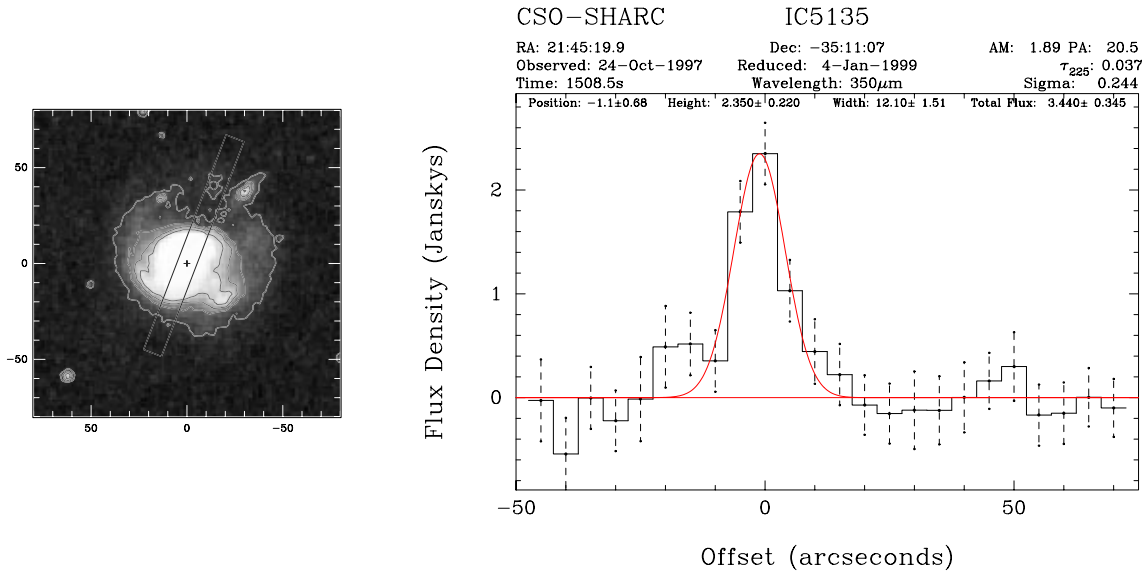

Figure 3.16 POSS image and 350μm observation of IC 5135.

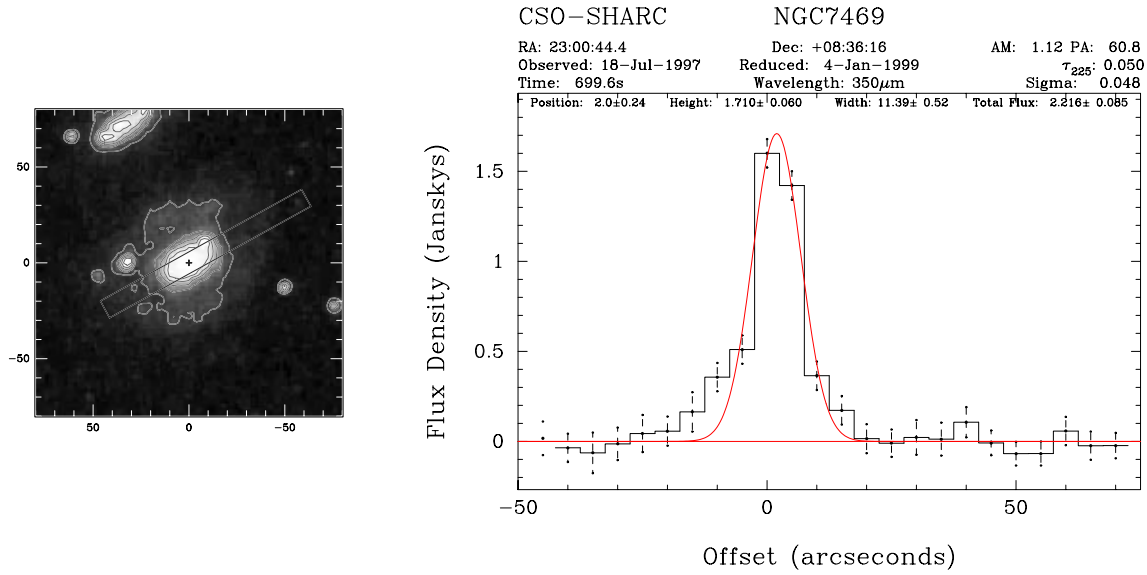

Figure 3.17 POSS image and 350μm observation of NGC 7469.

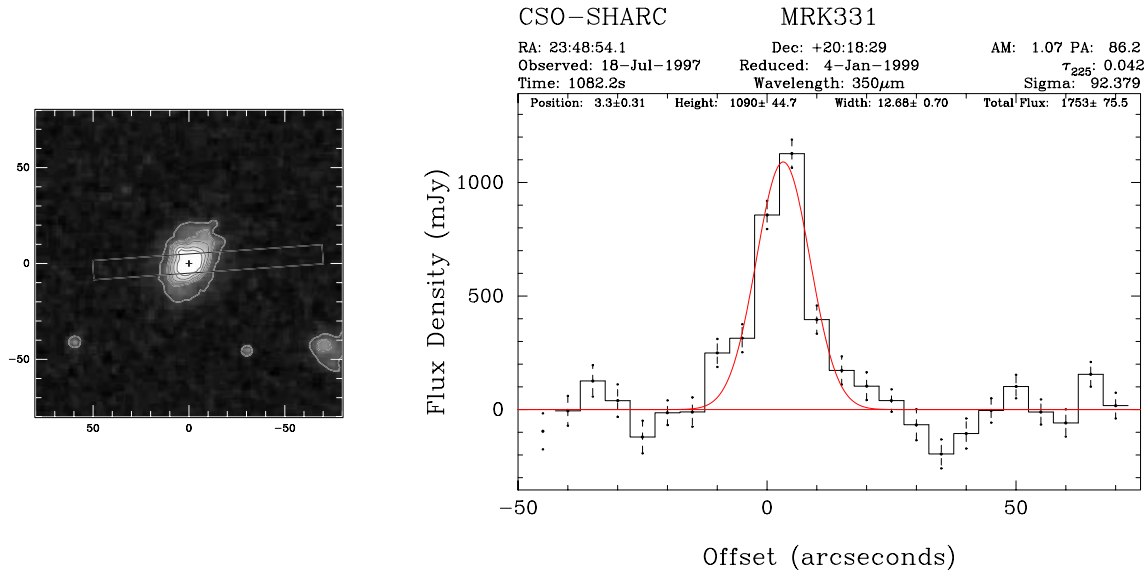

Figure 3.18 POSS image and 350μm observation of Mrk 331.

3.4 Data at Other Wavelengths

One major goal in observing this sample of galaxies is to derive the properties of the dust in luminous infrared galaxies by means of measuring the size of the emitting region at different wavelengths. As pointed out in WWB93, the mid- to far-infrared radiating region is very compact in highly luminous galaxies, being only a few arcseconds in extent as opposed to arcminutes in the optical. Using IRAS data combined with fixed-aperture observations (with either 5.″7 or 7.″6 apertures) from the IRTF[3] at 12μm and 25μm, WWB93 derived the compactness of each galaxy. The compactness is defined as the fraction of light passing through an aperture compared to the total passing through a very large aperture. With an aperture of $45'' \times 270''$ (Neugebauer et al. 1984), IRAS captures all the flux, so it is a good standard for determining compactness. If we model each galaxy's surface brightness distribution $\Xi(r)$ at radius r as

$$\Xi(r) \;=\; \exp\left(\frac{-r}{r_s}\right) \tag{3.2}$$

where r_s is the intrinsic source radius, then the total flux $\Phi(r)$ passing through an aperture of radius r is

$$\Phi(r) \;\equiv\; 2\pi \int_0^r \Xi(r)\, r \mathrm{d}r \;=\; r_s^2 \left[1 - \left(\frac{r}{r_s} + 1\right) \exp\left(\frac{-r}{r_s}\right)\right] \tag{3.3}$$

and then the compactness C is given by

$$\mathsf{C} \;\equiv\; \frac{\Phi(r)}{\Phi(\infty)} \;=\; \left[1 - \left(\frac{r}{r_s} + 1\right) \exp\left(\frac{-r}{r_s}\right)\right]. \tag{3.4}$$

This can be inverted numerically to derive source size from the compactness. Most of the sources are marginally resolved by the IRTF beam, yielding typical source sizes of $\sim 2''$. The results are given in Table 3.4. These source sizes can be converted to physical diameters using the assumed distance from Table 3.1; the mean of the 12

[3]NASA's InfraRed Telescope Facility, on Mauna Kea, is an infrared-optimized observatory.

Table 3.3 CSO-SHARC 350μm observations of luminous infrared galaxies. The error bars on the deconvolved and physical diameters are quoted at the $1\,\sigma$ levels for detections or $3\,\sigma$ levels for upper limits.

Source Name Name	Flux Density (Jy)	Raw Diameter ($''$)	Deconvolved Diameter[†] ($''$)	Physical Diameter[‡] (kpc)
NGC 520	4.89 ± 0.09	13.21 ± 0.30	$9.7\,^{+0.4}_{-0.6}$	$1.4\,^{+0.1}_{-0.1}$
NGC 1068	32.54 ± 0.82	43.41 ± 2.09	$42.5\,^{+2.1}_{-2.1}$	$3.1\,^{+0.2}_{-0.2}$
NGC 1614	1.87 ± 0.43	8.86 ± 2.07	≤ 6.2	≤ 1.9
NGC 2339	1.02 ± 0.10	9.65 ± 0.99	$3.5\,^{+2.2}_{-3.5}$	$0.5\,^{+0.3}_{-0.5}$
NGC 2388	1.38 ± 0.09	10.66 ± 0.71	$5.7\,^{+1.2}_{-1.5}$	$1.5\,^{+0.1}_{-0.1}$
NGC 2623	1.87 ± 0.08	12.07 ± 0.57	$8.04\,^{+0.8}_{-0.9}$	$2.9\,^{+0.3}_{-0.3}$
UGC 5101	2.09 ± 0.09	8.99 ± 0.41	≤ 2.7	≤ 2.1
NGC 4102	2.09 ± 0.83	8.23 ± 3.17	≤ 7.0	≤ 0.4
NGC 4194	0.97 ± 0.20	17.84 ± 5.07	$15.4\,^{+5.7}_{-6.3}$	$2.5\,^{+0.9}_{-1.0}$
NGC 4418	2.45 ± 0.74	8.05 ± 2.46	≤ 5.4	≤ 0.8
Mrk 231	1.05 ± 0.25	7.73 ± 1.71	≤ 2.8	≤ 2.3
NGC 4818	*– no data –*		–	
NGC 5135	*– no data –*		–	
Mrk 273	1.77 ± 0.22	7.07 ± 0.75	≤ 1.0	≤ 0.7
Arp 220	9.74 ± 0.34	10.66 ± 0.42	$5.7\,^{+0.8}_{-0.8}$	$2.0\,^{+0.3}_{-0.3}$
NGC 6000	7.26 ± 0.55	19.29 ± 2.16	$17.1\,^{+2.4}_{-2.5}$	$2.3\,^{+0.3}_{-0.3}$
NGC 6240	2.48 ± 0.25	11.95 ± 1.48	$7.9\,^{+2.1}_{-2.5}$	$3.7\,^{+1.0}_{-1.2}$
IC 5135	3.44 ± 0.35	12.10 ± 1.51	$8.1\,^{+2.1}_{-2.5}$	$2.5\,^{+0.7}_{-0.8}$
NGC 7469	2.22 ± 0.09	11.39 ± 0.52	$7.0\,^{+0.8}_{-0.9}$	$2.2\,^{+0.3}_{-0.3}$
Mrk 331	1.75 ± 0.08	12.68 ± 0.70	$8.9\,^{+1.0}_{-1.0}$	$3.2\,^{+0.4}_{-0.4}$

[†]Assuming Gaussian source distribution and beam.

[‡]Assuming H_0=75 km/s/Mpc.

most reliably determined diameters is $D = 0.5 \pm 0.2\,\mathrm{kpc}$. Additionally, observations at a wavelength of $\sim 1300\mu$m made by a variety of observers at several telescopes are listed.

3.5 Blackbody Fits

Using our measured flux densities and those at other wavelengths, we can fit a grey-body function as given by equation 1.1. As a check of the suitability of this fitting method, we have fit the complete spectrum of Arp 220, using data from the literature and from ISO-LWS observations (Fischer & Cox, private communication) at wavelengths longer than 60μm. This fit is shown in Figure 3.19 with its corresponding χ^2_ν hypersurface, demonstrating the excellent fit obtained. The best fit parameters are $T = 43.4 \pm 0.5\,\mathrm{K}$ and $\beta = 1.22 \pm 0.06$. The magnitude of the error (and, indeed, much of the extent in the hyperspace) is due to errors in the data themselves: flux density uncertainties are generally quoted as statistical errors. Without any compensation for the calibration uncertainties, the uncertainties assigned to each measurement are too small to allow a good fit. This kind of error does not decrease with additional data; the mean is determined more precisely but the variance remains constant.

Table 3.4 Data at other wavelengths.

Source Name	Mean 12 & 25μm Compactness $C^{\dagger}$	Source Diam. ($''$)‡	Diameter (kpc)$^{\flat}$	Flux Density at 1300μm (mJy)	Ref. No.
NGC 520	0.80 ± 0.12	2.5	0.37	50±25	1
NGC 1068		3.2$^{\natural}$	0.23	170±30	7,10
NGC 1614	1.01 ± 0.10	< 1.9	< 0.59	10.9±3.2	6
NGC 2339	0.73 ± 0.10	2.2	0.31	19.4±2.4	3
NGC 2388	0.50 ± 0.20	3.4	0.91		
NGC 2623	0.75 ± 0.22	2.1	0.75		
UGC 5101				< 36	5
NGC 4102	0.86 ± 0.07	1.6	0.09	50±6	4
NGC 4194	0.70 ± 0.09	2.3	0.37	< 9	6
NGC 4418	0.97 ± 0.12	< 1.7	< 0.24	72±12	4
Mrk 231		$< 3.0^{\natural}$	< 2.45	40±1.8	2,9
NGC 4818	1.03 ± 0.14	< 1.5	< 0.11		
NGC 5135	0.80 ± 0.15	1.9	0.50		
Mrk 273	0.85 ± 0.13	1.7	1.24	20.3±2	2
Arp 220	0.99 ± 0.11	< 1.6	< 0.56	226±20	5
NGC 6000	0.72 ± 0.08	2.2	0.30	42.7±3.9	8
NGC 6240	0.91 ± 0.11	1.4	0.66	20.5±10	1
IC 5135	0.85 ± 0.15	2.3	0.72	32.9±4.3	8
NGC 7469	1.04 ± 0.14	< 2.0	< 0.63	< 33	5
Mrk 331	1.01 ± 0.14	1.6	0.57	< 8.7	

†Mean compactness of measurements at 12μm and 25μm using a small aperture and IRAS data, from WWB93.

‡Source size calculated using exponential surface brightness falloff; see text for derivation.

$^{\flat}$Source diameter calculated using size and presumed distance.

$^{\natural}$Source size estimated using flux measurements from the literature (NED Database).

References. — 1. Braine & Dumke (1998); 2. Krügel et al. (1988); 3. Chini et al. (1995); 4. Roche & Chandler (1993); 5. Carico et al. (1992); 6. Chini et al. (1988) 7. Thronson et al. (1987); 8. Chini, Krügel & Lemke (1996); 9. Chini, Krügel & Kreysa (1992); 10. Rowan-Robinson (1992)

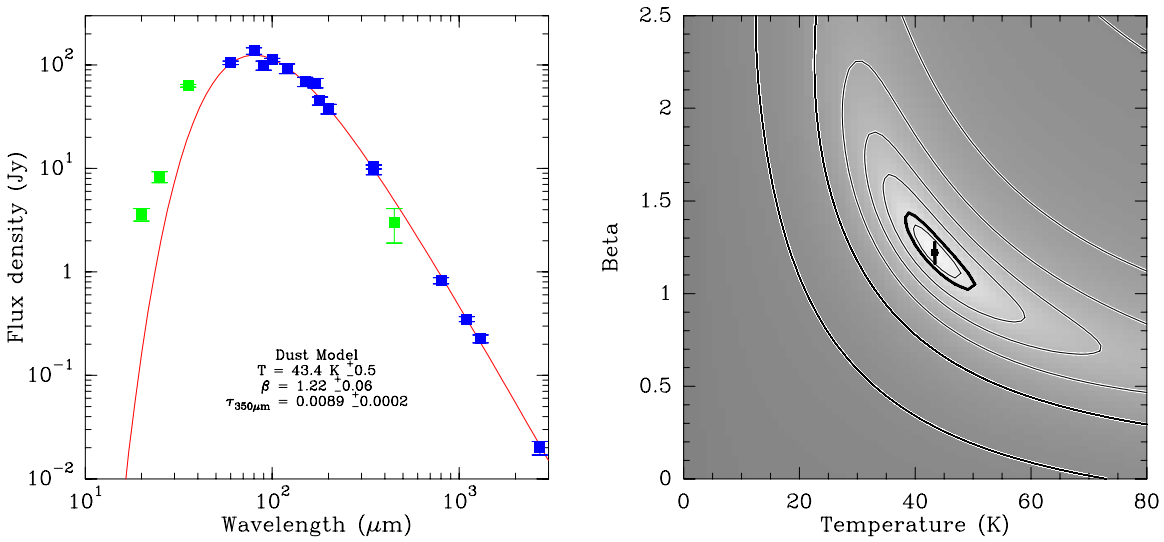

Figure 3.19 Greybody fit to the observed spectrum of Arp 220 from far-infrared to millimeter wavelengths. (Left) Derived spectrum (solid curve) with measurements (points); only the darker points were used in the fit. This data include points from ISO, IRAS, CSO, JCMT, IRAM, and OVRO observations. Here and in the following SEDs, the lighter points were not used in the fit. (Right) χ^2_ν hypersurface of this fit. The contours are multiples of 2,4,..., 64 times the minimum in χ^2_ν. The minimum is 1.38, while the heavy contour denotes the $3\,\sigma$ level.

Using only the IRAS 60μm and 100μm data, our measured 350μm detections, and 1300μm detections or upper limits from the literature where available, we are able to find a good greybody model for the spectrum of the cold dust component in each galaxy. For those galaxies in which our statistical errors in the determination of the flux density were small, an assumed uncertainty of 10% was used to allow for calibration errors. The longer-wavelength data for Mrk 231 was corrected for an assumed synchrotron component with a spectral index of $\alpha = -0.7$ (Bryant & Scoville 1996). These broadband SEDs are shown in figures 3.20–3.22. Additional submillimeter points are included from the references in Table 3.4 and Rowan-Robinson (1992), Chini, Krügel & Kreysa (1992), and Rigopoulou, Lawrence & Rowan-Robinson (1996).

Our four-band fit to the SED of Arp 220 yielded a temperature or 45.0 ± 0.2 K and $\beta = 1.17 \pm 0.03$. This is reasonably consistent with the fit from the decidedly different ISO dataset used for Figure 3.19, and demonstrates the efficacy of the greybody fitting routine in determining parameters accurately and precisely.

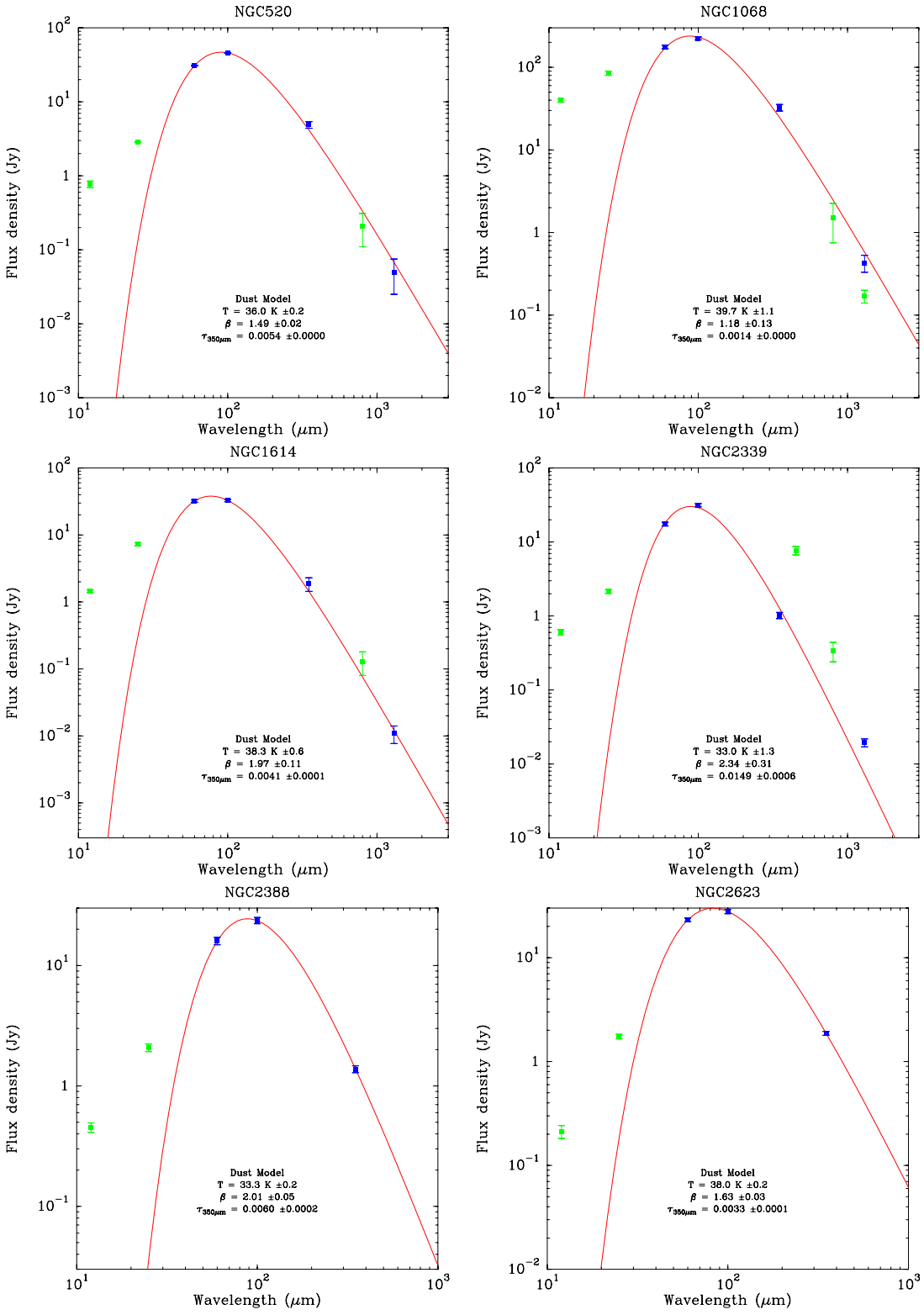

Figure 3.20 Greybody fits to the cold dust emission spectrum of NGC 520, NGC 1068, NGC 1614, NGC 2339, NGC 2388, and NGC 2623.

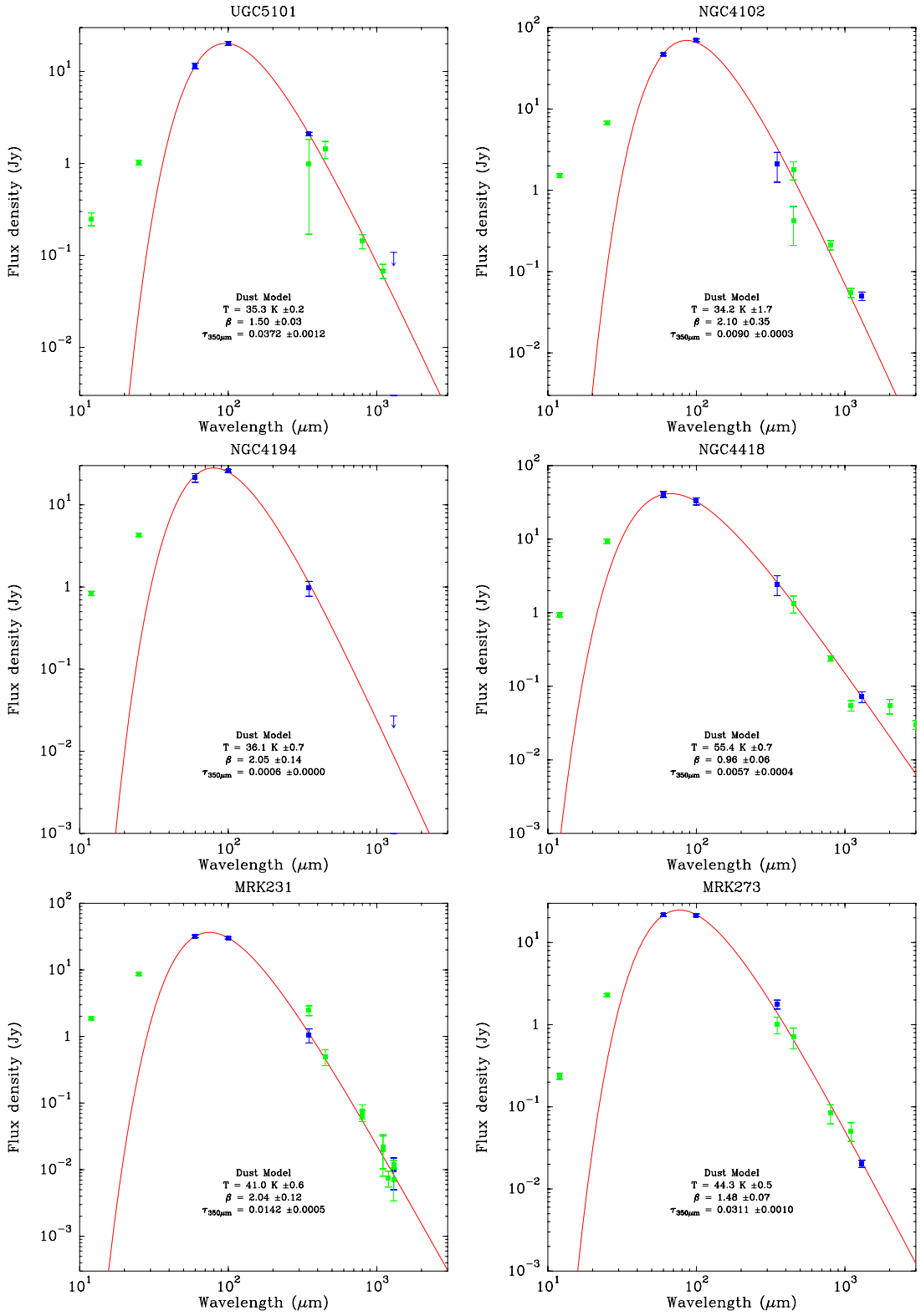

Figure 3.21 Greybody fits to the cold dust emission spectrum of UGC 5101, NGC 4102, NGC 4194, NGC 4418, Mrk 231, and Mrk 273.

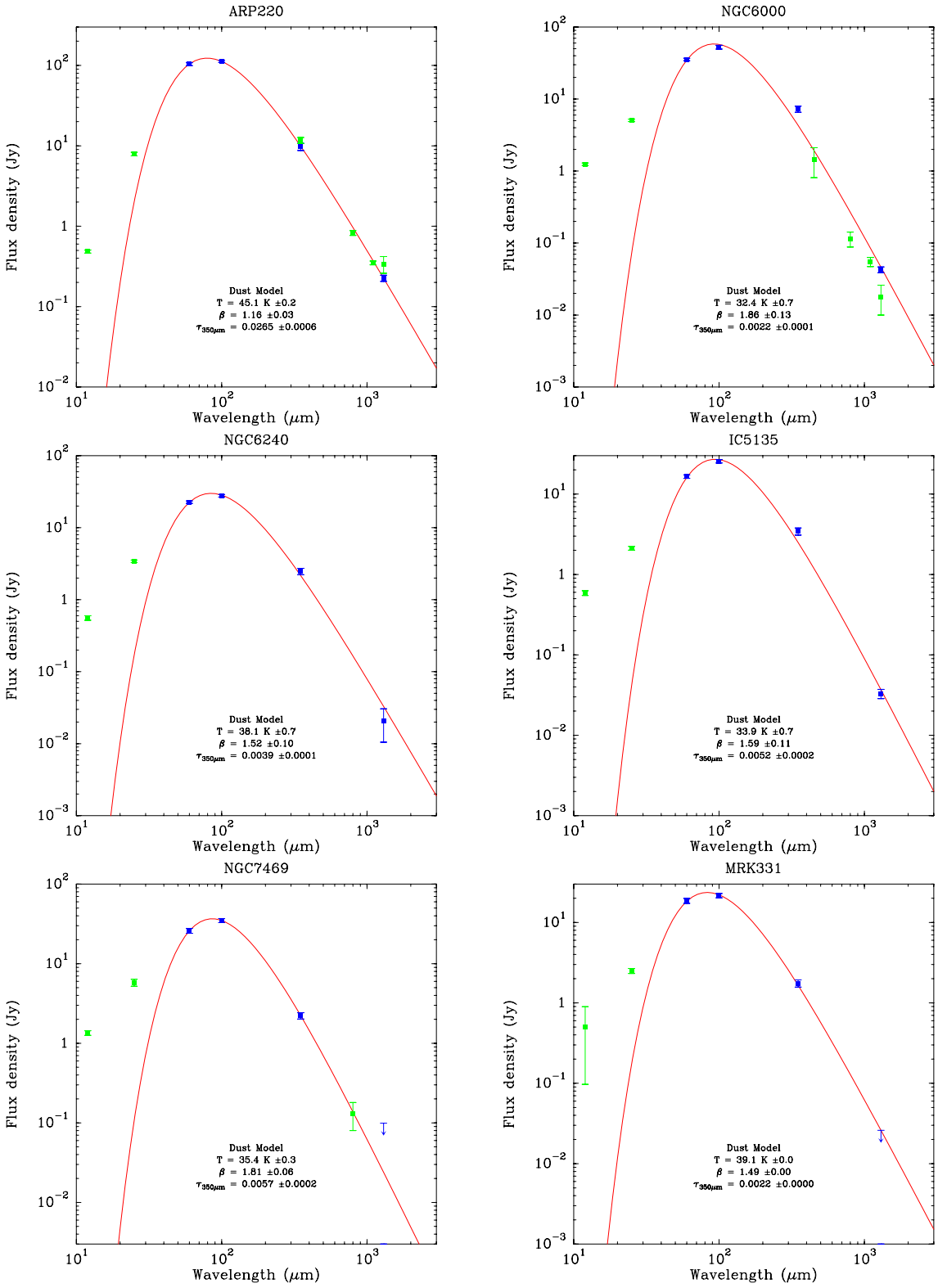

Figure 3.22 Greybody fits to the cold dust emission spectrum of Arp 220, NGC 6000, NGC 6240, IC 5135, NGC 7469 and Mrk 331.

The full parameters for the fits are given in Table 3.5. Listed there are the fitted temperature, emissivity index β, and 350μm opacity τ_{350} assuming a source size as given in Table 3.3. Derived parameters such as the luminosity of the cold dust component and the dust mass are given, assuming an emissivity at 2.4 THz of 7.5×10^{-4} and a mass opacity coefficient $\kappa = 18.75$ cm^2 g^{-1} (Hildebrand 1983). Furthermore, the fraction of the total far infrared luminosity emitted by the cold dust component and the luminosity to mass ratio are given. The fraction of the total far infrared luminosity shall be defined as the ratio of the luminosity carried by the cold component (and hereafter labeled $L_{\rm FIR}$) to the total infrared luminosity as measured by IRAS for the 1-1000μm range (hereafter denoted by $L_{\rm IR}$).

The relations between the three fitted parameters and the luminosity are shown in the graph in Figure 3.23. It is apparent that the values of temperature and β lie in a region shaped similarly to the χ^2_ν hypersurface shown in Figure 3.19. This is probably partly a reflection of the fact that with a limited number of spectral points, none of which are in the Wien limit, a greybody fit cannot be achieved in which the values of temperature and β are independently constrained. There appears to be a tendency for the most luminous objects to have a higher optical depth, although the statistics are too poor to establish a relation. There is, however, an apparent trend present in the luminosity vs. temperature, which will be discussed later.

3.5.1 The Luminosity and Mass of LIRGs

Relations between the derived parameters (luminosity, fractional FIR luminosity, mass, and luminosity-to-mass ratio) are shown in the nomograph in Figure 3.24. The most obvious relation is that between the dust mass and the luminosity – or equivalently, the generally increasing luminosity-to-mass ratio with increasing luminosity – which are well-fit by a power law:

$$\left(\frac{M}{10^6\,M_\odot}\right) = 2.7\left(\frac{L}{10^{10}\,L_\odot}\right)^{0.77} \qquad \left(\frac{L/M}{100\,L_\odot/M_\odot}\right) = 37\left(\frac{L}{10^{10}\,L_\odot}\right)^{0.23}. \tag{3.5}$$

Table 3.5 Dervied physical properties of the cold dust emission regions of the luminous infrared galaxies.

Source	Fitted Parameters			Derived Parameters			
Name	Temperature	β	$\tau_{350\mu m}$	L_{FIR} ($10^{10}\,L_\odot$)	L_{FIR}/L_{IR}	Dust Mass ($10^6\,M_\odot$)	L/M ($100\,L_\odot/M_\odot$)
NGC 520	36.1 ± 0.2	1.47 ± 0.02	0.0055	6.25 ± 0.08	0.93	10.4 ± 0.1	60
NGC 1068	39.7 ± 1.1	1.18 ± 0.13	0.0014	8.44 ± 0.63	0.43	9.4 ± 0.3	90
NGC 1614	38.3 ± 0.6	1.97 ± 0.11	0.0041	24.40 ± 1.39	0.59	23.4 ± 0.7	104
NGC 2339	33.3 ± 1.3	2.28 ± 0.30	0.0150	3.31 ± 0.36	0.62	8.6 ± 0.4	39
NGC 2388	33.3 ± 0.2	2.01 ± 0.05	0.0060	10.17 ± 0.32	0.72	22.3 ± 0.9	46
NGC 2623	38.3 ± 0.2	1.61 ± 0.03	0.0032	25.23 ± 0.58	0.78	28.4 ± 0.7	89
UCG 5101	35.2 ± 0.2	1.51 ± 0.03	0.0374	67.94 ± 1.43	0.85	165.2 ± 5.4	41
NGC 4102	34.4 ± 1.6	2.07 ± 0.34	0.0091	1.21 ± 0.17	0.30	2.2 ± 0.1	54
NGC 4194	32.9 ± 0.4	2.37 ± 0.09	0.0006	4.54 ± 0.24	0.59	8.5 ± 0.3	53
NGC 4418	55.2 ± 0.7	0.96 ± 0.06	0.0057	7.40 ± 0.41	0.68	1.8 ± 0.1	410
Mrk 231	40.9 ± 0.6	2.05 ± 0.12	0.0141	164.10 ± 8.41	0.52	131.4 ± 4.7	125
NGC 4818		*– no data –*				–	
NGC 5135		*– no data –*				–	
Mrk 273	44.3 ± 0.5	1.48 ± 0.07	0.0312	95.59 ± 3.55	0.74	66.8 ± 2.0	143
Arp 220	45.0 ± 0.2	1.17 ± 0.03	0.0266	111.20 ± 2.34	0.85	71.8 ± 1.7	155
NGC 6000	32.3 ± 0.7	1.86 ± 0.13	0.0022	6.18 ± 0.43	0.60	16.3 ± 0.5	38
NGC 6240	38.2 ± 0.7	1.51 ± 0.10	0.0039	44.12 ± 2.55	0.71	52.4 ± 1.5	84
IC 5135	33.9 ± 0.7	1.59 ± 0.11	0.0052	15.46 ± 0.95	0.72	34.8 ± 1.2	44
NGC 7469	35.5 ± 0.3	1.81 ± 0.06	0.0057	22.52 ± 0.88	0.60	36.7 ± 1.5	61
Mrk 331[†]	39.7 ± 0.5	1.47 ± 0.05	0.0022	20.58 ± 1.00	0.81	20.1 ± 0.7	102

[†] Uncertainties are estimated, as the lack of a 1300μm datum prevents solving for the true uncertainties.

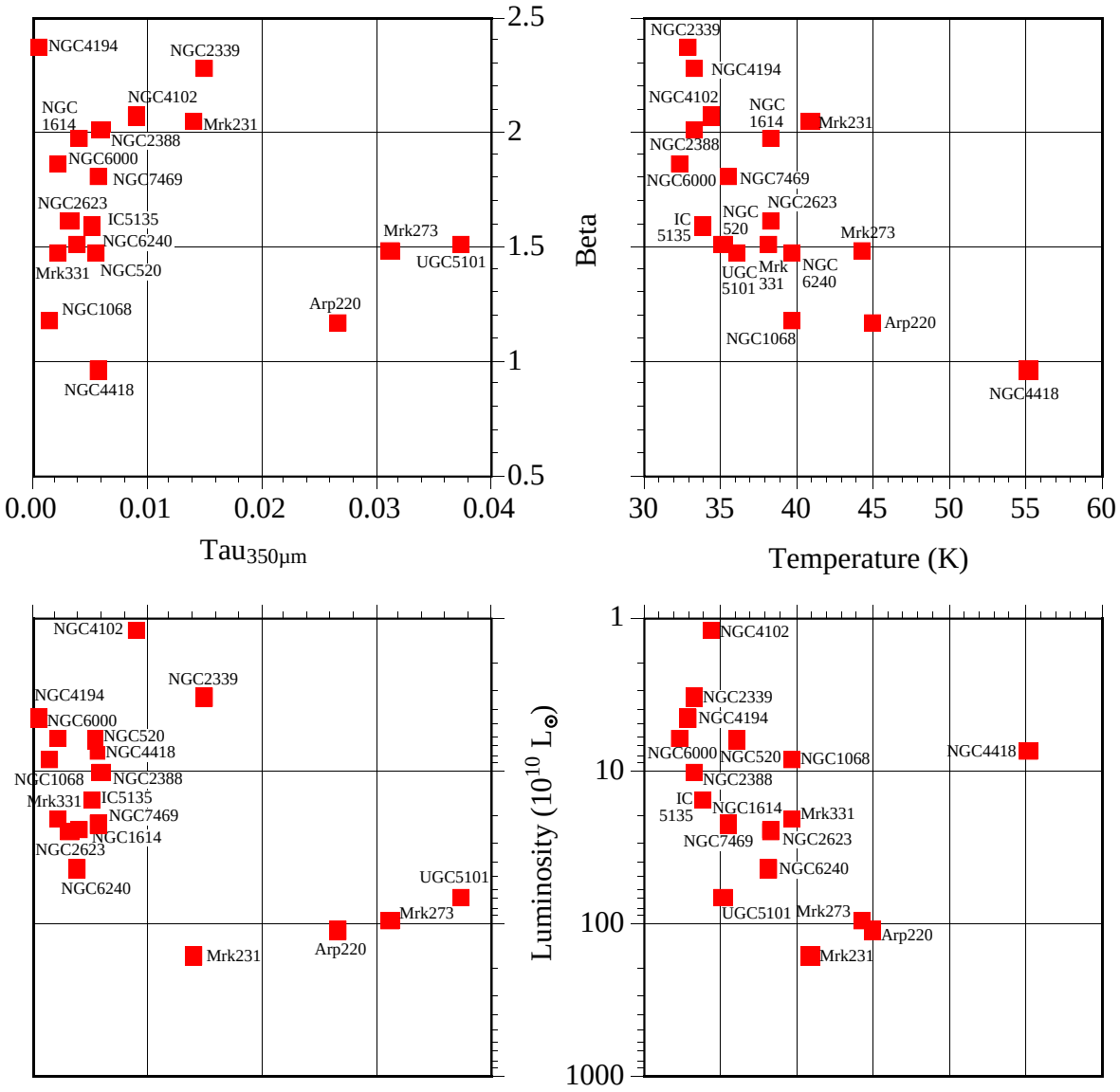

Figure 3.23 Graphs of the greybody fitting parameters (temperature, β, $\tau_{350\mu m}$) and luminosity in units of $10^{10}\,L_{\odot}$. A clear correlation can be seen in the two plots against temperature. In this quadrant plot, a single source can be traced through all four graphs as the axes are aligned, to simplify the comparison of parameters for various sources.

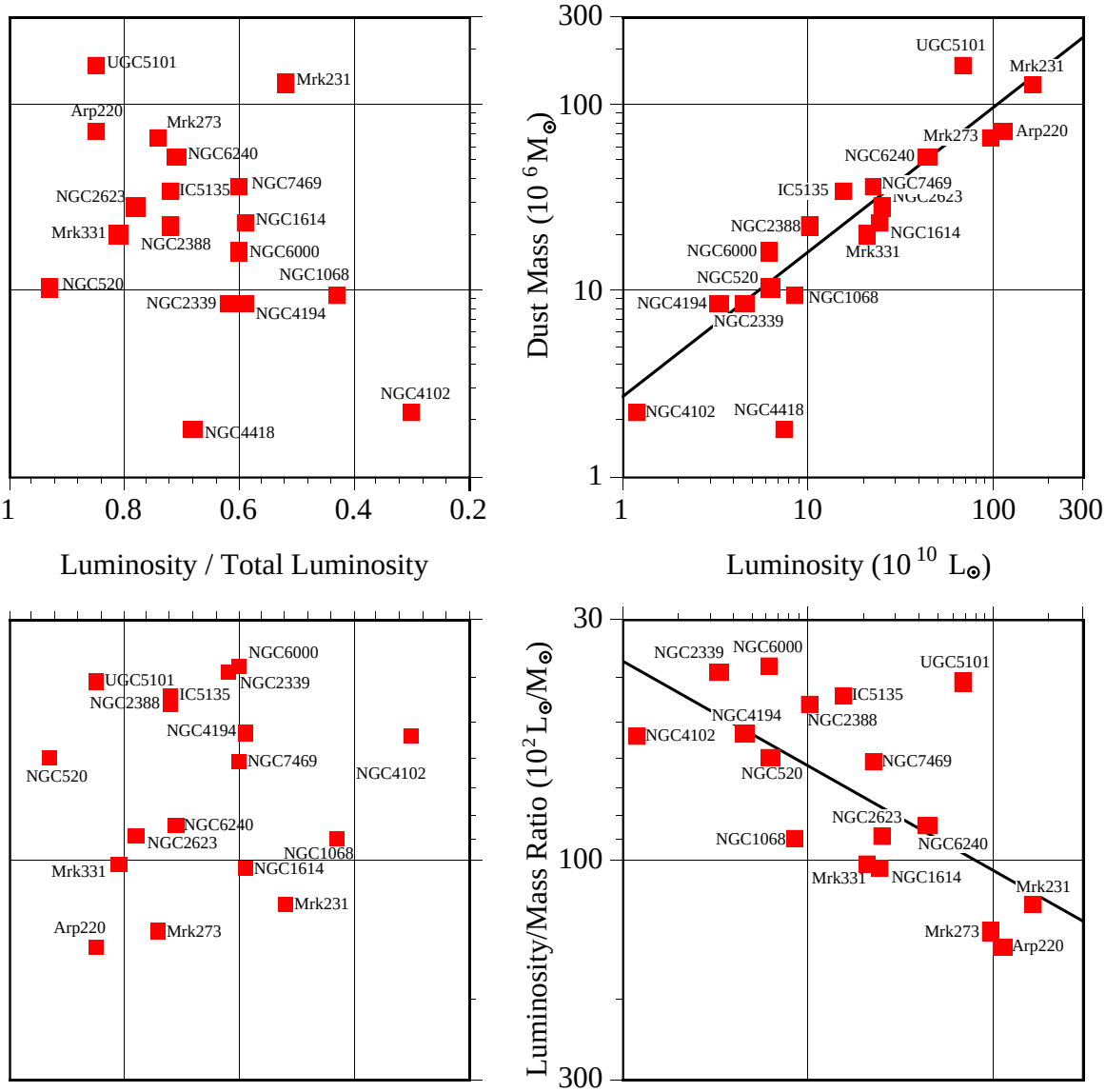

Figure 3.24 Graph of the derived parameters (FIR luminosity (that of the cold component, essentially at $\lambda > 40\mu$m), fractional FIR luminosity, mass, and luminosity-to-mass ratio). A correlation between the luminosity-to-mass ratio and the luminosity can be seen, as can a slight dependence of the fractional FIR luminosity on the luminosity. This plot is similar to Figure 3.23 in its quadrant format.

As noted before, there is a fairly reliable correlation between the luminosity and the temperature, as shown in Figure 3.25. In this plot, NGC 4418 is offscale because its parameters are substantially far off this correlation, implying an error in some of the data or a fundamentally different physical environment. The error bars are a reasonable estimate to the variance in each parameter. The line is a power law fit to the data, with

$$T \;=\; 31 \left(\frac{L}{10^{10}\, L_{\odot}} \right)^{0.06} \; K. \tag{3.6}$$

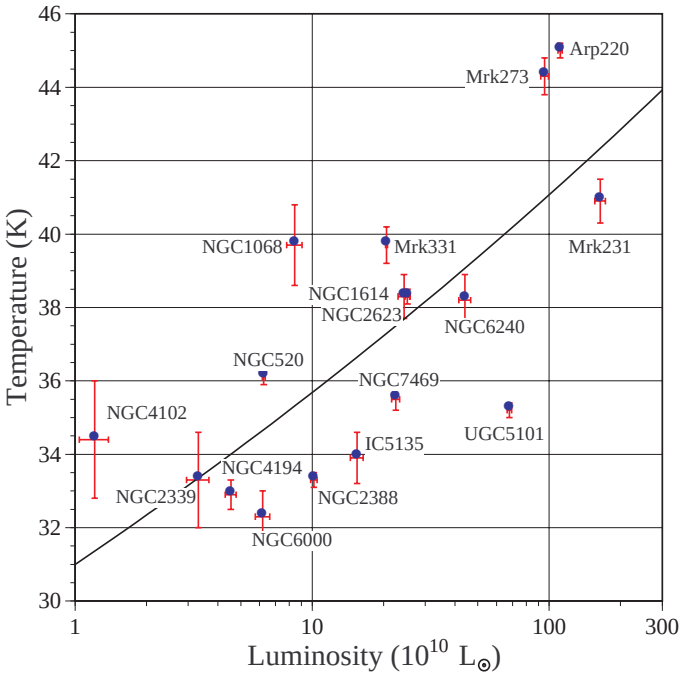

Figure 3.25 Temperature vs. luminosity (in units of $10^{10}\, L_{\odot}$) for 17 of the detected LIRGS; NGC 4418 is offscale because its parameters are very far off the norm.

The total far-infrared luminosity is proportional to the dust mass and the integrated greybody function, so the ratio $L_{\rm FIR}/M_{\rm dust}$ should be proportional to the integral of the modified Planck function. In other words,

$$\left(\frac{L_{\rm FIR}}{M_{\rm dust}} \right) \;\propto\; \int_0^{\infty} B_{\nu}(T_{\rm dust}) Q_{\nu}(\beta) {\rm d}\nu \;\propto T_{\rm dust}^{\beta'}, \tag{3.7}$$

where the weighted-average index β' has been introduced. This new index allows for the effective reduction in apparent β due to the fact that the dependence of $Q_{\nu}(\beta) \;\propto\; [1 - \exp(-(\nu/2.4\,{\rm THz})^{\beta})]$ becomes independent of β at frequencies above

$\sim 3\,\mathrm{THz}$ ($100\mu\mathrm{m}$), i.e., when the object becomes a blackbody.

For our observations this correlation is excellent, as shown in Figure 3.26. The relation is

$$\left(\frac{L/M}{100\,L_\odot/M_\odot}\right) = 9\times10^{-6}\,T^{4.4} \qquad \text{implying } \beta' = 0.4. \tag{3.8}$$

This can be compared with the result of Hunter (1997) wherein a sample of 26 ultra-compact HII regions exhibit $L/M = 1\times10^{-6}\,T^{4.7}$, a similar result.

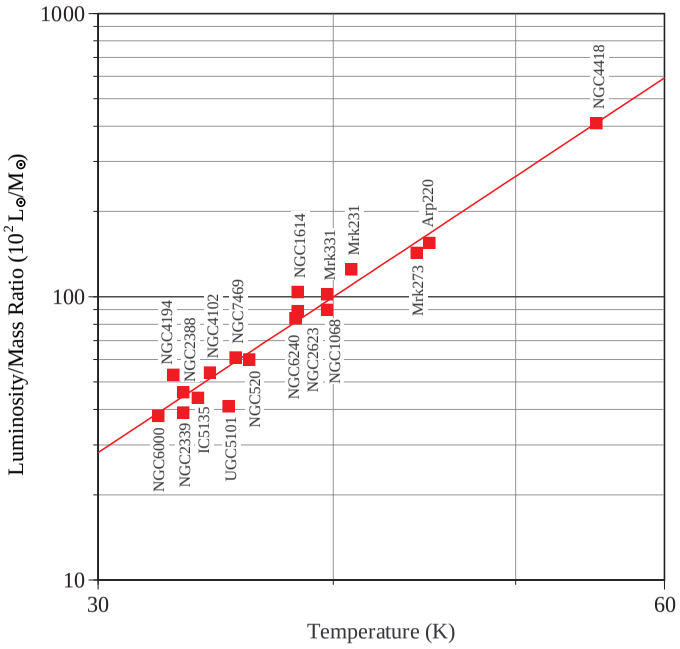

Figure 3.26 Luminosity to mass ratio (in units of $100\,L_\odot/M_\odot$) for the LIRGs.

Furthermore, in Figure 3.24 there is a slight proportional dependence visible in the fractional FIR luminosity as a function of mass. Because of the tight correlation between luminosity and mass, this indicates an increase in the fractional FIR luminosity with the cold dust component of the luminosity. This relation is shown in Figure 3.27, and follows $L_{\mathrm{FIR}}/L_{\mathrm{IR}} = 0.12\log(L/L_\odot) - 0.66$. This indicates that objects with larger luminosities in the cold dust component are increasingly dominated by that component, i.e., the infrared-to-millimeter SED is not linearly dependent on total luminosity, but changes shape to a colder SED as luminosity increases.

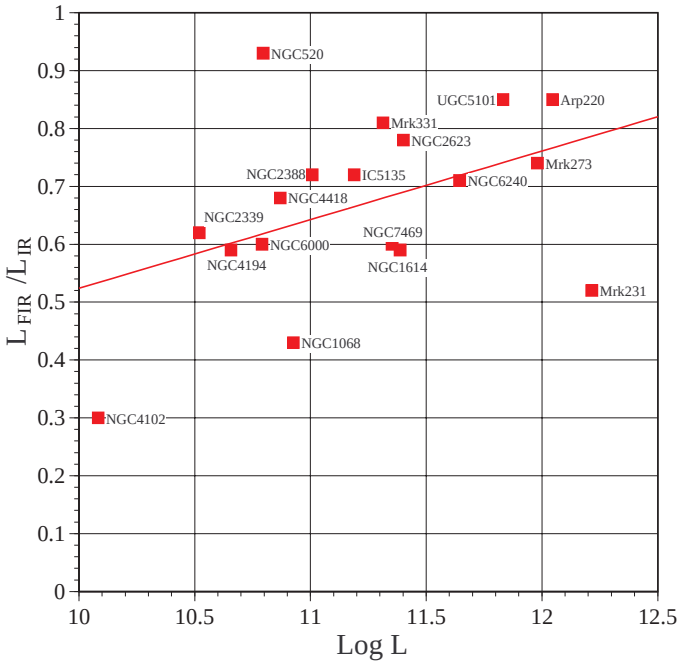

Figure 3.27 Fractional FIR luminosity vs. log luminosity (in $L_{\odot}$) for the LIRGs.

3.5.2 Emissivity Index

The mean value of the emissivity index β is 1.7 ± 0.4, as shown in the histogram on the left of Figure 3.28. As noted before, there is a correlation between the index β and the temperature, which may be partially due to an artifact of the curve fitting. For most galaxies, the product $T\beta$ is poorly constrained, so one would expect a decrease in β as the fitted temperature increases, as is shown in the right half of Figure 3.28. However, the variance σ_β of 0.4 is too large to be explained merely by poor fitting; hence, some of this variance is intrinsic to the sources, and has physical meaning. This curve is a fit to the data, following $\beta = 64/T$.

With an average emissivity index of 1.7, we can strongly reject models of pure amorphous carbon grains, which yield an index of 1.1 ± 0.1 (Colangeli et al. 1995; Mennella et al. 1998). However, our index is not well matched by silicates either, which require an index of $\beta \geq 2.0$. It is therefore likely that the dust is of mixed composition, with the silicate grains contributing more at shorter wavelengths and the carbonaceous at longer ones. Without improved spectral data, determining if this is indeed the case and measuring the crossover wavelength are not possible. Furthermore, the variance in the index intimates that some variation in the mixing

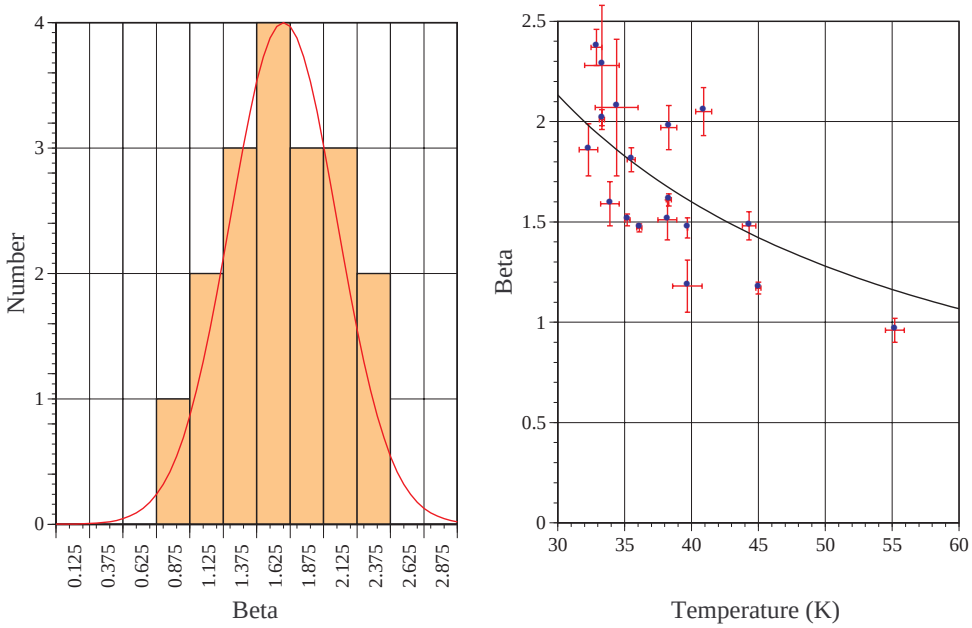

Figure 3.28 [Left] Histogrammed distribution of the observed values of the emissivity index β. The mean is 1.7, with a standard deviation of 0.4, as shown by the curve. [Right] Variation of β with temperature, approximately following $\beta = 64/T$.

ratio is present in the galaxies, but much better moderate-resolution spectroscopy is necessary to constrain this. It must be pointed out that the measured β can be less than the true index in the case of a source with large amounts of mass at colder temperatures (e.g., Lis, Carlstrom & Keene 1991), so we cannot entirely rule out a true index of 2. However, if we require $\beta = 2$ and fit a two-component model to Arp 220, we find we need an order of magnitude more mass in the second component with a temperature of ~ 15K. If this were the case, Arp 220 would become one of the most massive objects in the universe ($\mathrm{M_{H_2}} \sim 7 \times 10^{11} M_{\odot}$).

3.5.3 Gas-to-Dust Conversion Factor

The conversion factor used to estimate the total molecular gas mass from the derived dust mass is a subject of much uncertainty; local gas clouds have been measured at 100 (Helou 1989), while for a sample of luminous infrared galaxies, Sanders, Scoville & Soifer (1991) have found a value of 540 ± 290. Using the molecular gas masses derived from CO measurements of 12 galaxies in common with Sanders, Scoville &

Soifer (1991) and Solomon et al. (1997), we can derive a conversion factor to our observed dust masses. The mean factor is $M_{\rm H_2}/M_{\rm dust} = 480 \pm 290$, a very similar finding.

3.6 Size of the 350μm Emitting Region

If we assume that the cold dust component in the nuclear region of each galaxy can be approximated as a spherically symmetric dust distribution with a central heating source (in this case, a nuclear starburst or AGN), then the dust temperature will drop as a function of radius. By measuring the size of the nuclear dust region, we have determined the radius at which the dust radiates at 350μm with the measured temperature. We also derive the temperature of this shell using flux density measurements at additional wavelengths; this temperature is imprecise in our model due to the different source sizes at different wavelengths. However, without the ability to resolve the emission spatially at several wavelengths, this problem is not severe enough to warrant a more sophisticated solution.

We start by considering a spherically symmetric dust cloud with central heating provided by a source of UV luminosity (e.g., massive stars), and assume a radial density profile of $\mathcal{N}(r) \propto r^{-1}$. Assuming a greybody spectrum as in equation 1.1, the radiative transfer problem can be solved analytically (e.g., Bollea & Cavaliere 1976). The standard balance of absorption and emission, when corrected for a spectral index β, is given by $L e^{-\tau_{\rm UV}} (4\pi r^2)^{-1} Q_{\rm UV} = 4 Q_{\rm submm} \nu^{-\beta} \sigma_\beta T^{4+\beta}$. Following the formulation of Hughes et al. (1993), the radius r at which dust heated by a central source of luminosity L is in radiative thermal equilibrium at temperature T is given by:

$$r = \left(\frac{L}{T^{4+\beta}}\right)^{1/2} \left[\frac{e^{-\tau_{\rm uv}} Q_{\rm uv} \nu^\beta}{Q_{\rm submm}} \frac{c^2 h^{3+\beta}}{32\pi k^{4+\beta}} \frac{1}{\Gamma(4+\beta)\,\zeta(4+\beta)}\right]^{1/2}. \qquad (3.9)$$

In this formula, a greybody emission spectrum (equation 1.1) with emissivity spectral index β is assumed, $Q_{\rm uv}$ and $Q_{\rm submm}$ are the ultraviolet and submillimeter grain

absorptivities, $\tau_{\rm uv}$ is the ultraviolet optical depth to the heating continuum, and

$$\Gamma(\varkappa) \equiv \int_0^\infty \mathrm{e}^{-\varphi}\varphi^{\varkappa-1}\mathrm{d}\varphi \qquad \text{and} \qquad \zeta(\wp) \equiv \sum_{\mathrm{n}=1}^{\infty}\frac{1}{\mathrm{n}^{\wp}} \tag{3.10}$$

are the Gamma function and Riemann zeta function, respectively. Fortunately, these functions are very well-behaved over the interval $0 \leq \beta \leq 2$, as shown in Figure 3.29. The zeta function is very nearly 1.05, while the Gamma function can be approximated as $\Gamma(\beta) = 5.6\mathrm{e}^{1.5\beta}$. The net error is less than 10% across the entire range.

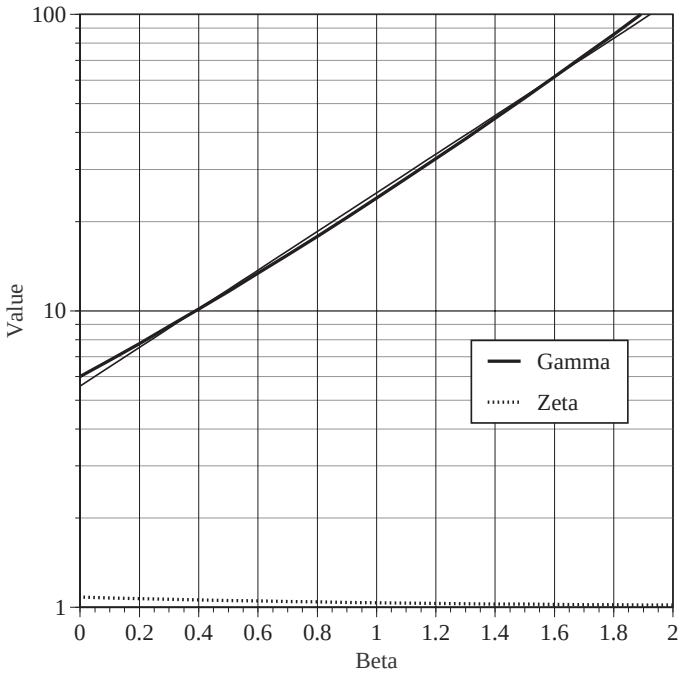

Figure 3.29 Values of the Gamma function and the Riemann zeta function of $(4+\beta)$ for β between 0 and 2. The thin line following the Gamma function is the approximation (see text).

For the other parameters, we must make further approximations; the easiest is the ultraviolet properties, as the emissivity $Q_{\rm uv}$ is nearly unity and the optical depth is sufficient to absorb all incident UV continuum by $\tau_{\rm uv} \simeq 3$. The submillimeter emissivity $Q_{\rm submm}$ can be estimated if we take the value of Hildebrand (1983) of $Q_{125\mu\mathrm{m}} = 10^{-3}$ and scale to arbitrary submillimeter frequency by:

$$Q_{\rm submm} = Q_{125\mu\mathrm{m}}\left(\frac{\nu}{2.4\,\mathrm{THz}}\right)^{\beta}. \tag{3.11}$$

We can now substitute these values into equation 3.9 and reduce it to

$$r \;=\; \left(\frac{L}{L_\odot}\right)^{1/2} \left(\frac{1}{T^{4+\beta}}\right)^{1/2} \left[4.94\,\mathrm{e}^{1.6\beta}\right] \qquad \mathrm{pc}. \tag{3.12}$$

It should be noted that the term in the last set of brackets is dependent on one's choice of dust parameters; as noted in Hughes et al. (1993) and Hughes, Dunlop & Rawlings (1997), the total uncertainty in the magnitude of that term is a factor of a few in either direction. Hence the absolute calibration of r should be taken as uncertain to a factor of two or so, but relative calibration should be excellent if the dust properties in each galaxy are similar.

To illustrate the range of values attainable in this model, I present in Figure 3.30 the diameter of the source as a function of temperature. To an observer, a measured temperature can be converted to the source size using this expression. As the diameter varies slowly with β for moderate temperatures over the expected range $1 \leq \beta \leq 2$, we can approximate the source size with $\beta = 1.5$. This results in a simple expression for the source diameter D:

$$D \;=\; 2.3 \left(\frac{T}{50\mathrm{K}}\right)^{-2.75} \left(\frac{L}{10^{12}\,L_\odot}\right)^{1/2} \qquad \mathrm{kpc}. \tag{3.13}$$

This is accurate to better than a factor of two for normal values of the temperature and β.

3.6.1 Measurements of the Sizes of LIRGs

We have used the fitted parameters for each galaxy as given in Table 3.5 and the equation 3.12 to model the size of the emitting region seen at 350μm in the SHARC data. The results yield diameters of 1.2 ± 0.6 kpc, a fairly small variation considering the large range of luminosities surveyed. Along with the measured mid-infrared size, the SHARC-derived sizes are tabulated in Table 3.6. The errors in each diameter determination are fairly similar, being $\sim 15\%$ for the mid-infrared measurement and $\sim 10\%$ for the far-infrared measurement and model.

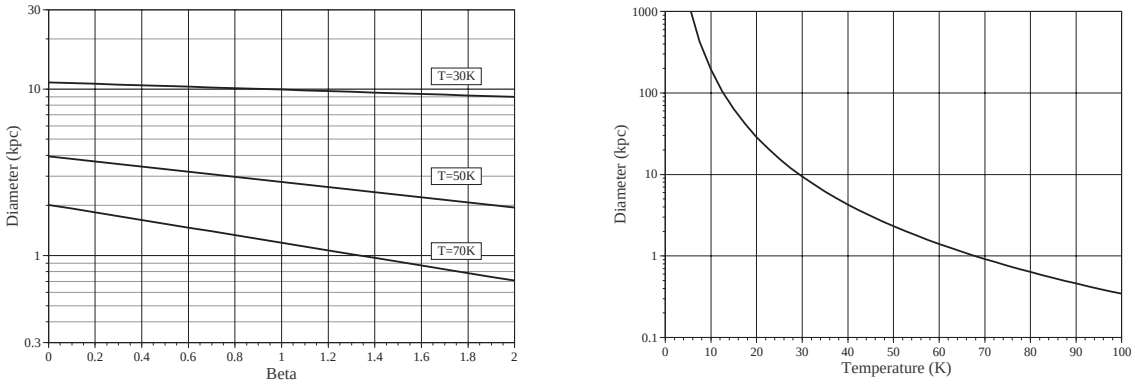

Figure 3.30 Source size from the central heating model, assuming a luminosity of $10^{12} L_{\odot}$. (Left) Variation of diameter with β for a typical range of temperatures. (Right) Variation of diameter with temperature assuming $\beta = 1.5$, a reasonable approximation.

Table 3.6 Comparison of sizes of LIRGs.

Source Name	Measured Mid-IR Diam. (kpc)	Measured Far-IR Diam. (kpc)	Modeled Far-IR Diam. (kpc)
NGC 520	0.37	1.4	1.4
NGC 1068	0.23	3.1	1.4
NGC 1614	< 0.59	< 1.9	2.1
NGC 2339	0.31	0.5	1.1
NGC 2388	0.91	1.5	2.1
NGC 2623	0.75	2.9	2.4
UGC 5101		< 2.1	5.0
NGC 4102	0.09	< 0.4	0.6
NGC 4194	0.37	2.5	1.4
NGC 4418	< 0.24	< 0.8	0.6
Mrk 231	< 2.45	< 2.3	4.5
NGC 4818	< 0.11	–	
NGC 5135	0.50	–	
Mrk 273	1.24	< 0.7	3.2
Arp 220	< 0.56	2.0	3.6
NGC 6000	0.30	2.3	1.8
NGC 6240	0.66	3.7	3.2
IC 5135	0.72	2.5	2.6
NGC 7469	< 0.63	2.2	2.7
Mrk 331	0.57	3.2	2.0

3.6.2 Comparison of Model and Measurement

It is most elementary to compare first the model predictions of the far-infrared sizes as compared to the measured mid-infrared sizes. The ratio of these two sizes is presented in Figure 3.31. The correlation between the model and the measurements is tight, but with a slope of 3.19 (excluding sources with upper limits), indicating that the far-infrared traces a colder, larger diameter component of the dust emission. This is not a surprising result, but rather serves as a demonstration that the model describes the radiative transfer of the dust emission from the nuclei of the galaxies fairly well.

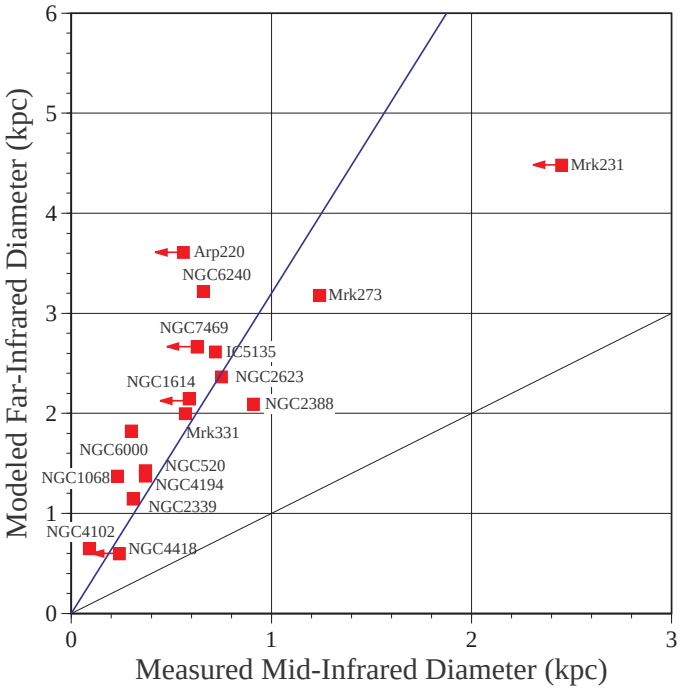

Figure 3.31 Modeled Far-IR sizes vs. measured Mid-IR sizes of LIRGs. The heavy line is a fit with a slope of 3.19.

When we compare the modeled predictions with the sizes measured at 350μm, however, we see a different result in Figure 3.32. The correlation is poor, especially when considering that had the unresolved sources been resolved, the scatter would increase further. The best fit to the sizes (excluding upper limits) yields a slope of 0.98, where 1.00 would indicate a perfect fit. This implies that the model does, on average, describe the continuum emission well even though the correlation is rather loose. However, even with the large scatter, since the measured sizes are similar to the predictions, averaging over all sources, the dust emission being traced by the 350μm

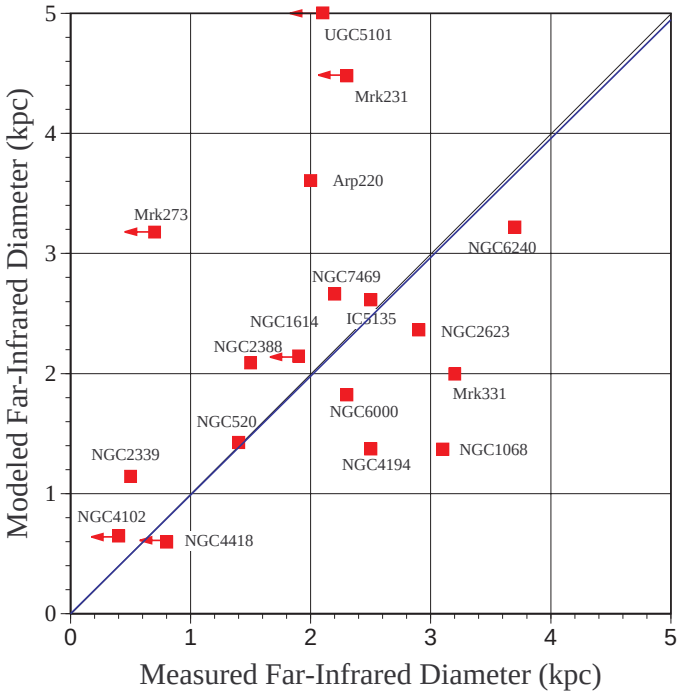

Figure 3.32 Far-IR sizes of LIRGs showing the ratio of the modeled vs. measured physical diameters. The heavy line is a fit of slope 0.98.

emission may be entirely centrally-heated.

That some of the galaxies are seen to be smaller than the model would predict may be indicative of a poor understanding of the properties of the dust in the extreme galaxies in that class: Mrk 231, Mrk 273, Arp 220 and UGC 5105. In the case of the larger galaxies, it is not surprising that once we reach temperatures of $T \lesssim 50\,\mathrm{K}$, the emission may come from a more diffuse component of the dust in the ISM or in a kiloparsec ring such as in the Milky Way or NGC 891. It is interesting to note that two of the three larger galaxies seen to be furthest from the modeled size are known to be extended from observations at other wavelengths: Mrk331 is the only source with *no* bright nucleus from the sample of Miles et al. (1996); NGC1068 has a molecular ring at a diameter of roughly 2.3 kpc (Scoville et al. 1988).

3.7 Conclusion

We have detected and measured the spatial extent of 18 luminous infrared galaxies at 350μm using the SHARC bolometer camera. Of these, 11 were clearly extended and the rest unresolved. Using data at other wavelengths, we have derived the cold dust

component of the SED of each galaxy. The greybody fits are quite good, and yield a mean temperature of $38.1 \pm 5.7\,\mathrm{K}$ and a mean emissivity index of $\beta = 1.7 \pm 0.4$. There is an inverse relationship between the temperature and β. Since a value of $\beta \sim 1.7$ implies that there is a mixture of dust composition, the relationship hints at a variation in the dust composition as a function of temperature. Furthermore, the variance in the index is real, and is indicative of an underlying variation in the mixing ratio from galaxy to galaxy.

We have demonstrated good correlations between several of the derived parameters. The temperature is found to increase slowly as a function of the luminosity. We further found that the luminosity-to-mass ratio also increases with the luminosity. These two relations are coupled, as (all other things being held constant) the increasing temperature raises the luminosity faster than does increasing the mass. Additionally, the cold fraction of the total luminosity increases as a function of the luminosity, requiring that the SED of highly luminous galaxies become more strongly peaked at longer wavelengths. This runs somewhat contrary to the increasing luminosity-to-mass vs. luminosity correlation, and hints at a reduction in the warm dust mass in galaxies as a function of luminosity.

Using a model for the surface brightness of galaxies, the compactness of 17 of these sources (primarily measured by WWB93) has been converted to a physical size. Using a simple, centrally-heated radiative transfer model with a density profile of $\mathcal{N}(r) \propto r^{-1}$, we have calculated the expected sizes of the galaxies based on their SEDs and compared them to the measured sizes. In general, the model fits well to the compactness-derived mid-infrared sizes, which trace only the nuclear component of the emission. However, the model fits the 350μm sizes poorly, indicating that there are underlying differences in the galaxies: the ultraluminous galaxies tend to be smaller than predicted, while galaxies which were previously known to be extended are larger. In the latter class, there is then a substantial component of the cold dust emission arising from more extended, locally heated sources such as distributed star formation in a spiral disk component. On average, however, the centrally-heated model does fit the measured sizes quite well, implying that a nuclear heating source

can account for most of the far-infrared luminosity in luminous infrared galaxies. Higher angular resolution observations of the ultraluminous galaxies will be necessary to better constrain the dust properties of these extreme sources.

Chapter 4 Distant Ultraluminous Infrared Galaxies

4.1 Searching for Dust at High Redshift

The first sign that the thermal emission from dust at temperatures below 100K could be detected at cosmological distances came with the discovery of the remarkable infrared-luminous galaxy IRAS F10214+4724 at $z = 2.286$ (Rowan-Robinson et al. 1991). This object has an apparent luminosity of several $10^{13}\,L_{\odot}$ in the far infrared, corresponding to billions of solar masses of dust. Although this galaxy is gravitationally lensed, this has not prevented more high-redshift objects from being detected in their dust emission. To date, the highest redshift yet detected is $z = 4.69$ (McMahon et al. 1994), nearly as distant as the highest redshift galaxies seen by optical telescopes. It is fundamental to our understanding of star formation in the early universe that we observe the far-infrared emission from such objects. IRAS detected only two objects at $z > 1$, so studies of this emission must currently be conducted from the ground in the available atmospheric windows (although the ISO and SIRTF satellites and the airborne observatory SOFIA do permit these observations, as of 1999 none of them are functioning). Millimeter-wavelength studies have proven quite fruitful (e.g., Omont et al. 1996b) but cannot constrain the temperatures – and therefore the luminosities and associated star formation rates – by themselves. Shorter wavelength (e.g., 350 or 450μm) studies are the best able to constrain the SEDs of high-redshift galaxies and thereby derive their properties.

In this chapter, I shall describe our effort to detect the 350μm continuum emission from a sample of roughly 20 quasars at redshifts of $1.8 \leq z \leq 4.7$. This work has been submitted for publication in the Astrophysical Journal Letters under the authorship of Benford et al. (1999). Following this, I detail our ongoing effort to determine

the nature of the far-infrared sources detected in deep blank-field surveys by the ISOPHOT instrument on ISO. I conclude with a summary of the CSO Deep Field, a 450μm survey for distant, dusty galaxies.

4.2 350 Micron Continuum Emission of High Redshift Quasars

4.2.1 Project Overview

We have observed a sample of high redshift sources ($1.8 \lesssim z \lesssim 4.7$), mainly radio-quiet quasars, at 350 μm using the SHARC bolometer camera at the Caltech Submillimeter Observatory. Nine sources were detected ($\gtrsim 4\sigma$) whilst upper limits were obtained for 12 sources with 350 μm flux densities limits $\lesssim 125$ mJy at the 3 σ level. Combining published results at other far-infrared and millimeter wavelengths with the present data, we are able to estimate the temperature of the dust emitting the observed radiation between 0.35-1.3 mm and find relatively low values, ranging from 40 to 60 K. From the spectral energy distribution, we derive dust masses of a few $10^8\,h^{-2}M_\odot$ and luminosities of 4-33$\times 10^{12}\,h^{-2}L_\odot$ (uncorrected for any magnification) implying substantial star formation activity. Thus both the temperature and dust masses are not very different from those of local ultraluminous infrared galaxies. For this redshift range, the 350μm observations trace the 60-100μm rest frame emission and is thus directly comparable with IRAS studies of low redshift galaxies.

4.2.2 Introduction

The study of molecular gas and dust is a significant observational tool for probing the physical conditions and star formation activity in local galaxies. Recent advances in observational techniques at submillimeter and millimeter wavelengths now permit such studies to be made at cosmological distances.

As a result of the IRAS survey, many local objects are recognized as containing

a large mass of dust and gas, such that the object may be more luminous in the far-infrared (FIR) than in the optical. The question as to how many such objects there may be at cosmological distances, and whether they can account for the recently discovered FIR cosmic background (Puget et al. 1996; Fixsen et al. 1998; Hauser et al. 1998), is attracting much interest and spawning new instrument construction and new surveys (Hughes et al. 1998; Ivison et al. 1998; Puget et al. 1998; Kawara et al. 1998). Existing submillimeter cameras on ground-based telescopes are not yet sensitive and large enough at 350μm to detect distant objects in arbitrary blank fields (e.g., the initial Caltech Submillimeter Observatory (CSO) SHARC survey, Phillips 1997). However, such cameras can measure the 350μm flux of objects of known position. A step forward in the field was the recognition of IRAS F10214+4724 as a high redshift object ($z = 2.286$) by Rowan-Robinson et al. (1991). However, it has proved difficult to find many such objects to study. On the other hand, quasars have sometimes proved to exist in the environs of dusty galaxies (Haas et al. 1998; Lewis et al. 1998; Downes & Solomon 1998). Omont et al. (1996b) have shown by means of a 1300 μm survey of radio-quiet quasars that the dust emission at high redshifts can be detected in a substantial fraction of their project sources.

In this section I present measurements at 350μm towards a sample of 21 sources with redshifts $1.8 \lesssim z \lesssim 4.7$, which were selected from different surveys and studies (references are given in Tables 4.1 & 4.2). This wavelength roughly corresponds to the peak flux density of highly redshifted ($z \simeq 3$) dust emission of objects with temperatures of 40 to 60 K. Together with measurements at longer wavelengths, it strongly constrains the dust temperature and, hence, the dust mass and luminosity of the object. Some of these results were first presented by Benford et al. (1998b). Throughout this section, I shall assume $\mathrm{H}_0 = h_{100} \times 100\,\mathrm{km\,s^{-1}\,Mpc^{-1}}$ and $\Omega_0 = 1$.

4.2.3 Observations and Results

The measurements were made during a series of observing runs in 1997 February and October and 1998 January and April with the 10.4 m Leighton telescope of the CSO on

the summit of Mauna Kea, Hawaii, during excellent weather conditions, with 225 GHz atmospheric opacities of ~ 0.05 (corresponding to an opacity of ≤ 1.5 at 350μm) or lower. We used the CSO bolometer camera, SHARC, described by Wang et al. (1996) and Hunter, Benford & Serabyn (1996). It consists of a linear 24 element close-packed monolithic silicon bolometer array operating at 300 mK. During the observations, only 20 channels were operational. The pixel size is $5''$ in the direction of the array and $10''$ in the cross direction. The weak continuum sources were observed using the pointed observing mode with the secondary chopping in azimuth by $30''$ at a rate of 4 Hz. The telescope was also nodded between the on and the off beams at a rate of $\sim$0.1Hz. The point-source sensitivity of SHARC at 350μm is $\sim 1\,\mathrm{Jy}/\sqrt{\mathrm{Hz}}$ and the beam size is $\sim 9''$ FWHM.

Pointing was checked regularly on nearby strong galactic sources which also served as secondary calibrators. Pointing was found to be stable with a typical accuracy of $\lesssim 3''$. The planets Mars, Saturn and Uranus served as primary flux calibrators. The absolute calibration was found to be accurate to within 20%. Repeated observations of H 1413 + 117 and F 10214 + 4724 confirmed a relative flux accuracy of $\sim$ 20%. The data were reduced using the CSO BADRS software package. Typical sensitivities (1σ) of $\sim$ 20 mJy were achieved, after $\sim$ 2500 s of on–source integration time.

Nine sources were detected at levels of $4\,\sigma$ and above, as outlined in Table 4.1. Included are the $z > 4$ quasars BR 1202−0725, BRI 1335−0417 and H 0000−263. Except for the Cloverleaf (H 1413+117) (Barvainis, Antonucci & Coleman 1992), the present measurements are the first reported detections for high redshift quasars at 350μm. Many of the sources were measured three or more times providing both consistency checks and improvements in the accuracy of the flux densities. The two strongest sources, H 1413+117 and IRAS F10214+4724, were often measured before starting the long (∼2-3 hours) integrations on the weaker sources.

As an illustration of the data quality, Figure 4.1 shows the 350μm CSO–SHARC measurement towards BR 1202−0725 at $z = 4.69$. This measurement corresponds to a total of 4 hours integration on source. The source is centered at offset zero. The other channels provide a measure of the neighboring blank sky emission and a

Table 4.1 Quasars detected at 350μm and derived properties. The luminosity refers to the integrated luminosity of the fitted greybody curve at the indicated temperature with $\beta = 1.5$.

Source	z	R.A. (B1950.0)	Dec. (B1950.0)	Flux Density (mJy, $\pm 1\,\sigma$)	T_{dust} (K)	Dust Mass ($10^8 h^{-2}$ $M_\odot$ †)	Luminosity ($10^{12} h^{-2}$ $L_\odot$ †)	Ref.
BR1202−0725	4.69	12 02 49.3	−07 25 50	106±7	50±7	$4.0^{+0.9}_{-0.8}$	$14.9^{+0.8}_{-0.7}$	1,2,3
BRI1335−0417	4.41	13 35 27.6	−04 17 21	52±8	43±6	$3.6^{+0.5}_{-0.8}$	$6.0^{+0.9}_{-0.5}$	4
H0000−263	4.10	00 00 49.5	−26 20 01	134±29	60‡	$2.0^{+0.2}_{-0.2}$	$20.7^{+1.5}_{-1.5}$	1
4C41.17	3.80	06 47 20.8	+41 34 04	37±9	52±6	$1.0^{+0.1}_{-0.1}$	$4.3^{+1.4}_{-1.3}$	5
PC2047+0123	3.80	20 47 50.7	+01 23 56	80±20	50‡	$2.3^{+0.6}_{-0.6}$	$8.5^{+2.2}_{-1.6}$	6
H1230+164	2.74	12 30 39.4	+16 27 26	104±21	49±12	$2.5^{+0.4}_{-0.4}$	$8.2^{+2.0}_{-2.0}$	1
Q0100+1300	2.68	01 00 33.4	+13 00 11	131±28	68±5	$1.2^{+0.5}_{-0.3}$	$23.8^{+0.2}_{-5.8}$	4
H1413+117†	2.54	14 13 20.1	+11 43 38	293±14	45±7	$8.9^{+1.9}_{-1.9}$	$17.7^{+1.3}_{-0.6}$	7
F10214+4724†	2.28	10 21 31.1	+47 24 23	383±51	55±3	$5.5^{+1.4}_{-1.4}$	$32.8^{+6.5}_{-5.3}$	8

† The dust masses and luminosities listed above have not been corrected for any lensing amplification. The probable intrinsic values may be found by dividing by $A = 7.6$ for H 1413+117 (Alloin et al. 1997) and $A = 13$ for F10214+4724 (Downes, Solomon & Radford 1995).

‡ Because of a lack of sufficient data at other wavelengths, the temperatures of these sources are poorly constrained. The available upper limits constrain H0000−263 to $50 \lesssim T_{dust} \lesssim 75$K, so we adopt 60K; PC2047+0.123 is essentially unconstrained, so we adopt 50K as that is roughly the median value.

References. — 1. Omont et al. (1996b); 2. McMahon et al. (1994); 3. Isaak et al. (1994); 4. Guilloteau et al. (1997); 5. Hughes, Dunlop & Rawlings (1997); 6. Ivison (1995); 7. Barvainis, Antonucci & Coleman (1992); 8. Rowan-Robinson et al. (1993)

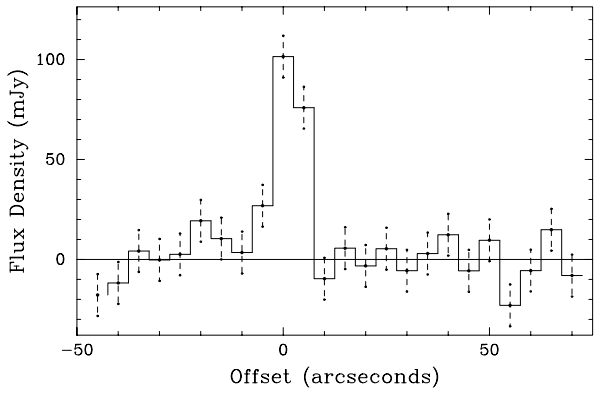

Figure 4.1 The 350μm flux density measured in the bolometers of the SHARC array towards BR1202−0725 at z=4.69. Offsets are given in arcsec with respect to the reference channel number 10. The source is centered at offset zero. Emission is also seen in the two neighboring pixels because the bolometers sample the diffraction pattern of the telescope with a Nyquist sampling.

reference for the quality of the detection.

12 sources with redshifts between 1.8 and 4.5 were not detected at 350μm with flux density upper limits at the 3 σ level of 30-125 mJy. Table 4.2 lists their names, redshifts, 350 μm flux density measurements with $\pm 1\,\sigma$ errors, and a 3 σ upper limit to their luminosities. The observations of each source are shown in figures 4.2 to 4.5.

4.2.4 Discussion

Figure 4.6 displays the spectral energy distributions of the six quasars detected at 350μm for which fluxes at two or more other wavelengths are available from the literature. In the following, we will first comment on individual sources and then discuss the physical properties of the objects.

The two radio-quiet $z > 4$ quasars BR 1202−0725 and BRI 1335−0417 are exceptional objects with large masses of gas ($\sim 10^{11}\,M_\odot$) which have been detected in CO by Omont et al. (1996a) and Guilloteau et al. (1997). They both are clearly detected at 350μm with flux densities of 106 ± 7 and 52 ± 8 mJy, respectively. However, BRI 0952−0115 which is the third $z > 4$ quasar in which CO has been measured (Guilloteau et al. 1999) is not detected at 350μm at a 3 σ level of 65 mJy. This upper limit is consistent with the weak flux density of BRI 0952−0115 at 1.3 mm, i.e.,

Figure 4.2 SHARC observations of high redshift sources.

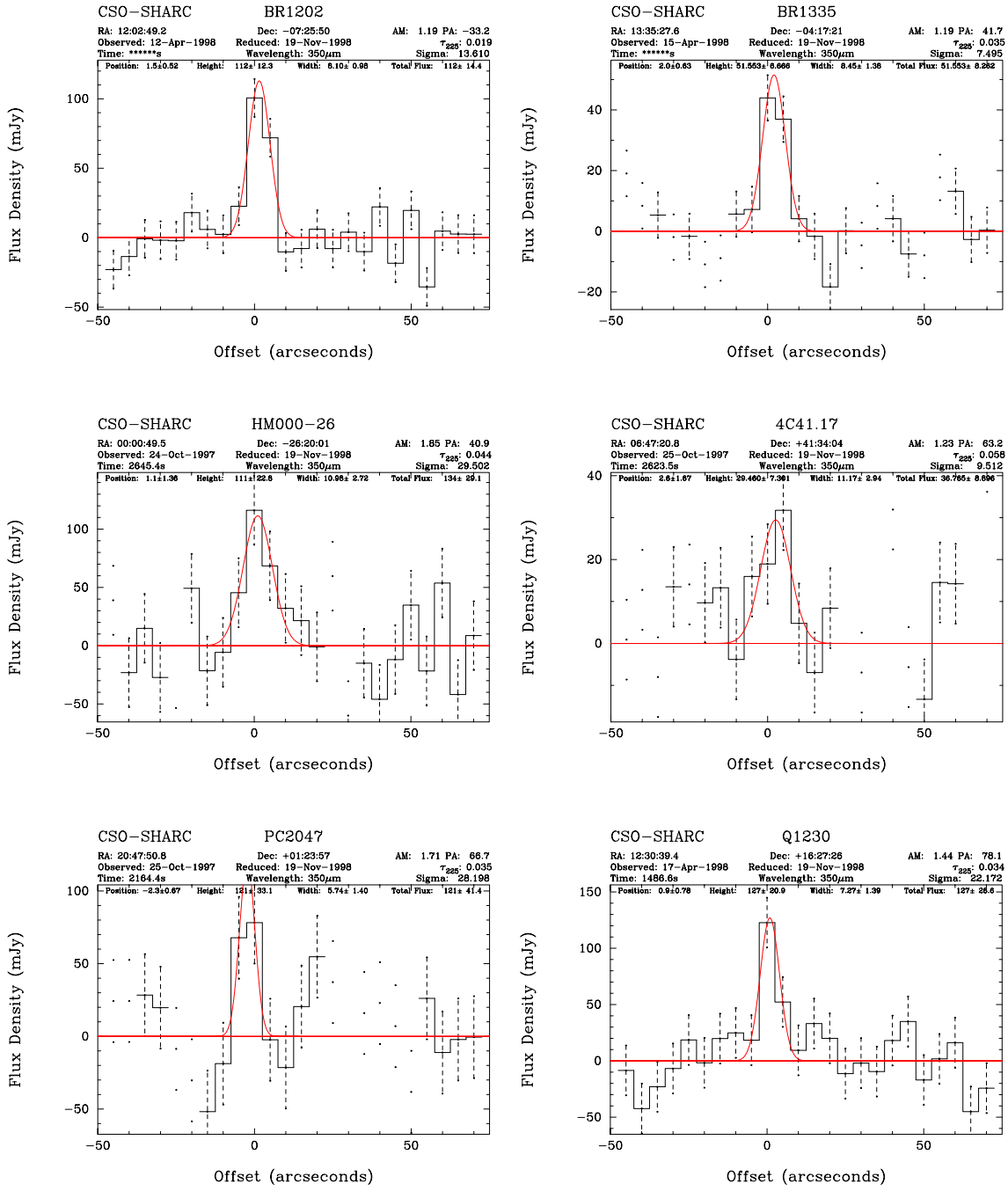

Figure 4.3 SHARC observations of high redshift sources (continued).

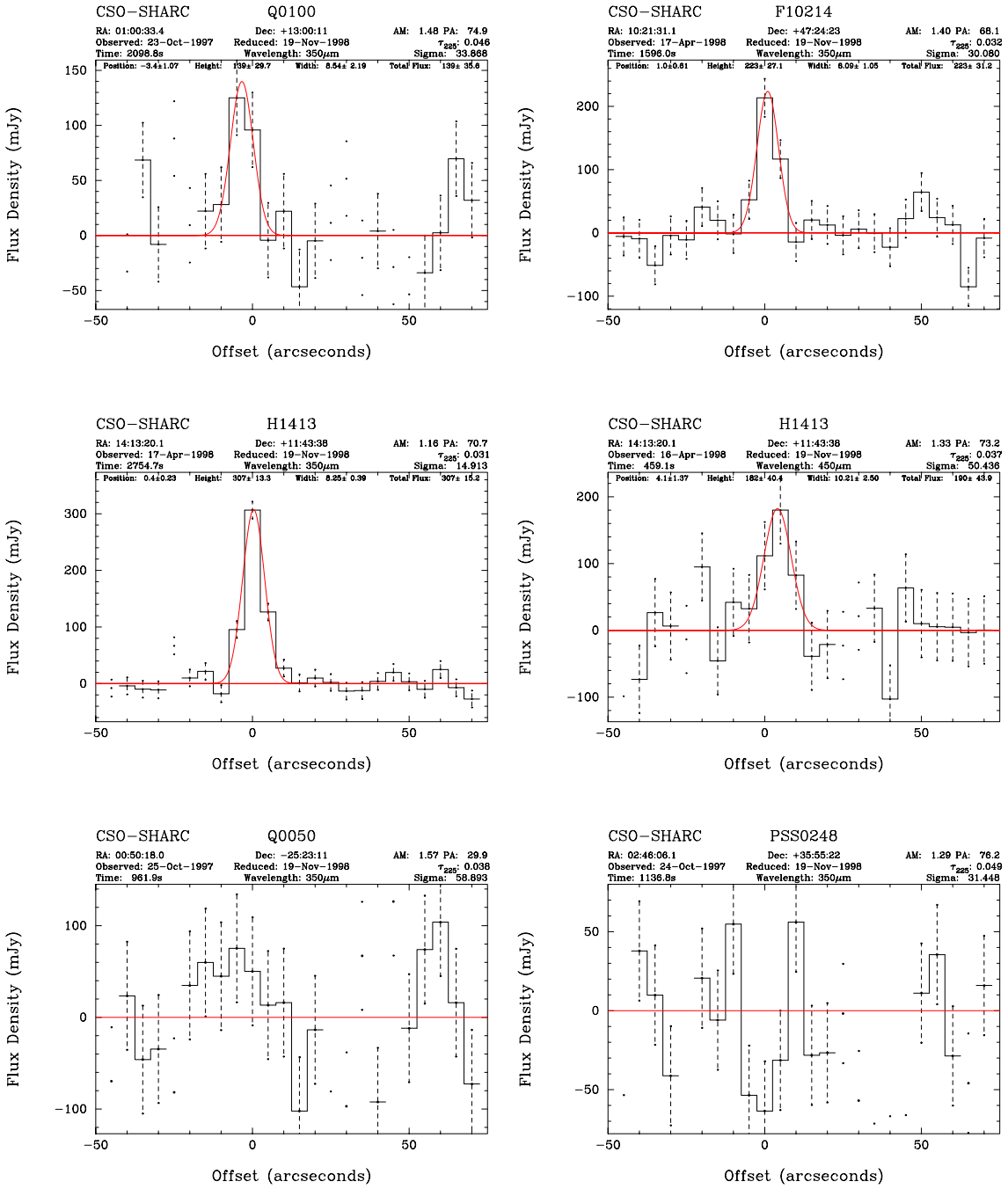

Figure 4.4 SHARC observations of high redshift sources (continued).

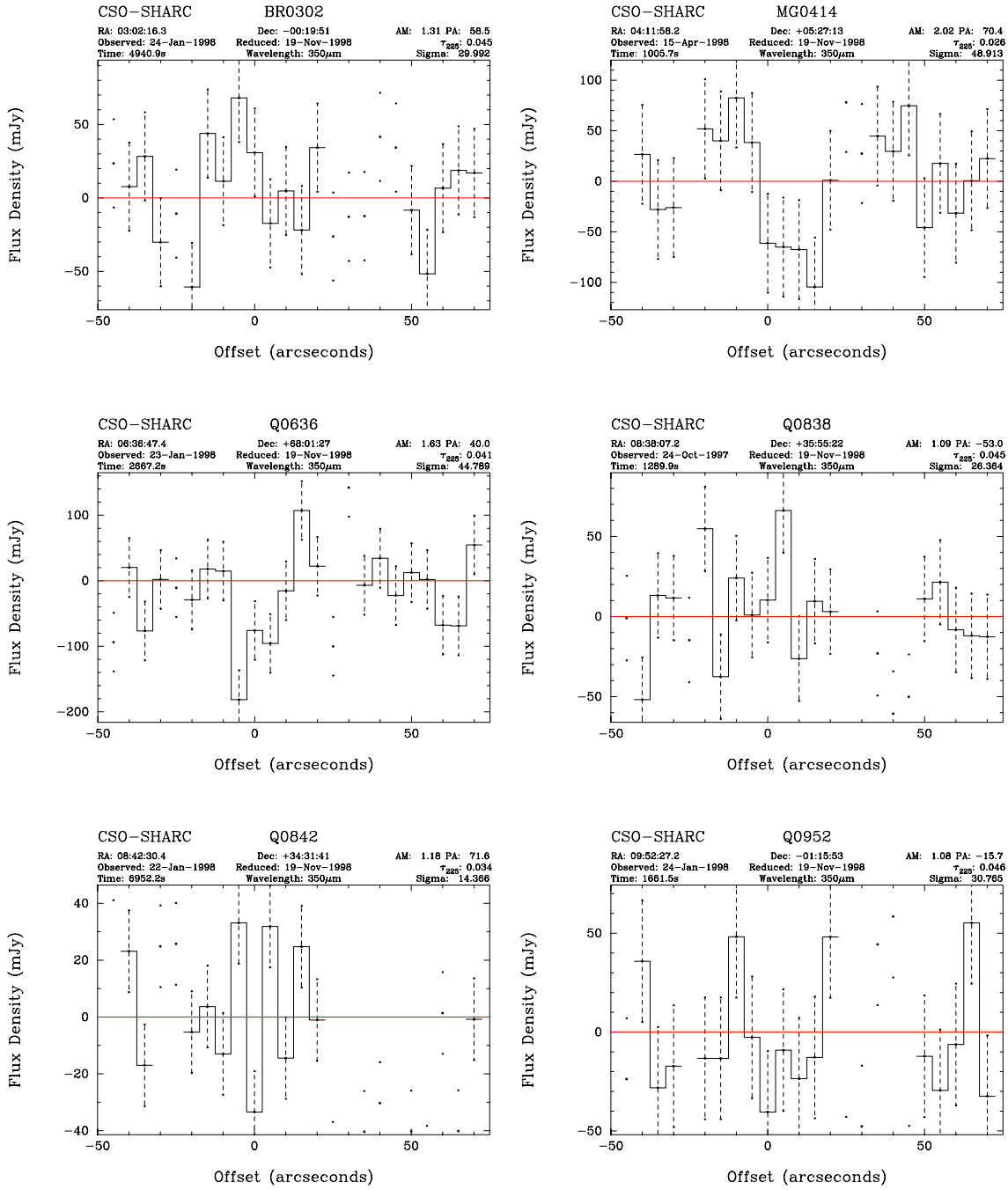

Figure 4.5 SHARC observations of high redshift sources (continued).

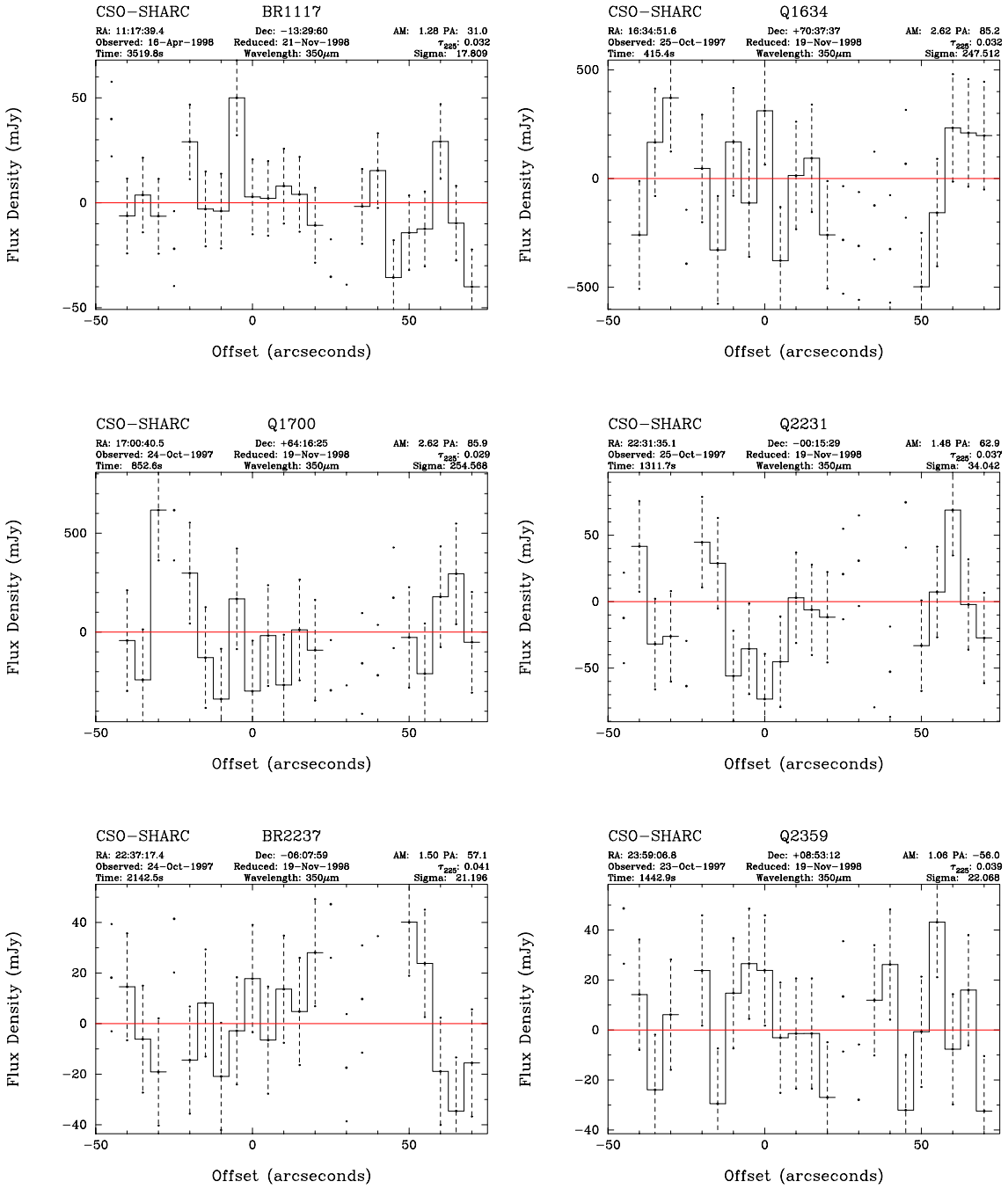

2.8 ± 0.6 mJy (Guilloteau et al. 1999) and a temperature of ~ 50 K (see below). The radio-quiet quasar H 0000−263 at $z = 4.11$, which was not detected at 1.25 mm using the 30m telescope (Omont et al. 1996b) due to its low declination, shows a surprisingly large flux density at 350μm (134±29 mJy). Measurements at other wavelengths would be useful to further constrain the properties of this object.

Table 4.2 Quasars with upper limits at 350μm.

Source	z	F_{350} (mJy, $\pm 1\,\sigma$)	L_{FIR} ($3\,\sigma$) ($10^{12} h^{-2}$ $L_\odot$)	Ref.
BR2237−0607	4.56	5 ± 15	< 6	1
BRI0952−0115	4.43	8 ± 22	< 8	1,2
PSS0248+1802	4.43	-75 ± 22	< 9	
BR1117−1329	3.96	27 ± 13	< 4	1
Q0302−0019	3.28	34 ± 21	< 5	
Q2359+0853	3.23	30 ± 16	< 4	
Q0636+680	3.18	-123 ± 38	< 9	
Q2231−0015	3.01	-65 ± 24	< 6	
MG0414+0534	2.64	-24 ± 35	< 8	3
Q0050−2523	2.16	69 ± 42	< 9	
Q0842+3431	2.13	16 ± 10	< 2	1
Q0838+3555	1.78	39 ± 19	< 4	1

References. — 1. Omont et al. (1996b); 2. Guilloteau et al. (1999); 3. Barvainis et al. (1998)

The detection of the $z = 3.8$ radiogalaxy 4C41.17 with a flux density of 37 ± 9 mJy at 350μm is one of the most sensitive measurements of this study. This sensitivity was reached after only 3/4 of an hour of on-source time and defines the limits which can be achieved with SHARC in the pointed observing mode under excellent weather conditions. A marginal $3\,\sigma$ detection was achieved at 350μm of PC 2047+0123, a $z = 3.80$ quasar (Ivison 1995). Finally, the 350μm flux density of the Cloverleaf (H 1413+117) is significantly higher than the value published by Barvainis, Antonucci & Coleman (1992), i.e., 293±14 mJy as compared to 189±56 mJy. We have also obtained for the Cloverleaf a 450 μm flux density of 226 ± 34 mJy in excellent agreement with the

measurement of 224 ± 38 mJy at 438 μm of Barvainis, Antonucci & Coleman (1992), as shown in Figure 4.6.

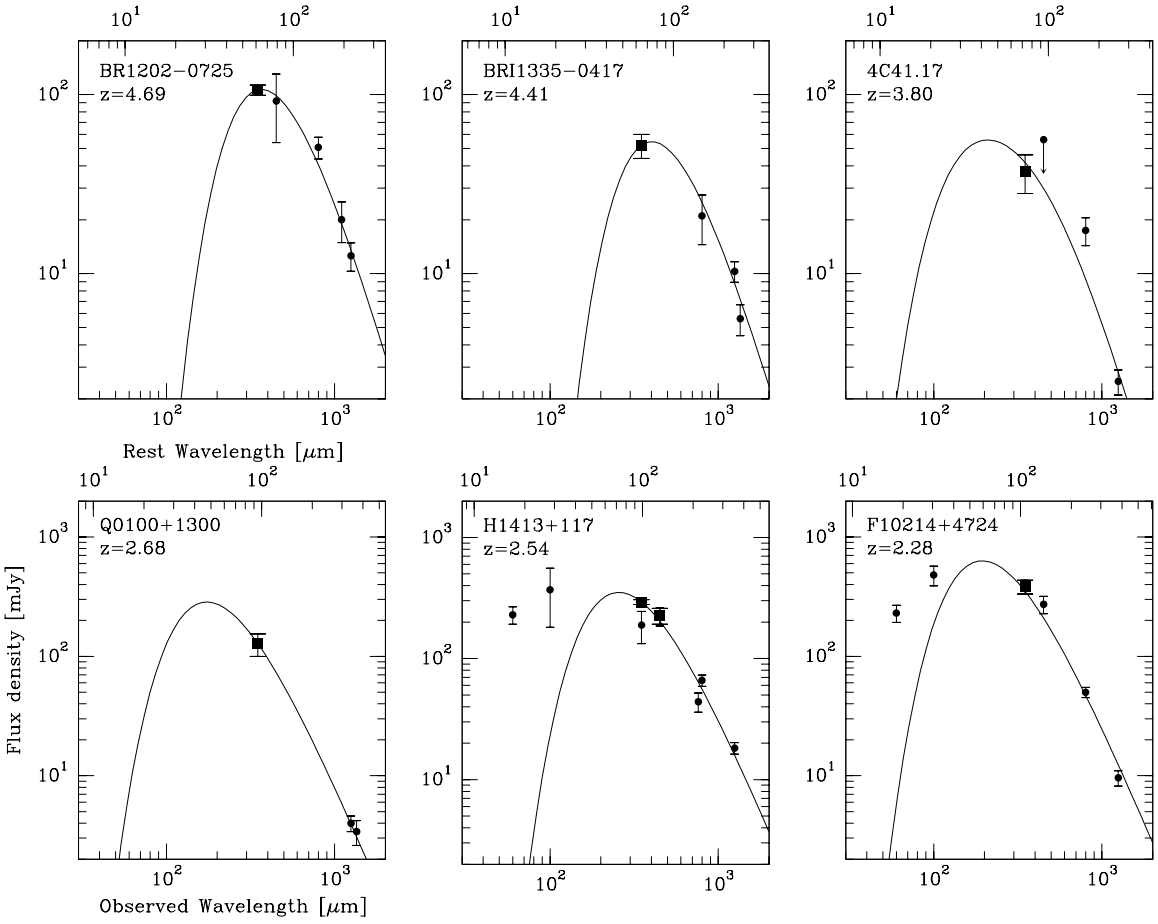

Figure 4.6 Spectral energy distributions of six of the high-redshift quasars discussed in this paper. The 350μm fluxes, shown as squares, are the measurements made with SHARC at the CSO. Fluxes taken from the literature are shown by circles. The observed fluxes at $\lambda_{\rm obs} \geq 350\mu$m were approximated by grey body spectra, shown as solid lines, assuming an emissivity index $\beta = 1.5$. The dust temperature results from a non-linear least-squares fit to the data - see text and references in Table 4.1.

4.2.4.1 Deriving the SED

A greybody was fit to the data points S_ν, for wavelengths of 350 μm and longward, as a function of the rest frequency $\nu = \nu_{\rm obs}/(1+z)$, of the form

$$S_\nu \; = \; B_\nu \Omega [1 - \exp(-\tau)] \text{ with } \tau \; = \; (\nu/\nu_0)^\beta, \tag{4.1}$$

where $\nu_0 = 2.4\,\mathrm{THz}$ is the critical frequency at which the source becomes optically thin and Ω is the solid angle of emission. The data were each weighted by only their statistical errors in the χ^2 minimization. This yields the dust temperature, dust mass (following Hildebrand (1983), using a dust mass emission coefficient at ν_0 of $1.9\ \mathrm{m^2\ kg^{-1}}$), and luminosity of the sources. When β is considered as a free parameter, we find that the average value of $\beta = 1.5 \pm 0.2$ for the detected sources. The fits shown in Figure 4.6 assume an emissivity index of $\beta = 1.5$. We estimated the $1\,\sigma$ uncertainty in the temperature by examining the χ^2_ν hypersurface in the range $1 \leq \beta \leq 2$, similar to the method of Hughes et al. (1993). To evaluate the uncertainties associated with the mass and luminosity, derived from the fitted temperature and $\beta = 1.5$, we used the maximum and minimum values of the mass and luminosity which are compatible with the data plus or minus the statistical error. No lensing amplification was taken into account. The temperature, dust mass and luminosities derived under these assumptions are given in Table 4.1. Three of the sources with upper limits have 1.25mm detections (Omont et al. 1996b), which, together with the 350μm data, yields an upper limit to their temperature. For $\mathrm{Q\,0842+3431}$ and $\mathrm{Q\,0838+3555}$, we find that $\mathrm{T_{dust}} < 40\mathrm{K}$, while for $\mathrm{BR\,1117-1329}$ a limit of $\mathrm{T_{dust}} < 60\mathrm{K}$ is found. If the dust is at the temperature limit, these quasars have dust masses $< 10^8 M_\odot$. For the other sources, an estimate of the maximum luminosity has been given under the assumption that each object has a temperature of 50 K and an emissivity index of $\beta = 1.5$.

The luminosities calculated in Table 4.1 underestimate the total infrared luminosity (1μm-1000μm in the rest frame), since a large luminosity contribution from higher temperature dust cannot be ruled out for most sources. However, in the case of H 1413+117 and IRAS F10214+4724, the available IRAS data allow us to fit an additional warm component. For IRAS F10214+4724, the cold component model carries roughly 60% of the total luminosity; in the case of H 1413+117, which has a hotter mid-IR spectrum, the total luminosity is underestimated by a factor of 3. The best-fit model of Rowan-Robinson et al. (1993) yields a radio-to-UV luminosity of $120 \times 10^{12} h^{-2}\,L_\odot$, nearly eight times larger. Under the assumption that the

majority of the luminosity is carried by the cold component (Table 4.1), the median luminosity-to-mass ratio is around 100 $L_\odot/M_\odot$, assuming a gas-to-dust ratio of ~ 500 similar to that of IRAS F10214+4724 and H 1413+117 (Downes et al. 1992; Barvainis et al. 1995) or of ultraluminous infrared galaxies (ULIRGs) (540 ± 290, Sanders, Scoville & Soifer 1991). We note that there is a slight correlation of temperature with luminosity, to the effect that $\mathrm{T} \sim \left[10 \log(\mathrm{L}_\odot/10^{12}) + 33\right]$ K.

The spectral energy distributions (SEDs) shown in Figure 4.6 clearly demonstrate the effect of redshift on the observed spectra. First, the peak of the energy distribution is around 350μm for redshifts $z \sim 4$, confirming the importance of this wavelength for the study of objects at these redshifts. Second, the shift of the SED's peak towards shorter wavelength as the redshift decreases is well illustrated when comparing the spectra of, e.g., BR 1202−0725 and H 1413+117. The peak emission in the rest frame is found to be in the wavelength range $\lambda_{\rm peak} \sim 60 - 80 \mu$m implying dust temperatures of 40-60 K (Table 4.1). These temperatures are nearly a factor of two lower than previously estimated for ultraluminous sources (e.g., Chini & Krügel 1994). This is in concord with the result of section 3.5.1 in which we noted that more luminous sources tended to have colder FIR components. If the temperature range we find is typical for the cold component of highly redshifted objects, multi-band photometric studies in the submillimeter/FIR, such as planned with FIRST, will provide reasonably accurate redshift estimates for the sources detected in deep field surveys.

For four of the quasars in this survey, CO measurements provide an estimate of the total gas mass using a standard CO-to-H_2 conversion factor. Using our derived dust masses and these gas masses, we estimate the ratio $M_{\rm H_2}/M_{\rm dust} = 440 \pm 130$. This is identical to the value of $M_{\rm H_2}/M_{\rm dust} \sim 540 \pm 290$ quoted above for local ULIRGs.

The global star formation rate in each quasar can be estimated using the relation of Thronson & Telesco (1986):

$$\mathrm{SFR} \sim \Psi \, 10^{-10} L_{\rm FIR}/L_\odot \, M_\odot \ \mathrm{yr}^{-1} \ \mathrm{with} \ \Psi \sim 0.8 - 2.1. \qquad (4.2)$$

For our mean luminosity of $1.7 \times 10^{13} \, h^{-2} \, L_\odot$, this yields a SFR of $\sim 2000 \, M_\odot \ \mathrm{yr}^{-1}$ if

all the submillimeter flux is from a starburst component. This value must be corrected for any lensing, but as the stellar mass is also being amplified (though not necessarily by the same factor), the timescale for formation may be only weakly dependent on the lensing amplification.If we assume a final stellar mass of $\sim 2 \times 10^{12} M_{\odot}$, a value appropriate to a giant elliptical like M87 (Okazaki & Inagaki 1984), then the timescale for formation in a single massive starburst is $\simeq 10^{9}$ yr. Given the large mass of dust already present in these quasars, a substantial amount of this star formation must already have occurred. From (Harrison 1981), the age of the universe for the highest redshift objects ($z \sim 4.5$) is

$$\frac{2}{3H_0}\left(\frac{1}{1+z}\right)^{3/2} \sim 500\,\mathrm{Myr}. \tag{4.3}$$

Thus, for the most distant quasars, the age of the universe is similar to the derived formation timescale. This implies a very high redshift ($z \gtrsim 5$) for the era of initial star formation, in agreement with models of high redshift Lyman-alpha emitters (Haiman & Spaans 1999). The presence of large amounts of dust in quasars out to $z \sim 5$ implies that more sensitive surveys should pick out dusty objects at even higher redshifts.

4.3 Discovering Galaxies in the Far-Infrared

It is only very recently that the discovery of distant galaxies by their far-infrared emission could be achieved. The first such results, using the bolometer camera SCUBA on the JCMT (Smail, Ivison & Blain 1997), turned up a small number of objects which were photometrically identified as distant galaxies (Smail et al. 1998). The ISO satellite has carried out similar surveys, towards the most blank areas of the sky (Clements et al. 1998; Kawara et al. 1998). The objects discovered in the former survey are the subject of a survey currently underway at the CSO. In this section, I shall present the most preliminary results of this survey, which is a collaboration including myself, Jean-Loup Puget, Pierre Cox, Bill Reach and others.

Using the ISOPHOT (Lemke et al. 1996) instrument on board ISO[1], Oliver et al. (1999) were able to detect the emission at 175μm from $\sim$ 1000 sources of unknown origin in a deep survey of a blank field. Many of these sources were undetected at 90μm, implying very cold dust temperatures ($T \leq 30$K) which is appropriate for highly redshifted dust emission. With follow-up observations at the VLA at 5 GHz, the detections were made secure and precise positions revealed (the ISOPHOT beamwidth of 90$''$ made for poor astrometry if further studies were to be made). The detections with the best positional associations are being studied at the CSO by using SHARC in its pointed observing mode at 350μm. In order to verify that this method would succeed, Pierre Cox and I chose to attempt to detect the emission from the best candidate.

The observations were made on April 13-15, 1998, using SHARC during excellent weather. Additional details regarding the observations may be found in the previous section (§ 4.2). We used the VLA position for FIRBACK 1608+544: RA (J2000) 16:08:58.0, Dec (J2000) +54:18:17. Both the 350μm and 450μm standard SHARC filters were used for the observations. At the shorter wavelength, with an effective band center of 353μm, the beamsize is 9$''$. The longer wavelength, at 449μm, yields a beamsize of 11$''$. The detectors subtend an angular size of $10'' \times 5''$ on the sky, with

[1]Infrared Space Observatory, an ESA infrared telescope satellite.

adjacent detectors in the narrow direction. In this way, a single diffraction-limited beam falls on approximately two detectors. A total of 5500s of on-source time were acquired at the shorter wavelength, yielding a $1\,\sigma$ noise of 14mJy per $5''$ pixel. At 450μm, we acquired 3000s of on-source integration for 12mJy noise.

4.3.1 Analysis

FIRBACK 1608+544 was detected at both wavelengths, with a 350μm flux density of 92 ± 12mJy ($7.5\,\sigma$) and a 450μm flux density of 68 ± 20mJy ($3.5\,\sigma$). The observations at both wavelengths are shown in Figure 4.7. The known flux densities in the far-infrared to millimeter regime are listed in Table 4.3. Using data from the IRAM 30m telescope and an ISOPHOT upper limit at 90μm, a greybody was fit to the data points as described in section 4.2.4.1. The resultant fit yields a temperature of 19.0±0.3K with an emissivity index of $\beta = 1.25$, as shown in Figure 4.8. The χ^2_ν hypersurface for this fit is shown in Figure 4.9, showing the excellent temperature constraint on this object.

Table 4.3 Flux densities of FIRBACK 1608+544.

Wavelength (μm)	Flux Density (mJy)	Telescope
90	<16 ($1\,\sigma$)	ISOPHOT
175	150 ± 30	ISOPHOT
350	92 ± 12	CSO
450	68 ± 18	CSO
1300	6 ± 3	IRAM-30m

The measured flux density ratios can be used to determine a photometric redshift. If we assume a source emission dominated by a cold greybody component at a temperature between 40K and 80K with an index of $\beta = 1.5$, the flux density ratios can be calculated as a function of redshift. Since each of the three ratios used (170μm, 350μm, and 1300μm in all combinations) yield slightly different best-fit redshifts, the overlapping region of redshift space can be quite narrow, as shown in Figure 4.10. For

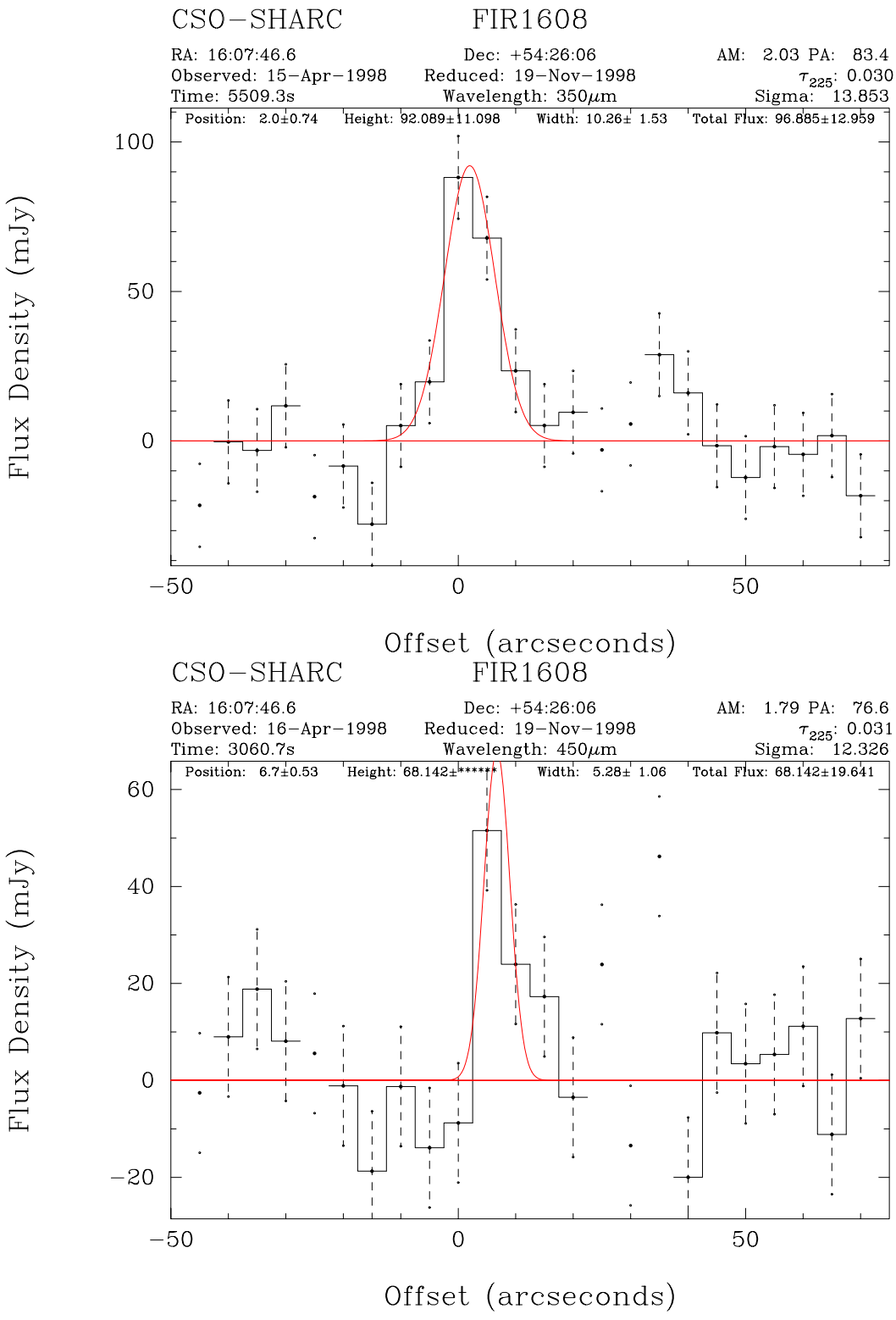

Figure 4.7 SHARC detections of FIRBACK 1608 at 350μm (top) and 450μm (bottom).

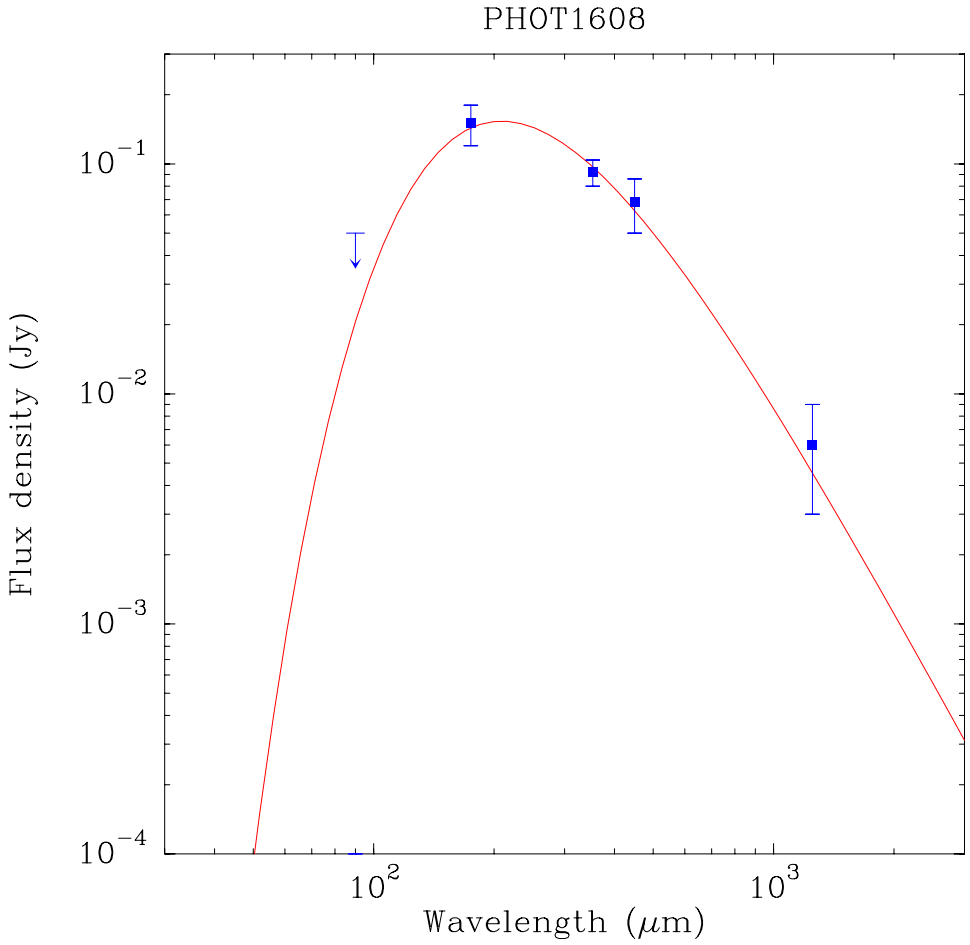

Figure 4.8 Spectral energy distribution of FIRBACK 1608. The fit is a greybody of temperature 19K (observed frame) and emissivity index $\beta = 1.25$.

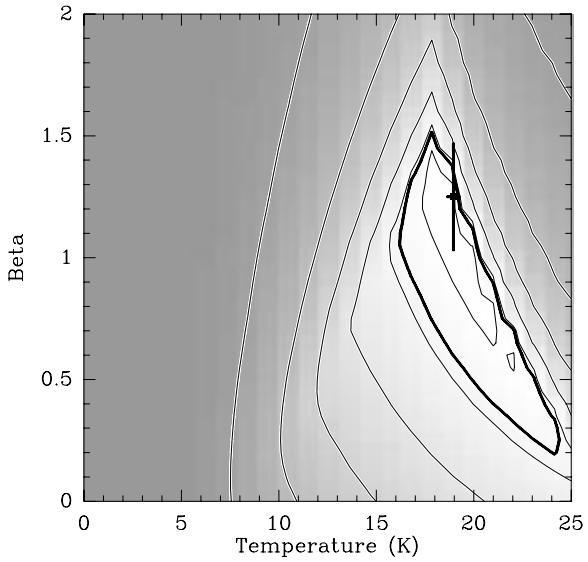

Figure 4.9 The χ^2_ν hypersurface for the greybody fit to FIRBACK 1608+544. The contours are 1.4, 2, 4, 8,..., 64 in χ^2_ν; the absolute minimum is 1.12, showing the excellent quality of the fit. Note that the upper limit at 90μm provides a very stiff bound on the maximum temperature.

an assumed cosmology of $h = 0.75$, $\Omega = 1$, we find that the redshift is quite tightly constrained in the region $1.3 \lesssim z \lesssim 1.8$. This corresponds to a rest temperature of $44 \lesssim T \lesssim 53$K, a reasonable range.

Additional evidence for the high-redshift origin of FIRBACK 1608+5444 is obtained by using the newly-developed radio-to-submillimeter spectral index test (Carilli & Yun 1999). The 1.4 GHz flux density measured at the VLA is 3.0mJy, and our fit to the observed-frame flux density at 350 GHz is 12 ± 2mJy. The spectral index between these two frequencies is a function of redshift:

$$\alpha_{1.4}^{350} \; = \; 0.24 - [0.42 \times (\alpha_{\rm radio} - \alpha_{\rm submm}) \times \log(1+z)] \tag{4.4}$$

If we assume spectral indices in the radio and submillimeter of -0.8 and $+3.3$, respectively, then the redshift is given by:

$$z \; = \; 10^{(\ln(S_{350}) - \ln(S_{1.4}) + 0.24)/9.5} \; - \; 1 \; = \; 0.5 \tag{4.5}$$

While this value is substantially lower than estimated above, we implicitly assumed

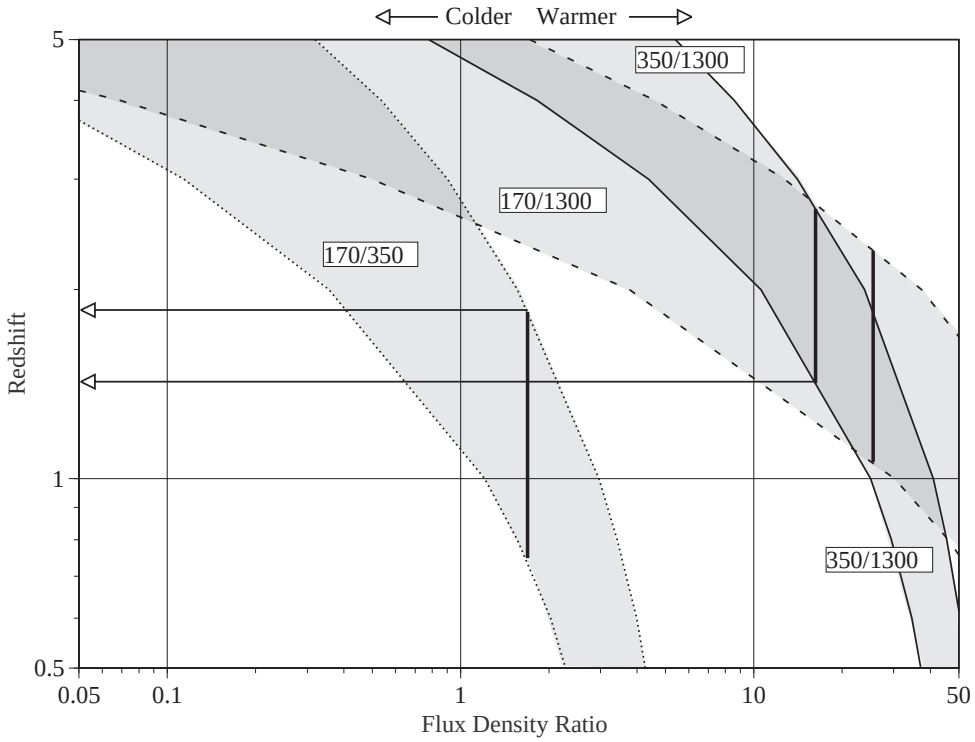

Figure 4.10 Determination of the redshift using photometry at 175μm, 350μm, and 1300μm. Each flux density ratio defines a limited region of redshift space, with the intersection of the three regions being $1.3 \lesssim z \lesssim 1.8$.

that this galaxy should have a temperature of $\sim$ 40K, as we have seen in many local and high-redshift galaxies. With $z = 0.5$, the cold dust is only 25K, much lower than in any other source described in this chapter or the previous. It may be that there is a class of colder, massive galaxies yet to be discovered. The derived properties of FIRBACK 1608+544 for various redshifts are given in Table 4.4.

Table 4.4 Derived properties of FIRBACK 1608+544.

Parameter	$z = 0.5$	$z = 1$	$z = 1.7$	$z = 3$
Temperature (K)	24.6±0.5	32.5±1.0	40.0±1.1	60.4±1.7
Dust Mass ($10^8 h^{-2} M_\odot$)	0.17±0.02	7.4±0.2	8.8±0.9	5.1±0.5
Luminosity ($10^{12} h^{-2} L_\odot$)	0.013±0.001	2.4±0.3	9.9±0.8	53.6±6.6
SFR ($M_\odot$ yr^{-1})	1	240	990	5360

4.3.2 Conclusion

A fair amount of evidence points towards a cosmologically distant origin for FIRBACK 1608+544. Spectroscopic evidence will, however, be required to prove or disprove this assertion. Some hints of a more local origin are found in a faint 12μm IRAS detection seen when coadding the raw scans. Future observations will be obtained this year.

4.4 DEEPFIELD: the CSO Survey for Unknown ULIRGS

As soon as heavy elements have formed from the initial episode of massive star formation, galaxies in the early Universe are expected to shine brightly in the submillimeter and far-infrared as they form the bulk of their stars. We expect the wavelength of peak emission to be similar to that seen in local starburst galaxies, roughly 80μm, and that the epoch of formation should be at redshifts in the range of 2 to 5. Hence, the redshifted dust emission of these protogalaxies peaks in the 200 to 500μm region. We have conducted a survey with SHARC of a large ($\sim 15^{\square}$) field in order to search for this emission (Phillips 1997).

In order to bias our sample towards detecting cosmologically distant objects only, we chose a field which was maximally free of diffuse IRAS emission, IRAS point sources, and VLA sky survey sources. In order that it be easily visible from the CSO during the winter when conditions are best, we selected a field at RA (B1950) = $10^h00^m00\overset{s}{.}0$, Dec (B1950) = $30°00'00''$. The field was first mapped in the conventional manner, via beam-switched mapping and image restoration, on several runs during the winter of 1996. The following winter, maps were made using a small beam-switch but without the image restoration and associated noise. This latter method does not produce a sky image, but can be used to detect sources by searching for the dual-beam signature of a source. The data I shall present relies solely on the first method.

We mapped a region roughly $5'$ on a side at several position angles, such that the final map will have little striping. The maps were made at a wavelength of 450μm and flux calibrated against Uranus. Approximately 10 hours of integration time made during the best weather were used to generate the final sky image. In order to improve our sensitivity and to reduce large-scale drifts, an unsharp-masking routine was applied to the final image. An image convolved with a $30''$ Gaussian was subtracted from an image smoothed with a $10''$ Gaussian, roughly the beamsize. In this manner, only information on spatial scales between the diffraction-limited resolution and $\sim 30''$ is preserved.

The final map of the CSO Deep Field is presented in Figure 4.11. The final $1\,\sigma$ noise level in the central $10'$, where the coverage was greatest, is roughly 90mJy. No sources are detected with any statistical significance in the image, but this can still be used to constrain the luminosity density of sources at cosmological distances. An ultraluminous galaxy with $L = 10^{12}\,L_{\odot}$ such as Arp 220 will produce a flux density of roughly 100mJy at the expected redshifts (see section 1.3.1 for this calculation). We can therefore state that no galaxies like Arp 220 were seen in this field.

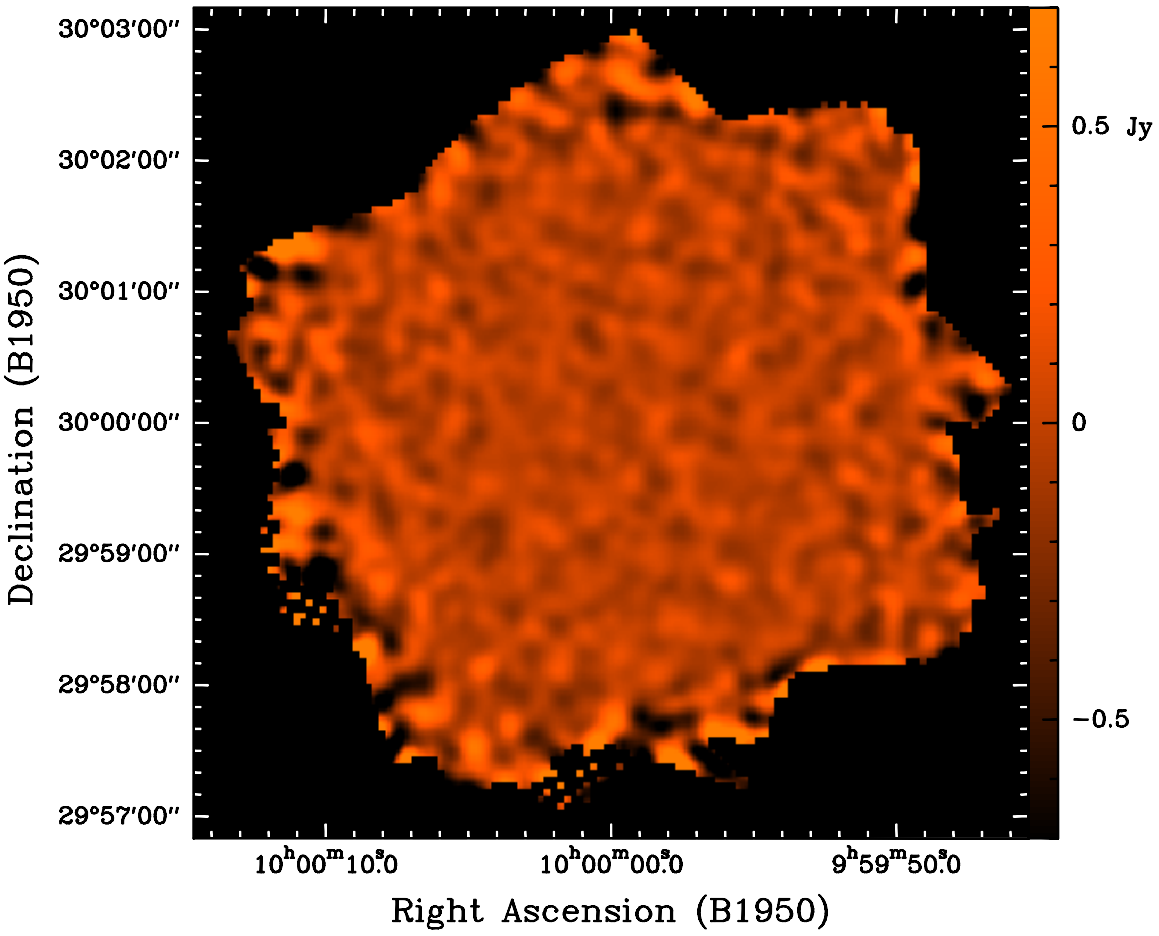

Figure 4.11 The CSO Deep Field at 450μm. The RMS noise achieved in the center of the map is better than 90 mJy. The noise degrades towards the edges due to decreased integration time.

Calculating our measured detection limit as a function of inverse area yields a limit on the maximum number of galaxies brighter than our $1\,\sigma$ noise. This can be compared to the models of Blain & Longair (1993) for source counts at 450μm. Using

their figure 11a, I plot the region excluded by the CSO Deep Field in Figure 4.12 as a grey area. While our results do not yet invalidate any models, we are close to doing so.

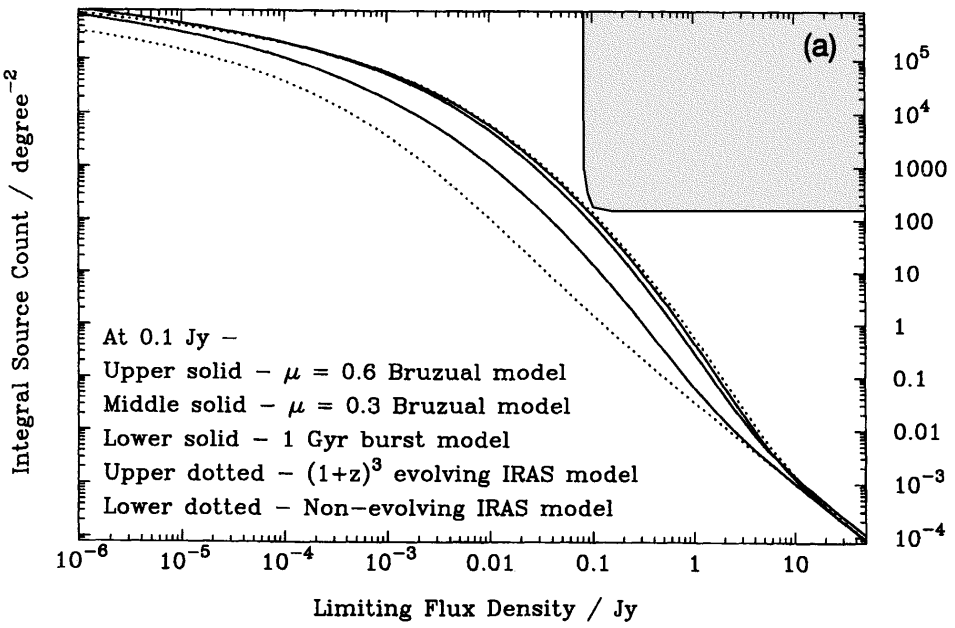

Figure 4.12 The CSO Deep Field constraints on models of source counts. The excluded area has been shaded, and comes quite close to validating or rejecting several of the models.

A separate way to discuss the problem is with respect to the average submillimeter deep sky background. Discussed in section 1.1.3, it is the result of reprocessing by dust of visible and UV radiation from initial star-formation events in distant galaxies to far-infrared wavelengths. The analysis of the COBE FIRAS data by Puget et al. (1996) shows an apparent isotropic background after subtraction of known local effects. The intensity of this background is modeled as

$$B_\nu = 3 \times 10^{-9} (\nu/400\mu\mathrm{m})^{-3} \text{ W m}^{-2} \text{ sr}^{-1}, \tag{4.6}$$

which at 400μm translates to about 50 mJy per square arcminute. Given that modern deep galaxy counts (HST and ground-based) find roughly 100 sources in this area and that about 1/3 are E/S0s (the expected final product of the ultraluminous IR starburst/merger events), and that the starburst phenomenon may last a few percent of

the Hubble time, there should be roughly one distant starburst in a square arcminute. Thus the recently reported apparent detection of a submillimeter sky background is consistent with the idea that there is typically one distant primeval starburst galaxy per square arcminute, at the 50 mJy level (at 400μm), corresponding to a galaxy of very approximately $10^{12}\,L_{\odot}$ at $z = 3 - 5$. Since we surveyed about 10 square arcminutes, we are already well within a factor of a two of a significant cosmological result.

It must be pointed out that the SCUBA bolometer camera on the JCMT is also conducting such surveys, three of which have been presented (Hughes et al. 1998; Barger et al. 1998; Eales et al. 1999). While some sources have been detected at 850μm, the statistics to date are sufficient to reject only those models with no evolution, e.g., the lowest curve in Figure 4.12. It is therefore probable that an improvement of a factor of a few in the CSO Deep Field, perhaps by the next-generation camera SHARC II, will produce detections of the first blank field at wavelengths of $\sim 400\mu$m.

Chapter 5 CO Emission from Nearby Ultraluminous Infrared Galaxies

5.1 The Characteristics of CO Emission from 4Jy ULIRGS

In the past five years, millimeter and submillimeter detections of highly redshifted CO transitions have been measured. As of this writing, eight such objects have been detected: IRAS F10214+4724 (Rowan-Robinson et al. 1991), H 1413+117 (Barvainis et al. 1994), BR 1202−0725 (Ohta et al. 1996; Omont et al. 1996a), BRI 1335−0415 (Guilloteau et al. 1997), 53W002 (Scoville et al. 1997), MG 0414+0534 (Barvainis et al. 1998), APM 08279+5255 (Downes et al. 1999), and SMM 02399−0136 (Frayer et al. 1998). Transitions from $J = 1 \rightarrow 0$ through $J = 7 \rightarrow 6$ have been seen, complicating the interpretation of this molecular emission. To date, almost all the published work on CO in galaxies has concentrated on the $1 \rightarrow 0$ emission, such as in the FCRAO 300-galaxy survey of Young et al. (1995). Because of the difficulty in detecting lines at higher frequencies, there is a relatively shallow knowledge of the state of molecular gas as traced by the higher-J transitions of CO, especially in infrared-luminous galaxies. A systematic study of even the $2 \rightarrow 1$ and $3 \rightarrow 2$ transitions in a complete sample of sources in several transitions has yet to be undertaken, though there have been some notable efforts (Aalto et al. 1995; Mauersberger et al. 1999). It is therefore difficult to compare the high-redshift galaxies with their local counterparts. We have undertaken a systematic survey of the CO $J = 2 \rightarrow 1$ and $J = 3 \rightarrow 2$ emission from ultraluminous infrared galaxies (ULIRGs) with the goal of leading to a greater understanding of the higher-J transitions of CO. This work is being prepared for publication under the authorship of myself, Min Yun, Lee Armus, Todd Hunter, and Tom Phillips.

5.1.1 Observations

Our sample is derived from the IRAS 2Jy catalog of galaxies used by Strauss et al. (1992) and with an incremented minimum flux cutoff at 60μm of 3.72Jy. This survey determined the redshifts and infrared luminosities of 2658 galaxies brighter than 1.936Jy at 60μm. We have selected a subset of this sample via three criteria, the foremost being a minimum luminosity of $10^{11.9}\,L_{\odot}$. This yields only ultraluminous galaxies ($11.93 \leq \log L \leq 12.55$), which we expect to be the most similar to the galaxies being detected in molecular line emission at high redshifts. We further cut out all those not readily observable from the CSO (available declination range $+70^{\circ} \geq \delta \geq -30^{\circ}$). This subset of 22 ULIRGs covers a redshift range of $0.018 \leq z \leq 0.134$ (shown histogrammatically in Figure 5.1) and includes several well-studied sources such as Arp 220, Mrk 231 and Mrk 273. Our goal was to observe each galaxy in both the $J = 3 \rightarrow 2$ and $J = 2 \rightarrow 1$ emission lines of CO. A few of the $3 \rightarrow 2$ transitions were not observed due to obscuration by an atmospheric water line at 325 GHz. Properties of our final sample, called the 4Jy CO sample, are listed in Table 5.1.

5.1.2 Observational Results

With our list of 22 objects and two transitions, a maximum of 44 spectra can be obtained. However, atmospheric absorption near 325 GHz prevents us from attempting to detect three of the $3 \rightarrow 2$ transitions. Additionally, two of the sources were not detected at $2 \rightarrow 1$ with a $1\,\sigma$ noise level of less than 3mK, so it was deemed not prudent to spend telescope time searching for the $3 \rightarrow 2$ emission. Still two more galaxies require $3 \rightarrow 2$ observations to complete the survey. The 37 collected spectra are presented in the following figures (5.2-5.23) along with the digital POSS plate for the observed position. Each spectrum has been calibrated in main beam temperature and is shown at a velocity resolution of 20km/s. Circles indicate the beamsize of the CSO at CO $J = 2 \rightarrow 1$ of diameter $\approx 30''$ and $J = 3 \rightarrow 2$ of diameter$\approx 20''$. The observed central position is marked by a crosshair of about the size of the pointing

Table 5.1 Positions and IRAS data for the 22 galaxies of the 4Jy CO survey.

IRAS Name	RA (B1950)	Dec	cz (km/s)	12μm	25μm	60μm	100μm	log($L_{\rm IR}$) ($L_\odot$)	Notes:
				Flux Density (Jy)					
03158+4227	03 : 15 : 51.7	+42 : 27 : 32	40288	< 0.07	0.45	4.3	4.3	12.55	highest cz
05189−2524	05 : 18 : 58.9†	-25 : 24 : 40	12816	0.74	3.44	13.7	11.4	12.11	Sy2
08311−2459	08 : 31 : 11.6†	-24 : 59 : 17	29988	0.33	1.10	5.0	5.8	12.40	v=13070
08572+3915	08 : 57 : 13.0	+39 : 15 : 39	17480	0.32	1.70	7.4	4.6	12.08	Sy2
09111−1007	09 : 11 : 13.1†	-10 : 06 : 54	16275	0.17	0.47	7.0	11.1	11.98	first detection
09320+6134	09 : 32 : 04.8	+61 : 34 : 37	11800	0.25	1.03	11.5	20.2	11.95	U0501, pair
10035+4852	10 : 03 : 35.7	+48 : 52 : 23	19371	0.10	0.28	4.6	6.2	11.93	pair
10565+2448	10 : 56 : 36.2	+24 : 48 : 40	12926	0.22	1.21	12.1	15.1	11.98	double
12112+0305	12 : 11 : 12.5	+03 : 05 : 22	21788	< 0.11	0.51	8.5	10.0	12.27	
12540+5708	12 : 54 : 05.0	+57 : 08 : 38	12650	1.87	8.66	32.0	30.3	12.50	Mrk231, Sy1
13428+5608	13 : 42 : 51.7	+56 : 08 : 14	11350	0.24	2.28	21.7	21.4	12.10	Mrk273, Sy2
14348−1447	14 : 34 : 53.4	-14 : 47 : 25	24732	< 0.14	0.49	6.9	7.1	12.28	merger
15250+3609	15 : 25 : 03.7	+36 : 09 : 01	16602	< 0.20	1.32	7.3	5.9	11.99	ring galaxy
15327+2340	15 : 32 : 47.0	+23 : 40 : 08	5450	0.48	7.92	103.8	112.4	12.11	Arp220, Sy2
17208−0014	17 : 20 : 47.2†	-00 : 14 : 15	12836	0.20	1.66	31.1	34.9	12.38	radio source
18470+3233	18 : 47 : 00.9†	+32 : 33 : 58	23626	< 0.11	0.42	4.1	3.4	12.02	
19297−0406	19 : 29 : 42.9	-04 : 06 : 31	25674	< 0.13	0.59	7.1	7.7	12.36	merger
19458+0944	19 : 45 : 52.0†	+09 : 44 : 31	29940	0.25	0.28	3.9	7.1	12.31	
20087−0308	20 : 08 : 47.1†	-03 : 08 : 49	31700	< 0.13	0.24	4.6	6.5	12.39	radio source
20414−1651	20 : 41 : 29.2	-16 : 51 : 09	26107	< 0.65	0.35	4.4	5.2	12.19	
22491−1808	22 : 49 : 09.0	-18 : 08 : 20	23300	< 0.12	0.55	5.4	4.5	12.12	merger
23365+3604	23 : 36 : 32.3	+36 : 04 : 33	19338	< 0.10	0.81	7.1	8.4	12.13	LINER

† Sources with Faint Source Catalog coordinates only – otherwise radio coordinates.

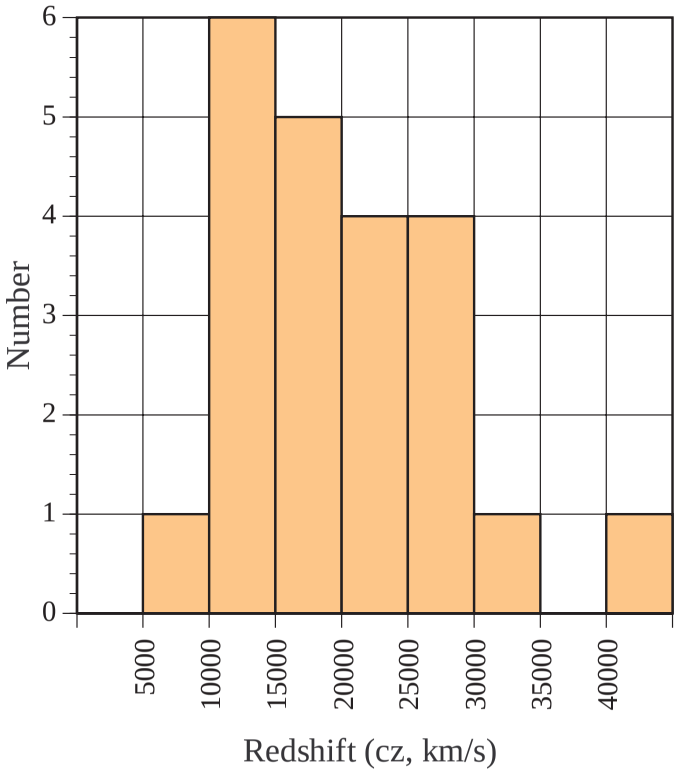

Figure 5.1 Histogram of the redshifts in the 4Jy sample.

accuracy. Of these 37 spectra, 32 are considered to be detections, a favorable yield considering the distance of the sources.

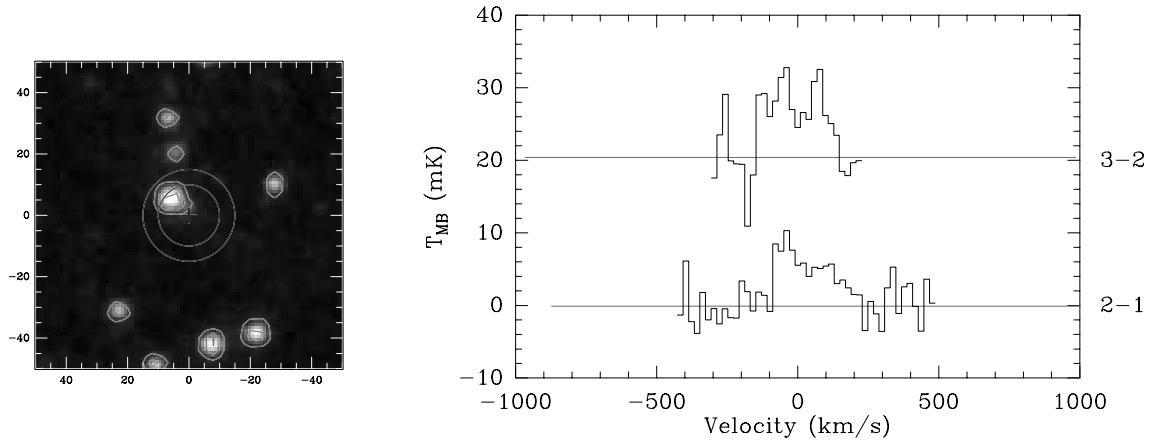

Figure 5.2 POSS image and CO $J = 3 \rightarrow 2$ (upper) and $J = 2 \rightarrow 1$ (lower) spectra for IRAS 03158+4227 at a redshift of $cz = 40,288$ km/s. The beamsize at CO $J = 2 \rightarrow 1$ of $\approx 30''$ and $J = 3 \rightarrow 2$ of $\approx 20''$ are shown, and the center is marked by a cross of about the size of the pointing accuracy.

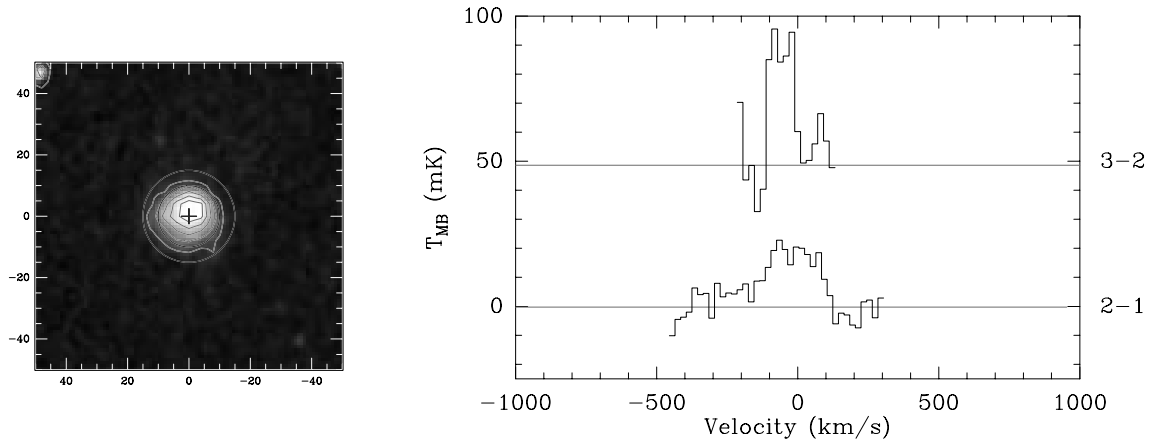

Figure 5.3 POSS image and CO spectra for IRAS 05189−2524 at $cz = 12,816$ km/s.

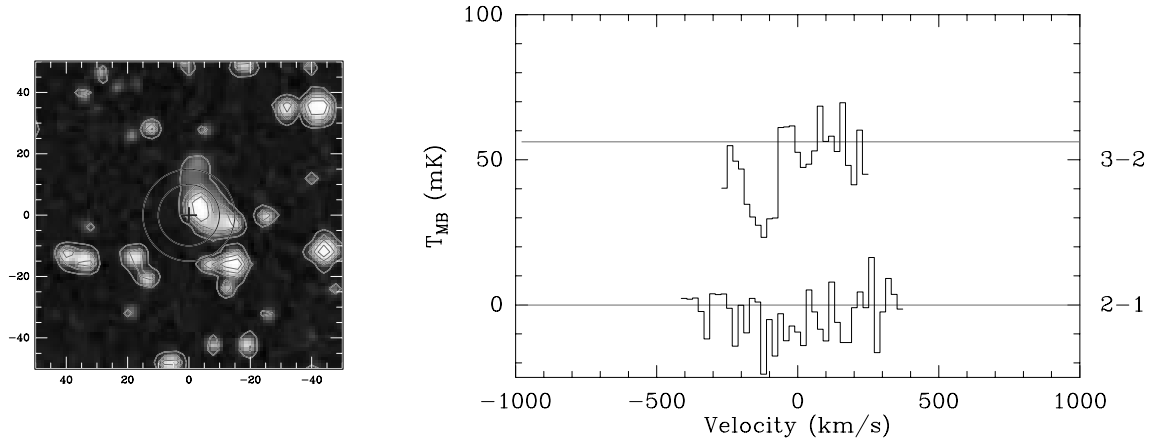

Figure 5.4 POSS image and CO spectra for IRAS 08311−2459 at $cz = 29,988$ km/s.

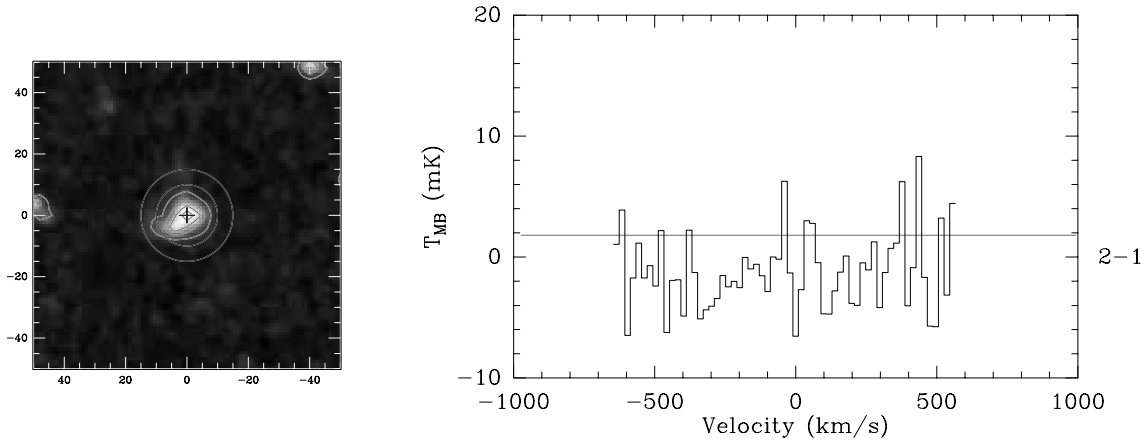

Figure 5.5 POSS image and CO spectra for IRAS 08572+3915 at $cz = 17,480$ km/s. The 3-2 line is blocked by atmospheric absorption.

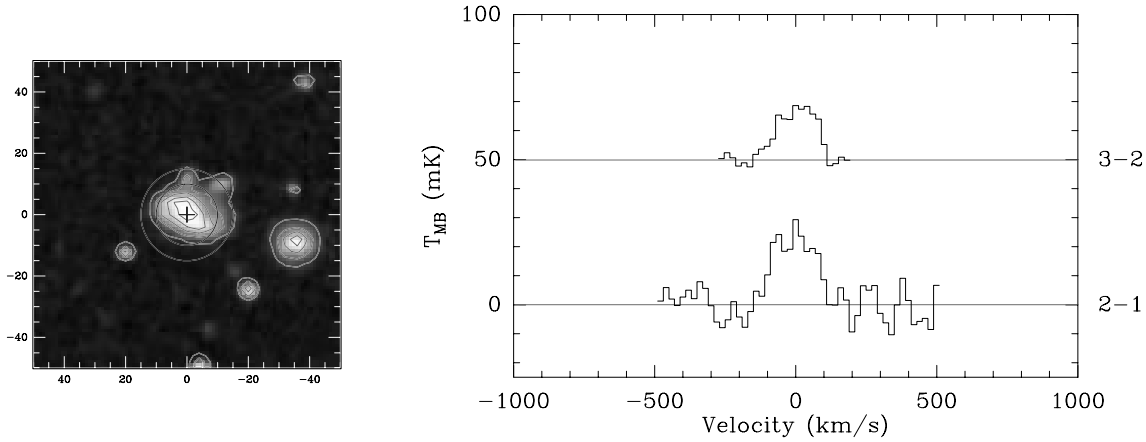

Figure 5.6 POSS image and CO spectra for IRAS 09111−1007 at $cz = 16,275$ km/s.

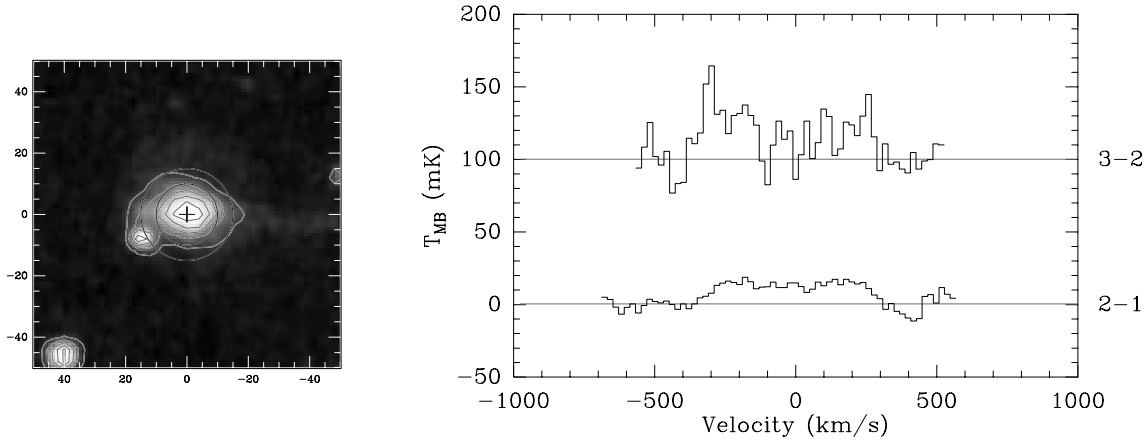

Figure 5.7 POSS image and CO spectra for IRAS 09320+6134 at $cz = 11,800$ km/s.

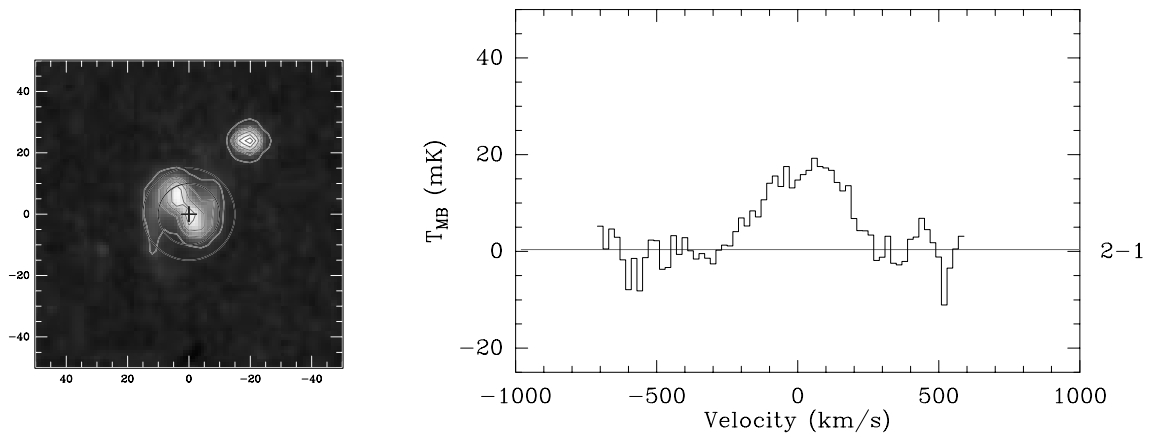

Figure 5.8 POSS image and CO spectra for IRAS 10035+4852 at $cz = 19,371$ km/s. The 3-2 line is blocked by atmospheric absorption.

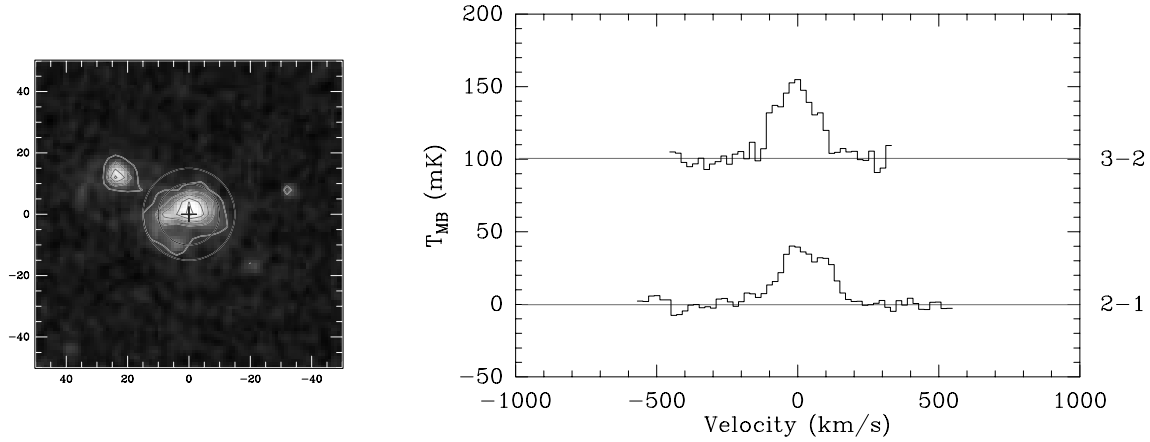

Figure 5.9 POSS image and CO spectra for IRAS 10565+2448 at $cz = 12,926$ km/s.

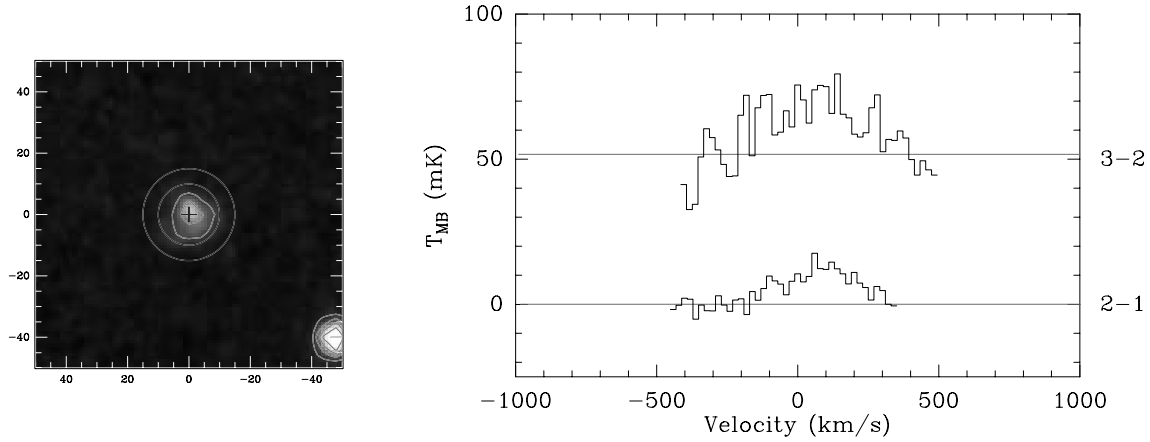

Figure 5.10 POSS image and CO spectra for IRAS 12112+0305 at $cz = 21,788$ km/s.

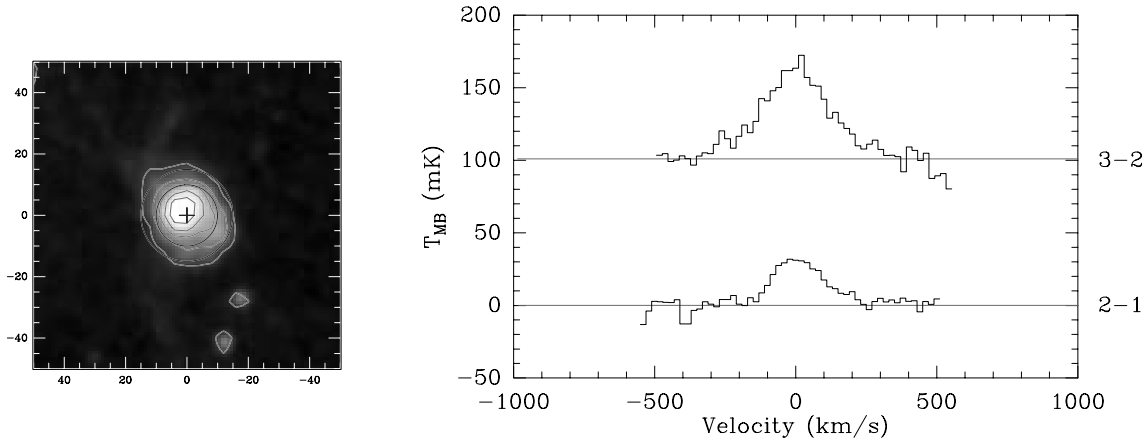

Figure 5.11 POSS image and CO spectra for IRAS 12540+5708 (Mrk 231) at $cz = 12,650$ km/s.

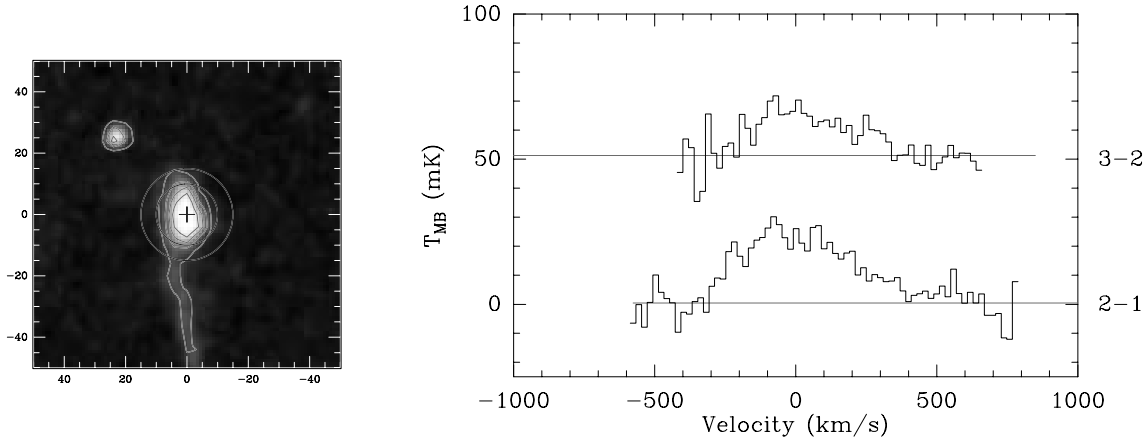

Figure 5.12 POSS image and CO spectra for IRAS 13428+5608 (Mrk 273) at $cz = 11,350$ km/s.

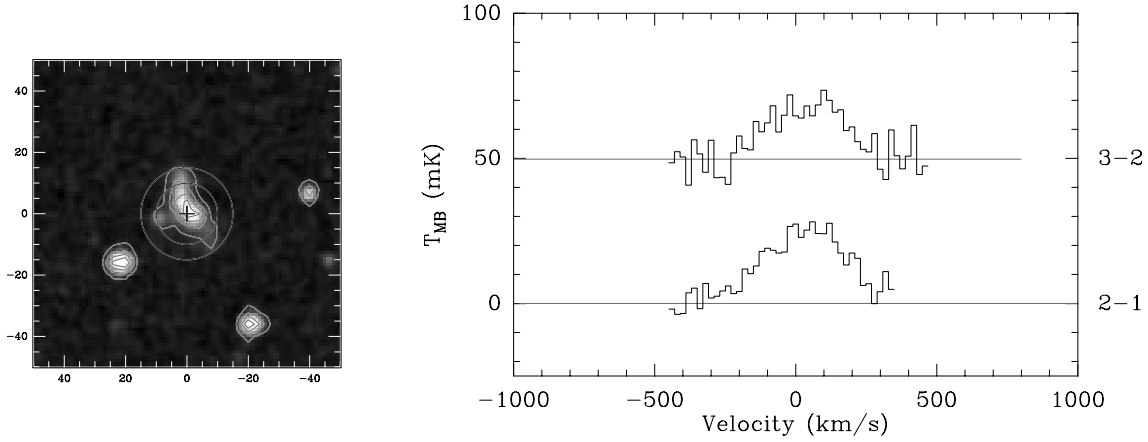

Figure 5.13 POSS image and CO spectra for IRAS 14348−1447 at $cz = 24,732$ km/s.

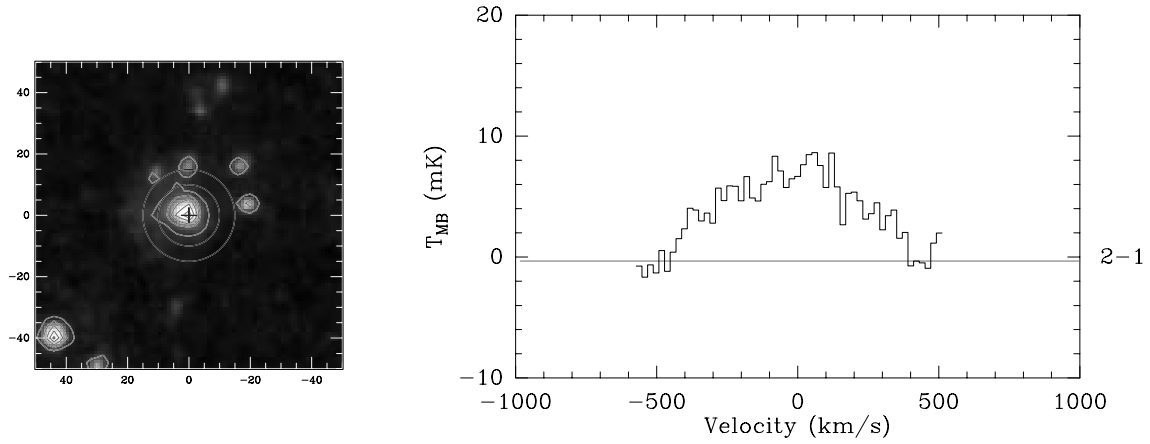

Figure 5.14 POSS image and CO spectra for IRAS 15250+3609 at $cz = 16,602$ km/s. The 3-2 line is blocked by atmospheric absorption.

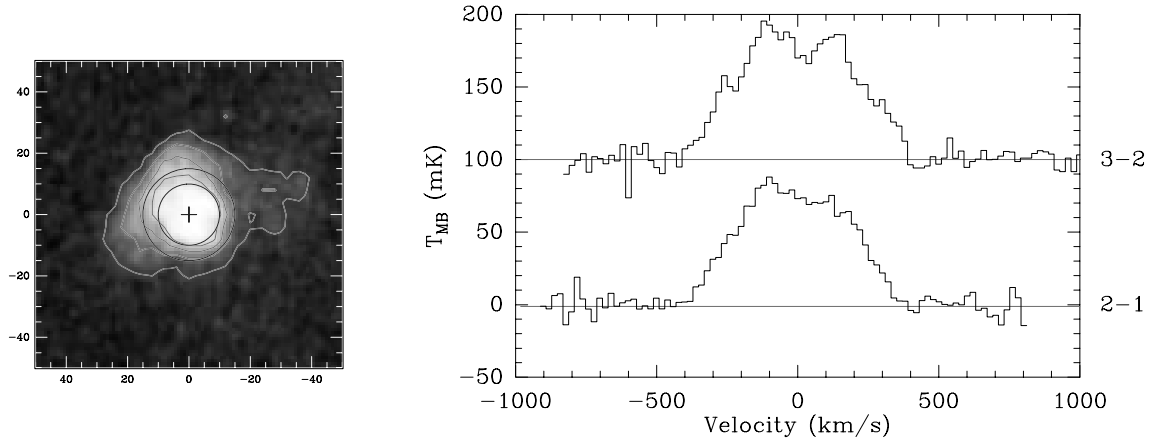

Figure 5.15 POSS image and CO spectra for IRAS 15327+2340 (Arp 220) at $cz = 5,450$ km/s.

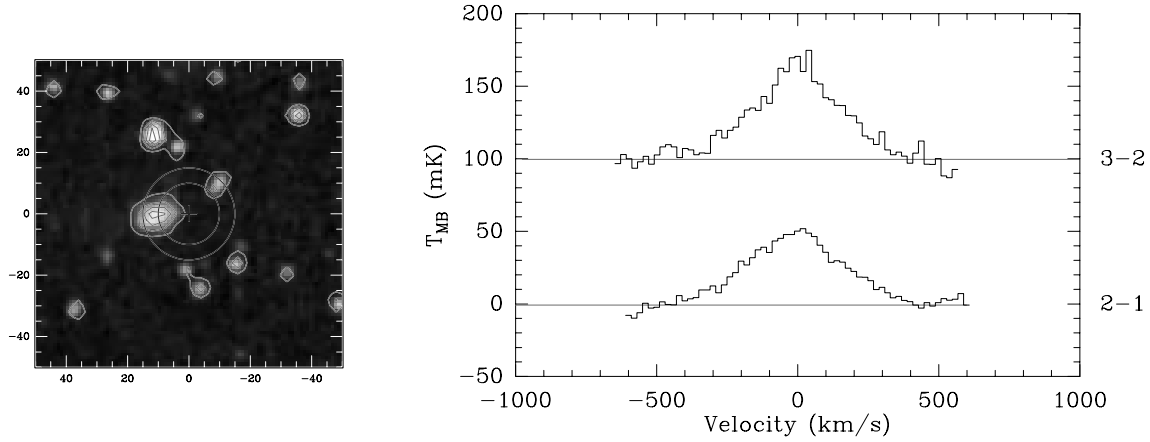

Figure 5.16 POSS image and CO spectra for IRAS 17208−0014 at $cz = 12,836$ km/s.

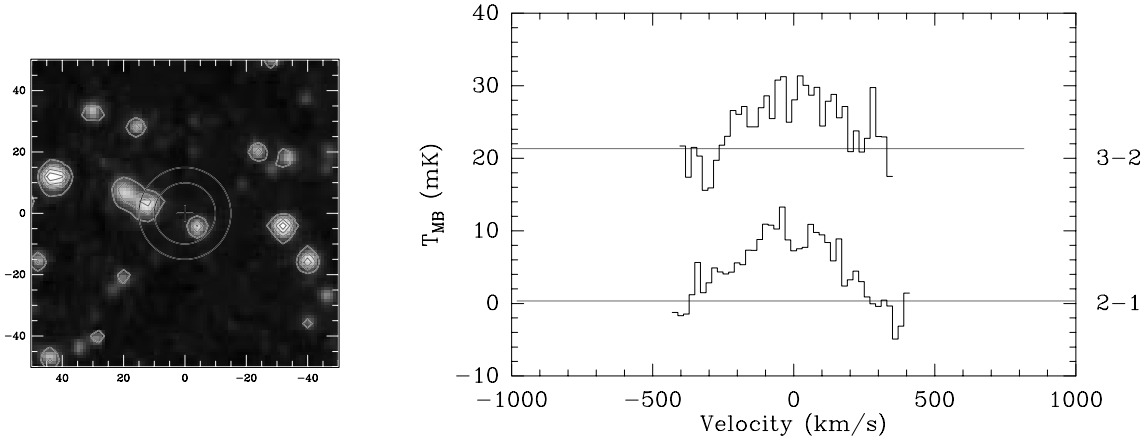

Figure 5.17 POSS image and CO spectra for IRAS 18470+3233 at $cz = 23,626$ km/s.

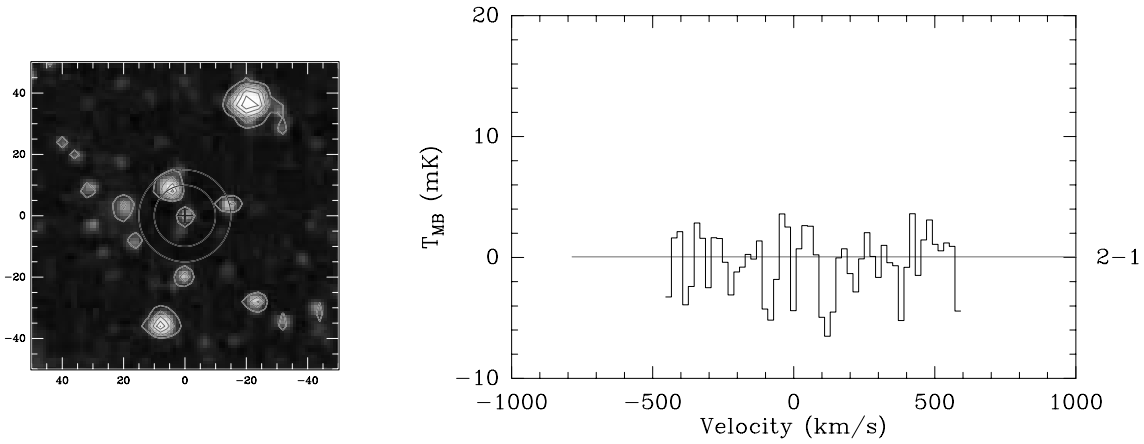

Figure 5.18 POSS image and CO spectra for IRAS 19297−0406 at $cz = 25,674$ km/s. No observations were made of the 3-2 transition due to the faintness of the 2-1 transition.

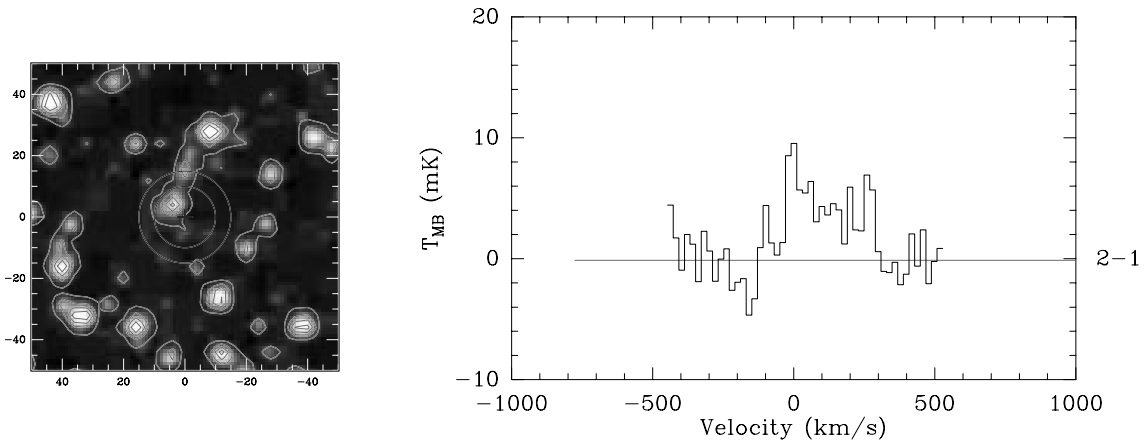

Figure 5.19 POSS image and CO spectra for IRAS 19458+0944 at $cz = 29,940$ km/s.

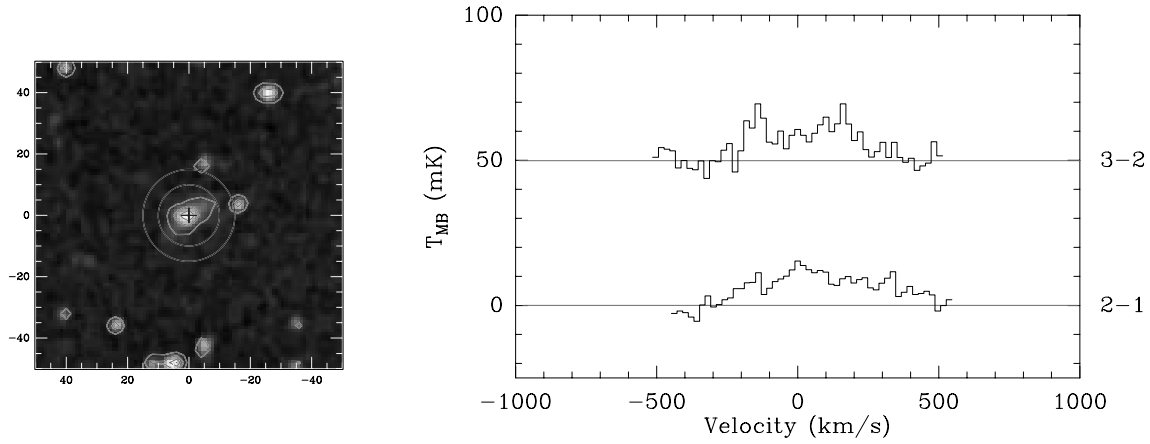

Figure 5.20 POSS image and CO spectra for IRAS 20087−0308 at $cz = 31,700$ km/s.

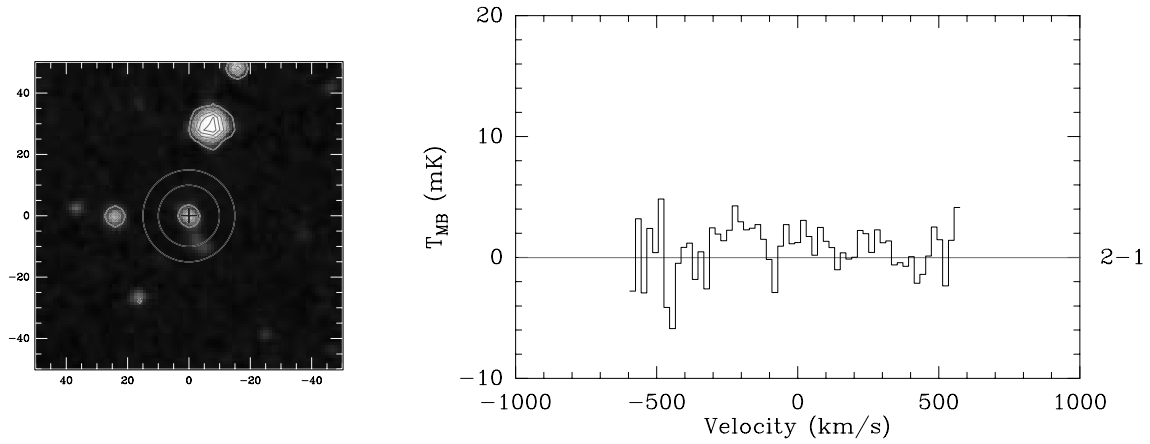

Figure 5.21 POSS image and CO spectra for IRAS 20414−1651 at $cz = 26,107$ km/s. No observations were made of the 3-2 transition due to the faintness of the 2-1 transition.

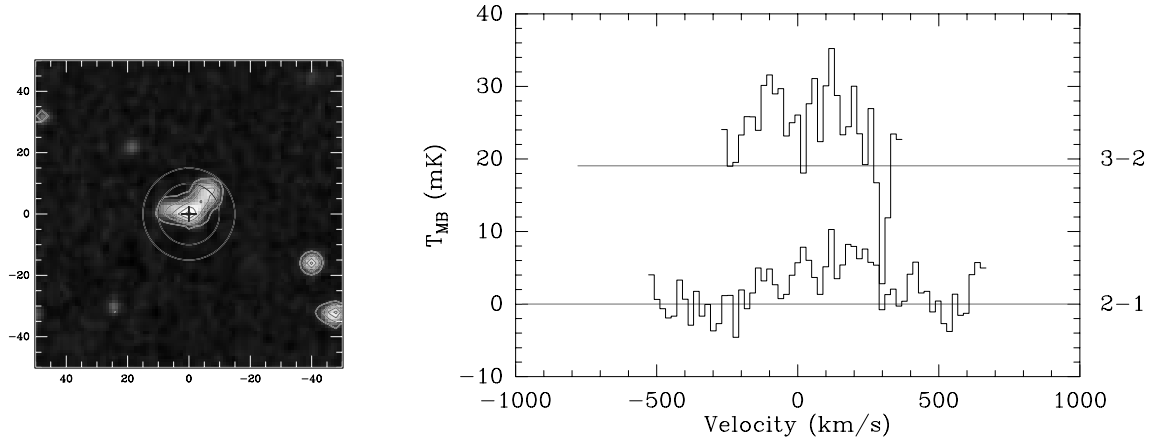

Figure 5.22 POSS image and CO spectra for IRAS 22491−1808 at $cz = 23,300$ km/s.

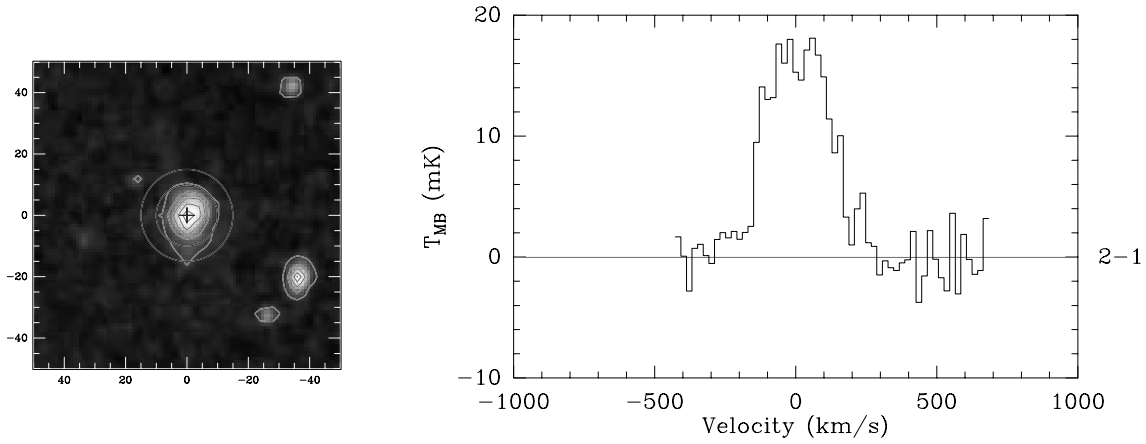

Figure 5.23 POSS image and CO spectra for IRAS 23365+3604 at $cz = 19,338$ km/s.

5.1.3 Determination of Galaxy Properties

Using the detections, we determine the antenna-temperature-weighted mean velocity $\overline{V}$ and width $\overline{W}$ using the formulations:

$$\overline{V} = \frac{\sum \mathrm{T}_i \, \mathrm{v}_i}{\sum \mathrm{T}_i} \qquad \overline{W}^2 \propto \frac{\sum \mathrm{T}_i \, \mathrm{v}_i^2}{\sum \mathrm{T}_i} - \overline{V}^2 \tag{5.1}$$

where the spectra consist of a series of antenna temperatures T_i at velocity v_i. The resultant derived parameters for our CO $2 \rightarrow 1$ observations in a $30''$ beam and $3 \rightarrow 2$ observations in a $20''$ beam are given in Table 5.2. In this table, all the limits are quoted at the $1\,\sigma$ level. Additionally, all the peak and intensity errors are statistical only, and do not reflect an estimated 20% calibration error. The velocities and widths have estimated errors from the integrated signal-to-noise of each line, but do not reflect any uncertainty due to inadequate baseline subtraction. The mean width of all the detected lines is 296 ± 115 km/s, as shown in the histogram in Figure 5.24.

5.1.4 Line Ratios

Observations of the CO $1 \rightarrow 0$ transition have already been made of all but four from our sample of galaxies. Using the available detections in the works of Mirabel et al. (1990), Sanders, Scoville & Soifer (1991), and Solomon et al. (1997), we have converted the measured fluxes into the equivalent fluxes in a $20''$ beam, so that comparison of the

Table 5.2 CO $2 \rightarrow 1$ and $3 \rightarrow 2$ detections and the derived parameters. Upper limits are $1\,\sigma$.

IRAS Name	CO 2→1 Peak T_{MB} (mK)	CO 2→1 Velocity (km/s)	CO 2→1 Width (km/s)	CO 2→1 Flux (K km/s)	CO 3→2 Peak T_{MB} (mK)	CO 3→2 Velocity (km/s)	CO 3→2 Width (km/s)	CO 3→2 Flux (K km/s)
03158+4227	6.2 ± 2.4	$40\,292 \pm 8$	206 ± 16	1.66 ± 0.23	8.8 ± 2.9	$40\,281 \pm 7$	166 ± 14	2.18 ± 0.35
05189−2524	18.7 ± 4.1	$12\,779 \pm 7$	170 ± 14	4.22 ± 0.47	38.6 ± 7.1	$12\,785 \pm 5$	113 ± 10	4.63 ± 0.80
08311−2459	< 9.7	...	...	< 0.78	< 9.4	...	...	< 0.80
08572+3915	< 4.1	...	...	< 0.70	*– no data (atmosphere) –*			
09111−1007	21.7 ± 4.3	$16\,261 \pm 3$	60 ± 6	4.00 ± 0.45	16.3 ± 2.3	$16\,273 \pm 5$	97 ± 9	2.65 ± 0.16
09320+6134	14.3 ± 2.7	$11\,791 \pm 12$	413 ± 27	8.17 ± 0.54	30.3 ± 6.6	$11\,727 \pm 13$	500 ± 32	13.47 ± 1.47
10035+4852	16.9 ± 2.3	$19\,395 \pm 9$	267 ± 20	5.71 ± 0.31	*– no data (atmosphere) –*			
10565+2448	35.0 ± 3.8	$12\,943 \pm 7$	197 ± 16	8.23 ± 0.30	51.6 ± 4.6	$12\,921 \pm 7$	179 ± 15	9.66 ± 0.47
12112+0305	13.0 ± 3.6	$21\,862 \pm 9$	265 ± 20	3.90 ± 0.23	22.1 ± 6.9	$21\,834 \pm 10$	340 ± 24	9.34 ± 0.66
12540+5708	30.7 ± 1.0	$12\,660 \pm 8$	232 ± 18	7.39 ± 0.53	66.0 ± 4.4	$12\,648 \pm 10$	312 ± 22	19.98 ± 0.81
13428+5608	24.8 ± 4.8	$11\,373 \pm 12$	438 ± 29	12.63 ± 0.90	19.3 ± 3.7	$11\,392 \pm 11$	384 ± 26	7.52 ± 0.60
14348−1447	25.7 ± 2.6	$24\,761 \pm 11$	344 ± 24	9.59 ± 0.55	16.8 ± 5.1	$24\,791 \pm 8$	295 ± 16	5.06 ± 1.07
15250+3609	7.0 ± 1.0	$16\,582 \pm 13$	476 ± 31	4.09 ± 0.21	*– no data (atmosphere) –*			
15327+2340	77.7 ± 4.7	$5\,434 \pm 11$	394 ± 27	38.74 ± 0.89	87.4 ± 5.3	$5\,448 \pm 12$	431 ± 28	45.39 ± 0.90
17208−0014	47.7 ± 2.4	$12\,821 \pm 11$	376 ± 26	19.65 ± 0.50	65.9 ± 8.5	$12\,828 \pm 11$	359 ± 25	23.52 ± 0.69
18470+3233	11.1 ± 1.9	$23\,605 \pm 10$	332 ± 23	9.60 ± 0.55	10.1 ± 2.9	$23\,649 \pm 11$	347 ± 24	4.39 ± 0.38
19297−0406	< 2.9	...	...	< 0.25	*– no data (faint) –*			
19458+0944	5.5 ± 2.2	$30\,021 \pm 7$	178 ± 15	1.51 ± 0.19	*– no data –*			
20087−0308	12.4 ± 1.8	$31\,772 \pm 12$	411 ± 27	5.65 ± 0.39	12.8 ± 3.5	$31\,730 \pm 11$	370 ± 25	5.14 ± 0.41
20414−1651	< 1.5	...	...	< 0.28	*– no data (faint) –*			
22491−1808	6.5 ± 1.9	$23\,426 \pm 11$	372 ± 25	2.58 ± 0.32	6.7 ± 4.3	$23\,306 \pm 9$	291 ± 21	3.26 ± 0.58
23365+3604	16.5 ± 1.1	$19\,353 \pm 9$	248 ± 19	5.13 ± 0.22	*– no data –*			

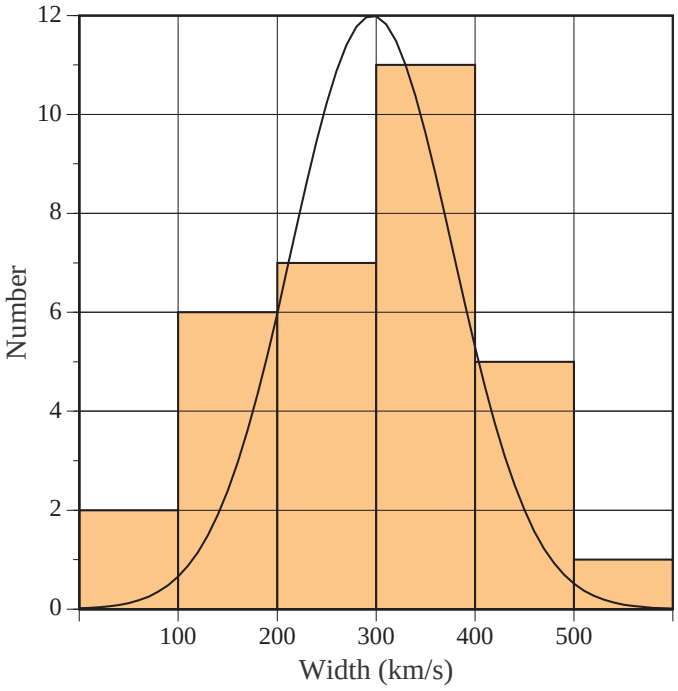

Figure 5.24 Histogram of the widths in the 4Jy CO detections. The Gaussian distribution has a width 115 km/s, centered at 296 km/s.

antenna temperatures can be made. A similar conversion is used for our $J = 2 \rightarrow 1$ CSO spectra. We make the assumption that a simple geometric factor to allow for beam dilution is a sufficient correction, which is true if all the CO emission comes from a compact nuclear region. As can be seen in the POSS images, the galaxy with the greatest optical extent is Arp 220, which contains a CO source only a few arcseconds in diameter. This lends us hope that the CO is similarly compact in the other (generally much more distant) galaxies. However, if it is not valid, the CO $J = 1 \rightarrow 0$ flux is likely to be overestimated.

Using our corrected measured fluxes integrated over the full width of the line, $I_{\rm CO}$, in the $2 \rightarrow 1$ and $3 \rightarrow 2$ transitions in addition to the $1 \rightarrow 0$ fluxes from the literature, we can construct the ratios

$$\mathbb{R}_{32} = \frac{I_{\rm CO\ 3\rightarrow2}}{I_{\rm CO\ 2\rightarrow1}} \qquad \text{and} \qquad \mathbb{R}_{12} = \frac{I_{\rm CO\ 1\rightarrow0}}{I_{\rm CO\ 2\rightarrow1}} \tag{5.2}$$

where $2 \rightarrow 1$ has been used as the reference since it was detected in the greatest fraction of the 4Jy galaxies. A graph of these ratios is shown in Figure 5.25, highlighting the excellent correlation between them. The mean of the line ratios is $\mathbb{R}_{12} = 1.13 \pm 0.51$

and $\mathbb{R}_{32} = 0.61 \pm 0.31$. In the optically thick limit with a thermalized population at high temperature, every transition traces the emission from a blackbody at a temperature much higher than the excitation temperature of the transition (5.53K for $1 \rightarrow 0$, 16.6K for $2 \rightarrow 1$, and 33.2K for $3 \rightarrow 2$). Thus one would expect that the ratios should be $\mathbb{R}_{12} = \mathbb{R}_{32} = 1$. Since the ratio of the lower two transitions, $\mathbb{R}_{12}$, is consistent with the optically thick assumption, the ratio of the upper two implies a cool distribution. Using the radiative transfer models of $\mathbb{R}_{12}$ from Aalto et al. (1995) and $\mathbb{R}_{32}$ from Mauersberger et al. (1999), we can estimate the most likely average temperature and density in the ULIRGS. We have plotted the acceptable regions of the parameter space in Figure 5.26. While the parameters are poorly constrained (largely due to a large error bar in $\mathbb{R}_{12}$), we can estimate a reasonable temperature range of $20 \lesssim T \lesssim 60$K and a density of $n(\mathrm{H}_2) = 10^{3.2 \pm 0.4}\,\mathrm{cm}^{-3}$. With a mean IRAS 60μm/100μm temperature of 70K, it is probable that the CO is colder than the dust.

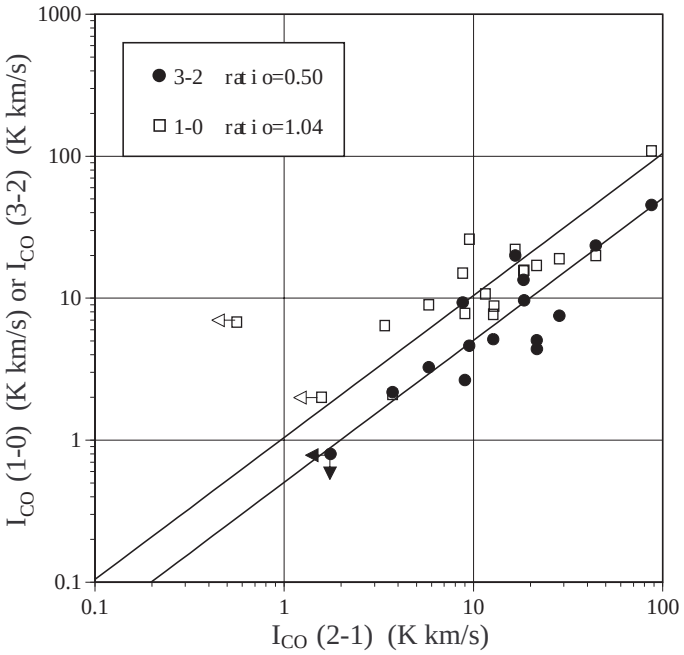

Figure 5.25 Line intensity ratios for the 4Jy survey galaxies, where the integrated intensities carried by the $3 \rightarrow 2$ and $1 \rightarrow 0$ transitions are plotted against the intensity carried by the $2 \rightarrow 1$ transition.

Our intensities track the 100μm flux in all transitions, again implying optically thick emission inasmuch as the 100μm emission is optically thick (Figure 5.27). That the gas may be optically thick and coupled to the dust can be seen in the good correlation ($> 95\%$ probability) between CO intensity and 100μm flux; indeed, Solomon et al. (1997) use this argument to suggest that their $1 \rightarrow 0$ observations trace optically

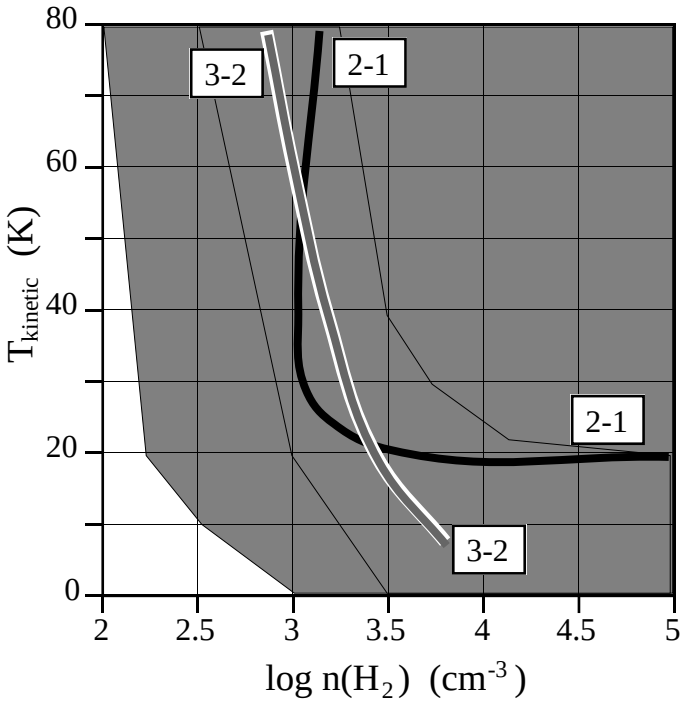

Figure 5.26 The allowed regions of the temperature-density parameter space are diagrammed schematically: the light hatched region with the solid dark curve is the area which satisfies the $\mathbb{R}_{12}$ ratio, while the doubly-hatched region with the outlined grey curve is the region allowed by the $\mathbb{R}_{32}$ measurement.

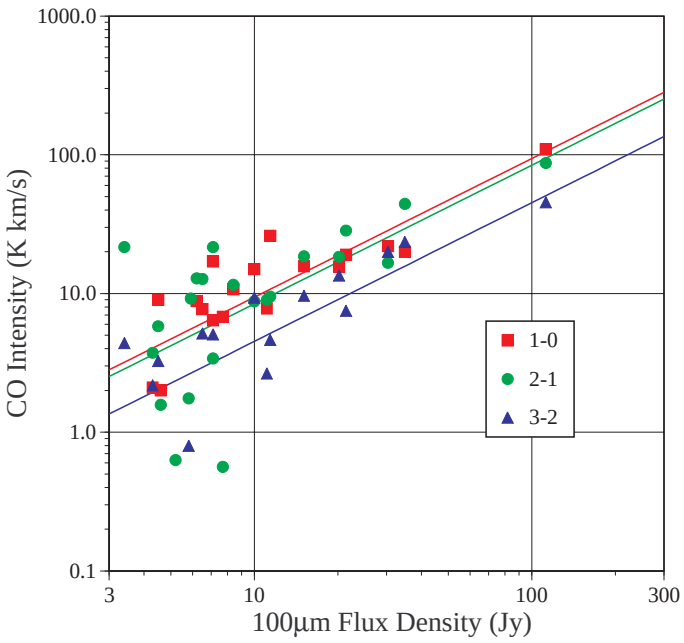

Figure 5.27 Line intensities as a function of the 100μm flux densities.

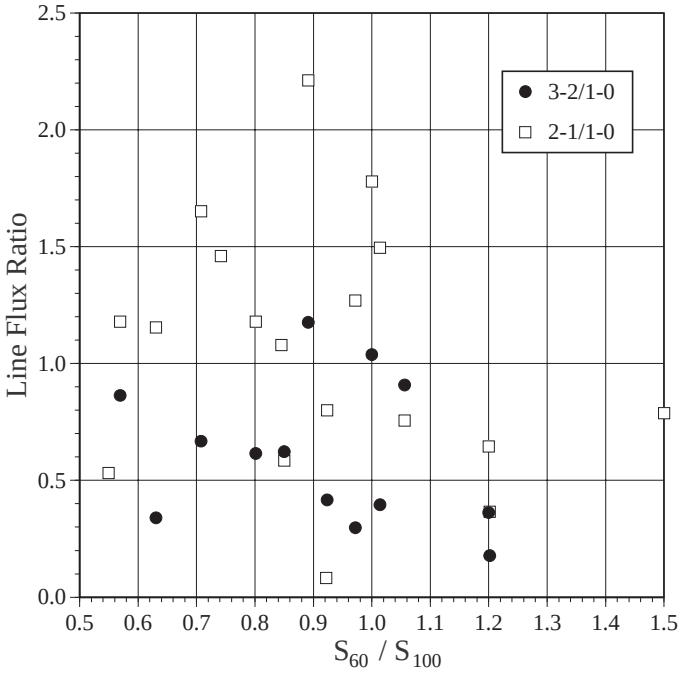

Figure 5.28 Line intensity ratios as a function of the 60μm/100μm color. No correlation is apparent.

thick ($\tau_{\rm CO\ 1-0} \sim 1$) emission. Interestingly, no correlation ($< 5\%$ probability) can be seen between the flux ratios and the FIR color as determined by the ratio of the IRAS 60μm and 100μm flux densities (Figure 5.28). Further modeling of the line ratios in each galaxy will be necessary to constrain the optical depth, density and temperatures.

5.1.5 Molecular Gas Mass

We can convert our measured integrated fluxes in each transition into a total line luminosity $L'_{\rm CO}$ in units of K km s^{-1} pc^2 (e.g., Solomon et al. 1997):

$$L'_{\rm CO} \;=\; 1.05 \times 10^9\, I_{\rm CO}\, \frac{D_L^2}{\nu_{\rm rest}(1+z)} \tag{5.3}$$

where the luminosity distance D_L in Mpc has been defined in equation 1.3 and the constant factor assumes a 10.4m antenna, $\nu_{\rm rest}$ in GHz and $I_{\rm CO}$ in K km s^{-1}.

Using the galactic conversion factor of CO $1 \rightarrow 0$ luminosity to H_2 mass of

$$M({\rm H_2}) \;=\; 4.6\, M_\odot \times \left(\frac{L'_{\rm CO\ 1-0}}{\rm K\ km\ s^{-1}\ pc^2} \right) \tag{5.4}$$

(Solomon et al. 1987) results in an overestimation of the total mass, probably by a factor of 2-3 (Solomon et al. 1997). However, as it is a standard value, we shall use it here to derive a conversion factor for CO $2 \rightarrow 1$ and CO $3 \rightarrow 2$ luminosities as well. Using the mass derived using equation 5.4, we can determine a linear fit for our other measured luminosities, as shown in Figure 5.29. We derive the conversion factors:

$$M(\mathrm{H_2}) \;=\; 2.5\,M_\odot \times \left(\frac{L'_{\mathrm{CO\ 2-1}}}{\mathrm{K\ km\ s^{-1}\ pc^2}}\right) \qquad M(\mathrm{H_2}) \;=\; 5.0\,M_\odot \times \left(\frac{L'_{\mathrm{CO\ 3-2}}}{\mathrm{K\ km\ s^{-1}\ pc^2}}\right) \tag{5.5}$$

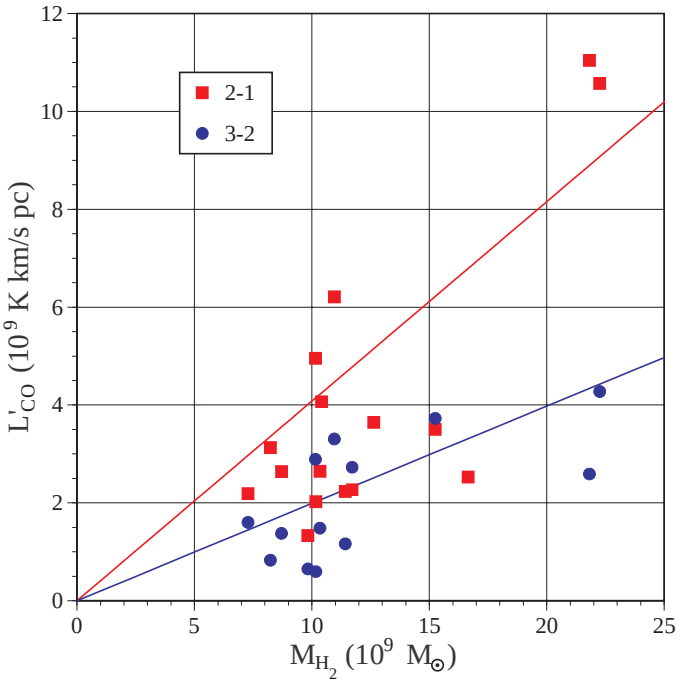

Figure 5.29 Line luminosities vs. the CO $1 \rightarrow 0$-derived molecular gas masses.

5.1.6 Conclusion

While we have been able to detect a substantial number of ultraluminous galaxies in CO $2 \rightarrow 1$ and $3 \rightarrow 2$, our line ratios are not suitable for tightly constraining the optical depth and temperature of the molecular gas in these galaxies. The excitation temperature of $3 \rightarrow 2$ is only 33.2K, whereas the dust temperatures derived from the IRAS measurements are 70 ± 15. It is therefore likely that the only effect we are sensitive to is a change in the optical depth. Unfortunately, observations of these

galaxies in the CO $4 \rightarrow 3$ and $5 \rightarrow 4$ transitions is impossible due to atmospheric absorption, but $6 \rightarrow 5$ at 691.473 GHz is accessible. We have initiated attempts to detect this transition, as with an excitation temperature of 83K, it should trace only the warm component of the molecular gas near the nucleus of ultraluminous galaxies. However, our instantaneous bandwidth at $\nu \sim 650$ GHz is less than 400km/s, too narrow for most of the galaxies on our list. Furthermore, with the existing receiver (Kooi et al. 1994), in one hour of on-source integration in good weather we can achieve a noise level of roughly 30mK (main beam) in a 20km/s channel, which would fail to detect most of the galaxies even at the $1\,\sigma$ level. It is therefore of scientific interest to attempt to detect the $6 \rightarrow 5$ transition with broader-bandwidth instrumentation in order to improve our understanding of the higher-J transitions of CO. Much of the rest of this thesis shall be oriented towards this and related goals.

5.2 Measuring the CO Ladder

The previous section highlights the difficulties inherent in measuring a range of submillimeter CO rotational transitions: differing beamsizes, different telescopes, the lack of simultaneity of observations (which substantially reduces relative calibration errors) and the resulting uncertainty in absolute calibration all contribute to make the physical conditions all the harder to evaluate. However, it may be possible to exploit the techniques of Fourier transform spectrometry to detect bright galaxies in several CO transitions simultaneously with the same beamsize. The difficulty with this approach is that the background power from the atmosphere, since the power would have to cover the entire submillimeter waveband, would load the detector so heavily as to reduce its sensitivity below the point of being able to detect weak sources. To combat this problem, Gene Serabyn and I have developed a specialized filter to pass only the CO transitions while blocking the atmospheric emission. This work has been submitted to the journal Applied Optics under the authorship of Benford, Wu, Pardo & Serabyn (1999).

5.2.1 Introduction

The simplest technique to perform astronomical spectroscopy with broad spectral coverage at moderate resolution in the far-infrared and submillimeter is through the use of a Fourier transform spectrometer (FTS) (Serabyn & Weisstein 1995). Linear molecules have nearly-harmonic rotational states which give rise to line emission at multiples of some fundamental frequency (e.g., Townes & Schawlow 1955). Thus, for studies of a single such molecule, the interesting regions of the spectrum are regularly spaced narrow windows, separated by broad empty regions. However, if the lines are narrow compared to their spacing, as in astronomical applications, then a detector at the output of an FTS will see an excessive continuum background power from the atmosphere. In the background-limited regime, this substantially limits the minimum detectable line brightness. A filter resonant at multiples of a fundamental frequency, such as a Fabry-Perot étalon, can reduce this background power, and so we have developed a resonant filter optimized for this application.

CO is the species with the brightest submillimeter rotational spectrum in astronomical objects such as molecular clouds (Groesbeck 1994). It is also the second most abundant interstellar molecule after H_2. CO also is an important species in a diverse range of objects from planets to distant galaxies. In galaxies, the narrow bandwidth of heterodyne spectrometers makes it impossible to measure simultaneously more than one CO transition per spectrometer. In fact, it is often difficult to detect even the CO $J = 7 \rightarrow 6$ line, where the bandwidth of existing facility spectrometers corresponds to less than 400 km/s. An FTS can address this issue by measuring the line integrals at low spectral resolution. An FTS has the further capability of measuring a large range of CO transitions simultaneously with a common beamsize, limited by the acceptance angle of the horn illuminating the detector. Thus what is desired is a resonant filter of spacing equal to the CO line spacing, 115 GHz, and with a passband width of many times the expected linewidth (perhaps 2 GHz) after allowing for small amounts of redshifting. For extragalactic observations, such a filter should be able to receive the CO $J = 7 \rightarrow 6$ line with a frequency shift of up to 15 GHz, i.e., from

extragalactic objects at a redshift of up to 5000 km/s (more distant objects being to faint to detect). Thus, a passband width of order 10-20 GHz at the $\sim 80\%$ transmission level is desirable. As an approximate design criterion, a FWHM of ~ 25 GHz is probably appropriate.

Even at the high, dry site of Mauna Kea, the atmosphere is transparent to CO transitions only up to about 1000 GHz (33 cm^{-1}) (Serabyn et al. 1998), which covers the lowest rotational transitions up to $J = 7 \rightarrow 6$ ($J = 5 \rightarrow 4$ and $J = 8 \rightarrow 7$ are blocked by atmospheric water vapor emission). However, the atmosphere is at most only $\sim 50\%$ transmissive above 500 GHz, so that the thermal radiation power loading a detector will be very large compared to the power from CO lines. In order to reduce the thermal power as much as possible, it is then necessary to achieve an out-of-band rejection of at least a factor of 10. For observing purposes, a wide, flat profile in both the passbands and the rejected bands is optimal.

The simplest method of fabricating a Fabry-Perot filter is to use the reflectivity of the two dielectric-to-vacuum boundaries of a thin slab of material. Silicon is an attractive material, since with a refractive index of $n \sim 3.4$ (Lamb 1996), its single-surface reflectivity is 30%. Germanium would be even better, with $n = 3.9$, but it is somewhat more difficult to obtain appropriate pieces. Silicon based Fabry-Perots have been made in the past (Bock et al. 1995), and can provide high resolving power with low loss. Furthermore, silicon can be manufactured by etching to a precise thickness with very parallel faces. However, a single slab of silicon does not have a sufficiently high finesse to be useful. Therefore, a double slab of silicon with an air gap was considered.

5.2.2 Calculation

The fundamental frequency of CO is the ($J = 1 \rightarrow 0$) transition at 115.271 GHz (3.842 cm^{-1}) (Townes & Schawlow 1955). Because the rotational constant $B_e = 57.8975$ GHz is so much larger than the centrifugal stretching constant $D_e = 183.4$ kHz (which gives a first-order correction to the rigid harmonic oscillator Hamiltonian), sub-

sequently higher transitions in the submillimeter are very nearly exact integer multiples of the fundamental frequency, to a precision of better than 10^{-3} at 1000 GHz. Our goal is to detect all of the submillimeter rotational transitions transmitted by the atmosphere, from the $J = 2 \rightarrow 1$ transition at 230.528 GHz or the $J = 3 \rightarrow 2$ transition at 345.796 GHz to the $J = 7 \rightarrow 6$ transition at 806.652 GHz. The lowest reachable frequency is determined by the cutoff wavelength of the horn illuminating the detector.

The transmission of a Fabry-Perot interferometer at normal incidence, ignoring losses, is given by the Airy function (Hecht 1987)

$$T = \frac{1}{1 + F \sin^2(2\pi nd/\lambda)} \text{ with } F = 4R/(1-R)^2 \tag{5.6}$$

where F is the coefficient of finesse and R is the single surface power reflectivity of a single interface of an étalon spaced by a distance d at a wavelength λ. For an air-dielectric, $R = [(n-1)/(n+1)]^2$, which yields

$$T = \frac{1}{1 + [(n+1)(n-1)/2n]^2 \sin^2(2\pi nd/\lambda)}. \tag{5.7}$$

This function is periodic in frequency with period $c/2nd$. The peaks of this function are unity while the transmission at each minimum is $(4n^2)/(n^2+1)^2$. The finesse $\mathfrak{F} = \frac{\pi}{2}\sqrt{F}$ is the ratio of the peak-to-peak spacing to the FWHM of each transmission peak, and is a useful figure of merit for a Fabry-Perot filter. The finesse rises from $\mathfrak{F} = 0$ at $n = 1$ (trivially) to $\mathfrak{F} = 3$ at $n = 4$. For our application, the CO filter must achieve a finesse of $\mathfrak{F} \sim 115/25 \sim 5$, requiring an impractical index of $n = 6.5$. Worse, for silicon the out-of-band transmission minima are 30%, implying only a factor of 3 rejection. A double Fabry-Perot stack would likely perform better as the square of 0.3 implies a rejection of a factor of ten.

The theory of the double Fabry-Perot is established (Dufour 1951), and results in analytical expressions for simple cases (e.g., identical Fabry-Perot étalons spaced so as to make a triple étalon). In order to calculate the transmission as a function of

frequency of an arbitrary double Fabry-Perot, we used a numerical algorithm based on the matrix formalism of Born & Wolf (1959) as developed by Woody & Keene (private communication). We started by assuming two identical étalons resonant at 115 GHz, which requires thicknesses of $d = 385\mu$m. The spacing between étalons can be estimated by requiring that the resonant frequency between them be higher than the maximum frequency of interest, around 1 THz. This requires the spacing to be smaller than 195μm. Through repeated refinement of our model, we were able to design a double Fabry-Perot which would satisfy the astronomical requirements. The theoretical transmission of this device is compared to that of a single Fabry-Perot étalon in Figure 5.30.

The geometry of this étalon requires silicon disks of thickness $385.5\pm1.0\mu$m spaced by a vacuum gap of $140\pm10\mu$m. The error on the silicon thickness is determined by requiring that the frequency error near 1 THz be substantially smaller than the bandwidth of ~ 20 GHz. The period of the Airy-like variation in the minimum transmission regions is dependent on the spacing between the two silicon étalons. In order that the out-of-band rejection be optimized for the frequencies of interest (200–900 GHz), the vacuum gap must have a resonant frequency of 1100 ± 100 GHz. The out-of-band rejection is at best a factor of 30, ten times better than with a single étalon. The FWHM of the passbands is unaffected in the region of interest, but the transmission peaks become more flat-topped, also a desirable characteristic. In the lowest six minima, the average transmission is reduced to $\sim 7\%$.

5.2.3 Fabrication

We acquired pre-thinned, double-side-polished 25mm diameter 100-oriented silicon wafers (Virginia Semiconductor), $390 \pm 7\mu$m thick. This is thicker than desired so that they could be etched away to the precise thickness required. The two sides were parallel such that the thickness variation across the free aperture of the final filter is less than 0.5μm. The thickness of each wafer was then determined by two methods. First, the transmittance spectrum was measured for room temperature samples

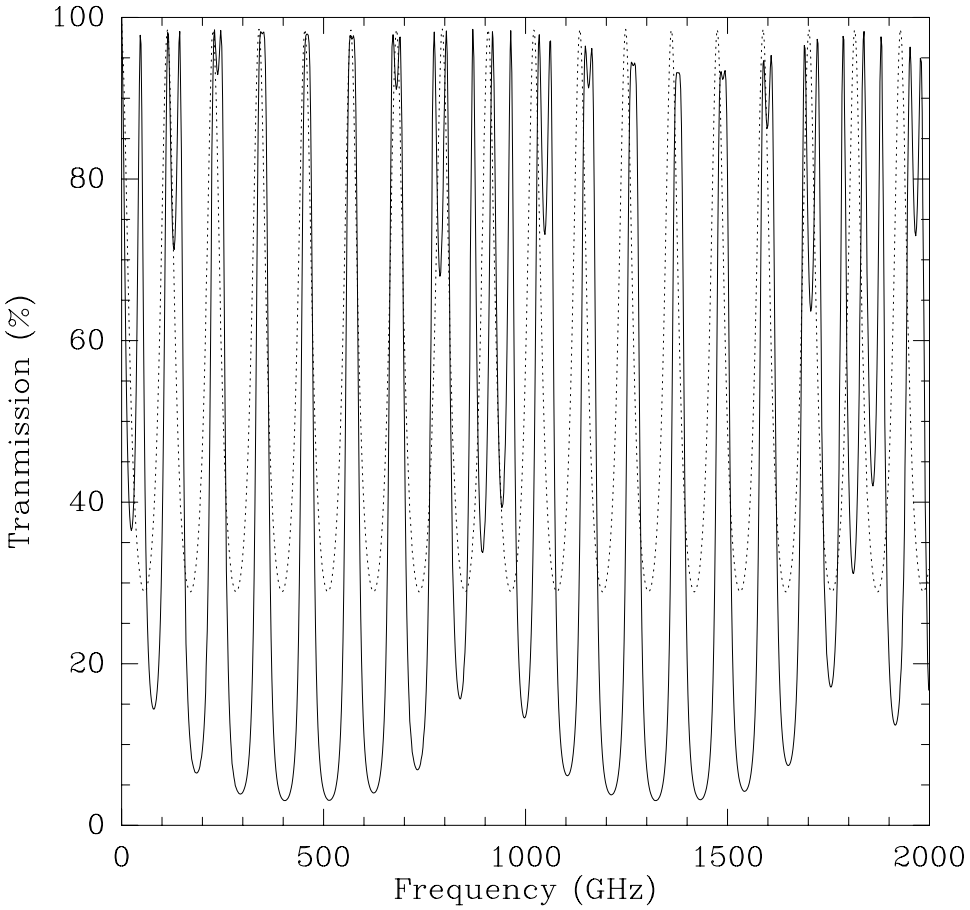

Figure 5.30 Theoretical transmission of a single (dotted) vs. a double (solid) Fabry-Perot étalon, constructed from silicon disks of $n = 3.42$ of 385μm thickness with a 140μm air gap between them.

at wavelengths between 7 and 12 μm using an infrared FTS (Nicolet Instruments, graciously provided for our use by George Rossman). In this spectral region, the refractive index is 3.4184 and constant to 100 ppm (Salzberg & Villa 1957). Over 150 fringes may be counted, allowing the determination of the thickness to $\lesssim 0.05\mu$m absolute accuracy. The second method used a temperature-controlled Mahr Universal Measuring Machine (Accurate Instrument Repair) with a precision and relative accuracy of $\sim 0.12\mu$m. Although the absolute accuracy of this instrument is only 0.24μm, its relative accuracy permits the verification of flatness to better than 300 ppm. The measurements were typically found to agree between the two methods to within the experimental accuracy, although a few were inconsistent.

The silicon wafers were thinned uniformly in order to adjust the thicknesses by growth and removal of a thermal oxide layer on the silicon surface. We first cleaned the silicon in a hydrogen peroxide and sulfuric acid solution at 120° C. Next, an approximately 1.4μm deep layer of surface silicon was converted to 3μm of SiO_2 in a thermal oxidation furnace at 1050° C for 18 hours. Finally the oxide was stripped away by buffered HF, resulting in a slightly thinner silicon wafer which remained optically flat. A second set of measurements indicated that 1.368μm were removed from each side in one etching process. Several of the wafers were then chosen to be thinned one additional time. The final "best" wafers were again measured and found to be 384.8μm and 386.4μm thick, bracketing the desired thickness of 385.5μm and within the desired tolerance of 1.0μm.

The filter stack is comprised of the two silicon disks each forming a Fabry-Perot étalon, spaced by a thin stainless steel washer nominally 140μm thick as shown in Figure 5.31. The stack is set in an aluminum cup for easy heat sinking, with a beryllium-copper washer screwed into place above the filter stack to hold it in the cup with some spring-loading to account for thermal contraction. Because of the small thicknesses of the components, thermal contraction changes the physical size of each part by much less than the associated error in each dimension. The clear aperture of the filter is about 2cm in diameter.

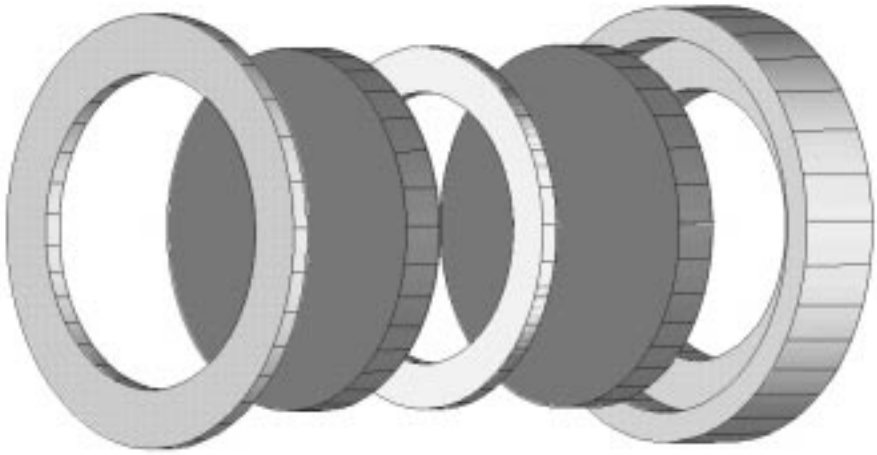

Figure 5.31 Diagram of Fabry-Perot layout. The thickness of the components has been substantially enhanced for clarity. The components are, from left to right: beryllium-copper spring washer, silicon disk (386μm thick), stainless steel spacer ring (140μm), silicon disk (385μm), aluminum mounting cup.

5.2.4 Measurements

The double Fabry-Perot was installed in a cryogenic dewar with a bolometer operating at 1.5K (Infrared Laboratories) and a filter wheel. The dewar looked through our laboratory Michelson submillimeter FTS (Bin et al. 1999) at a chopped hot/cold load at 150 Hz. An aperture stop was placed in the collimated beam portion of the FTS; an off-axis paraboloidal mirror near the dewar window reimaged this aperture stop onto the filter inside the dewar. The FTS was scanned 40cm to achieve a spectral resolution of 3.66 GHz covering the region from 300 to 1600 GHz. Two spectra were taken, one with the filter in place and the other with the filter moved out of the beam. This was then repeated with a thicker beamsplitter optimized for longer wavelengths, 100 to 900 GHz. The two resulting spectra were averaged together and the regions of poor signal-to-noise were removed.

The measured transmission of the double Fabry-Perot filter is compared to the theoretical calculation as shown in Figure 5.32. The agreement is excellent when one allows for a change in the index of refraction of silicon upon cooling to 1.5K. Loewenstein, Smith & Smith (1973) have found that the refractive index decreases on cooling to $n = 3.382$. We measured the index of refraction of silicon with the laboratory FTS

using a single silicon disk of a known thickness determined interferometrically in the mid-IR. At 1.5K, our measured index of silicon is 3.36 ± 0.01. Fitting the double Fabry-Perot model to the measured data yields an index in the 500-1500 GHz range of $n = 3.385 \pm 0.010$ at 1.5K, nearly within the joint $1\,\sigma$ error bars.

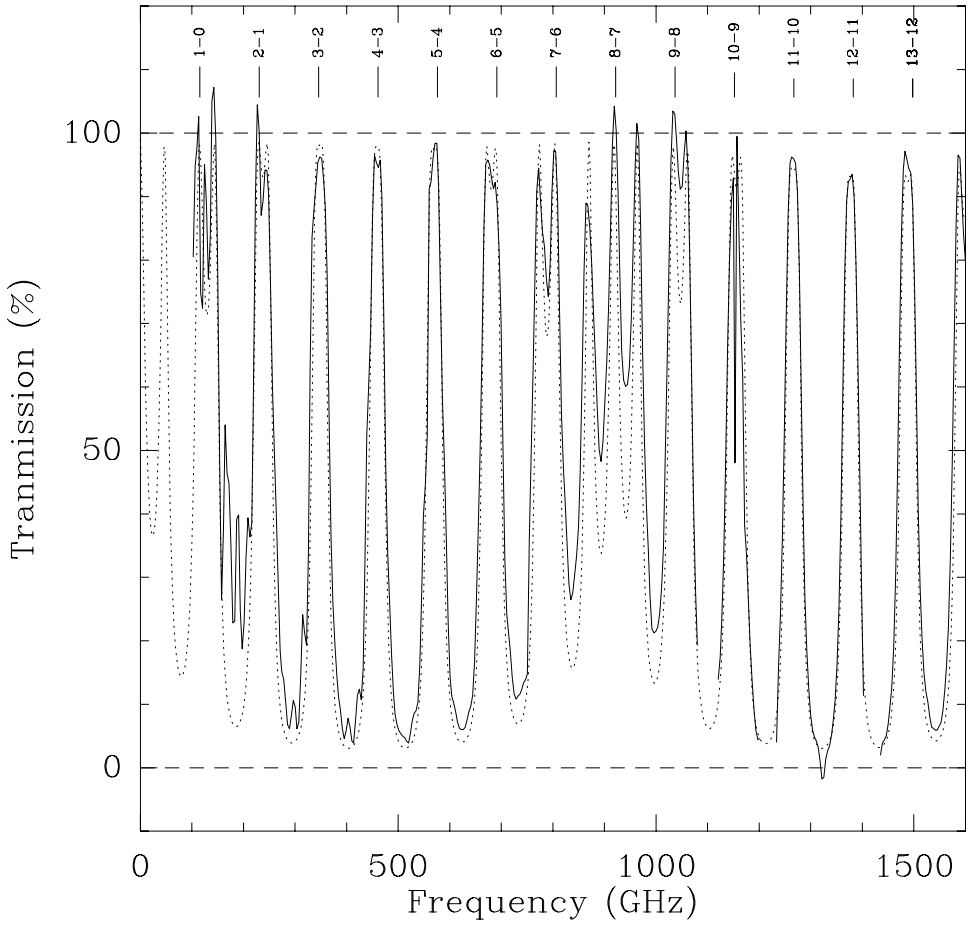

Figure 5.32 Measured transmission (solid curve) vs. theoretical (dotted curve). The CO transitions are indicated to demonstrate the excellent matching to the filter passbands. The data below 150 GHz have been smoothed to account for the decreasing signal at longer wavelengths.

The Airy-like variation in the minimum transmission regions has a period of $\sim$ 920 GHz, less than the designed 1110 GHz. If the spacing ring is not perfectly flat, it may be possible that the distance between the silicon disks is slightly larger than was initially planned. The theoretical curve in Figure 5.32 assumes an étalon spacing of 160μm rather than the designed $140 \pm 10\mu$m.

5.2.5 Initial Observations of Venus

The constructed filter[1] was next taken to the Caltech Submillimeter Observatory (CSO) to observe the CO absorption spectrum in the atmosphere of Venus. Venus makes an ideal test source, as its lines are bright enough to be detectable and broad enough to warrant the use of our filter with an FTS for scientific purposes. The filter was placed in front of the bolometric detector of the CSO facility FTS (Serabyn & Weisstein 1995; Serabyn & Weisstein 1996) and observations of Venus were carried out on 1998 April 1. Approximately 40 minutes of on-source integration time was available before sunrise. The relevant sections of the Fourier-transformed spectrum of Venus are shown in Figure 5.33, blown up around the regions containing the lines. All four lines available within our 300-1000 GHz passband were detected. The lines are slightly resolved, even at 200 MHz resolution. Interpretation of these results will be presented elsewhere, but it is clear from a first look at the data that the line integrals are significantly larger than is suggested by integrating over the line cores seen with narrow band heterodyne receivers. These integrated line wings thus probe deeper into the atmosphere than the narrow line cores seen in all previous observations of Venus (Clancy & Muhleman 1991; Gurwell et al. 1995).

5.2.6 Conclusion

We have fabricated a double Fabry-Perot resonant filter for astronomical use which will selectively pass the rotational transitions of CO. When used with an FTS on a submillimeter telescope, simultaneous measurements of all available submillimeter CO transitions are possible. When compared with a single Fabry-Perot étalon, the out-of-band rejection of the filter is enhanced by a factor of $\gtrsim 5$ for frequencies below 1 THz. The passband becomes more flat-topped while maintaining a similar width around each transition. For a source with strong CO lines, this filter thus allows very accurate relative calibrations of the line strengths with a reduction in the required integration time of 4. The relative accuracy of the calibrations should be limited only

[1] The filter is called the CO-DFPI filter, as it is the CO Double Fabry Perot Interference filter.

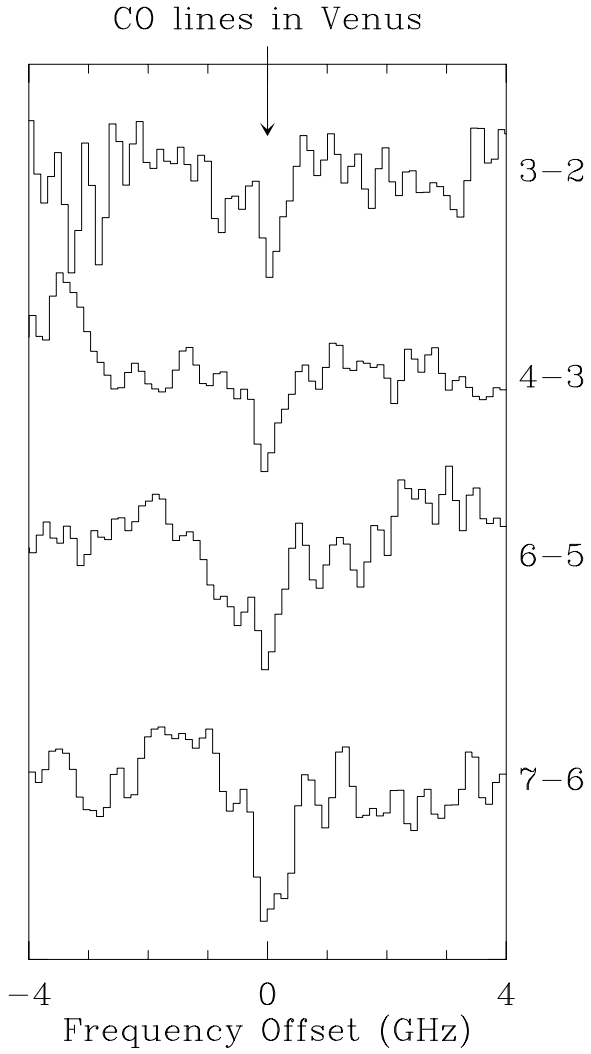

Figure 5.33 Simultaneous measurement of absorption by multiple transitions of CO in the atmosphere of Venus. The $5 \rightarrow 4$ and $8 \rightarrow 7$ transitions are blocked by atmospheric absorption due to water lines at 557 GHz and 916 GHz. The spectrum has been normalized by the spectrum of Jupiter to remove pass-band features.

by the model of the temperature of the planet which is used as a primary calibrator during the FTS observations. This time savings, plus the time no longer needed for filter switching between different CO lines, is especially critical for observations of the faint emission from galaxies. The measured sensitivity is such that a galaxy like M82 should be detectable ($\sim 5\,\sigma$) in all four available submillimeter CO transitions with approximately one hour of total telescope time (Serabyn & Weisstein 1995).

Chapter 6 Searching for Line Emission at High Redshift

The idea of probing the ISM in protogalaxies by searching for their far-infrared emission lines has been proposed by several authors, most notably for the use of the 158μm line of singly-ionized carbon (CI; e.g., Loeb 1993; Stark 1997), but also of the commonly observed rotational transitions of carbon monoxide (CO; e.g., Spaans 1997). A great amount of effort has gone into attempting to detect these lines in a variety of objects with little success (see the surveys of, e.g., Evans et al. 1996; van Ojik et al. 1997). As of this writing, eight objects – at least three of them gravitationally lensed – have been detected: IRAS F10214+4724 (Rowan-Robinson et al. 1991), H 1413+117 (Barvainis et al. 1994), BR 1202−0725 (Ohta et al. 1996; Omont et al. 1996a), BRI 1335−0415 (Guilloteau et al. 1997), 53W002 (Scoville et al. 1997), MG 0414+0534 3 → 2 (Barvainis et al. 1998), APM 08279+5255 (Downes et al. 1999), and SMM 02399−0136 (Frayer et al. 1998). This small sample represents the first forays into the detection of molecular and atomic far-infrared emission from high-redshift objects, a field of study destined to become important for learning about star formation in the early universe. In this chapter, I present our endeavors at the CSO to detect highly redshifted emission lines from known sources culled from the list above.

6.1 Detections of CII in Nearby Galaxies

Many detections of the CII 158μm line emission in nearby galaxies were made over the past two decades using the KAO (e.g., Stacey et al. 1991). Altogether, the net result is that the fractional contribution of the luminosity of CII line to the total

luminosity of the galaxy, which I shall call ϱ, was found to be

$$\varrho \equiv \frac{L_{\rm CII}}{L_{\rm FIR}}; \qquad 0.001 \leq \varrho \leq 0.01. \tag{6.1}$$

This is a substantial amount of luminosity considering that line emission is confined to such a narrow band. The first truly broadband, high spectral resolution spectra including the CII line were produced by the ISO satellite's Long Wavelength Spectrometer (LWS)[1], which permitted the detection of the continuum and other lines as well.

Perhaps the most comprehensive study published to date is that of Malhotra et al. (1997), which shows a trend of a decreasing ϱ with increasing temperature. The initial data are shown in Figure 6.1. A preliminary result of one study of bright infrared galaxies is that the line-to-continuum ratio varies tremendously. As shown in Figure 6.2 (pre-publication spectra, Fischer et al. 1999), the line can be dominant (e.g., Cen A) or almost undetected (Arp 220). Gerin & Phillips (1998) have used the CI line in Arp 220 to show that the lack of CII is due to the high gas density and high UV flux.

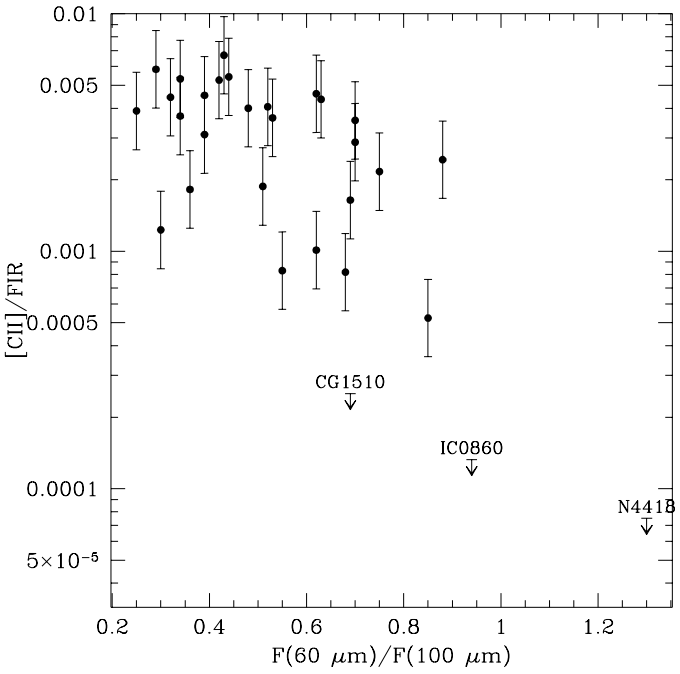

Figure 6.1 Ratio of CII emission to luminosity vs. ratio of 60μm to 100μm flux density for a sample of galaxies observed by ISO, from Malhotra et al. (1997).

[1]See chapter 8 for a description of the function of a similar instrument.

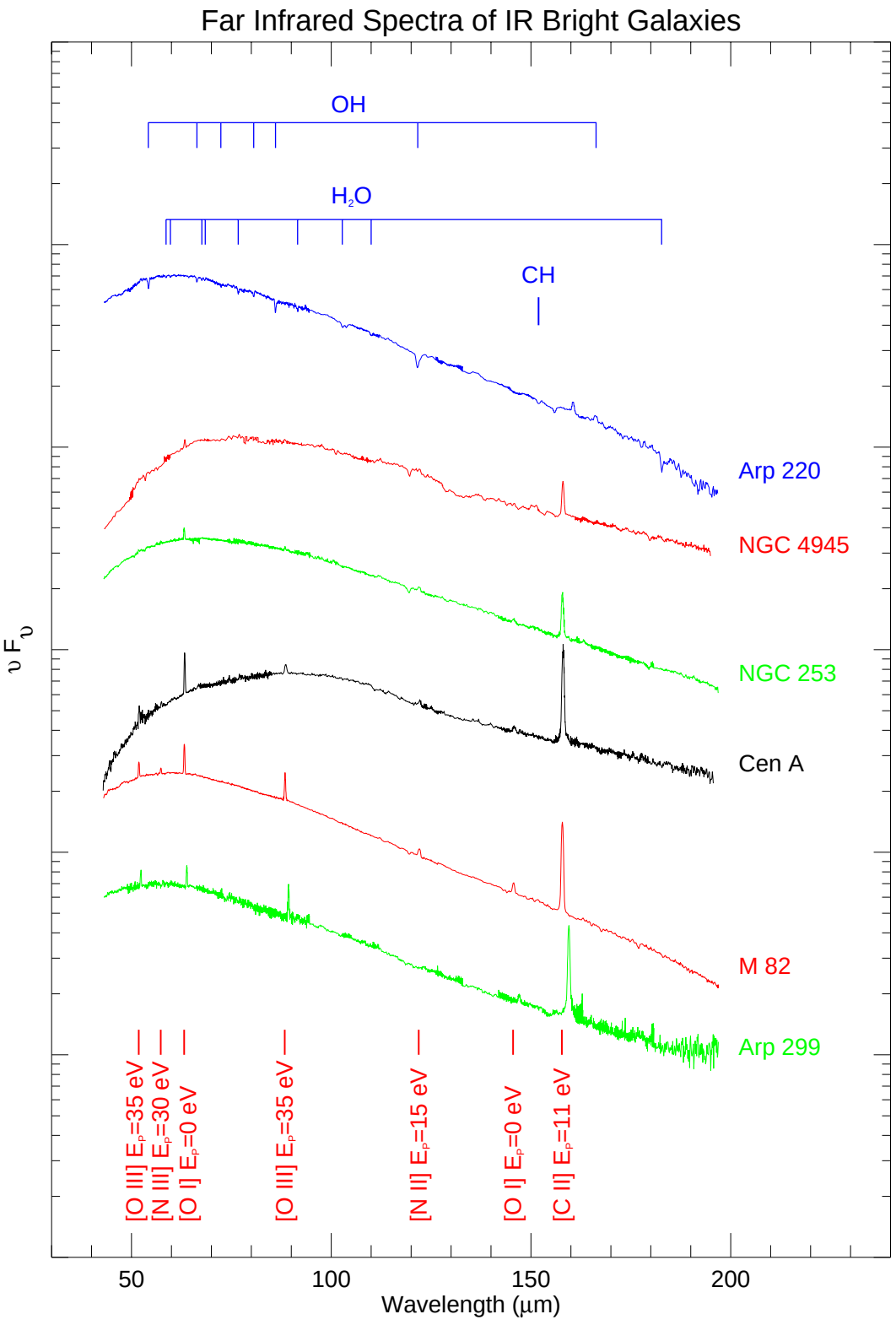

Figure 6.2 Far-infrared spectra of six bright galaxies, as seen by the ISO-LWS (Fischer et al. 1999).

6.1.1 Expectations

Recalling the derivation in section 1.3.2, specifically equation 1.6 and Figure 1.15 (repeated below as Figure 6.3), I calculated the expected flux density from the CII 158μm line at redshifts of $z \leq 10$. From the figure, it is evident that the best sensitivity for instruments at the CSO is in the range $4 < z < 6$, where the receivers are the lowest-noise currently available. One would expect the flux densities from a $10^{12}\,L_{\odot}$ galaxy to be a few tens of milliJanskys based on local measurements. This is just within the realm of detectability with existing CSO instruments.

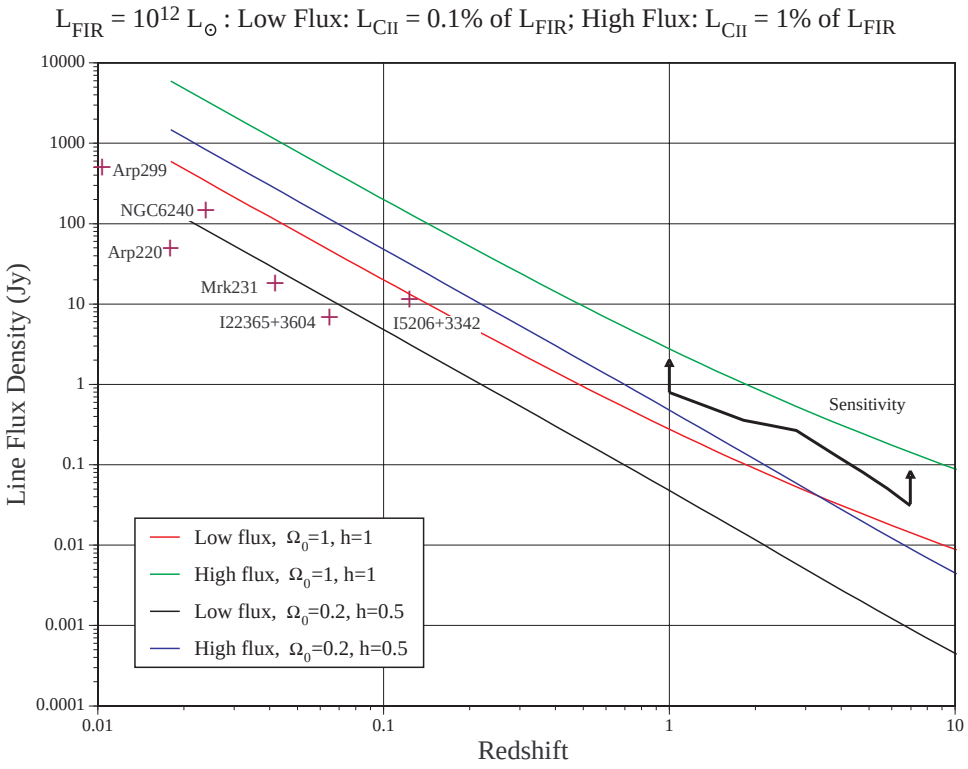

Figure 6.3 Predicted flux density in the CII line as a function of redshift. Two different cosmological models are plotted for each of two estimators: $L_{\rm CII} = 0.01 L_{\rm FIR}$ and $L_{\rm CII} = 0.001 L_{\rm FIR}$. The sensitivity is estimated for a 5σ detection in one hour of on-source integration, and should be considered only as an estimate.

One caveat has to be attached to this prediction: the local galaxies are, by and large, brighter in CII than more distant, ultraluminous galaxies such as Arp 220. If the galaxies we see at high redshifts are more like the latter class, then our expected flux densities might be a factor of 10 lower – $0.01\%\,L_{\rm FIR}$ – making them undetectable.

6.2 Search for CII in $z \sim 4$ Quasars

We have chosen for our deepest observations to attempt the discovery of the CII emission from the two $z > 4$ quasars detected in CO emission, BR 1202 − 0725 (Ohta et al. 1996; Omont et al. 1996a) at $z = 4.69$ and BR 1335 − 0415 at $z = 4.41$ (Guilloteau et al. 1997). The CO detections from these two works are shown in Figure 6.4. These galaxies were also observed using SHARC as described in chapter 4, yielding an excellent estimate of their total far infrared emission. Table 6.1 details the known far-infrared properties of these two quasars. This work has benefited from the contributions of Todd Hunter, Min Yun, Sangeeta Malhotra, Tom Phillips and myself.

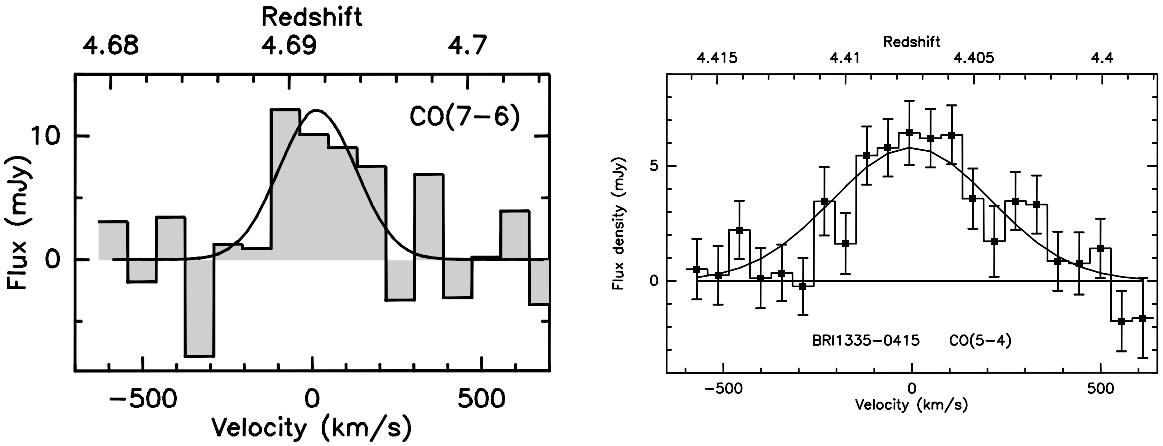

Figure 6.4 Detections of CO emission made using the Plateau de Bure interferometer. (A) BR 1202 − 0725 in CO $J = 7 \rightarrow 6$ at $z = 4.6916$ from Omont et al. (1996a). (B) BRI 1335 − 0415 in CO$J = 5 \rightarrow 4$ at $z = 4.4074$ from Guilloteau et al. (1997).

The observations were carried out at the CSO during periods of excellent weather ($\tau_{225\,\mathrm{GHz}} \sim 0.05$); BR 1202 − 0725 was observed in January of 1998, BRI 1335 − 0415 in March of 1998. With a rest frequency of 1900.537 GHz, the lines are redshifted to 333.920 GHz and 351.470 GHz, respectively. A total of 469 minutes of data were collected on the former galaxy, using the two facility 500 MHz AOS spectrometers with a frequency shift of ±150 MHz to cover a band 800 MHz wide. At this frequency, this covers 730km/s in the rest frame. The latter galaxy was observed for 480 minutes

Table 6.1 The far-infrared properties of the two quasars, from the CO $J = 5 \rightarrow 4$ observations of Omont et al. (1996a) and Guilloteau et al. (1997) and the continuum measurements of Benford et al. (1999).

Source:	BR $1202-0752$	BRI $1335-0415$
$z_{\rm CO}$	4.6916	4.4074
$T_{\rm dust}$ (K)	50 ± 4	43 ± 3
$M_{\rm dust}$ ($10^8\,h^{-2}\,M_\odot$)	4.0 ± 0.5	3.6 ± 0.5
$L_{\rm FIR}$ ($10^{12}\,h^{-2}\,L_\odot$)	15.6 ± 2.6	6.0 ± 1.0
Width (FWHM, km s^{-1})	350	420
$S_{\rm CO}\Delta v$ (Jy km s^{-1})	2.4	2.8
$L_{\rm CO}$ ($10^7\,h^{-2}\,L_\odot$)	9	9
M(H_2) ($10^{10}\,h^{-2}\,M_\odot$)	6	9

using only the facility 1.5 GHz spectrometer, achieving a usable range of roughly 800km/s. In a channel width of $\sim$ 34km/s, rms noise levels of 42mJy and 81mJy were achieved, respectively, assuming a conversion factor of 32 Jy $K_{\rm MB}^{-1}$. No significant emission was detected at either frequency, as is evident from the spectra shown in figures 6.5 and 6.6.

Rearranging equation 1.6 for a cosmology with $\Omega = 1$ and $H_0 = 100\,{\rm km\,s^{-1}\,Mpc^{-1}}$, we find that the total luminosity carried in a line of integrated flux density $S_\nu\Delta v$ is:

$$\frac{L_{\rm C\,II}}{L_\odot} \;=\; 7.13 \times 10^7 \left(\frac{S_\nu \Delta v}{\rm Jy\ km\ s^{-1}}\right) \left[(1+z) - 2\sqrt{1+z} + 1\right] \qquad (6.2)$$

Thus, we find $3\,\sigma$ upper limits to the total line luminosity of the two quasars of:

$$L_{\rm C\,II,BR\,1202-0725} \;\leq\; 1.9 \times 10^9\,L_\odot \qquad L_{\rm C\,II,BRI\,1335-0415} \;\leq\; 3.5 \times 10^9\,L_\odot .$$

This and other derived quantities are summarized in Table 6.2. For the estimated luminosity carried in the CO $J = 1 \rightarrow 0$ line, we have assumed that the brightness temperature remains fairly flat up to the $J = 5 \rightarrow 4$ transition, as is suspected in the Cloverleaf by Barvainis et al. (1994). Therefore, the luminosity scales as $\left(\frac{J=1}{J=5}\right)^2 = 0.04$

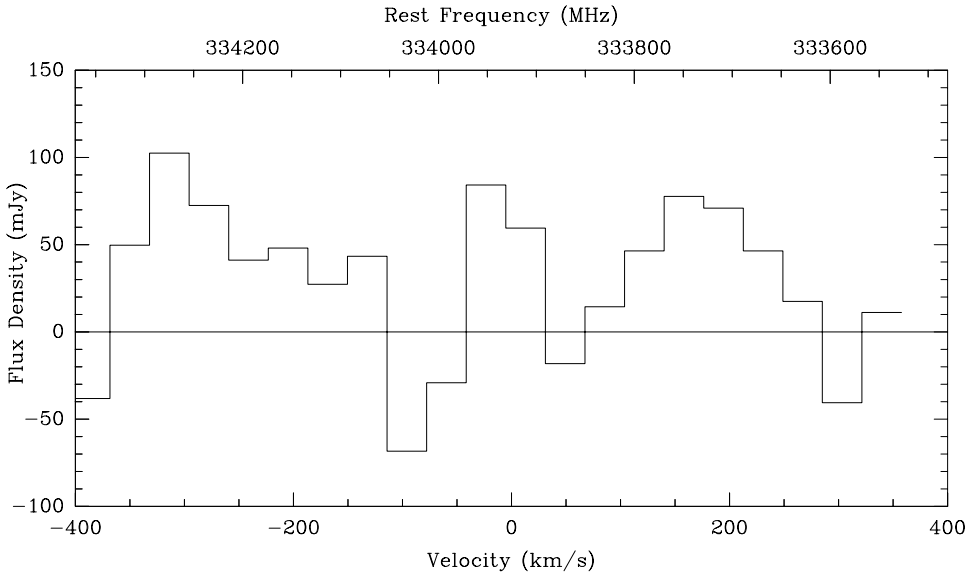

Figure 6.5 The composite spectrum from the quasar BR 1202 − 0725 as observed in January 1998; the velocity scale corresponds to $z = 4.6916$. With a noise level of 42mJy in a 36km/s channel, the integrated emission in a 400km/s band is determined to be less than 40mJy ($3\,\sigma$).

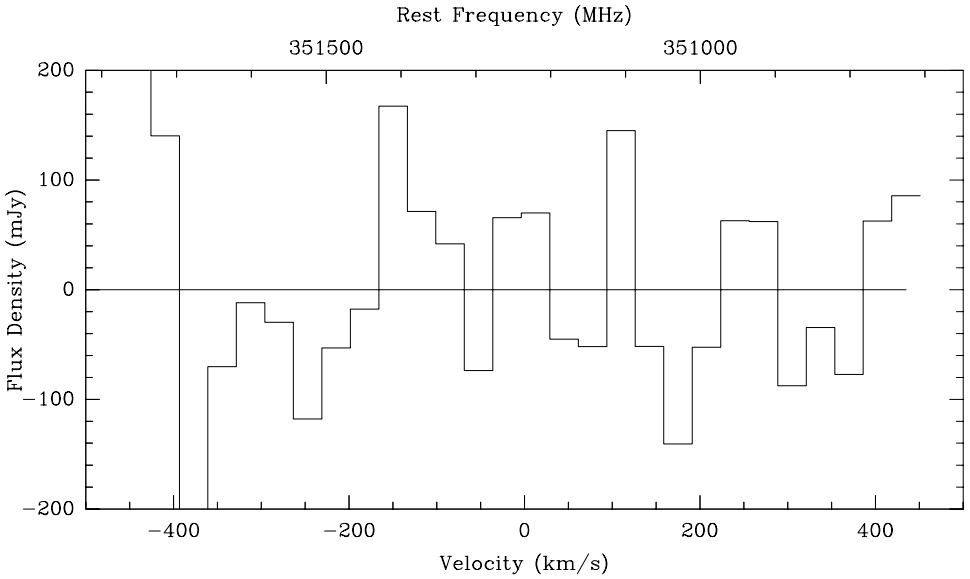

Figure 6.6 The composite spectrum from the quasar BRI 1335 − 0415 as observed in March 1998; the velocity scale corresponds to $z = 4.41$. With a noise level of 81mJy in a 32km/s channel, the integrated emission in a 400km/s band is determined to be less than 69mJy ($3\,\sigma$).

to yield a luminosity of $3.6 \times 10^6\, L_\odot$ for the 1-0 transition.

Table 6.2 Constraints on the CII emission from the two $z \geq 4$ quasars, where $3\,\sigma$ upper limits have been given.

Source:	BR $1202-0752$	BRI $1335-0415$
$S_\nu \Delta v$ (Jy km s^{-1})	< 14	< 28
$L_{\rm C_{II}}$	$\leq 1.9 \times 10^9\, L_\odot$	$\leq 3.5 \times 10^9\, L_\odot$
$\varrho = L_{\rm C_{II}}/L_{\rm FIR}$	$\leq 0.01\%$	$\leq 0.06\%$
$L_{\rm C_{II}}/L_{\rm CO\ 1-0}$	≤ 500	≤ 1000

The constraints in Table 6.2 are fairly restrictive on the nature of the atomic gas in these quasars. From the review of van der Werf (1998a), the CO line-to-continuum luminosity ratio ϱ is at least 0.05% in all the source considered therein. Our limit of $\varrho \leq 0.01\%$ $(3\,\sigma)$ implies that very different physics must be at work in the generation of the high luminosity of BR $1202-0725$. Furthermore, the ratio of CII to CO $1 \rightarrow 0$ emission is found to be at $\gtrsim 1500$ in all objects, well above our derived limit.

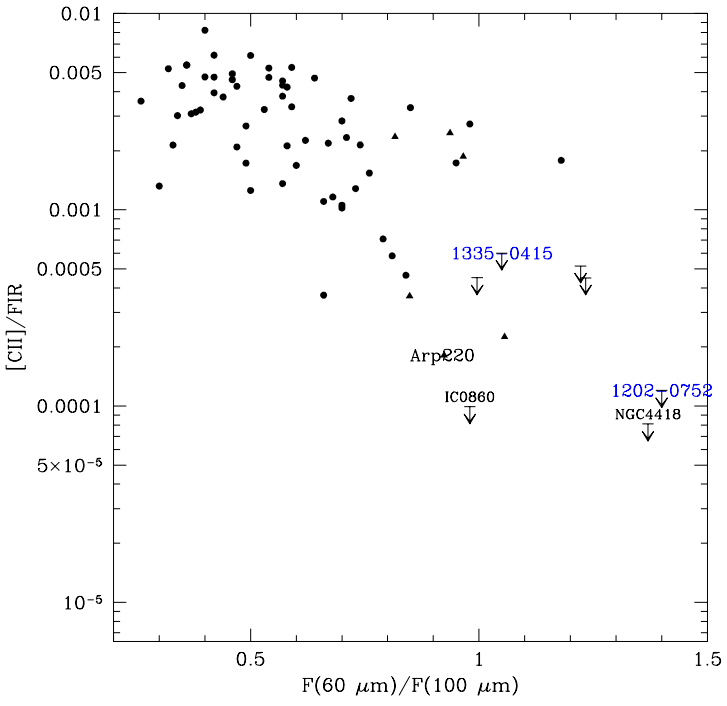

Figure 6.7 Ratio of CII emission to luminosity vs. ratio of the 60μm and 100μm flux densities for a sample of galaxies, from Malhotra et al. (1997), Luhman et al. (1998) and this work.

Since we have derived excellent SEDs for both of these quasars, a good estimate of

the local $S_{60\mu m}/S_{100\mu m}$ flux density ratio can be made. This can then be used to place our upper limits on the plot of Malhotra et al. (1997) along with the data of Luhman et al. (1998), as shown in Figure 6.7, where the $3\,\sigma$ upper limits have been plotted. Our results are consistent with the few other data points for galaxies with high 60/100 ratios. Since this ratio is similar in other ultraluminous galaxies, it follows that the CII line is likely to be similarly suppressed in other luminous high-redshift sources as compared to galaxies like the Milky Way. This is in agreement with recent (and yet-to-be-published) findings that ultraluminous sources are quite weak in CII emission as a fraction of the total FIR luminosity relative to less luminous sources. As mentioned before, Gerin & Phillips (1998) have demonstrated that the lack of CII is attributable to the high gas density and high UV flux. Our nondetections are consistent with this being the case in ultraluminous galaxies at high redshifts as well.

6.3 Search for NII in H 1413+117

Recent millimeter and submillimeter detections of molecular gas in high redshift objects have yielded new information and constraints on star formation at early epochs. Only CO transitions and atomic carbon transitions have been detected from these objects. Bright far-infrared lines such as CII at 158μm and NII at 205μm should be fairly readily detectable when redshifted into a submillimeter atmospheric window. Therefore, it is surprising that only published results thus far have been nondetections (Isaak et al. 1994; Ivison & Harrison 1996; van der Werf 1998a; Ivison et al. 1998). Remaining undiscouraged, we have attempted to detect the NII line at 205μm from the Cloverleaf quasar, H 1413+117. This section describes this work, which is being prepared for publication under the authorship of myself, Tom Phillips, and Karl Menten.

Observing at the redshift of the CO (3→2) line ($z = 2.558$), no NII emission is detected at a 1σ flux level of 9.2 Jy km s^{-1}. Predictions based on measured CO (3→2) lines imply a 205μm flux of 32.7 Jy km s^{-1}. This observation provides a constraint on the emitting regions of each of the two transitions in H 1413+117.

6.3.1 Introduction

COBE measurements (Wright et al. 1991) show that the 205μm line of ionized nitrogen is the second brightest in our Galaxy. It arises predominantly from the diffuse ionized ISM and HII regions. To date, this NII line has been detected in only one external galaxy, M82 (Petuchowski et al. 1994), predominantly because the atmosphere is opaque at this wavelength from all ground-based observatories. We have conducted a search for this line at the Caltech Submillimeter Observatory in an effort to extend the search for far-infrared lines to include NII. For comparison, we additionally set out to detect the CO $J = 7 \rightarrow 6$ transition, which traces warm gas in a way similar to NII. We have detected the CO $J = 7 \rightarrow 6$ line, which yields information on the molecular content of the Cloverleaf quasar. Combined with a nondetection of NII, this information can be used to provide a constraint on the emission source.

6.3.2 Observations and Data Reduction

The observations of H 1413+117 in NII were made at the CSO on 28-29 July 1995. The central position for the observations was $\alpha(1950) = 14^h13^m20^s.1$, $\delta(1950) = +11°43'38''$. This corresponds to both the optical and CO position from BIMA (Wilner, Zhao & Ho 1995) to within $1''$. The CSO facility 345 GHz receiver was used with both a 500 MHz and a 1.5 GHz AOS as backends. The 205 μm $^3P_1 \rightarrow ^3P_0$ ground state fine structure line of NII lies at 1461.13190 (61) GHz (Brown et al. 1994). Using the CO redshift of Barvainis et al. (1994) of $z = 2.5584 \pm 0.0001$ yields an observed frequency of 410.6149±0.0115 GHz.

Typical atmospheric transmissions during the two nights were measured using the NRAO tipping radiometer operating at 225 GHz. The measured tau value was ~ 0.04, yielding transmission at 410 GHz of ~ 0.85. Typical system temperatures were 800 K (DSB) for both nights. The data were reduced using the CLASS package. Because the 1.5 GHz AOS has a wider bandwidth than the receiver (about 900 MHz), the channels outside the receiver bandwidth were removed. Each individual spectrum from both nights and both AOSs was analyzed to determine the total noise contribution from

linear and quadratic components. Such components tend to look like broad emission lines when many such scans are added together. Approximately 15% of the scans had much more noise in these components than the average, so they were discarded. Then both nights' data from a given AOS were summed with equal weight to yield a final spectrum from each AOS. No evidence for any emission was present in either spectrum, but a small (-0.004 K) baseline offset was seen in the 1.5 GHz AOS data and removed. The two spectra were summed together and smoothed to 25 km s^{-1} resolution. The resulting composite spectrum comprises 8400s of integration time and is ∼650 km s^{-1} wide, more than the full width at zero intensity of 400 km s^{-1} from Barvainis et al. (1994).

The observations in CO $J = 7 \rightarrow 6$ were carried out in a similar fashion to the NII observations, but on two separate observing runs in February and May of 1996. With a rest frequency of 806.652 GHz, the redshifted emission should be centered at 226.715 GHz. A total of 7300s of integration time went into this spectrum, using both the 1.5 GHz AOS and the second 500 MHz AOS.

6.3.3 Results and Analysis

The final spectrum of the NII emission is shown in Figure 6.8. The RMS noise level is 92 mJy in a channel of width 25 km s^{-1}. Integrating over the entire width of the presumed line emission (∼400 km s^{-1}) yields a standard deviation in the mean flux of 9.2 Jy km s^{-1}.

We have detected the CO $J = 7 \rightarrow 6$ emission line in H 1413+117, as shown in Figure 6.9. The line peaks at the correct redshift ($z = 2.5573 \pm 0.00016$) and is the right width (425 ± 22 km s^{-1}), thereby securing the detection: the results of Barvainis et al. (1997) indicate $z = 2.5579$ and 400 km s^{-1}. Table 6.3 lists the measured and derived properties of H 1413 + 117 as determined by our measurements.

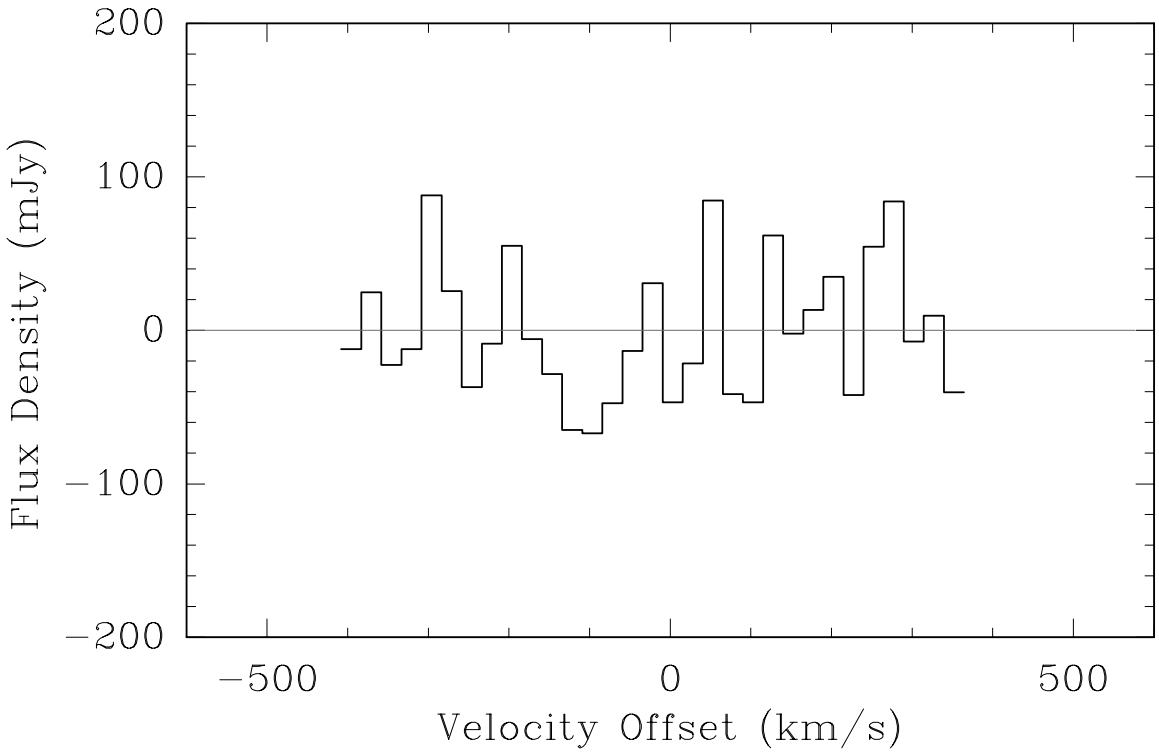

Figure 6.8 The composite spectrum at the frequency of NII from H 1413+117. No emission is detected at the $1\,\sigma$ level of 9.2 Jy km s^{-1}.

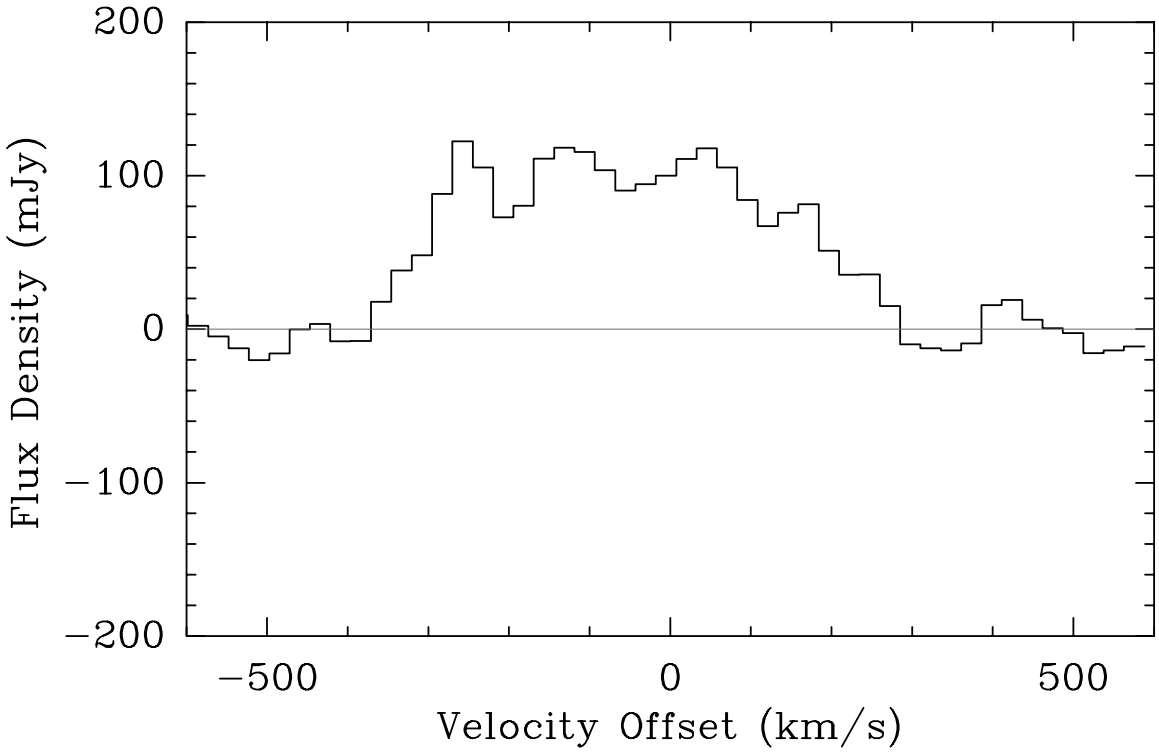

Figure 6.9 Spectrum of the CO $J = 7 \rightarrow 6$ emission from the H 1413+117.

Table 6.3 Measured and derived quantities relating to the far-infrared line emission from H 1413+117.

Quantity	CO $J = 7 \rightarrow 6$	NII
Peak Flux Density (mJy)	106 ± 6	...
Width (FWHM, km s^{-1})	425 ± 22	...
$S_\nu \Delta v$ (Jy km s^{-1})	52.5 ± 2.7	$< 9.2\ (1\,\sigma)$
$L_{\rm line}$	$1.25 \pm 0.06 \times 10^9\ L_\odot$	$\leq 3.9 \times 10^8\ L_\odot$
$L_{\rm line}/L_{\rm FIR}$	6×10^{-5}	$\leq 2 \times 10^{-5}$

6.3.4 Discussion

As reported in Barvainis et al. (1994), the flux from H 1413+117 in CO $3 \rightarrow 2$ is 9.9 Jy km s^{-1}. COBE observations (Wright et al. 1991) give the conversion factor

$$\left(\frac{F_{NII\,^3P_1 \rightarrow {}^3P_0}}{F_{CO3 \rightarrow 2}} \right) = 3.2 \pm 0.4 \tag{6.3}$$

averaged over the whole Galaxy. The only external galaxy with both CO and NII detections is M82. From Petuchowski et al. (1994), the NII flux of M82 in a 54″ beam is $52 \pm 9 \times 10^4$ Jy km s^{-1}. From maps of M82 in CO $3 \rightarrow 2$ by Tilanus et al. (1991) and Turner, Martin & Ho (1990), we estimate a total flux of 12×10^4 Jy km s^{-1}. This yields a flux ratio of 4.3 ± 1.3. Taking the weighted average of these values, 3.3 ± 0.4, implies that H 1413+117 should be seen in NII at a flux of 32.7 Jy km s^{-1} if it has similar CO/NII line ratios to the Milky Way and M82.

Alternatively, a value for the expected NII flux density can be estimated by scaling from the measured continuum flux density, assuming a consistent ratio in H 1413+117 and M82. From Petuchowski et al. (1994), the continuum flux density adjacent to the NII line is ~ 1300 Jy, while the line peaks at just more than twice that, implying a line-to-continuum ratio of ~ 1. A close approximation to the continuum level can be estimated from the 390 GHz measurement of 44mJy from Barvainis, Antonucci & Coleman (1992), which yields an NII peak flux density of $\sim$ 50mJy. Our measured variance in the mean is 23mJy, a factor of two below this prediction.

Using the estimate from CO $3 \rightarrow 2$ observations, we can reject the presence of any NII emission from H 1413+117 at the $3.6\,\sigma$ level. When compared to the continuum emission, we can reject it at the $\sim 2\,\sigma$ level. The nondetection can be explained by a difference in the distribution of emitting regions. The morphology of the NII line detected in the Galaxy by COBE does not show a strong peak in the direction of the nucleus as is seen in CO (Bennett et al. 1994). One explanation is that a substantial fraction of the NII emission arises from the warm ionized medium (Petuchowski & Bennett 1993) which is extended compared to CO, arising from denser regions. Interferometer observations of H1413+117 have shown that the emitting region in CO is $\sim$1 kpc in linear extent (Yun et al. 1997), and therefore does not sample the same region as that would emit NII. Since the magnification may well be largest for the nuclear region (hence its discovery), the NII emission may be magnified by a smaller amount and thus be undetectable. This is bolstered by the fact that the NII/CO flux ratio in M82 is smaller in the nucleus than the ratio averaged over the Galaxy. Calculating this ratio in the nucleus of the Milky Way gives a factor of $\sim$2, which predicts a flux from H 1413+117 close to our detection limit.

The CO $J = 7 \rightarrow 6$ detection can be compared to the well-detected transitions of CO of Barvainis et al. (1997), $3 \rightarrow 2$, $4 \rightarrow 3$, and $5 \rightarrow 4$ (they also detected $7 \rightarrow 6$ at a similar level to our observation, but with a large uncertainty in calibration). In temperature units, the ratios are:

$$\frac{7 \rightarrow 6}{3 \rightarrow 2} = 0.9 \qquad \frac{7 \rightarrow 6}{4 \rightarrow 3} = 0.8 \qquad \frac{7 \rightarrow 6}{5 \rightarrow 4} = 1.0 \tag{6.4}$$

If the brightness temperatures were decreasing systematically as J increases, the series of ratios would tend to drop. As this is not the case, it implies a warm ($T > 100\,\mathrm{K}$), optically thick (and therefore dense) gas. The optical depth is somewhat larger than predicted by Barvainis et al. (1997), and therefore more like the measurements of Galactic molecular clouds.

6.3.5 Conclusion on H 1413+117

We report an upper limit of the total flux in the NII $^3P_1 \rightarrow ^3 P_0$ line at 1461 GHz rest frequency from H 1413+117 at 9.2 Jy km s^{-1}. This is a factor of ~ 3 below predictions based on scaling the observed CO flux using a locally derived conversion factor. Comparison to line ratios in the Galaxy and M82 indicate that the NII emission and CO emission must come from different emitting regions. Furthermore, we have detected the CO $J = 7 \rightarrow 6$ transition and have demonstrated the existence of warm ($T > 100$ K) and dense ($n_{\rm H_2} \sim 10^4\ cm^{-3}$) molecular gas.

6.4 What We Conclude

Combining our nondetections of CII and NII with those in the literature, we see that the detection of far-infrared atomic lines is a much more difficult enterprise than had previously been supposed. Part of the reason that millimetric CO measurements have been successful (though with a detection rate of less than 10%) is that the velocity coverage is more than sufficient to contain the entire width of a line with a substantial amount of baseline on the sides. At frequencies of > 500 GHz, this is not yet true using any facility instrument at a submillimeter telescope. The logical conclusion is that a further improvement of a factor of a few in sensitivity and bandwidth will permit the detection of these lines, or at the least the determination of much stronger constraints on atomic and molecular gas at high redshifts.

Chapter 7 Design of a Bolometer Spectrometer

7.1 Introduction

The results of the previous two chapters highlight the need for more sensitive, broader band instrumentation. With available heterodyne spectrometer bandwidths (~ 1 GHz) at the CSO and JCMT limited to a velocity coverage of ~ 400 km/s in the high-frequency windows, the redshift of a distant object must be known to a precision of a few parts in 10,000. Furthermore, the total width (at zero intensity) must then be only 300km/s to allow proper baseline determination. These requirements are, in general, unreasonable constraints on the observability of high-redshift galaxies.

We have undertaken an effort to develop a spectrometer drawing from technologies proven in the infrared: an array of bolometric detectors with dispersing optics providing a velocity resolution of ~ 200 km/s and an instantaneous coverage of at least 3 000 km/s. The following chapters detail the optics which can provide this capability, either as a broadband Fabry-Perot or a tunable immersion grating. This chapter describes the spectrometer detectors, cryostat, electronics, and optical filtering; these elements are common to the spectrometer in either optical configuration. Since this instrument required bolometers an order of magnitude more sensitive than SHARC's, a substantial amount of testing has been undertaken at NASA-Goddard in order to prove that sufficiently low-noise detectors can be manufactured. This part of the instrument has been contributed to by Christine Allen, Harvey Moseley and myself. At Caltech, we have been developing the cryostat for the optics and detectors; this is the result of many people's contributions, but primarily those of Todd Hunter, Tom Phillips and myself.

7.2 Bolometer Sensitivity Requirement

Knowing the spectral resolution of the bolometer spectrometer, the expected incident power can be used to determine the necessary detector sensitivity. In the case of bolometric detectors, the zero-background noise sources include Johnson noise in the thermistor; phonon noise between the detector and its cooling bath; and the combined voltage and current noise of the amplifiers. The noise equivalent power (NEP), which is the required signal power required to achieve a unity signal-to-noise ratio in a unity bandwidth, is given by equation 2.16.

In the background-limited case, the NEP is entirely determined by the incident photon fluctuations. The expression for the background radiation equivalent NEP for a telescope of main beam efficiency η_{MB} was derived earlier and is given by equation 2.26. In the case of a grating spectrometer with resolution $\Re$, we find:

$$\mathrm{NEP}_{bkgnd} \approx \frac{2 \times 10^{-14}}{\sqrt{\Re}} \ \mathrm{W}/\sqrt{\mathrm{Hz}} \tag{7.1}$$

for $\nu = 750$ GHz, $\epsilon = 0.5, \eta_{optics} = 0.3, \eta_{MB} = 0.4$. This yields an NEP_{bkgnd} of $\sim 6 \times 10^{-16}$ W/$\sqrt{\mathrm{Hz}}$. When referred to the power received by the bolometer, however, the worst case noise power is lower due to optical losses, $\sim 10^{-17}$ W/$\sqrt{\mathrm{Hz}}$. Using equation 2.43 for the power, we find that $P = 0.6$pW for an NEP of $10^{-17}\sqrt{T}$ W/$\sqrt{\mathrm{Hz}}$. Comparing these two NEPs implies that a background limited instrument, which for safety's sake can be stipulated to be half as noisy, can be constructed only if $T \leq 0.25$K. Furthermore, we can use equations 2.38 with $G_0 \sim \frac{2P}{T^4}$ to determine that the conductance needed for this amount of power must be of order

$$G(T) \sim \left(\frac{T}{1\ \mathrm{K}}\right)^3 \qquad \mathrm{nW/K}. \tag{7.2}$$

Using the expression for NEP_{bkgnd}, we can calculate the noise equivalent flux density (NEFD) for the CSO, a telescope with area $A = 80\mathrm{m}^2$. Since

$$NEFD \equiv \frac{2\ NEP}{A \times \Delta\nu} = \frac{2\ NEP \times \Re}{A \times \nu}, \tag{7.3}$$

we find $NEFD \sim 4$ Jy/$\sqrt{\text{Hz}}$. This number is useful for comparison to the expected brightness of galaxies at high redshift. From Stark (1997), we can estimate a CII line flux from a galaxy emitting $10^9 L_\odot$ in CII at $z = 1.2$ as $F_\nu \sim 150$ mJy, detectable at the 3σ level in two hours. With an instantaneous bandwidth of ~ 3000 km/s, the redshift need only be known to ± 0.005.

7.2.1 Detector Array for the Bolometer Spectrometer

Micromachined silicon bolometers have been fabricated at the Goddard Space Flight Center for 15 years (Moseley, Mather & McCammon 1984). They have been proven as sensitive far-infrared detectors on the KAO (Casey et al. 1993), MSAM balloon platform (Farroqui et al. 1997), and at the CSO in SHARC (Wang et al. 1996). For the past decade, the state-of-the-art technology has been 24-element linear arrays of close-packed detectors, typically 1mm×2mm×10μm thick. Each bolometer has an implanted thermistor which is quite similar in properties across an array. The arrays are fabricated using conventional silicon micromachining techniques, enabling many arrays to be made per wafer with yields of $\sim 50\%$.

Current processes are sufficiently advanced that the detectors are now made from far thinner silicon, with a single bolometer being 1mm×1mm×1μm. These detectors are discussed more fully by Moseley (1998). The thermal conductance at 0.1K can be as low as 3×10^{-13} W/K, corresponding to an ultimate NEP of 5×10^{-19} W/$\sqrt{\text{Hz}}$, a factor of ten better than with the previous technology. The thermal conductance can be changed to suit the expected background power by coating the legs with normal or superconducting metals such as gold or aluminum. More details on the tests I have conducted on these detectors will be presented in the following section.

7.3 Bolometer Testing

We wish to construct a background-limited spectrometer, i.e., one in which the photon background noise is larger than the instrumental noise. The primary component of the instrumental noise derives from the noise of the bolometers, as discussed in

section 2.2.2. In this section, I describe the work I have performed in verifying that background-limited bolometers can be produced.

7.3.1 Optical Loading

It is straightforward to estimate the amount of power falling on the bolometer; then, for a given bolometer thermal conductance $G(T)$, one can derive the optimal operating temperature. Recalling equation 2.43:

$$P = 2\epsilon\eta_{\rm optics} k T_{\rm bkgnd} \Delta\nu,$$

we use $\eta_{\rm optics} = 0.1$, $\Delta\nu = 10^9$Hz, which is appropriate for a resolution of ~ 1000. This results in a power of slightly less than 1pW falling on a detector. Since we wish to achieve a thermal conductance (from equation 2.38)

$$G(T) \;=\; G_0 T^3 \;=\; \frac{2P}{T}, \tag{7.4}$$

we can measure G_0 for an actual bolometer (since it depends on the manufacturing), then estimate the operating temperature as $T = (2P/G_0)^{\frac{1}{4}}$.

The SHARC bolometers, made from the MIRA-II array (described in section 2.3.5) have a known G_0 from measurements we made at Caltech (Wang et al. 1996) of $G_0 = 3.2 \times 10^{-8}$ W/K. Therefore we must achieve a temperature of $\lesssim 80$mK in order to yield a sufficient temperature rise for the power we expect in spectrometer mode. Because this temperature is difficult to achieve for a full night of observing time with an ADR, we have investigated alternative bolometer designs for the spectrometer that will reduce the burden on the refrigeration.

7.3.2 1μm-Process Bolometers

In 1996, Christine Allen at GSFC fabricated the first generation of ultrathin bolometer arrays, where the thickness of the silicon bolometer has been reduced to $\sim 1\mu$m, as opposed to the $\sim 14\mu$m MIRA process. This, in principle, will reduce the thermal

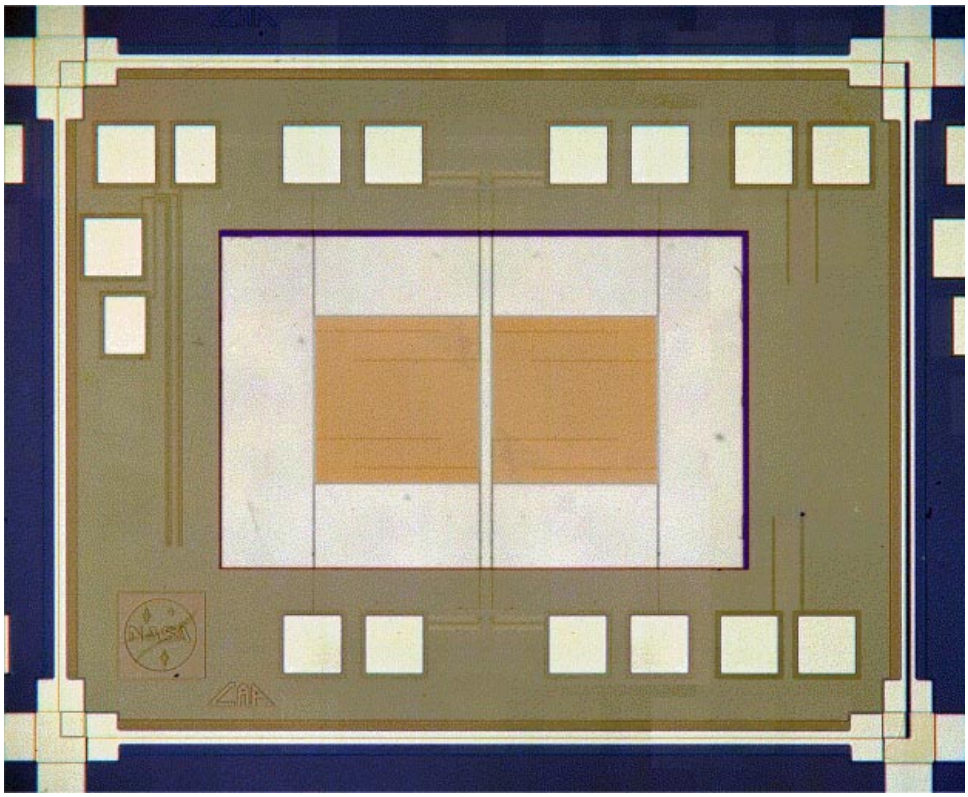

Figure 7.1 Photograph of the two-element bolometer array used to verify the viability of the 1μm fabrication process. At this thickness, silicon is visibly translucent.

conductance by an order of magnitude. The test detectors consisted of a two-element array shown in Figure 7.1. Each bolometer held two thermistors, nominally identical. There were also two more thermistors implanted in the bulk silicon of the bolometer frame, connected to the pairs of pads on the right. Additionally, a 4-wire thermometer was implanted to help verify the temperature of the frame, although it was not used in the following experiments to determine the thermal and electrical properties of the devices.

7.3.2.1 Resistance and Thermal Conductance

By applying a variable current up to $I \sim 1.5\mu$A to the bolometer, the voltage across each thermistor V was measured using a low bias current voltmeter. This yielded the resistance R at a temperature T which results in the application of the bias power VI. After taking a variety of points using base temperatures of 1.7K and 4.2K and applying power between a few pW and 50nW, we can derive both the electrical and thermal properties of the bolometer (Mather 1984b). This temperature range is ideal for bolometers with $T_0 \sim 30\,\mathrm{K}$ (Zhang et al. 1993). Although a first order solution is simple to attain via algebraic calculations, a complete χ^2–minimization routine was written by Attila Kovacs for this purpose using the formulations of Griffin & Holland (1988) and Grannan, Richards & Hase (1997). Using this code, I have derived the averaged properties of the four thermistors in the two bolometers:

$$R(T) = (314.5 \pm 4.5) \exp\left[\sqrt{\frac{49.46 \pm 0.11}{T}}\right] \quad \Omega \tag{7.5}$$

$$G(T) = (2.15 \pm 0.10) \times 10^{-9}\, T^3 \quad \mathrm{W/K}. \tag{7.6}$$

Figure 7.2 demonstrates the excellent fit of the sets of data to the desired functional form. The thermal conductance is reduced by almost precisely the geometric ratio ($14\mu\mathrm{m} \rightarrow 1\mu\mathrm{m}$), inasmuch as the ratio can be measured. This eases our temperature criterion to $\sim$ 150mK, a temperature easily achieved by an ADR (but still too low for a ^{3}He refrigerator).

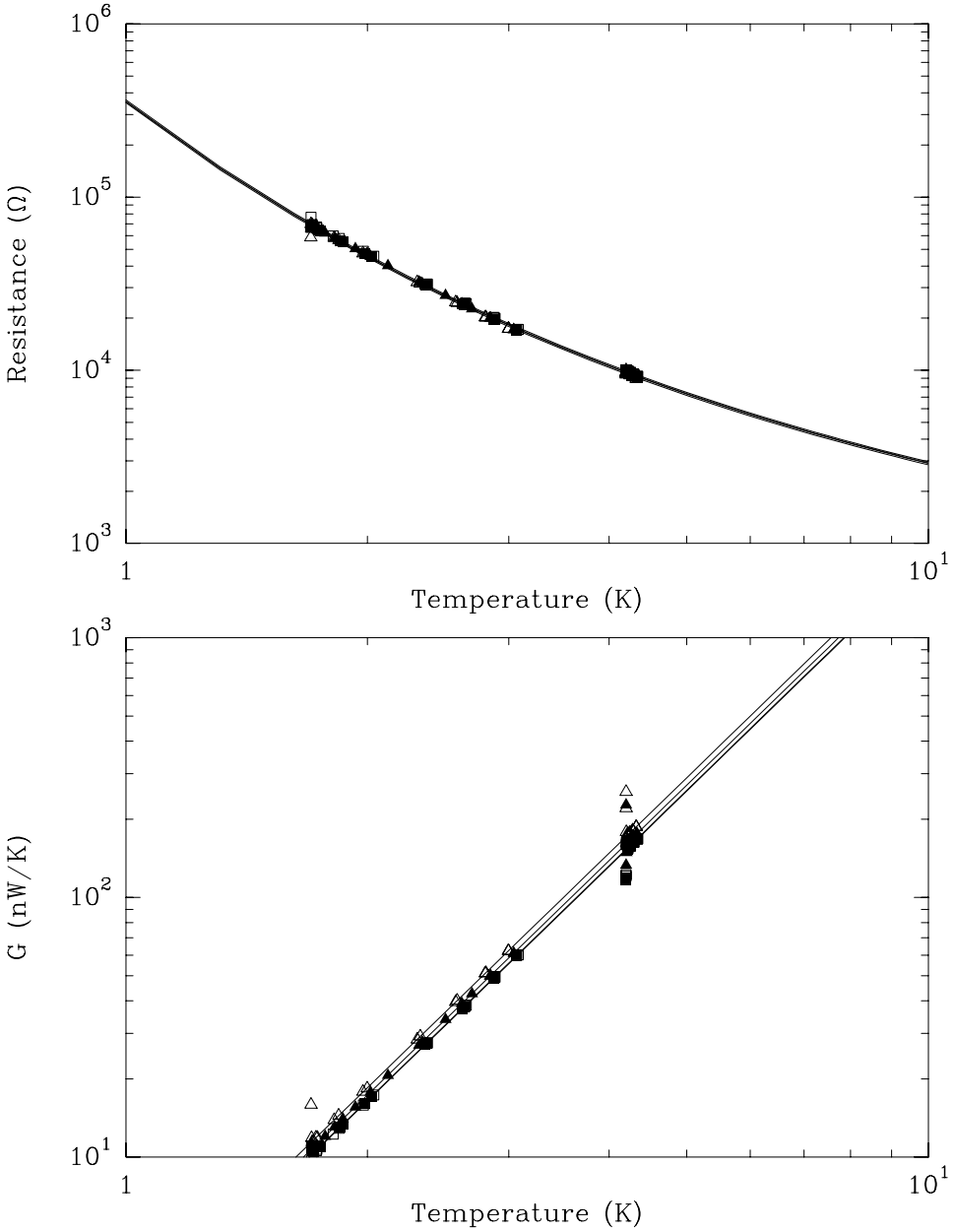

Figure 7.2 (TOP) Resistance versus temperature for the four 1μm bolometer thermistors; (BOTTOM) Thermal conductance of the two bolometers as determined by the four thermistors.

7.3.2.2 Electrical Nonlinearities and Heat Capacity

The electrical nonlinearity arising from the resistance dependence on the electric field V in bolometers has been modeled empirically (as per, e.g., Grannan et al. 1992; Grannan, Richards & Hase 1997) and can be compared to the linear approximation:

$$\frac{R_{\rm true}}{R_{\rm linear}} \;=\; \exp\left[-\frac{eVL}{dkT}\right] \;\sim\; 0.99 \tag{7.7}$$

where the ratio L/d has been solved for. This shows that the electrical nonlinearities are a small effect for these thermistors.

I have also tried to determine the heat capacity of these bolometers via a thermal relaxation time measurement. Power is applied to a thermistor in a step function and the resultant temperature is read out on the other thermistor. However, this measurement requires a faster data-taking method than was available, so only an upper limit of the time constant of $\tau \leq 10$ms could be determined. Since $\tau = C/G$, we can infer that $C(1.7K) \leq 10^{-11}$ J/K. From Downey et al. (1984), we calculate our bulk heat capacity to be

$$C_{\rm Si}(T) \;=\; 6.4 \times 10^{-13}\, T^3 \;=\; 3.1 \times 10^{-12}\ {\rm J/K}, \tag{7.8}$$

consistent with our measured upper limit.

7.3.2.3 Responsivity

Having determined the thermal and electrical parameters of the 1μm-process bolometers, one can then derive the responsivity S which relates the two (e.g., equation 7, Downey et al. 1984):

$$S \;=\; \frac{|\varsigma V|}{G(T) - \varsigma V^2/R(T)},\ \text{where}\ \varsigma \;\equiv\; d(\ln R)/dT \;=\; -\sqrt{T_0}/(2T^{\frac{3}{2}}) \tag{7.9}$$

in which V refers to the bias voltage on the bolometer. It must be pointed out that the voltage is a poorly controlled parameter - some bolometers can even exhibit an

instability where the dynamic resistance dV/dI is negative (Dowell et al. 1998) - but it is independent of the load resistance. The results of this modeling of the responsivity and the bolometer resistance are shown in Figure 7.3. This detector could achieve an electrical NEP of $\sim 10^{-17}\mathrm{W}/\sqrt{\mathrm{Hz}}$. For comparison, the responsivity of SHARC is shown in Figure 7.4.

One note regarding the 1μm bolometer process: because of the extreme thinness of the leads (placed in the legs by arsenic implantation), the series resistance is $\simeq 7\mathrm{k}\Omega$, a large value. However, even to achieve this low a resistance, the doping is quite large, leading to a strong thermistor effect in the legs themselves.

7.3.3 Pop-Up Detector Bolometers

In 1997, GSFC fabricated the first of the *Pop-Up Detector* (PUD) bolometer arrays. These are still being developed, with the eventual goal of producing two-dimensional arrays. These detectors are made using the 1μm process, but with one additional twist – literally. The suspending legs are made with torsion bars, as shown in Figure 7.5. Silicon is extremely flexible when made into a very thin sheet; the legs are 1μm thick, 4μm wide and roughly 1mm long. The suspending frame (out of view to the left and right in the figure) can thus be folded below the bolometer element, making the footprint of an array equal to the area of the pixels alone. Stacking these arrays will permit the manufacture of large-format, close-packed two-dimensional arrays of roughly 12×32 detectors.

The current generation of PUDs have a geometry of $1\mathrm{mm}\times 1\mathrm{mm}\times 1\mu\mathrm{m}$[1]. A schematic diagram of the bolometer array with an electron micrograph of a single pixel is shown in Figure 7.5. The implanted thermistor is invisible, as are the implanted leads continuing down the legs to bonding pads on the array frame. Despite the extreme thinness, the arrays are quite rugged due to the extreme elasticity of the very thin silicon legs: as described above, this design is intended to be folded so that the legs support the bolometers vertically rather than horizontally. These detectors are discussed more

[1] As Todd Hunter puts it, "The PUDs are analogous to erecting a one-inch-thick basketball court on four one-inch-diameter rods as tall as Millikan library."

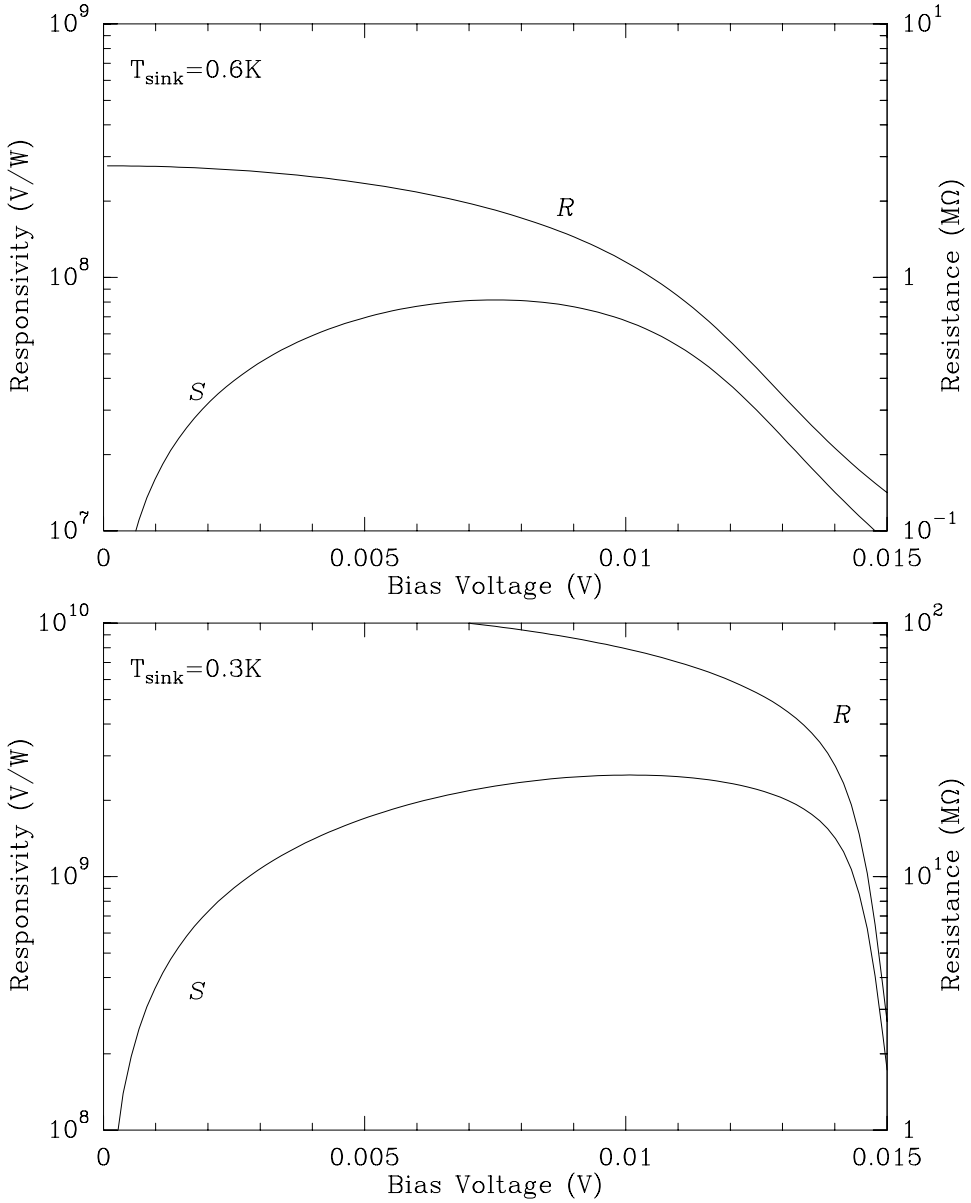

Figure 7.3 (TOP) Responsivity S and resistance R of a 1μm bolometer operated with a heat sink temperature of 0.6K; (BOTTOM) Same as above, but for a heat sink of 0.3K. These two values bracket the usable region of this detector based on the resistance value. Note that the responsivity is roughly 30 times lower when operated at twice the temperature, a very rapid change.

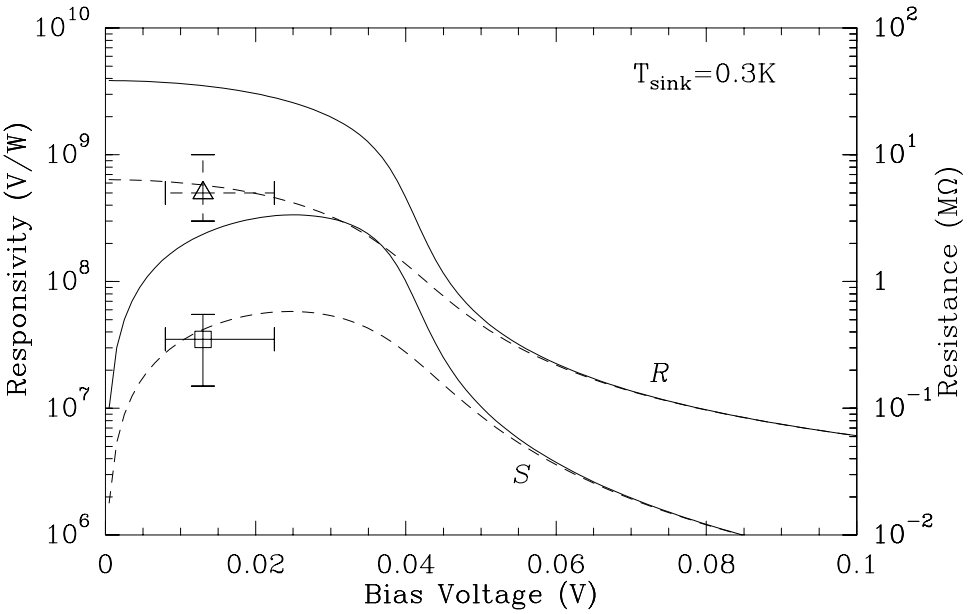

Figure 7.4 (TOP) Responsivity S and resistance R of the SHARC bolometers with no optical power (solid curve) and with the estimated optical loading (dashed curve). A measurement of the responsivity under normal operating conditions is shown as a square; the estimated bolometer resistance is shown as a triangle.

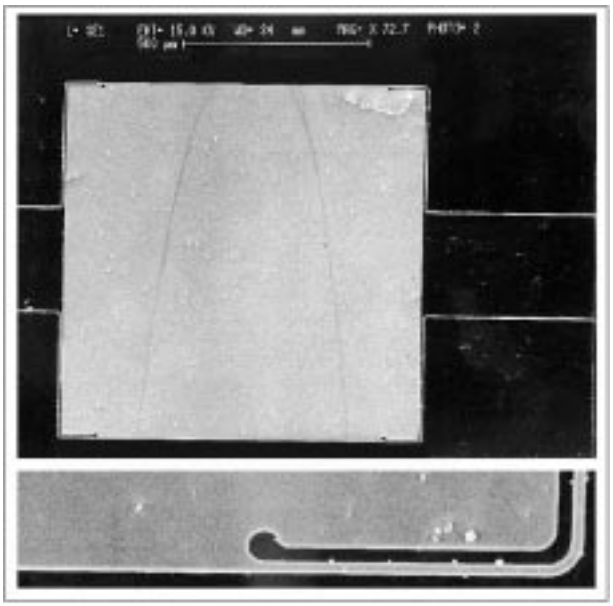

Figure 7.5 (A) Schematic diagram of a pop-up detector array. (B) Electron micrograph of a single bolometer pixel, 1mm on a side and 1μm thick. Optically, the pixel is a translucent brown color. Below is an enlargement of the lower right leg attachment point, showing the rounded cutout for strain relief when the array is folded to enable two-dimensional stacking.

fully by Moseley (1998). The thermal conductance at 0.1K can be as low as 3×10^{-13} W/K, corresponding to an ultimate NEP of 5×10^{-19} W/$\sqrt{\text{Hz}}$, a factor of ten better than with the previous technology. The thermal conductance can be changed to suit the expected background power by coating the legs with normal or superconducting metals such as gold or aluminum.

In September 1997, I tested the first run of these arrays using a ^{3}He refrigeration system. It could achieve temperatures as low as $\sim$ 315mK. Three arrays from different wafers were tested, named 3EHAK100, 3EHAK232, and 3SCRL181-M1. All the arrays had several bolometers wired up for tests, with two thermistors per bolometer. The last array had aluminum deposited on the legs, allowing a direct metallic contact to the implanted thermistor. Aluminum has a superconducting transition temperature of 1.18K (White 1979); hence the thermal conductance may have a very different behavior above and below this temperature depending on which mechanism for thermal conduction dominates.

The two EHAK arrays were tested by providing power to one thermistor while reading out the resistance at constant (and very small) current using a Keithley electrometer (Keithley Instruments, Inc.). This method of thermometry reduces the possibility of electrical nonlinearities as the voltage across the bolometer is much smaller. The SCRL array was tested in the standard manner, with bias current applied to the thermistor under test. Unfortunately, I was not able to acquire a sufficient range of data for the temperatures below 1K due to lack of time with the ^{3}He refrigerator operating. The results of the tests on a single bolometer from each of the three arrays is shown in Figure 7.6. The properties of the bolometers in a given array were very similar, so the data from only one detector per array are sufficient to illustrate the differences in the three wafers. Calculations of the responsivities and resistances of the three wafers for temperatures of 0.3K, 0.2K, and 0.1K are shown in figures 7.7, 7.8, and 7.9, respectively. All these calculations assume no optical loading; the responsivity drops quite substantially when additional optical power is allowed to fall on the bolometer (e.g., Figure 7.4).

It is apparent from the responsivity calculations that the array 3SCRL181-M1

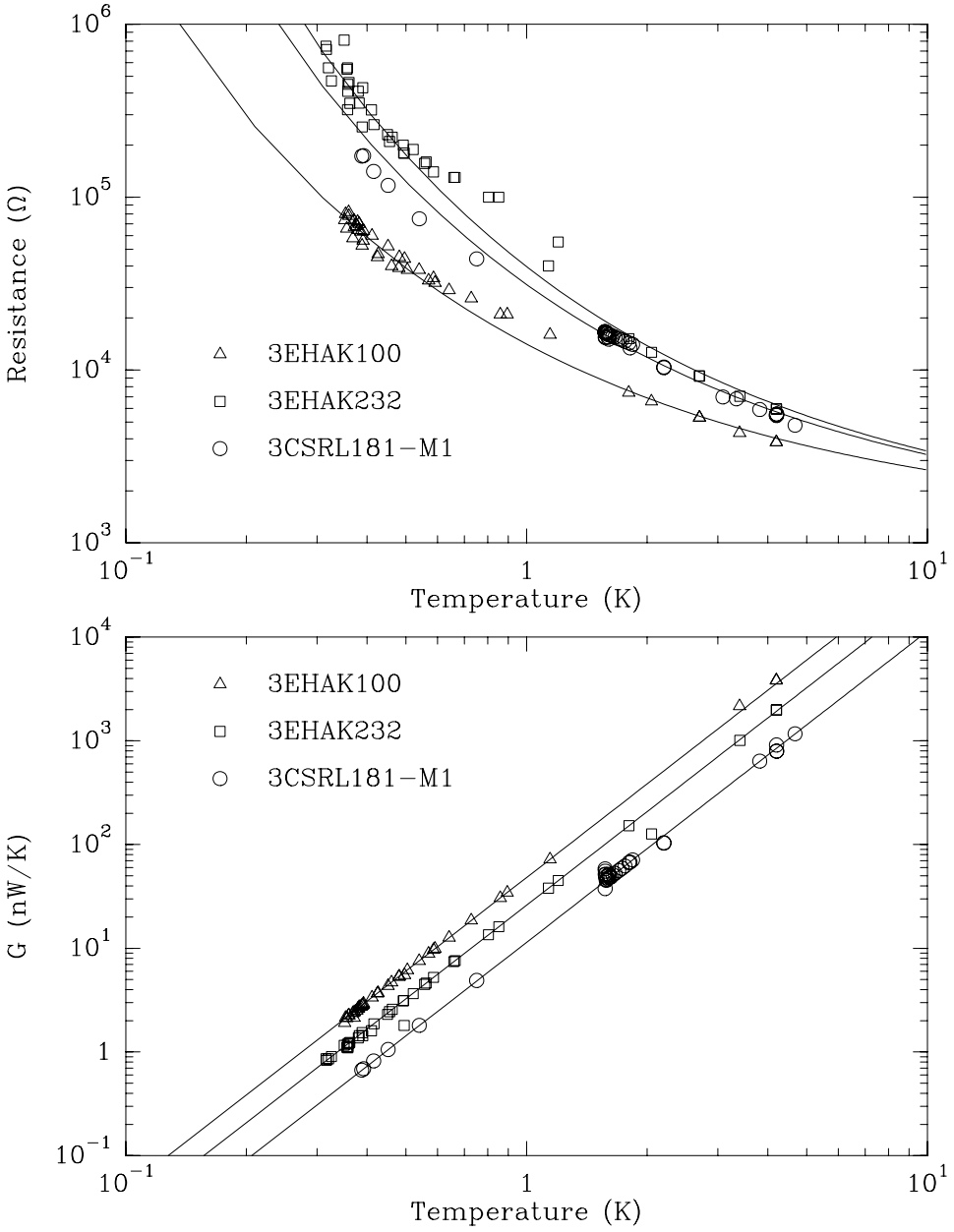

Figure 7.6 (TOP) Resistance versus temperature for three PUD bolometer thermistors; (BOTTOM) Thermal conductance of the arrays.

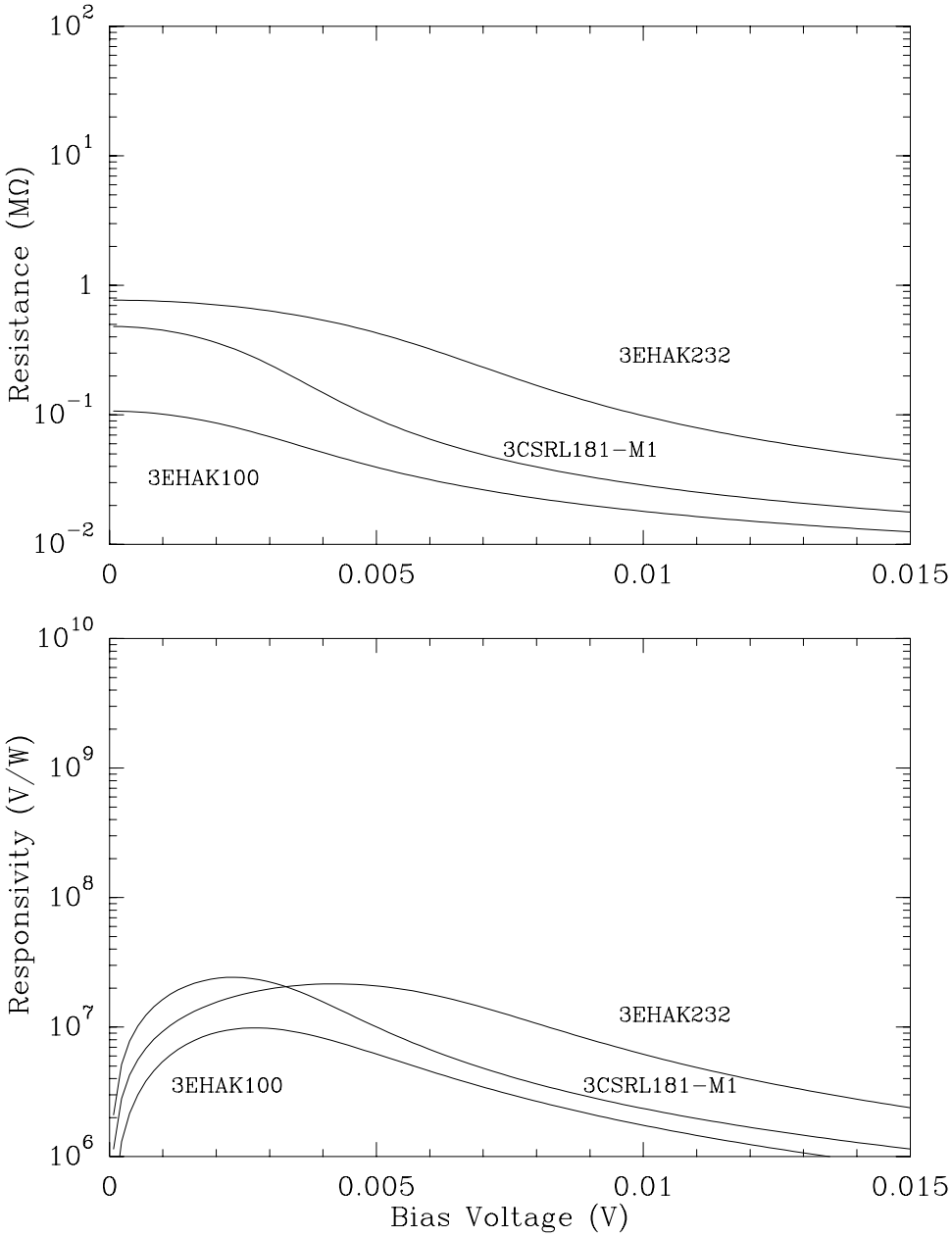

Figure 7.7 (TOP) Resistance R of the three PUD wafers at a sink temperature of 0.3K; (BOTTOM) Responsivity S of the three PUD wafers at a sink temperature of 0.3K. These calculations assume no optical loading.

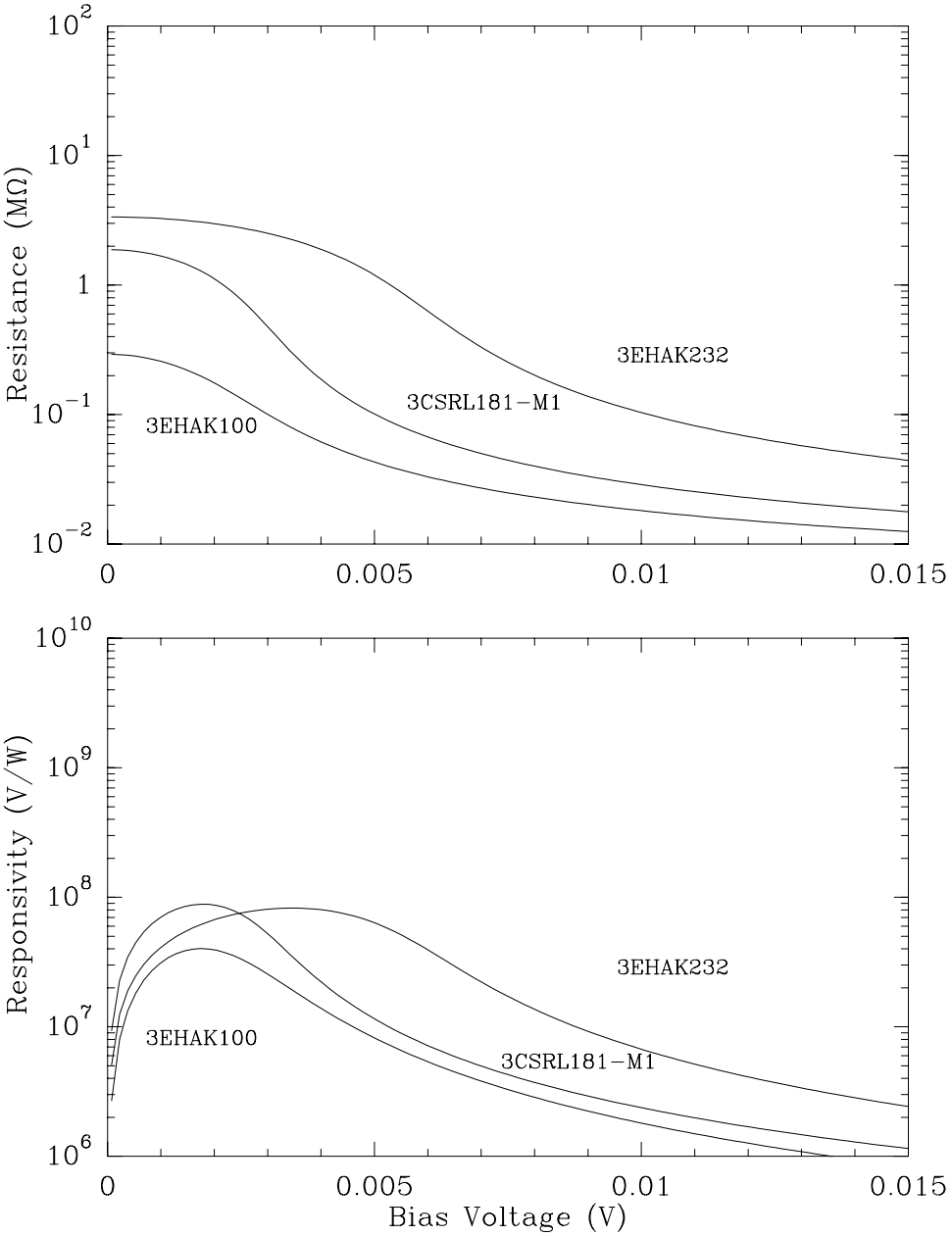

Figure 7.8 Same as in Figure 7.7, but with a sink temperature of 0.2K.

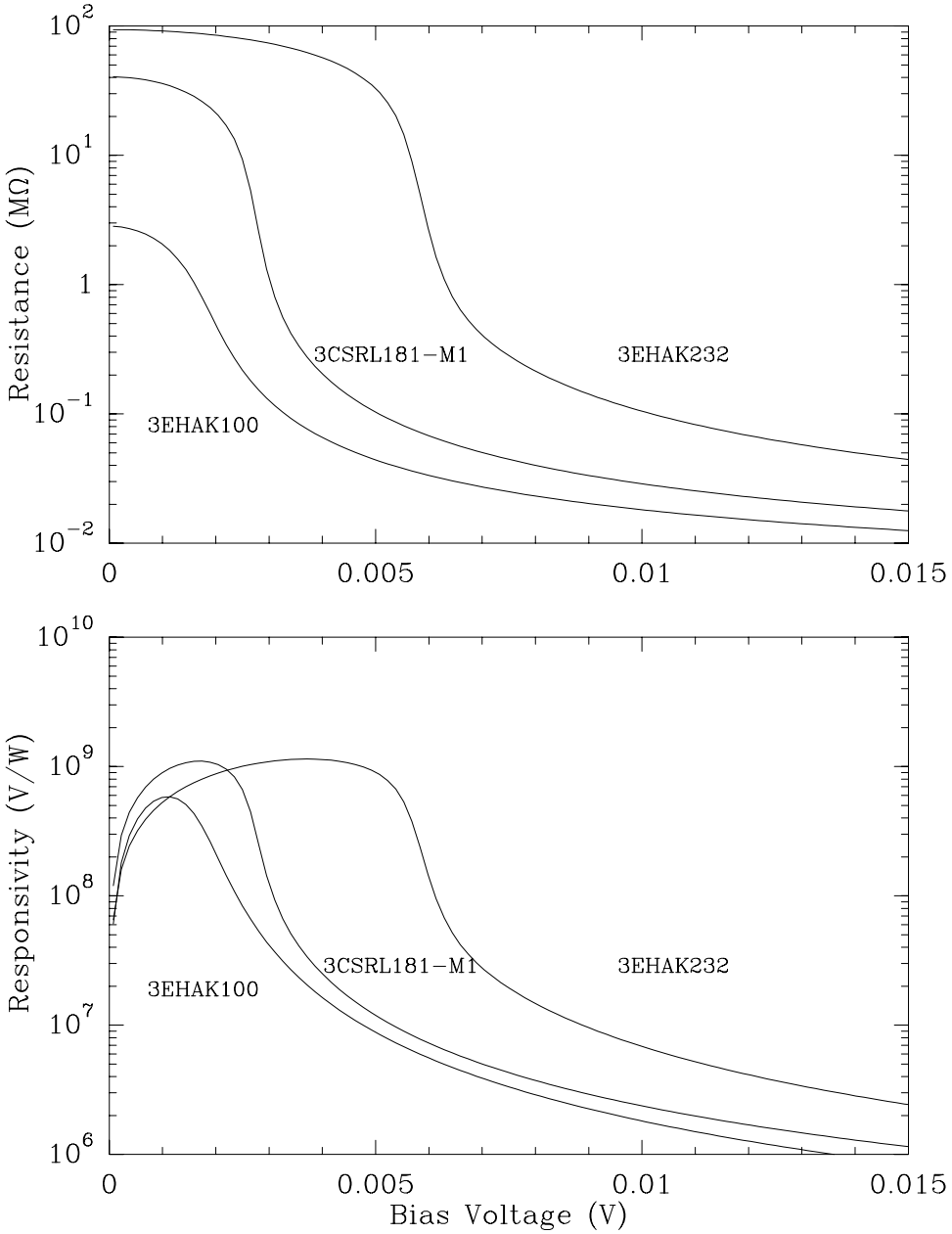

Figure 7.9 Same as in Figure 7.7, but with a sink temperature of 0.1K.

has the best combination of properties: high responsivity and resistance of $\simeq 5\mathrm{M}\Omega$ at roughly 150mK. With its thermal conductance of $G = 11.4\,T^3$ nW/K, the ideal sink temperature would be roughly 100mK. Optimally biased, its electrical responsivity under optical load would be roughly 10^8 V/W. Of course, the responsivity to optical power is reduced by the bolometer absorptivity, since not all incident light is converted into thermal energy. This bolometer array would achieve an NEP referred to the cryostat entrance of 10^{-15} W/$\sqrt{\mathrm{Hz}}$ and an ultimate no-load electrical NEP of 10^{-17} W/$\sqrt{\mathrm{Hz}}$.

A summary of the properties of the measured PUD arrays appears in Table 7.1.

Table 7.1 Properties of the Pup-Up Detector arrays tested at GSFC.

Wafer	Doping	T_0 (K)	R_0 (Ω)	G_0 (10^{-8} W/K)
3EHAK100	0.7625	6.01 ± 0.02	1217 ± 8	4.8 ± 0.2
3CSRL181-M1	0.7250	10.99 ± 0.07	1135 ± 9	1.1 ± 0.1
3EHAK232	0.7125	12.91 ± 0.04	1090 ± 8	2.6 ± 0.1

7.3.4 AXAF Bolometers

As part of the testing of the ADR cryostat, I have installed a bolometer array designed for operation near 100mK. This array was originally designed for the X-Ray Spectrometer (XRS) aboard the Advanced X-Ray Astrophysics Facility (AXAF), but was descoped in 1994 and is now scheduled to be launched as an instrument on Astro-E in 2000, but with a different detector configuration.

This test array consists of 12 bolometers in a linear array, much like the MIRA–II array in SHARC. However, its elements are 0.5mm $\times$ 2.0mm in size, inappropriate for the optical designs considered for the bolometer spectrometer. After the cryostat had been tested and commissioned for all components operating at temperatures above 2K, the ADR was installed and has been in testing since early 1997. The bolometers were acquired from GSFC, then installed on the ADR cold plate in August 1997. Two of the bolometers are thermally isolated, while two thermistors of similar construction

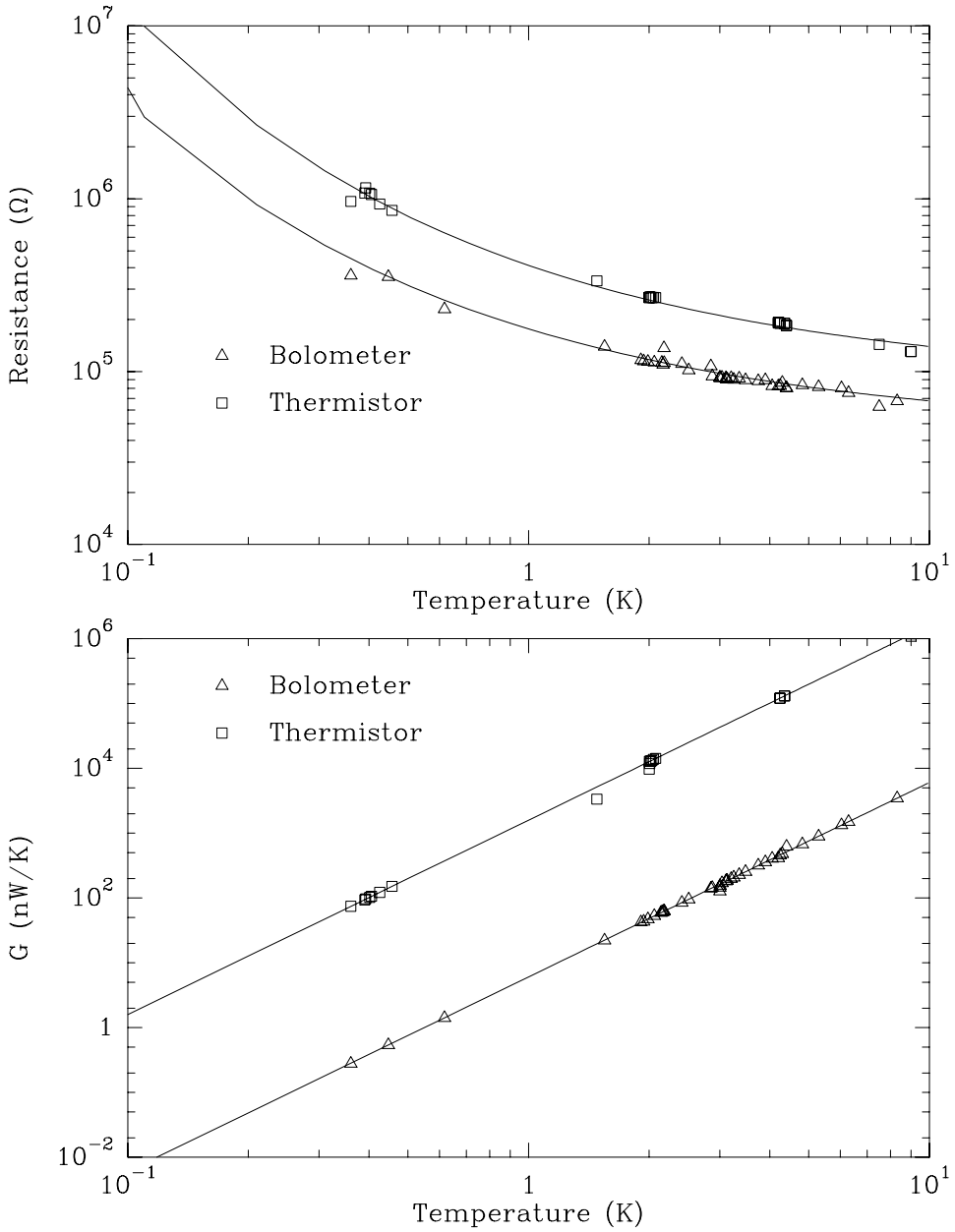

Figure 7.10 (TOP) Resistance versus temperature for an isolated bolometer and a buried thermistor; (BOTTOM) Thermal conductance of the bolometer and thermistor.

were implanted in the silicon frame of the array. Several tests of these bolometers result in the compiled data shown in Figure 7.10. Lack of accurate thermometry has made it more difficult to perform these tests, but the results show preliminarily that the cryostat is functioning well (i.e., no measurable RF heating) to temperatures of below 500mK.

7.4 Overview of the Instrument

Producing a stable 0.1K bath for the bolometers requires the use of many technologies. The cryostat used for this instrument is a hybrid using both a closed-cycle refrigerator and a pumped liquid ^{4}He bath which has a hold time at 1.5K of approximately 4 days with no optical loading. The closed-cycle refrigerator is decoupled from the cryostat mechanically via a pneumatic vibration isolator. The 1.5K stage provides the mounting surface for the optics, which shall be discussed in chapters 8 and 9. It also serves as the thermal bath for the operation of the 0.1K refrigeration system with its associated detector mount. Furthermore, the cryostat is designed to be a Faraday cage in order to reduce radiofrequency interference. As such, the detector electronics are contained in enclosures mounted on the cryostat.

Cooling a detector array to 0.1K typically requires either an adiabatic demagnetization refrigerator (ADR) or a dilution refrigerator. The disadvantages of dilution refrigeration for our purpose are the temperature change upon tilting the dewar and the large plumbing assembly necessary to achieve this degree of cooling. An ADR is compact and gravity-insensitive, requiring only electrical power to operate. This particular version of an ADR is based on technology developed for use in SIRTF (Timbie, Bernstein & Richards 1990). A ferric ammonium alum salt pill is used as the working element and was manufactured at Goddard using the techniques developed for AXAF (Serlemitsos, SanSebastian & Kunes 1992). The ^{4}He bath is contained in a toroidal can which surrounds a high-field, low-current magnet (Cryomagnetics Inc.) producing a central field of 3T at 6A. Duty-cycle-optimized brass wires are used as high-current leads to prevent the thermal runaway problems associated with copper

leads. The salt pill is suspended rigidly in the bore of the magnet by Kevlar cords. A constant-ramp-rate current controller has been built to enable the demagnetization to compensate for the heat leak into the ADR, thus stabilizing the temperature. A self-contained 0.35K ^{3}He refrigerator of the Torre & Chanin (1985) heritage has been constructed to reduce the heat load on the ADR, considering the necessarily separate suspension of the bolometer array and the heat load from the wiring. The hold time at 0.1K is designed to be at least 12 hours, enough to last a single night of observing before recycling.

7.5 Spectrometer Cryostat

The cryostat used for this instrument is a hybrid dewar (Dewar 1893) of the Ellison (1988) heritage (custom manufactured, Precision Cryogenic Systems Inc.). A pumped liquid ^{4}He bath of 5.2l capacity is contained within this cryostat, surrounded by two radiation shields. The helium bath has a hold time at 1.5K of approximately 4 days. A level meter is built into the cryogen tank to enable occasional monitoring of the liquid level. These three primary temperature stages are rigidly attached to each other by G10 fiberglass standoffs to prevent flexure in the optics during cooldown or during changing orientation on the back of the telescope. A diagram of the layout of the cryostat is shown in Figure 7.11.

Two of the most insidious parasitic heat loads in cryostats are through radiative loading (merely by absorptive areas or through light leaks) and residual gas conduction. Every metallic surface at low temperatures which could easily be plated has an electroplated coating of at least 0.5μm of gold. This prevents unwanted absorption, as clean gold has an emissivity of $\sim$ 0.7% in the far-infrared (Xu, Lange & Bock 1996). Radiative loading in the cryostat is reduced by the use of aluminized mylar superinsulation. Multiple layers of mylar (approximately 10 in this cryostat) tend to remain thermally coupled to each other, especially at high temperatures, due to residual gas conduction (Sarwinski, private communication). In order to facilitate evacuation to high vacuum levels (since, according to Scialdone (1993), Mylar su-

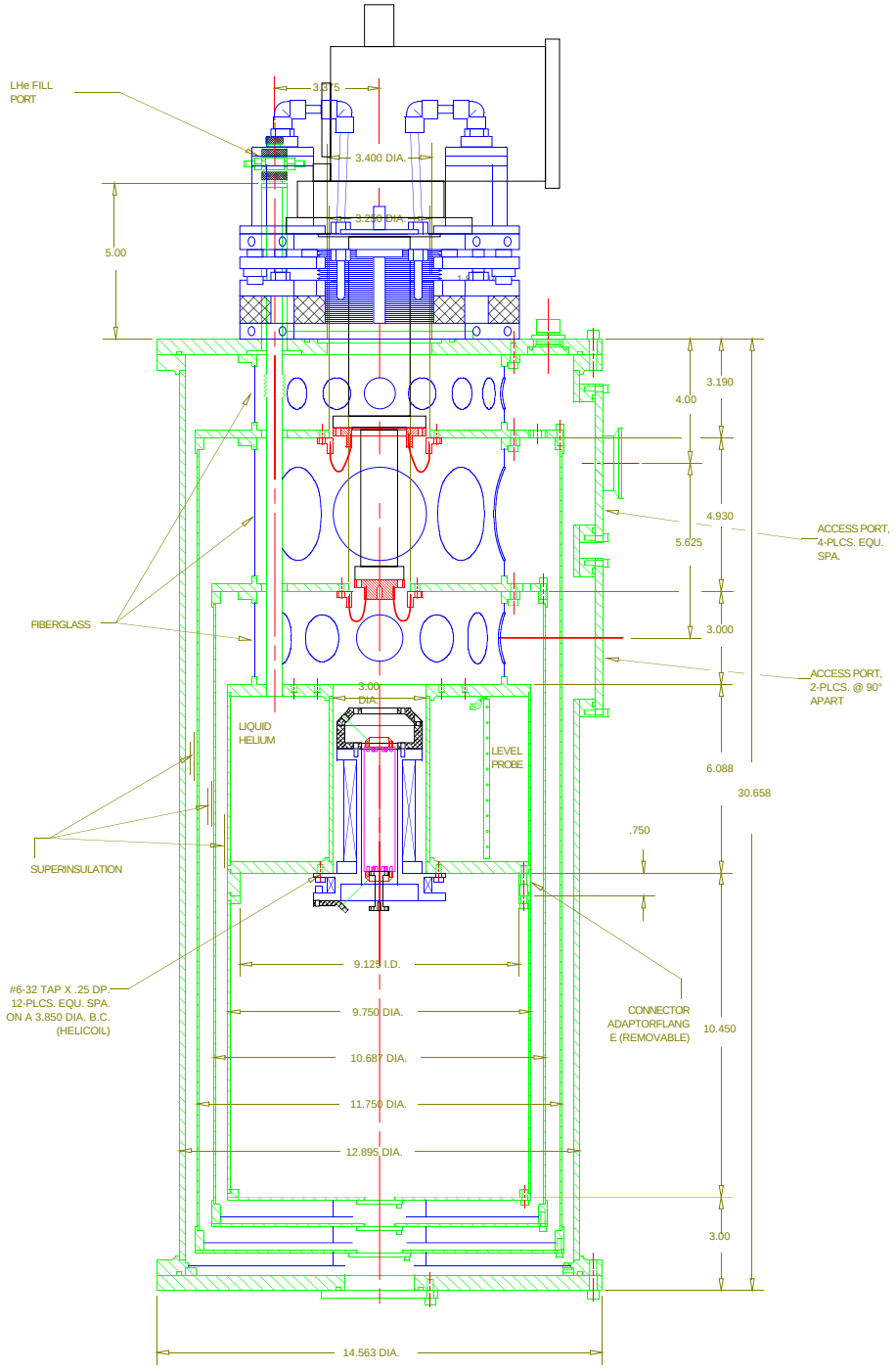

Figure 7.11 Side view of the cryostat with the major components included. The closed-cycle refrigerator is at the top, isolated from the dewar mechanically by the vibration isolator and thermal strapping. The ADR magnet and salt pill can be seen near the center. The optics space is the large volume in the right half of the dewar, surrounded by a shield at 2K with windows at the far right. In actual operation, the cryostat is downward-looking, although it can tilt $\pm 45°$ as the telescope slews between zenith and horizon.

perinsulation becomes saturated with gas when kept in atmosphere for one day), the superinsulation has been slit every $\sim$ 10cm to provide a path for gas to escape. Additionally, there are light-proof holes in every stage allowing for gas to escape easily from the inner volumes. In the case of the 65K and 12K stages, where the cooling power is quite large, the light baffles are in the form of a Z−shaped hole coated internally with glass- and carbon-loaded Stycast epoxy (Emerson & Cuming). In this way, light passing through the baffle must bounce off a blackened surface at least twice but probably much more often. With an estimated emissivity of $> 90\%$ (Bock 1994), this should provide at best a 1% transmissive baffle. On the 2K stage, where light must be blocked to a very high level, sintered brass filters are used to allow gas to pass. These devices, sold for use in fluid systems as breather valves, have also had carbon black applied to them. The number of bounces inside the sintered brass is quite large because of the large ratio of thickness to particle size (~ 10). I have made a measurement using a lock-in detected LED and proven that the optical transmission is less than 1% even without the carbon black. Finally, in order to insure that the residual gas conduction is low, several charcoal adsorbers have been placed in the cryostat. There is one such adsorber on the cold end of the mechanical refrigerator, which has an equilibrium temperature of about 10K. Furthermore, several adsorbers have been place in the 2K work space, which will ensure that no residual gas remains to adsorb on the bolometers, which can increase their heat capacity dramatically (A. Clapp, private communication).

Most of the electrical leads in the cryostat are made using twisted pairs of 125μm (0.005") manganin with heavy Formvar insulation (California Fine Wire). In order to heat sink the wires adequately, an estimated $\sim$ 5cm of thermal anchoring length at each temperature was deemed to be adequate. The wires are wrapped tightly and uniformly over cylindrical metallic spools and varnished in place using GE varnish (GE 7031 Varnish). With a $\sim$ 3cm circumference and around 4 wraps, these wires should be heat sunk more than enough (one wrap being calculated to be sufficient) to guarantee a low heat load to the cryogen bath. These spools are tightly screwed down to their respective stages, which are gold plated to enhance the thermal contact.

7.5.0.1 Thermometry

In order to understand well the performance of the cryostat, I have installed several thermometers at critical points around the system. For the lower temperatures ($T < 20$K), most thermometry is provided by commercially acquired DT-470 diode thermometers (Lakeshore Cryotronics, Inc.). At the higher temperatures ($T > 30K$), I have calibrated a large supply of diode thermometers using plastic-encapsulated 1N4002 rectifier diodes. These diodes are inexpensive (4 orders of magnitude less than the Lakeshore diodes!), repeatable, and similar to each other, as shown in Figure 7.12. By batch-calibrating a cluster of them at several temperatures, a reliable calibration curve can be generated. These thermometers yield a temperature which is accurate to better than 1% and approximately twice as sensitive (in terms of the dimensionless sensitivity ${}^{T}/_{V} \times {}^{\mathrm{d}V}/_{\mathrm{d}T}$) as the DT-470 series. The temperature is given by $T(\mathrm{K}) = 430 - 350\ V$, where V is the voltage across the diode with 10μA DC excitation. I have also developed an inexpensive compact, precision low-power current source for this purpose (see Appendix C).

7.5.1 Mechanical Refrigeration and Vibration Isolation

A CTI Cryodyne 350 (CTI Cryogenics) closed-cycle Gifford-McMahon refrigerator (McMahon & Gifford 1960) is used to cool the two outer radiation shields with approximate temperatures of 65K and 12K. The mechanical refrigerator is decoupled from the cryostat mechanically via a pneumatic vibration isolator (National Electrostatics Corporation). The thermal connections between the CTI cold head and the dewar stages needed to be sufficiently conductive to insure adequate cooling of the stages, but mechanically soft to allow compliance for vibration isolation. Several contact designs were tried, based on a variety of attachments made from tinned copper braid. Using the measurements of temperatures based on the early designs, an optimized thermal connection was made using 75μm (0.003") thick, 12mm wide, 10cm long copper straps. The 65K stage uses 36 such straps while the 12K stage has 24, each hard soldered into copper end pieces for easy attachment. The straps are made

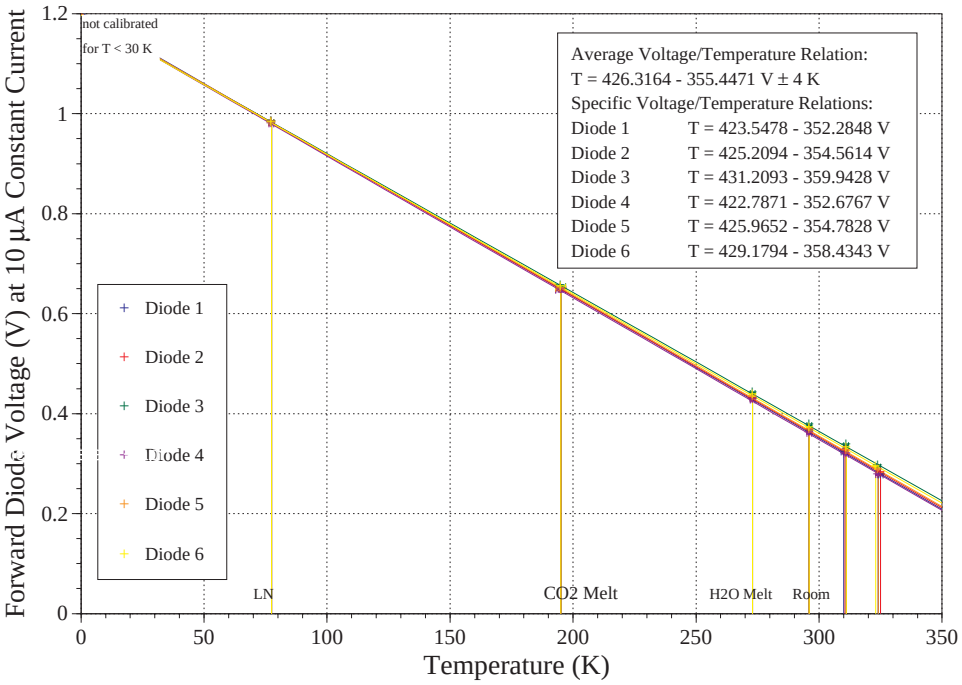

Figure 7.12 Calibration curves for six 1N4002-series plastic encapsulated diode thermometers. At any temperature, the standard deviation is less than 1% of the temperature.

from half-hard electrolytic copper to achieve a good balance between mechanical and thermal stability with high thermal conductivity. Each connection allows the stages and cold heads to move relative to each other over a 20mm range.

The vibration isolator is a customized pneumatic isolator for use with the CTI 350 cold head (National Electrostatics Corporation). The warm end of the cold head rides on a four-piston air cell with external ballast tanks. The air cells are additionally isolated from the cryostat by means of passive rubber vibration absorbers. A vacuum seal is maintained by means of a butt-welded bellows which allows for a large range of motion with minimal mechanical coupling. The isolator has a nominal range of motion of ± 25 mm, but has been reduced to ± 12 mm by means of rigid mechanical stops in order to limit the motion requirements on the thermal connections outlined above. The isolator uses a constant supply of pressurized air at 35psi, which bleeds through two symmetric sides of the vibration isolator to provide a constant soft air spring with variable bleed valves acting to restore the DC position of the isolator under changing

loads. The two sides of the isolator are oriented such that the varying direction of the cold head loading on the cryostat while moving on the telescope can be compensated for. According to the manufacturer's specifications, this system reduces the amount of vibration coupled into the cryostat by over an order of magnitude for frequencies above ~ 1 Hz. However, this has not yet been verified with cold bolometers.

7.6 Achieving 100mK

A compact ADR has been constructed in the spectrometer cryostat. Based on the design of a compact, efficient, low-power ADR intended for SIRTF (Timbie, Bernstein & Richards 1990; Bernstein et al. 1991; Hagmann, Benford & Richards 1994; Hagmann & Richards 1995), most of the refrigerator assembly is mounted inside a toroidal helium tank to yield good heat sinking of the magnet while not sacrificing space for optical components.

7.6.1 Adiabatic Demagnetization

Adiabatic demagnetization was first proposed conceptually and independently by Debye (1926) and Giauque (1927). It dominated the field of ultralow-temperature refrigeration from its first use (de Haas, Wiersma & Kramers 1933; Giauque & MacDougall 1933) until the development of the dilution refrigerator in the late 1960s. The adiabatic demagnetization cycle is illustrated by the entropy-temperature diagram in Figure 7.13. Beginning at point (A) with a high temperature and low external magnetic field, a paramagnetic substance (often a hydrated salt) is subjected isothermally by an increasing magnetic field towards point (B). Some thermal contact with a controlled heat bath, such as pumped liquid ^{4}He, is needed at this point. As the magnetic field increases, the paramagnetic spins will align, a configuration of low entropy. This requires that heat be extracted from the system, which flows into the bath. Upon reaching point (B), the thermal connection to the bath is broken and the magnetic field reduced isentropically (adiabatically). During this stage, as shown in the figure, in order to remain at constant entropy in a decreasing magnetic field,

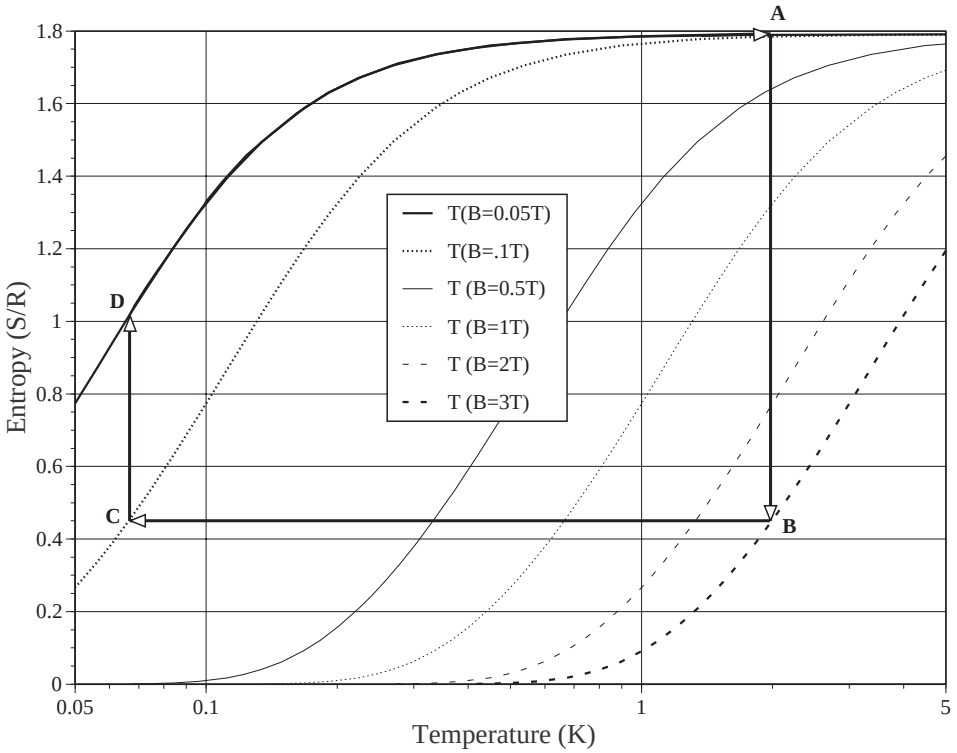

Figure 7.13 Diagram of the cycle of an adiabatic demagnetization refrigerator cycle, as described in the text.

the temperature must decrease. Physically, the paramagnetic spins are disaligning again, removing entropy (and therefore thermal energy) from the lattice of the salt crystal. In a controlled ADR being operated at constant temperature, upon reaching point (C) the demagnetization ceases. Because some residual parasitic heating (from mechanical supports or electrical power) will cause entropy to flow into the crystal lattice, the salt will tend to warm up. However, a slow demagnetization will continue to remove this entropy, keeping the salt isothermal until point (D) is reached, at which point the cooling power of the ADR is exhausted. The thermal contact to the bath is then reestablished, bringing the system back to point (A) where the cycle can begin again. ADRs can achieve near-Carnot efficiency due to their adiabatic cooling.

7.6.2 Paramagnetic Salts

The working element of every ADR is the paramagnetic salt, typically referred to as the salt pill. Many choices of salt are available, depending on the temperature

and power requirements of the cold stage (Kittel 1980a). Most of these are unusable at 0.1K, but were historically useful before the development of ^{3}He sorption-pumped refrigerators for producing temperatures below the 1K achievable by pumping liquid ^{4}He. At temperatures between 0.05 and 0.15K, the most efficient salt in terms of entropy density (cooling power per unit volume) is Ferric Ammonium Alum ($Fe(NH_4)(SO_4)_2 \times 12H_2O$, FAA), as shown in Figure 7.14. Its zero field entropy density is 53 kJ K^{-1} m^{-3}.

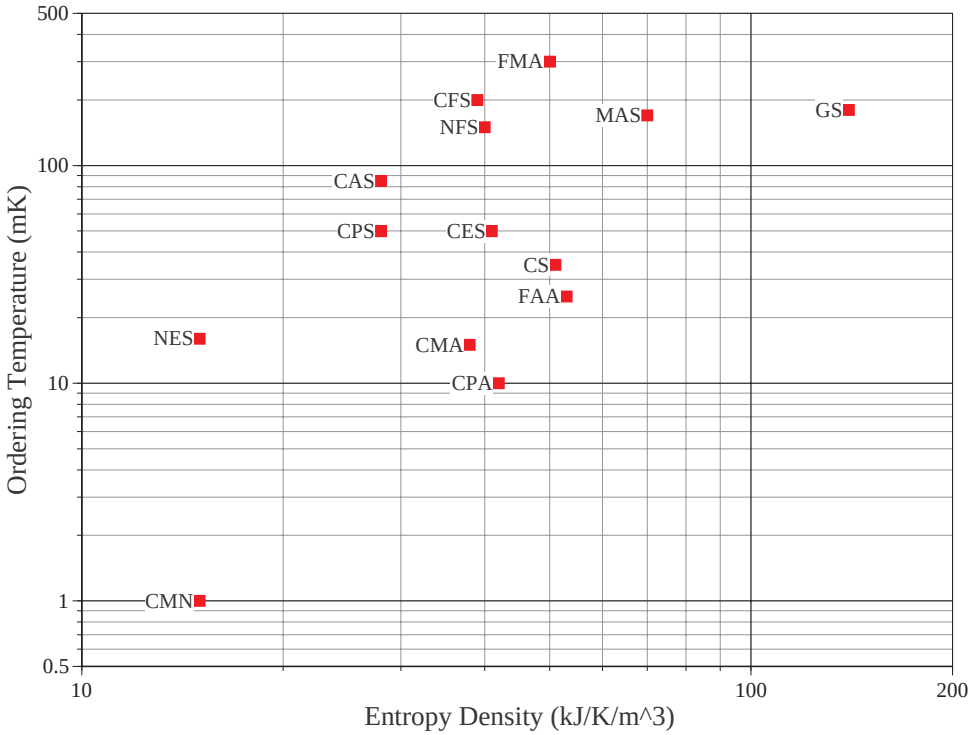

Figure 7.14 Comparison of the entropy density and ordering temperature of a variety of paramagnetic salts (from, Kittel 1980a). FAA is the salt with the highest entropy density for operation below 100mK.

The entropy of FAA can be calculated using the equation for the entropy in a paramagnetic system. Consider a lattice of paramagnetic ions in which the interaction energy between dipoles is small compared to the thermal energy. In this case, the ions are free to align in any orientation, resulting in a net entropy contribution of $R\ln(2J+1)$ per mole for an ion with angular momentum quantum number J. For FAA, the iron atom is in the $^6S_{5/2}$ state (Hudson 1972), which indicates that $L = 0$,

$S = 5/2$, and $J = 5/2$. If the lattice contribution to the entropy is smaller than the paramagnetic contribution, then the total entropy is constant with temperature until such time as the thermal energy becomes smaller than the interaction energy, at which point the dipoles will align, thereby removing virtually all remaining entropy from the system. We define $x = \beta gJB/kT$ to be the ratio of the maximum interaction energy βgJB to the thermal energy kT, with $\beta = 9.274 \times 10^{-24}$ J/T (the Bohr magneton), $g = 3/2 + [S(S+1) - L(L+1)]/[2J(J+1)] = 2$ (the Landé factor) and B the applied magnetic field. Manipulations of the equations for the entropy and the magnetization as a function of temperature and field result in the final expression for the magnetic entropy of a paramagnet (Betts 1976; Lounasmaa 1974; de Klerk 1956):

$$S = nR\left[\frac{x}{2J}\coth\left(\frac{x}{2J}\right) - \frac{(2J+1)x}{2J}\coth\left(\frac{(2J+1)x}{2J}\right) + \ln\left[\frac{\sinh\left(\frac{(2J+1)x}{2J}\right)}{\sinh\left(\frac{x}{2J}\right)}\right]\right] \tag{7.10}$$

It should be noted that the above expression is a function only of the ratio (B/T), which implies that, during the adiabatic demagnetization, B/T must stay constant. In truth, there is an effective internal residual field (which, in the case of FAA, is $B_{\rm internal} = 0.02$T) which should be added in quadrature to the applied field (Betts 1976). This equation is a valid approximation only for the regime $B > B_{\rm internal}$. Furthermore, it breaks down at the ordering temperature of FAA (0.025K), when the paramagnetic spins self-align.

The entropy for FAA is shown in Figure 7.15. Experimental data from Vilches & Wheatley (1966) are used for the zero field curve (B=0), while the remaining data are calculations from equation 7.10. Also shown is the heat capacity of FAA multiplied by 10, and the heat capacity of copper multiplied by 1000.

During the isothermal regulation, the entropy available for cooling is, conservatively, $0.5R$ J mol^{-1} K^{-1}. In our compact configuration, a total of $\sim$ 50g of FAA – about 0.10 moles using the measured coefficient of 482g/mol of Mendoza (1961) – is available. Then the total available magnetic entropy at 100mK is roughly 40mJ. Thus, to achieve a hold time at 100mK of 12 hours, the heat leak must be reduced to

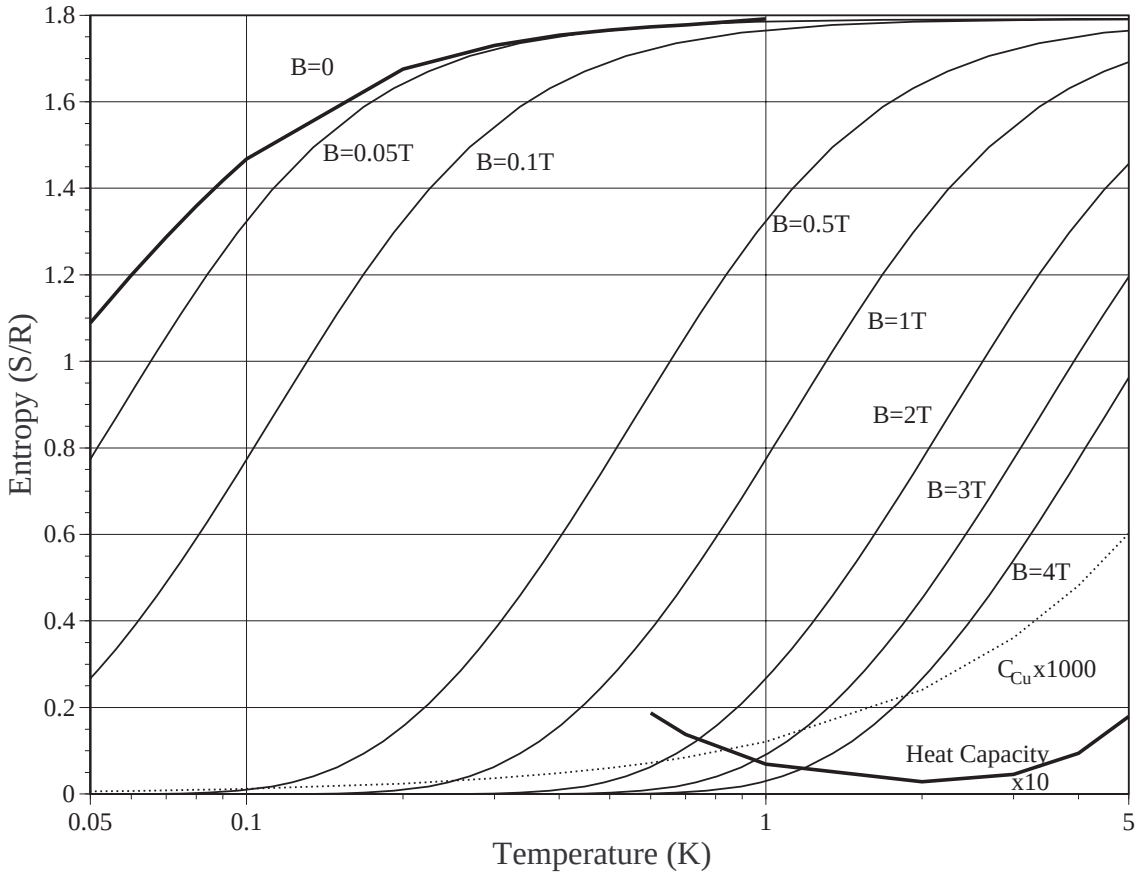

Figure 7.15 Entropy of Ferric Ammonium Alum as a function of temperature and applied magnetic field, in units of the molar gas constant $R = 8.3145$ J mol^{-1} K^{-1}.

$\lesssim 1\mu$W. Towards this goal, simple, symmetric mechanical suspension using Kevlar, an aramid fiber of high strength and modulus of elasticity (DuPont Company), has been constructed. The salt pill and magnet are coaxial cylinders, with the salt pill suspended by three tensioned cords pulling radially away from the center of the system (Figure 7.16). The 6 cords are made of braided Kevlar 29, each with a cross-sectional area of approximately 0.1mm^2 and a length of 2cm. Based on the measurements of the thermal conductivity K of Kevlar (Duband, Hui & Lange 1993; Duband, Lange & Bock 1996), $K = 2.4 \times 10^{-5} T^{1.62}$ W cm^{-1} K^{-1}, the heat load onto the cold stage is then $P_{\rm ADR} = 3 \times 10^{-8} T_{\rm bath}^{2.6}$ W, where $T_{\rm bath}$ is the temperature of the ^{4}He bath. In order to guarantee that the heat load remains low even with additional, separately suspended addenda (detector arrays, thermal links), it is safe to require that the conducted power be 10% of the maximum heat load. This assumes that the additional

parasitic loads from wiring, radiation, and residual gas conduction are negligible. With proper design, this is true. Then the maximum allowed $T_{\rm bath} = 1.6$K, just within the range conveniently available by using pumped ^{4}He. Fortunately, the base temperature of the spectrometer dewar is below 1.4K, corresponding to a pressure of less than 2 Torr (White 1979).

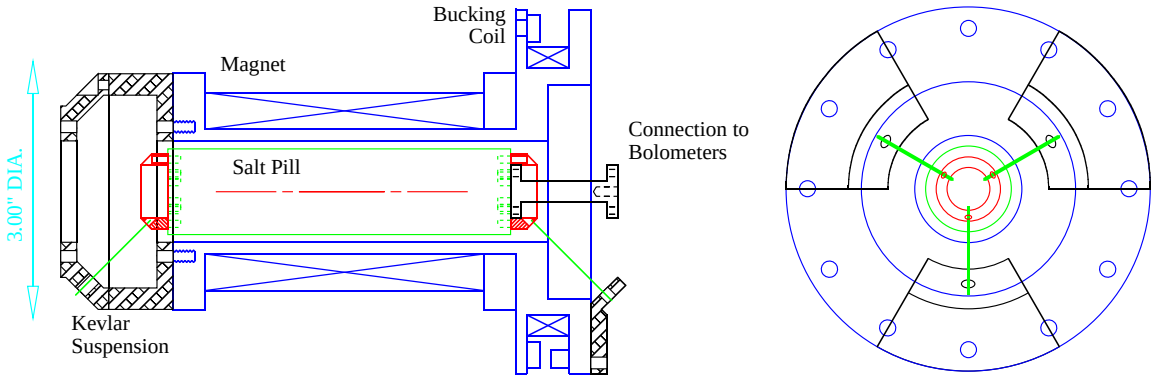

Figure 7.16 Side and end views of the ADR assembly, illustrating the Kevlar suspension system and the placement of the salt pill in the magnet.

7.6.3 Heat Switches

The ADR requires a thermal connection between the cold stage and the bath which can be made and broken at will. Generally, these "heat switches" are required to have a high ratio of thermal conductance when "on" compared to the conductance when "off," called the switching ratio κ. This ratio is critical to the performance of the ADR, since it relates the maximum power a heat switch can conduct to its parasitic heat leak. If we assume that we wish to have a hold time of 12 hours and a 5% fractional parasitic heat leak due to the switch, then the effective hold time based on the switch alone is 60 hours. As all the energy entering the system during this 60 hour period must be withdrawn at the start each cycle, the time for removal is then $60/\kappa$.

The simplest heat switch is merely a thermal link between the two stages wherein the thermal conductance is a rapid function of temperature near the switching point. Typical materials include the amorphous carbon in a cheap resistor (Pandorf, Chen

& Daunt 1962), which has a low switching ratio, and superconducting wires. The superconducting heat switch (Lawson 1982; Schuberth 1984; Coccia & Modena 1993) can have a switching ratio at liquid helium temperatures of > 100 (Lounasmaa 1974), but is often difficult to handle and may have strange interactions with the ADR magnetic field.

Perhaps the most common passive heat switch in ADR design is the use of a helium gas-gap switch (Torre & Chanin 1984; Frank & Nast 1986; Duband, Hui & Lange 1990). In this design, a small thermally insulating cylinder with conductive ends is used to thermally connect the bath and cold stage. A small reservoir of helium gas (volume less than 1 ml) adsorbed onto charcoal opens onto the inside of this cylinder. If the reservoir is heated, the adsorbed gas is released and causes the cylinder to be a thermal short due to the high conductivity of helium gas. When the reservoir cools, the charcoal acts as a sorption pump and evacuates the cylinder. This type of heat switch can also achieve switching ratios of ~ 5000, but at the expense of switching speed (several minutes) and mechanical complexity in construction due to tight tolerances.

The highest switching ratio is that achieved by a mechanical heat switch, wherein thermal contact is made through a pressed mechanical contact which can be broken, thereby achieving total thermal isolation. Because of the large mechanical forces necessary, such switches are usually large and complex, but the infinite switching ratio makes them a commonly used switch nevertheless. Initially, I designed a simple solenoid-actuated switch in which a copper finger from the cold stage is drawn against a plate in good thermal contact with the bath. The solenoid was hand-wound with NbTi superconducting wire (California Fine Wire) to limit heat dissipation. This switch suffered from low thermal conductance (due to a reasonably small mechanical pressure) and from substantial misalignment problems due to its being inherently asymmetrical. This meant that, quite often, the switch would close by itself during cooldown. A new heat switch has recently replaced this one, using symmetrical pair of jaws on reciprocal screws which can be clamped or removed from the cold finger. It is driven by a stepper motor fabricated at Caltech using as a commercially available

motor as a basis (Bearing Engineers). The heat switch is opened and closed by driving the stepper motor in opposite directions.

7.6.4 Magnet Current Controller

In order to control the temperature during the isothermal stage (*C-D* in Figure 7.13), an approximately constant heat load must be tolerated. This involves a slow demagnetization at a rate sufficient to compensate for the parasitic heat load, which is performed by a linearly ramping current source. Ideally, excellent stability (deviations of a few μK) can be achieved using feedback to adjust the ramp rate slowly (timescales of seconds). Discussions of the control of ADRs have been presented by Kittel (1980b), Kittel (1983), Nara et al. (1982), and Skyba et al. (1994). Fortunately, a nearly linear ramp rate will control the temperature to within a few percent. The demagnetization paths for an ADR operating at 100mK and 200mK are shown in Figure 7.17, in which the thick lines are the optimal paths for constant temperature and the thin lines are the approximated linear fits. When operating at 100mK or 200mK, the RMS temperature deviations using a linear ramp are calculated to be 3% and 5.5%, respectively, with much of the error determined by the excursion near zero field. Since the zero field time occurs at the end of the cycle (after observations have ceased at daybreak), this time will probably not be used and so the stability is even better.

I have designed and constructed a controller for the ADR based loosely on the design of Bernstein et al. (1991). The controller features a dual ramp, one for the isothermal magnetization and adiabatic demagnetization stages (A-B and B-C in Figure 7.13), called the "fast ramp," and one for the isothermal demagnetization (C-D), the "slow ramp." The user can ramp either or both of these sources in either direction with different, adjustable rates or hold them constant. Both ramps are digitally controlled using a variable-speed clock, 16-bit counter, and 16-bit digital-to-analog converter. The weighted sum of these two counters produces a voltage signal in the range 0-7V. A voltage-to-current driver was designed to convert this

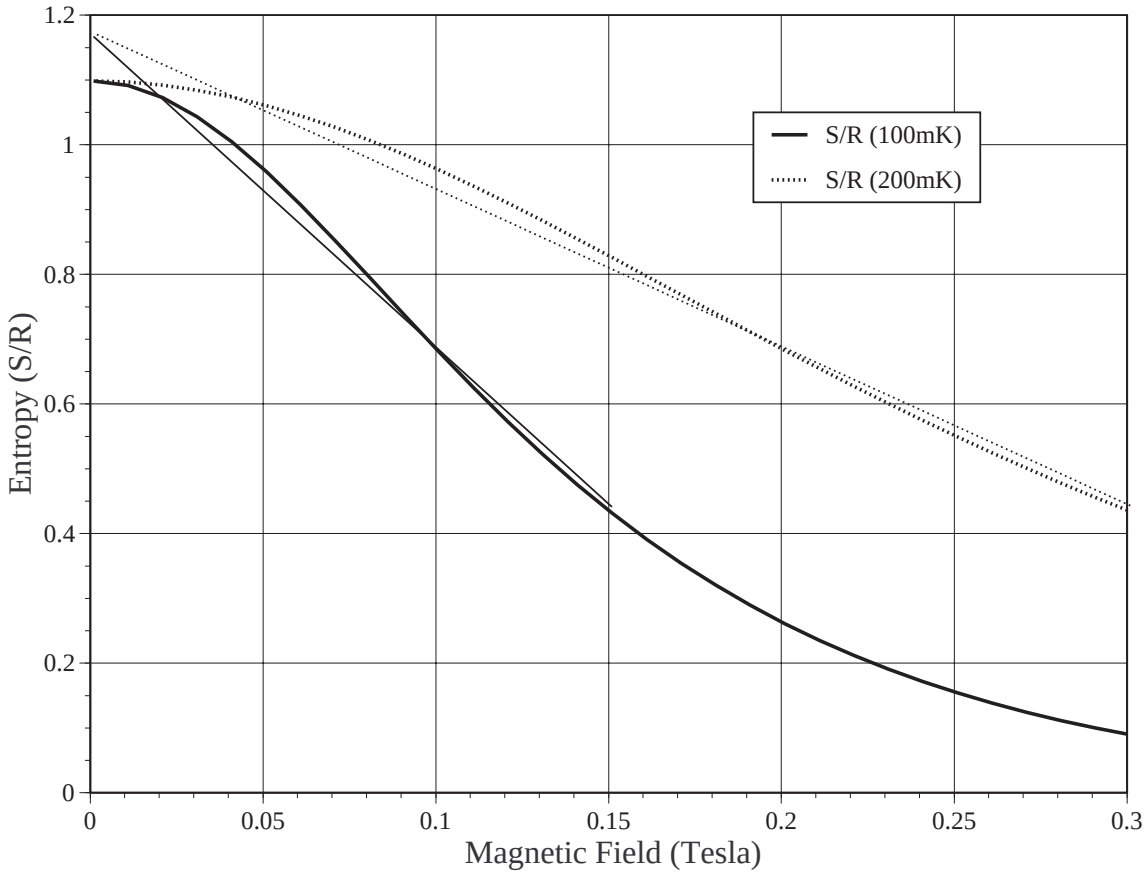

Figure 7.17 Graph of the paths for isothermal demagnetization at 100mK and 200mK, assuming an optimal demagnetization ($\Delta T = 0$, heavy curve) and linear demagnetization ($\Delta T_{\rm rms} \sim 3$mK and 5mK, respectively, light curve).

voltage into a current through the magnet with a conversion factor of 1.000A/V. In this way, the fast ramp can be raised from 0 to 6A, held during equilibration, then slowly reduced to 0A. In the meantime, the slow ramp is brought up to 0.6A, then, during the isothermal demagnetization, ramped down very slowly. With 16 bits, a 12-hour hold time implies switching at a rate of 1.5 bits/second. Since this is much faster than the electrical time constant of the 30H magnet (tens of seconds) and the thermal equilibration time of the ADR (probably also tens of seconds), the magnet field produced changes smoothly with time. Diagnostics in the form of a readout of voltage, current, power, and resistance are provided. The schematic for this circuit is shown in the Appendix C as Figure 10.6.

7.7 Electronics for Detectors

The electronics for reading out the detectors use the KAO data system developed at the Goddard Space Flight Center. A block diagram of the system is shown in Figure 7.18. The bolometers are biased by a constant voltage source, and are placed at the focus of a modulated beam of submillimeter light. Each signal impedance is transformed by a FET at 120K acting as a source follower in order to reduce microphonics, as the output impedance of $\sim$ 1kΩ is smaller than the impedance of the bolometer by 4 orders of magnitude. This signal is then amplified and digitized at 1kHz with 16 bits of resolution. The stream of signals from all digitizers (one per bolometer) is sent to a DSP card located in a Macintosh control computer. Software digital lock-in detection is performed by a set of DSPs, resulting in a readout of each bolometer signal at the optical modulation frequency (typically 4Hz).

The Preamplifier schematic diagram for a single detector is shown in Figure 7.19. There is a DC signal path with gain of 2, along with a two-stage AC amplifier yielding a nominal gain of 500 or 8000 with 3dB rolloffs at 0.3Hz and 1kHz. The final result is summed and output to the digitizing electronics. A noise analysis has been made of the various parts of the circuits, using the manufacturers' specifications for the operational amplifiers and calculating the FET noise from the manufacturer's speci-

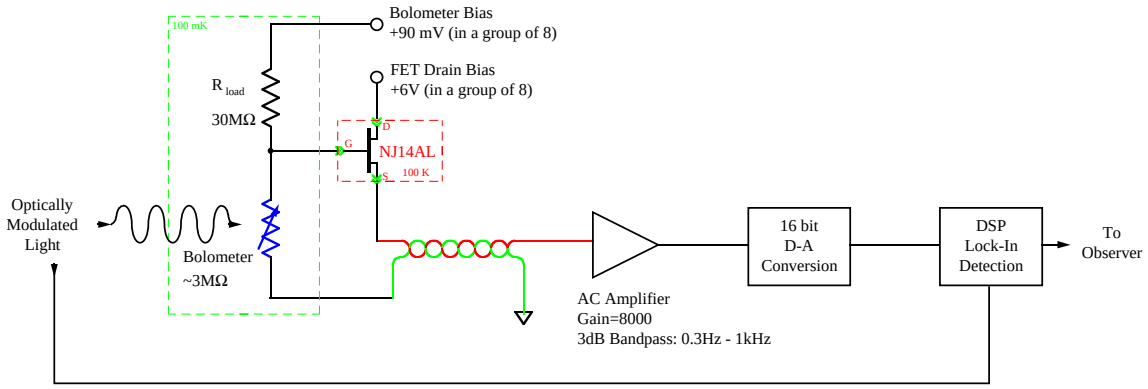

Figure 7.18 Block diagram of the KAO data system developed at GSFC.

fications and theory (Das 1972). A good introduction to estimating the noise sources in the first stages of a bolometer amplifier is given by Timbie et al. (1994).

In order to prevent electrical noise pickup, whether from RF interference, grounding and shielding problems, or microphonics, the amplifiers must be located as close as is possible to the cryostat. I have built a set of three electronics boxes (amplifiers, housekeeping, and ADR control) which bolt onto the side of the cryostat as shown in Figure 7.20. Each of these boxes is in and of itself an RF-shielded box, using metallized gasketing to ensure that all seals are RF-tight. The cables leading from the cryostat to each box are sealed in stainless steel bellows tubing and gold plated for optimal electrical shielding. At the input of each box, an RF-suppressing connector is used to ensure that no RF power can enter the cryostat from the room-temperature electronics. Additionally, the output connectors leading to external electronics (such as the A/D box) are RF-shielded. The ADR connector is custom-made to suppress RF while permitting the contacts to carry up to 15A without difficulty.

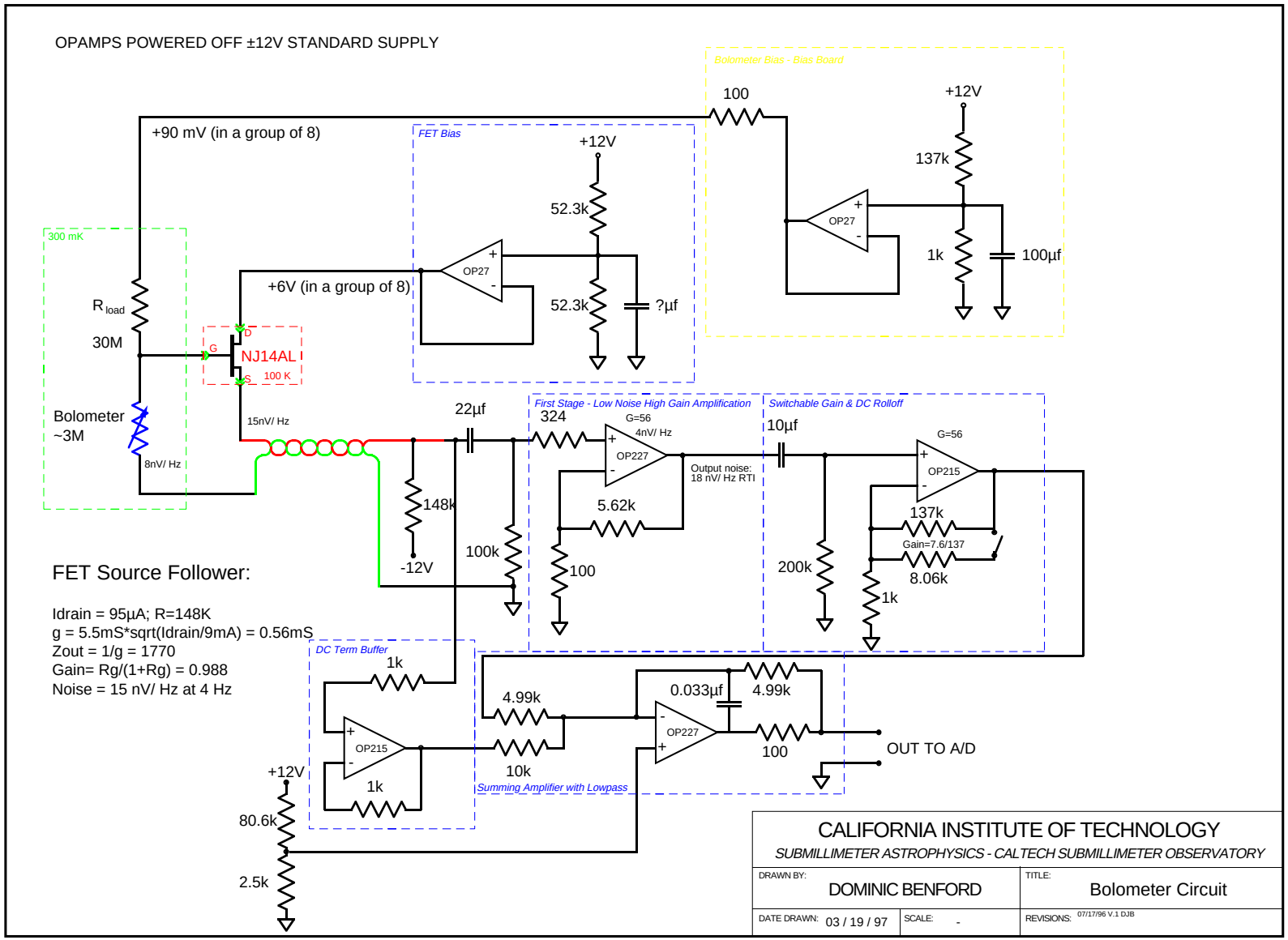

Figure 7.19 Schematic diagram of the GSFC KAO PreAmp.

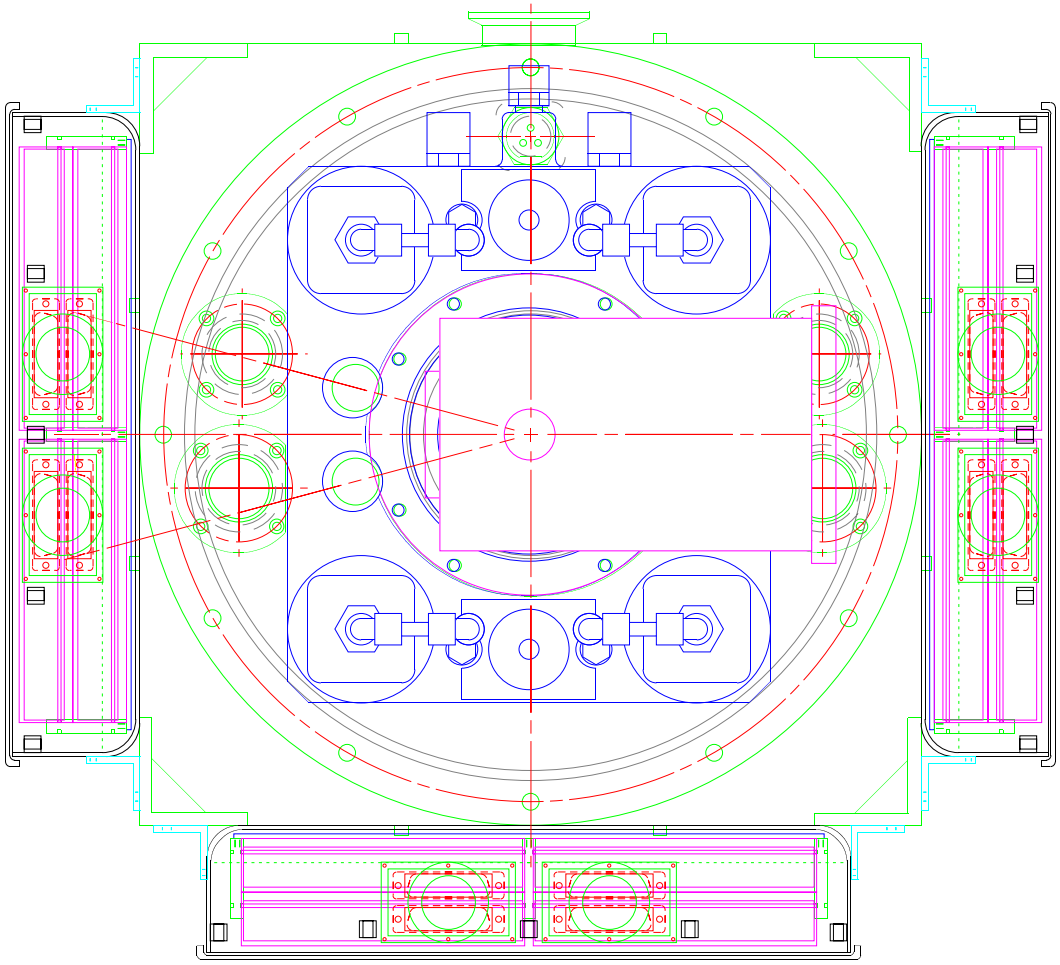

Figure 7.20 Diagram of the top of the spectrometer cryostat, showing the placement of the electronics boxes around the outside. The leftmost contains the housekeeping electronics (thermometer controller, Fabry-Perot driver and grating motor/encoder controller); the middle contains the ADR control and power circuitry; the rightmost houses the bolometer bias and readout electronics. This is a top view of a downward-looking cryostat, so we see here the vibration isolator and mechanical refrigerator head.

7.8 Optical Filtering

As described in section 2.4.7, optical filtering is necessary in a submillimeter spectrometer of high sensitivity, since with low temperature detectors, it is crucial to limit the radiative heat load on the cryogenic detectors. Because of the broad wavelength response of the detectors, far-infrared through optical radiation must be rejected by a stack of blocking filters. We have available three cooled shields, at temperatures of about 75K, 15K, and 2K. The filters are mounted at the entrance to each of the shields of the cryostat. In order to accurately determine the amount of filtering needed to meet our requirements of high efficiency and low total out-of-band power transmission, the filter model of section 2.4.7 was again used. Given that we have available three shields, a filter stack with nearly 60% transmission is possible, with the total transmitted out-of-band power only a few percent of the in-band power. The model of the filter stack chosen for the spectrometer is shown in Figure 7.21. An analysis of each component follows, with all the measurements shown in Figure 7.22. Again, the vacuum window of the cryostat is a 1.0 mm-thick disk of high density clear white polyethylene as described in section 2.4.7

7.8.1 Zitex

The infrared blocking at the 70K and 15K stages is provided by Zitex (Norton Performance Plastics), a porous Teflon material which scatters strongly at wavelengths $\lambda < 50\mu$m, providing excellent rejection of optical through mid-infrared radiation. Its properties are described more fully by Benford, Gaidis & Kooi (1999). I have chosen to use two sheets of 250μm thick Zitex on each of the two shields. Assuming that each layer scatters out of an $f/4.48$ beam into a uniform sphere, the transmission is:

$$\left(\frac{\mathrm{Area}_{f/4.48}}{\mathrm{Area}_{4\pi}}\right)^4 = \left(\frac{0.04\,\mathrm{sr}}{4\pi\,\mathrm{sr}}\right)^4 = 10^{-10}. \tag{7.11}$$

A more pessimistic model would assume that each layer of two sheets acts as one, which yields a theoretical transmission of 10^{-5}. This is sufficient to block virtually all

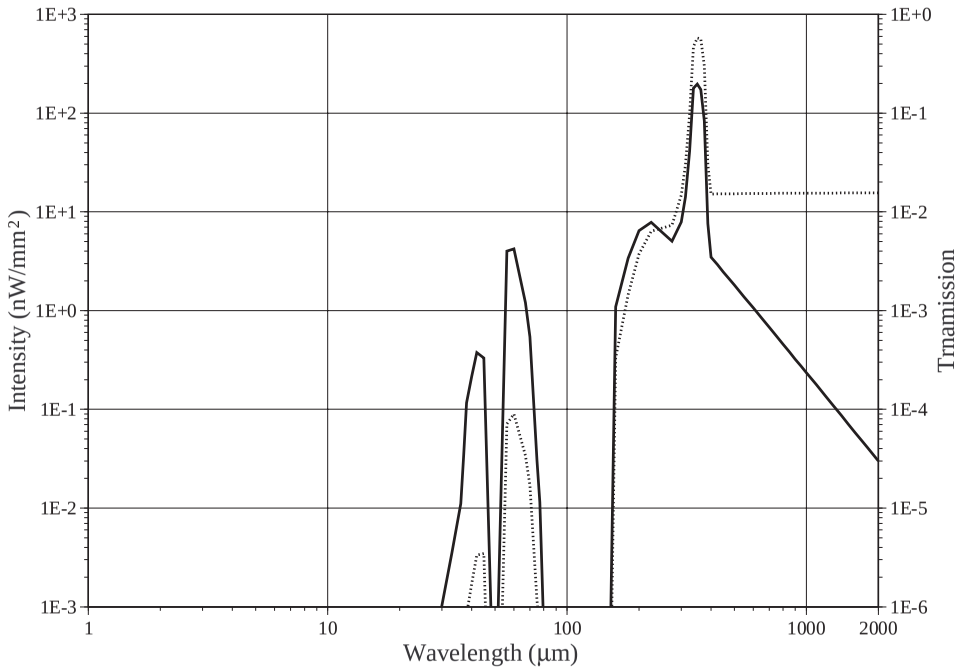

Figure 7.21 Modeled transmission (dotted line) and total intensity (solid line) in unity bandwidth for the spectrometer filter stack.

radiation shortward of 50μm, with a slow rolloff to nearly perfect transmission ($< 5\%$ loss) at wavelengths longer than about 200 μm.

7.8.2 CsI

The first filter on the helium shield is a 1 mm thick crystalline cesium iodide (CsI) filter with clear polyethylene anti-reflection coating (Josse, Gerbaux & Hadni 1993) on both sides. At 4 K, the CsI filter yields nearly zero transmission of incident radiation between 80 and 150μm while rising to 90% transmission at 350μm (Hadni et al. 1962; Vergnat et al. 1969). There is still a very small peak of transmission at about 50μm, where neither the Zitex nor the CsI block efficiently. The power transmitted in this peak is roughly 1% of the in-band power, a negligibly small optical loading.

7.8.3 Bandpasses

The bandpass of the spectrometer is defined by one of a pair of narrow-band ($\lambda/\delta\lambda \sim 10$) metal mesh filters. According to measurements made by the manufacturer (Cochise

Instruments), the bandpass filters effectively block all wavelengths $\lambda > 150\mu$m except, of course, for their specified bandpass at 350μm, 450μm. However, they do typically have a few percent transmission at the third harmonic, which corresponds to the absorption band of the CsI filter.

In the grating spectrometer configuration, the filters are mounted on a liquid He-cooled filter wheel which is located just above the aperture stop, between the helium shield and the 15K shield. In the Fabry-Perot configuration, the bandpass filter is held in a small block immediately before the field stop. The bandpass filter wheel is a 102 mm diameter geared circular plate with two round milled slots that can hold metal-mesh bandpass filters of 25 mm clear aperture. A drive shaft for the filter wheel extends from the wall of the dewar radially inward. At each shield, the shaft is coupled via a set of small gears so that no one section of shaft touches more than two temperatures. The shaft is well heat sunk at 15K, then again at 2K. The shaft drives the filter wheel with a 16:1 turn ratio with manual operation from the outside.

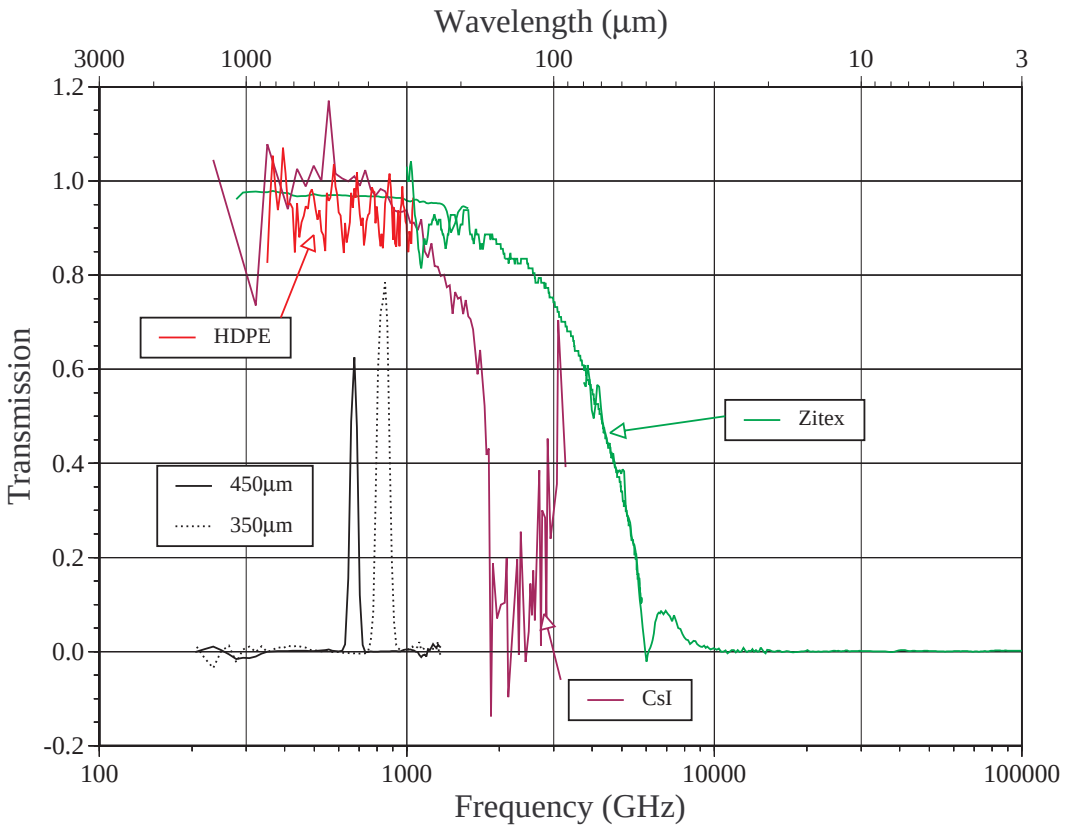

Figure 7.22 Measured transmissions of the components of the spectrometer filter stack.

7.9 Project Status

We have developed a cryostat with a hybrid of many cryogenic technologies, including closed-cycle refrigeration, liquid Helium, and adiabatic demagnetization refrigeration. Additionally, an integrated electronics package allows for bolometric detectors in the dewar to be biased and amplified for easy readout by a pre-existing data-taking system. Many tests on bolometric detectors have led to the characterization of a new generation of bolometer arrays which are ideally suited to operation at temperatures of $100 \leq T \leq 300$ mK under the thermal background loading assumed for a spectrometer with a resolving power of ~ 1000 (300km/s). A set of blocking filters has been designed, and each component fabricated and tested, which will enable the bolometers to remain background-limited for optimal performance.

The only portion of this instrument yet to be discussed is the spectrometric optics package itself. For both scientific and political reasons, two parallel packages have been developed for use in the spectrometer cryostat. Using the same detector array, a Fabry-Perot spectrometer and an immersion grating spectrometer can be installed in the cryostat. The Fabry-Perot was developed by a group at the IAS[2] headed by François Pajot. It has been undergoing integration and testing for the past few months, and is likely to receive first light at the CSO in the second half of 1999. The immersion grating has been developed at Caltech by myself and Gene Serabyn, and will be integrated and tested starting in mid-1999 during gaps in the Fabry-Perot testing sequence. I have designed the cryostat such that changing the optics from one configuration to the other (assuming a warm, non-evacuated cryostat) should take only about two hours. Therefore, the spectrometer can be changed at the telescope on a fairly regular basis to accommodate a wide variety of astronomical projects. The Fabry-Perot is optimized for searching for line emission in a wide band at either 350μm or 450μm with a warm-up required to change bands. In contrast, the immersion grating is designed to search for very broad emission lines with known redshifts (at least to a part in 100) and is tunable anywhere in the allowed atmospheric windows between 330μm and 500μm.

[2]Institute d'Astrophysique Spatiale in Paris.

Chapter 8 Fabry-Perot Optics

As discussed in chapter 5, the current bandwidth limitations of submillimeter heterodyne receivers and spectrometers make the search for emission lines of unknown or poorly known redshift extremely difficult. While more of the specifics of this limitation are discussed in chapter 9, the basic problem for surveying is that the total usable bandwidth of the receivers at the Caltech Submillimeter Observatory is such that the redshift must be known to roughly one part in 10^4, uncommon for optical spectra. Searching for weak lines at a totally unknown redshift (for instance, from a source found in a far-infrared deep survey) with such an instrument would seem a Sisyphean task. The reason that spectra can be taken at optical and near-infrared wavelengths is that grating spectrometers such as LRIS on Keck (Oke et al. 1996) use CCD detectors 2048 pixels on a side covering a wavelength range of 5500Å-11000Å(a theoretical redshift coverage of a part in two) with a resolution of $R \equiv \lambda/\delta\lambda \sim 2000$. No such instruments yet exist in the submillimeter, but being able to cover even a redshift range of one part in 10 at similar resolution would be an improvement. With the recent discovery of far-infrared sources of an unknown extragalactic origin (Clements et al. 1998; Kawara et al. 1998; Oliver et al. 1999), the capability to conduct broadband searches in the submillimeter becomes an important observational tool.

One method to achieve this would be to use a Fabry-Perot filter to achieve high resolution followed by an order-sorting grating and an array of detectors to get wider redshift coverage. While this may seem like an arbitrary choice (and to some extent it is, although the best alternatives to this, a grating or a Fourier transform spectrometer, suffer from large mechanical size and poorer sensitivity, respectively), there is a precedent for this. Such an instrument was used on a balloon-borne instrument over a decade ago (Poulter & Jennings 1983; Poulter 1984) and became the progenitor for the Long Wavelength Spectrometer (LWS) aboard the Infrared Space Observatory (ISO)

(Clegg et al. 1996; Swinyard et al. 1996). This remarkable instrument has produced many exciting results regarding the far-infrared emission of galaxies (Malhotra et al. 1997; Luhman et al. 1998). Its capabilities include a high-resolution mode ($R \sim 8000$) covering the wavelength range 70-197μm. For the CSO, a similar instrument could be produced for the wavelength range 300-500μm, with a diminished spectral resolving power of $R \sim 1000$ but better angular resolution.

This chapter describes one possible configuration for the bolometer spectrometer. The Fabry-Perot optics were developed at the IAS in Paris, under the supervision of François Pajot. Other major contributors to the integration phase of this project from the French collaboration include Cyrille Rioux, Bruno Maffei (currently at QMC), Jean-Claude Renault, and Frédéric Schuller. At Caltech, Jeff Groseth has built some of the electronics for the Fabry-Perot unit.

8.0.1 Fabry-Perot Theory

In a mechanical sense, the Fabry-Perot is perhaps the simplest multiple-beam interferometer, being comprised only of two plane-parallel partially reflecting surfaces. It was the desire of Fabry & Perot (1899) to have a compact, tunable, high resolution interferometer, which they made from two pieces of partially-silvered glass on a movable carriage. This device now bears their name, the Fabry-Perot etalon.

If one imagines a beam of light propagating through an etalon comprised of two planar surfaces of reflectivity r separated by a distance d, one can calculate the transmission of the beam through the device by summing an infinite series of ever smaller reflections (hence the multiple beams). The transmission at wavelength λ for an etalon in vacuum at normal incidence is given by the Airy function (Born & Wolf 1959):

$$T = \frac{1}{1 + \Upsilon \sin^2(\frac{\delta}{2})} \text{ where } \Upsilon \equiv \frac{4r}{(1-r)^2} \text{ and } \delta \equiv \frac{4\pi}{\lambda} d. \tag{8.1}$$

The variable Υ is related to the *finesse* $\mathcal{F}$ through $\mathcal{F} = 2\sqrt{\Upsilon}/\pi$. The finesse describes the resolving power of the Fabry-Perot through application of Rayleigh's criterion,

that two wavelengths separated by $\Delta\lambda$ should each have their intensity maximum at the first intensity minimum of the other (Lord Rayleigh 1879). This results in a resolving power of

$$R \sim \frac{2\mathcal{F}d}{\lambda}, \tag{8.2}$$

which drives the design at long wavelengths to large separations and high finesse. However, it is apparent from the form of equation 8.1 that there are many maxima to the transmission function, spaced every $\delta = 2\pi m$, where $m = 2d/\lambda$ is the *order*. This means that for a sufficiently large separation $\Delta\lambda_{\rm SR}$, two orders will begin to overlap. This wavelength is called the *free spectral range* and is given by $\Delta\lambda_{\rm SR} = \lambda^2/2d$. Therefore large separations lead to a decrease in free spectral range. These equations can be combined to yield

$$\mathcal{F} = \frac{R\Delta\lambda_{\rm SR}}{\lambda}, \tag{8.3}$$

which demonstrates that high resolving power and large free spectral range imply a high finesse.

One disadvantage of using a high finesse cavity is that as finesse increases and the effective beam passes through the etalon more times, any absorption losses will compound rapidly. In our application, we wish to achieve a resolution of $R = 1000$ with a free spectral range of around $\Delta\lambda_{\rm SR}/\lambda = 40$, which implies $\mathcal{F} = 25$. While this does not sound like a particularly stiff requirement for a finesse, it does require a surface reflectivity of around 86%. The optical efficiency of a Fabry-Perot etalon can easily be seen to be $[(1-r-\alpha)/(1-r)]^2$, where α is the single-pass power absorptivity. Hence, in order to achieve an efficiency of 50% (an arbitrary minimum), this requires $\alpha < 4\%$. At long wavelengths this is most easily met by the use of a capacitive metal mesh grid.

While the optical theory of ideal metal mesh grids has been around for a century (Lamb 1898), a complete description of the far-infrared transmission properties of a

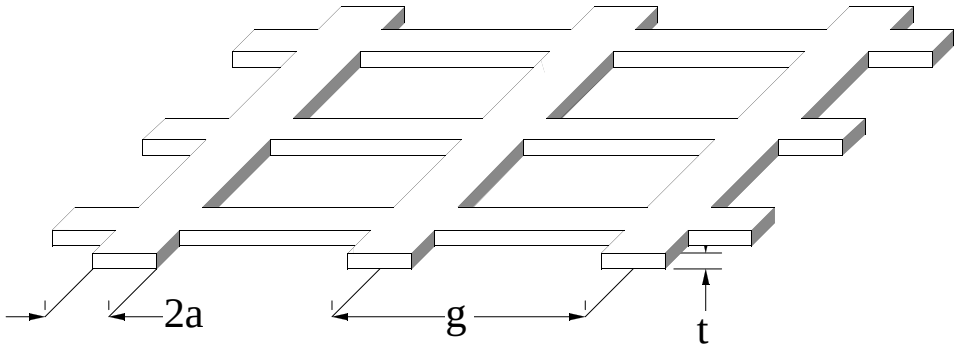

Figure 8.1 Geometry for an inductive wire grid, showing the trace width $2a$, the grid spacing g, and the thickness t.

two-dimensional, finitely conducting metal grid has only existed for 30 years (Ulrich 1967). A grid of this sort is shown in Figure 8.1, where $2a$ is the width of each metal strip of effective resistivity ρ and thickness t, and the center-to-center grid spacing is g. In the long wavelength limit of $\lambda >> g$, the reflectivity becomes fairly weakly dependent on the wavelength, and is given by:

$$r = \frac{1}{1 + (g/2a)\sqrt{\frac{\pi\rho}{Z_0\lambda}}}, \tag{8.4}$$

where $Z_0 \equiv 377\Omega/\Box$ is the impedance of free space. The remaining wavelength dependence arises from the variation of the resistance of the metal due to the skin effect. The effective resistivity ρ should not be confused with the DC bulk resistivity, as a metal at infrared wavelengths is subject to both the anomalous skin effect, wherein the electron mean free path is much greater than the skin depth, and the electron relaxation effect, where the mean time between collisions is much greater than the reciprocal of the frequency of the light. Fortunately for those of us in need of a simple empirical value for the resistivity, at far-infrared wavelengths many common metals have an effective resistivity of $\rho \simeq 2.2 \times 10^{-9}\ \Omega\,\mathrm{m}$ at cryogenic temperatures (Davis et al. 1995). The transmission of a metal mesh using the complete formulation of Ulrich (1967) and Sakai & Genzel (1983) is shown in Figure 8.2. It should be noted that in the long wavelength regime, the transmission is rather strongly dependent on the effective resistance of the grid. The transmission shown in Figure 8.2 uses

a resistance suitable for the grids which were actually manufactured for the Fabry-Perot.

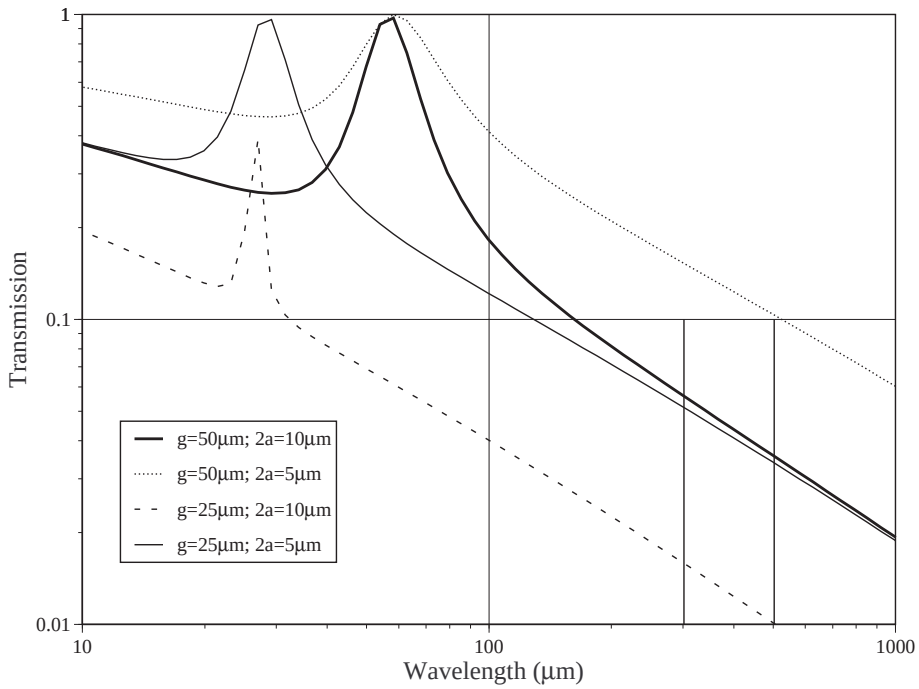

Figure 8.2 Transmission of inductive wire grids for several useful geometries. The wavelength range of interest is indicated by two short vertical lines at 300μm and 500μm, where low and fairly constant transmission implies high, reasonably constant finesse. The quantities in the legend are defined in Figure 8.1.

Naturally, the performance of a Fabry-Perot etalon will never reach the theoretical value due to real-world problems which degrade it. For instance, a divergent beam will exhibit a walk-off effect in an etalon, a problem which becomes worse as the finesse increases. Adequate control of the collimation of the beam eliminates this problem. Nonparallel reflectors will also suffer from walk-off, so a well-designed etalon will be able to correct the parallelism as the etalon moves. Also, nonplanar reflecting surfaces will degrade the finesse due to slightly different path lengths (and therefore phase differences upon recombination) in various parts of the etalon.

8.1 Design of a Submillimeter Fabry-Perot

The Fabry-Perot etalon intended for use at the CSO has been described by Maffei et al. (1994). The etalon itself, with the motors and grids, has been developed by the CEA-CESTA[1] laboratory and is virtually identical mechanically to that used on the ISO LWS (Davis et al. 1995; Davis et al. 1995). However, instead of freestanding wire meshes, it was decided that a grid evaporated on quartz substrates would be more rugged and less subject to surface irregularities. If these grids are on the inner faces of the quartz plates, the transmission of the Fabry-Perot cavity will be unaffected by absorption in the quartz. Additionally, one grid is placed on the planar side of a planoconvex lens which acts as the collimator for the Fabry-Perot. The other quartz plate is wedged to prevent its self-Fabry-Perot effect, as shown schematically in Figure 8.3 (at right). The finished Fabry-Perot (without the quartz plates) is shown in Figure 8.4. The mechanical support structure has since been stripped of its black coating and gold plated.

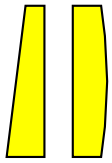

Figure 8.3

The theoretical transmission of the Fabry-Perot with a grid reflectivity of 95% and a spacing of 7500μm is shown in Figure 8.5. In actuality, the reflectivity is somewhat lower at wavelengths of $\sim 350\mu$m, as illustrated in Figure 8.2. A small amount of absorption is included in the model, resulting in an efficiency of $\sim 50\%$. The measured reflection for a single mesh of geometry $g = 40\mu$m, $2a = 11\mu$m was 92.6%, yielding a finesse of 41 and a theoretical resolving power of about 1800. The measured absorption loss was about 2.2%. One can calculate the theoretical efficiency ϖ using $\varpi = (1 - \alpha/(1 - r))^2 = 49\%$.

The complete Fabry-Perot etalon with a fixed spacing was measured using a Fourier Transform Spectrometer (FTS). The resulting spectrum shown in Figure 8.6 verifies that the maximal transmission is approximately 30%, less than that theoretically achievable but reasonable for losses due to manufacturing error.

The layout of the Fabry-Perot spectrometer is shown in Figure 8.7. Although

[1] Commissariat à l'Énergie Atomique (the Atomic Energy Commission in France) operates a (primarily military) research laboratory in Gironde called CEA/Cesta.

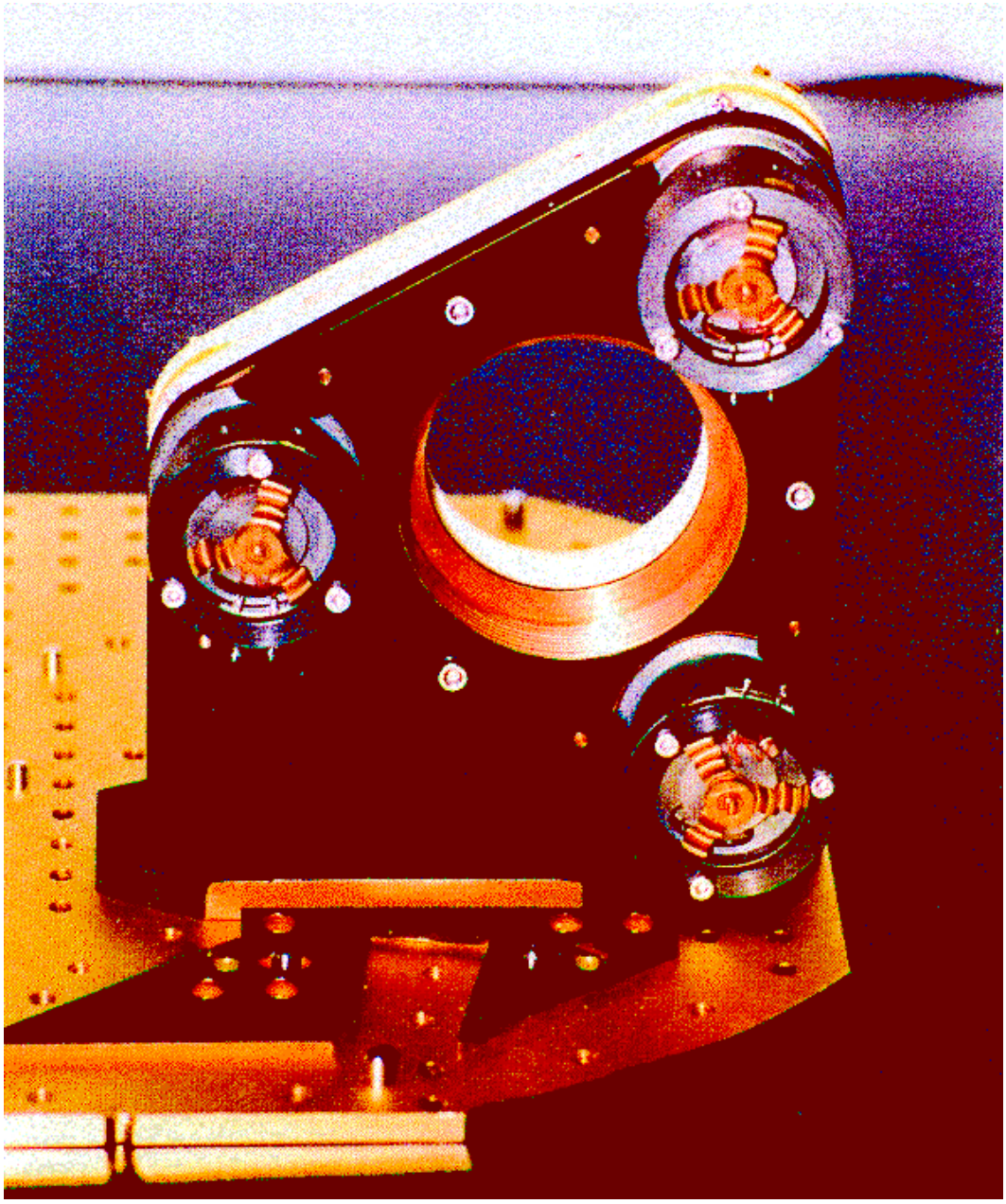

Figure 8.4 Photograph of the Fabry-Perot etalon, showing the placement of the three solenoidal motors. The grids sit in the large central aperture, but were removed for this photo; with their parylene antireflection coating, they appear opaque and white.

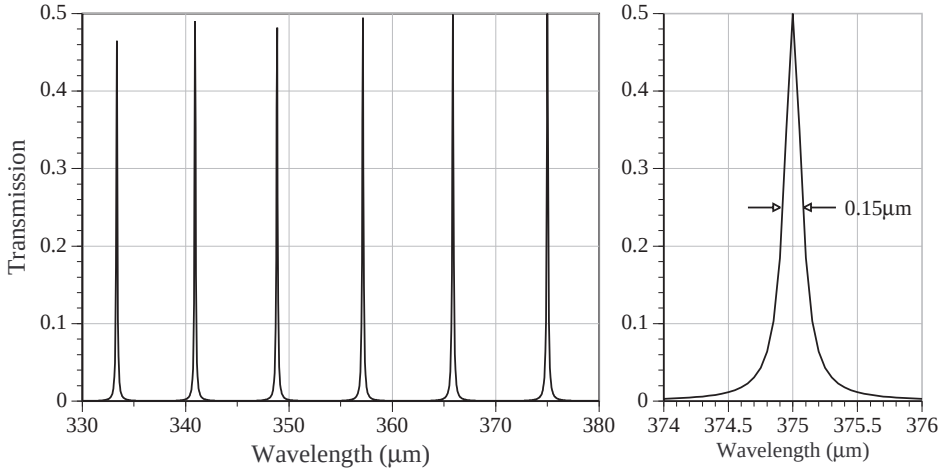

Figure 8.5 Theoretical transmission of the Fabry-Perot. The FWHM of each resonance is approximately 0.15μm, for a resolving power of ~ 2000.

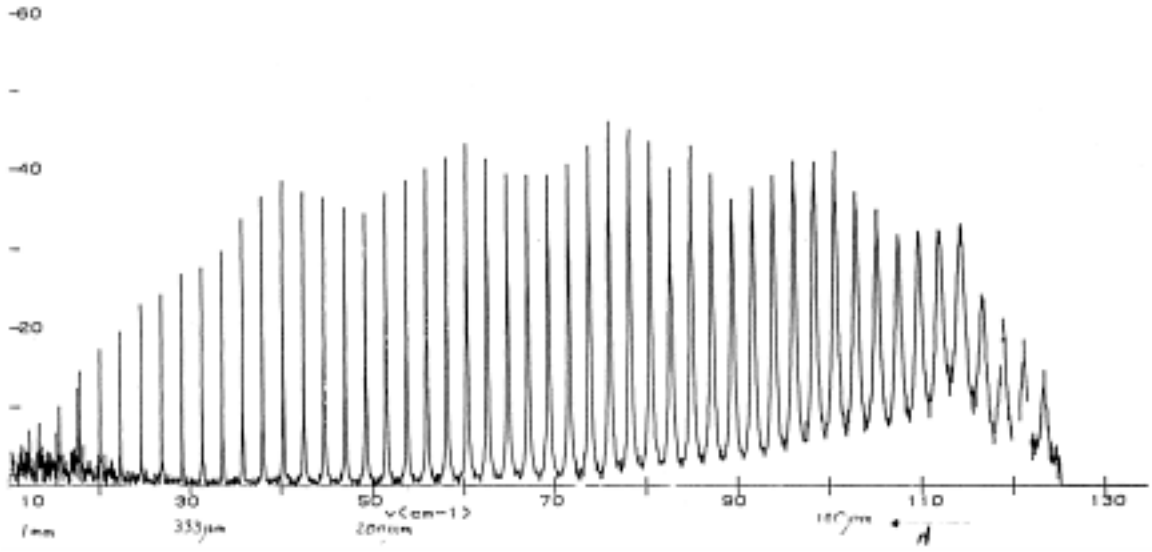

Figure 8.6 Scan of the Fabry-Perot transmission made on an FTS. The peak transmission is about 40% over the wavelength range of interest. The horizontal axis is in wavenumbers ($1\text{cm}^{-1} = 30\text{GHz}$). From Maffei (1994).

the filtering scheme will be changed in February 1999 to accommodate lower-loss filter elements, the basic optical path shall be unchanged. Light from the telescope enters at the top and is collimated at the Fabry-Perot etalon. The Fabry-Perot passes several orders in the window defined by the bandpass filter (330-360μm). This light is then diffracted off a grating which divides the orders by a sufficient angle such that, after being focused by a quartz lens, the different orders fall on the detector array separated by about 3mm. The detectors are each 1mm wide, so that the orders are well separated. After scanning the Fabry-Perot, matrix inversion can be used to restore the spectrum of the source.

From the long wavelength to short wavelength cutoff, the Fabry-Perot transmits orders 40 (375μm) to 45 (333μm), as shown in Figure 8.5. To create a continuous spectrum, the Fabry-Perot must be scanned over the full free spectral range $\Delta\lambda_{\rm SR} = 8.4\mu$m. The motion of the etalon is then $\Delta d = \lambda/2 = 188\mu$m. In order that we be able to use this etalon at longer wavelengths (up to 500μm), a minimum motion of 250μm is desirable.

8.2 Electronics for a Fabry-Perot Motor

8.2.1 Motor Servo Loop

In order that the Fabry-Perot be positioned to micron precision in a cryogenic environment, a spring-reciprocated solenoidal driver has been developed. A coil around the pole piece of a permanent magnet is energized such that its field either pulls it towards or pushes it away from the pole piece. A beryllium-copper leaf spring provides a restoring force that tends to bring the coil back into its rest position. The position of the coil is measured via a capacitive micrometer in which the capacitance of a moving plate with respect to a fixed plate is compared to a fixed reference capacitance. The motor servo loop for each of the three Fabry-Perot motors drives the coil such that the capacitive micrometer capacitance is some fraction of the reference capacitance. By adjusting the fraction, the capacitance (and hence the position) can

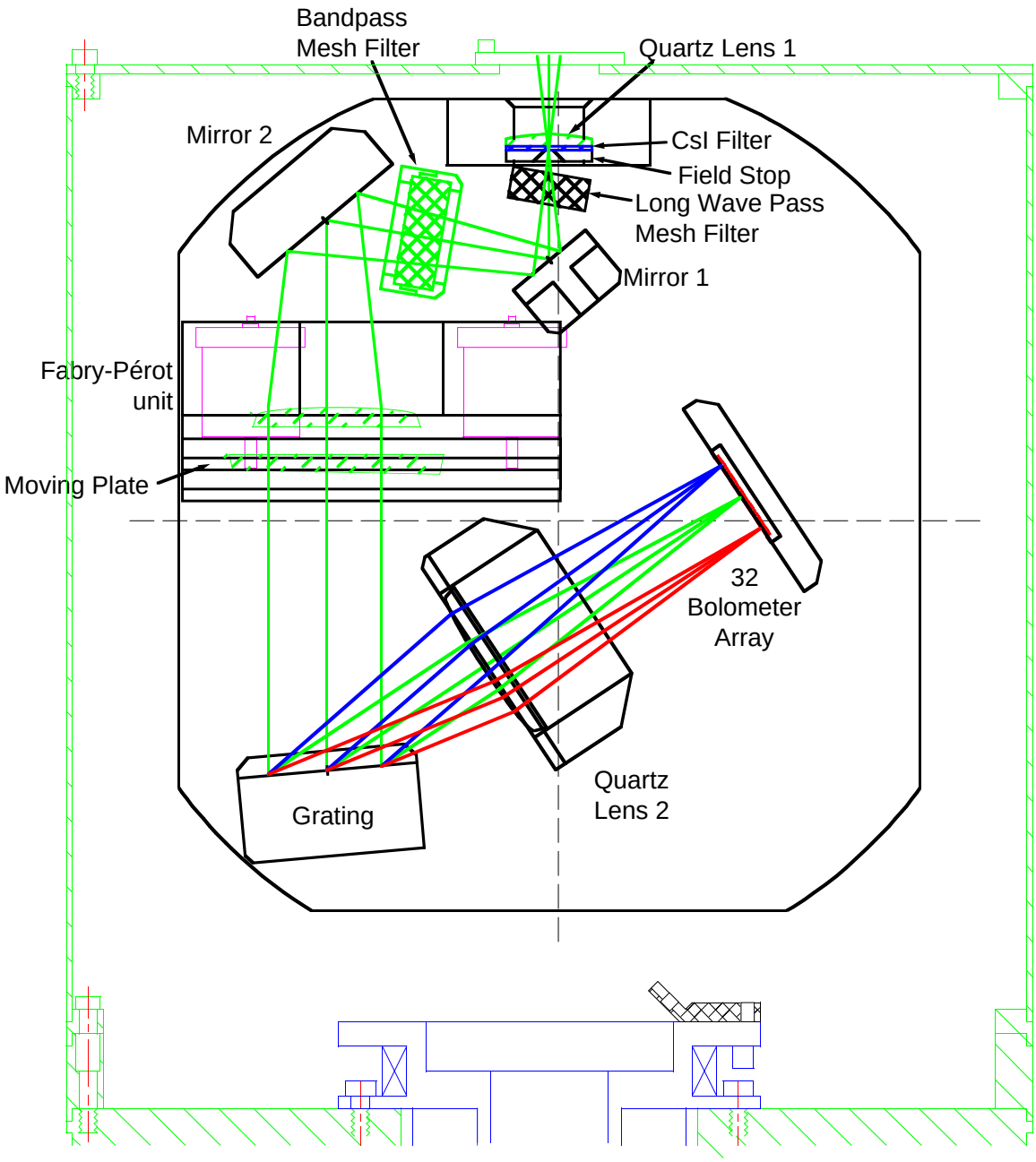

Figure 8.7 Layout of the optics of the Fabry-Perot spectrometer. Light enters at the top near the tertiary (relay optics) focus of the CSO. The expanding beam passes through the band-defining filters, then is collimated for the Fabry-Perot and order sorting grating. The final quartz lens focuses the ~ 8 transmitted orders onto the 32 element bolometer array. Each order is received by ~ 3 detectors.

be controlled. Drawing heavily on a design made by CEA, I have designed and constructed (with electronics technician Jeff Groseth) a compact, low power Fabry-Perot controller board.

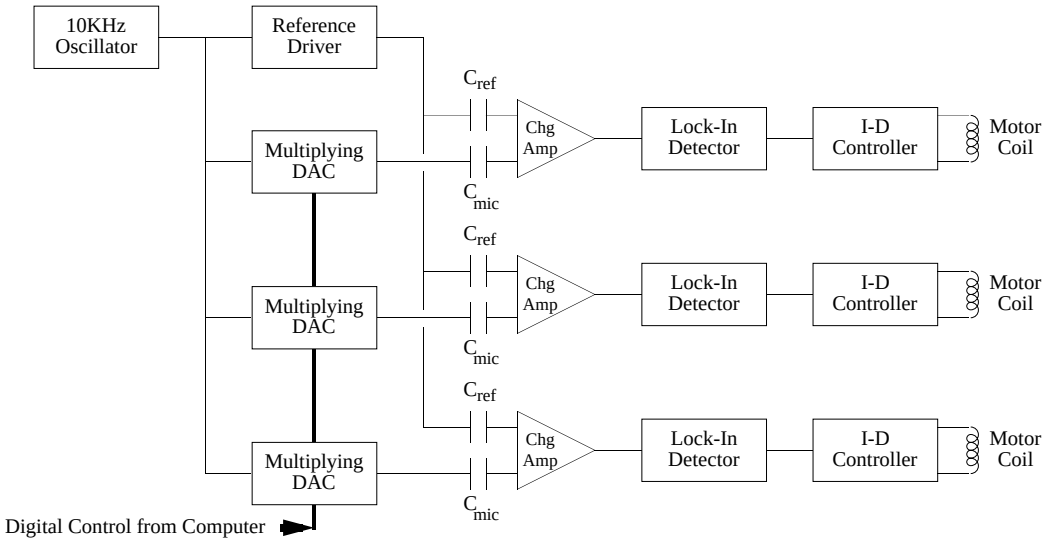

Figure 8.8 Block diagram of the control electronics for the three motors of the Fabry-Perot.

A block diagram of the electronics for controlling the Fabry-Perot motors is shown in Figure 8.8. A Wien oscillator produces a reference 10kHz sine wave which is used by the whole system. The user sends a set of three 16-bit digital commands to a multiple-channel multiplying digital-to-analog converter, which produces an excitation sine wave for each micrometer capacitor. This signal is used in a capacitive bridge circuit which reads out a capacitive micrometer. The error signal from the bridge is used in an integral-derivative (ID) controller which forces current through the motor coil to bring the bridge back into balance.

8.2.1.1 Capacitive Micrometer Readout

The micrometer readout circuit can be written schematically as a simple capacitive bridge, shown in Figure 8.9.

A fixed fraction of the 10kHz, 20 volt peak-to-peak sine wave is applied to the bridge. One arm passes through a resistive divider and is applied to a reference capacitor (C_{ref}). The other arm of the bridge is an effective resistive divider, where a

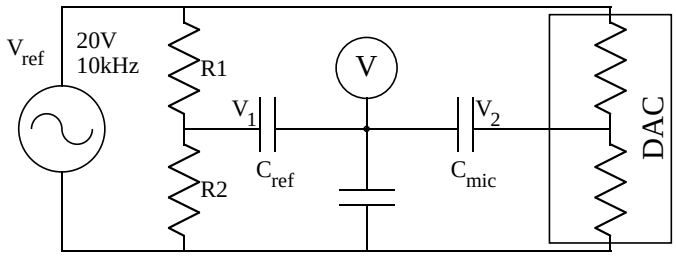

Figure 8.9 Schematic of the capacitive bridge circuit used to read the capacitive micrometers.

multiplying DAC allows the user to vary the voltage applied to the micrometer capacitor, $\mathrm{C_{mic}}$. The resolution of the DAC is 12 bits, providing control of the output voltage up to 20 volts peak-to-peak with a 5mV step. If one considers the instantaneous application of the voltages, the left arm of the bridge will build up a charge $\mathrm{Q_{ref}} = \mathrm{C_{ref}V_1}$ and, similarly, the right arm $\mathrm{Q_{mic}} = \mathrm{C_{mic}V_2}$. The capacitor $\mathrm{C_{ref}} = 100\,\mathrm{pf}$, while $\mathrm{C_{mic}}$ is formed of two optically polished copper plates held on either side of the Fabry-Perot etalon. With an area of $A = 6.16 \times 10^{-4}\,\mathrm{m}^2$, the capacitance (neglecting edge effects) is then:

$$\mathrm{C_{mic}} = \frac{\epsilon_0 \mathrm{A}}{\mathrm{d}} \;=\; \frac{5449}{\mathrm{d}(\mu\mathrm{m})}\ \mathrm{pf}. \tag{8.5}$$

The voltages must balance such that

$$V_{\mathrm{ref}} C_{\mathrm{ref}} \frac{R_2}{R_1 + R_2} \;=\; V_{\mathrm{ref}} C_{\mathrm{mic}} \frac{N}{4096} \tag{8.6}$$

for digital command $0 \leq N \leq 4095$. This can be rearranged to yield:

$$d(\mu\mathrm{m}) \;=\; \frac{N}{75.17} \frac{R_1 + R_2}{R_2}. \tag{8.7}$$

The resistance on the right is made adjustable, and is typically operated with $R_1 \simeq 10.7\mathrm{k}\Omega$ and $R_2 \simeq 0.9\mathrm{k}\Omega$, which gives the relationship between the etalon spacing and the digital command. Given that there is a fixed offset d_0 between the actual wire grid position and the measured capacitive sensor position, we have:

$$d(\mu\mathrm{m}) = d_0 + \frac{N}{5.83}, \tag{8.8}$$

which implies a step size of 0.172μm. The constants were measured by Schuller (1998) and found to be $d_0 = 7840\mu$m (but changeable upon each reassembly) and a step size of 0.176μm, correct to the precision to which the values of the components are known.

8.2.1.2 Controller Stage

In order to avoid losing valuable telescope time, the etalon must be able to acquire a new position during the time between successive dwells of the CSO chopping secondary. The output of the charge amplifier is lock-in detected using a synchronous rectifier and low pass filter, producing an error signal which can vary on time scales of milliseconds. An integral-derivative controller is used to produce an output current to the coil which is accurate over long time scales due to the integral term yet can respond quickly to requests for a new position due to the derivative term. Because the etalon must be acquire a new position while the chopping secondary mirror of the CSO is in motion, a process which takes about 40ms, the etalon servo loop must find its new position with a time constant of roughly 10ms.

8.2.2 Motor Coil Design

The motor coil bobbin must be an electrical insulator because it is attached directly to one side of the capacitive micrometer. The initial coils were made using fine (60μm diameter) copper wire on a sapphire bobbin for heat dissipation. With a maximal load of $\sim$ 10mW per motor at 1.4K, the etalon can rise in temperature to $\sim 6K$. In order to reduce this parasitic loading on the helium bath and the optical loading on the bolometers, I have redesigned the motor to operate using copper-clad NbTi superconducting wiring of 50μm diameter. This eliminates the thermal dissipation entirely, permitting the use of a macor (machinable ceramic) bobbin instead of the costly sapphire bobbin. With a thermal conductivity at liquid helium temperatures of 10^{-3} of sapphire (Childs, Ericks & Powell 1973; Lawless 1975), the macor would heat up substantially if any power were dissipated into it. The redesigned Fabry-Perot motor will be tested this spring.

8.3 Verification of the Fabry-Perot Spectrometer

We have used the Fabry-Perot to detect the output of a Gunn oscillator and multiplier source. Shown in Figure 8.10 is a Fabry-Perot spectrum of a phase-locked Gunn oscillator and multiplier local oscillator source. A polyethylene lens was used to focus the output of the multiplier onto the Fabry-Perot such that the coupling efficiency was not unreasonably small. A test set of bolometers operating at 1.5K were used as detection elements to record the spectrum. At an output of 894.831GHz (335.027μm), the Fabry-Perot spectrum has a wavelength resolution of $\Delta\lambda = 0.34\mu$m, or $R = 985$. While this is worse than the design value of 1500−2000, this spectrum validates the optical setup, the capacitive readout and servo control, the wavelength calibration, and the inversion software.

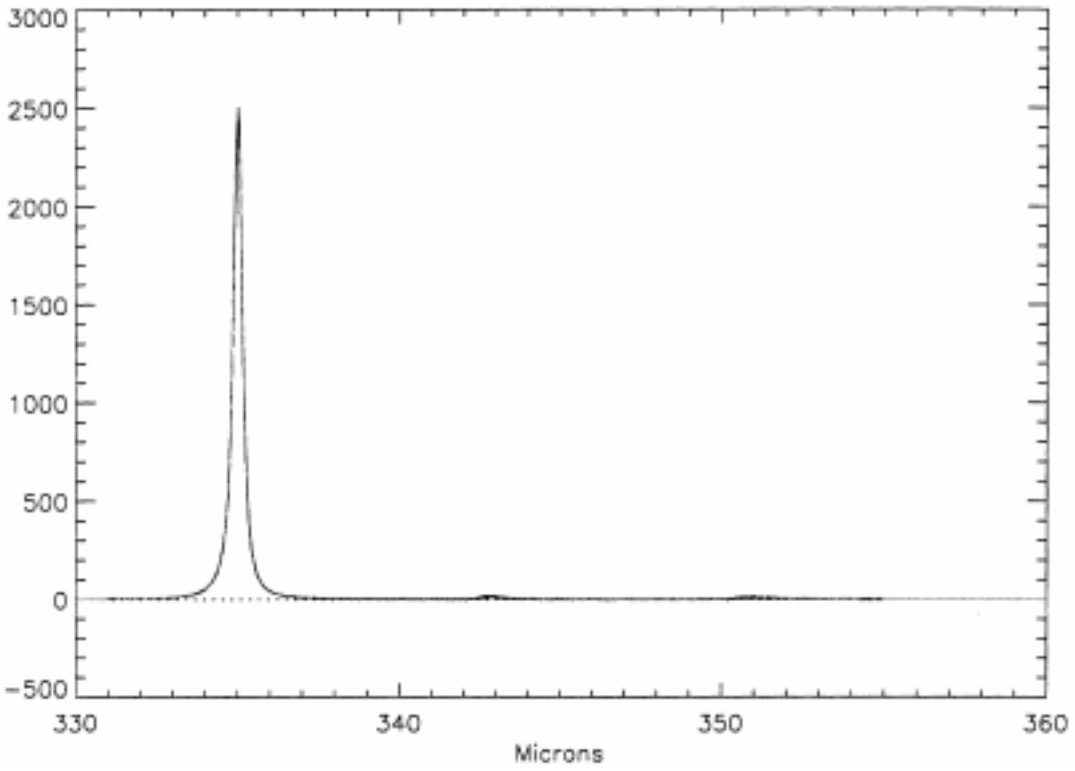

Figure 8.10 Spectrum made using the Fabry-Perot with a Gunn oscillator and multiplier as a source. The vertical scale is in arbitrary units. From Schuller (1998).

During the system integration in July of 1998, the Fabry-Perot unit was tested at Caltech using a similar local oscillator system (courtesy of Jonas Zmuidzinas & Dave

Miller) phase-locked at 830.02 GHz (361.44μm). The Fabry-Perot was stepped in $\partial = 0.8\mu$m intervals, resulting in a sampling interval of $\sim 2\partial/m = 0.04\mu$m. Approximately $^1/_3$ s of data were taken at each point until a complete spectrum around the peak had been recorded. Shown in Figure 8.11 is a Fabry-Perot spectrum of this source, showing the main peak and several ghosts. The inversion algorithm was optimized for the setup in France, and small changes during the system integration at Caltech result in an inversion which yields ghosts. Evidence of a miscalibration can be seen if we look at a blowup around the main peak (Figure 8.12, and see that the line falls 0.7μm shortward of its true position. At this wavelength, the FWHM of the main peak is 0.45μm for a resolution of about $R = 800$. It may be possible that the line is artificially broadened by the poor inversion: studying the variation in flux during the scan permits an estimation of the resolution at $R \sim 1000 - 1100$ (Schuller 1998). Furthermore, a test of the finesse based on measurements with a visible laser estimate a resolution of ~ 1300 (Maffei 1994), dominated by a lack of parallelism of the reflecting surfaces. We hope to improve the spectral resolution and generalize the inversion software in the near future.

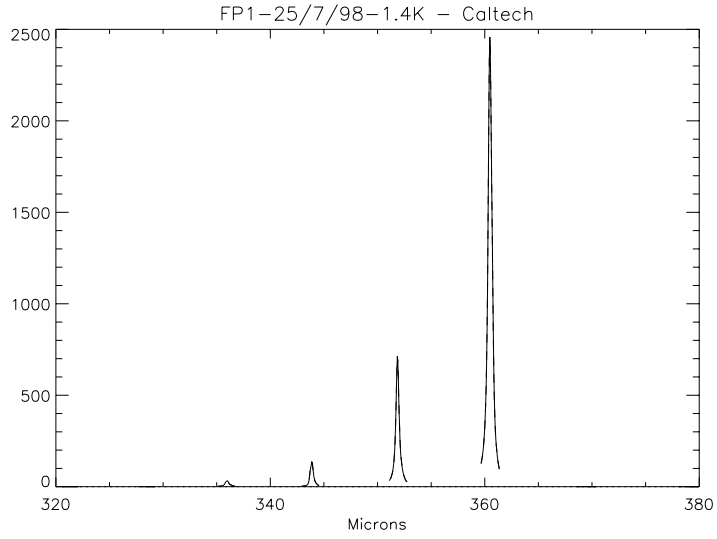

Figure 8.11 Spectrum made at Caltech using the Fabry-Perot with a Gunn oscillator operating at 361.44μm.

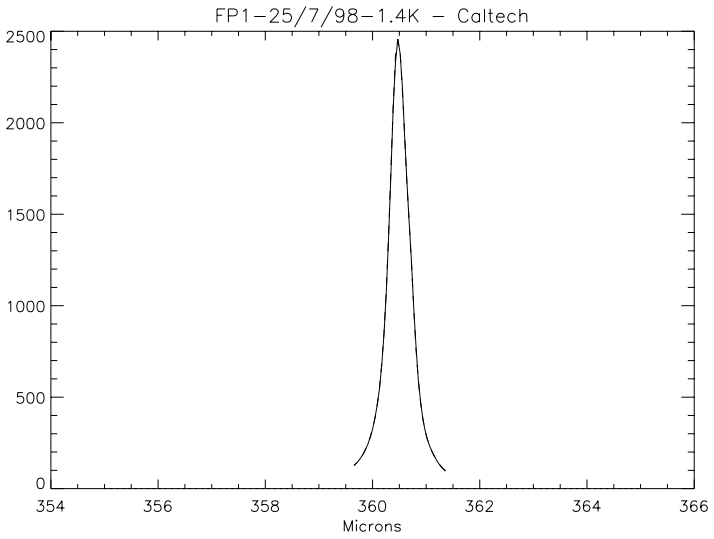

Figure 8.12 Spectrum made at Caltech using the Fabry-Perot with a Gunn oscillator operating at 361.44μm.

Chapter 9 Design of a Submillimeter Grating Spectrometer

Whereas it became apparent, roughly five to ten years ago, that the detection of highly redshifted emission lines in the observed wavelength band of $300\mu\mathrm{m} - 500\mu\mathrm{m}$ would be scientifically useful but not possible with the existing instrumentation, several people at Caltech and elsewhere began to conceive of new instruments designed specifically for this purpose. Background-limited spectrometry with instantaneous velocity coverages approaching 10,000 km/s cannot currently be achieved with any existing submillimeter spectrometers. Heterodyne spectrometers will eventually reach this limit, but this will take time. A bolometer-based Fabry-Perot, as described in the preceding chapter, can achieve this coverage at the expense of requiring more integration time (by an order of magnitude) to build up a complete spectrum. It was realized by Gene Serabyn, Tom Phillips, and myself that a tunable grating spectrometer would be a far more appropriate instrument for observing galaxies with known redshifts. As a consequence, I have developed such a spectrometer and provided proof-of-principle using laboratory measurements and optical modeling of the required components. This design was published under the authorship of myself, Gene Serabyn, Tom Phillips, and Harvey Moseley (Benford et al. 1998a).

9.1 Necessity of a Grating Spectrometer

One of the central issues in astronomy is the formation and evolution of galaxies at large redshifts. Submillimeter observations are essential to understanding these processes. One of the best prospects for high redshift submillimeter observations is the study of the CII 158μm fine-structure line, which carries about 0.2% of the total luminosity of nearby starburst galaxies (Stacey et al. 1991). However, current hetero-

dyne receivers at submillimeter observatories have insufficient bandwidth to detect the full extent of highly broadened emission lines. We are developing a broadband grating spectrometer for the Caltech Submillimeter Observatory with a total bandwidth of ∼3400 km/s and a velocity resolution of 200 km/s. The detectors will be a linear array of 32 close-packed monolithic silicon bolometers developed at NASA's Goddard Space Flight Center. In order to achieve background-limited sensitivity, the bolometers will be cooled to 100mK by an adiabatic demagnetization refrigerator. The spectrometer optics will consist of a tunable cryogenic immersion grating using broadband filters as order sorters. The spectrometer will be optimized to operate in the 350μm and 450μm atmospheric windows. Calculations of the sensitivity of the spectrometer reveal that an ultraluminous infrared galaxy of 10^{12} $L_{\odot}$ at a redshift of $z = 1$ would be detectable at the 5σ level in the CII line with one hour of on-source integration time.

The growing interest in submillimeter spectroscopy is evident from the amount of work reported in recent astronomical results (Phillips 1997). Heterodyne spectrometers in the ∼1 THz region use SIS junctions, Schottky diodes or HEB detectors[1] as the sensing element, mixing incident radiation down to a low enough frequency for subsequent amplifier and spectroscopic technologies. These include acousto-optical spectrometers (Schieder 1998), digital correlators (Von Herzen 1998) and analog correlators (Harris & Isaak 1998). While such technologies allow virtually unlimited spectral resolution, the practical limit to total bandwidth is still small: 1 GHz is typical for current telescopes. Future improvements will increase this by a factor of ∼4 in the coming decade, but heterodyne spectrometers with total bandwidths of several percent of the observing frequency are still far away. A good review of present heterodyne technologies is given by Carlstrom & Zmuidzinas (1996). A comparison with direct detection techniques is given by Phillips (1998).

As detection technology has improved, astronomers have pushed detections out to ever-greater distances. For objects at redshifts greater than 2, many lines with rest frequencies which are inaccessible from the ground are redshifted into atmospheric

[1]Hot Electron Bolometers (e.g., Kawamura et al. 1998).

windows. These include the higher J CO transitions and fine-structure lines of CI, CII, OI and NII, spanning frequencies from 500 to 5000 GHz. To date, only the lower frequency lines have been detected. Millimeter telescopes have provided most of the scientific results thus far (e.g., Barvainis et al. 1997; Scoville et al. 1997; Guilloteau et al. 1997), in part due to their greater fractional bandwidths. The ability to search a large segment of velocity space will be crucial in the coming years to enable the study of high-redshift galaxies.

9.1.1 Submillimeter Spectrometers

We shall compare the optical techniques for submillimeter instrumentation in terms of their background-limited noise performance, bandwidth, and spectral resolution. Specifically, we choose as our figures of merit: the noise bandwidth $\delta\nu_{\rm noise}$; the total instantaneous inverse fractional bandwidth of the instrument, which we define as $B \equiv \nu/\Delta\nu$; and the spectral resolution ($\Re \equiv \nu/\delta\nu$). Scientific goals demand a velocity coverage much greater than the kinematic width of a galaxy's emission, so 2000 km/s requires $B \leq 150$. Similarly, in order to achieve the greatest signal-to-noise we need only to barely resolve the lines spectrally; 100 km/s necessitates $\Re \geq 3000$. If we consider the highest submillimeter frequencies observable from the ground, $\sim$850 GHz, then the desired $\Delta\nu = 6$ GHz and the desired $\delta\nu \leq 0.3$ GHz.

Whilst current heterodyne receiver technologies are limited by backend spectrometers to $\sim$1 GHz, 4 GHz will soon be available. With a 1000 channel spectrometer, this yields $\Re = 3 \times 10^5$ and $B = 850$ (improving to 280 in the near future). Fourier transform spectrometers like that at the CSO (Weisstein & Serabyn 1994) can achieve $\Re = 5000$ and $B \sim 3$. A Fabry-Perot used in an imaging mode (i.e., no order sorting) can achieve a resolution of $\Re = 2000$ using 95% reflective surfaces (finesse $F = 50$), with a bandwidth limited only by atmospheric windows to $B = 10$. Continuum (bolometric) instruments are at the $\Re \sim 10$ level with no spectral information, so $B = 10$. A hypothetical grating spectrometer with 32 detectors to cover 16 spectral elements is listed along with the above instruments in Table 9.1. The noise bandwidth for

each instrument as a function of its resolution is also listed, indicating the differences in different optical methods. Figure 9.1 compares the existing high resolution spectrometers to the astronomical objects observable.

Table 9.1 Resolutions, bandwidths, and noise bandwidths of submillimeter instrumentation operating near 850 GHz. $\Delta\nu$ is the total instantaneous bandwidth, whilst $\delta\nu$ is the bandwidth per spectral element; the noise bandwidth is a somewhat vague figure of merit, since Fabry-Perot and FTS techniques require scanning which changes the effective integration time per spectral element as compared to the other spectrometers.

Technology	$\Re$	B	$\delta\nu_{noise}$
Heterodyne Spectrometers	300,000	850-280	$\delta\nu$
Fourier Transform	5,000	3	$\Delta\nu/2$
Imaging Fabry-Perot	2,000	10	$\Delta\nu/F$
Grating Spectrometer	1,500	100	$\delta\nu$
Continuum Bolometers	10	10	$\delta\nu$

Based on the simple outline above, a grating spectrometer is the most desirable possibility for targeted observations where the redshift is known to $\sim 1\%$. Fabry-Perots are well suited to imaging spectroscopy unless an order sorting grating is used, which puts them on an equal footing with grating-only spectrometers. FTS methods are better suited to objects with unknown redshifts, but because of their large noise bandwidth are not very sensitive. Heterodyne spectrometers are most useful when the redshift is very well known. We have therefore designed a grating spectrometer to achieve sufficient bandwidth and sensitivity to detect distant galaxies with approximate redshifts known from optical and near-infrared techniques.

9.2 Grating Spectrometer Fundamentals

The principle of the diffraction grating was discovered by Rittenhouse (1786), though not applied until somewhat later (Fraunhofer 1823). The theory is well explained in Born & Wolf (1959). Basically, the idea is to divide a collimated beam of light into

several subsections, introducing a phase delay into each subsection. This can be done by requiring the input and output beams to be at an angle to a reflective surface with grooves in it, as indicated schematically in Figure 9.2 below. In this sketch, the grooves are angled ("blazed") so that the direction of diffracted light is also the direction of specularly reflected light. The path length difference between any two adjacent rays is then

$$\xi\big[\sin(\vartheta) - \sin(\varphi)\big], \tag{9.1}$$

where φ and ϑ denote the input and output beam angles with respect to the grating normal $G_\perp$, and ξ is the center-to-center spacing of the grooves. Requiring that the net result be in phase, we find that for a wavelength λ the maxima in reflection off a

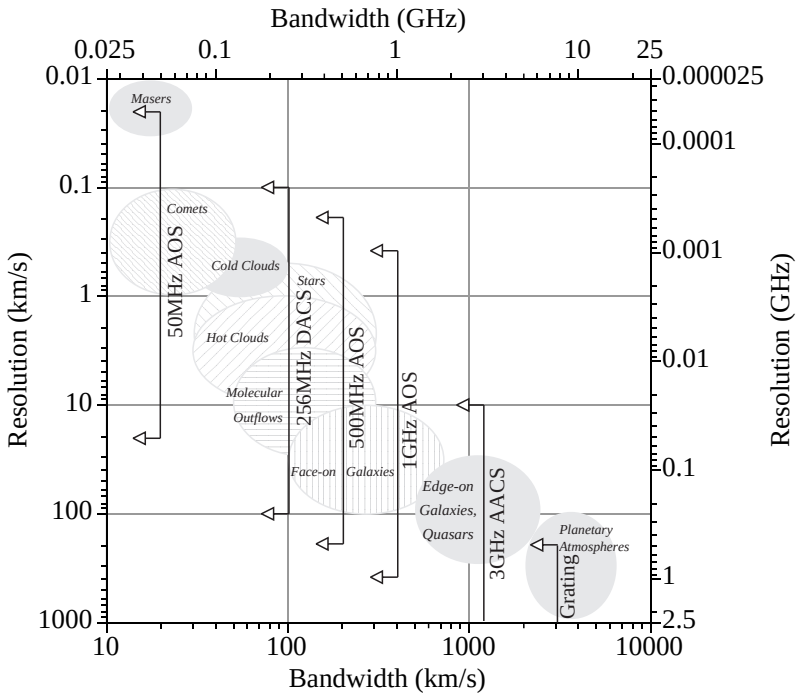

Figure 9.1 Resolution and bandwidth for existing spectrometers operating at 750 GHz (plain text and arrows) and astronomical sources (italicized text and grey areas). FTS/Fabry-Perot techniques have sufficiently broad bandwidths that they do not appear on this chart; they lie off the lower right edge.

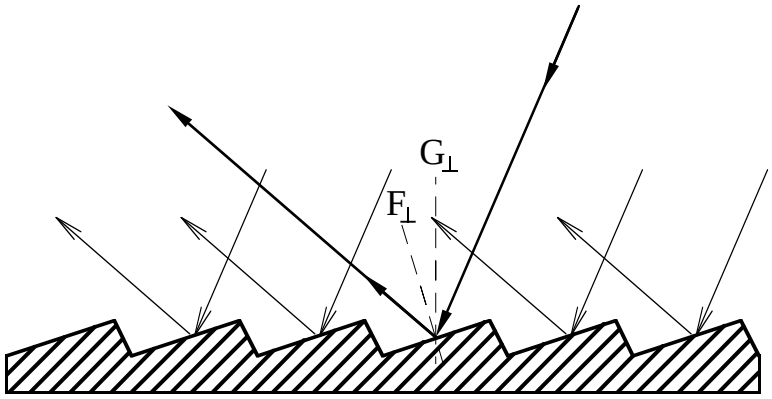

Figure 9.2 Geometric layout of a blazed grating indicating the normal direction of the facets ($F_\perp$) and the grating plane ($G_\perp$).

grating occur when

$$\sin(\vartheta) - \sin(\varphi) = \frac{m\lambda}{\xi}, \tag{9.2}$$

where m is the *order* of interference and takes on integral values. We can see from equation 9.2 that a source of white light limited to a sufficiently narrow band at an angle φ will produce a dispersed spectrum of light at the output, with ϑ proportional to $\sin^{-1}(\lambda)$. The term "sufficiently narrow band" is necessary because a wider band will cause orders to overlap, i.e., $m\lambda_1 = (m+1)\lambda_2$ if λ_1 and λ_2 are widely separated. This defines the *free spectral range* of a grating, analogous to that of the Fabry-Perot. Numerically, it is given by

$$\frac{\Delta\lambda_{\mathrm{SR}}}{\lambda} = \frac{1}{m} \tag{9.3}$$

which is dependent upon the order alone, whereas for the Fabry-Perot it depended on the etalon spacing.

9.2.1 Immersed Gratings

A general guiding principle for interferometric techniques is that the resolution is given by the number of wavelengths of path difference between beams. In the case

of a reflection grating, this difference is merely twice the grating depth. A resolution of 3000 at 400μm thus requires a 60cm grating, unwieldy in a cryogenic environment but possible (Erickson et al. 1984). A well-known method for increasing the spectral resolution of a grating is to immerse it in a medium of high index n (Dekker 1996), as shown in Figure 9.3. An *immersed grating* therefore reduces the volume requirement on a cryogenic environment by a large factor.

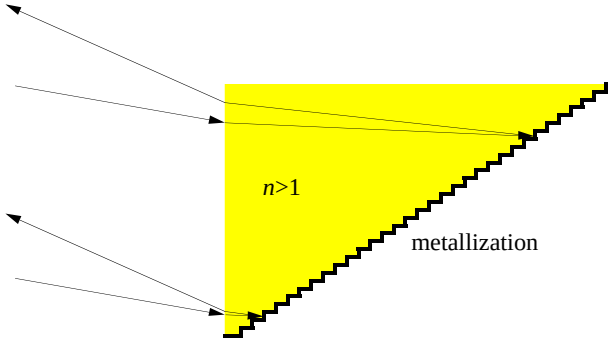

Figure 9.3 Schematic of an immersion grating. The grating depth is increased in number of wavelengths by a factor of n.

The grating equation for a plane grating immersed in a material of index n is:

$$m\lambda = n\xi[\sin(\vartheta) \pm \sin(\varphi)], \tag{9.4}$$

where again m is the order, ξ is the grating constant, and φ and ϑ the incident and reflected angles. In near-Littrow configuration, when the incident and reflected beams are nearly parallel, this reduces to $m\lambda = 2n\xi\sin(\varphi)$. A given grating has fixed n and ξ, so we can choose φ to illuminate detectors with light at wavelength λ. The order m must be determined, usually through prefiltering or (in the near-infrared) using a cross-dispersing grating.

Ground-based submillimeter telescopes can access only two windows at frequencies above 500 GHz: the 350μm and 450μm windows. The ratio of these wavelengths is 7:9, implying that for a fixed φ, the windows are transmitted through a grating operating in the 9th and 7th order, respectively. It is then possible to order sort using bandpass filters, thereby reducing the angle through which the grating must

be rotated to cover the full range of both windows. This is particularly important in the case of immersion gratings: Snell's law shows that a small angular change at the grating corresponds to a larger angular change in vacuum. Put another way, a beam of collimated light in vacuum entering the grating block at an angle φ' will be incident upon the grating surface at $\varphi = sin^{-1}(sin(\varphi')/n)$. This relationship is shown in Figure 9.4. The grating depth increases as $\sin(\varphi)$, making it favorable to operate with $\varphi > 45°$. It is also possible to increase the width of the collimated beam, but this increases the mass and cost of the immersing medium.

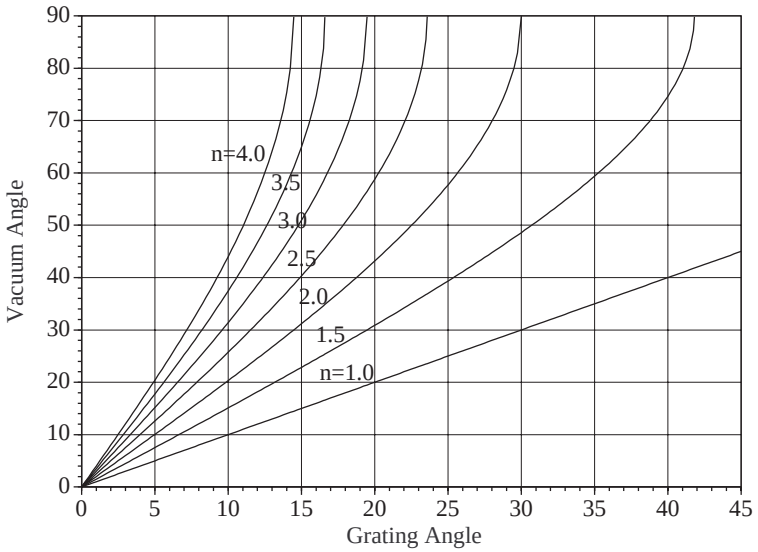

Figure 9.4 Rotation angle for given grating angle (assuming that blazed operation is at 0°) as a function of index.

The choice of an immersing medium is driven toward maximizing the index of refraction, but one must also try to minimize cost, difficulty of manufacture, and absorption coefficient. Typically, these immersed materials must be cooled, as the absorption coefficients drop substantially between room and liquid helium temperatures. Considering frequencies of ~ 1 THz, polymers typically (Lamb 1996) have refractive indices of $n \sim$1.5 and absorption coefficients of $\alpha \sim 0.3$ cm^{-1}, quite poor parameters. Quartz is better in both respects, with $n = 2.131$ and $\alpha = 0.1$ cm^{-1} at 10K (Bréhat & Wyncke 1997). Silicon is an attractive material, with $n = 3.382, \alpha = 0.1 \pm 0.2$ at 1.5K (Loewenstein, Smith & Smith 1973). Unfortunately, it is a difficult material to

machine using conventional techniques, though the method of etching a grating into a silicon surface is well-established (Graf et al. 1994). A still higher refractive index is found in germanium, with $n = 3.928$ (Loewenstein, Smith & Smith 1973); an upper limit to the absorption coefficient of $\alpha = 0.1 \pm 0.2$ at 1.5K. Therefore, we chose to explore designs using germanium.

9.3 FTS Studies of Germanium

A germanium-immersed grating with $\Re \sim 1500$ near 400μm requires a grating depth of 7.5cm. Should the absorption coefficient be even as much as 0.1 cm^{-1}, the intensity of the beam on the most-delayed path will be only 25% of that of the least-delayed path, reducing the grating efficiency. If we set a minimum differential absorption between paths at 75%, the germanium must have an absorption coefficient of less than 0.02 cm^{-1}. While the absorption of germanium has been measured at higher temperatures (Loewenstein, Smith & Smith 1973), a pure semiconductor should have no far-infrared absorption mechanisms as it cools towards absolute zero. Only the impurities will contribute at liquid helium temperatures. To determine if this is the case, we performed accurate measurements of the loss of germanium at 1.5K.

The optical measurements of germanium were made using a large-throughput, high resolution Fourier transform spectrometer (FTS). This instrument has been described by Bin et al. (1999). Our detector was a 1.5K bolometer (Infrared Laboratories) using an $f/6$ Winston cone as a light concentrator. A cold filter wheel with six spaces sits immediately in front of the entrance aperture to select between the various thicknesses of germanium samples. The cryostat, also made by Infrared (Laboratories), has a custom-machined paraboloidal mirror immediately in front of the entrance window. The paraboloid is placed after the final focus of the FTS, such that the optically modulated light from the FTS is then collimated when entering the dewar. In this way, changes in the optical depth of the material in the beam (e.g., when a thick germanium slab is moved in and out of the beam) do not change the focus. An aperture in the collimated portion of the FTS itself (just before the final paraboloidal

mirror) restricts the field of view to that appropriate to an $f/6$ beam. The lowpass filters in the cryostat provide an effective usable bandpass of 300 to 1600 GHz. At lower frequencies, optical efficiencies and source powers drop rapidly.

For the highest quality data, the samples were provided by Oxford Instruments. We used four right circular cylinders of 2.5cm diameter and thicknesses of 2, 4, 8, and 18mm. Each cylinder was cut from the same boule of highest purity, single crystal germanium and ground and polished to have planar end surfaces. One additional sample, 16mm thick, was used. The sixth space was left blank for calibration. While chopping between a hot ($\sim$ 900 K) load and a cold ($\sim$ 80 K) load at 200 Hz, the moving mirror of the FTS was scanned at 40μm s^{-1} with an integration time constant of 300ms. The unapodized frequency resolution was 14.6 GHz, requiring approximately 35 minutes per symmetric scan. This resolution is coarse enough so that the Fabry-Perot fringes in all samples were smeared out to an acceptable level. Two scans were taken on each of the five samples. Additionally, a higher resolution (920 MHz) scan was taken on the thinnest piece and the clear aperture in order to measure the index of refraction accurately.

The scans were Fourier transformed and phase corrected to compensate for zero-

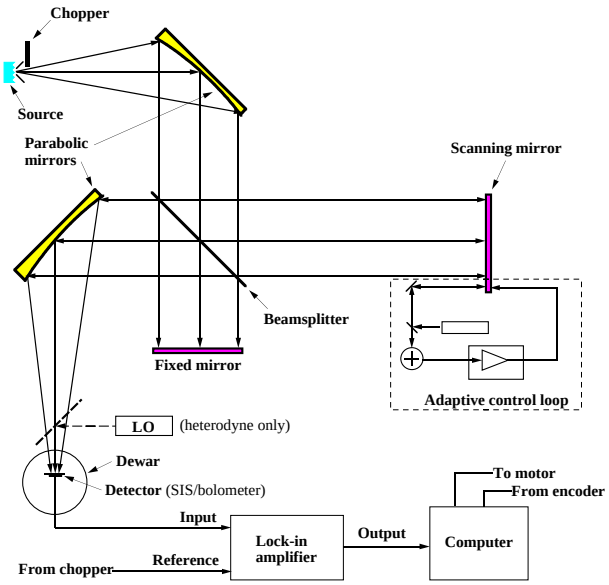

Figure 9.5 Schematic layout of the FTS system used for studying the optical properties of materials at submillimeter wavelengths.

position error. Each sample's two scans were averaged to improve the signal-to-noise. The final five spectra were than paired together in the ten possible combinations and ratioed to find the transmission $T_{\rm net}$ of the effective germanium slab with a thickness given by the difference of the thickness between the two pieces. This method reduces the chance of systematic effects in the data due to reflection at the vacuum-germanium interface. Since the absorption $A \equiv 1 - T_{\rm net}$ for an effective thickness of t is given by $A = \exp[-\alpha t]$, we found the absorption coefficient for each of the ten pairs by inverting this expression. The mean of the ten pairs of transmission and absorption coefficient measurements is presented in Figure 9.6. If we further take the variance of the absorption coefficient measurement between 500 and 1000 GHz, we find that absorption coefficient is $\alpha \leq 0.009$ cm^{-1} $(1\,\sigma)$.

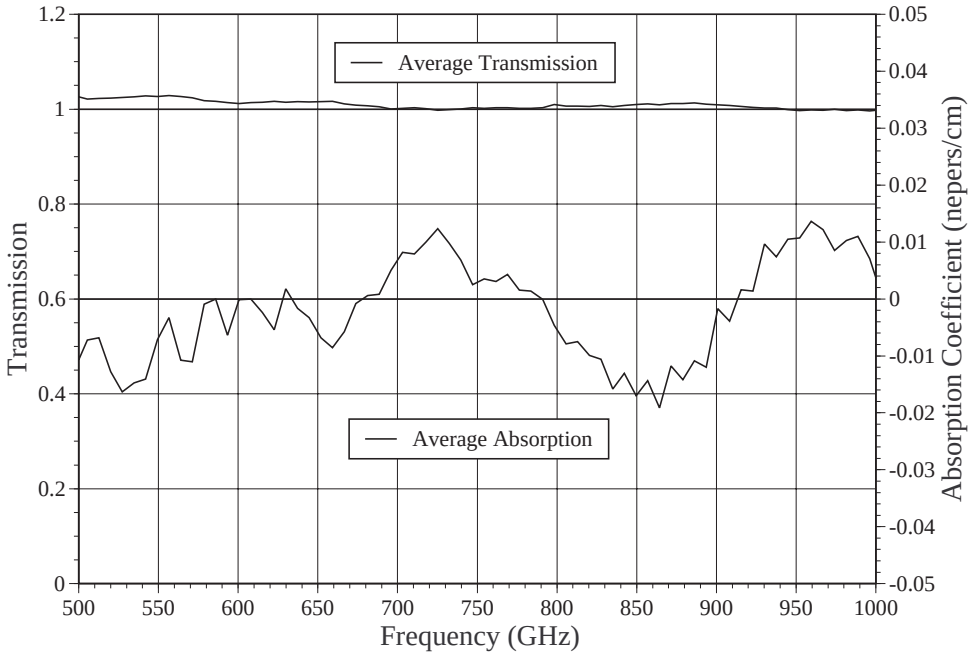

Figure 9.6 Mean transmission (top) and derived absorption coefficient (bottom) for germanium between 500 and 1000 GHz. The variance in the absorption coefficient yields $\alpha \leq 0.009$ cm $^{-1}$.

We used the high spectral resolution measurement to fit the Fabry-Perot fringes in the germanium, and found $n = 3.937 \pm 0.020$. In the past, our previous set of samples yielded $n = 3.907 \pm 0.015$. Taking the mean, we find that $n = 3.92 \pm 0.01$, in excellent agreement with Loewenstein, Smith & Smith (1973). Our precision is

limited by our knowledge of the thickness of the samples, which are typically only 2mm thick.

Using this measured limit, a grating depth of 7.5 cm implies a transmission through the germanium (neglecting surface effects) is $> 87\%$ ($1\,\sigma$) or $> 67\%$ ($3\,\sigma$). This is sufficiently high efficiency for our purposes.

9.4 Optical Design of the Grating Spectrometer

The optical design of the grating spectrometer was carried out using *Code V* (Optical Research Associates) software. The CSO has a Cassegrain reimaging system (Serabyn 1997) which yields a low-aberration $f/4.48$ focus with a convenient mounting surface for dewars. The design also places an image of the primary 142mm from the focus, enabling a closed cold optics system to be used to define the beam (Hunter, Benford & Serabyn 1996). However, a Gaussian optics calculation reveals that for an instrument with a single diffraction-limited beam, an aperture stop can be placed as close as 50mm from the focus. After many possible designs were considered, the simple design illustrated in Figure 9.7 was chosen. The grating is operated in Littrow[2] mode, with the beams displaced from each other in the direction normal to the page; this is highlighted in Figure 9.8. A single off-axis paraboloid is first used to collimate, then refocus the diffracted beam. The collimated beam is 50mm in diameter, which (with an $f/4.48$ beam) requires a focal length of 224mm. Parallel light is then incident on the germanium surface followed by the grating surface, tilted at an angle of 55° with respect to the germanium surface. A 50mm diameter collimated beam with this angle provides a grating depth of

$$2 \times 50 \tan(55^\circ) n \;=\; 560\,\mathrm{mm} \qquad \text{so that at } \lambda \;=\; 400\mu\mathrm{m}, \qquad \Re \;=\; 210\,\mathrm{km/s}. \tag{9.5}$$

The whole immersion grating is rotated about an axis lying in the plane of the germanium surface rather than the grating surface, because in this configuration the

[2]This is the configuration in which the grating input and output beams are superposed

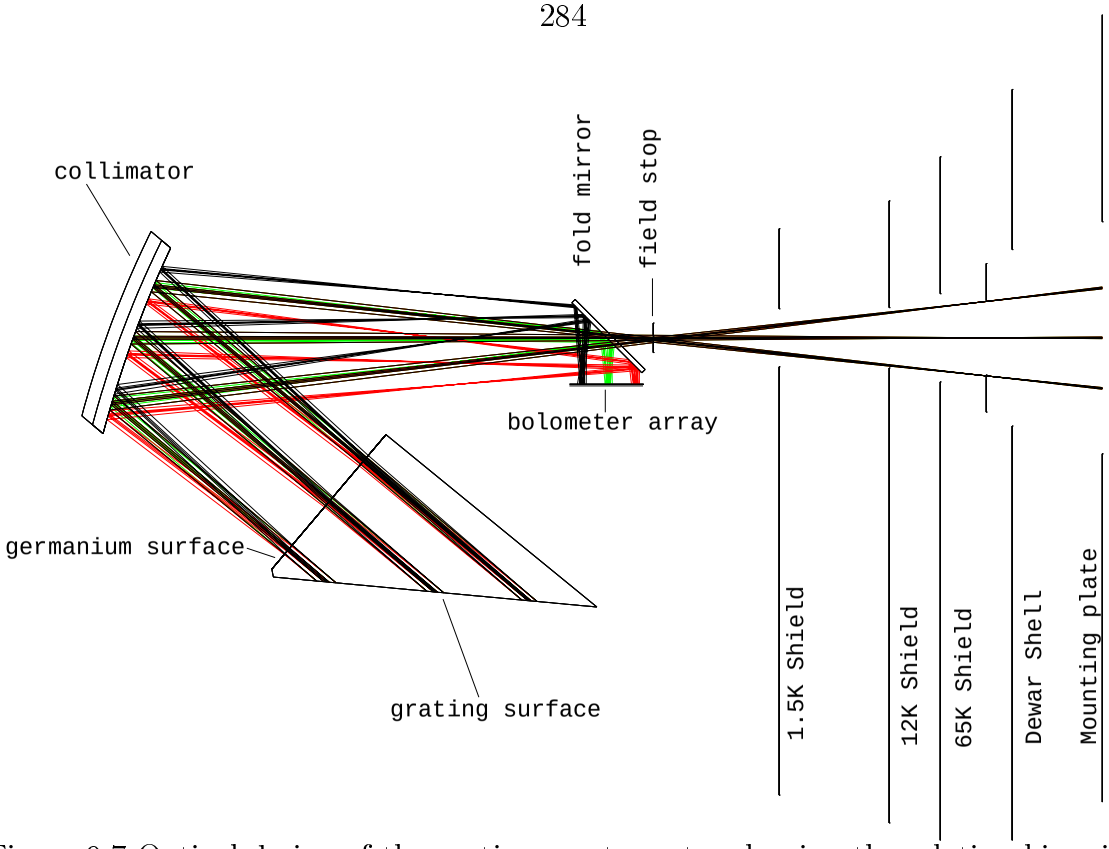

Figure 9.7 Optical design of the grating spectrometer showing the relationship with the cold surfaces. The three sets of rays indicate wavelengths of 452, 450, and 448 μm. The grating is rotated about an axis directed out of the page, at the center of the germanium surface.

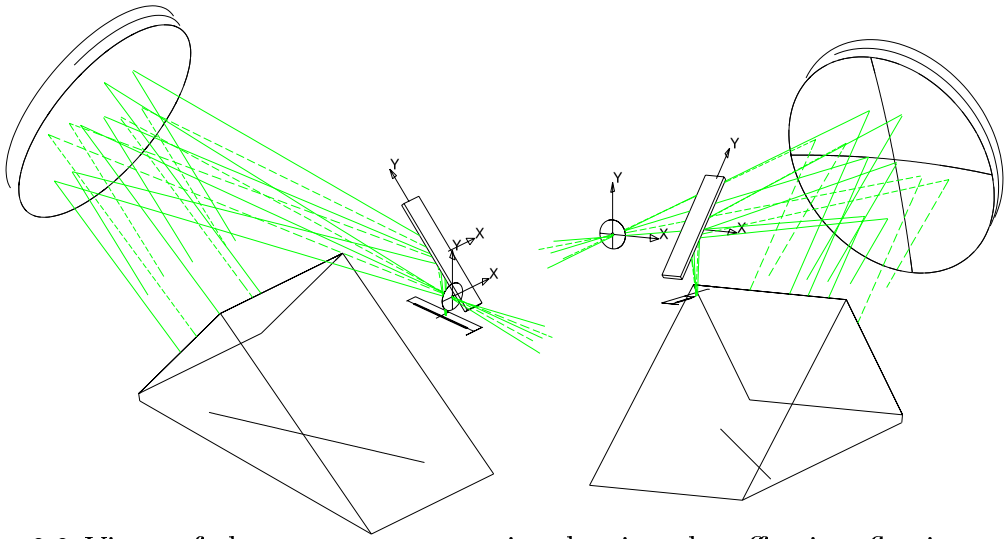

Figure 9.8 Views of the spectrometer optics showing the off-axis reflection used to separate the field stop from the final focus. The triangular piece represents the germanium, with the grating surface indicated by a diagonal line. The long, thin slab at 45° is the fold mirror, while the flat rectangular surface beneath it represents the detector array.

angular changes in the beams do not also involve positional changes. The germanium surface is chosen to be normal to the incident beam at the center of the grating rotation range. Velocity resolutions and channel widths as a function of wavelength are shown in Figure 9.9. A diagram of the optical layout, for wavelengths of 425, 450 and 475μm, is shown in the complete configuration in the cryostat in Figure 9.10.

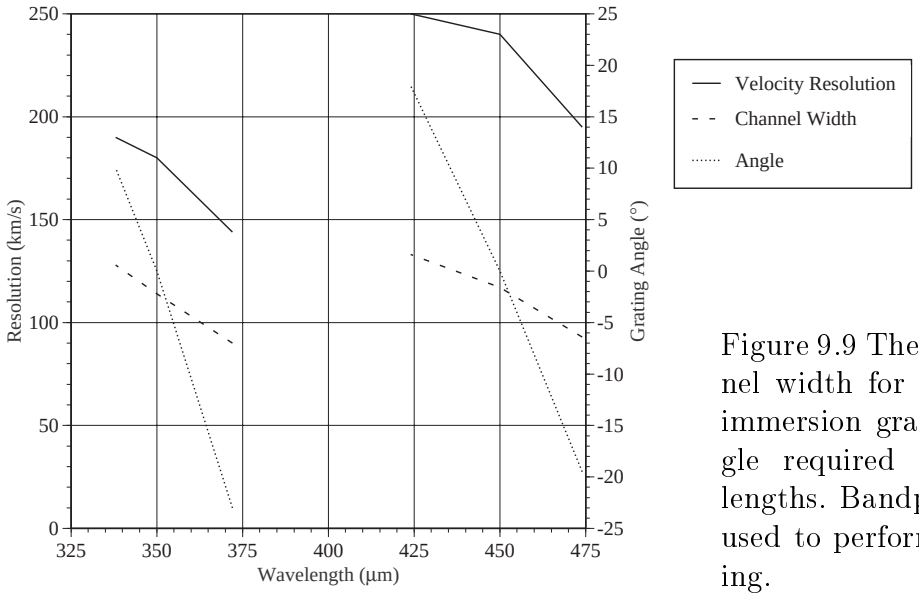

Figure 9.9 The resolution, channel width for 1mm pixels, and immersion grating rotation angle required for given wavelengths. Bandpass filters will be used to perform the order sorting.

The germanium block is a 7cm×10cm cylinder cut diagonally to produce an oval face for the grating surface. Antireflection coating on the planar surface will be provided by a dielectric coating. Using a 50μm thick layer of quartz on the front surface will yield an average transmission after two passes of $> 90\%$ for the wavelengths of interest. The mechanical design uses a stepper motor to rotate the grating with a direct position readout provided in situ by a potentiometer. Optical baffling is used to prevent stray light from other orders from reaching the detector.

9.5 Project Status

Currently, foreoptics (dewar extension, filter wheel components) and grating motion components have been fabricated and tested. A detector array mount and the associated circuit board and FET amplifier boxes have been manufactured and are in the process of being commissioned. The remaining work is to machine the optics

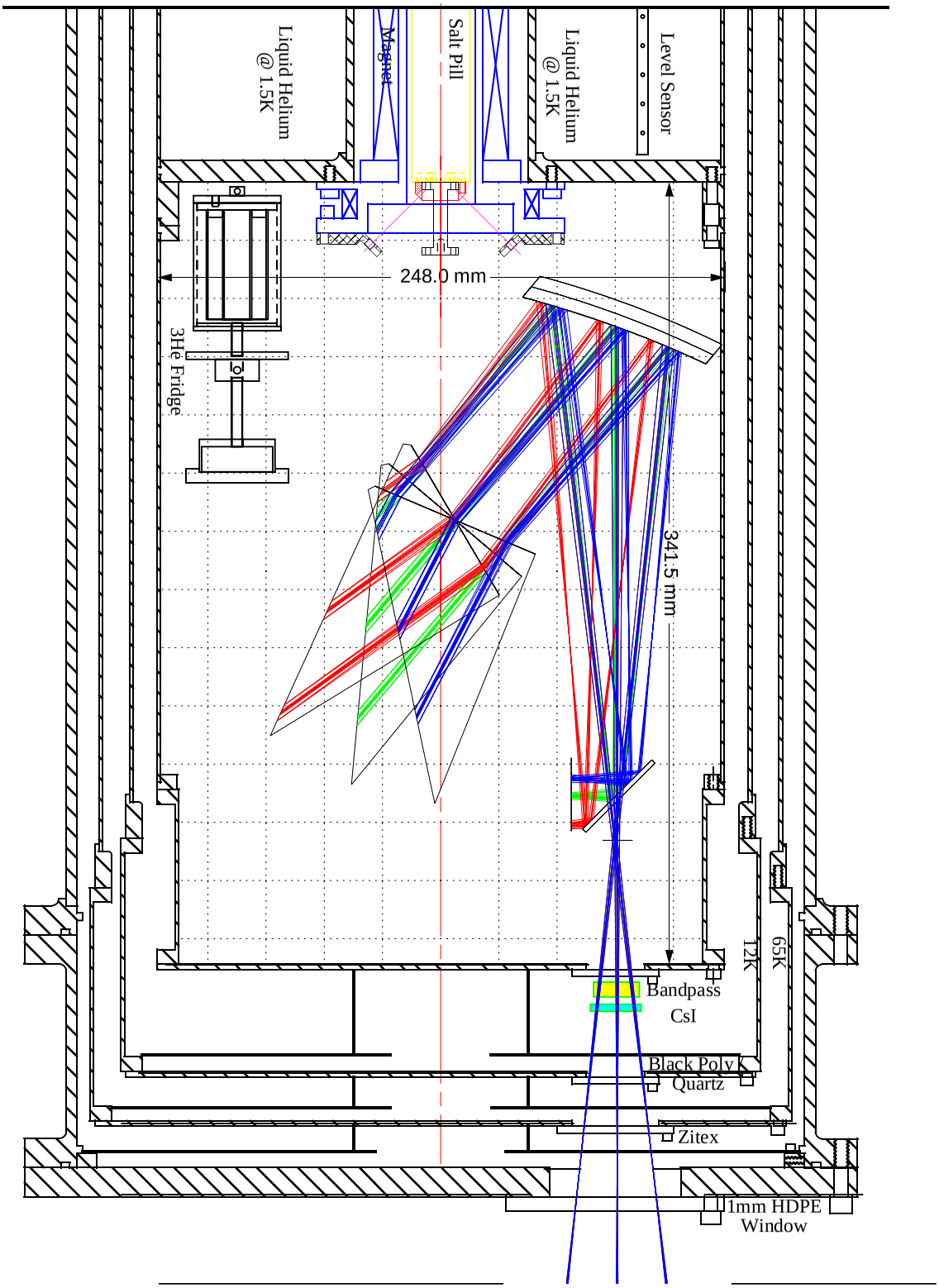

Figure 9.10 Diagram of the immersion grating spectrometer highlighting the grating rotation necessary to achieve 425, 450, or 475μm operation. Note the dewar extension which has been added onto the cryostat as shown in Figure 7.11.

framework and the paraboloidal mirror and to have the germanium grating machined. Funding for this has already been acquired. For the time being, a metallic reflection grating with the same optical parameters will be used for testing; it will achieve a velocity coverage of $\sim 12,000$ km/s with a resolution of around 800 km/s.

9.6 Summary

We have designed a grating spectrometer for use in the 350μm and 450μm atmospheric windows from the ground. Using a germanium-immersed grating, velocity resolutions between 150 and 250 km/s can be achieved. Using a 32-element bolometer array, the total velocity coverage is 2700-4100 km/s. The bolometers will be cooled to 0.1K by an adiabatic demagnetization refrigerator to achieve an NEP of $\sim 6 \times 10^{-16}$ W/$\sqrt{\text{Hz}}$ for an NEFD of ~ 4 Jy/$\sqrt{\text{Hz}}$. An hour of integration time will yield noise levels of the order of a few tens of mJy. At this level and with this bandwidth, 10^9 $L_\odot$ of CII 158μm line emission from a galaxy a redshift of 1 would be detectable at the 3 σ level. Ultraluminous infrared galaxies out to $z = 0.1$ will be detectable in the higher-J lines of CO and the fine-structure transition of CI. This instrument is intended to be a facility spectrometer for the CSO.

Chapter 10 Summary:

Toward the Future with Broadband Submillimeter Studies

"Although the Universe is under no obligation to make sense, students in pursuit of the Ph.D. are."

– Robert P. Kirshner (1991)

In the hopes of not repeating what was referred to in the abstract and detailed in the intervening pages, I shall endeavor to paint this work and, indeed, the whole field of far-infrared extragalactic studies with a broad brush.

Much of this thesis describes efforts at detecting the emission from dust and molecular gas in nearby galaxies. We have made some very good measurements, and can begin to constrain the temperature and properties of dust and molecular gas in luminous infrared galaxies at $z \lesssim 0.1$. In the case of dust emission in nearby LIRGs, we find a typical temperature of 37 ± 4 and an emissivity index of $\beta = 1.7 \pm 0.4$ for a single component greybody fitted to the $60\mu\text{m} \leq \lambda \leq 1300\mu\text{m}$ data points. On average, a centrally-heated model with the derived temperatures is consistent with the measurement of the far-infrared and mid-infrared source sizes. We have studied molecular gas in ULIRGs by means of the first systematic study of CO $J = 3 \rightarrow 2$ and $2 \rightarrow 1$ emission in external galaxies. The resultant averaged line intensities imply optically thick molecular gas with a temperature in the range of 20-60K and a density of $n(\text{H}_2) \approx 1500$ cm^{-3}.

The majority of the remaining astronomy content concerns the few detections and many upper limits found when attempting to observe high redshift objects. These galaxies and quasars should be similar to their local counterparts, but are still just

beyond the reach of our telescopes. We have successfully detected the 350μm (observed wavelength) emission from nine sources at redshifts $2.3 \leq z \leq 4.7$, which makes this the first detections from a survey at this wavelength. A median temperature of 50K is quite cold, implying a large dust mass of $\sim 3 \times 10^8\, h^{-2}\, M_\odot$. We find a wide range of luminosities ($4 - 33\ \times 10^{12}\, h^{-2}\, L_\odot$), implying large amounts of star formation ($\sim 1000\, M_\odot\ \mathrm{yr}^{-1}$) if this emission arises from a starburst. This survey, which also yielded 12 nondetections, used a target list of known sources (predominantly radio-quiet quasars). Our attempt at a blank-field survey turned up no detections, but does not strongly constrain any models of galaxy formation. We have also made some forays into the detection of highly redshifted line emission, but have detected only the Cloverleaf quasar in CO $J = 7 \rightarrow 6$. With the sensitivities achieved in our searches for CII and NII emission lines, we should have detected the targeted quasars if our models for the line fluxes are correct. It seems that we must revised downward our estimates for the flux carried by these elusive fine-structure lines, which promised to be the most informative in terms of protogalaxy studies. They are too faint to be seen with existing technology, which cries out for new instruments.

Elsewhere in this thesis, I have detailed the development of instrumentation technologies aimed at making these astronomical studies more fruitful. The commissioning of the SHARC bolometer camera has made the detection of dust emission from high redshift quasars described above a possibility, though blank-field surveys are still not sensitive enough to constrain galaxy evolution significantly. In the realm of broadband spectroscopy, we have proven the technologies necessary to build a bolometer spectrometer with velocity coverage in the thousands of kilometers per second. When installed at the CSO, it promises to achieve a factor of several increase in the sensitivity of searches for the CII 158μm line. If we should still fail to detect this line, it would be indicative of a very different nature of star formation in high redshift galaxies.

While the past few years of efforts in understanding the optically dark side of galaxies and galaxy evolution have seen a substantial number of advances (of which this work is but a very small part), there is much left to be done. By the end of

the millennium[1], the CSO will feature two new instruments: the aforementioned bolometer spectrometer and the SHARC II bolometer camera, an instrument which will achieve a factor of 20 improvement in areal coverage for use in the surveying of the universe for protogalaxies. Future airborne and space-based platforms (SOFIA, SIRTF and FIRST) will be available shortly thereafter for observations across the entire far-infrared. With the hindsight available to us in two decades, this thesis will seem primitive, but every journey begins with a single step.

[1]I use the true end: December 31, 2000. History will prove me right.

References

Aalto, S., Booth, R.S., Black, J.H. & Johansson, L.E.B. 1995, A&A 300, 369

Aannestad, P.A. 1975, ApJ, 200, 30

Alloin, D., Guilloteau, S., Barvainis, R. & Tacconi, L. 1997, A&A, 321, 24

Accurate Instrument Repair, Orange, CA 92667

Armstrong, K.R. & Low, F.J. 1974, Applied Optics, 13 (2) 425

Ashby, M.L.N., Hacking, P.B., Houck, J.R. Soifer, B.T. & Weisstein, E.W., 1996, ApJ, 456, 428

Barger, A.J., Cowie, L.L., Sanders, D.B., Fulton, E., Taniguchi, Y., Sato, Y., Kawara, K. & Okuda, H. 1998, Nature, 394, 248

Baron, E. & White, S.D.M. 1987, ApJ, 322, 585

Barvainis, R., Antonucci, R. & Coleman, P. 1992, ApJ, 399, L19

Barvainis, R., Tacconi, L., Antonucci, R., Alloin, D. & Coleman, P. 1994, Nature, 371, 586

Barvainis, R., Antonucci, R., Hurt, T., Coleman, P. & Reuter, H.-P. 1995, ApJ, 451, L9

Barvainis, R., Maloney, P., Antonucci, R. & Alloin, D. 1997, "Multiple CO transitions, CI, and HCN from the Cloverleaf quasar," *ApJ* **484**, pp. 695–701

Barvainis, R., Alloin, D., Guilloteau, S. & Antonucci, R. 1998, ApJ, 492, L13

Bearing Engineers, 27 Argonaut, Aliso Viejo, CA 92656; (714) 586-7442. Provided stepper motor #17PM-K004-02V.

Benford, D.J., Serabyn, E., Moseley, S.H. & Phillips, T.G. 1998a, in *Advanced Technology MMW, Radio, and Terahertz Telescopes*, T.G. Phillips, ed., *Proc. SPIE* 3357

Benford, D.J., Hunter, T.R. & Phillips, T.G. "Noise equivalent power of background limited thermal detectors at submillimeter wavelengths," *Int. J. IR MM Waves* **19** (7), 1998, p. 931-938

Benford, D.J., Cox, P., Omont, A. & Phillips, T.G. 1998b, BAAS, 192, 11.04

Benford, D.J., Cox, P., Omont, A., Phillips, T.G. & McMahon, R.G. 1999, ApJL, *submitted*

Benford, D.J., Gaidis, M.C. & Kooi, J.W., 1999, in preparation.

Benford, D.J., Wu, S., Pardo, J.R. & Serabyn, E. 1999, Applied Optics, *submitted*

Bennett, C. L., Fixsen, D. J., Hinshaw, G., Mather, J. C., Moseley, S. H., Wright, E. L., Eplee, R. E., Jr., Gales, J., Hewagama, T., Isaacman, R. B., Shafer, R. A. & Turpie, K., 1994, ApJ, 434, 587

Bernstein, G., Labov, S., Landis, D., Madden, N., Millet, I., Silver, E. & Richards, P. 1991, Cryogenics, 32, 99-101

Betts, D.S. 1976, Refrigeration and Thermometry Below One Kelvin, Sussex University Press, London

Bevington, P.R. 1969, Data Reduction and Error Analysis for the Physical Sciences, (New York: McGraw-Hill), p. 63 (2nd edition)

Bin, M., Benford, D.J., Gaidis, M.C., Büttgenbach, T.H., Zmuidzinas, J., Serabyn, E. & Phillips, T.G. 1999, "A large throughput high resolution Fourier Transform Spectrometer for submillimeter applications," *Int. J. IR MM Waves*, 20 (3), *in press*

Birch, J.R., Dromey, J.D. & Lesurf, J. 1981, Infrared Physics, 21, 225

Birch, J.R. 1990, Infrared Physics, 30, 195

Blain, A.W. & Longair, M.S. 1993, MNRAS, 264, 509

Blea, J.M., Parks, W.F., Ade, P.A.R. & Bell, R.J. 1970, J. Opt. Soc. America, 60 (5), 603

Bock, J.J. 1994, "Rocket-Borne Observation Of Singly Ionized Carbon 158 Micron Emission From The Diffuse Interstellar Medium"; Ph.D. Thesis, University of California at Berkeley

Bock, J.J., Kawada, M., Matsuhara, H., Richards, P.L. & Lange, A.E. 1995, "Silicon-gap Fabry-Perot filter for far-infrared wavelengths," Applied Optics **34,** 3651-3657

Bollea, D. & Cavaliere, A. 1976, A&A, 49, 313

Bond, J.R., Carr, B.J. & Hogan, C.J. 1986, ApJ, 306, p. 428-450

Born, M. & Wolf, E., 1959, "Principles of Optics," Pergamon Press, London

Braine, J. & Dumke, M. 1998, A&A, 333, 38

Bréhat, F. & Wyncke, B. 1997 "Measurements of the optical constants of crystal quartz at 10K and 300K in the far infrared spectral range: 10-600 cm^{-1}," *Int. J. IR MM Waves* **18** (9) p. 1663–1679

Brown, R.L. & Vanden Bout, P.A. 1991, AJ, 102, 1956

Brown, J.M., Varberg, T.D., Evenson, K.M. & Cooksy, A.L. 1994, ApJ, 428, L37

Bryant, P.M. & Scoville, N.Z. 1996, ApJ, 457, 678

Bussone, D.D. 1989, in Modern Plastics Encyclopedia (New York: McGraw-Hill), p. 66

California Fine Wire Company, P.O. Box 446, Grover Beach, California 93483-0446; (805) 489-5144

Carico, D.P., Keene, J.B., Soifer, B.T. & Neugebauer, G. 1992, PASP, 104, 1086

Carilli, C.L. & Yun, M.S. 1999, ApJL, in press

Carlstrom, J.E. & Zmuidzinas, J. 1996, "Millimeter and submillimeter techniques," in *Reviews of Radio Science 1993-1995*, W.R. Stone, ed., Oxford University Press

Casey, S.C., Moseley, S.H., Chan, K.W. & Loewenstein, R.F. 1993, "The Goddard cooled grating spectrometer," *BAAS* **182** #34.19

Childs, G.E., Ericks, L.J. & Powell, R.L. 1973, *Thermal Conductivity of Solids at Room Temperature and Below*, NIST-NBS Monograph 131

Chini, R., Steppe, H., Kreysa, E., Kirchbaum, T., Quirrenbach, A., Schalinski, C. & Witzel, A. 1988, A&A 192, L1

Chini, R., Krügel, E. & Kreysa, E. 1992, A&A, 266, 177

Chini, R., Krügel, E., Lemke, R. & Ward-Thompson, D. 1995, A&A, 295, 317

Chini, R. & Krügel, E., 1994, A&A, 288, L33

Chini, R., Krügel, E., & Lemke, R. 1996, A&AS, 118, 47

Church, S.E. 1995, MNRAS, 272, 551

Clancy, R.T. & Muhleman, D.O. 1991, "Long-term (1979-1990) changes in the thermal, dynamical, and compositional structure of the Venus mesosphere as inferred from microwave spectral line observations of C-12O, C-13O, and CO-18," Icarus **89**, 129-146

Clapp, Andre. Private communication regarding his calculation of the heat capacity of a monolayer of adsorbed ^{4}He.

Clarke, J., Hoffer, G.I., Richards, P.L. & Yeh, N.-H. 1977, J. Appl. Phys. 48(2), 4865

Clegg, P.E., Ade, P.A.R., Armand, C., Baluteau, J.-P., Barlow, M.J., Buckley, M.A., Berges, J.-C., Burgdorf, M., Caux, E., Ceccarelli, C., Cerulli, R., Church, S.E., Cotin, F., Cox, P., Cruvellier, P., Culhane, J.L., Davis, G.R., Di Giorgio, A.,

Diplock, B.R., Drummond, D.L., Emery, R.J., Ewart, J.D., Fischer, J., Furniss, I., Glencross, W.M., Greenhouse, M.A., Griffin, M.J., Gry, C., Harwood, A.S., Hazell, A.S., Joubert, M., King, K.J., Lim, T., Liseau, R., Long, J.A., Lorenzetti, D., Molinari, S., Murray, A.G., Naylor, D.A., Nisini, B., Norman, K., Omont, A., Orfei, R., Patrick, T.J., Pequignot, D., Pouliquen, D., Price, M.C., Nguyen-Q-Rieu, Rogers, A.J., Robinson, F.D., Saisse, M., Saraceno, P., Serra, G., Sidher, S.D., Smith, A.F., Smith, H.A., Spinoglio, L., Swinyard, B.M., Texier, D., Towlson, W.A., Trams, N.R., Unger, S.J. & White, G.J. 1996, A&A 315, L38

Clements, D.L., Puget, J.-L., Lagache, G., Dole, H., Cox, P., Gispert, R., Reach, W.T., Cesarsky, C., Elbaz, D., Aussel, H., Bouchet, F., Guiderdoni, B., Omont, A., Désert, F.-X., Franceschini, A., Moorwood, A. & Lemke, D. 1998, "The FIRBACK 175 Micron Survey," to appear in *Astrophysics with Infrared Surveys: A Prelude to SIRTF*, proceedings of the first SIRTF conference, ed. M. Bicay

Coccia, E. & Modena, I. 1993, "Smooth Heat Switch Below 1K," Cryogenics, 33 (2), 228

Cochise Instruments Incorporated, 6304 deMello St., Hereford, AZ 85615: (602) 378-6321

Colangeli, L., Mennella, V., Palumbo, P., Rotundi, A. & Bussoletti, E. 1995, A&AS, 113, 561

Cowan, W.D., Levan, P.D., Barnaby, D., Johnson, R.L. & Duncan, T.S. 1995, Proc. SPIE Vol. 2475, p. 236, Infrared Detectors and Instrumentation for Astronomy

Cowie, L. L., Gardner, J. P., Hu, E. M., Songaila, A., Hodapp, K.-W. & Wainscoat, R. J. 1994, ApJ, 434, 114

Cryomagnetics Incorporated, 1006 Alvin Weinberg Drive, Oak Ridge, TN 37830: (423) 482-9551

CTI Cryogenics, 9 Hampshire Street, Mansfield, Massachusetts, 02048-9171: (508) 337-5000

Cunningham, C.R. & Gear, W.K. 1990, in SPIE Symposium on Astronomical Telescopes and Instrumentation for the 21st Century

Das, M.B. 1972, "FET Noise Sources and their Effects on Amplifier Performance at Low Frequencies," IEEE Trans. Elect. Devices, 19 (3), 328

Davis, G.R., Furniss, I., Patrick, T.J., Sidey, R.C. & Towlson, W.A. 1991, Proc. 25th Aerospace Mechanisms Symposium (NASA Conference Publication #3113), p. 151-59

Davis, G.R., Furniss, I., Towlson, W.A., Ade, P.A.R., Emery, R.J., Glencross, W.M., Naylor, D.A., Patrick, T.J., Sidey, R.C. & Swinyard, B.M. 1995, Applied Optics, 34 (1), 92

Debye, P. 1926, "Einige Bemerkunden zur Magnetisierung bei teifer Temperatur," Annalen der Physik, v. 81, p. 1154-1160

de Haas, W.J., Wiersma, E.C. & Kramers, H.A. 1933, Physics, 1, 1

Dekker, H. 1987, "An immersion grating for an astronomical spectrograph," in *Instrumentation for ground-based optical astronomy*, L. B. Robinson, ed., pp. 183–188, Springer-Verlag, Berlin

de Klerk, D. 1956, "Handbuch der Physik," Springer-Verlag, v. 15, p. 38

De Propris, R., Pritchet, C.J., Hartwick, F.D.A. & Hickson, P. 1993, AJ, 105, 4

Désert, F.-X., Boulanger, F. & Puget, J.L. 1990, A&A 237, 215

Dewar, J. 1893, Proc. Inst. Gt. Br. 14, 1

Djorgovski, S. & Weir, N. 1990, ApJ, 351, 343

Djorgovski, S. 1992, "On the Observability of Primeval Galaxies," in *Cosmology and Large-Scale Structure in the Universe*, ASP Conferences v. 24, R.R. de Carvalho, ed.

Dowell, C.D., Hildebrand, R.H., Schleuning, D.A., Vaillancourt, J., Dotson, J.L., Novak, G., Renbarger, T. & Houde, M., 1998, ApJ, 504, 588

Downes, D., Radford, S.J.E., Greve, A., Thum, C., Solomon, P.M. & Wink, J.E. 1992, ApJ, 398, L25

Downes, D., Solomon, P.M. & Radford, S.J.E. 1995, ApJ, 453, L65

Downes, D. & Solomon, P.M. 1998, ApJ, 507, 615

Downes, D., Neri, R., Wiklind, T., Wilner, D.J. & Shaver, P. 1999, ApJL, in press

Downey, P.M., Jeffries, A.D., Meyer, S.S., Weiss, R., Bachner, F.J. et al. 1984, Appl. Op., 23, 910

Draine, B.T. & Lee, H.M. 1984, ApJ, 285, 89

Duband, L., Hui, L. & Lange, A.E. 1990, "Space-Borne ^{3}He Refrigerator" Cryogenics, 30, p. 263-269

Duband, L., Hui, L. & Lange, A.E. 1993, "Thermal Isolation of Large Loads at Low Temperature Using Kevlar Rope" Cryogenics, 33, p. 643-647

Duband, L., Lange, A.E. & Bock, J.J. 1996, "Helium Adsorption Coolers for Space" Proc. 30th ESLAB Symposium, ESA SP-388, p. 289-292

Dufour, C. 1951, "Recherches sur la Luminosité, le Contraste et la Résolution de Systèmes Interferéntiels A Ondes Multiples," Ann. Phys. **6**, 5-107

DuPont Co.: Kevlar aramid; P.O. Box 80,0705, Wilmington, DE 19880-0705; (800) 453-8527. I use 40lb pull cord, which is 1000 denier (1d=weight in grams of 9000m of cord; 1000d$\simeq$0.45mm diam)

Dwek, E. & Smith, R.K. 1996, BAAS, 188, 0703

Dwek, E. & Arendt, R.G. 1998, ApJL, 508, L9

Eales, S. A. & Edmunds, M.G., 1996, MNRAS, 280, 1167

Eales, S. A. & Edmunds, M.G., 1997, MNRAS, 286, 732

Eales, S. A. & Edmunds, M.G., 1998, MNRAS, 299, L29

Eales, S., Lilly, S., Gear, W., Dunne, L., Bond, J.R., Hammer, F., Le Fèvre, O. & Crampton, D. 1999, ApJL, submitted

Eldridge, J.E. 1991, in Handbook of Optical Constants of Solids II, ed. E.D. Palik, p. 853

Ellison, B.N. 1988, "Hybrid liquid helium cryostat for radio astronomy use," *Cryogenics* **28** p. 779–782

Elston, R., 1991, ed., Astrophysics with Infrared Arrays, ASP Conf. Ser., v. 14 (San Francisco: ASP)

Emerson, D.T., Klein, U. & Haslam, C.G.T. 1979, A&A, 76, 92

Emerson & Cuming: Stycast 2830 FT epoxy; 77 Dragon Court, Woburn MA 01888; (617) 938-8630

Erickson, E.F., Matthews, S., Augason, G.C., Houck, J.R., Rank, D.M. & Haas, M.R. 1984. "All-aluminum optical system for a large cryogenically cooled far infrared echelle spectrometer," in *Cryogenic Optical Systems and Instruments*, Proc. SPIE **509** p. 129–139

Evans, A.S., Sanders, D.B., Mazzarella, J.M., Solomon, P.M., Downes, D., Kramer, C. & Radford, S.J.E. 1996, ApJ, 457, 658

Fabry, A. & Perot, C., 1899, Ann. Chim. Phys., 7, **16**, 115

Farroqui, K. *et al.* 1997, "The single-mode monolithic silicon bolometer as an ultrasensitive detector for millimeter wavelengths," in *Proceedings of the Eighth International Symposium on Space Terahertz Technology*, p. 546–555

Fellgett, P., Jones, R.C. & Twiss, R.Q. 1959, Nature, 4691, 967

Fischer, J. et al. 1999, in preparation. (The work in question is a study of the ISO-LWS far-infrared spectra of bright IR galaxies.)

Fischer, J. and Cox, P. Private communication regarding the ISO-LWS spectrum of Arp220.

Fisher Scientific 1995, Fair Lawn, NJ 07410, (201) 796-7100

Fixsen, D.J., Dwek, E., Mather, J.C., Bennett, C.L. & Shafer, R.A., 1998a, ApJ, 508, 106

Fixsen, D.J., Bennett, C.L. & Mather, J.C., 1998b, ApJ, submitted

Franceschini, A., Mazzei, P., De Zotti, G. & Danese, L., 1994, ApJ, 427, 140

Frank, D.J. & Nast, T.C. 1986, "Getter-Activated Cryogenic Thermal Switch," Adv. Cryog. Eng. 31, p. 933-940

Fraunhofer, J. 1823, Annalen der Physik, 74, 337

Frayer, D. T., Ivison, R. J., Scoville, N. Z., Yun, M., Evans, A. S., Smail, Ian, Blain, A. W. & Kneib, J.-P. 1998, ApJ, 506, L7

Gerin, M. & Phillips, T.G. 1998, ApJ, 509, L17

GE Varnish: available from many companies, including:

Part No. IMI 7031, Lakeshore Cryotronics, Inc., 64 East Walnut St., Westerville, OH 43081-2399; (614) 891-2243

Part No. TVZ 0001, Oxford Instruments, 130A Baker Ave., Concord, MA 01742; (978) 369-9933

Giauque, W.F. 1927, J. Am. Chem. Soc., 49, p. 1864-1870

Giauque, W.F. & MacDougall, D.P. 1933, "Attainment of Temperatures Below 1° Absolute by Demagnetization of $Gd_2(SO_4)_3 \cdot 8H_2O$" Phys. Rev. 43, 768

Gordon, M.A. 1988, ApJ, 331, 509

Graf, U.U. Jaffe, D.T., Kim, E.J., Lacy, J.H. Ling, H., Moore, J.T. & Rebeiz, G. 1994, "Fabrication and evaluation of an etched infrared diffraction grating," *App. Opt* **33** (1) p. 96–102

Grannan, S.M., Lange, A.E., Haller, E.E. & Beeman, J.W. 1992, Phys. Rev. B., 45 (8), 4516

Grannan, S.M., Richards, P.L. & Hase, M.K. 1997, "Numerical optimization of bolometric infrared detectors including optical loading, amplifier noise, and electrical nonlinearities," *Int. J. IR MM Waves* **18** (2) p. 319

Gregorich, D. T., Neugebauer, G., Soifer, B. T., Gunn, J. E. & Herter, T. L. 1995, AJ, 110, 259

Griffin, M.J. & Holland, W.S. 1988, "The influence of background power on the performance of an ideal bolometer," *Int. J. IR MM Waves* **9** (10) p. 861–875

Groesbeck, T.D. 1994, "The Contribution of Molecular Line Emission to Broadband Flux Measurements at Millimeter and Submillimeter Wavelengths," Ph.D. Thesis, California Institute of Technology

Grossman, E., 1989, Airhead Software, 2069 Bluff St., Boulder, CO 80302

Guiderdoni, B., Hivon, E., Bouchet, F.R. & Maffei, B., 1998, MNRAS, 295, 877

Guilloteau, S., Omont, A., McMahon, R.G., Cox, P. & Petitjean, P. 1997, "The second detection of CO at redshift larger than 4," A&A, 328, pp. L1–L4

Guilloteau, S., Omont, A., McMahon, R.G., Cox, P. & Petitjean, P. 1999, A&A, submitted

Gurwell, M.A., Muhleman, D.O., Shah, K.P., Berge, G.L. and Rudy, D.J. 1995, "Observations of the CO bulge on Venus and implications for mesospheric winds," Icarus **115**, 141-158

Haas, M., Chini, R., Meisenheimer, K., Stickel, M., Lemke, D., Klaas, U. & Kreysa, E. 1998, ApJ, 503, L109

Hacking, P., Condon, J.J. & Houck, J.R. 1987, ApJ, 316, L15

Hacking, P. B. & Soifer, B. T. 1991, ApJ, 367, L49

Hadni, A., Claudel, J., Décamps, E., Gerbaux, X. & Strimer, P. 1962, C.R. Acad. Sci. Paris, 255, 1595

Hagmann, C., Benford, D.J. & Richards, P.L. 1994, Cryogenics, 34, 213

Hagmann, C. & Richards, P.L. 1995, Cryogenics, 35, 303

Haiman, Z. 1998, Proc. 32nd COSPAR Scientific Assembly - Adv. Space Research

Haiman, Z. & Spaans, M. 1999, ApJ, in press.

Halpern, M., Gush, H.P., Wishnow, E. & De Cosmo, V. 1986, Appl. Op., v. 25, n. 4, p. 565

Harris, A.I. & Isaak, K.G. 1989, "WASP: wideband analog correlator spectrometer," in *Advanced Technology MMW, Radio, and Terahertz Telescopes*, T. G. Phillips, ed., *Proc. SPIE* **3357**

Harrison, E.R. 1981, *Cosmology, the Science of the Universe*, Cambridge University Press, Cambridge

Haslam, C.G.T. 1974, A&AS, 15, 333

Hauser, M.G., Arendt, R.G., Kelsall, T., Dwek, E., Odegard, N., Weiland, J.L., Freudenreich, H.T., Reach, W.T., Silverberg, R.F., Moseley, S.H., Pei, Y.C., Lubin, P., Mather, J.C., Shafer, R.A., Smoot, G.F., Weiss, R., Wilkinson, D.T. & Wright, E.L., ApJ, 508, 25

Hecht, E. 1987, *Optics*, Addison-Wesley, Reading, Massachusetts

Helou, G. 1989, in *Interstellar Dust*, I.A.U. Symposium #135, p. 285-301

Herschel, W., 1800, "Experiments on the Refrangibility of the Invisible Rays of the Sun," Philosophical Transactions, p. 294

Hewett, P.C., Foltz, C.B., & Chaffee, F.H. 1995, AJ, 109, 1498

Hildebrand, R.H. & Winston, R. 1982, Appl. Op., v. 21, n. 10, p. 1844

Hildebrand, R.H. 1983, QJRAS, 24, 267

Hildebrand, R.H. 1986, Optical Engineering, vol. 25, no. 2, p. 323

Holland, W.S., Ade, P.A.R., Griffin, M.J., Hepburn, I.D., Vickers, D.G., Cunningham, C.R., Hastings, P.R., Gear, W.K., Duncan, W.D., Baillie, T.E.C., Haller, E.E. & Beeman, J.W. 1996, Int J IR MM Waves, 17, 669

Holland W. S., Cunningham C. R., Gear W. K., Jenness T., Laidlaw K., Lightfoot J. F., Robson E. I. 1998, in *Advanced Technology MMW, Radio and Terahertz Telescopes*, T.G. Phillips, ed., *Proc. SPIE* 3357

Holzapfel, W.L., Wilbanks, T.M., Ade, P.A.R., Church, S.E., Fischer, M.L., Mauskopf, P.D., Osgood, D.E. & Lange, A.E. 1997, ApJ, 479, 17

Horowitz, P. & Hill, W. 1989, "The Art of Electronics," Cambridge University Press, Cambridge

Hudson, R.P. 1972, "Principles and Application of Magnetic Cooling," Elsevier Publishing, New York

Hughes. D.H., Robson, E.I., Dunlop, J.S. & Gear, W.K. 1993, MNRAS, 263, 607

Hughes, D.H., Dunlop, J.S. & Rawlings, S., 1997, MNRAS, 289, 766

Hughes, D.H., Serjeant, S., Dunlop, J., Rowan-Robinson, M., Blain, A., Mann, R.G., Ivison, R., Peacock, J., Efstathiou, A., Gear, W., Oliver, S., Lawrence, A., Longair, M., Goldschmidt, P. & Jenness, T. 1998, Nature, 394, 241

Hunter, T.R., Benford, D.J. & Serabyn, E. 1996, PASP, 108, 1042

Hunter, T.R. 1997, "A Submillimeter Imagine Survey of Ultracompact HII Regions"; Ph.D. Thesis, California Institute of Technology

Infrared Labs, 1808 East 17th Street, Tucson, AZ 85719-6505; (520) 622-7074

InterFET, 322 Gold Street, Garland TX 75042; (972) 487-1287

Isaak, K.G., McMahon, R.G., Hills, R.E. & Withington, S. 1994, MNRAS, 269, L28

Ivison, R.J. 1995, MNRAS, 275, L33

Ivison, R.J. & Harrison, A.P. 1996, A&A 309, 416

Ivison, R.J., Harrison, A.P. & Coulson, I.M. 1998, A&A 330, 443

Ivison, R.J., Smail, I., Le Borgne, J.-F., Blain, A.W., Kneib, J.-P., Bézecourt, J., Kerr, T.H. & Davies, J.K. 1998, MNRAS, 298, 583

James Rex, *The Holy Bible*, King James version, 1611.

Jones, R. Clark 1953, J.O.S.A., v. 43, n. 1, p. 1

Josse, M., Gerbaux, X. & Hadni, A. 1993, Int. J. of IR & MM Waves, v. 14, n. 7, p. 1381

Kawada, M., Bock, J. J., Christov, V. V., Lange, A. E., Matsuhara, H., Matsumoto, T., Matsuura, S., Mauskopf, P. D., Richards, P. L. & Tanaka, T. 1994, ApJ, 425, L89

Kawamura, J., Paine, S. & Papa, D.C. 1996, Proc. Seventh International Symposium on Space Terahertz Technology, Charlottesville

Kawamura, J.H., Tong, C.-Y.E., Blundell, R., Papa, D.C., Hunter, T.R., Gol'tsman, G., Cherednichenko, S., Voronov, B. & Gershenzon, E. 1998, *ASC*, submitted

Kawara, K., Sato, Y., Matsuhara, H., Taniguchi, Y., Okuda, H., Sofue, Y., Matsumoto, T., Wakamatsu, K., Karoji, H., Okamura, S., Chambers, K. C., Cowie, L. L., Joseph, R. D. & Sanders, D. B. 1998, A&A, 336, L9

Keithley Instruments, Inc., 28775 Aurora Road, Cleveland, OH 44139; 216-248-0400

Kennefick, J. D., De Carvalho, R. R., Djorgovski, S. G., Wilber, M. M., Dickson, E. S., Weir, N., Fayyad, U. & Roden, J. 1995, AJ, 110, 78

Kirshner, R.P. 1991, QJRAS, 32, 233-244

Kittel & Kroemer 1980, *Thermal Physics*, W.H. Freeman & Co., San Francisco, publisher

Kittel, P. 1980a, "Magnetic Refrigeration in Space - Practical Considerations" Journal of Energy, 4, 6, p. 266

Kittel, P. 1980b, "Temperature stabilized adiabatic demagnetization for space applications" Cryogenics, 599

Kittel, P. 1983, "Ultimate stability of a magnetic refrigerator" Cryogenics, 477

Kooi, J.W., Walker, C.K., LeDuc, H.G., Benford, D.J., Hunter, T.R. & Phillips, T.G. 1994, International Journal of Infrared and Millimeter Waves, v. 15, p. 477

Kraus, J.D. 1986, Radio Astronomy, 2nd ed. (Powell, Ohio: Cygnus-Quasar Books)

Kreysa, E., Haller, E.E., Gemünd, H.-P., Haslam, C.G.T., Lemke, R. & Sievers, A.W. 1993, in Fourth International Symposium on Space Terahertz Technology, p. 296

Krügel, E., Chini, R., Kreysa, E. & Sherwood, W.A. 1988, A&A, 190, 47

Kürti, N. & Simon, F. 1934, Nature, 133, 907

Lakeshore Cryotronics, Inc., 64 East Walnut St., Westerville, OH 43081-2399; (614) 891-2243

Lamb, H. 1898, "On the Reflection and Transmission of Electric Waves by a Metallic Grating," Proc. London Math. Soc., 29, p. 523-544

Lamb, J.W. 1996, "Miscellaneous data on materials for millimetre and submillimetre optics," *Int. J. IR MM Waves* **17** (12) p. 1997–2034

Langley, S.P. 1881, "The Bolometer," Nature, 25, 14

Lawless, W.N. 1975, Cryogenics, 15, 273

Lawson, N.S. 1982, "A Simple Heat Switch for Use at Millikelvin Temperatures," Cryogenics, 667

Lemke, D., Klaas, U., Abolins, J., Abraham, P., Acosta-Pulido, J., Bogun, S., Castaneda, H., Cornwall, L., Drury, L., Gabriel, C., Garzon, F., Gemuend, H.P., Groezinger, U., Gruen, E., Haas, M., Hajduk, C., Hall, G., Heinrichsen, I., Herbstmeier, U., Hirth, G., Joseph, R., Kinkel, U., Kirches, S., Koempe, C., Kraetschmer, W., Kreysa, E., Krueger, H., Kunkel, M., Laureijs, R., Luetzow-Wentzky, P., Mattila, K., Mueller, T., Pacher, T., Pelz, G., Popow, E., Rasmussen, I., Rodriguez Espinosa, J., Richards, P., Russell, S., Schnopper, H., Schubert, J., Schulz, B., Telesco, C., Tilgner, C., Tuffs, R., Voelk, H., Walker, H., Wells, M., Wolf, J. 1996, A&A, 315, 64

Lewis, W.B. 1947, Proc. Phys. Soc., 59, 34

Lewis, G.F., Chapman, S.C., Ibata, R.A., Irwin, M.J. & Totten, E.J., ApJ, 505, L1

Lis, D.C., Carlstrom, J.E. & Keene. J.B. 1991, ApJ, 380, 429

Lis, D.C., Serabyn, E., Keene, J.B., Dowell, C.D., Benford, D.J., Phillips, T.G., Wang, N. & Hunter, T.R. 1998, ApJ, 509, 299

Loeb, A. 1993, ApJ, 404, L37

Loewenstein, E.V., Smith, D.R. & Smith, R.L., "Optical constants of far infrared materials. 2: Crystalline solids," *App. Opt.* **12** (2) p. 398–406, 1973

Lonsdale, C. 1996, in "Unveiling the Cosmic Infrared Background," AIP Proceedings v. 348, p. 147, E. Dwek, ed.

Lord Corporation Industrial Coatings, 2000 West Grandview Blvd., P.O. Box 10038, Erie, PA 16514-0038, (814) 868-3611

Lounasmaa, O.V. 1974, Experimental Principles and Methods Below 1K, Academic Press, London

Low, F.J. 1961, J.O.S.A., v. 51, n. 11, p. 1300

Luhman, M. L., Satyapal, S., Fischer, J., Wolfire, M. G., Cox, P., Lord, S. D., Smith, H. A., Stacey, G. J. & Unger, S. J. 1998, APJ 504, L11

Madau, P., Ferguson, H.C., Dickinson, M.E., Giavalisco, M., Steidel, C.C. & Fruchter, A. 1996, MNRAS, 283, 1388

Maffei, B. 1994, "Etude des Galaxies dans le Domains Submillimétrique et Réalisation d'un Spectromètre Refroidi"; Ph.D. Thesis, Université de Paris VII

Maffei, B., Pajot, F., Phillips, T.G., Benford, D.J., Caux, E., Gispert, R., Halverson, N., Hunter, T., Jegoudez, G., Josse, M., Lamarre, J.M., Lepeltier, J.P., Moseley, S.H., Origné, A., Petuchowksy, S., Rabottin, M., Renault, J.C., Rioux, C., Serabyn, E. & Wang, N. 1994, Infrared Phys. Technol. 35, 321

Malhotra, S., Helou, G., Stacey, G., Hollenbach, D., Lord, S., Beichman, C. A., Dinerstein, H., Hunter, D. A., Lo, K. Y., Lu, N. Y., Rubin, R. H., Silbermann, N., Thronson, H. A., Jr. & Werner, M. W., ApJ, 491, L27

Marshall, H.L., Tananbaum, H., Avni, Y. & Zamorani, G. 1983, ApJ, 269, 35

Mather, J.C. 1981, Appl. Op., v. 21, n. 6, p. 1125

Mather, J.C. 1984a, Appl. Op., v. 23, n. 4, p. 584

Mather, J.C. 1984b, Appl. Op., v. 23, n. 18, p. 3183

Mather, J. C., Cheng, E. S., Eplee, R. E., Jr., Isaacman, R. B., Meyer, S. S., Shafer, R. A., Weiss, R., Wright, E. L., Bennett, C. L., Boggess, N. W., Dwek, E., Gulkis, S., Hauser, M. G., Janssen, M., Kelsall, T., Lubin, P. M., Moseley, S. H., Jr., Murdock, T. L., Silverberg, R. F., Smoot, G. F. & Wilkinson, D. T. 1990 , Ap. J., 354, L37

Matsuura, S., Kawada, M., Matsuhara, T., Noda, M. & Tanaka, M. 1994, PASP, 106, 770

Mattila, K. 1990, in IAU Symposium 139, *The Galactic and Extragalactic Background Radiation*, ed. S. Bowyer & C. Leinert (Dordrecht: Kluwer), 257

Mauersberger, R., Henkel, C., Walsh, W. & Schulz, A. 1999, A&A 341, 256

McCammon, D., Edwards, B., Juda, M., Plucinsky, P., Zhang, J., Kelley, R., Holt, S., Madejski, G., Moseley, S. & Szymkowiak, A. 1989, in Low Temperature Detectors for Neutrinos and Dark Matter III (Edition Fronteres: Gif sur Yvette Cedex)

McCammon, D., Juda, M., Zhang, J., Holt, S.S., Kelley, R.L., Moseley, S.H. & Szymkowiak, A.E. 1987, Japanese. J. of Appl. Phys., 26 Suppl 26-3, 208

McLean, I.S. 1994, ed., Infrared Astronomy with Arrays: The Next Generation (Dordrecht: Kluwer)

McMahon, H.O. & Gifford, W.E. 1960, Advances in Cryogenic Engineering, 5, 354

McMahon, R.G., Omont, A., Bergeron, J., Kreysa, E. & Haslam, C.G.T. 1994, MNRAS, 267, L9

Mendoza, E. 1961, in "Experimental Cryophysics," Butterworths, London, p. 165

Mennella, V., Brucato, J.R., Colangeli, L., Palumbo, P., Rotundi, A. & Bussoletti, E. 1998, ApJ, 496, 1058

Miles, J.W., Houck, J.R., Hayward, T.L. & Ashby, M.L.N. 1996, ApJ, 465, 191

Mirabel, I.F., Booth, R.S., Garay, G., Johansson, L.E.B. & Sanders, D.B. 1990, A&A, 236, 327

Mitsuishi, A., Yamada, Y. & Yoshinaga, H. 1962, J. Optical Society of America, 52, 14

Moseley, S.H., Mather, J.C. & McCammon, D.J. 1984, "Thermal detectors as x-ray spectrometers," *J. Appl. Phys.* **56** p. 1257–1262

Moseley, S.H. 1995, in New Developments in Array Technology and Applications, eds. A.G. Davis Philip et al. (Netherlands: International Astronomical Union), 95

Moseley, S.H. 1998, "Pop-up bolometer arrays," in *Advanced Technology MMW, Radio, and Terahertz Telescopes*, T. G. Phillips, ed., *Proc. SPIE* **3357**

Nara, K., Fujii, I., Kaneko, K. & Ikushima, A.J. 1982, Jap. J. App. Physics, 21, p. 1083-1085

National Electrostatics Corporation, 7540 Graber Road box 620310, Middleton, WI 53562-0310: (608) 831-7600

National Instruments, Inc., 6504 Bridge Point Parkway, Austin, TX 78730-5039

NED: NASA/IPAC Extragalactic Database, `ned.ipac.caltech.edu`; described by Madore, B.F., Helou, G., Corwin, H.G., Schmitz, M., Wu, X. & Bennett, J. 1992, in *Astronomical Data Analysis Software and Systems I*, ASP Conference Proceedings v. 25, p. 47

Netzer, Y. 1981, Proc. IEEE, 69(6), 728

Neugebauer, G., Habing, H.J., Van Duinen, R., Aumann, H.H., Baud, B., Beichman, C.A., Beintema, D.A., Boggess, N., Clegg, P.E., De Jong, T., Emerson, J.P., Gautier, T.N., Gillett, F.C., Harris, S., Hauser, M.G., Houck, J.R., Jennings,

R.E., Low, F.J., Marsden, P.L., Miley, G., Olnon, F.M., Pottasch, S.R., Raimond, E., Rowan-Robinson, M., Soifer, B.T., Walker, R.G., Wesselius, P.R., Young, E. 1984, ApJ, 278, L1

Nicolet 60SX spectrometer, Nicolet Instruments, 5225 Verona Rd., Madison, WI 53711; (800) 232-1472

Nishioka, N.S., Richards, P.L. & Woody, D.P. 1978, Appl. Op., 17, 1562

Noda, M., Christov, V. V., Matsuhara, H., Matsumoto, T., Matsuura, S., Noguchi, K. & Sato, S. 1992, ApJ, 391, 456

Norton Performance Plastics, Wayne, New Jersey; (201) 696-4700

Ohta, K., Yamada, T., Nakanishi, K., Kohno, K., Akiyama, M. & Kawabe, R. 1996, Nature, 382, 426

Okazaki, A. T. & Inagaki, S. 1984, PASJ, 36, 17

Oke, J.B., Cohen, J.G., Carr, M., Cromer, J., Dingizian, A., Harris, F.H., Labrecque, S., Lucino, R., Schaal, W., Epps, H. and Miller, J., 1995, PASP, 107, 375-385

Oliver, S., Rowan-Robinson, M., Cesarsky, C., Danese, L. Franceschini, A., Genzel, R., Lawrence, A., Lemke, D., McMahon, R., Miley, G., Puget, J-L., Rocca-Volmerange, B., Ciliegi, P., Efstathiou, A., Gruppioni, C., Héraudeau, P., Serjeant, S., Surace, C. and the ELAIS consortium 1999, To appear in 'Wide-field surveys in cosmology', Proc. XIV IAP meeting

Omont, A., Petitjean, P., Guilloteau, S., McMahon, R.G, Solomon, P.M. & Pécontal, E. 1996a, Nature, 382, 428

Omont, A., McMahon, R.G., Cox, P., Kreysa, E., Bergeron, J., Pajot, F. & Storrie-Lombardi, L.J. 1996b, A&A, 315, 1

Optical Research Associates, 3280 E. Foothill Blvd., Pasadena, CA 91107; (626) 795-9101

Oxford Instruments, 601 Turnpike, Oakridge, TN 37831; (423)483-8405

Padman, R. 1994, in Multi-Feed Systems for Radio Telescopes, eds. D.T. Emerson & J.M. Payne, ASP Conf. Ser., v. 75 (San Francisco: ASP)

Pahre, M.A. & Djorgovski, S.G. 1995, ApJ, 449, L1

Pandorf, R.C., Chen, C.Y. & Daunt, J.G. 1962, Cryogenics, p. 239-242

Partridge, R.B. & Peebles, P.J.E. 1967, ApJ, 148, 377

Penzias, A.A. & Wilson, R.W. 1965, "A Measurement of Excess Antenna Temperature at 4080 Mc/s," ApJ 142, 419

Petuchowski, S.J. & Bennett, C.L. 1993, ApJ, 405, 591

Petuchowski, S.J., Bennett, C.L., Haas, M.R., Erickson, E.F., Lord, S.D., Rubin, R.H., Colgan, S.W.J. & Hollenbach, D.J. 1994, ApJ, 427, L17

Phillips, T.G., 1988, in *Millimetre and Submillimetre Astronomy*, Wolstencroft & Burton, eds, p. 1

Phillips, T.G. & Keene, J.B., 1992, Proc. IEEE, 80, 1662

Phillips, T.G. 1997, "Recent results from the Caltech Submillimeter Observatory," in *The Far Infrared and Submillimeter Universe, ESA Conference SP-401, p. 223, A. Wilson, ed.*

Pignatel, G.U., Pedrolli, F., Cavalleri, A., Bonaldi, M. & Vitale, S. 1994, Physica B, 194-196, 1183

Pompea, S.M., Bergener, D.W., Shepard, D.F. & Russak, S. 1984, Optical Eng., v. 23, n. 2, p. 149

Potters Industries, Inc., Waterview Corporate Center, 20 Waterview Blvd., Parsippany, NJ 07054-1282, (201) 229-2900. Part number A-glass 1922 and 2024

Poulter, G. & Jennings, R.E. 1983, Infrared Physics, 23, 43

Poulter, G. 1984, Infrared Physics, 24, 35

Pozzetti, L., Madau, P., Zamorani, G., Ferguson, H. C. & Bruzual, G. A. 1998, MNRAS, submitted

Precision Cryogenic Systems, Inc., 7804 Rockville Road, Indianapolis, Indiana 46214: (317) 273-2800

Pritchet, C.J. 1994, PASP, 106, 1052-1067

Puget, J.-L., Abergel, A., Bernard, J.-P., Boulanger, F., Burton, W.B., Desert, F.-X. & Hartmann, D., 1996, A&A, 308, L5

Puget, J.-L. et al., 1998, A&A, accepted

Randell, C.M. & Rawcliffe, R.D. 1967, "Refractive Indices of Germanium, Silicon, and Fused Quartz in the Far Infrared," Applied Optics, 6 (11), p. 1889-1895

Lord Rayleigh, 1879, Phil. Mag., Series 5, 8 (49), 261

Richards, P.L. & Greenberg, L.T. 1982, Infrared And Millimeter Waves, Volume 6, Chapter 3, Academic Press, Inc.

Richards, P.L. 1994, "Bolometers for infrared and millimeter waves," *J. Appl. Phys* **76** p. 1, 1994.

Rigopoulou, D., Lawrence, A. & Rowan-Robinson, M. 1996, MNRAS, 278, 1049

Rittenhouse, D. 1786, *"An Optical Problem, propofed by* Mr. HOPKINSON*, and folved by* Mr. RITTENHOUSE." Trans. Amer. Phil. Soc., 2, 201

Robinson, F.N.H. 1979, *Noise in Electronic Devices & Circuits*

Roche, P.F. & Chandler, C.J. 1993, MNRAS, 265, 486

Rowan-Robinson, M., et al., 1991, Nature, 351, 719

Rowan-Robinson, M. 1992, MNRAS, 258, 787

Rowan-Robinson, M., Efstathiou, A., Lawrence, A., Oliver, S., Taylor, A., Broadhurst, T.J., McMahon, R.G., Benn, C.R., Condon, J.J., Lonsdale, C.J., Hacking, P., Conrow, T., Saunders, W.S., Clements, D.L., Ellis, R.S. & Robson, I. 1993, MNRAS, 261, 513

Sakai, K. & Genzel, L. 1983, Reviews of Infrared and Millimeter Waves, p. 155-247

Salzberg, C.D. & Villa, J.J. 1957 "Infrared refractive indexes of Silicon, Germanium and modified Selenium glass," J. Opt. Soc. Am. **47**, 244

Sandell, G. 1994, MNRAS 271, 75

Sanders, D.B., Scoville, N.Z. & Soifer, B.T. 1991, ApJ, 370, 158

Sargent, W.L.W., Steidel, C., & Boksenberg, A. 1989, ApJSS, 69, 703

Sarwinski, R.E.; in technical brochure distributed by R.G. Hansen & Associates, 631 Chapala St., Santa Barbara, CA 93101; (805) 564-3388

Sato, S., Hayakawa, S., Matsumoto, T., Matsuo, H., Murakami, H., Sakai, K., Lange, A.E. & Richards, P.L. 1989, Appl. Op., v. 28, n. 20, p. 4478

Schieder, R. 1998, "Design of large bandwidth acousto-optical spectrometers," in *Advanced Technology MMW, Radio, and Terahertz Telescopes*, T. G. Phillips, ed., *Proc. SPIE* **3357**

Schmitt, H.R., Kinney, A.L., Calzetti, D. & Storchi-Bergmann, T., 1997, AJ, 114, 592

Schroeder, D.J. 1987, Astronomical Optics, (San Diego: Academic Press)

Schuberth, E. 1984, Rev. Sci. Inst., 55 (9), 1486

Schuller, F. 1998, "Spectromètre Submillimétrique au Sol"; Thesis, Université Paris VI

Scialdone, J.J. 1983, J. Spacecraft & Rockets, 30 (2), 208-215

Scoville, N.Z., Matthews, K., Carico, D.P. & Sanders, D.B. 1988, ApJ, 327, L61

Scoville, N.Z., Yun, M.S., Windhorst, R.A., Keel, W.C. & Armus, L. 1997, "CO J=3-2 emission in the radio galaxy 53W002 at z=2.394," ApJ, **485**, pp. L21–L24

Serabyn, E. 1994, in Multi-Feed Systems for Radio Telescopes, eds. D.T. Emerson & J.M. Payne, ASP Conf. Ser., v. 75, (San Francisco: ASP)

Serabyn, E. & Weisstein, E.W. 1995 "Fourier-Transform Spectroscopy of the Orion Molecular Cloud Core," ApJ, **451**, 238-251

Serabyn E. & Weisstein, E.W. 1996 "Calibration of Planetary Brightness Temperature Spectra at Near-Millimeter and Submillimeter Wavelengths with a Fourier-Transform Spectrometer," Applied Optics **35,** 2752-2763

Serabyn, E. 1997, "A wide-field relay optics system for the Caltech Submillimeter Observatory," *Int. J. IR MM Waves* **18** (2) p. 273–284

Serabyn, E., Weisstein, E.W., Lis, D.C. and Pardo, J.R. 1998, "Submillimeter Fourier-transform spectrometer measurements of atmospheric opacity above Mauna Kea," Applied Optics **37**, 2185-2198

Serlemitsos, A.T., SanSebastian, M. & Kunes, E., "Design of a spaceworthy adiabatic demagnetization refrigerator," *Cryogenics* **32** p. 117–121, 1992

Shafer, R. A., Mather, J. C., Fixsen, D. J., Jensen, K. A., Reach, W. T., Wright, E. L., Dwek, E., & Cheng, E. S. 1998, preprint

Shklovskii, B.I. & Efros, A. L. 1984, *Electronic properties of the doped semiconductors* (Springer-Verlag, New York)

Silva, L. & Danese, L., 1998, ApJ, submitted

Skyba, P., Gréser, Z., Krasnya, Z. & Smolka, N., "Digitally Controlled Current Source for Demagnetization Refrigerators," Cryogenics, 34 (9), 739

Smail, I., Ivison, R.J. & Blain, A.W. 1997, ApJL, 490, L5

Smail, I., Ivison, R.J., Blain, A.W. & Knieb, J.-P. 1998, BAAS, 192, #48.13

Smith, S.M. 1984, Appl. Op., v. 23, n. 14, p. 2311

Smoot, G. F., Bennett, C. L., Kogut, A., Wright, E. L., Aymon, J., Boggess, N. W., Cheng, E. S., De Amici, G., Gulkis, S., Hauser, M. G., Hinshaw, G., Jackson, P. D., Janssen, M., Kaita, E., Kelsall, T., Keegstra, P., Lineweaver, C., Loewenstein, K., Lubin, P., Mather, J., Meyer, S. S., Moseley, S. H., Murdock, T., Rokke, L., Silverberg, R. F., Tenorio, L., Weiss, R. & Wilkinson, D. T. 1992, Ap. J., 396, L1

Soifer, B.T., Neugebauer, G., Helou, G., Lonsdale, C.J., Hacking, P., Rice, W., Houck, J.R., Low, F.J., Rowan-Robinson, M. 1984, ApJ, 283, L1

Soifer, B.T. & Neugebauer, G., 1991, AJ, 101, 354

Solomon, P.M., Rivolo, A.R., Barrett, J.W. & Yahil, A. 1987, ApJ, 319, 730

Solomon, P.M., Downes, D., Radford, S.J.E., Barrett, J.W. 1997, ApJ, 478, 144

Spaans, M. 1997, ApJ, 488, L79

Stacey, G.J., Geis, N., Genzel, R., Lugten, J.B., Poglitsch, A., Sternberg, A. & Townes, C.H. 1991, ApJ, 373, 423

Stapelfeldt, K., JPL; Private communication regarding the temperature of Mars at a wavelength of $\sim 400\mu$m using the method & software of D. Rudy (JPL).

Stark, A. 1997,"Potential measurement of the luminosity function of 158 micron CII at high redshifts: a test of galaxy formation models," ApJ, **481** p. 587–593

Steidel, C.C. & Sargent, W.L.W. 1991, ApJ, 382, 433

Steidel, C.C., Giavalisco, M., Pettini, M., Dickinson, M. & Adelberger, K.L. 1996, ApJ, 462, L17

Strauss, M.A., Huchra, J.P., Davis, M., Yahil, A., Fisher, K.B. & Tonry, J. 1992, ApJS, 83, 29

Stützel, P., Tegtmeier, H.D. & Tacke, M. 1988, Infr. Phys., v. 28, n. 2, p. 67

Swinyard, B.M., Clegg, P.E., Ade, P.A.R., Armand, C., Baluteau, J.-P., Barlow, M.J., Berges, J.-C., Burgdorf, M., Caux, E., Ceccarelli, C., Cerulli, R., Church, S.E., Colgan, S., Cotin, F., Cox, P., Cruvellier, P., Davis, G.R., Digiorgio, A., Emery, R.J., Ewart, D., Fischer, J., Furniss, I., Glencross, W.M., Greenhouse, M., Griffin, M.J., Gry, M.R., Haas, C., Joubert, M., King, K.J., Lim, T., Liseau, R., Lord, S., Lorenzetti, D., Molinari, S., Naylor, D.A., Nisini, B., Omont, A., Orfei, R., Patrick, T., Pequignot, D., Pouliquen, D., Price, M.C., Nguyen-Q-Rieu, Robinson, F.D., Saisse, M., Saraceno, P., Serra, G., Sidher, S.D., Smith, H.A., Spinoglio, L., Texier, D., Towlson, W.A., Trams, N., Unger, S.J. & White, G.J. 1996, A&A, 315, L43

TGV, Inc., 603 Mission St., Santa Cruz, CA 95060-3653

Thronson, H. & Telesco, C. 1986, ApJ, 311, 98

Thronson, H.A., Walker, C.K., Walker, C.E. & Maloney, P. 1987, ApJ, 318, 645

Tilanus, R.P.J., Tacconi, L.J., Sutton, E.C., Zhou, S., Sanders, D.B., Wynn-Willaims, C.G., Lo, K.Y. & Stephens, S.A. 1991, ApJ, 376, 500

Timbie, P.T., Bernstein, G.M. & Richards, P.L. 1990, "Development of an adiabatic demagnetization refrigerator for SIRTF," *Cryogenics* **30** p. 271–275

Timbie, P.T., Zhou, J-W., Farroqui, K. & Wilson, G. 1994, "Issues in the Readout of FIR and MM-Wave Bolometers for Astrophysical Applications," Proc. SPIE, v. 2226, p. 2-13

Torre, J.P. & Chanin, G. 1984, "Heat Switch for Liquid-Helium Temperatures," Rev. Sci. Inst., 55 (2), 213

Torre, J.P. & Chanin, G. 1985, "Miniature liquid-^{3}He refrigerator," *Rev. Sci. Inst.* **56** p. 318–320

Townes, C.H. & Schawlow, A.L. 1955 *Microwave Spectroscopy*, McGraw-Hill, New York, NY

Trimble, V. & McFadden, L.-A., 1998, PASP, 110, 223

Turner, J.L., Martin, R.N. & Ho, P.T.P 1990, ApJ, 351, 418

Ulrich, R. 1967, Infrared Physics, 7, p. 37-55

van der Werf, P.P. 1998a, in *Highly Redshifted Radio Lines*, ASP Conference Series; Carilli, Radford, Menten & Langston, eds.

van der Werf, P.P. 1998b, in *The Most Distant Radio Galaxies*, Röttgering, Best & Lehert, eds.; Kluwer Academic Publishers, Dordrecht.

van Ojik, R., Röttgering, H.J.A., van der Werf, P.P., Miley, G.K., Carilli, C.L., Visser, A., Isaak, K.G., Lacy, M., Jenness, T., Sleath, J. & Wink, J. 1997, A&A, 321, 389

Vergnat, P. et al. 1969, Journal de Physique, 30 723

Vilches, O.E. & Wheatley, J.C. 1966, Rev. Sci. Inst., 37, p. 819-831

Virginia Semiconductor, 1501 Powhatan Street, Fredricksburg, VA 22401; (540) 373-2900

von Herzen, B. 1998, "Digital cross-correlation at 250 MHz using high-performance FPGAs," in *Advanced Technology MMW, Radio, and Terahertz Telescopes*, T. G. Phillips, ed., *Proc. SPIE* **3357**

Wang, B, 1991a, ApJ, 374, 456

Wang, B, 1991b, ApJ, 374, 465

Wang, N., Hunter, T.R., Benford, D.J., Serabyn, E., Phillips, T.G. and Moseley, S.H. 1994, SPIE Symposium on Astronomical Telescopes and Instrumentation for the 21st Century, Kona, Hawaii

Wang, N., Hunter, T.R., Benford, D.J., Serabyn, E., Lis, D.C., Phillips, T.G. & Moseley, S.H. et al. 1996, Appl. Op., 35, 6629

Weinberg, S. *Gravitation and Cosmology: Principles and Applications of the General Theory of Relativity*, Wiley & Sons, New York.

Weinberg, S. 1977, "The First Three Minutes", Bantam Books, New York

Weisstein, E. & Serabyn, E. 1994, "Detection of the 267 GHz J=1-0 rotational transition of PH_3 in Saturn with a new Fourier-Transform spectrometer," *ICARUS* **109**, p. 367

Wells, D.C., Greisen, E.W. & Harten, R.H. 1981, A&AS, 44, 363

White, G.K., "Experimental Techniques in Low-Temperature Physics," 1979, Oxford University Press, New York

Williams, R.E., Blacker, B., Dickinson, M., Dixon, W.V.D., Ferguson, H.C., Fruchter, A.S., Giavalisco, M., Gilliland, R.L., Heyer, I., Katsanis, R., Levay, Z., Lucas, R.A., Mcelroy, D.B., Petro, L., Postman, M., Adorf, H.-M. & Hook, R. 1996, AJ, 112, 1335

Wilner, D.J., Zhao, J.-H. & Ho, P.T.P. 1995, ApJ, 453, L91

Winston, R. 1970, J. Opt. Soc. Am. 60, 245

Woody, D.P. & Keene, J.B.; private communication regarding the analytic calculation of the optical transmission of arbitrary dielectric layers. Resulting program is called *FILTER* and is available as a module of *UAP*.

Wright, E. L., Mather, J. C., Bennett, C. L., Cheng, E. S., Shafer, R. A., Fixsen, D. J., Eplee, R. E., Jr., Isaacman, R. B., Read, S. M., Boggess, N. W., Gulkis, S.,

Hauser, M. G., Janssen, M., Kelsall, T., Lubin, P. M., Meyer, S. S., Moseley, S. H., Jr., Murdock, T. L., Silverberg, R. F., Smoot, G. F., Weiss, R. & Wilkinson, D. T., 1991, ApJ, 381, 200

Wynn-Williams, C.G. & Becklin, E.E. 1993, ApJ, 412, 535

Xu, J., Lange, A.E. & Bock, J.J. 1996, "Far-Infrared Emissivity Measurements of Reflective Surfaces," Proc. 30th ESLAB Symposium, ESA SP-388

Yamada, Y., Mitsuishi, A. & Yoshinaga, H. 1962, J. Optical Society of America, 52, 17

Young, J.S., Xie, S., Tacconi, L., Knezek, P., Viscuso, P., Tacconi-Garman, L., Scoville, N., Schneider, S., Schloerb, F.P., Lord, S., Lesser, A., Kenney, J., Huang, Y.-L., Devereux, N., Claussen, M., Case, J., Carpenter, J., Berry, M. & Allen, L., 1995, ApJS, 98, 219

Yun, M.S., Scoville, N.Z., Carrasco, J.J. & Blandford, R.D. 1997, ApJ, 479, L9

Zhang, J., Cui, W., Juda, M., McCammon, D., Kelley, R.L., Moseley, S.H., Stahle, C.K., Szymkowiak, A.E. 1993, Phys. Rev. B, 48, 2312

Zhang, J., Cui, W., Juda, M., McCammon, D., Kelley, R.L., Moseley, S.H., Stahle, C.K. & Szymkowiak, A.E. 1998, Phys. Rev. B, 57(8), 4472

Appendix A: Pundit's Guide to the SHARC Cryostat

Note: don't try this unless you consider yourself very experienced with SHARC!

Pumping on liquid helium

1. Close both the pot and the pump heat switches.
2. Turn on the Lake Shore thermometer; it should be ~52 Ω.
3. Fill the helium can of the dewar from the storage dewar.
4. Put the SHARC pump fitting on the helium fill tube.
5. Begin pumping by cracking open the large alidade valve slowly until the Lake Shore reading rises at a rate = 0.02 to 0.04 per update. Remember the time delay of ~10 seconds between when you change the valve and when the rate changes.
6. Monitor this rate every 5-10 minutes and continue opening the valve slightly to maintain the rate.
7. Re-top the LN_2 jacket while you wait.
8. After ~45 minutes, you reach a pressure of 38 Torr (the lambda point) on the vacuum gauge, and the Lake Shore reads ~90 ohms. Open the valve all the way!
9. After another ~15 minutes, the Lake Shore thermometer will rise above 105 Ω.

Condensing Helium-3

1. Connect an ohm-meter to the pump thermometer port; it will be about 70 KΩ.
2. Close the knurled green valve on the ^{3}He tank outside the dewar.
3. Verify that the pot heat switch is closed; open the pump heat switch; the pump thermometer will drop quickly to ~25 KΩ.
4. Connect the long BNC from "Heater 2: Charcoal pump." on the battery box to the pump heater BNC port on the housekeeping breakout box.
6. Plug in the AC line; press the big green "1" button; Unplug the AC line.
8. Turn on the pump heater switch on the battery box and adjust voltage to 8.0 Volts.
9. After about 8-9 minutes, the pump thermometer will drop to 2400 ohms, and the LakeShore will read ~40ohms. Turn off the pump heater switch on the battery box.

Setting up the electronics

1. Move the long BNC cable to the JFET heater port on both ends.
2. Connect a BNC between the JFET thermometer port on top of the preamp box to the small blue 10 microamp current source. Voltage will be ~1.9V.
3. Turn on the JFET heater switch and adjust the meter voltage to 6.25 V.
4. When the JFET thermometer drops below 1V after a ~15 minutes, turn on the preamp & A/D power switches on the boxes & the battery box.
5. When the JFET thermometer reading stabilizes near 0.87 V, turn off the ten microamp current source and the Fluke meter to prevent noise pickup.
6. Unplug all BNCs from the dewar.

Pumping on Helium-3

1. Wait until the Lake Shore thermometer again reads >=105 ohms.
2. Open the pot heat switch; Close the pump heat switch. The Lake Shore will rise.
3. You're set when the Lake Shore thermometer reading reaches ≥ 5000 Ω. Turn off the Lake Shore thermometer and unplug the IEEE cable; the only cable plugged into the dewar housekeeping port at this point should be the JFET heater.
4. Open the knurled green valve on the ^{3}Helium tank 1-$^1/_4$ turns.
5. Be sure the fan is running to keep ice off the dewar window.
6. Uncover the flat tertiary mirror and the big ellipsoidal mirror before observing. The Cassegrain flip mirror should be out of the beam to allow SHARC to observe.

Appendix C: Schematics

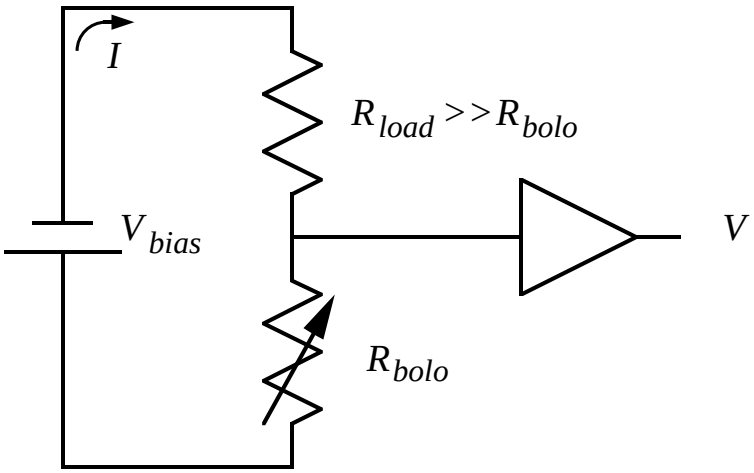

Figure 10.1 A simplified schematic for a bolometer using the classic unlooped voltage amplifier.

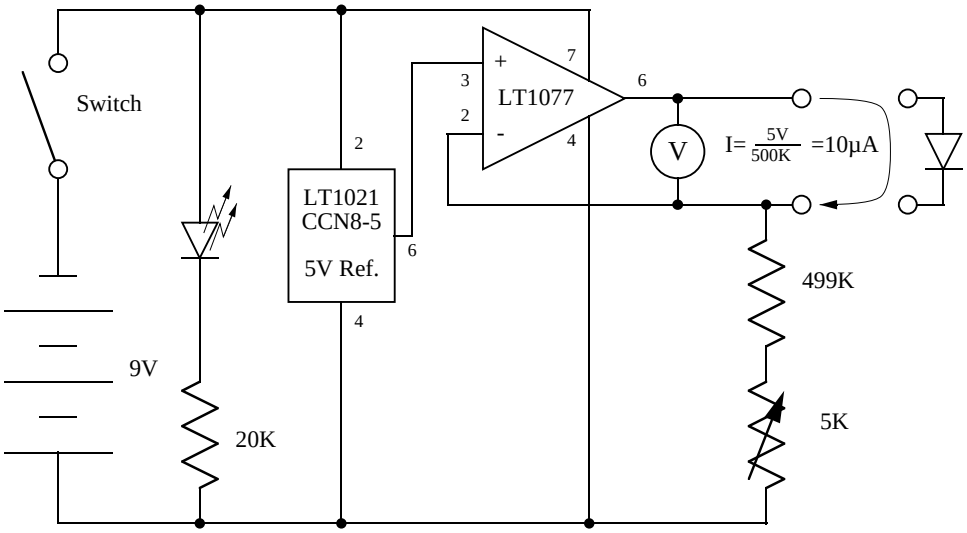

Figure 10.2 Schematic for the ubiquitous 10μA current sources I have used everywhere for diode thermometer readouts.

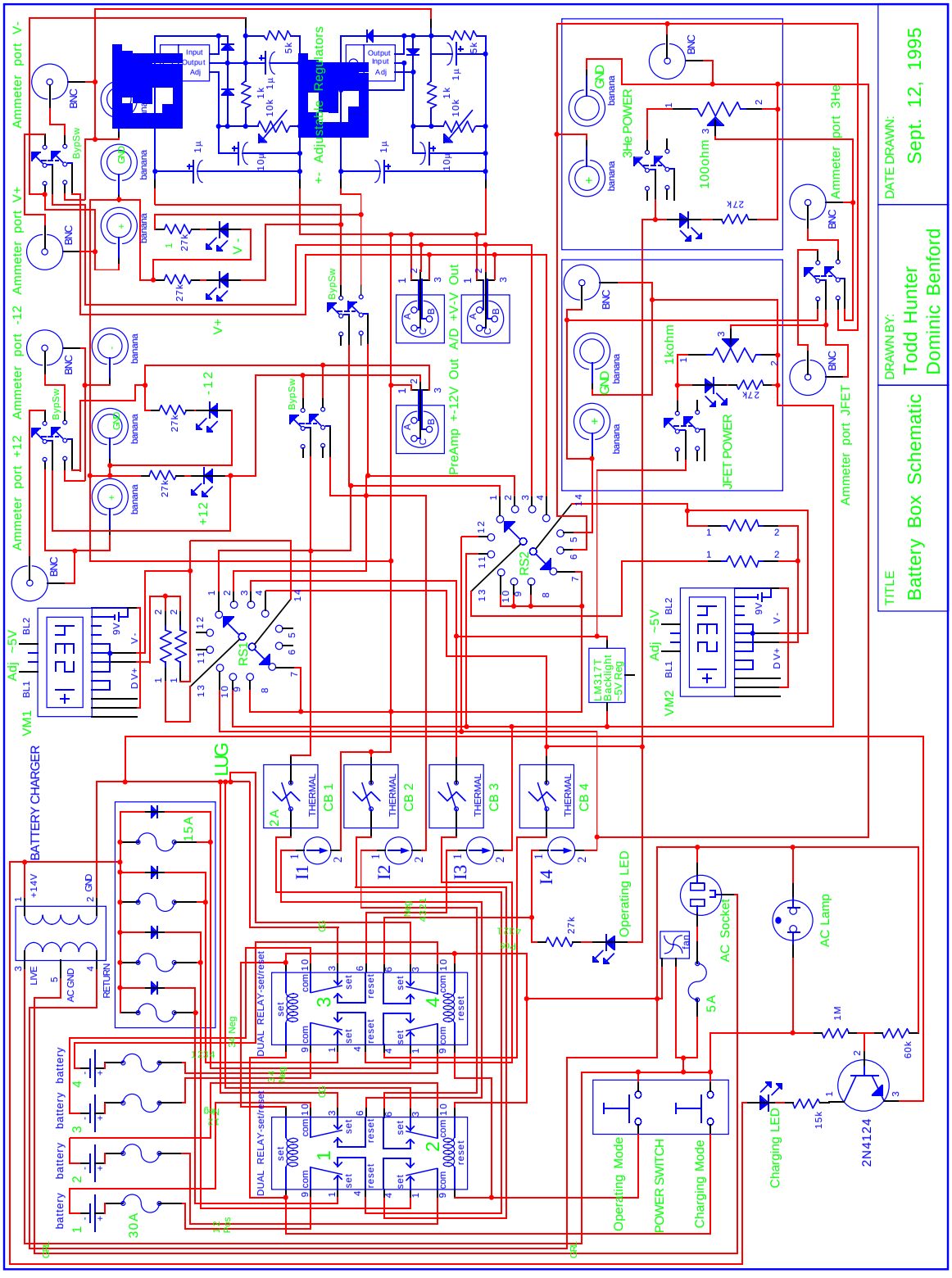

Figure 10.3 SHARC Battery Box, as delivered. Although the layout has changed upon its redesign in August 1998, the fundamental circuitry is still similar.

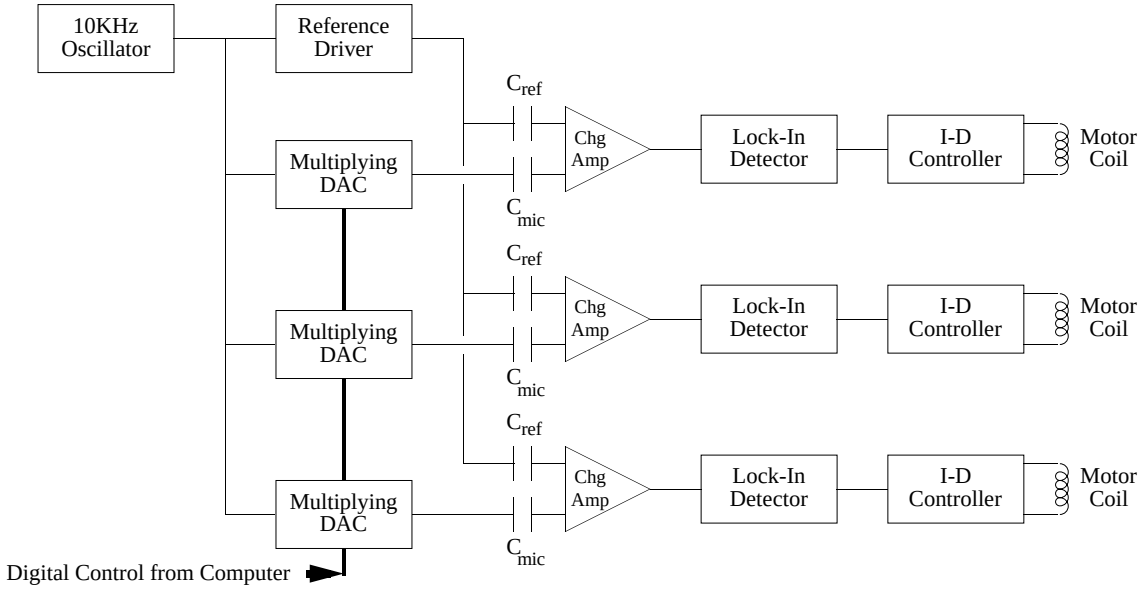

Figure 10.4 Block diagram of the control electronics for the three motors of the Fabry-Perot.

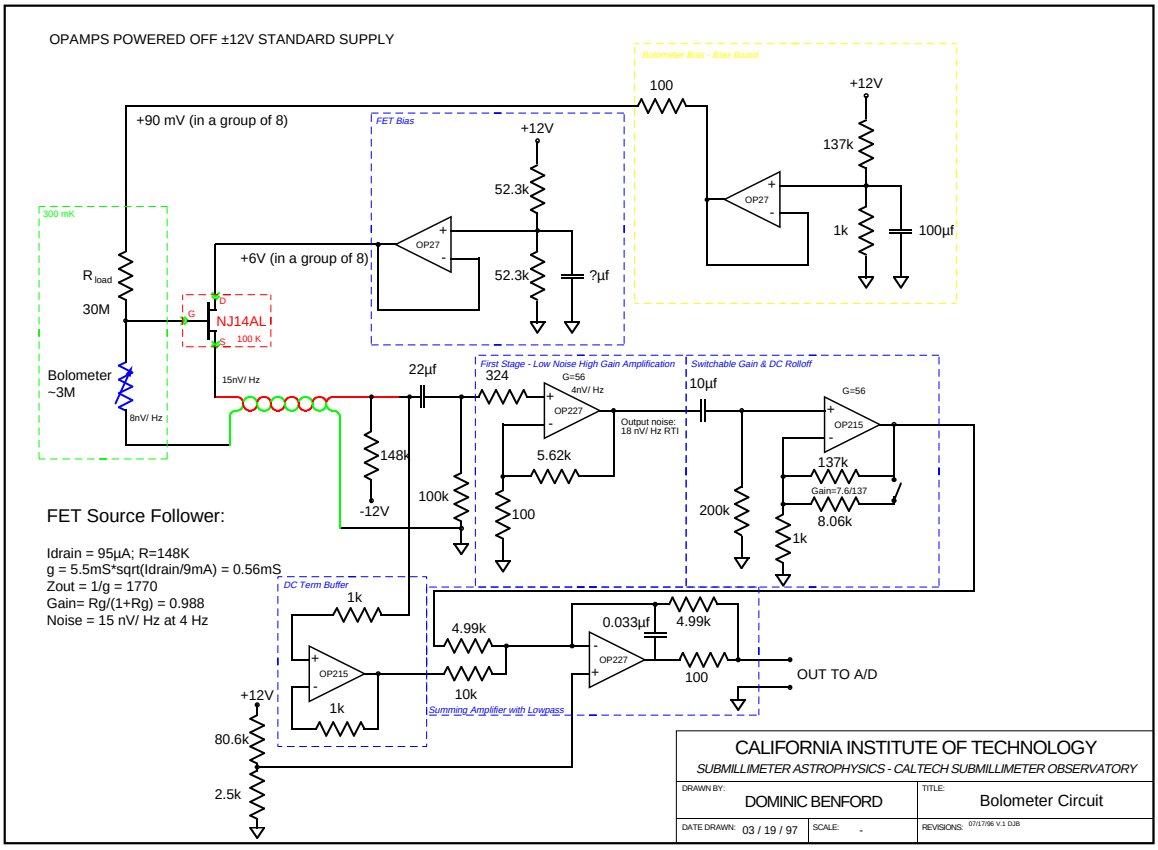

Figure 10.5 Schematic diagram of the GSFC KAO PreAmp.

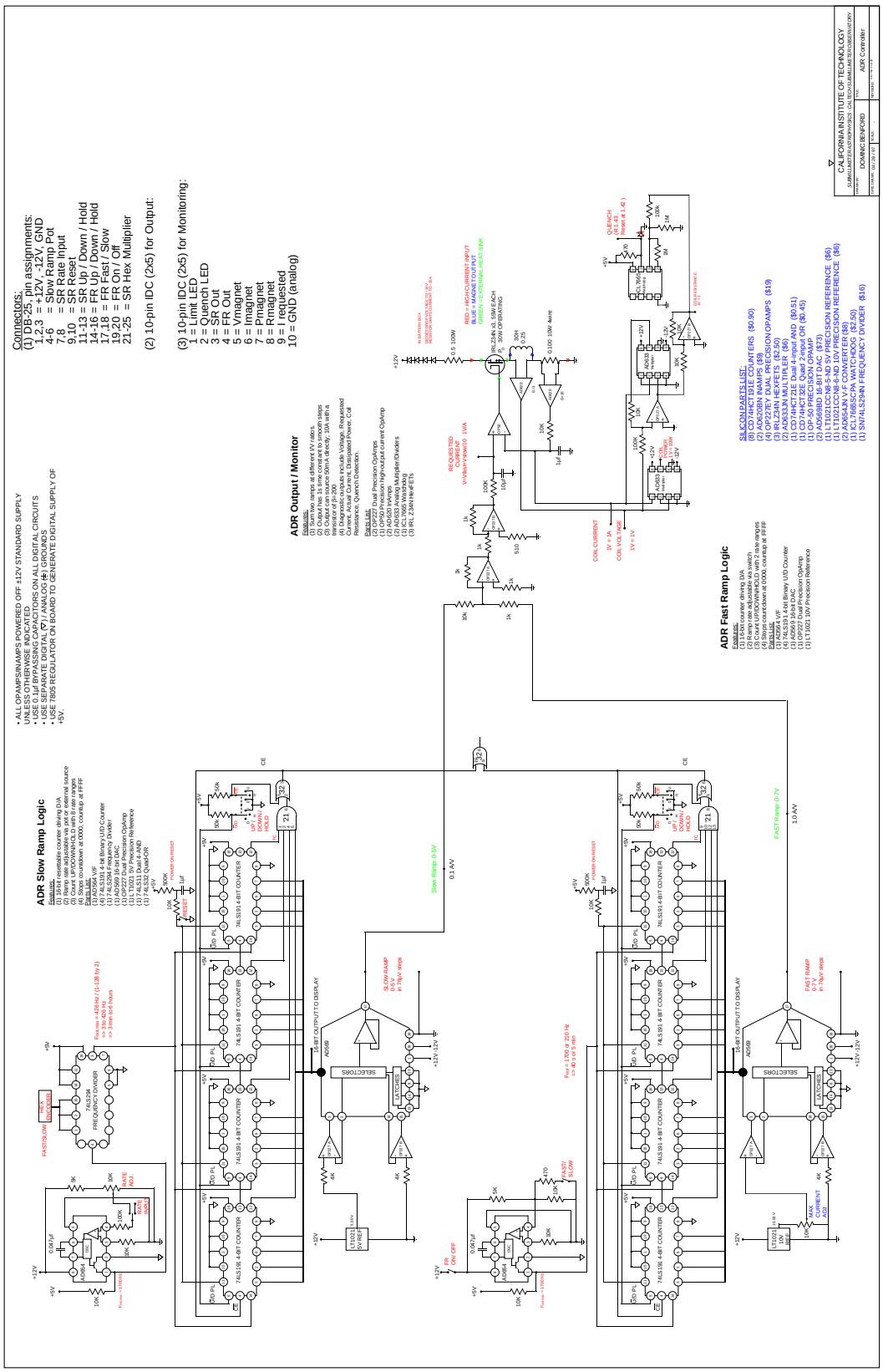

Figure 10.6 Schematic of the ADR controller, a dual digitally-controlled, linear-ramping, constant-current power supply optimized for a superconducting magnet.

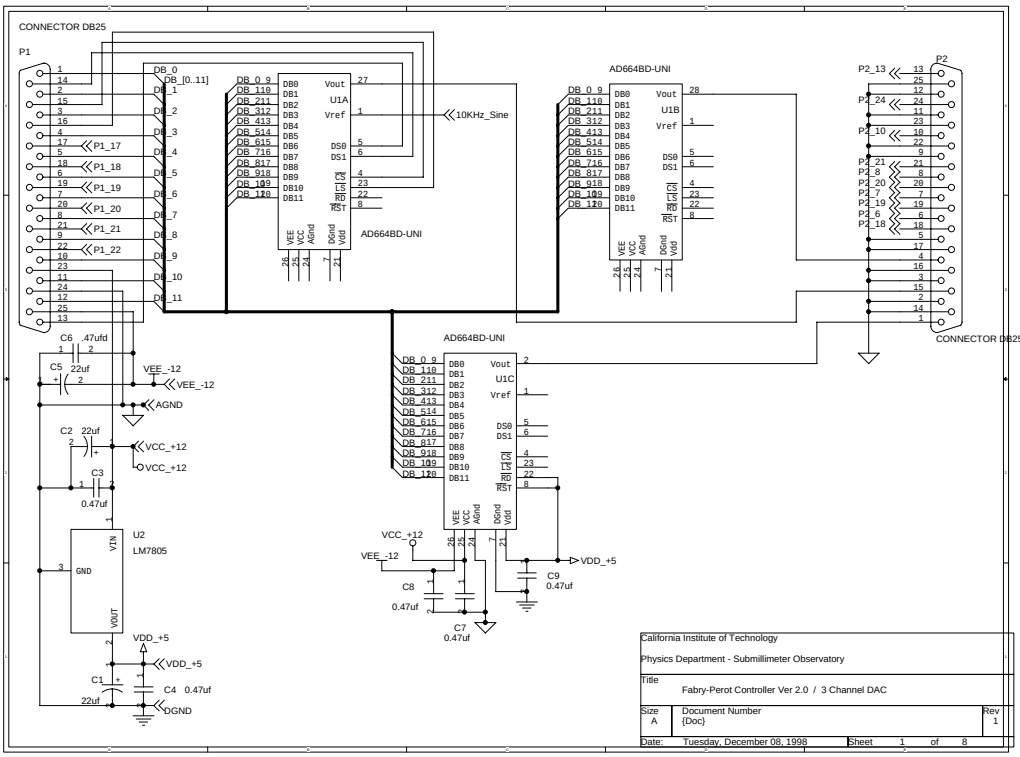

Figure 10.7 Fabry-Perot DAC computer interface. This and the following figures appear courtesy of Jeff Groseth, who drafted the Fabry-Perot schematics.

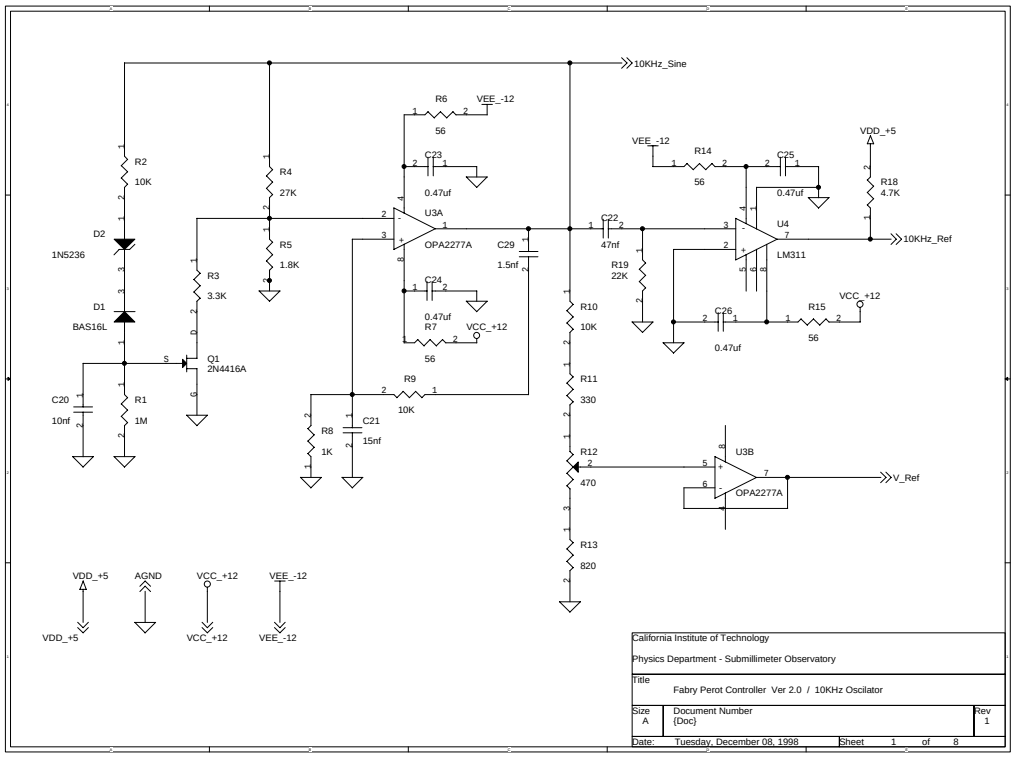

Figure 10.8 Fabry-Perot oscillator.

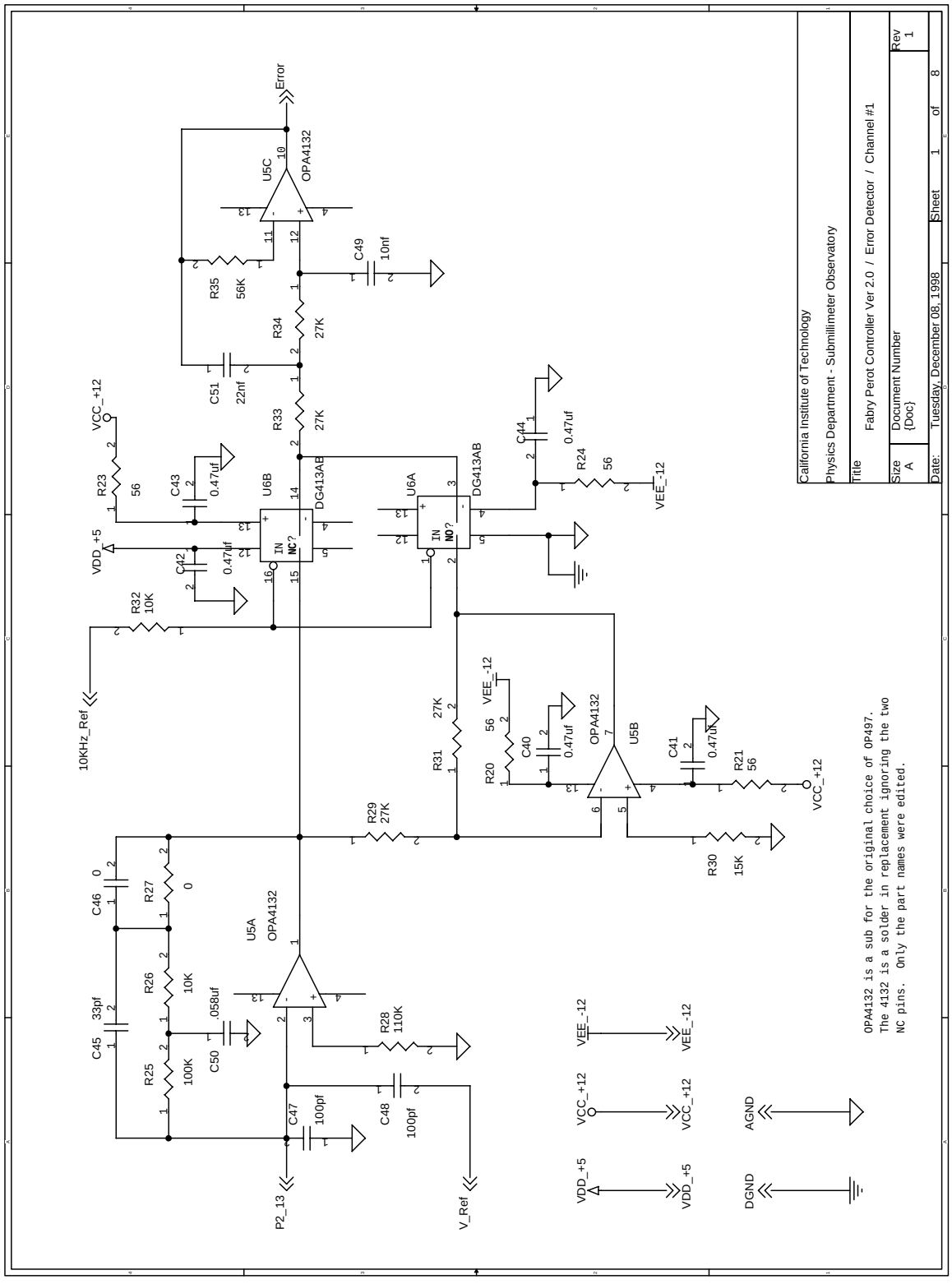

Figure 10.9 Fabry-Perot error detector (motor 1).

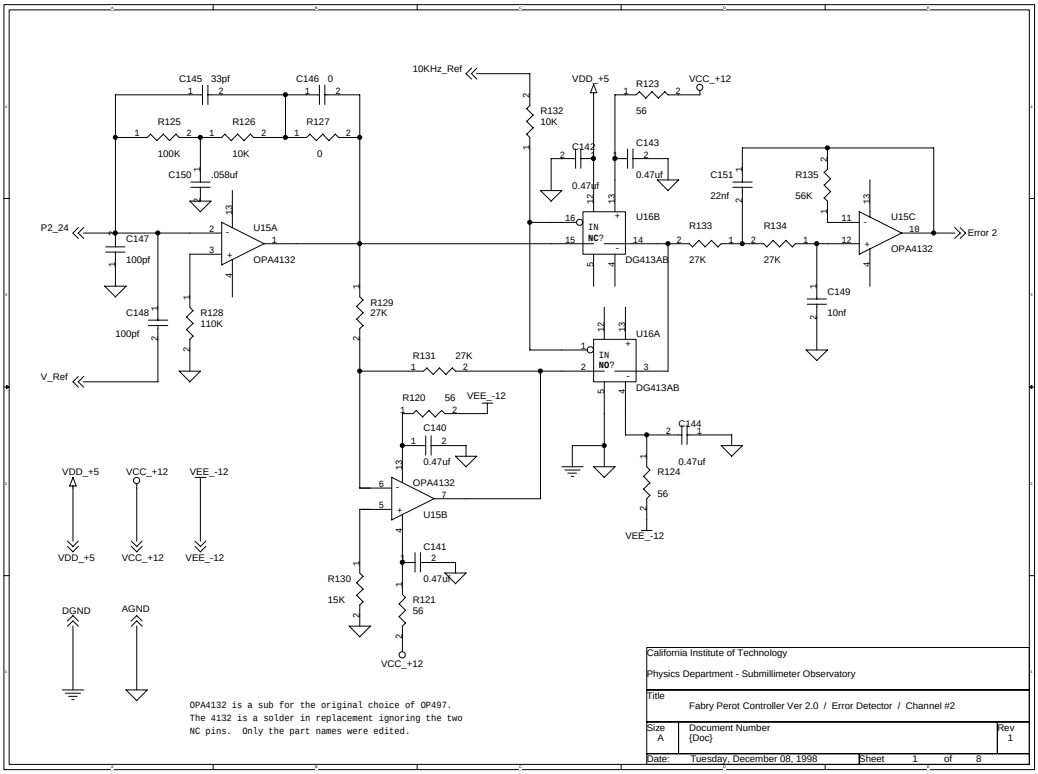

Figure 10.10 Fabry-Perot error detector (motor 2).

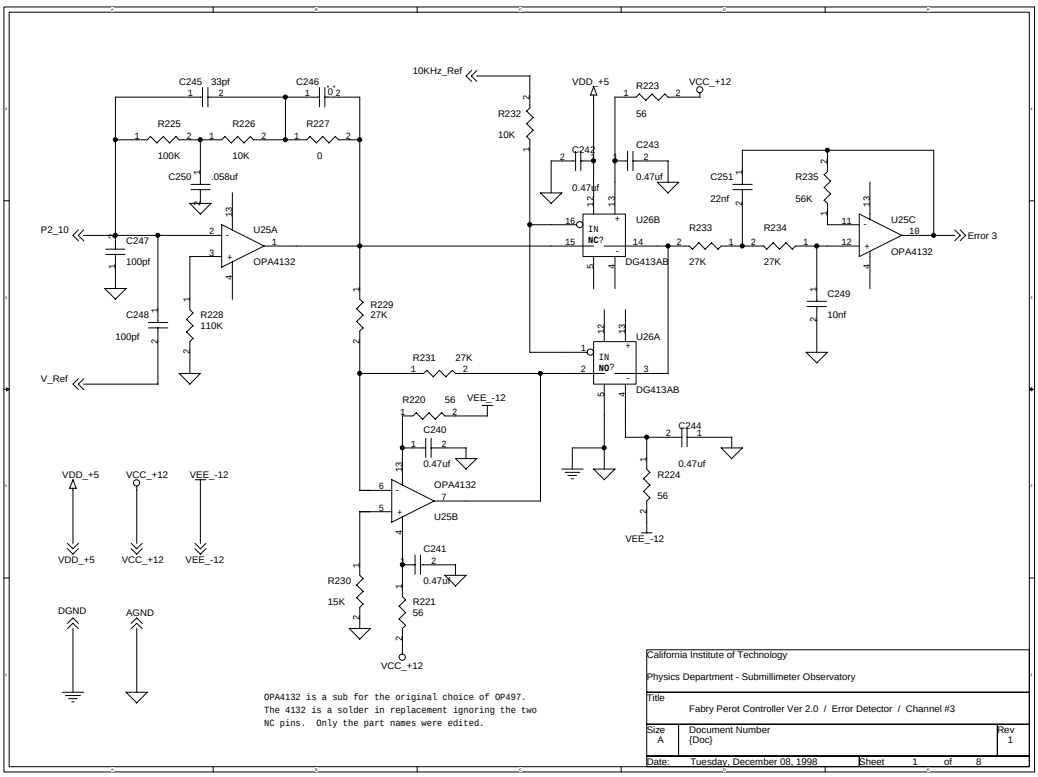

Figure 10.11 Fabry-Perot error detector (motor 3).

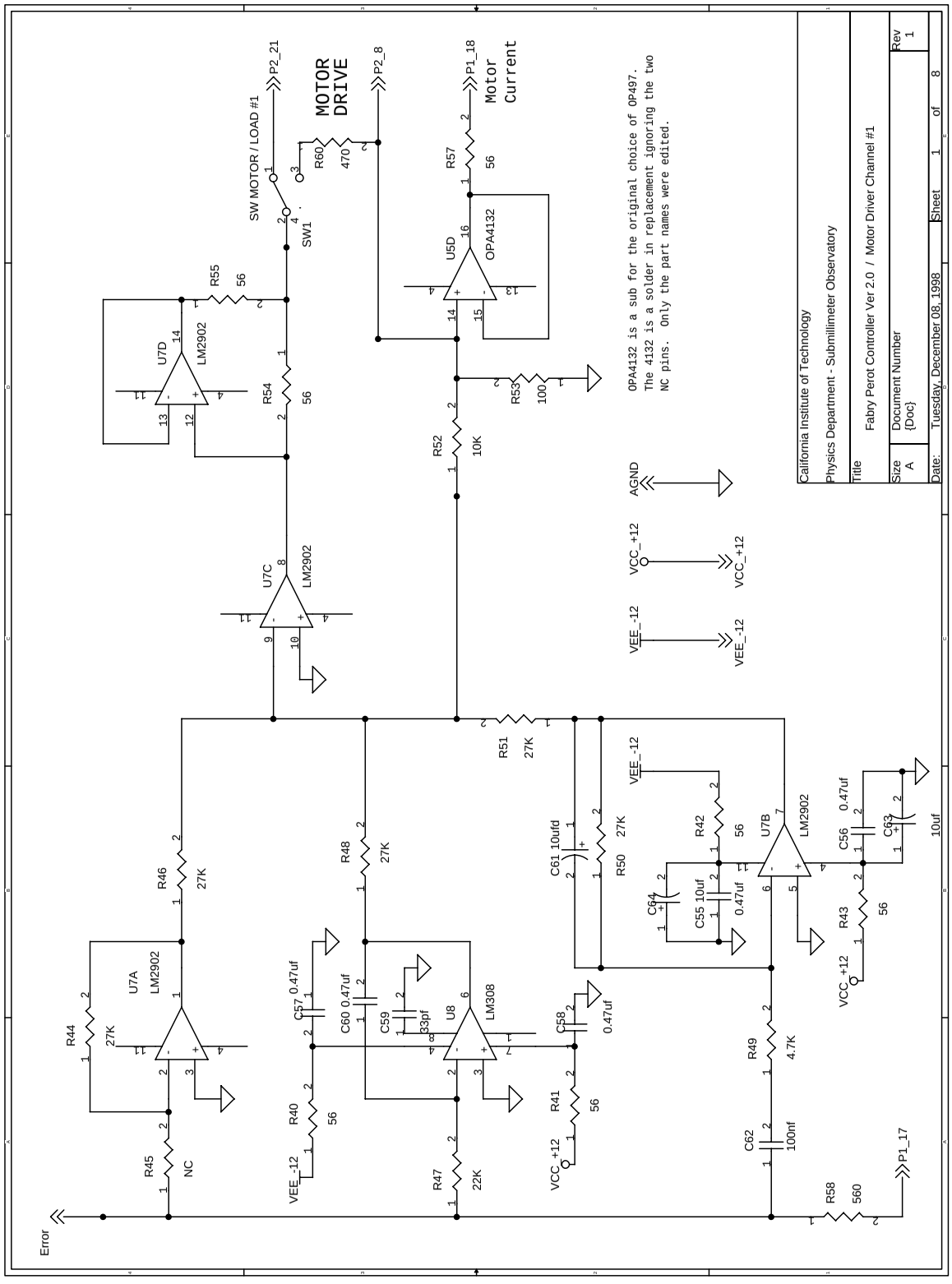

Figure 10.12 Fabry-Perot PID & driver (motor 1).

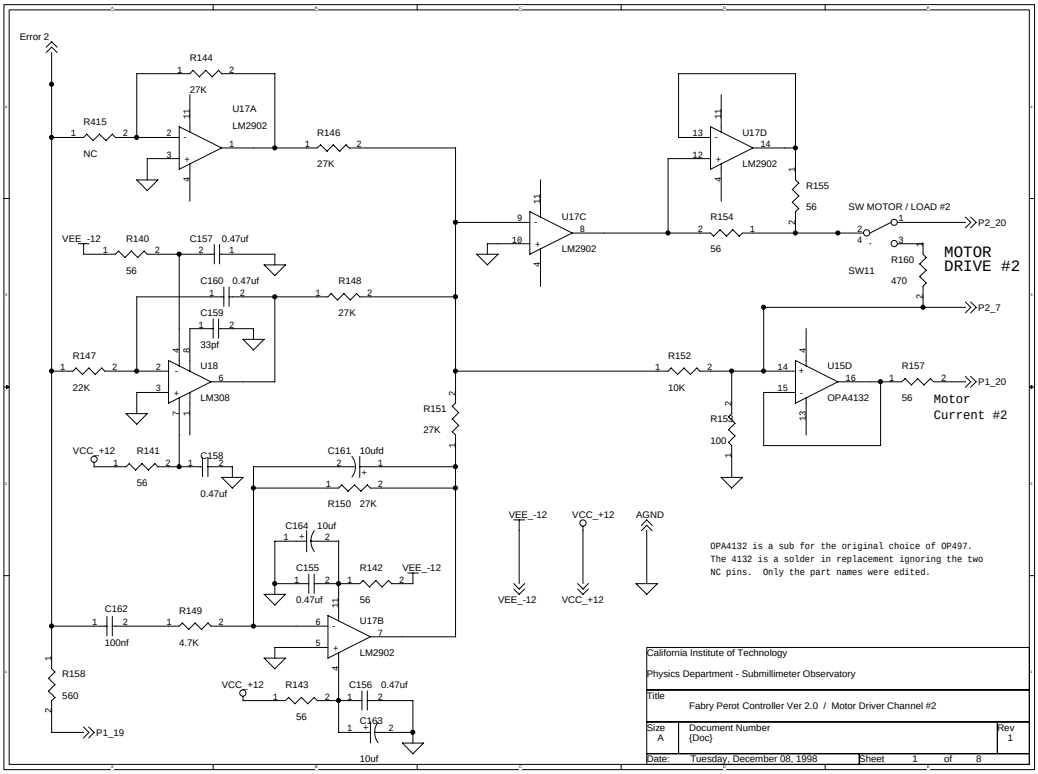

Figure 10.13 Fabry-Perot PID & driver (motor 2).

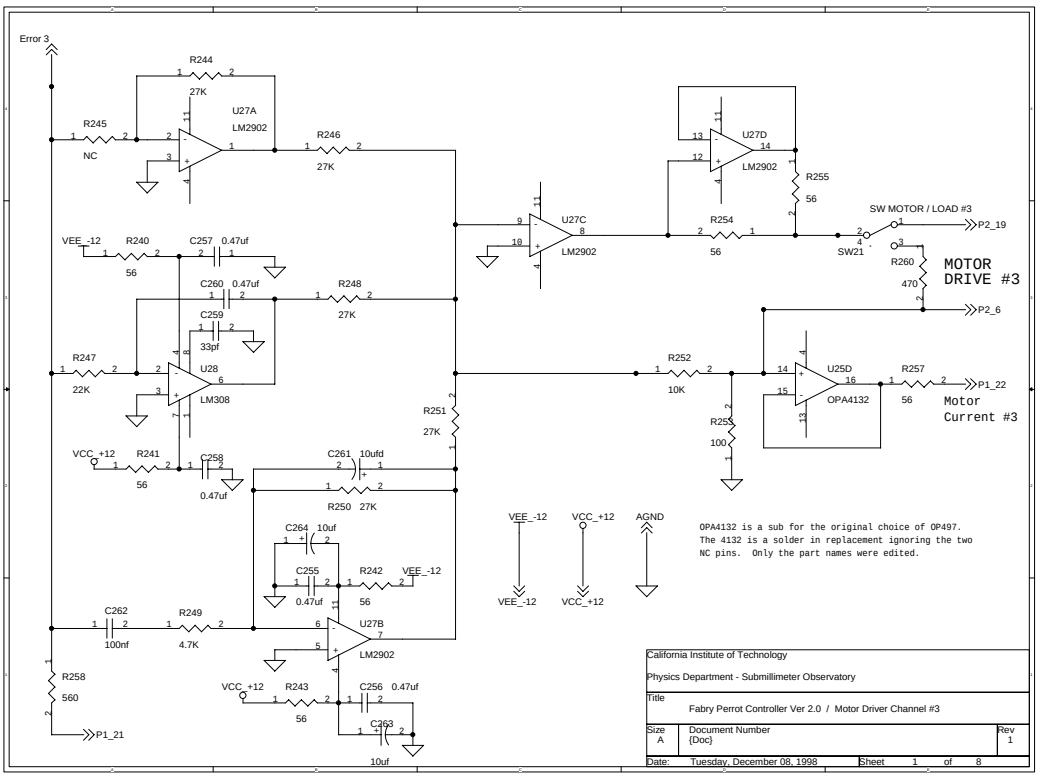

Figure 10.14 Fabry-Perot PID & driver (motor 3).

Appendix D: BADRS Manual

I have authored the *Bolometer Array Data Reduction Software* (BADRS, pronounced Bad-Riss) package, an interactive, scriptable software language for the cleaning, calibration, and display of pointed observations with SHARC. It is currently in release under version 3.15 (99/01/02) and is available on the web via anonymous FTP at `[www.submm.caltech.edu/pub/badrs/badrs_19Nov98.tar.gz]`. It is updated approximately every other month. The command line interface uses the SIC package developed at IRAM for heterodyne spectroscopy and featured in *CLASS* and *GRAPHIC*. This enables scripting, some degree of platform independence, and a useful VMS-like `HELP` command. This chapter serves as a command reference guide to *BADRS*. After a brief introduction to data reduction using *BADRS*, there is a complete command listing explaining the actions of all *BADRS* commands. Standard commands in `SIC` are beyond the purvue of this document, but can be found most easily via the online help.

It is crucial in the processing of CHOP_SLEWY observations that one understand how the data are taken and stored. A single CHOP_SLEWY command directs the telescope to move between the "on" and the "off" beams of the telescope (since the chopping secondary is running), integrating for some time in each beam and writing the data to disk. After some number of these integrations, each of which lasts about 10 seconds of telescope time, the average is written to disk. This is called a *scan* and represents somewhere in the neighborhood of 50 up to 250 seconds of on-source integration time. Because the raw data is written as well as the averages, a standard deviation can be calculated for each data point in the data set of scans. In order to represent the true standard deviation closely, a minimum of ten raw data points must be used in the determination (Bevington 1969). One of the most important functions of *BADRS* is the determination of the standard deviation, which is used for weighting sums or removal of spikes, and ultimately determines the noise remaining in the final

summed data.

One of the first things to do in *BADRS* is to calibrate the data to correct for atmospheric opacity and pixel-to-pixel gain variations. As these calibrations bring the data into real units (Janskys/beam), the concept of a true standard deviation becomes valid. The data set can then be viewed as a two-dimensional array, with the vertical axis being position on the sky along the detectors and with the horizontal axis being time, since each scan is just another sampling of the same astronomical source. After calibrating, removal of a constant offset from each bolometer in each scan is necessary. This is analogous to the destriping algorithm in mapping mode. After removing these offsets the despiking, as outlined above, is applied. *BADRS* allows the removal of spikes using a cutoff based either on the data viewed as a time sequence (taking the standard deviation in the signal from one bolometer) or as a spatial sequence (each scan has its own standard deviation in the detectors). Finally, another baseline is subtracted to compensate for the despiked pixels. Once this processing has been applied, the standard deviation for every data point in the two-dimensional array using the raw data from that point and the neighboring two points in time (i.e., the same pixel immediately before and after). The array is then ready for final summation.

Adding together the processed scans into a final, single scan can be done in a variety of ways. The simplest is to weight all scans by the time taken to acquire them, so that the final scan is equivalent to what would have been recorded at the telescope if it had simply been integrating for the entire time, and wrote only the final result. This can be improved upon if one weights scans more heavily if the noise level is less (sigma weighting). This is a valid approach in that the true signal-to-noise changes during the observation due to the rising and setting of the source through a varying amount of atmosphere. The sigma used for this weighting can be either the standard deviation of each pixel or of each scan as a whole. After summing, a baseline (usually linear) can be removed to subtract off any remaining spurious offset.

One more subtlety exists: there is a low-level discrepancy in the digitizing electronics for SHARC in that odd and even bolometers use equivalent but separate

channels of a dual digital-to-analog converter. There is therefore a small amount of residual signal which varies consistently from channel to channel, like a square wave of fixed amplitude. Accordingly, this can be modeled and subtracted, and is typically (for long integrations, appropriate to observations of distant galaxies) a correction on the order of a few mJy. Nevertheless, it contributes to the overall standard deviation of the final scan.

BADRS has a routine for fitting a Gaussian to the final data and can plot the results for inclusion in publications. A final scan on the Cloverleaf quasar, H1413etc, is shown below to illustrate the excellent quality of data obtainable.

Because of an unfortunate correspondence between the SIC command option designator and the Unix directory delimiter (/), all directory names used in *BADRS* commands must be placed in double quotes to avoid parsing them as qualifiers.

A few terms to remember: each integration from the telescope is a scan; the input file is the data you wish to reduce; the output file is the data you are writing (which is, one would hope, reduced); the current found list is the list of scans which are being processed; and the current scan is the scan in memory being acted upon by processing.

DEBUG Turns on debugging messages, which are useful to a programmer but otherwise pretty worthless.

DIRECTORY Lists the contents of the current directory. Optionally, a command of the form `DIRECTORY ''/home/mirkwood/dbenford''` will list the contents of another directory.

FLIP Causes all the data to be multiplied by -1. This is useful in the event that one inadvertently swaps the meaning of the "on" and "off" beams of the telescope. Using the built-in UIP macro *PHASE_12* or any of its variants will guarantee that the beams are defined correctly.

DEVICE Opens a graphics device for display. This uses the conventional PGPLOT devices installed on the host system, but aliases to the most commonly used are allowed via the qualifiers */XWINDOW*, */VT125*, */GF*, and */XSERVER*.

FILE Opens a file for either input or output. `FILE IN filename` will read in

the contents of a preexisting file named `filename` (in double quotes if a directory is specified). `FILE OUT filename` will open a new or preexisting file for output. The file header written to a new output file will be identical to the file header of the current input file; therefore, the `FILE OUT` command should never be used without previously opening an input file. The `NEW` command will reread the current input file, which is useful if it has changed (for instance, at the telescope when new data has been written).

PLOT Plots the current data to the output display or to a postscript file on disk. Qualifiers are `/HARD filename` which will write a hardcopy to disk with the default filename `badrs.ps` unless an alternative is specified. It is also sent to the printer defined by the Unix environment variable `BADRS_PRINTER`. The option `/SPECTRUM` will plot only the data, analogous to the *CLASS* command `SPECTRUM`. The option `/BAD_INCLUDED` will plot the bad channels (see `SET BAD`, while the opposite option `/BLANK_BAD` will not. If a Gaussian fit has been calculated, the option `/GAUSS_FIT` will draw the curve on top of the data. The option `/ARCSECONDS` will plot the scan in units of spatial offset in arcseconds rather than the default unit, detector number. You can specify a title to plot in the upper right-hand corner using the option `/TITLE title` and specifying a valid character string `title`. Because SHARC is a lock-in detected system, you can plot either the `/IN_PHASE`, `/QUADRATURE`, or `/TOTAL_POWER` as your signal. The quadrature data is not written to disk correctly, so will be useless until somebody corrects that software bug, so neither of the last two options are recommended. Therefore, `/IN_PHASE` is selected by default. The plot will be drawn in color if the option `/COLOR` is specified. A more publication-ready hardcopy can be produced using the option `/PUBLICATION`.

GET Brings a scan into the current memory. The current scan is used for most operations, so the `GET` command is necessary before attempting them.

SET/SHOW This command is used to set any of several parameters which affect the operation of *BADRS*. They include:

1. `WEIGHT` sets the weighting method, by `SIGMA` or by `TIME`.

2. SIGMA sets the definition of the standard deviation to be either the standard deviation of the SCAN or the standard deviation in each CHANNEL.

3. SOURCE sets the name of the source you wish to search for in FIND.

4. BAD is used to flag channels as bad (so they are not used in calculating standard deviations or baselines) or to set them back to good. Up to 8 channels may be specified on each line.

5. NUMBER sets the range of scan numbers which can be found using the FIND command.

6. CALIBRATION sets a numerical factor for converting from millivolts (mV) to Janskys (Jy). This is used when you want a quick look at your data with some calibration applied. After calibrating your data using the CALIBRATE command, the conversion factor from mV (calibrated to zero airmasses!) to Jy is roughly 0.4.

7. UNIT chooses between VOLTS or JANSKYS for the display unit. This has no effect on the data, only on the display - it does not calibrate anything!

LIST_SCANS Provides a listing of the currently found scans. Using the /FULL option will give you more information than you'll know what to do with, while SCAN number will give you all the information on a single scan number. The ALL option lists all the scans in the current input file.

CALIBRATE Corrects all data in the currently found scans list for either atmospheric opacity or pixel-to-pixel gain variations. Selecting the /GAIN filename option will calibrate for the gain variations, reading in from a data file of the same format as the *CAMERA* calibration file, CAMERA.DAT.

BASE Removes a baseline from a scan or scans. The baseline order can be 0 (constant offset) or 1 (linear offset). A command like BASE 0 /ALL will remove a constant offset from all scans in the currently found list.

DROP Removes a scan of scans from the current found list. Without any parameters, it will drop the current scan; otherwise up to 9 scans may be dropped on a single command line.

FIND Searches through the current input file to produce the current found list. All scans between the `SET NUMBER` limits matching the `SET SOURCE` sourcename will be found, unless they have previously been `IGNORE`ed. Use the `FIND/ALL` command to find all scans regardless of ignore status.

DESPIKE Removes spikes from the data, both raw and averaged. `DESPIKE` takes a parameter indicating the sigma cutoff; i.e., `DESPIKE 3` will remove all spikes more than 3 standard deviations away from the mean. With no options, it will apply a despiking to all scans, using the sigma definition set by `SET SIGMA`. With the `/TIME` option, instead of despiking a scan, the algorithm will look at the "scan" made up of the time series of data seen by a given pixel. In either case, `DESPIKE` replaces any bad data points with the average of the neighboring two points. Failing this, it merely decreases its deviation to less than the sigma limit.

HEADER Prints a header to the screen. The option `FILE` will print out the file header. The option `SCAN` prints out the current scan header or (with `SCAN n`) the header for scan `n`. Using `/FULL` prints out all the information, rather than just what I deem useful.

GAUSS_FIT Performs a nonlinear least-squares fitting of a single Gaussian function to the current scan. By default, it searches for a peak near the reference pixel (0 arcseconds offset), but `GAUSS_FIT x` will attempt to fit a peak near pixel `x`. The option `/BEAM` will constrain the Gaussian width to be equivalent to the diffraction limited beam. This option is useful for the `CLEAN` routine.

IGNORE Removes a scan from the currently found list. Without a parameter, the current scan is removed; otherwise, up to 9 scans may be removed on a single command line. `IGNORE` differs from `DROP` in that the `FIND` command does not recover `IGNORE`d scans.

NEW Rereads the current input file. In the event that new data has been added (as at the telescope when the next scan has been written to disk), this command gives

you access to it. In *BADRS*, the file is read in all at once, then closed, so that the file does not remain open and (in principle) no opportunity for data corruption exists.

PRINT Writes a *CLASS* style output of the data, in a friendly ASCII format that anyone can import into other programs. The `/ALL` option will write out the entire file, so that *BADRS* can be used as a file translator.

SUM Sums the scans in the current found list and puts the result in the current scan. The *BADRS* settings `WEIGHT` and `SIGMA` control how the data is weighted.

WRITE Writes the current scan to the output file. Be aware that no raw data is written since, in general, there is no raw data for the current scan. Only the scan average and the standard deviation are written.

SMOOTH Performs a Hanning smoothing on the current scan. This combines each pixel with the neighboring pixel (if good) using the weights (0.5, 1, 0.5). The effective resolution is changed, so the flux calibration should also change. Use this routine with caution.

CLASS Writes a CLASS format output file.

SHIFT Nudges the current scan data to the `RIGHT` or `LEFT`, depending on the parameter you specify, by one pixel. This can be used to correct for pointing drifts in $5''$ jumps. The channel on one end is thrown away, and that on the other end set to the neighboring pixel.

MULTIPLY Multiplies the current scan by a constant factor. This is useful when you want to calibrate by a fixed conversion factor in Jy/mV, and preserve this calibration when you `WRITE` the scan.

INTERPOLATE Interpolates the bad pixels based on the good. The two nearest neighboring pixels (or one if at an edge) are used to interpolate the bad pixel. This is reasonably valid if there is only one bad pixel with two neighbors, since the bolometer array oversamples the telescope diffraction pattern and so the pixels are inherently quite correlated with their neighbors.

STAMP Provides a nifty two-dimensional view of the data set, in greyscale. By default, it will show the averaged data; using the `/RAW`, `/SIGMA`, or `/QUADRATURE` options will display the raw data, the standard deviations, or the quadrature data,

respectively. The output of `STAMP` can be printed using the `/HARD` option.

MAP Prints a two-dimensional image of the data set in Ra-Dec coordinates, in greyscale. This is useful to give you some idea of the source distribution in sky coordinates, in the case of asymmetric sources. There is an option `/COVERAGE` which merely plots the coverage of the Ra-Dec area; this is useful to show where the data was taken even if there is no source.

SIGMA Calculates the standard deviation in the averaged data using the standard deviation in the raw data from each pixel in a given scan and its two neighbors. This should result in a minimum of 12 data points being used for the standard deviation calculation, which is sufficient to represent the true statistical standard deviation accurately. Recent data taken at the CSO will already have a (probably) correct standard deviation in the file written at the telescope; for older data, this command is imperative. In order to accurately represent the standard deviation of the average, all data processing (calibration, despiking, baselining) should be performed before calculating the standard deviations. One note: the windowed area defined by `SET WINDOW` will use the average standard deviation of the remaining pixels, as the presence of signal can artificially increase the standard deviation. There is also an option `/COMPENSATE` which will use the Gaussian fitted parameters from `GAUSS_FIT` to estimate the standard deviation increase from the signal-to-noise in each scan and remove it accordingly.

RESIDUAL Puts the residual data after subtracting the Gaussian fit from `GAUSS_FIT` into the current scan. Use `PLOT` to display it.

CLEAN Performs a peculiar sort of CLEAN-like algorithm on the current scan. It takes a parameter which is the number of sources to remove - 10 is the default. A diffraction-limited Gaussian is removed from the peak flux density of the scan this number of times, and stored in an alternate memory. Then the residual after all the subtraction is displayed, and this alternative memory stored as the current scan (which is then cleaned in some sense). Use `PLOT` to display it.

AVERAGE Calculates the average data based on the raw data.

COSINE Removes a cosinusoidal-like fit from the data. This is essentially a base-

line removal, but the baseline is a function of the form $A(-1)^i$ where A is a fitted constant and i is the ith bolometer number. Mathematically, the baseline function $B(\imath)$is

$$B_\imath = \begin{cases} -A & \text{if } \imath \text{ is odd,} \\ A & \text{if } \imath \text{ is even,} \end{cases}$$

with the caveat that A can be positive or negative. The option `DOUBLE` will fit a different constant A to the bolometers 1–12 and 13–24. The fundamental cause of this is an even/odd asymmetry in the analog-to-digital conversion in SHARC, which cannot be caused by physical processes (because it is an anticorrelation between pixels, whereas optically there must be a correlation between pixels).

Appendix F: Submillimeter Astrophysics Bible

While some might consider it sacrilegious to use the term above, it behooves me to point out that *no* mention of submillimeter astrophysics *whatsoever* appears in the Bible (James 1611). Therefore I shall take it upon myself to compose, much as the Talmudic scholars in Tiberias on the banks of the Sea of Galilee did these millenia ago, what I consider to be an Explanatory Supplement to the Bible, Submillimeter Astrophysics Volume. Herein I encapsulate all those parameters of our physical universe which I have found useful over the years.

Table 10.1 Planetary data.

Name	Mass (kg)	Radius (m)	Period (yr)	Semimajor (AU)	Eccentricity
Mercury	3.30×10^{23}	2.44×10^{6}	0.24	0.387	0.206
Venus	4.87×10^{24}	6.05×10^{6}	0.62	0.723	0.007
Earth	5.98×10^{24}	6.38×10^{6}	1.00	1.000	0.017
Mars	6.42×10^{23}	3.40×10^{6}	1.88	1.524	0.093
Jupiter	1.90×10^{27}	7.14×10^{7}	11.9	5.205	0.048
Saturn	5.69×10^{26}	6×10^{7}	29.5	9.575	0.053
Uranus	8.66×10^{25}	2.62×10^{7}	84.0	19.30	0.050
Neptune	1.03×10^{26}	2.43×10^{7}	164.8	30.21	0.004
Pluto	1×10^{22}	1.2×10^{6}	247.7	39.91	0.257

The blackbody formulae (B_ν is the brightness, S_ν the flux density for a source subtending $\Omega_{\rm source}$):.

$$B_\nu \equiv \frac{2h\nu^3}{c^2}\frac{1}{e^{h\nu/kT}-1}\ \mathrm{W\ m^{-2}\ Hz^{-1}\ rad^{-2}} \qquad S_\nu \equiv \frac{2h\nu^3\Omega_{\rm s}}{c^2}\frac{1}{e^{h\nu/kT}-1}\ \mathrm{W\ m^{-2}\ Hz^{-1}}$$

Blackbody peaks: 5.1 mm K in frequency units, 2.9 mm K in wavelength units.

Table 10.2 Astrophysical data.

Name	Symbol	Value	Units (SI)
Astronomical unit	AU	1.496×10^{11}	m
Parsec	pc	3.0856×10^{16}	m
Light year	ly	9.4605×10^{15}	m
Solar mass	$M_\odot$	1.989×10^{30}	kg
Solar radius	$R_\odot$	6.953×10^{8}	m
Solar luminosity	$L_\odot$	3.83×10^{26}	W
Solar temperature	$T_\odot$	5780	K
Moon mass	$M_{\rm moon}$	6.7×10^{22}	kg
Moon distance	$D_{\rm moon}$	3.8×10^{8}	m
Moon radius	$R_{\rm moon}$	1.738×10^{6}	m
Flux density	Jy	10^{-26}	W m^{-2} Hz^{-1}

Table 10.3 Emission line transitions.

Name	Transition	Frequency (GHz)	Wavelength (μm)	$E_{\rm lower}$ (K)	$\mu^2 S$ (D^2)
CII	$2p\ ^2P_{3/2} \rightarrow {}^2P_{1/2}$	1900.537	157.7409	0.00	...
NII	$2p^2\ ^3P_1 \rightarrow {}^3P_0$	1460.59	205.1782	0.00	...
H_2		1.420405	211061.3		
CO	$J = 1 \rightarrow 0$	115.2712	2600.7579	0.00	0.012
CO	$J = 2 \rightarrow 1$	230.5380	1300.4038	5.53	0.024
CO	$J = 3 \rightarrow 2$	345.7960	866.9634	16.60	0.036
CO	$J = 4 \rightarrow 3$	461.0408	650.2515	33.19	0.048
CO	$J = 5 \rightarrow 4$	576.2968	520.2310	55.32	0.060
CO	$J = 6 \rightarrow 5$	691.4730	433.5563	82.97	0.072
CO	$J = 7 \rightarrow 6$	806.6518	371.6504	116.16	0.084
CO	$J = 8 \rightarrow 7$	921.7997	325.2252	154.87	0.097
CI	$2p\ ^2P_1 \rightarrow {}^2P_0$	491.1607	609.1353	0.00	...
CI	$2p\ ^2P_2 \rightarrow {}^2P_1$	809.3446	370.4139	23.62	...
H_2O	1 1 0 $\rightarrow$ 1 0 1	556.9360	538.2889	34.23	15.480
H_2O	2 1 1 $\rightarrow$ 2 0 1	752.0332	398.6426	100.84	7.122
H_2O	2 0 2 $\rightarrow$ 1 1 1	987.9268	303.4562	53.43	2.605

Table 10.4 Common interstellar molecules.

Molecule	Common Name	Characteristics
CO	Carbon Monoxide	no electronic angular momentum
H2O	Water	anorganic; asymmetric rotor
NO	Nitrus Oxide	eam
CCH	Ethynyl	linear; eam
HCN	Cyanic Acid	linear; no eam; also HNC
SO	Sulphur Oxide	eam
CH3OH	Methanol	organic; asymmetric rotor
SO2	Sulfur Dioxide	anorganic; asymmetric rotor
HDO	Deuterated Water	anorganic; asymmetric rotor
HCOOCH3	Methyl Formate	organic; asymmetric rotor
OCS	Carbonyl Sulfide	linear; no eam
CH3OCH3	Dimethyl Ether	organic; asymmetric rotor
H2CO	Formaldehyde	organic; asymmetric rotor
CS	Carbon Monosulfide	no eam
SiO	Silicon Monoxide	no eam
CH3CN	Methyl Cyanide	symmetric rotor
C2H5CN	Ethyl Cyanide	organic; asymmetric rotor
HCCCN	Cyanoacetylene	linear; no eam
C2H3CN	Vinyl Cyanide	organic; asymmetric rotor
CH3CCH	Methyl Acetylene	symmetric rotor
HCO+	Formyl Ion	linear; no eam
CN	Cyanogen	eam
H2CS	Thioformaldehyde	organic; asymmetric rotor
HCOOH	Formic Acid	organic; asymmetric rotor
C2H5OH	Ethanol	organic; asymmetric rotor
CH2CO	Ketene	organic; asymmetric rotor, also H2CCO
HNCO	Isocyanic Acid	organic; asymmetric rotor
NH2CHO	Formamide	organic; asymmetric rotor
HCS+		linear; no eam

Table 10.5 Universal constants.

Name	Symbol	Value	Unit (SI)
Speed of light	c	2.99792458×10^{8}	m s^{-1}
Planck constant	h	6.62608×10^{-34}	J s
	$\hbar$	1.054573×10^{-34}	J s
Gravitational constant	G	6.6726×10^{-11}	m^3 kg^{-1} s^{-2}
Electron charge	e	1.60218×10^{-19}	C
Electron volt	eV	1.60218×10^{-19}	J
Electron mass	m_e	9.10939×10^{-31}	kg
Proton mass	m_p	1.67262×10^{-27}	kg
Neutron mass	m_n	1.67493×10^{-27}	kg
Hydrogen mass	m_H	1.6733×10^{-27}	kg
Atomic mass unit	amu	1.66054×10^{-27}	kg
Avogadro's Number	N_A	6.02214×10^{23}	
Boltzmann constant	k	1.38066×10^{-23}	J K^{-1}
Stefan-Boltzmann const.	σ	5.60705×10^{-8}	W m^{-2} K^{-4}
Molar gas constant	R	8.31451	J mol^{-1} K^{-1}
Molar volume	V_m	0.022414	m^3 mol^{-1}
Atmosphere	atm	1.01325×10^{5}	Pa
Standard acceleration	g	9.80665	m s^{-1}
Permeability of Vacuum	μ_0	1.25664×10^{-6}	N A^{-2}
Permittivity of Vacuum	ϵ_0	8.85419×10^{-12}	F m^{-1}
Impedance of Vacuum	Ω_0	376.73	Ω
Planck mass	m_{pl}	2.1767×10^{-8}	kg
Planck length	l_{pl}	1.6161×10^{-35}	m
Planck time	t_{pl}	5.3906×10^{-44}	s
Magnetic flux quantum	Φ_0	2.0678×10^{-15}	Wb
Josephson quotient		483.598	GHz mV^{-1}
Bohr magneton	μ_β	9.2740×10^{-24}	J T^{-2}
Fine structure const.	α	1/137.0360	
Bohr radius	a_0	5.29177×10^{-11}	m
Electron radius	r_e	2.81794×10^{-15}	m
Logarithm base	e	2.718282	
Circle constant	π	3.14159265	
Radian	rad	57.2958	$^\circ$
Steradian	sr	3282.806	$^{\circ 2}$
Year	yr	3.1556925×10^{7}	s
Hunter's ATM constant		206265	$''$ sr^{-1}
Knop's Gravity constant		0.8	

Table 10.6 NATO phonetic alphabet

A -	Alpha	H -	Hotel	O -	Oscar	V -	Victor
B -	Bravo	I -	India	P -	Papa	W -	Whiskey
C -	Charlie	J -	Juliet	Q -	Quebec	X -	X-Ray
D -	Delta	K -	Kilo	R -	Romeo	Y -	Yankee
E -	Echo	L -	Lima	S -	Sierra	Z -	Zulu
F -	Foxtrot	M -	Mike	T -	Tango		
G -	Golf	N -	November	U -	Uniform		

Table 10.7 Order of magnitude prefixes

Magnitude	Prefix
10^{-24}	Yocto-
10^{-21}	Zepto-
10^{-18}	Atto-
10^{-15}	Femto-
10^{-12}	Pico-
10^{-9}	Nano-
10^{-6}	Micro-
10^{-3}	Milli-
10^{-2}	Centi-
10^{-1}	Deci-
10^{+1}	Deca-
10^{+2}	Hecta-
10^{+3}	Kilo-
10^{+6}	Mega-
10^{+9}	Giga-
10^{+12}	Tera-
10^{+15}	Peta-
10^{+18}	Exa-
10^{+21}	Zeta-
10^{+24}	Yotta-

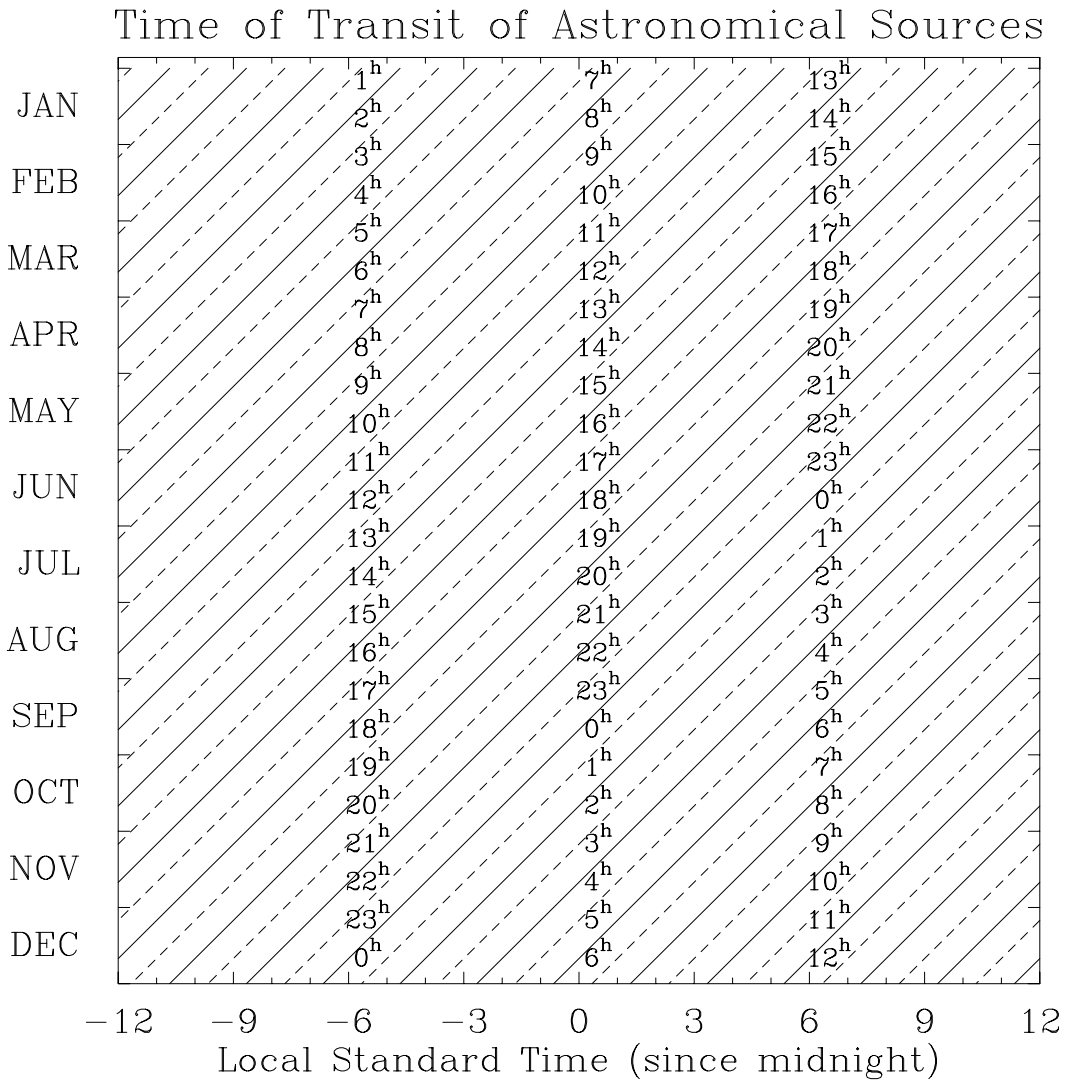

Figure 10.15 Chart illustrating the relationship between local standard time and sidereal time (LST). To find out what Right Ascension is transiting, look up the current local time and the month, then find the line denoting which hour of RA is overhead. This chart was assembled with extreme cleverness by Todd R. Hunter.

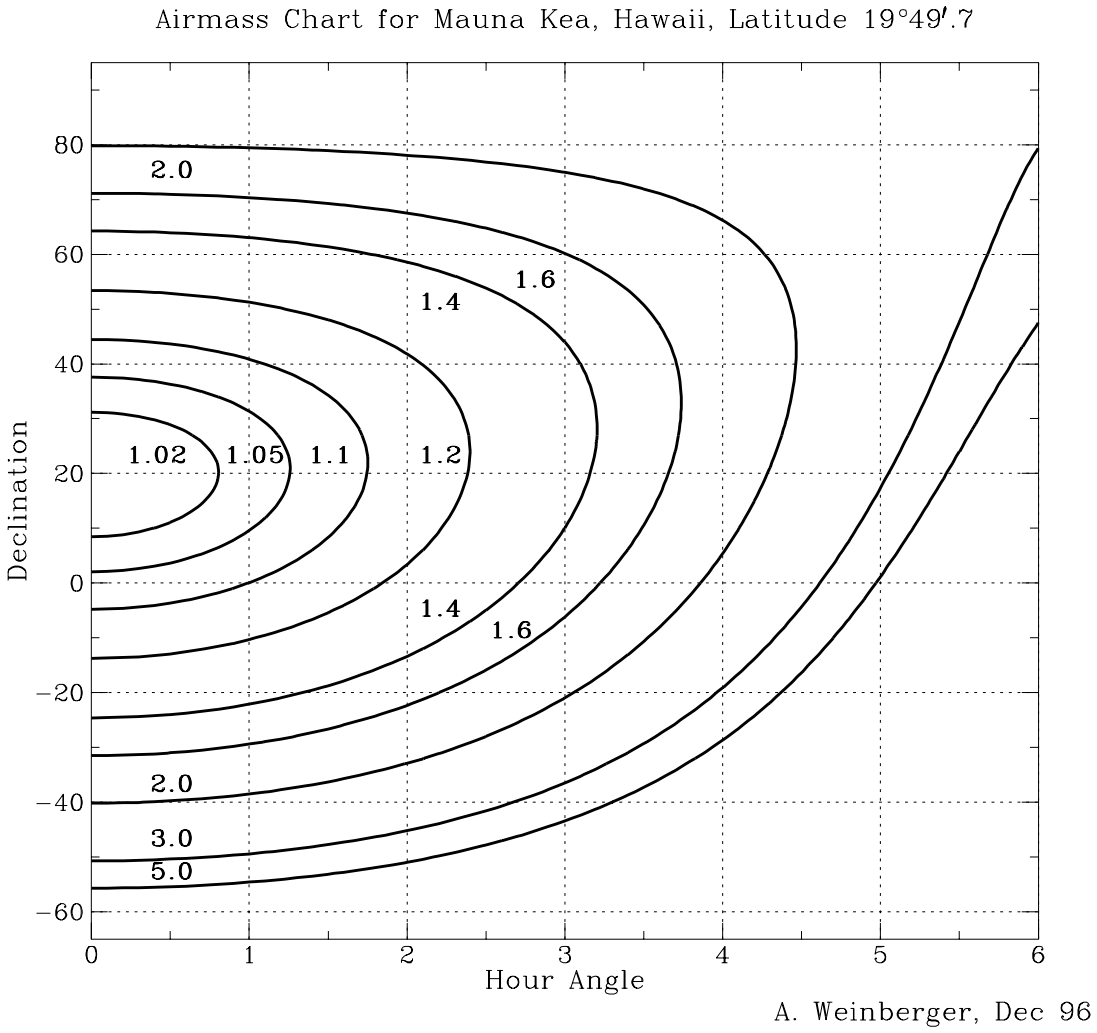

Figure 10.16 Chart illustrating the airmass being looked through when observing a source at a specified Hour Angle and Declination. This chart is appropriate for Mauna Kea Observatory and is provided courtesy of Alycia J. Weinberger.

Appendix F: Quotes from Astronomers

"Zey come out of ze trenches viss ze hands up." - Fritz Zwicky

"Pundits are self-proclaimed experts of dubious credentials." - W.L.W. Sargent

"It's a case of fools rushing in where pundits fear to tread." - W.L.W. Sargent

"Dixitque Deus: fiat lux campusque magneticus." Genesis 1:3 according to Fritz Zwicky

"Nimium opinionum, parum horarum." - E. Sterl Phinney

"Now everybody take a deep breath and say in chorus 'more work is needed."' - Virginia Trimble

"'Aromatic' means 'containing at least one benzene ring' rather than 'smelly"' - Virginia Trimble on PAHs

"No federal funds were diverted to support this curiosity-based research." - F.C. Michel

"ISO is dead? Thank goodness I won't have to reduce any more ISOPHOT data!" - anonymous

"Never observe anything twice." - E. Serabyn

"R.P., T.S., and C.H. made pertinent comments on the manuscript; T.L. made impertinent comments." - Barbara S. Ryden

"Following the precedent set by van der Kruit & Searle, the order of the author's names has been determined by spinning a Moody graphite squash raquet." - Richard J. Rand & James M. Stone

"The Martian rocks all have names, but it is no use remembering them, because, like

cats and Victor Borge's children, they don't come when you call them anyway." - Virginia Trimble & Lucy-Ann McFadden on Pathfinder

"In summary, nothing simple works." - Francesco R. Ferraro et al.

"[IRC+10216 is] the best-studied carbon star in the universe (by humans)." - M.A.T. Groenewegen

"[One of us] once shared nights on the 48-inch Palomar Schmidt telescope with a colleague who kept awake by singing music of the early Polish church." - Virginia Trimble & Lucy-Ann McFadden

"Well, [seeing zero events] is a lot for that experiment." - Maurice Goldhaber

"Ve hef known ziss for thirty years." - Fritz Zwicky

"It is difficult to explain something even when you understand it, and almost impossible when you don't." - Ehrenfest

"Astrophysics... [is] all parts of astronomy that do not require you to recognize the constellations." - Virginia Trimble

"Simulate: to represent with the intent to deceive." - Ned Wright

"Rob, you and I need to get married and start having kids." - Alycia Weinberger

"The problem with L.A. is that the poor people have cars." - Alycia Weinberger

"If this is true, and if they are suns having the same nature as our sun, why do not these suns collectively outdistance our sun in brilliance?" - Kepler, *Conversation with the Starry Messenger*, the original Olber's Paradox.

"A theory has only the alternatives of being right or wrong. A model has the third possibility: it may be right, but irrelevant." - Manfred Eigen, *The Physicist's Conception of Nature*

"Now my own suspicion is that the universe is not only queerer than we suppose, but queerer than we can suppose." - John Haldane, *Possible Worlds and Other Papers*

"Of course, I do not believe in flying saucers; however, I realize that they may exist, whether I believe in them or not." - Peter Sturrock

"The probability of success is difficult to estimate; but if we never search, the chance of success is zero." - Giuseppe Cocconi & Philip Morrison

"Nature gives most of her evidence in answer to the questions we ask her." - C.S. Lewis

"Looking at Orion is like looking at a bowl of porridge and trying to figure out why there is a carrot over here and a bean over there." - Taco

"With increasing distance, our knowledge fades, and fades rapidly. Eventually, we reach the dim boundary – the utmost limits of our telescopes. There, we measure shadows, and we search among ghostly errors of measurement for landmarks that are scarcely more substantial." - Edwin Hubble, *The Realm of the Nebulae*

"To sum up: (1) The cosmos is a gigantic fly-wheel making 10,000 revolutions a minute. (2) Man is a sick fly taking a dizzy ride on it. (3) Religion is the theory that the wheel was designed and set spinning to give him the ride." - Henry Mencken

"Sir, I had no need of that hypothesis." - Pierre Simon de Laplace, responding to Napoleon's query on why Laplace's *Celestial Mechanics* contained no mention of God.

"This is a case when physics is stranger than fiction." - R.B. Laughlin

"This is not that long of a time. I think it's just one age of the universe." - R.B. Laughlin

"This is an experiment only God can do." - R.B. Laughlin

Appendix G: Astérix Novels

These *Bandes Dessinées*, so beloved of the French-speaking world, have helped me (and Trudi!) get through my thesis work. Here is a tribute to René Goscinny & Albert Uderzo, in the French release order.

1. Astérix le Gaulois (Asterix the Gaul)
2. La serpe d'or (Asterix and the Golden Sickle)
3. Astérix et les Goths (Asterix and the Goths)
4. Astérix gladiateur (Asterix the Gladiator)
5. Le tour de Gaule (Asterix and the Banquet)
6. Astérix et Cleopatre (Asterix and Cleopatra)
7. Le combat des chefs (Asterix and The Big Fight)
8. Astérix chez les Bretons (Asterix in Britain)
9. Astérix et les Normands (Asterix and the Normans)
10. Astérix Legionnaire (Asterix the Legionary)
11. Le bouclier arverne (Asterix and the Chieftain's Shield)
12. Astérix aux jeux olympiques (Asterix at the Olympic Games)
13. Astérix et le chaudron (Asterix and the Cauldron)
14. Astérix en Hispanie (Asterix in Spain)
15. La zizanie (Asterix and the Roman Agent)
16. Astérix chex les Helvêtes (Asterix in Switzerland)
17. Le domaine des dieux (The Mansions of the Gods)
18. Les lauriers de César (Asterix and the Laurel Wreath)
19. Le devin (Asterix and the Soothsayer)
20. Astérix en Corse (Asterix in Corsica)
21. Le cadeau de César (Asterix and Caesar's Gift)
22. La grande traversée (Asterix and the Great Crossing)
23. Obelix et compagnie (Obelix and Co.)
24. Astérix chez les Belges (Asterix in Belgium)
25. Le grand Fossé (Asterix and the Great Divide)
26. L'Odyssée d'Astérix (Asterix and the Black Gold)
27. Le Fils d'Astérix (Asterix and Son)
28. Astérix chez Rahâzade (Asterix and the Magic Carpet)
29. La rose et le glaive (Asterix and the Secret Weapon)
30. La galère d'Obélix (Asterix and Obelix all at sea)